Imperial College London
Centre for Doctoral Training in Theory and Simulations of Materials
Department of Materials

# Imaging the breakdown of phonon *quasi*particle theory in MgO and $BaTiO_3$ with atomistic simulations

Gabriele Coiana

THESIS

Submitted in part fulfilment of the requirements for the degree of
Doctor of Philosophy in Materials Science of Imperial College London, January 2023

## Statement of originality

I, Gabriele Coiana, declare that this thesis and the work presented in it is generated as the result of my own original research. When information, data or plots are extracted from other sources, they are appropriately referenced in the text.

## Copyright

The copyright of this thesis rests with the author. Unless otherwise indicated, its contents are licensed under a Creative Commons Attribution-Non Commercial 4.0 International Licence (CC BY-NC).

Under this licence, you may copy and redistribute the material in any medium or format. You may also create and distribute modified versions of the work. This is on the condition that: you credit the author and do not use it, or any derivative works, for a commercial purpose.

When reusing or sharing this work, ensure you make the licence terms clear to others by naming the licence and linking to the licence text. Where a work has been adapted, you should indicate that the work has been changed and describe those changes.

Please seek permission from the copyright holder for uses of this work that are not included in this licence or permitted under UK Copyright Law.

# Abstract

The anharmonic effects in crystals have been commonly studied in the assumption that the phonon-phonon interactions are weak. However, unlike strong electronic interactions, which have been studied for decades, strong phononic interactions have not gained the same attention.

In this thesis, I study phonon-phonon interactions that are so strong that the *quasi*particle picture of the phonons breaks down, and I call this event the melting of phonons. After performing molecular dynamics simulations, I calculate the distribution of kinetic energy in reciprocal spacetime, $\tilde{\mathcal{E}}(\omega, \boldsymbol{k})$, from the Fourier transform in space and time of the atomic velocity-velocity correlation function. This method, which is known but has not been used extensively in the literature, is fully anharmonic and fully non-perturbative, and hence is possibly the only method that allows to compute phonon spectra at extreme conditions of temperature or for very anharmonic materials in any phase they might be, even liquid.

The melting of the phonon bands and its physical consequences are investigated in two oxides, magnesium oxide (MgO) and barium titanate ($BaTiO_3$).

In MgO, the departure from a band structure is progressive, and the quasiparticle picture of the phonons holds until temperatures close to its melting point.

In $BaTiO_3$, band melting happens suddenly in approaching the phase transition temperature. I show that one of the transverse optical (TO) modes of $BaTiO_3$, the Slater mode, melts because its energy is widely spread out both in $\omega$-space and in $\boldsymbol{k}$-space. The broadening in $\omega$-space suggests the presence of a hopping motion of Ti-O atoms between wells of the potential energy surface. The broadening of the Slater mode in $\boldsymbol{k}$-space creates a flat band over an area in reciprocal space, and implies linear correlations of the atomic motions. The results strongly support the conclusion that the phase transitions in $BaTiO_3$ are of the order-disorder type.

## Acknowledgements

I would like to express my deepest gratitude to my supervisors Paul Tangney and Johannes Lischner. Turning an engineer into someone who resembles a physicist is more properly a herculean task than an act of normal supervising. I wish to thank Paul for his patience, constant availability, brilliance, precious lessons he gave me about Science, and for allowing me in his office whenever I needed. I wish to thank Johannes for his brilliant supervising and for the support he gave me throughout these years, especially during the difficult times of the pandemic.

London can be overwhelming sometimes, and it would be were it not for the many friends I have met along the way. First, Giulia, who was a constant presence over these five years. Then Giorgino, Mitso and Katerina. My PhD was sponsored by the EPSRC and was undertaken at the CDT in Theory and Simulation of Materials. I wish to thank Zainab for her precious friendship, Zac, Carlos, Matthew, and all the people in my and other cohorts. Thanks to Chris, Federica, Marta and Victoria for the great time we had together, on and off campus.

I wish to thank my mum, my family and my friends Davide, who encouraged me to embark in the PhD, Gianmarco and Enrica, Giuseppe, Pietro and Filippo. They all have in common that they have never understood what I was doing. And, probably, neither have I.

*A papà, tutto.*

# Contents

**Statement of Originality and Copyright** **i**

**Abstract** **iii**

**Acknowledgements** **iii**

**1 Introduction** **1**

1.1 Motivations and objectives: thermal degradation of the phonon bands and phonon melting . . . . . 1

1.2 The choice of the method: why use classical MD? Beyond-zero-temperature methods . . . . . 5

1.3 Why study the breakdown of phonon theory: possible applications . . . . . 10

1.4 Overview . . . . . 11

**2 Background Theory** **15**

2.1 Introduction . . . . . 15

2.2 The Hamiltonian . . . . . 16

2.3 The harmonic approximation . . . . . 18

2.3.1 Phonon energies and Bose-Einstein distribution . . . . . 20

2.4 The quasi-harmonic approximation . . . . . 21

2.5 Anharmonic terms: phonon-phonon interactions . . . . . 22

2.5.1 The phonon linewidth from perturbation theory . . . . . 24

2.6 Fully non-perturbative method: the velocity-velocity correlation function . . . . 30

2.7 Quasiparticle thermodynamics . . . . . 36

2.7.1 The isobaric heat capacity within the QHA . . . . . 36

2.7.2 The isobaric heat capacity within the QPA . . . . . 36

2.8 The scattering cross section . . . . . 39

2.8.1 The case of fixed atoms . . . . . 39

2.8.2 The case of mobile atoms . . . . . 40

2.9 Simulating infra-red spectra . . . . . 44

2.10 Molecular dynamics . . . . . 47

2.10.1 NVT ensemble . . . . . 48

2.10.2 NPH ensemble . . . . . 52

2.10.3 NPT ensemble . . . . . 56

2.11 The force field . . . . . 56

**3 Progressive breakdown of phonon theory in MgO** **60**

3.1 Introduction . . . . . 60

3.1.1 Motivation for studying MgO . . . . . 60

3.1.2 Experimental literature review . . . . . 61

3.1.3 Gaps in the literature . . . . . 69

3.1.4 Chapter's overview . . . . . 70

3.2 Simulation and calculation details . . . . . 70

3.2.1 MD . . . . . 70

3.2.2 Lattice dynamics . . . . . 72

3.2.3 VVCF and its Fourier transform . . . . . 74

3.3 Sources of imprecision of the force field . . . . . 74

3.4 Results . . . . . 76

3.4.1 Phonon spectra at finite temperatures in the $V(T)$ simulations . . . . . 77

3.4.2 Phonon spectra at finite temperatures in the $V(0)$ simulations . . . . . 81

3.5 The broadening of the LO mode near the $\Gamma$ point . . . . . 83

3.5.1 The conservation of energy and momentum for the LO mode . . . . . 85

3.5.2 Classical view of acoustic-LO coupling . . . . . 89

3.6 The quasiparticle approximation (QPA) . . . . . 94

3.6.1 The phonon quasiparticles as a function of temperature . . . . . 95

3.7 Quasiparticle thermodynamics . . . . . 99

3.7.1 Isobaric heat capacity from quasiparticle thermodynamics . . . . . 102

3.8 Conclusions . . . . . 104

**4 Interlude** **107**

**5 Introduction to $BaTiO_3$** **109**

5.1 Ferroelectricity and ferroelasticity of $BaTiO_3$ . . . 109

5.2 The phases of $BaTiO_3$ . . . 111

5.3 Theories for phase transitions . . . 112

5.3.1 Displacive theory . . . 113

5.3.2 Order-disorder theory . . . 116

5.3.3 Displacive vs order-disorder . . . 120

5.3.4 Spectroscopic evidence of displacive *and/or* order-disorder transition . . 124

5.3.5 Other experimental evidence of displacive *and/or* order-disorder transition 127

5.4 Taxonomy of phonon modes: group theoretical and spectroscopic notation . . . 128

5.5 Applications of $BaTiO_3$ . . . 133

**6 Experimental literature review for $BaTiO_3$** **136**

6.1 Infra-red and THz spectroscopy . . . 137

6.2 X-ray diffuse scattering . . . 143

6.3 Neutron scattering . . . 152

6.3.1 $SrTiO_3$ and other perovskites . . . 154

6.3.2 The early INS dispersion of the Slater mode in $BaTiO_3$ . . . 155

6.3.3 The spectra of the low-frequency excitations away from $\Gamma$ . . . 157

6.4 Local probes: X-ray absorption fine structure (XAFS) . . . 163

6.4.1 The XAFS of $BaTiO_3$ . . . 167

6.5 Local probes: nuclear magnetic resonance (NMR) . . . 172

6.5.1 Summary of experimental results for local probes: NMR vs XAFS . . . . 177

6.6 Electron microscopy . . . . . 180

6.7 Summary of experimental literature . . . . . 181

**7 Sudden melting of the transverse optical Slater phonon in $BaTiO_3$ 189**

7.1 Scope of the chapter . . . . . 189

7.1.1 Overview of this chapter . . . . . 191

7.2 Simulation details . . . . . 191

7.2.1 Force field . . . . . 191

7.2.2 Molecular Dynamics . . . . . 192

7.2.3 Calculation details . . . . . 193

7.3 Simulated phases and accuracy of the force field . . . . . 195

7.4 Results: an overview of the sections . . . . . 201

7.5 IR spectra . . . . . 203

7.6 Diffuse scattering . . . . . 209

7.6.1 Harmonic diffuse scattering . . . . . 211

7.6.2 MD diffuse scattering . . . . . 214

7.7 The melting of the Slater TO . . . . . 219

7.7.1 The Slater TO at $T < T_C$ . . . . . 221

7.7.2 The Slater TO at $T \geq T_C$ . . . . . 229

7.8 Displacements in real spacetime . . . . . 241

7.8.1 The displacements of Ti and O atoms . . . . . 241

7.8.2 The displacement distribution function of the titaniums . . . . . 245

7.8.3 The displacement distribution function of chains and planes of titaniums 248

7.8.4 The local structure of $BaTiO_3$ and the chain dynamics . . . . . 254

7.9 The melting of the Slater TO mode and the loss of correlation . . . . . 256

7.9.1 Cases where the energy is perfectly localized . . . . . 256

7.9.2 Cases where the energy is delocalized . . . . . 258

7.10 Discussion . . . . . 265

7.10.1 The phase transitions from the point of view of a single unit cell . . . . . 265

7.10.2 The phase transitions from the point of view of many unit cells . . . . . 267

7.11 Conclusions . . . . . 270

**8 The physical consequences of the melting of the Slater TO phonon 275**

8.1 Ferroelectricity . . . . . 275

8.1.1 The fit of the Debye mode to a damped harmonic oscillator . . . . . 278

8.1.2 The simulated static dielectric constant . . . . . 279

8.1.3 Ferroelectricity and the chains dynamics . . . . . 282

8.2 Ferroelasticity . . . . . 284

**9 Conclusion 290**

9.1 Summary of thesis achievements . . . . . 290

9.2 Future work . . . . . 293

9.2.1 MgO: phonon sidebands . . . . . 294

9.2.2 $BaTiO_3$: the effect of pressure . . . . . 296

9.2.3 $BaTiO_3$: ferroelasticity and other elastic anomalies. Is the material auxetic? 297

9.2.4 $BaTiO_3$: the thermal conductivity . . . . . 299

9.3 Other avenues of future work . . . . . 300

**A The force field parameters for MgO** **302**

**B The force field parameters for $BaTiO_3$** **303**

**C The relationship between the distribution of kinetic energy and the velocity-velocity correlation function** **304**

**D Planning on a modern neutron scattering experiment** **307**

**E The phonon band structures of $BaTiO_3$** **313**

**F The simulated IR spectra from NVT simulations** **319**

**G The diffuse scattering for $BaTiO_3$ in the HA broken down into modes** **321**

**H The diffuse scattering of $BaTiO_3$ from NPT simulations** **323**

**I The distribution of vibrational energy for $BaTiO_3$ projected onto different eigenvectors** **325**

**Bibliography** **325**

# List of Tables

3.1 Comparison between QHA and MD lattice constants, in Å. The numbers in brackets are the percentage changes in volume with respect to the $T \to 0$ volume. The bigger value of the QHA equilibrium volume is caused by the additional contribution of the zero-point energy, which is absent in classical MD. Note that the QHA overestimates the volumes at all $T$s, but the lattice expansivity (proportional to the numbers in brackets) is smaller than the one predicted by MD, up to temperatures in between 1000-2000 K. . . . . 75

6.1 Features of $S(\boldsymbol{Q})$ and what they imply in the real space distribution of atoms. This table is entirely taken from [76]. . . . . 150

A.1 The force field parameters for MgO in atomic units. . . . . 302

B.1 The force field parameters for $BaTiO_3$ in atomic units. . . . . 303

# List of Figures

2.1 Schematic representation of phonon-phonon scattering events, taken from Dove [38]. Upper row: three-phonon scattering, with one phonon annihilating with another one to create a new phonon (left) and one phonon annihilating to create two phonons (right). Lower row: four-phonon scattering events. All events must conserve energy and momentum. . . . . 24

2.2 Schematic of sum and difference processes, with the conservation of energy and momentum. . . . . 27

3.1 Experimental optical conductivity $\sigma_{\text{exp}}$ of MgO at room $T$, taken from Giura *et al.* [52]. The upper right inset shows their calculated spectrum. The bottom left inset shows the raw reflectivity obtained from the experiment, to which they applied the Kramers-Kronig relations to obtain $\sigma_{\text{exp}}$ [89, 52]. The excess of spectral weight (ESW) is denoted by '*' symbols. . . . . 63

3.2 Reflectivity (left) and optical spectra (right) of a MgO single crystal obtained at various $T$s and $P$s, taken from Calandrini *et al.* [16]. In the right hand side, plots (a) and (c) show the imaginary part of the dielectric function, $\varepsilon_2$ as a function of $T$ and $P$, respectively; these plot contain only TO modes. Plots (e) and (g) show the imaginary inverse loss function, defined as $1/\varepsilon = (\varepsilon_1^2 + \varepsilon_2^2)/\varepsilon_2$, which contains information about LO modes, as a function of $T$ and $P$, respectively; the peaks of these plots correspond to LO modes. The other spectra are theoretical calculations of the similar quantities. The red lines are the result from a Kramer-Kronig analysis, the black lines are Lorentzian fits to the spectra. The excess of spectral weights (ESWs) are denoted by '*' symbols. . . . . 63

3.3 The spectra of the LO mode obtained from IXS, taken from Giura *et al.* [52], obtained for various $\boldsymbol{q}$-points in the {100} and {111} directions of the BZ. The LO is damped near $\Gamma$, it is maximally damped at $\boldsymbol{q} = \frac{3}{10}\boldsymbol{k}_X$ and $\boldsymbol{q} = \frac{3}{10}\boldsymbol{k}_L$, and minimally damped at $X$ and $L$. . . . . 66

3.4 Theoretical results from Giura *et al.* [52]. The variable-width bands in the dispersion plot denote the linewidths of the corresponding phonons. The left panel shows the optical conductivity and the right panel shows the global DOS. The middle 3D plots show the MgO BZ, in which coloured surfaces denote the final state decomposition of the LO phonon at the $\Gamma$ point and at the $\boldsymbol{q}$-point indicated by the dotted arrow. The bottom sketches denote the photon-phonons absorption process which is deemed to produce the ESW and the phonon-phonon scattering which produces the broadening of the LO. . . . . 67

3.5 Distribution of vibrational energy in reciprocal spacetime, $\tilde{\mathcal{E}}(\omega, \boldsymbol{k})$, at a selection of temperatures ($T$) up to and above the melting temperature, $T_m$, computed for MgO after MD at constant pressure. The values of $T$ are approximate, precise values are provided in Sec. 3.2. The blue and white background image is data from the MD simulations using the *ab initio*-parameterized force field: at each $T$, $\tilde{\mathcal{E}}(\omega, \boldsymbol{k})$ was calculated and normalized to one so that the same map between colours and energy density values could be used at each $T$. The image is pixelated, with the width and height of each pixel equal to the resolutions imposed on our simulations by our finite simulation cell size and simulation times, respectively. We also project the full spectrum onto the normal mode eigenvectors calculated at zero temperature, and plot the locations of the quasiparticle peaks as orange symbols in the lower right panel. The red and green symbols on each plot are the phonon frequencies calculated with the force field at zero temperature and using the quasiharmonic approximation, respectively. The frequencies measured by Sangster *et al.* experimentally [106] are plotted with blue squares and the black lines have been calculated by density functional perturbation theory (DFPT) using the quasiharmonic approximation [52]. The side plots at each temperature are plots of $\tilde{\mathcal{E}}(\omega) = \sum_{\boldsymbol{k}} \tilde{\mathcal{E}}(\omega, \boldsymbol{k})$ versus $\omega$, with $\omega$ on the vertical axis. 78

3.6 Distribution of vibrational energy in reciprocal spacetime, $\tilde{\mathcal{E}}(\omega, \boldsymbol{k})$, at a selection of temperatures ($T$) computed for MgO after MD at constant volume. The values of $T$ are approximate, precise values are provided in Sec. 3.2. For further details, see Fig. 3.5. . . . . 82

3.7 The LO spectra at $T = 1000$ K along the $\Gamma - X$ path, showing an anomalously large broadening at $\boldsymbol{k} = \frac{1}{5}\boldsymbol{k}_X$. The experimental spectra can be found in Fig. 2 of Ref. [52]. The LO frequency at $\Gamma$ lacks the additional contribution of the long-range electric field, which is absent in the supercell calculation. . . . . 83

3.8 Two-phonon density of states (TPDOS, on the left) and weighted two-phonon density of states (wTPDOS, on the right) calculated for a reference Γ phonon. Solid lines and broken lines represent summation and difference processes, respectively. On the left, vertical lines are drawn in the correspondence of the TO and LO frequencies, the latter one of which has been augmented after applying the non analytical correction. The height of the vertical lines corresponds to the sum of the contributions of the summation and difference processes at the relevant frequency. The star "*" and double star "**" indicate peaks of the TPDOS where infra-red spectroscopy performed by Giura *et al.* and Calandrini *et al.* found excess of spectral weight [52, 16]. On the right, the evolution of the wTPDOS with increasing temperature is shown, highlighting that the Bose-Einstein prefactors open more and more decay channels as the crystal is heated, and that summation processes happen with greater probability than difference processes. 86

3.9 Results of fitting Lorentzian functions to optical mode spectra at, from left to right, the wavevectors $\frac{1}{5}\boldsymbol{k}_X$, $\boldsymbol{k}_X$, $\frac{1}{5}\boldsymbol{k}_L$ and $\boldsymbol{k}_L$. The upper panels show the phonon frequency shifts versus $T$, obtained through the difference between the fitted Lorentzian's peak frequency and the $T \to 0$ phonon frequency. The lower panels plot the fitted Lorentzians' full widths at half maximum versus $T$ and the leftmost plot includes a comparison to the values measured by Calandrini *et al.* at a much smaller wavevector [16]. The insets specify the meanings of the symbols and their colors in all eight plots. . . . . 95

3.10 Hierarchy of methods for calculating the isobaric heat capacity. Symbols denote experimental values of Ref. [67], the yellow line denotes QHA calculation from Karki *et al.* [71] and the blue line corresponds to the quasiparticle calculation of $C_P^{\mathrm{QP}}$ from Eqs. 2.44-2.43. The broken lines denote $C_V$ computed from the HA through the quantum mechanical formula (in red) and the classical Dulong-Petite law (in green). . . . . 101

5.1 Schematic structure of perovskites, featuring the A and B cations and the X anions. . . . . 110

5.2 2D model ferroelectric-ferroelastic lattice, readapted from Gigli *et al.* [50]. Different atoms are shown with different colors. The left plot shows the cubic cell, which is stable at high $T$, and since it has a center of inversion symmetry, gives a paraelectric phase. The middle plot shows the behaviour of a ferroelectric material as $T$ is lowered: the central atom displaces along the square diagonal, the inversion symmetry is broken and a spontaneous polarization appears. If the material is also ferroelastic, the cubic cell is unstable: as the right plot shows, if we allow to cell change its shape freely (no stress applied), it distorts along the direction of the Ti displacement. . . . . 111

5.3 Schematic of a displacive phase transition, copied from Dove [38], where the soft mode is a BZ center one. Panel a) is a plot of the soft mode frequency as a function of the wavevector, showing the branch softening. Panel b) is the real-space picture showing that the atom in grey is displaced from the centrosymmetrical position when $T < T_C$. Panel c) shows the evolution of the soft mode at the BZ center vs temperature, according to Cochran's law. . . . . 114

5.4 The eight-site model of Comes, Lambert and Guinier, taken from Ref. [25]. The upper panel shows the spatial arrangement of the titaniums: the atoms are displaced in one of the eight equivalent positions along the cube's body diagonal, and they align their displacements on a [010] direction forming chains. The chains are differently polarized: chain 1 is polarized up and chain 2 is polarized down. The middle panel shows an enlarged version of the eight possible orientations of the Ti displacement, and their orientations in the two chains. The lower panel shows the total net polarization of the crystal: this is along [101], because [010] chains and $[0\bar{1}0]$ chains compensate: they average out in space to a net zero polarization along [010]. . . . . 117

5.5 Potential energy as a function of the collective displacement imposed by a macroscopic parameter, in panel (a), and as a function of the displacement of a single atom in panel (b). Panel (a) represents the case of a displacive transition, whereby the potential energy is in the form of a double well at $T < T_C$ and becomes a quadratic potential at $T > T_C$, hence it changes with $T$. The collective motion of the atoms is about a well of the potential energy, hence the atoms displace altogether at $T \to T_C$. Panel (b) is the case of an order-disorder transition. The potential energy surface does not change with $T$, hence in the $T > T_C$ phase the atom hops from one minimum to another. The phase has higher symmetry, on spatial and time average. The figure is taken from Stern and Yacoby [126]. . . . . 119

5.6 Lorentz-like spectrum of a phonon mode with frequency $\omega_{\mathrm{TO}}$ for four values of the damping factor $\Gamma$, taken from Ref. [148]. . . . . 125

5.7 Schematic plot of the temperature dependence of the $F_{1u}$ mode, taken from Luspin *et al.* [82]. The figure shows the splitting of this mode with decreasing the temperature from the C phase. The $F_{1u}$ is triply degenerate in the C phase. In the T phase, characterized by a polarization along an axis [001], the $F_{1u}$ splits into a mode $A_1$ polarized along [001] and two degenerate modes $E$ polarized along [100]-[010]. In the O phase, characterized by a polarization along [011], the $A_1$ mode rotates and is polarized along [011], the $E$ mode further splits into a $B_1$ mode polarized along $[0\bar{1}1]$ and a $B_2$ mode polarized along [100]. In the R phase with polarization along [111], the $A_1$ mode is polarized along [111], and the doubly degenerate $E$ mode are polarized perpendicular to it. The solid lines represent a fit to reflectivity measurements from Luspin *et al.*, but the broken lines were drawn by adjusting data from other perovskites, so the temperature dependence of the frequencies is mainly qualitative. The plot does not account for the LO/TO splitting. . . . . 131

5.8 The eigenvectors of the $F_{1u}$ modes, from Hlinka *et al.* [63]. Panel (a) shows the Slater mode, panel (b) shows the Last mode and panel (c) shows the Axe mode. 132

6.1 Imaginary part of the dielectric function $\varepsilon''(\omega)$ from two IR experiments from Hlinka *et al.* [62] and Luspin *et al.* [82]. The TO modes are labelled according to their spectroscopic names: D=Debye, L=Last, S=Slater and A=Axe. The shaded areas indicate the emergence of the Debye mode. Note the different scales for axes of the two plots: the Debye peak dominates the absorption spectrum at lower temperatures in the C phase. The vertical arrows indicate the undamped Debye frequencies as provided by Luspin *et al*, manifesting the hardening of the mode in the C phase. . . . . 140

6.2 Real and imaginary parts of the low-frequency dielectric function of $BaTiO_3$ in the C phase, taken from Ponomareva *et al.* [100]. The solid and broken lines denote the calculated and experimental spectra, respectively. In the imaginary spectrum, the first peak is the Debye mode, and the authors have claimed that the second small bump at $\approx 90$ cm$^{-1}$ is the Slater mode. . . . . 141

6.3 The X-ray diffuse patterns of $KNbO_3$, from Comes, Lambert and Guinier [26]. The panels (d)-(c)-(b)-(a) show the R-O-T-C phases of $KNbO_3$, which is isomorphous with $BaTiO_3$, respectively. I have added red arrows to point at the most striking features of the patterns. In the R phase, mainly the $\boldsymbol{G}$-points are visible. In the O phase, a set of horizontal $S_O$ appears. In the T phase, two sets of orthogonal $S_O$ appear. In the C phase, the two sets of tetragonal $S_O$ remain, but the background is darker, suggesting there is an additional diffuse *plane* parallel to the plane of the figure. . . . . 145

6.4 The X-ray diffuse scattering of $BaTiO_3$ obtained experimentally at 500 K, readapted from Pasciak *et al.* [94]. Panel (a) shows the reciprocal plane $[hk0]$, and panel (b) shows the reciprocal plane $[hk1.5]$. The latter plane does not show the Bragg peaks because it passes through the $X$ point, and hence allows to see the patterns more clearly. The red arrows point at the $S_A$ and $S_O$. Notice that diffuse streaks are present in both planes, suggesting they are diffuse sheets. . . . . 147

6.5 Neutron scattering spectra (left plot) and dispersion (right plot) of $SrTiO_3$ for the two lowest phonons, taken from Yamada and Shirane [147]. . . . . 154

6.6 Neutron scattering dispersion of $BaTiO_3$ in the $\Gamma - X$ path featuring a soft TO excitation, from Shirane *et al.* [119]. These results were retracted by the same authors four years later in Ref. [56]. . . . . 156

6.7 The low-frequency spectrum of the Slater TO and of the TA in cubic $BaTiO_3$. (a) the neutron scattering spectra, taken from Harada, Axe and Shirane [56], featuring a TO excitation softer than the TA (the black dots represent incoherent scattering and must be subtracted). (b) the spectra from the calculation of this work, obtained after MD, showing that the Slater TO melts and is spread out in $\omega$-space . . . . . 157

6.8 Neutron scattering results for C-$BaTiO_3$, taken from Harada, Axe and Shirane [56] in the $\boldsymbol{q} \sim \langle 110 \rangle$ path in reciprocal space. The left plot shows a const-$\boldsymbol{Q}$ scan, the right plot shows two const-$E$ scans and the central plot shows the proposed dispersion. Note that the authors suggest that the Slater branch (indicated by the physical group theoretical notation $\Sigma_3$) stands at frequencies higher than the acoustic modes. The red lines denote the Slater activity, the blue line indicates the TA mode and the broken lines denote the portions of the dispersion to which the scans correspond. . . . . 160

6.9 The pair correlation function obtained from XAFS for the Pb-O distance in $PbTiO_3$ [126, 122] (left plot) and for the Nb-O distance in $KTaO_3$:9%Nb [126] (right plot). . . . . 166

6.10 XANES spectra of perovskites, taken from Ravel *et al.* [102]. (a) comparison between T-$PbTiO_3$, T-$BaTiO_3$ and C-$EuTiO_3$ at 300 K showing that the pre-edge peak almost disappears in a cubic perovskite. (b) pre-edge peak in T-$PbTiO_3$ for the electric field polarized parallel and perpendicular to the tetragonal axis $c$, showing that the peak disappears in the latter case. (c) pre-edge peak in T-$BaTiO_3$ for the electric field parallel and perpendicular to the tetragonal axis $c$, showing that the peak almost does not change with the orientation of the electric field. This is the best XAFS indication that the T phase (and, by extension, the other phases) is characterized by a local rhombohedral distortion, hence is disordered. (d) temperature evolution of the pre-edge peak of $BaTiO_3$, showing that the distortion is present in all phases. . . . . 169

6.11 Model of T phases of $PbTiO_3$ (a) and of $BaTiO_3$ (b), according to XAFS authors Ravel *et al.* [102]. The T phase of $PbTiO_3$ is ordered, while the T phase of $BaTiO_3$ is disordered. . . . . 170

6.12 NMR spectra of $BaTiO_3$ from Zalar, Laguta and Blinc [150], with $\mathbf{B}||[001]$. a) C phase, with the central transitions of $^{47}$Ti and $^{49}$Ti sitting on a broad background. b) T phase, with well-resolved satellite peaks. The black arrows indicate $^{49}$Ti transitions in [100] or [010] domains, while the grey arrows indicate $^{47}$Ti transitions in [100] or [010] domains or $^{49}$Ti transitions in [001] ferroelectric domains [150]. The presence of a broad background in plot (a) indicates that the Ti atom is locally off-centered. . . . . 175

6.13 Scanning transmission electron microscopy (STEM) of a single-crystal domain within a polycrystalline sample of $BaTiO_3$ from Bencan *et al.* [9]. The left hand side shows the STEM image, and the right hand side shows the Ti vs Ba displacements according to the analysis of the authors. . . . . 180

7.1 The average MD 10×10×10 supercell vectors' lengths and angles. Error bars denote the standard deviations of the same quantities. . . . . 196

7.2 Experimental and simulated dielectric spectra of $BaTiO_3$. On the left is the imaginary part of the dielectric function $\varepsilon''_{zz}(\omega)$, and on the right is the permittivity $\chi''_{xx}(\omega)$ from NPT simulations. Both sides contain dielectric spectra of TO modes near Γ. The left hand plots are, in the bottom, experimental spectra of $A_1$ modes in the T phase from Hlinka *et al.* [62], and in the top, experimental spectra of $F_{1u}$ modes in the C phase from Luspin *et al.* [82]. In right hand plots are the simulated IR spectra, calculated from Eq. 2.61, in the R phase (bottom plot) and C phase (top plot). In the bottom right plot, I shifted the 100 K and 125 K spectra by 40 $cm^{-1}$ and 80 $cm^{-1}$ for visualization purposes. The naming of the modes follows the spectroscopic notations described in Sec. 5.4: D=Debye, L=Last, $S_1$ and $S_2$ are the two non degenerate Slater modes, and $A_1$ and $A_2$ are the two non degenerate Axe modes. The MD peaks are caused by the barostat, and are discussed in the body of the text. The Debye mode is highlighted by shaded areas in the bottom plots. In the simulated R-C transition, the two Slater modes shrink, and a Debye mode emerges. The Debye mode initially manifests as a noisy signal in between the MD and the Last peaks. Then, at $T \gtrsim T_C$ in the C phase, it dominates the spectrum and appears as a narrow peak (critical slowing down). The Debye peak then broadens and hardens, until it overlaps with the Last modes. . . . . 204

7.3 Harmonic calculation of diffuse scattering. Left: pixelated contrast plot. The $\boldsymbol{G}$-points are colored in white, because Bragg scattering has been subtracted. The broken blue line is a guide for the eye to identify the diffuse streaks, which are elongation of the Bragg peaks from the $\boldsymbol{G}$-points along a direction at 45° from the Cartesian axes. The coloured arrows in the bottom show an example of the scattering cross section around $\boldsymbol{G}$ = [-2 -2 0], showing that, for phonons propagating in the direction $\boldsymbol{q}$, the transverse modes having eigenvector $\boldsymbol{\varepsilon}_T$ have a maximum value of the selection rule $\boldsymbol{Q} \cdot \boldsymbol{\varepsilon}$, and hence form the 45° streaks. Right: a contour plot showing the typical butterfly and oval shapes around the $\boldsymbol{G}$ vectors. Mode decomposition of the scattering cross section is available in appendix G. . . . . 212

7.4 The neutron diffuse scattering in the R and C phase simulated from MD in the NVT ensemble. The phase transition is signalled by the additional presence of horizontal and vertical streaks $S_O$, of which [±3k0] and [h±30] are the most pronounced. . . . . 215

7.5 Comparison between the diffuse scattering obtained experimentally at 500 K [94] (left) and from MD at 150 K (right) for the planes (a) $[hk0]$ and (b) $[hk1.5]$. Notice that diffuse streaks are present in both planes, suggesting they are diffuse sheets orthogonal to the plane of the figure. . . . . 217

7.6 The distribution of vibrational energy, $\tilde{\mathcal{E}}(\omega, \boldsymbol{k})$ of $BaTiO_3$ along $\Gamma - X - M - \Gamma - R$ at several temperatures calculated after NPT simulations of a $10 \times 10 \times 10$ cell. In each panel, the right hand side plot is the plot of $\tilde{\mathcal{E}}(\omega) = \sum_{\boldsymbol{k}} \tilde{\mathcal{E}}(\omega, \boldsymbol{k})$. The Slater TO branches chosen in the rhombohedral (R) phase and cubic (C) phase are highlighted in the lower-right panel, which shows the harmonic band structures computed for the R and C unit cell. The red dots denote the harmonic phonon frequencies of the selected Slater branches for comparison with the limit of zero temperature. The upper panels show that in the R phase the Slater mode partially softens, burrows through the Last mode (orange arrow at 50 K), as explained in the text, and cedes its energy to the 0-5 THz range to create a Debye mode (green circles). The middle and lower panels show that the Slater mode forms an anomalous blotch in the C phase, which extends to the whole $\{100\}$ plane in the Brillouin zone. The purple and grey triangles in the $T = 300$ K panel show the HA frequencies of the Last and TA modes, respectively. The presence of white spots whose frequencies coincide with the TA and Last modes suggests mixing with these modes, which is at the heart of the ferroelectric-ferroelastic coupling. . . . . 220

7.7 Phonon spectra at $\boldsymbol{k} = \frac{2}{5}\boldsymbol{q}_X$ in the R-C transition of the model of $BaTiO_3$ obtained from NPT simulations. Each mode is drawn with a different color, as is described in the legend. In the legend, S stands for Slater, L stands for Last, TO and LO stand for transverse optical and longitudinal optical, respectively, and $A^*$ and $A^{**}$ denote the group theoretcial IRREPs of the modes. In the inset is shown the band structure in the harmonic approximation, at the relaxed configuration of the atoms (R phase). The coloring scheme is consistent with the spectra. The vertical dotted lines denote the average positions of the spectra, as explained in the text. Each Slater mode burrows through the Last mode with which it shares the same IRREP. This causes the presence of dips, highlighted by black arrows, in the Slater spectra at frequencies corresponding to the average positions of the Last modes. The more the Slater modes burrow through the Last modes, the more their spectra are sucked up in the 0-5 THz range, and they broaden heavily in this range. At the same time, the Last modes broaden noticeably the more the burrowing occurs, and its average frequency downshifts. 223

7.8 Phonon spectra at $\boldsymbol{k} = \frac{2}{5}\boldsymbol{q}_X$ in the C phase of the model of $BaTiO_3$ obtained from NPT simulations. Each mode is drawn with a different color, as is described in the legend. In the legend, S stands for Slater, and TA and LA stand for transverse acoustic and longitudinal acoustic, respectively, and $A_1$ and $E$ denote the group theoretcial IRREPs of the modes. The peaks denoted 'MD' are due to the fluctuations of the volume caused by the barostat, as explained in Sec. 7.5. In the inset is shown the band structure in the harmonic approximation, with the structure taken as the C phase. The coloring scheme is consistent with the spectra. The vertical dotted lines denote the average positions of the spectra, as explained in the text. The Slater mode is dramatically spread out in frequency, and the mixing with the TAs causes the interference dips indicated by the black arrows. The burrowing of the blotch through the TAs causes a large broadening of the latter modes. Such broadening is very non monotonic: it is large at $T \gtrsim 150$ K and small at $T = 1000$ K. the broadening of the LA mode is small throughout all temperatures. . . . . 230

7.9 Schematic of the different dynamical regimes that occur to a disordered model of $BaTiO_3$ as $T$ is varied. The motion of only *one titanium* (the black bead) in only *one unit cell* is considered. The $x$ axis corresponds to one direction of space. In the top panels the energy surface is plotted against the Ti displacement, and is assumed to have the form of a double well. In the bottom panels, I plot the expected probability distribution of the Ti position. The double arrows $\leftrightarrow$ indicate the scale of the thermal energy, $k_B T$,at each temperature. The figure shows the three different dynamical *regimes* that can happen. At $T_1 \ll T_C$, the motion is purely vibrational about one minimum of the potential. At $T = T_C$, the atom can overcome the barrier by hopping to the other minimum, and the vibrational and hopping motion coexist. At $T \gg T_C$, the motion is effectively a vibration about the center of the cell. The frequency of such vibration is proportional to the curvature of the broken red line. . . . . 232

7.10 $x$ components of the displacements of Ti and O atoms on the plane [$x$ $y$ 0.05] (scaled coordinates) averaged over a 0.5 ps time window, at 50 K in the R ferroelectric phase (a), and at 150 K in the C paraelectric phase (b). The Ti atoms positions averaged over time are denoted with a black dot, and the O atoms positions with a cross. These have been offset for visualization purposes. In the R phase, Ti-O couples are in phase, and the motion is characterized roughly by half of the plane being polarized to the right and half of it to the left, hence it indicates that we are probing a TA mode propagating in the $y$ direction of space. In the C phase, Ti-O are in anti phase: this suggests that the motion is characterized by a Slater eigenvector. The displacements of Ti vs O align to form chains in real space. The polarizations of the chains are uncorrelated with each other. If one chain is positively polarized, the chain above or below it can be polarized either positively or negatively, indifferently. . . . . 242

7.11 Displacement distribution function (DDF) of the Ti atom from MD simulations. The vertical segments denote the averages of the distributions. The DDF broadens progressively with $T$ at $50 < T < 125$ K, but there is a sharp broadening at $T = 150$ K $\approx T_C$. The DDF becomes very flat and asymmetrical at this temperature, and its average shifts a lot. In the top plot, the DDF is less flat. The view in the top plot is enlarged, so that the two plots share the $x$ axis but not the $y$ axis. . . . . 245

7.12 Displacement distribution function (DDF) of one chain (left) and of the whole plane (right) of atoms from MD. The distributions are not normalized. The chain DDF is narrow at $T = 50$ K, and it spreads at $T = 100$ K and $T = 125$ K. At $T = 150$ K, the DDF is sharply double peaked: this suggests that the motion of the centroid of the chains is not a pure oscillation. Increasing $T$, the chain DDF flattens out in the midpoint, signalling that the atomic hopping is increasing. The plane DDF remains roughly Gaussian at all temperatures, meaning that the different polarizations of the chains compensate, and the polarization of a plane is zero at any given time. . . . . 250

7.13 Schematic of the displacement pattern imposed by a mode of wavevector $\boldsymbol{q}$. The wavevector is drawn with a blue arrow, and the black arrows are schematic vectors indicating the direction of the eigenvector $\boldsymbol{e}(\boldsymbol{q})$ of the phonon involved. A TO phonon produces the coherent displacements of atoms belonging to a plane perpendicular to $\boldsymbol{q}$; the correlation in the displacements in parallel planes is modulated by the phase factor $\exp(i\boldsymbol{q}\cdot\boldsymbol{R})$. The transversal correlation of the atomic displacements is infinite: the planes are ordered. . . . . 257

7.14 Schematic of the displacement pattern imposed by a flat band. The narrow rectangle in blue shows the direction $\hat{\boldsymbol{q}}$ (1D structure) of the spread of the energy in reciprocal space. The black arrows are schematic vectors indicating the direction of the eigenvector $\boldsymbol{e}(\boldsymbol{k})$ of the flat band. A flat band induces displacements which are perfectly correlated on *planes* (2D structure) perpendicular to $\hat{\boldsymbol{q}}$. The correlation along $z$ between parallel planes is lost: each plane displaces independently from another. . . . . 259

7.15 Schematic of the displacement pattern imposed by a melted phonon. The rectangle in blue shows the area $A(\boldsymbol{q})$ (2D structure) of the spread of the energy in reciprocal space. The black arrows are schematic vectors indicating the direction of the eigenvector $\boldsymbol{e}(\boldsymbol{k})$ of the melted phonon. A melted phonon induces displacements which are perfectly correlated on *lines* (1D structure) perpendicular to $A(\boldsymbol{q})$. The correlation along $z$ between parallel planes is lost, and the correlation along $y$ between rows of atoms is also lost: each row of atoms along $x$ moves independently from another. . . . . 261

7.16 Schematic of the chain formation in $BaTiO_3$, taken from Senn *et al.* [112]. The upper row shows a view of a supercell, with the arrows representing the polarization of each cell in the bulk of the material. The black and white arrows represent the sum of the polarizations of face-sharing cells, along the Cartesian directions [100], [010] and [001]. There are three sets of chains, each pointing at a different Cartesian direction. In the R phase, each set is made of chains which are polarized all in the same direction, and the phase is ordered. In the O phase, the chains belonging to two sets are equally polarized, and the ones belonging to one set are disordered, meaning that they alternate their polarizations so that their spatial average is zero along one direction. In the T phase, one set is polarized and two sets are disordered, meaning that their averaged polarization is zero. In the C phase, all the three sets are disordered. The lower row shows the calculated diffuse scattering from the static structures indicated by the upper rows. . . . . 268

8.1 The low-frequency part of the susceptibility $\chi''(\omega)$ computed from MD (wiggly dotted lines) and from a fit to damped harmonic oscillators, Eq. 2.63 (solid lines). The vertical arrows indicate the undamped oscillators' frequencies. . . . . 278

8.2 Static dielectric constant as a function of temperature. The orange line is the Curie-Weiss fit. The red vertical line denotes the transition (Curie) temperature $T_C$. The errorbars are computed by means of the standard statistical formulae for the variance of the variance, as in Ref. [50]. Inset: Cochran's law and oscillator fit of the low-frequency spectrum, showing that the evolution of the Debye mode vs $T$ is not consistent with Cochran's law. . . . . 280

8.3 Temperature dependence of the LA and TA frequency shift (upper part) and broadening (lower part), obtained by fitting the phonon spectra to Lorentzian, and computing their peak positions and full width at half maximum at the simulated temperatures. Note the dip in the LA frequency, signalling a softening of the bulk modulus due to the unit cell's change of shape and the very non-monotonic behaviour of the TA broadening. . . . . 287

9.1 Emergence of a "ghost" (G) band in the phonon dispersion of NaBr and MgO. (a) inelastic neutron scattering results for NaBr, at 10 K and 300 K, taken from Ref. [115]; (b) the all-bands result of this work at 300 K for MgO; (c) the spectra projected onto the optical eigenvectors, with the G band being clearly visible; (d) the spectra projected onto the acoustic eigenvectors, with the G band basically disappeared; (e) the temperature evolution of the G band in the high-frequency spectrum of the phonons at the $X$ point, zoomed in so as to see the G band: the G band is very shallow at low temperatures, and its peak softens and gets more structured at higher temperatures. . . . . 295

9.2 Vibrational energy distribution in reciprocal space of the Slater TO phonons of $BaTiO_3$ highlighted in the rightmost panel after NPT simulations at $(T, P) = (50$ K, 0 GPa) and (50 K, 100 GPa). Pressure stabilizes the Slater Ti-O vibrations, making it resemble a phonon. . . . . 297

D.1 The variation of the neutron spectra obtained for a same $\boldsymbol{q}$ point, $\boldsymbol{q} = [0.2, 0, 0]\boldsymbol{a}^*$, around different $\boldsymbol{G}$-points, $\boldsymbol{G} = [0, 2, 2]\boldsymbol{a}^*$ (upper plot) and $\boldsymbol{G} = [1, 2, 2]\boldsymbol{a}^*$ (lower plot). The lines are fit to the experimental data, which is indicated by symbols. The spectra are obtained at two temperatures. Note that the acoustic peak is weaker at $\boldsymbol{Q} = [1.2, 2, 0]\boldsymbol{a}^*$. . . . . 311

E.1 The phonon band structure of $BaTiO_3$ in the HA at mechanical equilibrium. I have highlighted the Slater TO phonon modes near $\Gamma$. . . . . 314

E.2 The Slater TO modes at $\boldsymbol{k} = \frac{1}{5}\boldsymbol{k}_X$ for the R band structure at mechanical equilibrium. The red arrow is the wavevector, and the black arrows represent the eigenvector. . . . . 315

E.3 The phonon band structure of $BaTiO_3$ in the HA for the nominal C band structure with lattice parameter $a = 4$ Å. I have highlighted the optical phonon modes near $\Gamma$ and at $\Gamma$. . . . . 316

E.4 The Slater TO modes at $\boldsymbol{k} = \frac{1}{5}\boldsymbol{k}_X$ for the C band structure. The red arrow is the wavevector, and the black arrows represent the eigenvector. . . . . 317

E.5 The Slater TO modes at $\boldsymbol{k} = \boldsymbol{k}_M$ for the C band structure. The red arrow is the wavevector, and the black arrows represent the eigenvector. . . . . 318

F.1 Imaginary part of the dielectric function $\varepsilon''_{zz}(\omega)$ (left) and permittivity obtained from NVT simulations, $\chi''_{xx}(\omega)$ (right), containing the spectra of polar TO modes near Γ. The left hand side plots are, in the bottom, experimental spectra from Hlinka *et al.* [62] of $A_1$ modes in the T phase, and in the top, $F_{1u}$ modes in the C phase from Luspin *et al.* [82]. In the right hand side are the simulated IR spectra, calculated from Eq. 2.61, in the R phase (bottom plot) and C phase (top plot). In the bottom plot, I shifted the 100 K and 125 K spectra by 40 $cm^{-1}$ and 80 $cm^{-1}$ for visualization purposes. The naming of the modes follows the spectroscopic notations described in Sec. 5.4: D=Debye, L=Last, $S_1$ and $S_2$ are the two non degenerate Slater modes, and $A_1$ and $A_2$ are the two non degenerate Axe modes. This figure can be compared to Fig. 7.2, which shows the NPT results. Note the disappearance of the MD peaks in the NVT simulations. For the rest, the NPT and NVT spectra are similar. The Debye mode is highlighted by shadowed areas in the bottom plots. In the R-C transition, the two Slater modes shrink, and a Debye mode emerges. The Debye mode initially manifests as a noisy signal in the range $0 < f < 180$ $cm^{-1}$, which grows with approaching $T_C$ from below. Then, at $T \gtrsim T_C$ in the C phase, the Debye peak dominates the spectrum and appears as a narrow peak (critical slowing down). It then broadens and hardens, until it overlaps with the Last modes. . . . . 320

G.1 Decomposition of harmonic diffuse scattering into phonon branches. First row: acoustic modes ($TA_1$ $TA_2$ LA). Note that characteristic butterfly and oval shapes caused by the $TA_1$ mode, and compare this with Fig. 7.3. The $TA_1$ contributes maximally to the scattering. Second row: Last modes. Note that higher energy modes contribute much less than acoustic modes. The color scheme is the same for all plots. . . . . 322

H.1 The neutron diffuse scattering in the R and C phase simulated from MD in the NPT ensemble. Note that additional vertical and horizontal streaks appear in both phases, which are caused by the barostat. . . . . 324

I.1 The calculated vibrational energy $\mathcal{E}(\omega, \mathbf{q})$ of $BaTiO_3$ for all modes. The three peaks at low frequencies along $\Gamma - X$ visible at all $T$s are the MD peaks which I find in the IR spectrum of Fig. 7.2 as well, and result from the volume fluctuations caused by the barostat. I highlight with green arrows the partial softening and broadening of the Slater modes in the R-C transition, at 100 K and 125 K. At 150 K, I draw a green circle around $\Gamma - X$ where the melting of the mode is more apparent. Note that there is an evident splitting between $A_1$ or $B_1$ modes and $E$ modes at $\Gamma$ in the R phase, but in the C phase the phonon modes recover their degeneracies at $\Gamma$. Note also that the dispersion becomes broader at higher $T$; one striking feature is that the Slater LO mode, which is the highest frequency mode, becomes very broad at high $T$. . . . . 326

I.2 The calculated vibrational energy $\mathcal{E}(\omega, \mathbf{q})$ of $BaTiO_3$ projected onto the eigenvectors of modes 4,5,6 of the rhombohedral phase, denoted in red in the lower right panel. This set of modes includes the Last modes at $\Gamma$. However, because of the high mixing of the modes away from the BZ center, the modes at $X$ can differ quite a lot from the pure Last modes at $\Gamma$. This is evident if we consider that these three branches contribute to the blotch, as it is apparent from 150 K to 1000 K. In the body of the thesis, in Fig. 7.6, the blotch is contributed maximally by the Slater branch obtained for the C phase. Hence, there is mixing, in the R phase, between Last modes and Slater modes. . . . . 327

I.3 The calculated vibrational energy $\mathcal{E}(\omega, \mathbf{q})$ of $BaTiO_3$ projected onto the eigenvectors of modes 4,5,6,7,8 of the rhombohedral phase, denoted in red in the lower right panel. These modes cover the frequency range 5-10 THz in the spectrum, where the Slater modes lie. The melting of the Slater modes is clearly visible. . 328

I.4 The calculated vibrational energy $\mathcal{E}(\omega, \mathbf{q})$ of $BaTiO_3$ projected onto the eigenvectors of mode 15 (Slater LO) of the rhombohedral phase, denoted in red in the lower right panel. Note that it always stays hard, and broadens a lot with $T$. . . 329

# Chapter 1

# Introduction

In this chapter I introduce the subject of this thesis, explain the reasons for studying it, and outline my objectives. I justify the choice of the methods I have used in Sec. 1.2 and discuss some possible applications in Sec. 1.3. Finally, I present an overview of the thesis in Sec. 1.4.

## 1.1 Motivations and objectives: thermal degradation of the phonon bands and phonon melting

Phonon theory is the theory commonly used to describe lattice vibrations. Being a band theory, it is exact in the limit of zero temperature ($T$), $T \to 0$. In this limit, the lattice vibrations become a set of phonons, namely, a set plane waves with wavevector $\boldsymbol{q}$ and frequency $\omega_{\boldsymbol{q}\nu}$, $\sim \exp[i(\boldsymbol{q} \cdot \boldsymbol{r} - \omega_{\boldsymbol{q}\nu} t)]$, and whose spectrum is $\delta$-function in reciprocal spacetime, $(\omega, \boldsymbol{k})$-space. Then, the distribution in reciprocal spacetime of the vibrational energy, $\tilde{\mathcal{E}}(\omega, \mathbf{k})$, which is the portion of the energy related to the atomic vibrations, and which will be defined formally in Sec. 2.6, is composed of a set of sharp peaks centered at the frequencies $\omega_{\boldsymbol{q}\nu}$ and wavevectors $\boldsymbol{q}$ of the normal modes of vibration, i.e., $\tilde{\mathcal{E}}(\omega, \mathbf{k}) \sim \delta(\mathbf{k} - \boldsymbol{q}, \omega - \omega_{\mathbf{q}\nu})$. The $\delta$-functions which compose the distribution of vibrational energy are defined in the four-dimensional space $(\omega,\boldsymbol{k})$, and form three-dimensional surfaces called *bands*.

The spectrum of each normal mode is a $\delta$-function when $T \to 0$ because the harmonic approximation (HA) applies in this limit: truncating the Taylor expansion of the potential energy about the $T \to 0$ equilibrium structure after the quadratic terms becomes an accurate approximation. The harmonic Hamiltonian can be diagonalized as a set of independent harmonic oscillators that do not interact. When $T$ increases, however, anharmonic terms in the potential expansion are activated and phonons start to interact. If $T$ is finite but not too high, perturbation theory (PT) is accurate, and the spectrum of each phonon acquires a small frequency shift and a small broadening [15]. The rate at which the energy is exchanged between phonons depends on many factors, but it usually increases steadily with $T$. As it does so, phonon band theory becomes less accurate. At sufficiently high temperatures, therefore, phonon theory breaks down as an approximation.

The breakdown of phonon theory is inevitable if one considers that, as $T \to 0$, each phonon becomes a plane wave with a characteristic pattern of atomic displacements (the eigenvector) having periodicities $l_{\boldsymbol{q}} = 2\pi/|\boldsymbol{q}|$ and $t_{\boldsymbol{q}\nu} = 2\pi/\omega_{\boldsymbol{q}\nu}$ in space and time, respectively, and infinite correlation length $\lambda_{\boldsymbol{q}\nu}$ and time $\tau_{\boldsymbol{q}\nu}$. Therefore, it correlates the displacement and velocity of an atom at $\mathbf{R}$ with those of an atom at $\mathbf{R} + \Delta\mathbf{R}$, where $\Delta\mathbf{R}$ is a lattice vector. Similarly, the displacement and velocity of an atom at time $t$ are correlated with its own displacement and velocity at time $t + \Delta t$. In the limit of $T \to 0$, the correlation function is a perfect sinusoid, and the correlation length $\lambda_{\boldsymbol{q}\nu}$ and time $\tau_{\boldsymbol{q}\nu}$ of the wave diverge in this limit. At low finite $T$, due to phonon-phonon interactions, $\lambda_{\boldsymbol{q}\nu}$ and $\tau_{\boldsymbol{q}\nu}$ become finite and the correlation function can be approximated by an exponentially decaying sinusoid. In reciprocal spacetime, the phonon spectral lines broaden, and are no more $\delta$-functions. The broadening of the spectral line of a phonon in $\omega$-space of the amount $\Gamma_{\boldsymbol{q}\nu}$ signifies that the atomic motions lose correlation on a time scale $\tau_{\boldsymbol{q}\nu} = 1/\Gamma_{\boldsymbol{q}\nu}$. Similarly, the broadening of the phonon spectral lines in $\boldsymbol{k}$-space along a certain direction implies a reduction of the correlation length $\lambda_{\boldsymbol{q}\nu}$ in the corresponding direction in real space: the perfect plane wave which correlates the atoms becomes a sinusoid with a decaying amplitude. Just as a wave in a continuous medium (like a free particle in quantum mechanics) becomes a wavepacket when its wavevector acquires a continuous range of values, a lattice vibration whose wavevector is broadened in $\boldsymbol{k}$-space would correspond to an

excitation of the lattice which is spatially localized. Its size is reduced the more the spectrum of the excitation is spread in $\boldsymbol{k}$-space.

When $\lambda_{\boldsymbol{q}\nu}$ and $\tau_{\boldsymbol{q}\nu}$ become finite, the lattice waves lose coherence in space and time. As long as $\lambda_{\boldsymbol{q}\nu}$ and $\tau_{\boldsymbol{q}\nu}$ are big compared to $l_{\boldsymbol{q}}$ and $t_{\boldsymbol{q}\nu}$, the lattice dynamics can still be described with a set of *quasi*phonons which are lattice waves whose spectra have finite widths. They are still sharply peaked at a particular wavevector and a slightly-shifted frequency but a small range of slightly different wavevectors and frequencies contributes to each peak. However, if/when the correlation length (time) of a collective excitation is equal or smaller than $l_{\boldsymbol{q}}$ ($t_{\boldsymbol{q}\nu}$), the atomic motions lose correlation on a length-scale (time-scale) equal or smaller than the length-scale typical of the wave. Then, the oscillation decays faster in space and time than the length- and time- scales of its period, and the phonon ($\boldsymbol{q}\nu$) is no longer a plane wave. The motion becomes critically damped, and the dynamics is effectively not vibrational, but purely relaxational. Phonon theory breaks down in this case: I call this event the melting of phonons.

There are obvious mechanisms for why this would happen, one of which is thermal disorder, especially when $T$ is high. Another one is the presence of defects, which inevitably disrupt the coherence of lattice waves traversing them. Another one is the presence of a very anharmonic potential energy function: this is the case, for example, of a multiple-well potential whereby atoms hop between different minima. This motion cannot be described accurately by PT, and can cause a sudden loss of correlation in space and the melting of a phonon. The thermal disorder and atomic hopping scenarios are the subjects of Ch. 3 and 7, respectively, which are devoted to magnesium oxide (MgO) and barium titanate ($BaTiO_3$).

Band melting occurs at different rates for different materials: we will see that the degradation of the phonon bands in MgO happens progressively as $T$ is raised until it melts, whereas in $BaTiO_3$ it happens suddenly within three ranges of temperatures and each time is associated with a structural phase transition to a different crystalline structure. Band melting also occurs at different rates for different bands of the same material, since the eigenvectors of the bands and their relative frequencies differ. The melting of optical phonons has different implications than the melting of acoustic phonons: we shall see that the melting of a transverse optical

(TO) phonon in $BaTiO_3$ is the origin of a transition to a disordered paraelectric crystalline phase, while the melting of an acoustic mode makes the crystal unstable against displacements along its eigenvectors, which become elastic distortions at very small wavevectors. When all the acoustic bands melt, the crystal is unstable against any elastic deformation, hence it is possible to change its shape without any effort: the crystal has melted.

The picture of band melting as a localization of vibrations in real spacetime holds even in this case: in a liquid, correlations between atoms are very localized in space, i.e., atoms only interact with a few nearby atoms. Any oscillations quickly dissipate or disperse. Hence, the atomic motions have very short correlation lengths and times: $\tau_{\boldsymbol{q}\nu}$ and $\lambda_{\boldsymbol{q}\nu}$ reduce dramatically. Most of the motion is diffusive, rather than vibrational. We shall see in Ch. 3 that the phonons have completely degraded in this case, and do not form band structure.

Just as the band theory of electrons breaks down in the presence of strong electronic correlation, we can view the breakdown of the band theory of the phonons as being caused by strong phononic interactions. However, while strong electronic interactions have been long investigated in the literature, strong phononic interactions which can cause dramatic spread in the phonon line shapes in $\omega$-space and $\boldsymbol{k}$-space have not received the same attention. The motivation for this work is then clear: we want to explore physical conditions in which phonon-phonon interactions are so strong that the quasiparticle theory of the phonons breaks down, and perturbation theory is inaccurate or not applicable. One possible way to do so is to simulate a material at temperatures as high as its melting point; this is what was done for MgO, and is discussed in Ch. 3. Another way is to simulate a material as it undergoes $T$-induced phase transitions to other crystal structures, like $BaTiO_3$, which is the subject of Chs. 5-8.

## 1.2 The choice of the method: why use classical MD? Beyond-zero-temperature methods

In the last section, I discussed the motivation for this work. In this section I clarify the reason why I decided to opt for classical molecular dynamics (MD) combined with the calculation of the Fourier transform of the velocity-velocity correlation function (FT-VVCF) as my primary method of investigation.

### The option of perturbation theory

An obvious way to compute phonon-phonon interactions is via PT. This requires the calculation of the self energy of the phonons, by considering phonon-phonon scattering processes which involve the third- and higher-order terms in the Taylor expansion of the potential energy. The potential derivatives that appear in these higher order terms can be calculated by finite differences or directly within density functional perturbation theory (DFPT) [7]. Since finite differences are quite computationally expensive, only few authors have made use of them [137], while most of the authors opt for DFPT [78, 95, 18, 13]. This is because the implementation of DFPT exploits the "$2n + 1$" theorem, which states that the knowledge of the derivatives of the electronic wavefunction up to order $n$ enables to compute the derivatives of the energy up to order $2n + 1$ [7]. Within DFPT, the first-order perturbation to the wavefunction can be obtained, hence the third-order derivatives of the energy can be computed. However, if quartic terms in the potential expansion are non-negligible, one is necessarily forced to compute them by finite differences of the cubic terms [78, 13], at the expense of a high computational cost.

The reason why I did not choose to use PT, despite its accuracy at low $T$, is its obvious unreliability at conditions of high temperatures or for materials which are just too anharmonic to treat the phonons as *quasi*-independent particles or lattice waves. Perturbation theory is inaccurate in these cases, for multiple reasons. Firstly, PT rests on the assumption that the phonon-phonon interactions are small. Secondly, the number of scattering processes (or, equivalently, the number of Feynman diagrams [15]) to be considered in the calculation would

be too big, and this is computationally very expensive or possibly intractable. Thirdly, it is important to recognize that the perturbational treatment of the phonons enables to compute the broadening of the spectral lines in $\omega$-space, but not the broadening in $\boldsymbol{k}$-space. I.e., the phonon *quasi*particles acquire a linewidth $\Gamma_{\boldsymbol{q}\nu}$, and hence have a finite correlation time $\tau_{\boldsymbol{q}\nu}$, but they still have an infinite correlation length $l_{\boldsymbol{q}}$. This is obviously an approximation that PT inherits from the HA: it is the elementary excitations that interact and their energy broadens, but they remain elementary excitations with a well-defined wavevector $\boldsymbol{q}$.

**The distribution of kinetic energy in reciprocal spacetime, $\tilde{\mathcal{E}}(\omega, \boldsymbol{k})$ and the velocity-velocity correlation function**

The loss of correlation in space and time of the atomic motions can be assessed through the distribution of kinetic energy in reciprocal space, $\tilde{\mathcal{E}}(\omega, \boldsymbol{k})$. This is related to the VVCF by a Fourier transform. In the limit of $T \to 0$, $\tilde{\mathcal{E}}(\omega, \boldsymbol{k})$ becomes the $k_B T$-weighted phonon density of states (DOS). At any finite $T$, $\tilde{\mathcal{E}}(\omega, \boldsymbol{k})$ permits computation of the spread of phonon excitations. Hence, it allows us to reconstruct a band structure at any finite $T$. I defer the discussion of the relationship between the FT-VVCF and $\tilde{\mathcal{E}}(\boldsymbol{k}, \omega)$ to Sec. 2.6. If the kinetic energy of a phonon is localized at a single frequency and wavevector, meaning that $\tilde{\mathcal{E}}(\boldsymbol{k}, \omega) = \delta(\omega - \omega_{\boldsymbol{q}\nu})\delta(\boldsymbol{k} - \boldsymbol{q})$, then it is the kinetic energy of a normal mode $(\boldsymbol{q}\nu)$. This energy is infinitely delocalized in time, because it is a pure oscillation and pure oscillations do not dissipate their energies or disperse, so they last forever, $\sim \exp(i\omega_{\boldsymbol{q}\nu} t)$. The same reasoning can be applied to real $\boldsymbol{r}$- and reciprocal $\boldsymbol{k}$-space: anything localized in $\boldsymbol{k}$-space, say at $\boldsymbol{q}$, is delocalized in real space through the plane wave $\exp(i\boldsymbol{q} \cdot \boldsymbol{r})$, and viceversa, if anything is delocalized in $\boldsymbol{k}$-space then it is localized in real space. The consequence of the spread in reciprocal spacetime is a localization in real spacetime.

It is important at this point to specify what it means that the energy is localized in real spacetime. When I say that an excitation is localized in real space, I mean that almost all of its energy is within some small connected region of the crystal. When I say that an excitation is localized in time I mean that almost all of its energy exists within a small time interval, meaning that it is transient. If an excitation is composed of a wave, then the atomic motions

are very correlated with each other: as phonon theory illustrates, the portion of potential energy that is expressed as a function of a particular collective excitation can be regarded as energy shared by all atoms, therefore the energy is very *de*localized in real spacetime–hence localized in reciprocal spacetime. Therefore, two widely-separated atoms may both share in the same portion of interaction potential energy, despite not interacting with one another directly. Therefore, at higher $T$, the lifetime of each collective motion has shortened and the number of atoms participating in it has reduced. This produces a loss of long-range order in real space for the collective motions of the atoms and so the severe disruption of phonons.

**Classical MD**

To calculate $\tilde{\mathcal{E}}(\omega, \boldsymbol{k})$, I Fourier transform the VVCF after having obtained the atomic trajectories from MD simulations. The strength of this method is that the velocities come from the MD trajectories, which in turn are a computed by numerically solving the equations of motion with the forces acting on each atom obtained from the force field. Hence, this approach is *non*-perturbative, because the forces which produce the atomic motion do not come from a potential function truncation to some order. Hence, this approach includes *all* the terms in the Taylor expnasion of the potential, and virtually all the phonon-phonon scattering processes to all orders are present in the calculation.

An obvious competitor of classical MD is *ab initio* MD. This corresponds to solving Newton's equations but with forces calculated with density functional theory. However, MD is too expensive, when forces are calculated *ab initio*, to compute the phonon spectra at more than a few wavevectors in $\boldsymbol{k}$-space. The total number of wavevectors in the first Brillouin zone (BZ) at which phonon spectra can be calculated in an MD simulation is equal to the number of primitive unit cells being simulated. In *ab initio* MD simulations, this number tends to be $\sim$ 10 [151, 129], and the number of symmetry-inequivalent wavevectors is smaller by a factor of at least two.

On the other hand, when forces acting on the atoms are calculated with computationally-inexpensive empirical force fields, spectra can be calculated at a much larger number of wavevec-

tors, making the resolution of the calculated spectra in ($\omega$,$\boldsymbol{k}$) space high enough to see details of the band structure and to study the $T$-induced degradation of the bands or other important complex processes. However, many empirical force fields are so inaccurate that spectra calculated with them do not compare well with experiment; furthermore, they often lack physical ingredients, such as the response of electrons to changes in local electric fields, that play crucial roles in phonon dynamics. As a result, one can have little confidence that the calculated spectra are even qualitatively correct.

First-principle simulations are very accurate, as they account for electrons quantum mechanically: we shall call this quality *accuracy*. However, a real-world material is macroscopic, including some $\sim 10^{23}$ atoms: hence, to simulate a relevant portion of a material under periodic boundary conditions, a large supercell and a good amount of simulation time is needed: we shall call this quality *precision*. The necessity of large supercells will be evident in Sec. 7.3, where I will discuss the accuracy of the force field for simulating $BaTiO_3$. For many years, very accurate first-principle methods of calculating the phonon broadening, like *ab initio* methods, have existed, and other, less accurate methods that are fast enough to simulate atomic motions with large supercells, and therefore with high resolutions in reciprocal spacetime have existed, but it has not been possible to calculate both *accurate* **and** *highly-resolved* spectra by non-perturbative methods.

This situation has changed in recent years, thanks to advances in both computer hardware and atomistic force fields. Force fields have been developed that strike very useful balances between the accuracy of *ab initio* methods and the precision, or resolution, achievable with simpler and faster force fields [130, 131, 134, 109, 55]. Therefore detailed spectra can now be calculated with an accuracy comparable to DFT.

**Flaws of MD**

Of course, classical MD has its drawbacks. First of all, it pays the price of being a classical method, which neglects the quantum mechanical nature of electrons and of phonon themselves at low $T$. However, the force fields used in the present work have been derived by means of a

fit of energies, forces and stresses to DFT data, hence they are not empirical. Moreover, most of the phenomena we are concerned with in this work happen at either very high temperatures (MgO case) or at temperatures similar to or higher than the material's Debye $T$ ($BaTiO_3$ case). Hence, we can safely exclude that quantum mechanical corrections to the phonon occupation numbers would change my results much in our case studies.

Quantum mechanics is, of course, important: many of the quantities we compute for MgO, like the heat capacity (Sec. 3.7.1), to mention one, are derived from quantum mechanical expressions. In these cases, we can regard our approach as *semi-classical*: phonon frequencies are computed by means of a classical force field, and then they are used to compute thermodynamic functions in quantum mechanical formulae.

This is the flaw discussed in the previous paragraph. There are other flaws that impair an MD simulations, and these are related to the accuracy of the force field used. There are many possible sources of inaccuracy of the force field: the overscreening of the long wavelength electric fields that LO phonons create [109], the use of relatively simple ionic energetics to describe atomic interactions in materials with a degree of covalency [54], the difficulty in modelling the non-isotropic electronic response to the local electric field [130], the problem of the transferability to different phases [43]. All these are general issues, which have material-specific consequences: for example, the overscreening of the LO electric field determines a lower frequency for the LO branch in MgO (Sec. 3.4.1), and the problem of transferability in $BaTiO_3$ is one of the reasons, together with finite size effects, why we can only fully compute two of its phases out of four. Because these consequences are specific to the material which the force field simulates, I dedicate two full sections to assess the accuracy of the two force fields I used, Sec. 3.3 for MgO and Sec. 7.3 for $BaTiO_3$.

The force fields I used in my work were given to me ready for use. They were developed by my principal supervisor (Ref. [130]) and by Fallon (Ref. [43]). I am confident that they are quantitatively or at least qualitatively good. To show this and to assess their accuracy, I compare my results to experiments every time I can, if experimental data is available, and/or to first-principle methods. The impression is that the force fields I used strike a very good

balance between the accuracy of DFT and the precision, or resolution, of empirical force fields.

## 1.3 Why study the breakdown of phonon theory: possible applications

The range of possible applications of the calculation of vibrational spectra at finite $T$, or at very high $T$s, or across-phase-transition $T$s, is vast.

For example, it should help with the development of materials that are either transparent or opaque to THz radiation in a particular frequency window. In the IR and THz range, light is absorbed by an insulator through the excitation of phonons. This is true also for semiconductors, although narrow-band semiconductors, like InSb or HgCdTe, can absorb light in the IR range also through the excitation of electrons. Hence, the absorption spectrum in the IR range is directly dependent on the phonon density of states. So, knowing the frequency distribution of the vibrational energy should help to guide us in the rational design of materials that behave as THz bandpass filters for use as active or passive components of THz devices, which constitute a fast-growing field of technological interest [96, 87].

A second application is in the study of materials at very high $T$, such as thermal barrier coatings, where there are high densities of defects, and therefore high densities of vibrations that are localized in spacetime and delocalized in reciprocal spacetime.

A third application, which is related to the second, is in the identification or design of materials with reduced or enhanced thermal conductivities. For example, thermal conductivities of materials with low-frequency localized rattler modes [21] are low because the energy of these modes, being localized in spacetime, is delocalized in $(\omega,\boldsymbol{k})$-space. Therefore they overlap with acoustic modes in reciprocal spacetime, which allows the acoustic modes to couple with them, and to one another through them, to disperse their energy.

A theoretical application is in the possibility, once the phonon spectra are known, to assess the validity of the harmonic and quasi-harmonic approximations and of perturbation theory

for phonon-phonon interactions. In Ch. 3, we will see that these approaches breakdown for MgO at $T > 1000$ K, and for $BaTiO_3$ they cannot be applied at all, since the phonon mode involved in the phase transitions gives imaginary frequencies in the cubic phase. If, and only if, the phonons can be treated as quasiparticles, then thermodynamic state functions can be evaluated by means of the phonon quasiparticle frequencies. This approach, which is called "quasiparticle thermodynamics" [2], overcomes the problems encountered at high $T$ by other perturbational treatments, like the quasi-harmonic approximation. It is important to note, however, that the quasiparticle approximation (QPA) fails when $T$ is high enough.

Another theoretical application is in the study of order-disorder transitions between crystalline phases: this is the case of $BaTiO_3$ and other perovskites of a similar experimental behaviour. These occur when a single phonon band melts but the other bands do not, causing displacements and velocities along the eigenvectors of the melted band to become disordered. This critical weakening of correlations causes both the time average and the spatial average of the displacements to vanish. As a result, when the crystal is observed at either a low spatial resolution or a low temporal resolution, its symmetry appears to have increased. The ability to see how the vibrational spectrum changes as $T$ crosses the transition temperature may lead to step changes in our understandings of these transitions, or even to a step change in our understanding of this class of transitions.

## 1.4 Overview

The focus of the thesis is phonon band melting. This thesis is organized as follows.

#### Short overview

In brief, the thesis can be roughly subdivided into three parts: one dedicated to the theory and methods, one dedicated to MgO and one dedicated to $BaTiO_3$. Ch. 2 is concerned with the theoretical background and the methods used, Ch. 3 is concerned with MgO, Ch. 4 is an interlude and Chs. 5-8 are concerned with $BaTiO_3$. I close with final remarks in Ch. 9.

**Extended overview**

In Ch. 2 I present the theory which this thesis is based on. I discuss a hierarchy of methods for calculating phonon spectra: the harmonic approximation (Sec. 2.3), some highlights of the quasi-harmonic approximation (Sec. 2.4), some elements of perturbation theory (Sec. 2.5), and the fully non-perturbative method, which is the chief method I use in this work, the velocity-velocity correlation function (Sec. 2.6). I then discuss quasiparticle thermodynamics in Sec. 2.7, and derive a formula to calculate the isobaric heat capacity by means of the phonon quasiparticle frequencies. In Secs. 2.8 and 2.9 I discuss the quantities which neutron diffuse scattering and infra-red spectroscopy probe, respectively, and how to simulate these two types of experiments from MD. The second part of Ch. 2 focuses on the method I used to simulate the atomic trajectories, which is molecular dynamics. In Sec. 2.10 I briefly describe MD and the theoretical/numerical devices to simulate different ensembles, namely thermostats and barostats, and in Sec. 2.11 I describe the functional form of the force fields for MgO and $BaTiO_3$.

I then dedicate one chapter to MgO and two chapters to $BaTiO_3$.

In the MgO chapter, the first section, Sec. 3.1, is used to introduce the subject. I motivate the choice of this material in Sec. 3.1.1, introduce some important recent experimental and theoretical findings and point out why a non-perturbative approach is needed in Sec. 3.1.2. Sec. 3.2 collects the details of the simulations and calculations. Sec. 3.3 is used to assess the accuracy of the force field employed for MgO. The progressive melting of the phonon bands is presented for the first time in Sec. 3.4, where the distribution of the kinetic energy $\tilde{\mathcal{E}}(\boldsymbol{k}, \omega)$ is plotted as a function of $T$. A discussion of the broadening of the phonons' spectral lines is outlined, and one specific feature of the spectra, namely the anomalous broadening of the LO mode, is described in detail in Sec. 3.5. The validity of the *quasi*particle picture of the phonons is then quantitatively assessed in Sec. 3.6, and the concept of *quasi*particle thermodynamics is exploited in Sec. 3.7 to compute the anharmonic isobaric heat capacity, and to demonstrate that the quasiparticle picture holds well until temperatures close to the melting point.

The Interlude, Ch. 4, is used to draw a bridge between the two cases: MgO, where band melting occurs progressively as $T$ is raised to the melting point, and $BaTiO_3$, where band melting occurs suddenly at the temperatures of its structural phase transitions.

In the first chapter on $BaTiO_3$, Ch. 5, I introduce the material in Sec. 5.1, and its crystalline phases in Sec. 5.2. I review the main theories for the phase transitions, the displacive and the order-disorder one, in Sec. 5.3. I then briefly explain the taxonomy of the phonon modes for $BaTiO_3$ in Sec. 5.4. The rest of the chapter, Sec. 5.5, is devoted to outline some applications of $BaTiO_3$.

The second chapter of $BaTiO_3$, Ch. 6, is a literature review of the experiments which have been performed from the late 1960'es to the present. I review results of infra-red and THz spectroscopy in Sec. 6.1, X-ray diffuse scattering in Sec. 6.2 and neutron scattering in Sec. 6.3. I then discuss local probes, namely X-ray absorption fine structure and nuclear magnetic resonance in Secs. 6.4 and 6.5, respectively, and electron microscopy in Sec. 6.6. I then summarize the experimental findings in Sec. 6.7.

The third chapter on $BaTiO_3$, Ch. 7, focuses on the results of my simulations. I show that a particular phonon mode, the Slater mode, melts during a phase transition. Sec. 7.2 outlines the simulation and calculation details. The phases that the force field is able to reproduce and its accuracy are discussed in Sec. 7.3. The results are introduced in Sec. 7.4, where I suggest that Secs. 7.5-7.7, in which my results are reported, can be read alongside the experimental results discussed in the corresponding Secs. 6.1-6.3. Whenever I can, I plot the experimental results in the same figure of my calculated results, to facilitate the comparison. In Sec. 7.5 I discuss the simulated IR spectra, and in Sec. 7.6 the simulated neutron scattering patterns. Sec. 7.7 is possibly the most important one of this thesis: it contains the distribution of vibrational energy in reciprocal spacetime, $\tilde{\mathcal{E}}(\boldsymbol{k}, \omega)$, of the optical phonon which melts across the temperature of the phase transition. I hint what it means that this phonon melts by proposing a simple model for the motion of the Ti within one unit cell. In Sec. 7.8, I present the real spacetime picture by showing the displacements of the Ti atoms from the MD trajectories. This reveals what kind of correlations the atoms have in real space, and prepares for the next section. In Sec. 7.9, I explain

theoretically what I mean by phonon band melting, and this should complete the understanding. The results sections are followed by Sec. 7.10, where the mechanism underpinning the phase transitions is discussed, mostly qualitatively. Sec. 7.11 wraps everything up.

The physical consequences of the microscopic understanding just developed in terms of the multiferroicity of $BaTiO_3$ are then presented in Ch. 8. In Sec. 8.1 I discuss ferroelectricity, and in Sec. 8.2 I discuss ferroelasticity.

Ch. 9, which is the final chapter, summarizes the thesis achievements and points out some possible roads for future work in Sec. 9.2, where I highlight some of the unanswered questions on MgO and $BaTiO_3$, or phenomena which I could not understand, and possible ways in which the present work can be expanded in the future.

# Chapter 2

# Background Theory

## 2.1 Introduction

In this chapter, I introduce the main background theory of this thesis.

In the first part of the chapter, I present a hierarchy of methods for calculating phonon bands, starting from the least accurate at finite $T$ and finishing with the most general formula, which is valid at any $T$ and in any phase the material might be in. The hierarchy includes the harmonic approximation (HA), the quasi-harmonic approximation (QHA), perturbation theory (PT) and the quasiparticle approximation (QPA), and finally the non-perturbative method which composes the main results of this work: the Fourier transform of the velocity-velocity correlation function (FT-VVCF). In the second part of the chapter, I focus on the quantities probed by X-ray/neutron scattering and IR spectroscopy. In the third part of the chapter, I discuss molecular dynamics (MD).

I start with the reference Hamiltonian, in Sec. 2.2. Then I present theories which assume that phonons do not interact: the HA in Sec. 2.3 and the QHA in Sec. 2.4. Anharmonicity is introduced in Sec. 2.5. The way linewidths are calculated to lowest order in perturbation theory, which assumes weak interactions between the phonons, is the subject of Sec. 2.5.1. The chief method which I use in this thesis, which is the FT-VVCF and is fully non-perturbative,

is discussed in Sec. 2.6. Quasiparticle thermodynamics, which is a method to calculate thermodynamic state functions in the assumption that the phonons are quasiparticles, is presented in Sec. 2.7. The scattering cross section, which is the quantity probed by neutron and X-ray scattering, is discussed in Sec. 2.8, and the dielectric function, which is the quantity probed by infra-red spectroscopy, is presented in Sec. 2.9. Molecular dynamics and its extension to different ensembles with algorithmic devices, like thermostats and barostats, are discussed in Sec. 2.10. Finally, the force field used in this work is described in Sec. 2.11.

## 2.2 The Hamiltonian

Let us consider the bulk of a crystal in three-dimensional space. I will use the term crystal to refer to the bulk of it, because we shall assume periodic boundary conditions throughout this section, so that we can avoid surface effects and consider quantities as a function of the *relative* positions of the atoms. At mechanical equilibrium, the crystal can be partitioned into unit cells whose origins are the lattice points $\mathbf{R}_l$; each unit cell is composed of a number $n_a$ of atoms placed at $\mathbf{R}_{jl} = \mathbf{R}_l + \boldsymbol{\tau}_j$, for a total of $N$ atoms. I denote the positions $\mathbf{R}_{jl}$ *equilibrium positions*. The lattice potential energy is

$$U_0 = U(\mathbf{R}_{j_1 l_1}, \mathbf{R}_{j_2 l_1}, \dots, \mathbf{R}_{j_n l_m}, \dots) = U(\mathbf{R}_1, \mathbf{R}_2, \mathbf{R}_3, \dots) \tag{2.1}$$

where the numeral subscripts are a shorthand for $jl$. In the assumption of pairwise interactions, $U_0 = \frac{1}{2}\sum_{jj',ll'} \phi(\mathbf{R}_{jl} - \mathbf{R}_{j'l'})$ [4], where $\phi(\mathbf{R}_{jl} - \mathbf{R}_{j'l'})$ is the potential energy of the interaction between an atom at $jl$ and an atom at $j'l'$. However, we shall not make this simplistic assumption and use the general form of the potential expressed in Eq. 2.1, which may encompass many-body contributions. This function is minimized at mechanical equilibrium, hence its gradient $\nabla = [\frac{\partial}{\partial \mathbf{R}_1}, \frac{\partial}{\partial \mathbf{R}_2}, \frac{\partial}{\partial \mathbf{R}_3}, \dots]^T$, which is the negative of the forces acting on the atoms, vanishes at $T \to 0$. Let us now consider the case of finite $T$: I denote the position of an atom away from equilibrium as $\boldsymbol{r}_{jl} = \mathbf{R}_{jl} + \boldsymbol{u}_{jl}$, where $\boldsymbol{u}_{jl}$ is the displacement. Then the lattice energy becomes

[4]

$$U = U(\mathbf{r}_{j_1 l_1}, \mathbf{r}_{j_2 l_1}, \ldots, \mathbf{r}_{j_n l_m}, \ldots) = U(\mathbf{r}_1, \mathbf{r}_2, \mathbf{r}_3, \ldots). \tag{2.2}$$

In the hypothesis of small displacements, each term in Eq. 2.2 can be Taylor expanded about $\mathbf{R}_{jl}$, obtaining [4, 38, 15]

$$U = U_0 + \sum_{n \geq 2} \frac{1}{n!} \sum_{\substack{j_1 \ldots j_n \\ \alpha_1 \ldots \alpha_n \\ l_1 \ldots l_n}} \Phi_{\alpha_1 \ldots \alpha_n}(\mathbf{R}_{j_1 l_1}, \ldots, \mathbf{R}_{j_n l_n}) u_{\alpha_1}(\mathbf{R}_{j_1 l_1}) \ldots u_{\alpha_n}(\mathbf{R}_{j_n l_n}). \tag{2.3}$$

Here, $U_0$ is the equilibrium potential energy of the static lattice (excluding the zero-point energy) defined in Eq. 2.1, $u_\alpha(\mathbf{R}_{j_1 l_1})$ denotes the Cartesian component $\alpha$ of the displacement of atom $jl$, and the tensors $\Phi$s are the derivatives of the potential function with respect to atomic displacements, i.e., $\Phi_{\alpha_1 \ldots \alpha_n}(\mathbf{R}_{j_1 l_1}, \ldots, \mathbf{R}_{j_n l_n}) = \frac{\partial^n U}{\partial u_{\alpha_1}(\mathbf{R}_{j_1 l_1}) \ldots \partial u_{\alpha n}(\mathbf{R}_{j_n l_n})}\big|_{\text{eq}}$, calculated at equilibrium. The first-order terms in the expansion, $\frac{\partial U}{\partial u_{\alpha_1}(\mathbf{R}_{j_1 l_1})}$, vanish because they correspond to minus the forces acting on each atom, which vanish at equilibrium. The sum in $j$ and $l$ runs over all atoms in all lattice points, respectively.

The Hamiltonian is then composed of the usual expression for the atomic kinetic energy and a sum of terms which depend on the order $n$ at which the Taylor expansion is truncated. Denoting the momentum and mass of atom $i$ by $\boldsymbol{p}_i$ and $m_i$, respectively, the Hamiltonian is

$$\mathcal{H} = U_0 + \mathcal{K} + U_2 + U_3 + U_4 + \cdots = U_0 + \mathcal{H}_{\text{harm}} + U_3 + U_4 + \ldots, \tag{2.4}$$

where $\mathcal{K} = \sum_i \frac{|\boldsymbol{p}_i|^2}{2m_i}$ is the kinetic energy, $\mathcal{H}_{\text{harm}} = \mathcal{K} + U_2$ is the *harmonic* term, and $U_3$, $U_4$, and so on are the cubic and quartic *anharmonic* terms.

## 2.3 The harmonic approximation

The harmonic approximation is based on the truncation of the Taylor expansion for the potential energy in Eq. 2.3 to second order ($n = 2$). Hence,

$$\mathcal{H}_{\text{harm}} = \mathcal{K} + U_2 \tag{2.5}$$

.

From now on, I will use the shorthand $jl$ to indicate that a quantity refers to atom $j$ in the primitive cell $l$. For example, the displacement of an atom which at equilbrium is placed at $\mathbf{R}_{jl}$ is $u_\alpha(jl) \equiv u_\alpha(\mathbf{R}_{jl})$. Within the HA approximation, the equations of motion become

$$m_j \ddot{u}_\alpha(jl,t) = -\sum_{j'l'\beta} \frac{\partial^2 U}{\partial u_\alpha(jl)\partial u_\beta(j'l')} u_\beta(j'l'). \tag{2.6}$$

The equations of motion in 2.6 are very coupled, in the sense that the motion of atom $jl$ depends on the interaction with all the other atoms $j'l'$. However, the equations can be decoupled if we seek solutions of the form [38]

$$\boldsymbol{u}(jl,t) = \frac{1}{\sqrt{N_c m_j}} \sum_{\mathbf{q}\nu} \mathbf{e}(\mathbf{q}\nu, j) Q(\mathbf{q}\nu) e^{i(\boldsymbol{q}\cdot\boldsymbol{R}_{jl} - \omega_{\mathbf{q}\nu} t)}. \tag{2.7}$$

Here $N_c$ is the number of unit cells in the crystal, $m_j$ is the mass of atom $j$, $\mathbf{q}$ is the wave vector, $\nu$ runs over the modes' branches, $\mathbf{e}(\mathbf{q}\nu, j)$ is the eigenvector of atom $j$ in mode $\mathbf{q}\nu$, and $Q(\mathbf{q}\nu, t)$ is a complex quantity called phonon coordinate or mode amplitude. The sum runs over the $D \times N$ degrees of freedom, where $D$ is the dimensionality, which for us is always 3, since we work in a three-dimensional space.

**The dynamical matrix**

Eq. 2.7 is the plane waves decomposition of the atomic motion. Inserting Eq. 2.7 into 2.5 gives the eigenvalue problem

$$\boldsymbol{D}(\mathbf{q}) \cdot \mathbf{e}(\mathbf{q}\nu) = \omega^2_{\mathbf{q}\nu}\mathbf{e}(\mathbf{q}\nu), \tag{2.8}$$

where $\boldsymbol{D}(\mathbf{q})$ is a $3n_a \times 3n_a$ matrix called dynamical matrix. Each $3 \times 3$ sub-matrix which composes the dynamical matrix is

$$D_{\alpha\beta}(\mathbf{q}, jj') = \frac{1}{(m_j m_{j'})^{1/2}} \sum_{l'} \Phi_{\alpha\beta}(\mathbf{R}_{j0} - \mathbf{R}_{j'l'}) \exp(i\mathbf{q} \cdot [\mathbf{R}_{j'l'} - \mathbf{R}_{j0}]). \tag{2.9}$$

Written in this form, it is clear that the dynamical matrix is the lattice Fourier transform of the tensor $\Phi_{\alpha\beta}(\mathbf{R}_{j0} - \mathbf{R}_{j'l'})$. The components of $\Phi_{\alpha\beta}(\mathbf{R}_{j0} - \mathbf{R}_{j'l'})$ are called interatomic force constants. Each force constant is the derivative of the force acting on atom $j'l'$, $\boldsymbol{F}(j'l')$, with respect to the displacement of an atom $j0$. Hence, the interatomic force constants are

$$\Phi_{\alpha\beta}(\mathbf{R}_{j0} - \mathbf{R}_{j'l'}) \equiv \Phi_{\alpha\beta}(j0, j'l') = -\left.\frac{\partial F_\beta(j'l')}{\partial u_\alpha(j0)}\right|_{\text{eq}}. \tag{2.10}$$

In my work, when calculating the dynamical matrix explicitly, I approximated the interatomic force constants by finite differences. To do this, I displaced atom $j0$ slightly from equilibrium by the amount $\Delta u_\alpha(j0) = a_\alpha(j0)$, and calculated

$$\Phi_{\alpha\beta}(j0, j'l') \approx -\frac{\Delta F_\beta(j'l')}{\Delta u_\alpha(j0)} = -\frac{F_\beta(j'l')}{a_\alpha(j0)}. \tag{2.11}$$

In the numerator of the last equation, the value of the force acting on atom $j'l'$ when atom $j0$ is not displaced vanishes, because forces on atoms vanish at equilbrium. The dynamical matrix was then computed by means of Eq. 2.9, and the harmonic phonon frequencies $\omega_{\mathbf{q}\nu}$ and eigenvectors $\mathbf{e}(\boldsymbol{q}\nu)$ were calculated by diagonalizing it numerically. This is the standard method for calculating vibrational spectra in the low $T$ limit, since interactions between phonons vanish in this limit.

### 2.3.1 Phonon energies and Bose-Einstein distribution

Eq. 2.7 is the phononic assumption of atoms moving in the form of plane waves, which is exact only when $T \to 0$. In this limit, the Hamiltonian becomes [38, 132]

$$\mathcal{H}_{\text{harm}} = \frac{1}{2}\sum_{\mathbf{q}\nu} |P(\mathbf{q}\nu)|^2 + \frac{1}{2}\sum_{\mathbf{q}\nu} \omega_{\mathbf{q}\nu}^2 |Q(\mathbf{q}\nu)|^2, \tag{2.12}$$

where $P(\mathbf{q}\nu) = \dot{Q}^*(\mathbf{q}\nu) = \dot{Q}(-\boldsymbol{q}\nu)$ [132] is a complex quantity denoted phonon momentum, and is the conjugate time derivative of the mode amplitude $Q(\mathbf{q}\nu)$ defined previously. The first and second terms are the kinetic and the potential terms, and the sums run over the number of $\boldsymbol{q}$-points, which equals the number of unit cells $N_c$, and over the number of modes $\nu$, which is $3n_a$. In total, the sum runs over $3N_c n_a = 3N$ momenta and amplitudes. From Eq. 2.12, it is apparent that the Hamiltonian is a collection of $3N$ *independent* harmonic oscillators.

The quantum mechanical expressions for the Hamiltonian are identical to Eq. 2.12, but with the phonon momentum and coordinate *operators*. See for example Dove [38] for further details.

The energy of each non-interacting oscillator in quantized form is [38]:

$$E_{\mathbf{q}\nu} = \hbar\omega_{\mathbf{q}\nu}\left(\frac{1}{2} + n_{\mathbf{q}\nu}\right), \tag{2.13}$$

where $n_{\mathbf{q}\nu}$ is an integer quantum number representing the state of the oscillator. At thermal equilibrium in the canonical ensemble, relevant for the phonons, the expectation value of the energy can be expressed as

$$\langle E_{\mathbf{q}\nu}\rangle = \hbar\omega_{\mathbf{q}\nu}\left(\frac{1}{2} + \bar{n}_{\mathbf{q}\nu}\right), \tag{2.14}$$

where $\bar{n}_{\mathbf{q}\nu}$ is the mean occupation number of phonon $\mathbf{q}\nu$, expressed by the Bose-Einstein distribution

$$\bar{n}_{\mathbf{q}\nu} = \frac{1}{e^{\beta\hbar\omega_{\mathbf{q}\nu}} - 1}, \tag{2.15}$$

where $\beta = 1/(k_B T)$ and $k_B$ is the Boltzmann constant. Eq. 2.15 is the average number of particles which can be found at the microstate's energy $\varepsilon_j = \hbar\omega_{\mathbf{q}\nu}$ in the assumption that the

particles are bosons and that there is an infinite number of them [17].

In the classical limit of the spacing between energy levels being much smaller than the thermal energy, $\hbar\omega_{\mathbf{q}\nu} \ll k_B T$, the Bose-Einstein distribution becomes

$$\bar{n}^{\mathrm{CL}}_{\mathbf{q}\nu} = \frac{k_B T}{\hbar\omega_{\mathbf{q}\nu}}, \tag{2.16}$$

and the average energy of each oscillator is

$$\langle E_{\mathbf{q}\nu} \rangle \overset{CL}{\sim} k_B T. \tag{2.17}$$

Making the approximation that the Hamiltonian is a sum of independent harmonic oscillators $\{(\mathbf{q}\nu)\}$ is tantamount to assuming that there is no interaction between modes/phonons. For this reason, the HA becomes exact in the $T \to 0$ limit, but phonons interact to some degree at any finite $T$ and the strengths of their interactions increase with $T$.

## 2.4 The quasi-harmonic approximation

One of the most important ways in which the vibrational spectra of materials change with temperature is via thermal expansion, which usually weakens bonds by lengthening them, thereby reducing the phonon frequencies. This effect is often modelled using the so-called *quasi-harmonic approximation* (QHA). In the QHA, the phonon frequencies are calculated at a range of volumes and used to evaluate the Gibbs free energy $G(T, P) = \langle U \rangle - T\langle S \rangle + P\langle V \rangle$, where $\langle S \rangle$ is the entropy, $P$ is the pressure and $\langle V \rangle$ is the average volume [71, 2]. At a given $T$ and $P$, the volume $V_{\mathrm{min}}(P, T)$ that minimizes $G(T, P)$ is the volume at thermal equilibrium. At zero pressure, the Gibbs free energy coincides with the Helmholtz free energy $F$, whose expression is [38]

$$F(V, T) = U_0(V) + \sum_{\mathbf{q}\nu} \frac{1}{2}\hbar\omega_{\mathbf{q}\nu}(V) + k_B T \sum_{\mathbf{q}\nu} \ln\left(1 - e^{-\hbar\omega_{\mathbf{q}\nu}(V)/k_B T}\right). \tag{2.18}$$

In the last equation, I have made the $V$-dependence of the total potential energy $U_0(V)$ and of the phonon frequencies $\omega_{\mathbf{q}\nu}(V)$ explicit. The QHA consists of finding the values $V_{\min}(P,T)$ of the volume for which the free energy is at a minimum. At fixed temperature, and neglecting frequency renormalization by phonon-phonon interactions, the phonon frequencies as a function of the volume, $\omega_{\mathbf{q}\nu}(V) = \omega_{\mathbf{q}\nu}(V(T))$, can be obtained by calculating the dynamical matrix $\mathbf{D}(\mathbf{q})$ in Eq. 2.9 at the volume $V = V_{\min}(P,T)$ instead of at the equilibrium volume $V_{\mathrm{eq}}(P,0)$. Hence, within the QHA the *harmonic* phonon frequencies are calculated at a set of volumes $V_{\min}(P,T)$, with the assumption that this would mimic the real thermally expanded volumes.

The problem with the QHA is that it does not account for any phonon-phonon interaction explicitly. Hence, the QHA usually works well only until temperatures low enough that they are negligible. The cause of the breakdown of the QHA is that when the temperature is high enough, the self energies of the phonons calculated neglecting anharmonic terms are not correct. This can happen even to fairly harmonic materials at high $T$. For MgO, the breakdown of the QHA happens at $T \gtrsim 1000$ K [71] (see Sec. 3.4). Moreover, the QHA cannot describe other important effects of anharmonicity, such as the broadening of peaks in the mode spectra as $T$ increases.

## 2.5 Anharmonic terms: phonon-phonon interactions

We saw that in the HA and QHA phonons do not interact with each other. Their spectral peaks are $\delta$-functions in $(\omega, \boldsymbol{k})$-space and hence their correlation times and length diverge. This is not the case when anharmonicity is considered.

Let us now write the anharmonic terms in the potential expansion explicitly. The plane wave ansatz of Eq. 2.7, which is exact in the $T \to 0$ limit because it diagonalizes the Hamiltonian when $\mathcal{H} \equiv \mathcal{H}_{\mathrm{harm}}$, is only approximate at any finite $T$. Despite being non exact, the plane wave decomposition is still convenient, because it allows to introduce the coupling terms of interactions between the phonons, which is only possible if we express the potential energy in Eq. 2.3 as a function of the mode coordinates. Importantly, expressing the potential energy

in terms of the mode coordinates gives a complete description of the structure of the crystal, because the eigenvectors $\boldsymbol{e}(\mathbf{q}\nu)$ form a complete basis. After the change of variable from the single atomic displacements $u(jl)$ to the mode coordinates $Q(\mathbf{q}\nu)$, the Hamiltonian can be written as [38]

$$
\begin{aligned}
\mathcal{H} =& U_0 + \mathcal{K} + U_2 + U_3 + U_4 + \cdots = \\
& U_0 + \frac{1}{2}\sum_{\mathbf{q}\nu} |P(\mathbf{q}\nu)|^2 + \frac{1}{2}\sum_{\mathbf{q}\nu} \omega^2_{\mathbf{q}\nu} |Q(\mathbf{q}\nu)|^2 \\
& + \frac{1}{3!}\sum_{\mathbf{q}\nu}\sum_{\boldsymbol{q'}\nu'}\sum_{\boldsymbol{q''}\nu''} \mathcal{V}_3\binom{\boldsymbol{q},\boldsymbol{q'},\boldsymbol{q''}}{\nu,\nu',\nu''} Q(\mathbf{q}\nu) Q(\boldsymbol{q'}\nu') Q(\boldsymbol{q''}\nu'') \cdot \Delta(\boldsymbol{q}+\boldsymbol{q'}+\boldsymbol{q''}) + \\
& + \frac{1}{4!}\sum_{\mathbf{q}\nu}\sum_{\boldsymbol{q'}\nu'}\sum_{\boldsymbol{q''}\nu''}\sum_{\boldsymbol{q'''}\nu''} \mathcal{V}_4\binom{\boldsymbol{q},\boldsymbol{q'},\boldsymbol{q''},\boldsymbol{q'''}}{\nu,\nu',\nu'',\nu'''} Q(\mathbf{q}\nu) Q(\boldsymbol{q'}\nu') Q(\boldsymbol{q''}\nu'') Q(\boldsymbol{q'''}\nu''') \cdot \Delta(\boldsymbol{q}+\boldsymbol{q'}+\boldsymbol{q''}+\boldsymbol{q'''}) + \\
& o(||Q||^5)
\end{aligned}
\tag{2.19}
$$

in which I have adopted the same symbol as in Eq. 2.12 for the mode amplitudes, and $\mathcal{V}_3\binom{\mathbf{q},\mathbf{q'},\mathbf{q''}}{\nu,\nu',\nu''}$ and $\mathcal{V}_4\binom{\mathbf{q},\mathbf{q'},\mathbf{q''},\mathbf{q'''}}{\nu,\nu',\nu'',\nu'''}$ are the lattice transformations of the real-space tesnsors of Eq. 2.3; these correspond to the coupling constants between different phonons of the third- and fourth-order, respectively. While phonons are independent particles in the harmonic approximation, anharmonicity makes them couple with one another, through the terms $\mathcal{V}_3\binom{\mathbf{q},\mathbf{q'},\mathbf{q''}}{\nu,\nu',\nu''}$, $\mathcal{V}_4\binom{\mathbf{q},\mathbf{q'},\mathbf{q''},\mathbf{q'''}}{\nu,\nu',\nu'',\nu'''}$, and so on.

We can see this coupling both classically and quantum mechanically. Classically, when one phonon is excited and the Hamiltonian has the form $\mathcal{H} = U_0 + \mathcal{K} + U_2$, there are no effects on the other phonons whatsoever; the crystal can be considered to be a gas of non interacting phonons. However, when $\mathcal{H} = U_0 + \mathcal{K} + U_2 + U_3 + U_4 + \ldots$, the activation of a mode's coordinate $Q(\mathbf{q}\nu)$ produces effects on all the other phonons which the reference phonon is coupled to, via the coupling coefficients $\mathcal{V}_3$, $\mathcal{V}_4$ and so on. In the quantum mechanical language, phonons participate in collisions events, or scatter from one another. Each collision is an event in which one or more phonons annihilate to generate one or more other phonons. In a three-phonon scattering (only $\mathcal{V}_3$'s involved), either one phonon is generated from the annihilation of two others or two phonons are generated from the annihilation of one [38].

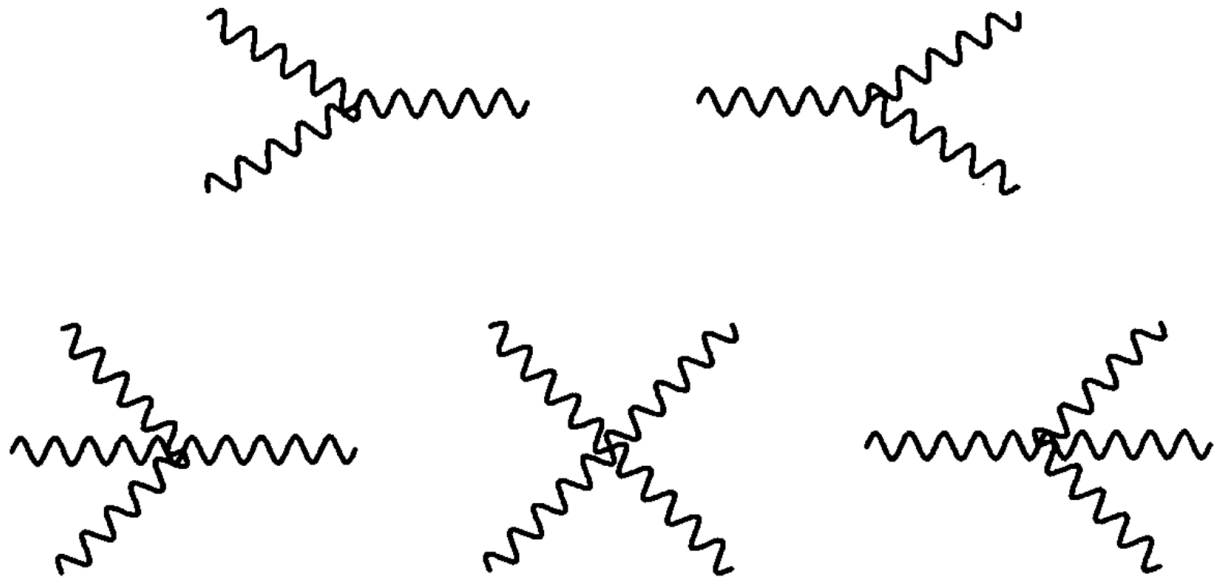


Figure 2.1: Schematic representation of phonon-phonon scattering events, taken from Dove [38]. Upper row: three-phonon scattering, with one phonon annihilating with another one to create a new phonon (left) and one phonon annihilating to create two phonons (right). Lower row: four-phonon scattering events. All events must conserve energy and momentum.

For example, in the three-phonon scattering process mediated by a term $\mathcal{V}_3(^{\mathbf{q},\mathbf{q}',\mathbf{q}''}_{\nu,\nu',\nu''})$ represented in the upper left part of Fig. 2.1, two phonons merge and annihilate to generate another phonon. In the process depicted in the upper right part of the same figure, one phonon decays to generate two phonons. It is important to note that the scattering events must obey strict conservation laws of energy and momentum, which stem from the time-invariance and from the translational symmetry of the Hamiltonian of Eq. 2.19, respectively. Using a three-phonon process as example, the conservation of momentum is $\boldsymbol{q} + \boldsymbol{q'} + \boldsymbol{q''} = \mathbf{0} + \boldsymbol{G}$, where $\boldsymbol{G}$ is a reciprocal lattice vector, and the conservation of energy is $\omega_{\mathbf{q}\nu} + \omega_{\boldsymbol{q'}\nu'} + \omega_{\boldsymbol{q''}\nu''} = 0$.

### 2.5.1 The phonon linewidth from perturbation theory

Phonon-phonon interactions of the simple forms discussed above are considered explicitly within perturbation theory (PT) [31, 15, 4]. The standard way of doing so is by computing the self energy of the phonons for a limited amount of phonon-phonon scattering events [35, 15]. Unfortunately, this is not the place to embark on a detailed discussion of PT. I believe that the theoretical developments of this theory for phonons were originally intended to be consistent

with the perturbational treatment of electrons, and to be compatible with that theory, so as to facilitate the development of theories of electron-phonon coupling. In fact, many reference textbooks on this subject focus on electronic interactions. One of these is the Mattuck [88]. For phonons, I would recommend the textbook by Reissland [104] and the thesis by Breeze [15], and the references therein.

The focus of PT is to treat the coupling constants $\mathcal{V}_3$, $\mathcal{V}_4$, etc., as small perturbations to the harmonic Hamiltonian, and to calculate the effect of this perturbation in the phonon frequencies and linewidths. Each scattering event is considered individually. Often, the scattering events are encapsulated into so-called Feynman diagrams [88], which are graphic representations of the collisions that can occur to a phonon injected into the interacting many-body system of phonons. The effect of the phonon-phonon interactions can be evaluated by calculating the self energy of the Feynman diagram. This is a complex quantity whose real part defines the frequency of the phonon *quasi*particle, and its imaginary part defines its linewidth. Though in principle many diagrams can be taken into account, in practise only three, to first- and second-order in the perturbation, are usually considered: the "bubble", the "tadpole" and the "loop" diagrams [15, 35]. This is because the computation of the self energy is often intractable for the more complicated diagrams. Although there are in the literature some cases of calculation of all the three diagrams [78], more often only the "bubble" is considered [52, 34].

The bubble diagram is interesting for us, because it is the lowest-order diagram whose self energy has an imaginary part, and hence produces a broadening of the phonon spectra, $\Gamma_\lambda$ [15, 35]. It represents the scattering of a phonon $\lambda$ with phonons $\lambda_1$ and $\lambda_2$: the $\lambda$ phonon gets annihilated with the creation of phonons $\lambda_1$ and $\lambda_2$, and it is recreated back through the annihilation of phonons $\lambda_1$,$\lambda_2$. Because for MgO we will be concerned with the broadening of the spectral lines in $\omega$-space, and because authors like Giura *et al.* [52] performed this type of calculation, we shall briefly discuss how the linewidth is calculated through this diagram.

With performing the self energy calculation for the bubble diagram, the linewidth of the phonon

with wavevector-branch $\lambda = (\mathbf{q}, \nu)$ is [15, 31, 34, 52]

$$\Gamma_\lambda = \frac{18}{\hbar^2}\sum_{\lambda_1\lambda_2}|\mathcal{V}_3(\lambda,\lambda_1,\lambda_2)|^2\Big[(n_{\lambda_1}+n_{\lambda_2}+1)\delta(\omega_\lambda-\omega_{\lambda_1}-\omega_{\lambda_2}) \\ +2(n_{\lambda_1}-n_{\lambda_2})\delta(\omega_\lambda+\omega_{\lambda_1}-\omega_{\lambda_2})\Big]. \tag{2.20}$$

Eq. 2.20 is the standard formula for the calculation of the linewidth of a phonon derived from considering a three-phonon scattering event [52, 34, 78]. Each color stands for a different part of the equation, and we will try to make sense of each term.

- the constant $18/\hbar^2$: often $\hbar$ is thought to be indicative of quantum mechanics. Here, $\Gamma_\lambda \to \infty$ as $\hbar \to 0$. Hence, we are within the quantum mechanical formalism: phonons are considered particles bearing a quantized amount of energy, and the differences in the energy levels are appreciable and non-vanishing;
- the sum $\sum_{\lambda_1,\lambda_2}$: this is typical of Feynmann diagrams. They are written down for one particular way the phonon $\lambda$ can interact with others, then we have to sum over all possible ways, a.k.a. intermediate momenta $\lambda_1, \lambda_2$;
- the coupling coefficient $\mathcal{V}_3(\lambda,\lambda_1,\lambda_2)$: this defines the energetics of the phonon-phonon scattering process. If $\mathcal{V}_3(\lambda,\lambda_1,\lambda_2)$ is high, it means that the couple of phonons $(\lambda_1,\lambda_2)$ is very likely to interact with the $\lambda$ phonon. In the harmonic approximation, $\mathcal{V}_2(\lambda_1,\lambda_2)$ reduces to $\frac{1}{4}\hbar\omega_{\lambda_1}\delta_{\lambda_1,\lambda_2}$ [15], where $\delta_{\lambda_1,\lambda_2}$ is a delta function assuring that $\lambda_1 = -\lambda_2 = \lambda$. This means that in the HA phonons do not interact at all. The coupling constant $\mathcal{V}_3(\lambda,\lambda_1,\lambda_2)$ can be calculated either with DFPT using the so-called "2n + 1" theorem, or by finite difference via the "frozen phonon method";
- the square brackets define two different processes:
  - the summation processes: these involve the decay of the reference $\lambda$ phonon into two of smaller frequencies, whose sum equals the frequency $\omega_\lambda$;
  - the difference processes: these involve the merging of the reference $\lambda$ phonon with either a $\lambda_1$ or a $\lambda_2$ phonon, to generate a $\lambda_2$ or $\lambda_1$ phonon;

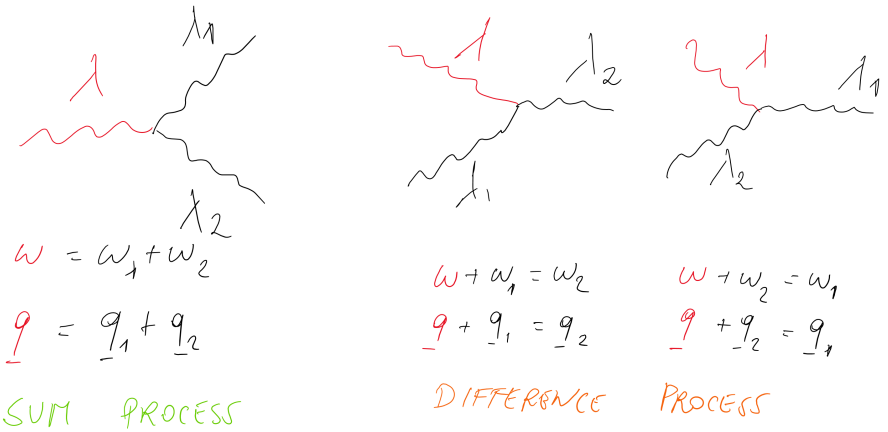



Figure 2.2: Schematic of sum and difference processes, with the conservation of energy and momentum.

  - the 2: takes care of the different situations on the right hand side of Fig. 2.2.

- the $\delta$-functions: these assure exact energy conservation, which is required by the time-independence of the Hamiltonian. If a phonon-phonon process is to happen, it must conserve the energy. It also must conserve the momentum, as a result of the translational symmetry of the Hamiltonian; this is left implicit, and the term $\delta(\boldsymbol{q}+\boldsymbol{q_1}+\boldsymbol{q_2})$ is subsumed into the coupling constants $\mathcal{V}_3$'s, which vanish when momentum is not conserved. The $\delta$-functions, with variable $\omega$ in place of $\omega_1$, are called "two-phonon density of states" (TPDOS), and are a sort of extension of the phonon DOS; their calculation is easy and very valuable.

### The two-phonon density of states

Within second-order PT, the linewidth of a phonon (Eq. 2.20) depends on the the coupling constants $\mathcal{V}_3$'s, the Bose-Einstein population of the phonons $n_{\lambda_i}$ and the $\delta$-functions which guarantee energy and momentum conservation. For this reason, it is useful to regard the linewidth calculated from Eq. 2.20 as a **weighted two-phonon density of states** (TPDOS) [15], where the weights are: (i) the Bose-Einstein pre-factors and (ii) the coupling constants.

The TPDOS is a sort of extension of the usual DOS that includes both summation and difference processes. It is calculated by replacing, in the energy-conserving $\delta$-functions of Eq. 2.20, $\omega_\lambda$

with the variable $\omega$. Hence, the TPDOS for the summation processes is defined as

$$\mathrm{TPDOS}_{sum}(\omega, \boldsymbol{k}) = \sum_{\boldsymbol{q_1}\nu_1\boldsymbol{q_2}\nu_2} \delta(\omega - \omega_{\boldsymbol{q_1}\nu_1} - \omega_{\boldsymbol{q_2}\nu_2})\delta(\boldsymbol{k} + \boldsymbol{q_1} + \boldsymbol{q_2}), \tag{2.21}$$

and the TPDOS for the difference processes is defined as

$$\mathrm{TPDOS}_{diff}(\omega, \boldsymbol{k}) = \sum_{\boldsymbol{q_1}\nu_1\boldsymbol{q_2}\nu_2} \delta(\omega + \omega_{\boldsymbol{q_1}\nu_1} - \omega_{\boldsymbol{q_2}\nu_2})\delta(\boldsymbol{k} + \boldsymbol{q_1} + \boldsymbol{q_2}). \tag{2.22}$$

If the wavevector $\boldsymbol{q}$ and frequency $\omega_\lambda$ of a reference phonon $\lambda = (\boldsymbol{q}\nu)$ lies where the TPDOS is high, then there are many pairs of phonons which fulfil the conservation of energy and momentum for phonon-phonon scattering, hence the reference phonon finds many decay channels; this is a necessary condition for its linewidth to be big. Of course, the energy conservation is only a necessary condition to open decay channels: the fact that a three-phonon scattering process *can* occur, it doesn't mean that it *will* with high probability.

The first thing that is necessary to check to see whether the linewidth of the reference phonon is high is the population of the phonons involved in the scattering: this is taken care of by the Bose-Einstein pre-factors of Eq. 2.20. Let us denote the the Bose-Einstein-weighted two-phonon density of states as wTPDOS. Then the wTPDOS for the summation processes is

$$\mathrm{TPDOS}_{sum}(\omega, \boldsymbol{k}) = \sum_{\boldsymbol{q_1}\nu_1\boldsymbol{q_2}\nu_2} (n_{\boldsymbol{q_1}\nu_1} + n_{\boldsymbol{q_2}\nu_2} + 1)\delta(\omega - \omega_{\boldsymbol{q_1}\nu_1} - \omega_{\boldsymbol{q_2}\nu_2})\delta(\boldsymbol{k} + \boldsymbol{q_1} + \boldsymbol{q_2}), \tag{2.23}$$

and the wTPDOS for the difference processes is

$$\mathrm{TPDOS}_{sum}(\omega, \boldsymbol{k}) = \sum_{\boldsymbol{q_1}\nu_1\boldsymbol{q_2}\nu_2} (n_{\boldsymbol{q_1}\nu_1} - n_{\boldsymbol{q_2}\nu_2})\delta(\omega - \omega_{\boldsymbol{q_1}\nu_1} - \omega_{\boldsymbol{q_2}\nu_2})\delta(\boldsymbol{k} + \boldsymbol{q_1} + \boldsymbol{q_2}). \tag{2.24}$$

The Bose-Einstein distribution of phonons is easily calculable in the HA; I show the calculation of the wTPDOS for MgO in Sec. 3.5.

The second thing that can trigger/hamper phonon scattering is the energetics of the phonon-phonon interactions: besides the conservation of energy and momentum and the population of phonons, there needs to be a mechanism for the scattering to occur. Within PT, this is

expressed by the coupling constants: if $\mathcal{V}_3$ is high for a certain process, it means that the three phonons couple more strongly.

The perturbational treatment of the phonons is not the focus of my thesis, and this section is surely not an exhaustive one. However, I have decided to include it because Eq. 2.20 is the standard equation for calculating phonon linewidths. Having introduced the TPDOS, which is the mathematical form for the conservation of momentum and energy, will help us interpret some features of the phonon spectra for MgO, which I will present in Sec. 3.5. However, it is important to realize that PT involves hypothesis over the strengths of the phonon-phonon interactions, namely that they must be small, and hence is an approximate method, which is based on the truncation of the Taylor expansion of the potential to some given order. In the following section, I introduce a fully non-perturbative method to calculate phonon spectra.

## 2.6 Fully non-perturbative method: the velocity-velocity correlation function

The velocity-velocity correlation function method (VVCF) is the chief method I use in this thesis. It allows one to calculate the distribution of vibrational energy in reciprocal spacetime, $\tilde{\mathcal{E}}(\omega, \boldsymbol{k})$, whose significance I introduced in Ch. 1. A more rigorous treatment than the one I am going to offer here is in Ref. [24], and especially in Ref. [132]. Here I limit myself to give a summary of the results for the quantities of interest.

### The correlation function

Let us consider a dynamical variable $\boldsymbol{A}(\boldsymbol{R}, t)$. Let us assume that the Hamiltonian is time independent, so that we only need to consider time *shifts*, $\Delta t$. I define the autocorrelation function of the variable $\boldsymbol{A}$ as [132]

$$C_{\boldsymbol{AA}}(\boldsymbol{R}, t) \equiv \langle \boldsymbol{A}(\boldsymbol{R}_0, t_0) \cdot \boldsymbol{A}^*(\boldsymbol{R}_0 + \boldsymbol{R}, t_0 + t) \rangle_{\boldsymbol{R}_0, t_0}, \tag{2.25}$$

where the average is taken over all $\boldsymbol{R}_0$'s and $t_0$'s, and the symbol $^*$ denotes the complex conjugate, which is only needed if $\boldsymbol{A}$ is a complex quantity. The correlation function measures how well variable $\boldsymbol{A}$ is correlated in time ($t$) and space ($\boldsymbol{R}$). At no shifts, ($\boldsymbol{R} = 0, t = 0$), the correlation function reduces to $C_{\boldsymbol{AA}}(\boldsymbol{R} = 0, t = 0) = \langle \|\boldsymbol{A}(\boldsymbol{R}_0, t_0)\|^2 \rangle_{\boldsymbol{R}_0, t_0} = \langle \|\boldsymbol{A}\|^2 \rangle$, which is just the second moment of the quantity $\boldsymbol{A}$, which corresponds to its variance or fluctuation in the case $\langle \boldsymbol{A} \rangle = 0$.

### The velocity-velocity correlation function

Let us now consider the dynamical variable $\mathbf{v}_{jl}(t) \equiv \mathbf{v}(\mathbf{R}_{jl}, t)$, defined as the $\sqrt{\text{mass}}$-weighted velocity of atom $jl$ at time $t$, that is, $\mathbf{v}(\mathbf{R}_{jl}, t) = \sqrt{m_j}\dot{\mathbf{u}}(\mathbf{R}_{jl}, t) \equiv \sqrt{m_j}\dot{\mathbf{u}}_{jl}$. Such a variable is a discrete function of space, because it is only defined at the positions of the atoms, namely, at $\boldsymbol{R} = \mathbf{R}_{jl}$. In the following, I will use $\boldsymbol{R} \equiv \mathbf{R}_{j'l'} - \mathbf{R}_{jl}$ to indicate a generic spatial *shift* where

atom $j'$ can be different than atom $j$, and $\boldsymbol{X} \equiv \mathbf{R}_{jl'} - \mathbf{R}_{jl}$ to denote a spatial shift between the same atom $j$, corresponding to an integer number of lattice vectors. The velocity-velocity correlation function is

$$C_{\mathbf{vv}}(\boldsymbol{R}, t) = \langle \mathbf{v}(\mathbf{R}_{jl}, t_0) \cdot \mathbf{v}(\mathbf{R}_{jl} + \boldsymbol{R}, t_0 + t) \rangle_{\mathbf{R}_{jl}, t_0} \equiv \langle \mathbf{v}_{jl}(t_0) \cdot \mathbf{v}_{j'l'}(t_0 + t) \rangle_{jl, t_0}, \tag{2.26}$$

where the average is performed over the ensemble of all atoms $\{\mathbf{R}_{jl}\}$ and over all initial times $\{t_0\}$. At no shifts, $(\boldsymbol{R} = 0, t = 0)$, Eq. 2.26 becomes

$$C_{\mathbf{vv}}(0, 0) = \langle \mathbf{v}_{jl}(t_0) \cdot \mathbf{v}_{jl}(t_0) \rangle_{jl, t_0} = \frac{1}{N} \sum_{\alpha jl} m_j \langle \dot{u}^2_{\alpha, jl} \rangle_{t_0}, \tag{2.27}$$

where the sum over $\alpha$ is the sum over the 3 dimensions of space. This is just $\frac{2}{N}$ times the average kinetic energy of the crystal, $\langle \mathcal{K} \rangle = \frac{3}{2} N k_B T$. Let us now consider the case of a finite time shift, $t \neq 0$, and no space shift $\boldsymbol{R} = 0$. Because the correlation function depends only on time *shifts*, we can write it as

$$C_{\mathbf{vv}}(0, t) = \langle \mathbf{v}_{jl}(0) \cdot \mathbf{v}_{jl}(t) \rangle_{jl, 0}, \tag{2.28}$$

where the subscript zero means that the average is over all initial times. Multiplying this function by $N$, and Fourier transforming it with respect to time gives [129, 151]

$$\tilde{\mathcal{E}}(\omega) = N \int_{-\infty}^{\infty} C_{\mathbf{vv}}(0, t) e^{i\omega t} dt. \tag{2.29}$$

This quantity is related to the average kinetic energy by $\langle \mathcal{K} \rangle = \int_0^\infty d\omega \tilde{\mathcal{E}}(\omega)$ [132]. In appendix C, I demonstrate this by showing that the frequency distribution of the kinetic energy of an atom (and of a vibrating string) equals the Fourier transform over time (and space) of its velocity-velocity correlation function. A more rigorous proof is in Ref. [132].

Because by the equipartition theorem the average energies of the terms appearing squared in the Hamiltonian are equal, $\langle \mathcal{H}_{\text{harm}} \rangle \equiv \langle \mathcal{K} + U_{\text{harm}} \rangle = 2\langle \mathcal{K} \rangle$, $\tilde{\mathcal{E}}(\omega)$ can be regarded as the distribution of the total vibrational energy in $\omega$-space, but only when anharmonic terms are

negligible. However, when anharmonic terms are not negligible in the Hamiltonian $\mathcal{H} = \mathcal{H}_{\text{harm}} + U_3 + U_4 + \ldots$, this quantity is more properly the distribution of kinetic energy. Throughout this thesis, I will sometimes call it distribution of vibrational energy, but it needs to be understood that strictly speaking $\tilde{\mathcal{E}}(\omega)$ is the distribution over frequency space of the kinetic energy of the crystal. In the limit of $T \to 0$, dividing it by $3Nk_BT$, $\tilde{\mathcal{E}}(\omega)$ becomes the total vibrational density of states (DOS). One proof of this is in the Dove [38], and a more rigorous one is in Refs. [24, 132].

For the remaining of the section, it is useful to define the the equal-atom correlation function

$$C^j_{\mathbf{vv}}(\boldsymbol{X}, t) = \langle \mathbf{v}(\mathbf{R}_{jl}, t_0) \cdot \mathbf{v}(\mathbf{R}_{jl} + \boldsymbol{X}, t_0 + t) \rangle_{\mathbf{R}_l, t_0} \equiv \langle \mathbf{v}_{jl}(t_0) \cdot \mathbf{v}_{jl'}(t_0 + t) \rangle_{l, t_0}, \tag{2.30}$$

where the average over space is performed over the sublattice of atom $j$, $\{\mathbf{R}_l\}$.

**The velocity-velocity correlation function projected onto a wave of wavevector $\boldsymbol{k}$**

The VVCF of Eq. 2.30 can be lattice transformed in space to give

$$C^j_{\mathbf{vv}}(\boldsymbol{k}, t) = \sum_l C^j_{\mathbf{vv}}(\boldsymbol{X}, t) e^{-i\boldsymbol{k}\cdot\boldsymbol{X}}, \tag{2.31}$$

where $\boldsymbol{X} = \mathbf{R}_{jl} - \mathbf{R}_{jl'}$ was defined previously, and equals an integer number of lattice spacings. From a mathematical point of view, this is equivalent to defining the collective variable [38]

$$\mathbf{v}_{\boldsymbol{k}j}(t) = \frac{1}{\sqrt{N_c}} \sum_l \mathbf{v}_{jl}(t) e^{-i\boldsymbol{k}\cdot\boldsymbol{R}_{jl}}, \tag{2.32}$$

and to calculating the correlation function over the initial times of this collective variable. In fact,

$$\begin{aligned} C_{\mathbf{v}_{\boldsymbol{k}j}\mathbf{v}_{\boldsymbol{k}j}}(t) &= \langle \mathbf{v}_{\boldsymbol{k}j}(0) \cdot \mathbf{v}^*_{\boldsymbol{k}j}(t) \rangle_0 = \frac{1}{N_c} \langle \sum_{ll'} \mathbf{v}_{jl}(0) e^{-i\boldsymbol{k}\cdot\boldsymbol{R}_{jl}} \cdot \mathbf{v}_{jl'}(t) e^{i\boldsymbol{k}\cdot\boldsymbol{R}_{jl'}} \rangle_0 & (2.33) \\ &= \frac{1}{N_c} \sum_{ll'} \langle \mathbf{v}_{jl}(0) \cdot \mathbf{v}_{jl'}(t) \rangle_0 e^{-i\boldsymbol{k}\cdot\boldsymbol{X}} \equiv C^j_{\mathbf{vv}}(\boldsymbol{k}, t), & (2.34) \end{aligned}$$

which is just Eq. 2.31, as can be proven by inserting Eq. 2.30 into 2.31. The collective variable is the lattice transform of the velocities $\mathbf{v}_{jl}$. It is the sum of the velocities of all atoms $j$ in the bulk of the crystal when these are projected onto a wave of wavevector $\boldsymbol{k}$. Eq. 2.33 is the equation I used to numerically compute the VVCF of waves of atoms. Fourier transforming in time this correlation function obtained with the $\boldsymbol{k}$-dependent velocities, and upon summation over the number of atoms in the unit cell, we obtain

$$\tilde{\mathcal{E}}(\omega,\boldsymbol{k}) = \int_{-\infty}^{\infty} \sum_{j}^{n_a} C^{j}_{\mathbf{vv}}(\boldsymbol{k},t) e^{i\omega t} dt = \int_{-\infty}^{\infty} \sum_{j}^{n_a} \langle \mathbf{v}_{\boldsymbol{k}j}(0) \cdot \mathbf{v}^{*}_{\boldsymbol{k}j}(t) \rangle_0 e^{i\omega t} dt, \tag{2.35}$$

which gives the distribution of kinetic energy projected onto the wave of wavevector $\boldsymbol{k}$. This quantity is the most important one of my work, and it is what I plot in Figs. 3.5-3.6 for MgO and in Fig. I.1 for $BaTiO_3$.

This quantity converges to the vibrational DOS for only one $\boldsymbol{k}$ point in the limit $T \to 0$. At finite $T$, however, this is just the distribution of kinetic energy in reciprocal spacetime. It allows us to reconstruct a band structure when it is calculated over many $\boldsymbol{k}$-points. It is important to note that the calculation of $\tilde{\mathcal{E}}(\omega,\boldsymbol{k})$ is strictly allowed for commensurate $\boldsymbol{k}$-points only, as the insertion of a non-commensurate $\boldsymbol{k}$-point in Eq. 2.32 would create a collective variable $\mathbf{v}_{\boldsymbol{k}j}$ which violates the translational symmetry of the MD supercell, therefore resulting in unphysical spectra.

**The velocity-velocity correlation function projected onto the modes ($\boldsymbol{k}\nu$)**

Recalling that the number of atoms in each unit cell is $n_a$, at low $T$ every lattice wave with wave vector $\boldsymbol{k}$ has $3 \times n_a$ modes of vibration, each one corresponding to a different eigenvector, $\boldsymbol{e}(\boldsymbol{k}\nu, j)$, of the dynamical matrix $\mathbf{D}(\boldsymbol{k})$. At finite $T$, the normal modes can mix and interact with other modes, and therefore can change character; mathematically, they do not exactly diagonalize the Hamiltonian $\mathcal{H} = \mathcal{H}_{\text{harm}} + U_3 + U_4 + \ldots$ when $T$ is high. However, we can use the fact that the eigenvectors form a *complete set*, and further project the collective variable

(Eq. 2.32) onto the *orthonormal* eigenvectors at $\boldsymbol{k}$, to obtain

$$v_{\boldsymbol{k}\nu}(t) = \frac{1}{\sqrt{3}} \sum_j \mathbf{v}_{\boldsymbol{k}j}(t) \cdot \boldsymbol{e}(\boldsymbol{k}\nu, j), \tag{2.36}$$

which is the velocity at which the phonon with wave vector $\boldsymbol{k}$, branch $\nu$, travels through the crystal. The Fourier transform of the correlation function obtained with this $\boldsymbol{k}$-$\nu$ projected velocity is

$$\tilde{\mathcal{E}}_\nu(\omega, \boldsymbol{k}) = \int_{-\infty}^{\infty} \langle v^*_{\boldsymbol{k}\nu}(0) v_{\boldsymbol{k}\nu}(t) \rangle_0 e^{i\omega t} dt, \tag{2.37}$$

and is the distribution of kinetic energy of the motion along the eigenvector $\boldsymbol{e}(\boldsymbol{k}\nu)$. In the limit of $T \to 0$, this is the $k_B T$-weighted DOS for the $\boldsymbol{k}\nu$ phonon, namely, the classical spectrum of one single phonon. The quantity $\tilde{\mathcal{E}}_\nu(\omega, \boldsymbol{k})$ is what I plot in Fig. 3.7 and 9.1c-9.1e for MgO and in Figs. 7.6, 7.7, 7.8 and I.2-I.4 for $BaTiO_3$.

Of course, $\tilde{\mathcal{E}}(\omega) = \sum_{\boldsymbol{k}} \tilde{\mathcal{E}}(\omega, \boldsymbol{k}) = \sum_{\boldsymbol{k}\nu} \tilde{\mathcal{E}}_\nu(\omega, \boldsymbol{k})$. The first equivalence can be proved by inserting Eq. 2.32 into 2.35 and using the lattice sum rule $\sum_{\boldsymbol{k}} \exp(i\boldsymbol{k} \cdot \boldsymbol{X}) = N_c \delta_{\boldsymbol{X},\boldsymbol{0}}$. The second equivalence follows after inserting Eq. 2.36 into 2.37 and from the properties of *orthonormality* and *completeness* of the eigenvectors $\sum_\nu e^*_\alpha(\boldsymbol{k}\nu, j) \cdot e_\beta(\boldsymbol{k}\nu, j') = \delta_{j,j'}\delta_{\alpha,\beta}$.

### The expected $\tilde{\mathcal{E}}(\omega, \boldsymbol{k})$ in the harmonic and quasi-harmonic approximations

In the limit $T \to 0$, where the HA holds, the phonons are independent of one another and do not interact. Hence, the spectrum of each phonon is a $\delta$-function in frequency space. The vibrational energy distribution in reciprocal spacetime, $\tilde{\mathcal{E}}(\omega, \boldsymbol{k})$, is a superposition of $\delta$-functions centered at the frequencies of the lattice vibrations $\omega_{\mathbf{q}\nu}$, and at the wavevectors $\mathbf{q}$ of the plane wave decomposition in Eq. 2.7 commensurate with the periodicity of the crystal. That is [132],

$$\tilde{\mathcal{E}}(\omega, \boldsymbol{k}) = \sum_{\boldsymbol{q}\nu} k_B T \delta(\omega - \omega_{\mathbf{q}\nu}) \delta(\boldsymbol{k} - \mathbf{q}) \tag{2.38}$$

In reciprocal spacetime, $\tilde{\mathcal{E}}(\omega, \boldsymbol{k})$ forms a set of quasicontinuous *bands*.

In the QHA, exactly like in the HA, the classical vibrational energy distribution in reciprocal spacetime, $\tilde{\mathcal{E}}(\omega, \boldsymbol{k})$, is made of $\delta$-functions centered at the QHA frequencies $\omega_{\mathbf{q}\nu}(V)$, and at the wavevectors commensurate with the periodicity of the crystal and its linear dimensions.

### The expected $\tilde{\mathcal{E}}(\omega, \boldsymbol{k})$ in the quasiparticle approximation

Under the assumption that phonons interact weakly, PT states that the phonon spectra are Lorentzian functions [15, 104, 52]. Hence, we expect the distribution of vibrational energy to be

$$\tilde{\mathcal{E}}(\omega, \boldsymbol{k}) = \sum_{\boldsymbol{k}\nu} k_B T L(\omega - \omega_{\mathbf{q}\nu}) \delta(\boldsymbol{k} - \mathbf{q}), \tag{2.39}$$

where $L(\omega)$ is the Cauchy distribution, which is a Lorentzian function.

### $\tilde{\mathcal{E}}(\omega, \boldsymbol{k})$ in the general case

In the general case, $\tilde{\mathcal{E}}(\omega, \boldsymbol{k})$ can take any form. Hence, the VVCF method allows to track the $k_B T$-weighted spectrum of each single phonon at any temperature or pressure, and in any phase the material might be, as long as the phonon wavevectors $\boldsymbol{k}$'s are commensurate with the MD supercell. The calculation of $\tilde{\mathcal{E}}_\nu(\omega, \boldsymbol{k})$ therefore allows image how the vibrational energy is among the modes in ($\omega$,$\boldsymbol{k}$)-space.

This method is not new. It was used in Refs. [133, 128, 129, 151]. However, it has not been extensively used. It is a very powerful method because it is fully non-perturbative, since it does not imply truncating the potential expansion 2.3 to any order, as the velocities are obtained from MD. It is possibly the most general method to obtain classical phonon spectra at finite $T$s.

## 2.7 Quasiparticle thermodynamics

In Sec. 3.7, I compute the isobaric heat capacity by means of the phonon quasiparticle frequencies. In this section, I show how this can be done.

### 2.7.1 The isobaric heat capacity within the QHA

It is common [38, 71] to calculate the isobaric heat capacity from the isochoric heat capacity through the formula $C_P = C_V(1 + \alpha\gamma T)$, where $\alpha$ is the thermal expansion coefficient, $T$ is the temperature and $\gamma$ is the thermal Grüneisen parameter [38]. More details can be found in standard textbooks, e.g. Dove [38]. Within the QHA, $\gamma$ can be computed through the first derivative of the phonon frequencies with respect to the volume $V$. The difference $C_P - C_V$ is thus a measure of the anharmonicity of the crystal [71]. I could have computed both $\alpha$ and $\gamma$, but these would have had the deficiency of being calculated within the QHA, which is inaccurate at high $T$. Hence, I went for another approach, which is more general and lies at the heart of quasiparticle approximation (QPA).

### 2.7.2 The isobaric heat capacity within the QPA

I hereby derive a closed formula for the heat capacity involving the temperature (rather than volume) derivatives of the phonon frequency shifts.

Within the QPA, the phonon quasiparticles have frequencies $\tilde{\omega}_{\mathbf{k}\nu}(V(T), T) = \tilde{\omega}_{\mathbf{k}\nu}(T)$, which are functions of $T$. Let us start from the definition of the entropy in the harmonic approximation:

$$\begin{aligned} S =& -\left(\frac{\partial F}{\partial T}\right)_V = k_B \sum_{\mathbf{k}\nu} [(\bar{n}_{\mathbf{k}\nu} + 1)\ln(\bar{n}_{\mathbf{k}\nu} + 1) - \bar{n}_{\mathbf{k}\nu} \ln \bar{n}_{\mathbf{k}\nu}] = \\ =& -k_B \sum_{\mathbf{k}\nu} \ln\left[1 - \exp(-\hbar\omega_{\mathbf{k}\nu}/k_B T)\right] - \frac{1}{T} \sum_{\mathbf{k}\nu} \hbar\omega_{\mathbf{k},\nu} \bar{n}_{\mathbf{k}\nu}, \end{aligned} \tag{2.40}$$

where $F$ is the Helmholtz free energy, $\bar{n}_{\mathbf{k}\nu} = \bar{n}(\omega, T) = [\exp(\hbar\omega_{\mathbf{k},\nu}/k_B T) - 1]^{-1}$ is the Bose-Einstein distribution and $k_B$ is the Boltzmann constant. In order to include anharmonic effects,

which shift the phonon frequencies, in the thermodynamic properties, I replace $\omega_{\mathbf{k}\nu}$ with its anharmonic counterpart $\omega_{\mathbf{k}\nu} \rightarrow \tilde{\omega}_{\mathbf{k}\nu}(T)$ in Eq. 2.40. This effectively corrects the phonon frequencies predicted within the harmonic approximation with their anharmonic values.

A question arises in doing the replacement $\omega_{\mathbf{k}\nu} \rightarrow \tilde{\omega}_{\mathbf{k}\nu}$: is it legitimate to do so in the entropy (Eq. 2.40) or should it be done in, for example, the energy, free energy or other state functions? Wallace [31] showed that it is correct to do the replacement in the entropy $S$; this gives results that are consistent, both in the low- and high- temperature limit, with first-order thermodynamic perturbation theory [31]. This is the approach which was used, for example, in Ref. [129].

This observation is an interesting one. It means that the entropy, rather than other state functions, is the most fundamental quantity when it comes to quasiparticle thermodynamics. Replacing $\omega_{\mathbf{k}\nu} \rightarrow \tilde{\omega}_{\mathbf{k}\nu}$ into the total energy $E$, for example, and calculating the heat capacity as $C_P = \partial E/\partial T$ would have given a wrong result. Note that if one replaces $\omega_{\mathbf{k}\nu} \rightarrow \tilde{\omega}_{\mathbf{k}\nu}(T)$ into the energy, they obtain a zero-point energy which is $T$-dependent.

The renormalized entropy is:

$$\tilde{S} = k_B \sum_{\mathbf{k}\nu} [(\tilde{n}_{\mathbf{k}\nu} + 1)\ln(\tilde{n}_{\mathbf{k}\nu} + 1) - \tilde{n}_{\mathbf{k}\nu} \ln \tilde{n}_{\mathbf{k}\nu}], \tag{2.41}$$

where $\tilde{n}_{\mathbf{k}\nu}$ is the Bose-Einstein distribution corrected with the temperature-dependent frequencies $\tilde{\omega}_{\mathbf{k}\nu}$. The physical meaning of this replacement is the following: we are assuming that phonons continue to follow the Bose-Einstein distribution, which however is corrected by including the quasiparticle phonon frequencies. We are hence exploiting the quasiparticle concept: the increased temperature makes the phonons become quasiparticles, and we use the phonon quasiparticle frequencies to calculate state functions, through quantum mechanical equations. Of course, this is only allowed *as long as the phonons are* bona fide *quasiparticles*.

Writing $\tilde{\omega}_{\mathbf{k}\nu}(T) = \omega_{\mathbf{k}\nu} + \Delta_{\mathbf{k}\nu}(T)$, and in the hypothesis of small shifts $\Delta_{\mathbf{k}\nu}(T)$ (so that $\Delta^2_{\mathbf{k}\nu}$ is negligible), one can Taylor expand $\tilde{n}_{\mathbf{k}\nu}$, $\ln(\tilde{n}_{\mathbf{k}\nu} + 1)$ and $\ln(\tilde{n}_{\mathbf{k}\nu})$ about $\omega_{\mathbf{k}\nu}$ to first order in $\Delta_{\mathbf{k}\nu}$

to obtain [31]:

$$\tilde{S} = k_B \sum_{\mathbf{k}\nu} [(n_{\mathbf{k}\nu}+1)\ln(n_{\mathbf{k}\nu}+1) - n_{\mathbf{k}\nu}\ln n_{\mathbf{k}\nu}] - \sum_{\mathbf{k}\nu} \hbar\Delta_{\mathbf{k}\nu}\frac{\partial n_{\mathbf{k}\nu}}{\partial T} = S_H + S_A \tag{2.42}$$

in which I separated out the harmonic part of the entropy $S_H$ and the (first-order in $\Delta_{\mathbf{k}\nu}$) anharmonic contribution to the entropy $S_A$. This formula for the anharmonic entropy is present in Wallace's textbook, but in a different form. Since the constant-pressure heat capacity is defined as $C_P = T(\partial S/\partial T)_P$, the harmonic and anharmonic contributions to the heat capacity are:

$$C_H = T\left(\frac{\partial S_H}{\partial T}\right)_{V,P=0} \equiv C_V; \tag{2.43}$$

$$\begin{aligned} C_{PA} =& T\left(\frac{\partial S_A}{\partial T}\right)_{P=0} = \sum_{\mathbf{k}\nu} T\frac{\partial}{\partial T}\left(-\hbar\Delta_{\mathbf{k}\nu}\frac{\partial n_{\mathbf{k}\nu}}{\partial T}\right)_{P=0} = \\ =& \sum_{\mathbf{k}\nu} -T\frac{\partial \hbar\Delta_{\mathbf{k}\nu}}{\partial T}\frac{\partial n_{\mathbf{k}\nu}}{\partial T} - T\hbar\Delta_{\mathbf{k}\nu}\frac{\partial^2 n_{\mathbf{k}\nu}}{\partial T^2} = \\ =& -\sum_{\mathbf{k}\nu} \frac{\hbar\omega_{\mathbf{k}\nu}}{k_B T}(n_{\mathbf{k}\nu}^2 + n_{\mathbf{k}\nu})\left[\frac{\partial \hbar\Delta_{\mathbf{k}\nu}}{\partial T} + \frac{\hbar\Delta_{\mathbf{k}\nu}}{T}\left((2n_{\mathbf{k}\nu}+1)\frac{\hbar\omega_{\mathbf{k}\nu}}{k_B T} - 2\right)\right]. \end{aligned} \tag{2.44}$$

In Eq. 2.43, the harmonic part of the heat capacity $C_H$ is obtained from the derivative of the harmonic part of the entropy. Because the harmonic crystal does not expand, $C_H \equiv C_V$, and the harmonic heat capacity corresponds to the constant-volume heat capacity. In Eq. 2.44, the $\Delta_{\mathbf{k}\nu}$'s are the quasiparticles shifts. I obtained $\tilde{\omega}_{\mathbf{k}\nu}(T) = \omega_{\mathbf{k}\nu} + \Delta_{\mathbf{k}\nu}(T)$ from the peaks of the Lorentzian fits to the phonon spectra computed from MD at constant pressure. In other words, they are obtained through a fit of Eq. 2.37 to a Lorentzian, for each phonon. Of course, in principle the anharmonic part of the constant-volume heat capacity $C_{VA}$ can be calculated by an exact same formula as Eq. 2.44, but with $\Delta_{\mathbf{k}\nu}$'s obtained from the spectra obtained at constant-$V$ simulations.

## 2.8 The scattering cross section

In this section, I discuss the quantity which inelastic X-ray scattering (IXS) or neutron scattering (INS) experiments probe, and which I simulate in Sec. 7.6. The two experimental techniques are discussed in more details in Secs. 6.2-6.3. For the sake of brevity, I do not derive all the equations. A good introductory textbook on this topic is the book by Dove [38], and a more comprehensive one is the book by Squires [124].

Let us consider a typical INS experiment. The rationale behind IXS is the same, the only difference being that the scattering lengths, valid for INS, have to be replaced with the atomic form factors [4, 73]. The incident and scattered beams have wavevectors $\mathbf{k}_i$ and $\mathbf{k}_f$, respectively. Their difference is called the scattering wavevector, and is denoted by $\boldsymbol{Q} = \mathbf{k}_f - \mathbf{k}_i$. Let us further use $\Phi$ to denote the flux of the incident beam, and $d\Omega$ the solid angle formed by the scattered beam in a direction $\hat{\mathbf{k}}_f$ at a distance $r$ apart from the sample. INS (or IXS) probes a quantity called *total scattering cross section*, $\frac{d\sigma}{d\Omega}$. This is defined as the number of neutrons (photons) scattered per second into the solid angle $d\Omega$ divided by the flux of the incident beam and by $d\Omega$. It is expressed as [124, 38]

$$\frac{d\sigma}{d\Omega} = S(\boldsymbol{Q}) = \langle \rho(\boldsymbol{Q})\rho(-\boldsymbol{Q}) \rangle, \tag{2.45}$$

where $\rho(\boldsymbol{Q}) = \sum_i b_i \exp(i\boldsymbol{Q} \cdot \mathbf{R}_i)$ is the scattering amplitude, with $\mathbf{R}_i$ being the position of atom $i$ (I dropped the lattice point subscript $l$ for convenience) and $b_i$ its scattering length, and the sum runs over all the number of atoms in the crystal.

### 2.8.1 The case of fixed atoms

Let us consider the atoms fixed at their equilibrium positions for the time being, i.e. $\mathbf{R}_i(t) = \mathbf{R}_i(0) = \mathbf{R}_i$. The scattering amplitude $\rho(\boldsymbol{Q})$ is the Fourier transform of the function $g(\mathbf{R}) = \sum_i b_i \delta(\mathbf{R} - \mathbf{R}_i)$. If we neglect the presence of the scattering lengths, $g(\mathbf{R})$ is the nuclear density function, i.e. a function composed of sharp peaks at the positions of the nuclei, $\{\mathbf{R}_i\}$. Let us

rewrite Eq. 2.45 as

$$S(\mathbf{Q}) = \sum_{ij} b_i b_j \langle e^{i\mathbf{Q}\cdot(\mathbf{R}_i - \mathbf{R}_j)} \rangle, \tag{2.46}$$

where the sums run over all atoms in the crystal again. Note that $S(\mathbf{Q})$ has the dimension of an area. In this form, it is easier to see that there exists a function $G(\boldsymbol{R})$ which is the inverse Fourier transform of $S(\boldsymbol{Q})$, namely,

$$S(\boldsymbol{Q}) = \int G(\boldsymbol{R}) e^{-i\boldsymbol{Q}\cdot\boldsymbol{R}} d\boldsymbol{R}. \tag{2.47}$$

This function is [124]

$$G(\boldsymbol{R}) = \sum_{ij} b_i b_j \langle \delta(\boldsymbol{R} - \mathbf{R}_i + \mathbf{R}_j) \rangle, \tag{2.48}$$

as can be proven by simply inserting Eq. 2.48 into 2.47.

Written in this form, it is easy to see that $G(\mathbf{R})$ is a *pair correlation function* (PCF). It is the probability that, sitting on an atom $n$, we find another atom $m$ at a distance $\mathbf{R}_n - \mathbf{R}_m$, weighted by the scattering lengths of the atoms. Let us further simplify the equation by considering the case of equal scattering nuclei, i.e. $b_m = b_n = b \quad \forall m, n$. Then Eq. 2.48 simplifies to [124]

$$G(\boldsymbol{R}) = b^2 N \sum_{ij} \langle \delta(\boldsymbol{R} - \mathbf{R}_i + \mathbf{R}_j) \rangle = b^2 N \sum_{i} \langle \delta(\boldsymbol{R} - \mathbf{R}_i + \mathbf{R}_0) \rangle, \tag{2.49}$$

for any reference nucleus $\mathbf{R}_0$ (which can be placed at the origin, so that $\mathbf{R}_0 = 0$). The PCF $G(\mathbf{R})$ is the probability of finding *any* particle at $\boldsymbol{R}$ from a reference atom $\mathbf{R}_0$ in the ensemble of atoms at $\{\mathbf{R}_j\}$. For the way we have defined it, the PCF is called *static* pair correlation function.

### 2.8.2 The case of mobile atoms

When we relax the assumption that atoms are fixed, we can define their positions as $\boldsymbol{r}_i(t) = \mathbf{R}_i + \boldsymbol{u}_i(t)$, where $\boldsymbol{u}_i(t)$ is the displacement of atom $i$ from the equilibrium position. The scattering amplitude is $\rho(\boldsymbol{Q}) = \sum_i b_i \exp(i\boldsymbol{Q}\cdot\boldsymbol{r}_i)$, and the scattering cross section defined in

Eq. 2.59 then becomes the *intermediate scattering cross section* [38, 124] [1]

$$F(\boldsymbol{Q},t)=\sum_{ij}b_ib_j\langle e^{i\boldsymbol{Q}\cdot[\boldsymbol{r}_i(t)-\boldsymbol{r}_j(0)]}\rangle=\sum_{ij}b_ib_je^{i\boldsymbol{Q}\cdot(\mathbf{R}_i-\mathbf{R}_j)}\langle e^{i\boldsymbol{Q}\cdot[\boldsymbol{u}_i(t)-\boldsymbol{u}_j(0)]}\rangle. \tag{2.50}$$

The term $\langle e^{i\mathbf{Q}\cdot[\boldsymbol{u}_i(t)-\boldsymbol{u}_j(0)]}\rangle$ can be manipulated by virtue of the equality $\langle\exp(A)\exp(B)\rangle = \exp(\langle(A+B)^2/2\rangle) = \exp(\langle 1/2(A^2+B^2)+AB)\rangle)$, yielding [38, 124]

$$\langle\exp\Big(i\boldsymbol{Q}\cdot[\boldsymbol{u}_i(t)-\boldsymbol{u}_j(0)]\Big)\rangle=\exp\Big(-\frac{1}{2}\langle[\boldsymbol{Q}\cdot\boldsymbol{u}_i(t)]^2\rangle-\frac{1}{2}\langle[\boldsymbol{Q}\cdot\boldsymbol{u}_j(0)]^2\rangle+\langle[\boldsymbol{Q}\cdot\boldsymbol{u}_i(t)][\boldsymbol{Q}\cdot\boldsymbol{u}_j(0)]\rangle\Big). \tag{2.51}$$

In this equation, the first two terms are the exponentials of the time-independent Debye Waller factors, $W_i = 2\langle[\boldsymbol{Q}\cdot\boldsymbol{u}_i]^2\rangle$, and the last term can be expanded in powers of $[\boldsymbol{Q}\cdot\boldsymbol{u}_i(t)][\boldsymbol{Q}\cdot\boldsymbol{u}_j(0)]$

$$\exp\Big(\langle[\boldsymbol{Q}\cdot\boldsymbol{u}_i(t)][\boldsymbol{Q}\cdot\boldsymbol{u}_j(0)]\rangle\Big)=\sum_{m=0}^{\infty}\frac{1}{m!}\big([\boldsymbol{Q}\cdot\boldsymbol{u}_i(t)][\boldsymbol{Q}\cdot\boldsymbol{u}_j(0)]\big)^m. \tag{2.52}$$

Hence, the intermediate scattering cross section can be written as

$$F(\boldsymbol{Q},t)=\sum_m\frac{1}{m!}\sum_{ij}b_ib_je^{i\boldsymbol{Q}\cdot(\mathbf{R}_i-\mathbf{R}_j)}e^{-(W_i+W_j)}\big([\boldsymbol{Q}\cdot\boldsymbol{u}_i(t)][\boldsymbol{Q}\cdot\boldsymbol{u}_j(0)]\big)^m=\sum_{m=0}^{\infty}F_m(\boldsymbol{Q},t). \tag{2.53}$$

This equation makes it clear that the scattering cross section is a series of terms $F_m(\boldsymbol{Q},t)$. The case $m=0$ is the case where no phonon is excited by the beam. The case $m=1$ is the case where the beam creates/annihilates one phonon, and so on [38]. The $m=1$ and $m=2$ cases are the higher order effects.

### The case $m=0$: Bragg scattering

The case $m=0$ corresponds to Bragg scattering. In fact, the quantity in Eq. 2.52 gives 1, and the Fourier transform of Eq. 2.53 gives [38]

$$S_{\text{Bragg}}(\boldsymbol{Q},\omega)\equiv S_0(\boldsymbol{Q},\omega)=\sum_{ij}b_ib_je^{i\boldsymbol{Q}\cdot(\mathbf{R}_i-\mathbf{R}_j)}e^{-(W_i+W_j)}\delta(\omega), \tag{2.54}$$

[1] as Squires [124] note, the equivalence $e^{i\boldsymbol{Q}\cdot\boldsymbol{r}_i(t)}e^{-i\boldsymbol{Q}\cdot\boldsymbol{r}_j(0)}=e^{i\boldsymbol{Q}\cdot(\boldsymbol{r}_i(t)-\boldsymbol{r}_j(0))}$ is only true if the operators $\hat{\boldsymbol{r}}_i(t)$ and $\hat{\boldsymbol{r}}_j(0)$ commute. In other words, Eq. 2.50 is strictly only valid within classical mechanics.

where the $\delta$-function represents the energy conservation for the incident beam, indicating that the scattering is elastic. The conservation of momentum requires that $\boldsymbol{Q} = \boldsymbol{G}$, where $\boldsymbol{G}$ is a reciprocal lattice vector [38, 124]. The integrated intensity, or total scattering cross section is then

$$S_{\text{Bragg}}(\boldsymbol{Q}) \equiv S_0(\boldsymbol{Q}) = \sum_{ij} b_i b_j e^{i\boldsymbol{Q}\cdot(\mathbf{R}_i - \mathbf{R}_j)} e^{-(W_j + W_l)} = \left| \sum_i b_i e^{i\boldsymbol{Q}\cdot\mathbf{R}_i} e^{-W_i} \right|^2 = |\rho(\boldsymbol{Q})|^2. \quad (2.55)$$

**The case $m = 1$: one-phonon scattering**

When the term $\langle \exp(i\boldsymbol{Q}\cdot(\boldsymbol{u}_i - \boldsymbol{u}_j)) \rangle$ inside Eq. 2.53 is expanded to first order in $\langle [\boldsymbol{Q}\cdot\boldsymbol{u}_i][\boldsymbol{Q}\cdot\boldsymbol{u}_j] \rangle$, we can use the assumption that the atoms move in the form of plane waves, Eq. 2.7 to obtain a the intermediate scattering cross section $F_1(\boldsymbol{Q}, t)$. This is the case in which a neutron is scattered by the crystal with the creation or annihilation of one phonon [38]. The momentum conservation is given by $\boldsymbol{Q} = \mathbf{q} + \boldsymbol{G}$, where $\mathbf{q}$ is the wavevector of the phonon involved. Fourier transforming it we get [38]

$$S_1^{\text{ph}}(\boldsymbol{Q}, \omega) = \sum_\nu \frac{\hbar}{2\omega_{\mathbf{q}\nu}} |F_\nu(\boldsymbol{Q})|^2 \Big[ (1 + n_{\boldsymbol{q}\nu}) \delta(\omega + \omega_{\boldsymbol{q}\nu}) + n_{\boldsymbol{q}\nu} \delta(\omega - \omega_{\boldsymbol{q}\nu}) \Big], \quad (2.56)$$

where the sum runs over the number of modes and the $\delta$-functions assure energy conservation for the one-phonon processes. The term $F_\nu(\boldsymbol{Q})$ is called *dynamical structure factor of mode* $\nu$, and is given by [38]

$$F_\nu(\boldsymbol{Q}) = \sum_j \frac{b_j}{\sqrt{m_j}} e^{-W_j} e^{i\boldsymbol{Q}\cdot\boldsymbol{R}_j} \boldsymbol{Q} \cdot \mathbf{e}(\mathbf{q}\nu, j). \quad (2.57)$$

The first term in the square brackets of Eq. 2.56 represents the case where the incident beam loses energy to the crystal by creating a phonon, and the second term represents the case where the incident beam gains energy from the crystal by annihilating a phonon. These two processes are not equally likely, because quantum mechanically it is easier to create a phonon than to annihilate it.

The scattering cross section reported in Eq. 2.58 is dependent upon three factors. It is inversely proportional to the excited phonon's energy, $S_1^{\text{ph}}(\boldsymbol{Q}, \omega) \sim 1/\omega_{\mathbf{q}\nu}$, meaning that phonons

with lower energy can be excited more easily. It is proportional to the phonon population, $S_1^{\mathrm{ph}}(\boldsymbol{Q},\omega) \sim T$, (the higher the temperature the more phonons are present, hence a bigger scattering cross section). Finally, it is and proportional to $\boldsymbol{Q}\cdot\mathbf{e}(\mathbf{q}\nu,j)$, which is regarded as the selection rule for neutron scattering. I illustrate schematically the selection rule is depicted in Fig. 7.3.

The integrated scattering cross section is then

$$S_1^{\mathrm{ph}}(\boldsymbol{Q}) = \sum_{\nu} \frac{\hbar}{2\omega_{\mathbf{q}\nu}} |F_\nu(\boldsymbol{Q})|^2 (1 + 2n_{\mathbf{q}\nu}). \tag{2.58}$$

**The *diffuse* scattering**

In the last section, in Eq. 2.58 I have used the superscript $^{\mathrm{ph}}$ to mean "phonons", because all the quantities appearing in the equation can be computed within the HA. This equation is obtained assuming a plane wave decomposition (Eq. 2.7), but truncating the expansion in Eq. 2.53 to first order. It is important, then, to realize that the one-phonon scattering cross section, Eq. 2.58, is an approximation, which is valid only at low $T$s. In the limit of low $T$, in fact, the excitation of more than one phonons, i.e. a process for which $m > 1$, is very unlikely, and $S(\boldsymbol{Q}) \to S_0(\boldsymbol{Q}) + S_1^{\mathrm{ph}}(\boldsymbol{Q})$.

At larger $T$s, however, it is convenient to refer to the scattering cross section without any approximation. This is easy to do if we consider the equation for Bragg scattering, Eq. 2.55: Bragg scattering represents the *square of the average* of the scattering amplitude. However, from Eq. 2.45 the total scattering cross section is defined as the *average of the square* of the scattering amplitude. Hence, we can define the total *diffuse* scattering cross section as the quantity [38]

$$S_{\mathrm{diffuse}}(\boldsymbol{Q}) = S(\boldsymbol{Q}) - S_{\mathrm{Bragg}}(\boldsymbol{Q}). \tag{2.59}$$

The diffuse scattering $S_{\mathrm{diffuse}}(\boldsymbol{Q})$, contains the terms in the expansion 2.53 to all orders. Subtracting Bragg scattering from the total scattering allows to avoid the sharp peaks in the correspondence of the $\boldsymbol{G}$-vectors, which are caused by the structure of the static lattice, rather than

the motion of the atoms. Recalling that the scattering cross section is the Fourier transform of the pair correlation function, the diffuse scattering then gives information on how correlated the *trajectories* of the atoms are in real space.

I discuss the X-ray diffuse scattering of $BaTiO_3$ in Sec. 6.2, and I simulate a neutron diffuse scattering experiment in Sec. 7.6. In the latter section, I calculate both $S_{\text{diffuse}}$ and $S_1^{\text{ph}}$, the former from MD and the latter by means of an harmonic calculation. The difference between the two cross sections gives information about how differently atoms are correlated in space as we increase $T$, namely, as we approach a phase transition.

## 2.9 Simulating infra-red spectra

In this section, I discuss how the infra-red (IR) optical spectra can be simulated from MD. The experimental IR spectra of $BaTiO_3$ are presented in Sec. 6.1, and the simulated spectra are presented in Sec. 7.5.

Typical IR studies measure the reflectance of a bulk material. From the reflectance, the real and imaginary parts of the dielectric function $\varepsilon(\omega) = \varepsilon'(\omega) + i\varepsilon''(\omega)$ are then obatined, either by means of the Kramer-Konig relations or by fitting $\varepsilon''(\omega)$ to a set of harmonic oscillators [63]. The latter method is often used in recent experiments; it has the advantage of producing smoother spectra, but the disadvantage of having assumed a form for the dielectric function and decided on the number of harmonic oscillators to fit the spectra *ex ante*. Often, the assumption that the IR response is the sum of a set of independent harmonic oscillators breaks down as a result of anharmonicity or coupling between polar phonon modes, and expedients must be put in place by the spectroscopist, such as a thorough modelling of the coupling between the modes [62].

### The static dielectric constant

From a theoretical point of view, the permittivity $\boldsymbol{\chi}$ (related to the dielectric function by $\boldsymbol{\chi} = \boldsymbol{\varepsilon} - 1$) gives the amount of polarization when a small electric field is applied to the crystal $\boldsymbol{P} = \boldsymbol{\chi}\boldsymbol{E}$. The static response, which is the response to a non-oscillating electric field, can be computed from MD via an Einstein-like relation [46]

$$\varepsilon_s^{\alpha\beta} = 1 + \varepsilon_\infty^{\alpha\beta} + \frac{\langle M_\alpha M_\beta \rangle}{3\epsilon_0 V k_B T}. \tag{2.60}$$

Here, $\varepsilon_s^{\alpha\beta}$ is the $\alpha\beta$ Cartesian component of the static dielectric tensor, $\varepsilon_\infty^{\alpha\beta}$ is the electronic part of the dielectric tensor, $V$ is the volume, $k_B$ is the Boltzmann constant and $T$ is the temperature. The quantity $\boldsymbol{M}$ is the total dipole moment of the MD supercell, made of its rigid-ion $\sum_i q_i \boldsymbol{r}_i$ contribution and distortable-ion contribution $\sum_i \boldsymbol{d}_i$, which within MD is evaluated every time step as described in Sec. 2.11. Eq. 2.60 is strictly valid only in cases in which the symmetry imposes a zero net polarization $\boldsymbol{P}$ of the crystal. In cases in which $\boldsymbol{P}$ is non-zero, such as in the FE phases of $BaTiO_3$, the square of the average polarization has to be subtracted from the numerator of Eq. 2.60. Hence, $\langle M_\alpha M_\beta \rangle \to \langle M_\alpha M_\beta \rangle - \langle M_\alpha \rangle \langle M_\beta \rangle$ [50].

Hence, the dielectric constant is directly proportional to the variance of the total polarization of the crystal. The variance of the dipole moments $\langle M_\alpha M_\beta \rangle - \langle M_\alpha \rangle \langle M_\beta \rangle$ appearing in Eq. 2.60 signifies that $\epsilon_s^{\alpha\beta}$ does not depend on the magnitude of $\boldsymbol{M}$, hence it does not depend on the choice of the unit cell, as we expect. In fact, the macroscopic polarization is notoriously an ill-defined quantity [43], meaning that it can change depending on the choice of the unit cells in which the crystal is partitioned. However, *changes* in $\boldsymbol{P}$ can still be quantified, even classically. I.e., the quantity $\partial \boldsymbol{P}/\partial \boldsymbol{E}$ can still be evaluated via the dipole moments' fluctuations, Eq. 2.60.

### The dielectric function

When the crystal initially at thermal equilibrium is radiated with light, it is excited with an oscillating electric field. This brings the crystal to a non-equilibrium state, making its energy change. The rate of change of the crystal's energy is the absorption. From linear response

theory and the fluctuation-dissipation theorem, the absorption is related to the autocorrelation function of the dynamical variable which couple to the electric field, namely, the total dipole moment $\boldsymbol{M}(t)$. The permittivity tensor is given by [46, 89, 17, 53, 50, 81]:

$$\chi^{\alpha\beta}(\omega) = \frac{1}{3\epsilon_0 V k_B T}\left(\langle M_\alpha M_\beta\rangle - \langle M_\alpha\rangle\langle M_\beta\rangle - i\omega\int_0^\infty \langle M_\alpha(0)M_\beta(t)\rangle e^{-i\omega t}dt\right). \quad (2.61)$$

Let us consider one of the three diagonal parts of the dielectric tensor. In the assumption that the dielectric response can be fitted to a damped harmonic oscillator (DHO), the dielectric function can be written as [63, 99]

$$\varepsilon_{\mathrm{DHO}}(\omega) = \varepsilon_\infty + \frac{A}{\omega_0^2 - \omega^2 + i\omega\Gamma_0}, \quad (2.62)$$

where $A$ is the strength of the oscillator (proportional to the Born effective charge of the mode [63, 99]), $\omega_0$ and $\Gamma_0$ its frequency and damping constant.

The imaginary part of the permittivity is proportional to the absorption spectrum of light from the crystal [89]. In the assumption of Eq. 2.62, this can be written as

$$\varepsilon''_{\mathrm{DHO}}(\omega) = \chi''_{\mathrm{DHO}}(\omega) + 1 = A\frac{\Gamma_0\omega\omega_0^2}{(\omega^2 - \omega_0^2)^2 + \Gamma_0^2\omega^2}, \quad (2.63)$$

where the subscript $''$ indicates the imaginary part. Eq. 2.63 is the functional form I used to fit the permittivity in Secs. 7.5-8.1.

## 2.10 Molecular dynamics

Molecular dynamics is the method I use in this thesis to obtain atomic positions and velocities. It involves solving Newton's equation of motion to compute the trajectories of the atoms in a material.

The trajectories of the atoms can be simulated when the forces acting on them are known. If the force acting on atom $i$ having mass $m_i$ at time $t$ is $\boldsymbol{F}_i(t)$, then its trajectory $\boldsymbol{r}_i(t)$ is a solution to the equation

$$\boldsymbol{F}_i(t) = m_i \frac{\mathrm{d}^2 \boldsymbol{r}_i(t)}{\mathrm{d}t^2}. \tag{2.64}$$

The set of forces acting on the atoms is the gradient of the potential energy surface, $\{\boldsymbol{F}(t)\} = -\nabla_{\boldsymbol{r}} U(\{\boldsymbol{r}(t)\}) = [\partial U/\partial \boldsymbol{r}_1, \partial U/\partial \boldsymbol{r}_2, \dots]^T$, where each derivative is taken at each one of the three directions of space. Hence, the forces can be calculated analytically if the PES $U(\{\boldsymbol{r}\})$ is known. The PES of my simulations is described in Sec. 2.11.

If one has the capability of evaluating the forces, then the trajectories $\{\boldsymbol{r}(t)\}$ of the atoms can be numerically approximated by, for example, the Verlet algorithm, whose formula is [1, 46]

$$\boldsymbol{r}_i(t + \Delta t) = 2\boldsymbol{r}_i(t) - \boldsymbol{r}_i(t - \Delta t) + \frac{\boldsymbol{F}_i(t)\Delta t^2}{m} + O(\Delta t^4). \tag{2.65}$$

Hence, the position of an atom at time $t + \Delta t$ can be approximated if its position is known at times $t - \Delta t$ and $t$, and the force is know at time $t$. In my simulations, I used an in-house code developed by my first supervisor and his coworkers, which implements the Verlet algorithm.

Despite its apparent simplicity, setting up an MD simulation can be tricky. The Newton's equations of motion, in fact, are valid at constant number of atoms, volume, and energy, hence they simulate the microcanonical ensemble (NVE). Often, it is desirable to simulate other ensembles, like the canonical esnemble (NVT), or the isoenthalpic-isobaric ensemble (NPH), or the isothermal-isobaric ensemble (NPT). Each ensemble represents the states that the system can have when it is in thermodynamic equilibrium with a reservoir. Such reservoir is characterized by having a certain fixed quantity. For example, in the NVT ensemble, the reservoir is

a heat bath having constant temperature $T$. In the NPT ensemble, the reservoir is at constant temperature $T$ and pressure $P$.

There are theoretical and numerical devices that enable to simulate a certain ensemble. I shall not describe all the methods in details, but I give an overview of the ones which I use in my simulations.

### 2.10.1 NVT ensemble

Often it is necessary to work in the canonical ensemble. I simulated the NVT ensemble for MgO (Ch. 3). I here described the two methods I used to approximate, in my MD simulations, such ensemble.

#### Velocity rescaling

A simulation which makes use of velocity rescaling as it is defined in the following is not properly considered a simulation of the NVT ensemble. Velocity rescaling, in fact, is more a "brute force" method to set the temperature to the desired value. The temperature is related to the kinetic energy of the atoms, $K$, by

$$K = \langle \sum_i \frac{|\boldsymbol{p}_i|^2}{2m_i} \rangle = \frac{D}{2} N k_B T. \tag{2.66}$$

In this equation, $\boldsymbol{p}_i$ is the momentum of atom $i$, $D$ is the dimensionality (it is always 3 for us because we work in 3D space), $N$ is the number of atoms, $k_B$ is the Boltzmann constant, and the right hand side results from the equipartition theorem. Note that this form of the equipartition theorem is valid only if the momenta appear squared in the Hamiltonian. This is the case, for instance, of the Hamiltonian of Eq. 2.4.

Eq. 2.66 links the kinetic energy of the atoms to the temperature $T$. If we want the system's temperature to reach the target value $T = T_{\text{target}}$, we could rescale the momenta every so often during the simulation so that the system's temperature is closer to the target $T_{\text{target}}$. In order

to do this, we define an "instantaneous kinetic temperature" [1]:

$$\mathcal{T}(t) = \sum_i \frac{|\boldsymbol{p}_i(t)|^2}{2m_i} = \frac{2\mathcal{K}(t)}{3Nk_B}, \tag{2.67}$$

This "instantaneous kinetic temperature" is not a proper thermodynamic quantity. Its definition is not unique, and as far as we are concerned this needs not even have a physical meaning, but its average gives exactly $T$. Hence, velocity rescaling entails artificially modifying the velocity of the atoms so that $\mathcal{T}(t) = T_{\text{target}}$. In order to do this, the atomic velocities are multiplied by a factor $\beta = \sqrt{T_{\text{target}}/\mathcal{T}}$ every $\Delta t$ time.

Velocity rescaling is not a very sophisticated method, and it does not properly simulate the canonical ensemble [1, 43]. It creates abrupt discontinuities on the atomic trajectories, because atoms are "slapped" every so often. I used it for setting the temperature in equilibration runs, but I never used it for my production runs.

**The Nosé-Hoover thermostat**

The Nosé-Hoover thermostat belongs to the class of methods called "extended Lagrangian formalism". The rationale of such formalism is to find an auxiliary Lagrangian or Hamiltonian which is extended with respect to the original one, because it includes one or more terms. As a result, the extended Lagrangian simulates a *virtual* system. Such virtual system is chosen *ad hoc* so that an average in its microcanonical ensemble, $\text{NVE}_{virtual}$, is equal to an average in the ensemble which we want to simulate, and which here is the $\text{NVT}_{real}$ ensemble. In other words, the microcanonical phase space distribution of the *virtual* system corresponds to the canonical phase distribution of the *real* system. This way, the Newton's equations of motion obtained for the virtual system allow to simulate the NVT ensemble of the real system.

Let us see the example of the Nosé-Hoover thermostat. The *physical* Hamiltonian is that of Eq. 2.4, and the Nosé virtual Hamiltonian is

$$\mathcal{H}_{\text{Nosé}}(\boldsymbol{r}, \boldsymbol{p}, s, p_s) = \sum_i^N \frac{p_i^2}{2m_i s^2} + U(\boldsymbol{r}_1, \ldots, \boldsymbol{r}_N) + \frac{p_s^2}{2Q} + gk_BT \ln s. \tag{2.68}$$

In this equation, I have used the simplified notation $\boldsymbol{r} = \{\boldsymbol{r}_i\}$ and $\boldsymbol{p} = \{\boldsymbol{p}_i\}$ to indicate *all* the positions and momenta of the atoms, and made clear that the Hamiltonian is extended by including, among its variables, a dimensionless quantity, $s$, and its conjugate momentum, $p_s$. $Q$ and $g$ are parameters of the thermostat: $Q$ is a "mass" parameter (although it does not have the dimensions of a mass), and $g$ is a real number, which needs to be set to $3N + 1$ [65]. I will always use no superscript for the virtual coordinates, and a prime $'$ for the real coordinates.

The effect of $s$ is to rescale the real system's momenta, so that one can define the real momentum $\boldsymbol{p}' = \boldsymbol{p}/s$ and obtain the real Hamiltonian $\mathcal{H}_{\text{real}}(\boldsymbol{r}, \boldsymbol{p}')$. Because of this relationship between real and virtual momenta, $s$ can be thought of a parameter which rescales time, $dt' = dt/s$. The strange logarithmical term present in the Nosé Hamiltonian guarantees that the $\text{NVE}_{virtual}$ ensemble corresponds to the $\text{NVT}_{real}$. In fact, we shall see soon that the microcanonical ensemble of the virtual system corresponds to the canonical ensemble of the real system.

The equations of motion coming from Eq. 2.68 are not convenient, because they contain the term $s(t)$ which makes the real system's time fluctuate. For this reason, Hoover [65] modified the Nosé equations of motion by using the equations of motion coming from the Lagrangian of Eq. 2.68, but substituting $\boldsymbol{p}'' \to \frac{p}{s}$ and $dt'' \to dt/s$ (in other words, he neglected the $1/s$ in the Nosé Hamiltonian so that the first part of it resembles the real Hamiltonian, $\mathcal{H}_{\text{real}}(\boldsymbol{r}, \boldsymbol{p})$). These transformations are called non-canonical, because the resulting equations of motion cannot be traced back to a Hamiltonian. The resulting system is called non-Hamiltonian. With this modification, the Nosé-Hoover equations of motion read [46, 138, 65, 85]

$$\begin{aligned}
\dot{\boldsymbol{r}}_i &= \frac{\boldsymbol{p}_i}{m_i} \\
\dot{\boldsymbol{p}}_i &= \boldsymbol{F}_i - \xi \boldsymbol{p}_i \\
\dot{\xi} &= \left( \sum_i \frac{p_i^2}{m_i} - dNk_BT \right) / Q \\
\frac{\dot{s}}{s} &= \frac{d \ln s}{dt}.
\end{aligned} \tag{2.69}$$

In this equation, I removed the subscripts $''$ for simplicity, and $\xi$ is a friction term defined as $\xi = p_s/Q$ [65]. Once again, such equations cannot be derived from a proper Hamiltonian,

because they are obtained from a modification of equations of motion which come from an Hamiltonian. Nonetheless, there is a conserved quantity associated to them, namely, a quantity whose total time derivative is zero during the motion. This quantity is [46, 138]

$$H_{\text{conserved}}(\boldsymbol{r}, \boldsymbol{p}, s, \xi) = \sum_i^N \frac{p_i^2}{2m_i} + U(\boldsymbol{r}_1, \ldots, \boldsymbol{r}_N) + \frac{Q\xi^2}{2} + gk_BT \ln s, \tag{2.70}$$

as it can be shown since $dH_{\text{conserved}}/dt = 0$. Hoover [65] and Martyna, Klein and Tuckerman [85] showed that the canonical density function in phase space, $f_{NVT}$, calculated assuming $H_{\text{conserved}}$ as the energy function, satisfies Liouville's equation. Hence, the equations of motion 2.69 properly sample the canonical ensemble.

Eqs. 2.69 are used when a Nosé-Hoover thermostat is applied. Note that the last equation is decoupled from the first three, so in practice it is neglected. The origin of the denomination "friction coefficient" can be understood by expressing the first two of the Eqs. 2.69 in terms of $\boldsymbol{r}_i$ and $\dot{\boldsymbol{r}}_i$, and noting that, by deriving the first equation with respect to time, we obtain $\ddot{\boldsymbol{r}}_i = \boldsymbol{F}_i/m_i - \xi\dot{\boldsymbol{r}}_i$, which is the equation of motion of a system with damping forces $\xi\dot{\boldsymbol{r}}_i$ applied to its atoms. The friction term then simulates the stochastic collisions which would happen when the crystal is put in contact with a heat bath, and which produce additional damping forces. Such friction term is a proper dynamical variable, since it has its own equation of motion.

The *parameter* of the Nosé-Hoover thermostat is the "mass" $Q$. In the third line of Eq. 2.69, the value of $Q$ defines the time scale of the oscillation of $\xi(t)$. It is more convenient to express $Q$ in terms of the frequency of such oscillations. The "mass" $Q$ is then recast in the following form:

$$Q = \frac{2DNk_BT}{(2\pi f_{\text{Nosé}})^2}, \tag{2.71}$$

where $f_{\text{Nosé}}$ is the frequency of the Nosé-Hoover thermostat. When I apply a Nosé-Hoover thermostat, like in the $BaTiO_3$ simulations of Ch. 7, I always quote its frequency, rather than its mass.

In general, the Nosé-Hoover thermostat is more damped than other thermostats, like the Berendsen one, in the sense that the system's instantaneous temperature $\mathcal{T}$ might take more

time to converge to its target value $T_{\text{target}}$. It can be shown that the Berendsen thermostat produces a completely relaxational convergence, namely $d\mathcal{T}/dt = (\mathcal{T} - T_{\text{target}})/\tau$ [10], where $\tau$ is the Berendsen thermostat parameter; the Nosé-Hoover thermostat, on the other hand, produces an oscillatory relaxation [11] $d^2 \ln \mathcal{T}/dt^2 = \omega^2_{\text{Nosé}}(1 - \mathcal{T}/T_0)$. This means that the time scale needed for the Nosé-Hoover thermostat to converge is higher than for the Berendsen thermostat. However, Hoover has shown that the Nosé-Hoover equations are the *only ones* which properly sample the canonical ensemble [65, 46]. Hence, the Berendsen thermostat does not sample the canonical ensemble correctly, although convergence of $\mathcal{T}$ is more rapid. Moreover, for the simulations I have run, convergence of $\mathcal{T}$ was never a problem, as the simulation time was always much larger than the time taken for the temperature to converge.

Finally, Eqs. 2.69, which are non Hamiltonian, do not guarantee ergodicity. This is an issue, because the sampling of the canonical ensemble is guaranteed if, and only if, the system is ergodic [85]. In other words, only if the system is ergodic a time average over the trajectories defined by Eqs. 2.69 corresponds to a canonical ensemble average. Hoover showed that, in the pathological case of the system being a harmonic oscillator, the integrated Nosé-Hoover equations give trajectories which occupied the available phase space very poorly. This issue prompted Martyna, Klein and Tuckerman to extend the Nosé-Hoover thermostat by considering chains of thermostats, each with its own variable $\xi_i$, and whose $\xi_i$'s are coupled to one another. The method is discussed in Ref. [85]. It did not seem necessary to implement the chains of thermostats in my simulations, so I only used a single $\xi$ thermostat.

### 2.10.2 NPH ensemble

So far, the types of simulations we have discussed are at constant volume, $V$. Most of the experiments, however, are performed at constant $T$ and $P$. Moreover, there are physical processes which involve the variation of the shape and volume of the unit cells constituting the crystal: among such processes are the phase transitions, as it happens to $BaTiO_3$. In these cases, it is necessary to perform simulations at constant $P$, and allow $V$ to fluctuate.

The theoretical/numerical device that allows volume fluctuations in an MD simulation is called

barostat. One of the first authors to ever propose such a device was Andersen [3]. In its form, Andersen's barostat only included fluctuations of the supercell's volume, but not of its shape. Parrinello and Rahman [93] later extended the barostat to allow the supercell's volume *and* shape to change. It is the latter type of barostat that is implemented in the code I used for the simulations.

### The Parrinello-Rahman barostat

The idea that extended Lagrangians could produce virtual systems whose equations of motion could be used to simulate real systems in different ensembles was used by Parrinello and Rahman [93] with the aim of simulating the isoenthalpic (NPH) ensemble.

The rationale behind the Parrinello-Rahman barostat is the same as the one behind the Nosé-Hoover thermostat. Let us consider a virtual system, which we call "scaled" system for a reason that will be clear soon. The scaled system has a Lagrangian built *ad hoc*. Equations relating the scaled dynamical variables $(\boldsymbol{s}, \dot{\boldsymbol{s}})$ to the real dynamical variables $(\boldsymbol{r}, \dot{\boldsymbol{r}})$ allow to always go from one system to the other. Then, it is demonstrated that the virtual Lagrangian correctly reproduces the NPH ensemble of the *real* system, which is the one we want to study, with $P = P_{\text{target}}$.

Let us first introduce the scaled coordinates. The real coordinates of the atoms can be referred to the matrix $\mathbf{h}$, which is a 3×3 matrix containing the values of the supercell's vectors $\mathbf{A}_1$, $\mathbf{A}_2$, $\mathbf{A}_3$ in column. Then, the position of an atom can be expressed as $\boldsymbol{r}_i = \mathbf{h}\boldsymbol{s}_i$, where $\boldsymbol{s}_i$ is the *scaled* coordinate of atom $i$. The volume is $V = \det\{\mathbf{h}\} = \mathbf{A}_1 \cdot \mathbf{A}_2 \times \mathbf{A}_3$. When $P$ is constant, the volume is allowed to fluctuate, hence the supercell matrix becomes time dependent $\mathbf{h}(t)$.

In the case of hydrostatic pressure applied, which is the case I study in this thesis, the Parrinello-Rahman Lagrangian is [93]

$$\mathcal{L}_{\text{P-R}}(\boldsymbol{s}, \dot{\boldsymbol{s}}, \mathbf{h}, \dot{\mathbf{h}}) = \sum_i^N \frac{1}{2}\dot{\mathbf{s}}_i^T(\mathbf{h}^T\mathbf{h})\dot{\mathbf{s}}_i + U(\mathbf{h}\boldsymbol{s}_1, \ldots, \mathbf{h}\boldsymbol{s}_N) + \frac{1}{2}W\text{Tr}\{\dot{\mathbf{h}}^T\dot{\mathbf{h}}\} + P_{\text{target}}\det\{\mathbf{h}\}. \quad (2.72)$$

In this equation, the Lagrangian of the scaled system is extended to include a "virtual piston",

as Andersen called it [3], or a variable supercell, as we should call it, whose mass is $W$ and whose kinetic energy is $T_{\text{cell}} = \frac{1}{2}W\text{Tr}\{\dot{\mathbf{h}}^T\dot{\mathbf{h}}\}$ and whose potential energy is $U_{\text{cell}} = P\det\{\mathbf{h}\} = PV(t)$.

It is important to make a short digression on the Lagrangian of Eq. 2.72, which is essentially an extension of Andersen's equation (which can be found in Ref. [3]) to allow the angles between the lattice vectors $\boldsymbol{A}_i$ to change. The best way to think of this Lagrangian is to see it as describing a system contained into a piston which is allowed to expand/contract. The atomic positions are rescaled on the basis of the equations of motion coming from The Lagrangian. However, Andersen pointed out that the barostat's Hamiltonian does not necessarily have a perfect physical meaning [3]. In fact, the condition $\boldsymbol{r}_i = \mathbf{h}\boldsymbol{s}_i$ implies that $\dot{\boldsymbol{r}}_i = \mathbf{h}\dot{\boldsymbol{s}}_i + \dot{\mathbf{h}}\boldsymbol{s}_i$. Hence, at time $t$, the real velocities depend on the scaled velocities $\mathbf{h}\dot{\boldsymbol{s}}_i$ plus an additional velocity term coming from the "dragging effect" of the piston, $\dot{\mathbf{h}}\boldsymbol{s}_i$. Such term is not present in Eq. 2.72, as Andersen highlighted [3]. Parrinello and Rahman did not comment on the physicality of the Lagrangian, maintaining that if the equations of motion would reproduce the correct ensemble, then that would be good enough.

The Lagrangian of Eq. 2.72 defines the scaled system. To obatin equations for the real system, we need further equations which relate the real and scaled coordinates. These relationships are [138, 3]

$$\boldsymbol{r}_i(t) = \mathbf{h}\boldsymbol{s}_i(t) \tag{2.73}$$

$$\boldsymbol{p}_i(t) = \boldsymbol{\pi}_i(t)\mathbf{h}^{-1}. \tag{2.74}$$

Eq. 2.73 relates the scaled and real positions. Eq. 2.74 is, in my opinion, a deliberate mistake. It is valid if and only if $\mathbf{h}$ is time-independent, but in principle it should contain the piston's dragging effect. Andersen made this clear by reporting them without and with the explicit time dependence, in Eqs. 3.12 and 3.13 of Ref. [3]. These equations are not compatible with the Lagrangian of Eq. 2.72, because in that Lagrangian $\mathbf{h}$ is a dynamical variable with its own equation of motion, and Eq. 2.74 would not be satisfied. However, Eqs. 2.73-2.74 allow to obtain equations of motion for the real system which possess an important and desired quality: an average in the microcanonical ensemble for the scaled system, $\text{NVE}_{scaled}$, corresponds to the

avareg in the isobaric-isoenthalpic ensemble for the real system, NPH$_{real}$. This is proved in Anderesen's paper [3]. So, although the real system's equations of motion are non-Hamiltonian [138], in the sense that they cannot be derived from a proper Hamiltonian, they correctly sample the NPH ensemble.

Taking the the equations of motion coming from the Lagrangian of Eq. 2.72 in $(\boldsymbol{s}, \dot{\boldsymbol{s}})$, and using the Eqs. 2.73-2.74 to refer back to the real system, the equations of motion for the real system can be written as [93]

$$\ddot{\boldsymbol{r}}_i(t) = \frac{\boldsymbol{F}_i}{m_i} - \boldsymbol{M}\dot{\boldsymbol{r}}_i \tag{2.75}$$

$$\ddot{\boldsymbol{h}} = \frac{V}{W}\boldsymbol{h}^{-1}(\boldsymbol{\mathcal{P}} - P_{\text{target}}\boldsymbol{I}). \tag{2.76}$$

In this equation, $\boldsymbol{F}_i = -\nabla U(\boldsymbol{r}_1, \ldots, \boldsymbol{r}_N)$ is the force acting on atom $i$, $-\boldsymbol{M}\dot{\boldsymbol{r}}_i$ is the additional acceleration coming from the barostat, $\boldsymbol{M} = \boldsymbol{h}[\boldsymbol{h}^T\dot{\boldsymbol{h}} + \dot{\boldsymbol{h}^T}\boldsymbol{h}]\boldsymbol{h}^{-1}$, $\boldsymbol{I}$ is the identity matrix, and $\boldsymbol{\mathcal{P}}$ the instantaneous pressure whose components are

$$\mathcal{P}_{\alpha\beta} = \frac{1}{V}\sum_i \left(\frac{p_i^\alpha p_i^\beta}{2m_i} + F_i^\alpha r_i^\beta\right). \tag{2.77}$$

In the simpler case that the volume is allowed to change, but not the shape, the equations, this time in terms of positions and momenta, $(\boldsymbol{r}, \boldsymbol{p})$, simplify to the ones proposed by Andersen [3]

$$\begin{aligned}
\dot{\boldsymbol{r}}_i &= \frac{\boldsymbol{p}_i}{m_i} + \frac{1}{3}\boldsymbol{r}_i\frac{\dot{V}}{V} \\
\dot{\boldsymbol{p}}_i &= \boldsymbol{F}_i - \frac{1}{3}\boldsymbol{p}_i\frac{\dot{V}}{V} \\
\ddot{V} &= \frac{1}{W}\left(\text{tr}\{\boldsymbol{\mathcal{P}}\} - P_{\text{target}}\right).
\end{aligned} \tag{2.78}$$

I quoted Andersen's equations because it is easier to see that the additional effect of the variation of the volume $\dot{V}/V$ on the velocities and accelerations of the atoms, and because it is easier to see that the MD cell undergoes an additional equation of motion which contains the hydrostatic internal pressure $\frac{1}{3}(\mathcal{P}_{\alpha\alpha} + \mathcal{P}_{\beta\beta} + \mathcal{P}_{\gamma\gamma})$ and the target pressure $P_{\text{target}}$. The target pressure is interpreted as the pressure of the bath surrounding the MD cell; whenever there

is an unbalance between the internal pressure $\mathcal{P}$ and the external pressure $P_{\text{target}}$, there is an acceleration of the MD volume, according to the third of Eqs. 2.78.

The cell's mass $W$ is the parameter of the Parrinello-Rahman barostat. It can be shown that, if the compressibility of the material is known, the mass parameter can be converted into a frequency parameter, similarly to the way we converted the "mass" of the Nosé-Hoover thermostat into a frequency in Eq. 2.71. Like in the case of the Nosé-Hoover thermostat, the Parrinello-Rahman barostat gives rise to an oscillatory relaxation of the volume $V$, which usually takes longer to converge than a Berendsen barostat [10]. The code I used for my simulations requires the mass $W$ as input. It is important to recognize that a smaller mass gives rise to a higher frequency of the fluctuations of the volume, and viceversa. Because higher frequency means higher disturbance on the atomic trajectories, much care needs to be taken in setting up this parameter. I discuss this in Sec. 7.2.2.

### 2.10.3 NPT ensemble

The NPT ensemble can be obtained by combining the Nosé-Hoover thermostat and the Parrinello-Rahman barostat. The complete equations of motion and relative conserved quantity can be found in Martyna, Tobias and Klein [86], and in fact are often quoted as MTK equations.

## 2.11 The force field

The force field I used in this work was pioneered by Tangney and Scandolo for silica [130], and subsequently applied for MgO [131], for $TiO_2$ by Han *et al.* [55], and for alumina by Sarsam, Finnis and Tangney [109]. For $BaTiO_3$, the force field's parameters were obtained by Fallon [43].

In the following, I denote $\boldsymbol{r}_{ij}$ the vector of the distance between ion $i$ and ion $j$, and $r_{ij}$ its

module. The form of the force field contains long range and short range terms. Hence:

$$U = U^{sr} + U^{lr}. \tag{2.79}$$

The short range interactions model the Pauli repulsion between electronic clouds when ions are brought closer to one another. The functional form that the force field adopts is the Morse-Stretch potential

$$U_{ij}^{sr} = D_{ij}[e^{\gamma_{ij}[1-(r_{ij}/r_{ij}^0)]} - 2e^{(\gamma_{ij}/2)[1-(r_{ij}/r_{ij}^0)]}], \tag{2.80}$$

where $D_{ij}$, $\gamma_{ij}$ and $r_{ij}^0$ are parameters of the model.

The long range terms are the electrostatic interactions. These are expressed as the sum of the contributions from charge-charge, charge-dipole and dipole-dipole interactions [1]. There are two mechanisms through which a dipole can be induced in an ion: one is via the electric field caused by all the other ions and dipoles, and one is by the short range forces which can deform the electronic cloud when ions are brought together [55]. The first mechanism produces a long range contribution $\boldsymbol{d}_i^{lr}$ and the second a short range contribution $\boldsymbol{d}_i^{sr}$. The long range contribution is

$$\boldsymbol{d}_i^{lr} = \alpha_i \boldsymbol{\mathcal{E}}(\boldsymbol{r}_i), \tag{2.81}$$

where $\alpha_i$ is the polarizability of ion $i$, and $\boldsymbol{\mathcal{E}}(\boldsymbol{r}_i)$ is the local electric field at the atomic site $i$.

The additional dipole moments caused by short range interactions are computed via a model proposed by Wilson and Madden [144], in the following way

$$\boldsymbol{d}_i^{sr} = \alpha_i \sum_{j \neq i} \frac{q_{ij}\mathbf{r}_{ij}}{r_{ij}^3} f_{ij}(r_{ij}), \tag{2.82}$$

where

$$f_{ij}(r_{ij}) = c_{ij} \sum_{k=0}^{4} \frac{(b_{ij}r_{ij})^k}{k!} e^{-b_{ij}r_{ij}}, \tag{2.83}$$

where $b_{ij}$ and $c_{ij}$ are parameters of the model.

Eq. 2.82 can be evaluated fairly easily, but Eq. 2.81 is more complicated, because the electric

field $\boldsymbol{\mathcal{E}}(\boldsymbol{r}_i)$ depends on the charges and dipoles. Hence, determining the dipoles entails knowing the electric field, which in turn depends on the dipoles. The strategy adopted by the force field is to iterate to self consistency, at each MD time step, the equation [130, 55, 109]

$$\boldsymbol{d}_i^{(n)} = \alpha_i \boldsymbol{\mathcal{E}}\left(\boldsymbol{r}_i; \{\boldsymbol{d}_j^{(n-1)}\}_{j\neq i}; \{\boldsymbol{r}_j\}_{j\neq i}\right) + \boldsymbol{d}_i^{sr}. \tag{2.84}$$

Hence, a trial dipoles' configuration is guessed, so that the dipole at each atomic site $\boldsymbol{d}_i^{(1)}$ can be obtained; then, the dipoles $\boldsymbol{d}_i^{(1)}$'s are plugged into Eq. 2.84 to get $\boldsymbol{d}_i^{(2)}$'s, and the process repeats until convergence is achieved to within a tolerance.

Once the dipoles are calculated self consistently, the long range electrostatic interactions are modelled via the dipole expansion

$$E_{ij}^{lr} = \frac{1}{4\pi\varepsilon_0}\sum_{i>j}\left(\frac{q_i q_j}{r_{ij}} + \sum_{\gamma}\nabla_\gamma \frac{d_i^\gamma q_j - q_i d_j^\gamma}{r_{ij}} + \sum_{\gamma,\beta}\nabla_\gamma\nabla_\beta\frac{d_i^\gamma d_j^\beta}{r_{ij}}\right) + \sum_{i,\gamma}\frac{(d_i^\gamma)^2}{2\alpha_i}. \tag{2.85}$$

Here, $\varepsilon_0$ is the vacuum permittivity, $\nabla_\alpha = \partial/\partial r_{ij}^\alpha$, and the last term is the sum of the self energies of the dipoles, namely, the energy cost for inducing a dipole at ion $i$. The long range electrostatic interactions are computed by means of the Ewald summation scheme [1].

**Comments on the force field**

The force field which I use calculates the dipole moments in such a way that the effects of the distortion of the electron clouds caused by the electric field at the atomic sites is included. It also models the further distortion coming from short range forces, which quantum mechanically are caused by the Pauli exclusion principle. Such model can be called distortable-ion model [131], and it is in principle more sophisticated than a shell model [38, 106]. In fact, the short range part of the dipole moment $\boldsymbol{d}_i^{sr}$ depends on the positions of the surrounding atoms (Eq. 2.82), hence it varies depending on the directions of the neighbouring ions $\hat{\boldsymbol{r}}_{ij}$ with respect to the reference ion. This is then an anisotropic contribution. Moreover, although it is a pair potential in its essence, the way the dipoles are calculated (Eq. 2.84) is a many body contribution.

Based on the tests of Refs. [131, 55, 109], the thorough modelling of short range polarization effects has been proven necessary to obtain potential energy functions which are in better agreement with density functional theory (DFT), and phonon frequencies in better agreement with DFT and experiments [131, 55, 109].

The force field's free parameters are $D_{ij}$, $\gamma_{ij}$ and $r_{ij}^0$, $q_i$, $c_{ij}$, $b_{ij}$ and $\alpha_i$. I have not performed the parametrization of the force fields I used. For MgO, I used the parameter set from Tangney and Scandolo [131], and for $BaTiO_3$ I used the one of Fallon [43]. The parameters were obtained by fitting the energies, forces and stresses tensors to DFT data. More details on the parametrization technique can be found in Refs. [131, 43].

The accuracy of the force field for MgO and $BaTiO_3$ will be discussed in the chapters dedicated to these materials, in Sec. 3.3 and Sec. 7.3.

# Chapter 3

# Progressive breakdown of phonon theory in MgO

## 3.1 Introduction

### 3.1.1 Motivation for studying MgO

Magnesium Oxide (MgO) is a prototypical oxide whose vibrational properties are of interest in a wide variety of fields.

Firstly, it is an important geophysical material because magnesiowüstite, (Mg,Fe)O, is one of the major constituents of the Earth's lower mantle, together with (Mg,Fe)$SiO_3$ perovskite [134]. Near the Earth's core-mantle boundary, at a depth of $\approx$ 2900 km, the Mg-based minerals exist at a pressure of up to 130 GPa [134] and temperature up to $\sim$ 3000 K [34]. These conditions are difficult to reproduce in a laboratory, so MgO and other lower mantle minerals have been studied computationally to find key physical properties, such as their melting temperature at 130 GPa, or the speed at which they transmit seismic waves at high $P$ and $T$ [134].

Secondly, MgO has a lot of industrial applications. Its stability in the rock-salt form up to high temperatures makes it an excellent refractory material. For example, MgO is an additive in

the Portland cement which is used in civil engineering. Its high thermal conductivity and low electrical conductivity make it suitable for many other industrial applications.

Thirdly, MgO is a technologically important material. It is used as thermal or electrical insulator or as a substrate for growing superconducting materials or electronic circuits [15]. Another application of MgO is in the field of microwave dielectric devices. The electromagnetic spectrum in the radio and microwave regions has a crucial importance in the field of telecommunication, where metal oxides like MgO are used to fabricate resonators, filters, antennas, etc. [15]. Moreover, MgO has been proposed also as a catalyst for the dissociation of water molecules [116], or as a component of magnetic tunnel junctions, for its high magnetoresistance [149].

Finally, we study MgO for its simplicity. It is a strong ionic material with a stable rocksalt structure up to its melting point (and at room temperature up to more than 227 GPa [71]). Therefore, it is a natural starting point for studying vibrational properties of oxides at extreme conditions. We shall see that much of the understanding which comes from the study of MgO can be extended to other materials with a similar degree of ionicity and hence a similar bonding type, such as CaO or other bi-atomic oxides or the alkali halides (e.g. NaCl and KBr [146, 145] and NaBr [115]), which show similar experimental behaviours (see Secs. 3.5 and 9.2). Most importantly, many of the theoretical concepts which we will explore in this chapter are rather general, and will be useful in the rest of this thesis: visualizing the melting of the phonon bands in MgO will guide our understanding of band melting in $BaTiO_3$, which we will deal with in Ch. 7.

### 3.1.2 Experimental literature review

The vibrational properties of MgO have been the object of a considerable amount of experimental and theoretical research.

**Inelastic neutron scattering and X-ray scattering**

From an experimental point of view, there are in the literature many inelastic neutron scattering (INS) studies performed on MgO. Among these, the one of Sangster *et al.* [106], who were the first to use "hot neutron" sources (see also appendix D) to study an MgO single crystal. The hot neutrons allowed the authors to measure phonon spectra, including those of the highest-frequency LO modes, along the main directions {100},{110},{111} of the BZ [106], and hence to measure the band structure of MgO at room $T$ along the high symmetry path $\Gamma-X-X^*-\Gamma-L$, which I show in the bottom right plot of Fig. 3.5. Their study also allowed to investigate the quality of different models of ion-ion interactions. Their analysis indicates that a simplistic rigid-ion model is not sufficiently accurate to describe atomic interactions in MgO. Instead, they concluded that a shell model, whereby the electronic distortion of the anion is mimicked by a classical spherically symmetric distortion of the ion's shell ("breathing shell model"), reproduces very well the experimental data [106]. This is a first indication that accounting for the distortion of the electrons' cloud, for example via a polarizable-ion force field, is necessary to compute with accuracy the interionic forces in MgO, which in turn determine the frequencies of its lattice vibrations.

Mei *et al.* [90] and Bosak *et al.* [14] performed inelastic X-ray scattering (IXS) experiments with synchrotron radiation to infer the vibrational properties of MgO. Their analysis allowed to obtain the phonon density of states and other thermal properties like the heat capacity. Mei *et al.* considered a theoretical model of MgO for their calculations and fitted the IXS data to equations which are valid only within the harmonic approximation, and their temperature range was $10 < T < 400$ K [90]. Bosak *et al.* did not go beyond $T = 935$ K.

**Recent reflectivity studies**

The group of P. Giura have recently performed infrared reflectivity [52, 16] measurements on MgO single crystals. From their analysis of the reflectivity, Giura *et al.* obtained in 2019 the optical conductivity [52] at room $T$, and Calandrini *et al.* obtained in 2021 the frequency-

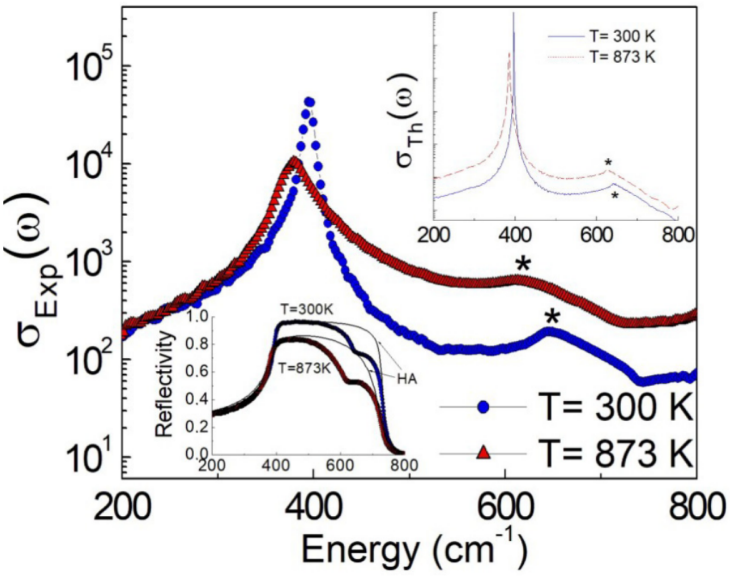



Figure 3.1: Experimental optical conductivity $\sigma_{\text{exp}}$ of MgO at room $T$, taken from Giura *et al.* [52]. The upper right inset shows their calculated spectrum. The bottom left inset shows the raw reflectivity obtained from the experiment, to which they applied the Kramers-Kronig relations to obtain $\sigma_{\text{exp}}$ [89, 52]. The excess of spectral weight (ESW) is denoted by '*' symbols.

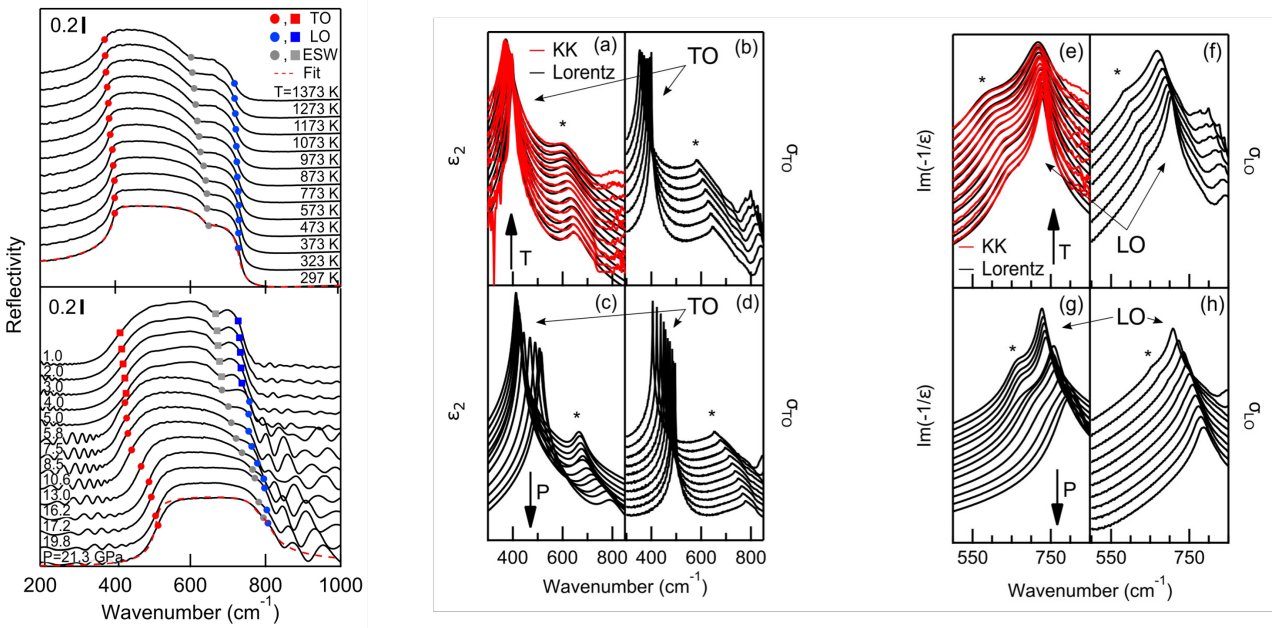



Figure 3.2: Reflectivity (left) and optical spectra (right) of a MgO single crystal obtained at various $T$s and $P$s, taken from Calandrini *et al.* [16]. In the right hand side, plots (a) and (c) show the imaginary part of the dielectric function, $\varepsilon_2$ as a function of $T$ and $P$, respectively; these plot contain only TO modes. Plots (e) and (g) show the imaginary inverse loss function, defined as $1/\varepsilon = (\varepsilon_1^2 + \varepsilon_2^2)/\varepsilon_2$, which contains information about LO modes, as a function of $T$ and $P$, respectively; the peaks of these plots correspond to LO modes. The other spectra are theoretical calculations of the similar quantities. The red lines are the result from a Kramer-Kronig analysis, the black lines are Lorentzian fits to the spectra. The excess of spectral weights (ESWs) are denoted by '*' symbols.

dependent dielectric function [16] at various temperatures and pressures. The optical conductivity, being proportional to the absorption spectrum of light, contains information about the TO modes at the BZ center, and the real and imaginary parts of the dielectric function allow to collect information about the TO and LO and modes at the BZ center.

The findings of Refs. [52, 16] are very interesting: an excess of spectral weight (ESW) was found in the optical spectra at frequencies slightly lower [52, 16] and higher [16] than the LO mode frequency. An ESW is an additional peak in the spectra which is not predicted by the harmonic theory of the phonons. The ESW can be seen in Fig. 3.1, which reports the experimental spectra of Ref. [52]. The plot shows the experimental optical conductivity, obtained from a Kramer-Kronig analysis of the reflectivity function, which is shown in the bottom left inset. Within the HA, the reflectivity is predicted to increase at the frequency of the TO mode, to be maximum and almost constant in the frequency region between the TO and the LO (the reststrahlen plateau), and to tail off after the LO modes' frequency [83]. In the reflectivity measurement, the ESW manifests itself as an additional shoulder to the reststrahlen region, which cannot be predicted within the HA (denoted by a black line in the inset of Fig. 3.1). When the absorption spectrum or the optical conductivity is obtained from the reflectivity, the ESW shows up as an additional peak indicated in Fig. 3.1 by a '*'.

On the left hand side of Fig. 3.2, which reports the results from Ref. [16], the reflectivity is shown as a function of $T$ and $P$. An ESW, drawn with grey symbols, was found in all spectra again. The right hand side of the same figure shows the measured imaginary part of the dielectric function $\varepsilon_2$ as a function of $T$ (plot a) and $P$ (plot c), and the inverse loss function $1/\varepsilon = (\varepsilon_1^2 + \varepsilon_2^2)/\varepsilon_2$, where $\varepsilon_1$ is the real part of the dielectric function, as a function of $T$ (plot e) and $P$ (plot g). The other spectra are theoretical calculations of the similar quantities. The red lines are the result from a Kramer-Kronig analysis, the black lines are Lorentzian fits to the spectra. The ESW is again denoted with a '*', and it lies at frequencies higher than the TO (plots a and c) and slightly lower than the LO (plots e and g). Note also that another extra band, outside the reststrahlen region, was found (see e.g. plot f), but the authors deferred its analysis to further dedicated studies.

Let us now discuss how these authors interpreted the ESW. If we look back at the bottom left inset of Fig. 3.1, it is clear that the solid black lines denoting the HA calculation are not able to predict the additional ESW shoulder, which is found in the experimental blue and red dotted lines. Hence, the existence of a ESW was interpreted as the result of a multiphonon process. Multiphonon processes are contributions to the absorption of light by a crystal whereby a photon of real momentum $\hbar\boldsymbol{k}$ and energy $E$ is absorbed with the creation of two phonons of crystal momenta $\hbar\boldsymbol{q}_1$ and $\hbar\boldsymbol{q}_2$ and energies $\hbar\omega_{\boldsymbol{q}_1\nu_1}$ and $\hbar\omega_{\boldsymbol{q}_2\nu_2}$. In order for this to occur, the process must fulfill the conservation of energy $E = \hbar\omega_{\boldsymbol{q}_1\nu_1} + \hbar\omega_{\boldsymbol{q}_2\nu_2}$ and momentum $\boldsymbol{k} = \boldsymbol{q}_1 + \boldsymbol{q}_2$ [52]. In other words, in a multiphonon process the photon excites a pair of phonons, rather than just one phonon. Of course, multiphonon processes occur with lower probability than single phonon processes, hence their signature, the ESW, produces a weaker signal. Because the wavevector of a photon in the IR range, which is the energy range of the phonons, is much smaller than the dimension of the BZ, the photon's wavevector can be considered vanishing, $\boldsymbol{k} \approx 0$, and so the conservation of momentum reads $\boldsymbol{q}_1 \approx -\boldsymbol{q}_2$. Now, if there are many phonons with equal and opposite wavevector, $\boldsymbol{q}$ and $-\boldsymbol{q}$, and whose energies sum up to $\omega_{\boldsymbol{q}\nu_1} + \omega_{-\boldsymbol{q}\nu_2} = E/\hbar$, then many decay channels open for the photon. The presence of an ESW shows that this is indeed the case.

The multiphonon contribution to the absorption spectrum is also an indication of anharmonicity. In fact, if a phonon near $\Gamma$, $\boldsymbol{q} \approx 0$, exists whose frequency is close to $E/\hbar$, then the conservation of momentum and energy for phonon-phonon scattering is exactly the same as the conservation of momentum and energy for the photon which we just described (cf. Sec. 2.5.1). Hence, the same decay channels open for this phonon. In the case of MgO, the long wavelength LO mode, LWLO, is at a frequency, $\omega_{\mathrm{LWLO}}$, very similar to the frequency $E/\hbar$ of the ESW. Hence, this mode has approximately the same decay channels of a photon, and we can expect it to be highly damped.

To summarize, the IR reflectivity spectra of Giura *et al.* and Calandrini *et al.* found evidence of multiphonon contributions in the vibrational spectra of MgO, and this is a hint that the LO mode might be very anharmonic.

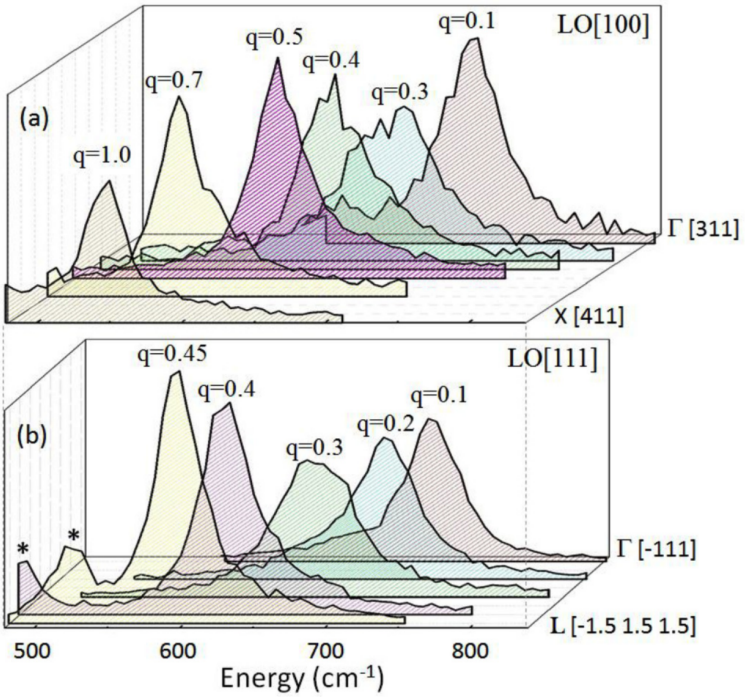



Figure 3.3: The spectra of the LO mode obtained from IXS, taken from Giura *et al.* [52], obtained for various $\boldsymbol{q}$-points in the {100} and {111} directions of the BZ. The LO is damped near Γ, it is maximally damped at $\boldsymbol{q} = \frac{3}{10}\boldsymbol{k}_X$ and $\boldsymbol{q} = \frac{3}{10}\boldsymbol{k}_L$, and minimally damped at $X$ and $L$.

### IXS spectra of the LO mode

Of course, the presence of decay channels for the LO mode is not a sufficient condition for the high broadening of the mode, but it is a necessary condition. In fact, as we saw in Sec. 2.5.1, the linewidth of a mode is proportional to the TPDOS, which quantifies the number of decay channels which fulfill energy and momentum conservation. The damping of the LO mode was further investigated by Giura *et al.* by means of high-resolution inelastic X-ray scattering [52]. The experimental spectra of the LO mode are reported in Fig. 3.3, and show a relatively large broadening of the LO mode, and a very non-monotonic broadening across the BZ, manifesting a high degree of anharmonicity for this mode.

In particular, it was found that the LO dampens a lot in regions of the BZ near the BZ center: it reaches the maximum broadening at $\boldsymbol{q} = \frac{3}{10}\boldsymbol{k}_X$ and $\boldsymbol{q} = \frac{3}{10}\boldsymbol{k}_L$, where $\boldsymbol{k}_X$ and $\boldsymbol{k}_L$ represent the $X$ and $L$ points, and its line shape becomes narrower at the BZ boundaries. This interesting anomalous broadening confirms the opening of decay channels for the LO found by reflectivity

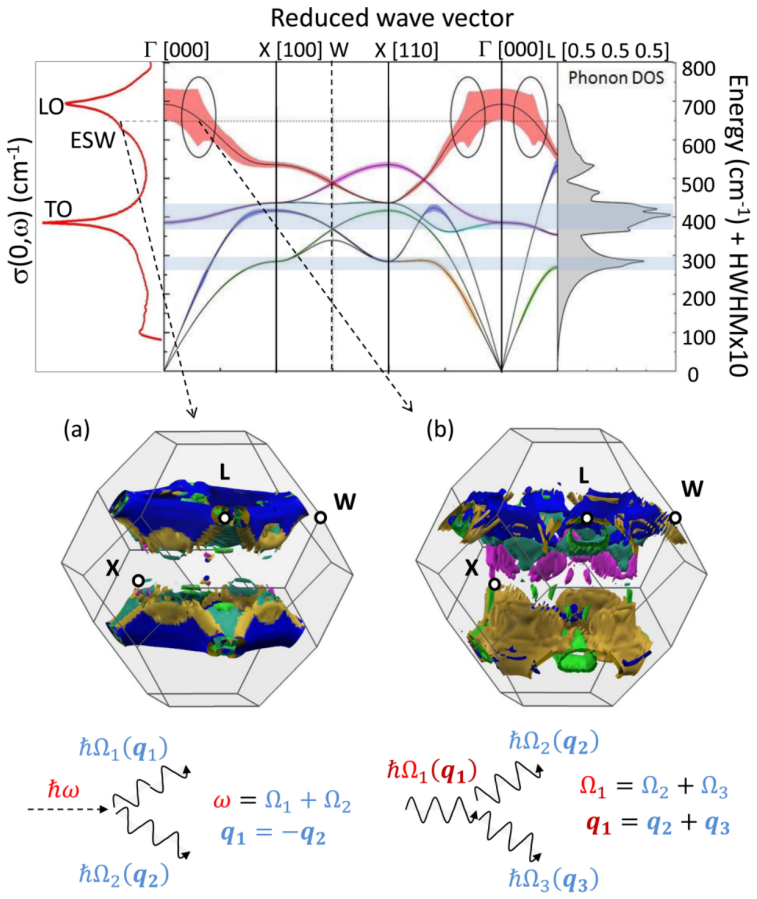



Figure 3.4: Theoretical results from Giura *et al.* [52]. The variable-width bands in the dispersion plot denote the linewidths of the corresponding phonons. The left panel shows the optical conductivity and the right panel shows the global DOS. The middle 3D plots show the MgO BZ, in which coloured surfaces denote the final state decomposition of the LO phonon at the Γ point and at the $\boldsymbol{q}$-point indicated by the dotted arrow. The bottom sketches denote the photon-phonons absorption process which is deemed to produce the ESW and the phonon-phonon scattering which produces the broadening of the LO.

measurements, and shows that the LO is very anharmonic, at least near Γ. This deserves an explanation; I dedicate a whole section to the LO mode, Sec. 3.5.

In general, the experimental evidence is that phonon-phonon interactions play an important role in the lattice dynamics of MgO, especially for the highest-energy mode, namely, the LO mode.

**Theoretical literature**

From a theoretical point of view, the experimental findings imply that the HA is not adequate when the temperature is raised so that anharmonicity is not negligible, a scenario which seems to happen already at room temperature [52].

Theoretical attempts to go beyond the HA by performing QHA calculations were undertaken by Karki *et al.* [71], and Erba *et al.* [41]. They proved themselves adequate for the prediction of thermodynamic properties of MgO only up to 1000 K, such as the heat capacity, thermal expanasivity or bulk modulus [71, 41], but they fail at higher temperatures and they cannot compute the phonon linewidths. This is because the QHA is a band theory, and hence it assumes that phonons do not interact with each other, but that their frequencies only change as a function of the volume.

Phonons linewidths can be computed with *ab initio* methods like DFPT within the framework of PT, but it is well known that perturbation treatments become intractable when the number of anharmonic terms to be considered becomes large. Giura *et al.* [52] evaluated the leading-order contribution to the anharmonic Hamiltonian, i.e. the "bubble" diagram, and calculated the phonon broadening up to a $T = 873$ K. The results are shown in Fig. 3.4. The width of the bands in the dispersion plot of the figure indicates the linewidths of the phonons computed at $T = 873$ K. The LO modes, denoted in red, are by far the most anharmonic ones, in accordance with experiments. Interestingly, the broadening of the LO is maximum not *at* the $\Gamma$ point, but *near* it. The grey, horizontal shaded areas are a guide for the eye for the phonon DOS, and highlight the van Hove singularity at $\approx 300$ cm$^{-1}$ and $\approx 400$ cm$^{-1}$. The sum of the two frequencies almost perfectly matches the frequency of the LO, indicating that many decay channels open for this mode. The middle plots represent the MgO Brillouin zone, in which surfaces are drawn that denote the final state decompositions of the LO mode at $\Gamma$ and of the LO mode near $\Gamma$. The color scheme is consistent with the upper dispersion. The final state decomposition quantifies the number and position in the BZ of the pairs of modes into which the LO can decay. The larger the area of the surfaces, the more decay channels are available. The bottom drawings sketch the processes which contribute to the ESW and to the

LO linewidth, that is, photon-phonon absorption and phonon-phonon scattering.

### 3.1.3 Gaps in the literature

Both theory and experiments clearly found that anharmonicity plays an important role in MgO. The most striking feature observed experimentally and theoretically is a high broadening of the LO mode.

Anharmonicity is triggered by temperature, and as long as $T$ is low enough, MgO can be considered a fairly harmonic material. In fact, from an experimental point of view, the HA formulae used to interpret the IXS results of Mei *et al.* were successful, but only up to a maximum temperature $T_{\max} = 400$ K [90]. Other experiments, like the one of Bosak *et al.*, were performed at $T = 935$ K [14].

From a theoretical point of view, the QHA is in strikingly good agreement with experiments at $T < 1000$ K [71, 41]. As for the phonon linewidths, the relatively low anharmonicity of MgO allowed Giura *et al.* the use of PT with success, at $T = 300$ K and $T = 873$ K [52]. However, phonon-phonon scattering has only been assessed theoretically within PT. PT is limited by the requirement that the strengths of phonon-phonon interactions are small.

If we consider that the melting temperature of MgO is $T_m \approx 3100$ K at ambient pressure [134], we have to recognize that there is a temperature range, $1000 < T < 3100$ K, amounting to more than 2000 K, where the vibrational spectrum of MgO, to my knowledge, has never been computed or measured. It has never been measured nor calculated because investigating phonon-phonon interactions at very high $T$ is neither simple theoretically nor simple experimentally. It is not simple experimentally, because the melting temperature of MgO is high, and high temperatures can be difficult to reproduce in a laboratory. It is not simple theoretically, because the bubble approximation, with which phonon linewidths are calculated most of the time [52, 78, 95, 18, 13], breaks down at high $T$, when higher-order terms in the potential expansion become non negligible. If we look back at Fig. 3.4, we immediately observe that the LO is much broader than the TO. If the bubble calculation is performed at high $T$, the ratio

between the linewidths of the LO vs the TO can only increase. On the contrary, we expect that higher-order contributions, like four-phonon processes, might become relevant at high $T$ and change the ratio between the linewidth of the LO and that of the TO modes.

Classical MD with near DFT precision, which is the method I use here, does not have the limitations imposed by having to reach extreme experimental conditions or by the range of applicability of PT. I showed in Sec. 2.6 that the approach of the FT-VVCF computed after classical MD simulations is completely general, being applicable at any condition of temperature and pressure, and even for liquids. The FT-VVCF allows us to compute the kinetic energy distribution in reciprocal spacetime, and classical MD strikes an excellent balance between accuracy and the need for reaching larger length- and time-scales. Here, we shall see a concrete example for MgO.

### 3.1.4 Chapter's overview

To give an overview of this chapter, we here investigate strong phonon-phonon interactions in MgO by computing the distribution of vibrational energy $\tilde{\mathcal{E}}(\omega, \boldsymbol{k}; T)$ at temperatures well beyond the limits of PT. I discuss the details of the MD simulations and of the calculations in Sec. 3.2 and the accuracy of the force field in Sec. 3.3. I show the results in Sec. 3.4, and then focus on one specific feature of the spectra, the broadening of the LO mode, in Sec. 3.5. I treat the phonons as quasiparticles and show the frequency shifts and linewidths in Sec. 3.6, and finally I assess the accuracy of the hierarchy of methods HA, QHA and QPA in Sec. 3.7.

## 3.2 Simulation and calculation details

### 3.2.1 MD

MD simulations were performed using the classical polarizable-ion potential whose mathematical form is described in Sec. 2.11. Its parameters were fitted to an effectively-infinite dataset

of forces, energy differences and stress tensors calculated from density functional theory using the PBEsol functional. The force field's parameters are provided in Appendix A.

I simulated under periodic boundary conditions and the supercell is a $N_c = N_1 N_2 N_3 = 10 \times 10 \times 10$ repetition of the 2-atom rhombohedral primitive unit cell. I used the velocity rescaling algorithm (cf. Sec. 2.10.1) followed by $\approx 10$ ps of equilibration in the NVE ensemble to prepare for $\approx 100$ ps production runs at each temperature. The production runs are also performed in the NVE ensemble and the reported values of the temperature are calculated from the average of the kinetic energy of the production runs. I used a time step of 0.725 fs for MD and sample the positions every 10 steps for later analysis. The velocities are obtained from finite differences of two successive snapshots of the atomic positions.

I performed one set of simulations at volumes $V(T)$ at each temperature chosen such that the average pressure $P$ is close to zero. I chose to perform NVE simulations with a volume tuned so that $P \approx 0$, instead of NPE simulations, for specific reasons: although the magnitudes of the fluctuations of each primitive cell's volume would be reduced, to some degree, by simulating with the supercell volume fixed, this was deemed preferable to polluting the spectra with unphysical artefacts of an MD barostat. The averages of $(T, P)$ are (100 K, 0.014 GPa), (301 K, -0.011 GPa), (502 K, -0.018 GPa), (1004 K, 0.158 GPa), (1995 K, 0.104 GPa), (2998 K, -0.059 GPa), (3521 K, 0.164 GPa) and finally (3813 K, 6.67 GPa), for the liquid phase of MgO. The pressure is large in the highest temperature simulation because the crystal has melted and I did not repeat the simulation with the volume adjusted for the liquid phase. The fact that the pressures of the simulations is not exactly zero, but $P \neq 0$, imposes an error in the simulated volumes, with respect to the condition $P = 0$. The volumetric error can be estimated as $|\Delta V/V| = P/B$, where $B \approx 160$ GPa [71] is the bulk modulus of MgO. The maximum estimated percentage error in the simulated volume with respect to the condition $P = 0$ is $\approx 0.1\%$, and therefore we can be confident that we reproduce well the zero pressure conditions.

Another set of simulations is carried out at the equilibrium $(T = 0, P = 0)$ density, this time keeping the volume fixed at the relaxed configuration of the atoms, i.e., at the volume that minimizes the enthalpy with respect to atomic positions. The averages of $(T, P)$ are in this

case (100 K, 1.125 GPa), (301 K, 2.441 GPa), (506 K, 3.765 GPa), (1008 K, 6.922 GPa), (1982 K, 12.791 GPa), (2986 K, 18.602 GPa), (3458 K, 21.285 GPa).

### 3.2.2 Lattice dynamics

#### HA calculation

To obtain the phonon band structure within the HA, I first relaxed the supercell to mechanical equilibrium $T = 0, P = 0$. Then, I calculated the dynamical matrix with this structure from finite differences of forces after displacing atoms slightly from equilibrium. To avoid artefacts of interpolation, I only plot the frequencies at commensurate $\boldsymbol{k}$-points, but increase their density in reciprocal space by calculating the phonon bands on $N \times N \times N$ supercells for $N \in \{6, 7, 8, 9, 10, 11\}$. The phonon dispersions are shown along the high-symmetry path $\Gamma \to X \to X^* \to \Gamma \to L$. Here $X^*$ is the the closest $X$ point in the BZ contiguous to the reference BZ, and the direction $\Gamma - X^*$ is the $\{110\}$ direction. These points correspond to the points $[0, 0, 0] \to [0.5, 0, 0.5] \to [0.5, 0.5, 1] \to [0, 0, 0] \to [0.5, 0.5, 0.5]$ in scaled coordinates of the primitive Brillouin zone (BZ) vectors, or equivalently to $[0, 0, 0] \to [1, 0, 0] \to [1, 1, 0] \to [0, 0, 0] \to [0.5, 0.5, 0.5]$ in scaled Cartesian coordinates in reciprocal space.

#### QHA calculation

As we discussed in Sec. 2.4, the QHA simply amounts to calculating the phonon band structure at the volumes that minimize the free energy $F(V, T)$, defined in Eq. 2.18. I calculated the free energy under the assumption that phonons do not interact with one another and that the vibrational energy is distributed among the phonon bands according to Bose-Einstein statistics. Therefore, when the QHA is applied we assume that band theory is a good approximation and I computed the phonon bands as a function of volume, $\omega^{\mathrm{QHA}}_{\boldsymbol{q}\nu}(V)$. I then used these frequencies in Eq. 2.18, which is exact in the $T \to 0$ limit where band theory is exact, to find the volume that minimizes $F(V, T)|_T$. For the QHA computation, to make the comparison with the MD supercell possible, I used again a $10 \times 10 \times 10$ supercell, and performed the summation in Eq.

2.18 with a commensurate $10 \times 10 \times 10$ regular grid of $\boldsymbol{k}$-points. This allows consistence with the MD supercell, which is of the same size. The free energy curves at fixed temperature $F(V)$ were obtained by isotropically varying the conventional lattice parameter of $\delta a = 0.02$ Å, from -3 $\delta a$ to 18 $\delta a$, and I interpolated between these values with cubic splines.

**Density of states (DOS) and two-phonon density of states (TPDOS)**

To calculate the total phonon DOS, I use Eq. 2.38, which is valid within the HA, and plot it alongside the FT-VVCF calculated from Eq. 2.29 for comparison with the fully-anharmonic method. The results are the harmonic phonon DOS and the MD DOS. The TPDOS for the summation and difference processes are defined in Eq. 2.20, with variable $\omega$ instead of $\omega_\lambda$.

The commensurate $10 \times 10 \times 10$ regular grid of $\boldsymbol{k}$-points is a poor $\boldsymbol{k}$-point sampling for the calculation of the DOS. To converge the results and achieve a smoother curve for the DOS, the common method is to Fourier interpolate to a denser grid in reciprocal space. Hence, to obtain the harmonic phonon DOS, I interpolated the force constant matrix obtained with the commensurate $10 \times 10 \times 10$ supercell to a denser $30 \times 30 \times 30$ regular grid of $\boldsymbol{k}$-points. The MD results, on the other hand, are never interpolated. In all cases, the real space supercell I used for the interatomic force constants was the $10 \times 10 \times 10$ supercell, in order to be comparable to the MD supercell.

**LO/TO splitting**

The supercell calculation does not account for the LO-TO splitting at $\Gamma$. Hence, when I consider the LO mode at $\Gamma$ from MD, the LO/TO splitting is not present. When it is necessary to do so, I apply the non-analytical correction by adding the non-analytical term to the force constants, whose equation can be found in Refs. [143, 7, 23].

### 3.2.3 VVCF and its Fourier transform

I computed the VVCF spectra exploiting the convolution theorem [1], using the fast Fourier transform. The resolution in reciprocal ($\boldsymbol{k}$-) and frequency ($\omega$-) space is determined by the size of the supercell and the length of the simulation, respectively. In $\boldsymbol{k}$-space, owing to the $10 \times 10 \times 10$ MD supercell, I was able to sample six commensurate $\boldsymbol{k}$-points between $\Gamma$ ($[0, 0, 0]$) and $X$ ($[0.5, 0, 0.5]$), $\Gamma$ and $X$ included. In $\omega$-space, on the other hand, the resolution is $1/\mathcal{T}$, where $\mathcal{T}$ is the duration of the simulation; in the present case, the resolution is $\approx 0.01$ THz. The fast Fourier transform produces noisy spectra: this is a result of imperfect statistics, due to the finite simulation time. There are several ways of smoothing a spectrum, such as applying a windowing function to the velocity data or the use of the maximum entropy method [1]. Here, the power spectra are convolved with Gaussians, whose standard deviation $\sigma$ was chosen as small as possible, in order to preserve the quality of the original spectra: I chose $\sigma = 0.05$ THz for $T \lesssim 1000$ K and $\sigma = 0.1$ THz for $T \gtrsim 1000$ K.

## 3.3 Sources of imprecision of the force field

MD, like any method for simulating materials, is not free from flaws and imperfections. We shall here comment on the possible sources of imprecision of the present simulations.

The first limitation is the use of a relatively simple functional form to describe interatomic interactions. The accuracy with which our force field predicts phonon frequencies at 300 K is evident in the bottom-right panel of Fig. 3.5, where I compare the present calculation with measured phonon frequencies and with those calculated using *ab initio* DFPT. The underestimation of longitudinal optical (LO) frequencies at small wavevectors is common for force fields of this kind [109, 131], and has been discussed in Ref. [109]. It is likely to be caused by the induced dipoles of the force field overscreening the long wavelength electric field that LO phonons create, and which increases the energies of LO phonons relative to transverse optical (TO) phonons.

| | 0 K | 100 K | 300 K | 500 K | 1000 K | 2000 K | 3000 K | 3500 K | 4000 K |
|---|---|---|---|---|---|---|---|---|---|
| $a_{\mathrm{QHA}}$ | 4.2294 (0.0) | 4.2296 (0.02) | 4.2350 (0.40) | 4.2441 (1.05) | 4.2726 (3.10) | 4.3557 (9.24) | - | - | - |
| $a_{\mathrm{MD}}$ | 4.2119 (0.0) | 4.2202 (0.59) | 4.2305 (1.33) | 4.2410 (2.09) | 4.2670 (3.98) | 4.3296 (8.62) | 4.4120 (14.9) | 4.4640 (19.1) | |

Table 3.1: Comparison between QHA and MD lattice constants, in Å. The numbers in brackets are the percentage changes in volume with respect to the $T \to 0$ volume. The bigger value of the QHA equilibrium volume is caused by the additional contribution of the zero-point energy, which is absent in classical MD. Note that the QHA overestimates the volumes at all $T$s, but the lattice expansivity (proportional to the numbers in brackets) is smaller than the one predicted by MD, up to temperatures in between 1000-2000 K.

The accuracy with which our force field describes thermal expansion is evident from Table 3.1. Its accuracy for other properties and at higher $T$ is more difficult to assess because I have neither other calculations nor experimental measurements to compare with. However, force fields of the same mathematical form, and parameterized in the same way, were successfully used in Refs. [131] and [134] for MgO. They accurately predict the pressure dependence of the crystal's volume and of the melting temperature, and to produce pair correlation functions for molten MgO in very good agreement with those produced by *ab initio* MD simulations.

To parameterize the force field used for MgO, DFT data was calculated with the PBEsol functional [97], which tends to be more accurate than the local density approximation used in Refs. [131] and [134]. Furthermore, the fit to the parameters to DFT calculations were obtained for crystalline MgO, whereas those used in Refs. [131] and [134] were required to describe MgO in both molten and crystalline forms, which meant compromising on the accuracy with which each phase was described. The tests performed here and in those previous works suggest that, at worst, the force field I am using in this thesis should be regarded as describing an oxide like MgO. I also suggest that some of the gross features of the $T$-dependence of the spectra calculated with it, including those that I have selected for the discussion below, are caused by simple physical mechanisms that would occur in other ionic crystals and therefore might be present in their vibrational spectra, too.

A second limitation of my calculations is that the MD simulations are classical simulations. Therefore, their accuracy at low $T$ is questionable. However, when $T$ is comparable to, or greater than, the Debye temperature ($\Theta_D \approx 760$ K [20]), which is the range of most interest for studying the breakdown of band theory, this approximation should not affect the results significantly.

Furthermore, I will show in Sec. 3.7.1 that the heat capacity calculated from the quasiparticle energies extracted from MD simulations is in very good agreement with measurements at all values of T between 300 K and 1800 K.

We should regard the use of a supercell of finite size in the MD simulations as by far the most important source of inaccuracy in the vibrational spectra presented. It means that the only lattice waves present in the MD simulations are those whose wavevectors are commensurate with the supercell. The use of a $10 \times 10 \times 10$ supercell means that the longest finite wavelength among the phonons in my simulation was only ten times the length of a primitive lattice vector. To make clear that I only calculate spectra at a finite number of points in $(\omega,\boldsymbol{k})$-space I have pixelated the spectra, with one pixel centered at each commensurate $\boldsymbol{k}$-point. However, the absence of any vibrations at incommensurate $(\omega,\boldsymbol{k})$-points would change how energy is distributed among the commensurate set of points; for example, in a real crystal there would be far more channels (modes) through which energy and momenta could be exchanged.

## 3.4 Results

This section is organized as follows: I first present the main result of this chapter, the distribution of vibrational energy, $\tilde{\mathcal{E}}(\boldsymbol{k},\omega;T)$, for the temperatures considered in the constant pressure ($V(T)$) simulations, in Sec. 3.4.1, and in the constant volume ($V(0)$) simulations, in Sec. 3.4.2. In these sections, I briefly outline some of the gross features which are then discussed in subsequent sections. Among these is the presence of a highly anharmonic phonon, the LO mode near the BZ center, to which I dedicate Sec. 3.5, where I show its spectrum and provide two possible explanations for why this phonon shows a large broadening. In Sec. 3.6, we look at the quasiparticle approximation of the phonons (QPA), after fitting the phonon spectra to Lorentzian functions. I demonstrate the breakdown, at high $T$, of the QHA by comparing it with the finite-$T$ phonon quasiparticle frequencies. Finally, in Sec. 3.7, I use the quasiparticle frequencies to calculate the fully-anharmonic isobaric heat capacity, which is compared to the measured one; this will enable to assess the temperature range of validity of the QPA.

### 3.4.1 Phonon spectra at finite temperatures in the $V(T)$ simulations

In this section, we are going to see the progressive melting of the phonon bands when MgO is heated. Details of the simulations and calculations were given in Sec. 3.2. The spectra are presented in Fig. 3.5, where regions of high and low $\tilde{\mathcal{E}}(\boldsymbol{k},\omega;T)$ are coloured dark blue and white, respectively. The plots appear pixelated because of the finite size of the supercell and simulation length (cf. Sec. 3.2.3). For comparison with the HA and QHA, the HA phonon frequencies and the finite-$T$ QHA phonon frequencies are drawn on top of the spectra with red and green triangles, respectively. I here start discussing some gross features of the spectra, and will then focus on some other selected features in subsequent sections.

Fig. 3.5 shows the progressive transition from two limiting conditions: the low $T$, where phonon bands are well defined, and very high $T$, where phonon bands are less well or not defined. At $T = 100$ K, the phonon dispersion does not substantially differ from the $T \to 0$ one, all the phonon line shapes are very narrow and their peaks are approximately at the harmonic frequencies. At $T = 3800$ K, on the other hand, it is not possible to recognize any phonon band[1]. This is because the spatial and temporal correlations are short when the crystal has melted, and so the phonon assumption of atoms moving altogether in the form of plane waves breaks down.

This confirms the prior observation which we discussed in Sec. 1.1. When the energy spreads out from the point in reciprocal spacetime at which it was localized in the $T \to 0$ limit, it means that the collective motions that possess this energy are becoming less wavelike and more localized in spacetime. In the low-$T$ limit, $\tilde{\mathcal{E}}(\boldsymbol{k},\omega)$ is very localized in reciprocal spacetime, hence the energy is delocalized in real spacetime, meaning that the motion is in the form of a collective excitation. In the high-$T$ limit, $\tilde{\mathcal{E}}(\boldsymbol{k},\omega)$ is very delocalized in reciprocal spacetime, hence the energy is localized in real spacetime, meaning that the motion is diffusive. The other temperatures can be seen as intermediate stages between the low-$T$ limit, where atoms move in the form of plane waves with a well-defined frequency ad wavevector, and the liquid, where

[1]Note that MgO melts at $T_m \lesssim 3100K$ [134], but it is well known that, by imposing a degree of long range order, the periodic boundary conditions used in MD simulations can prevent melting until $T$ is significantly larger than $T_m$. Therefore, the spectrum at $T = 3500$ K should be regarded as a superheated MgO crystal.

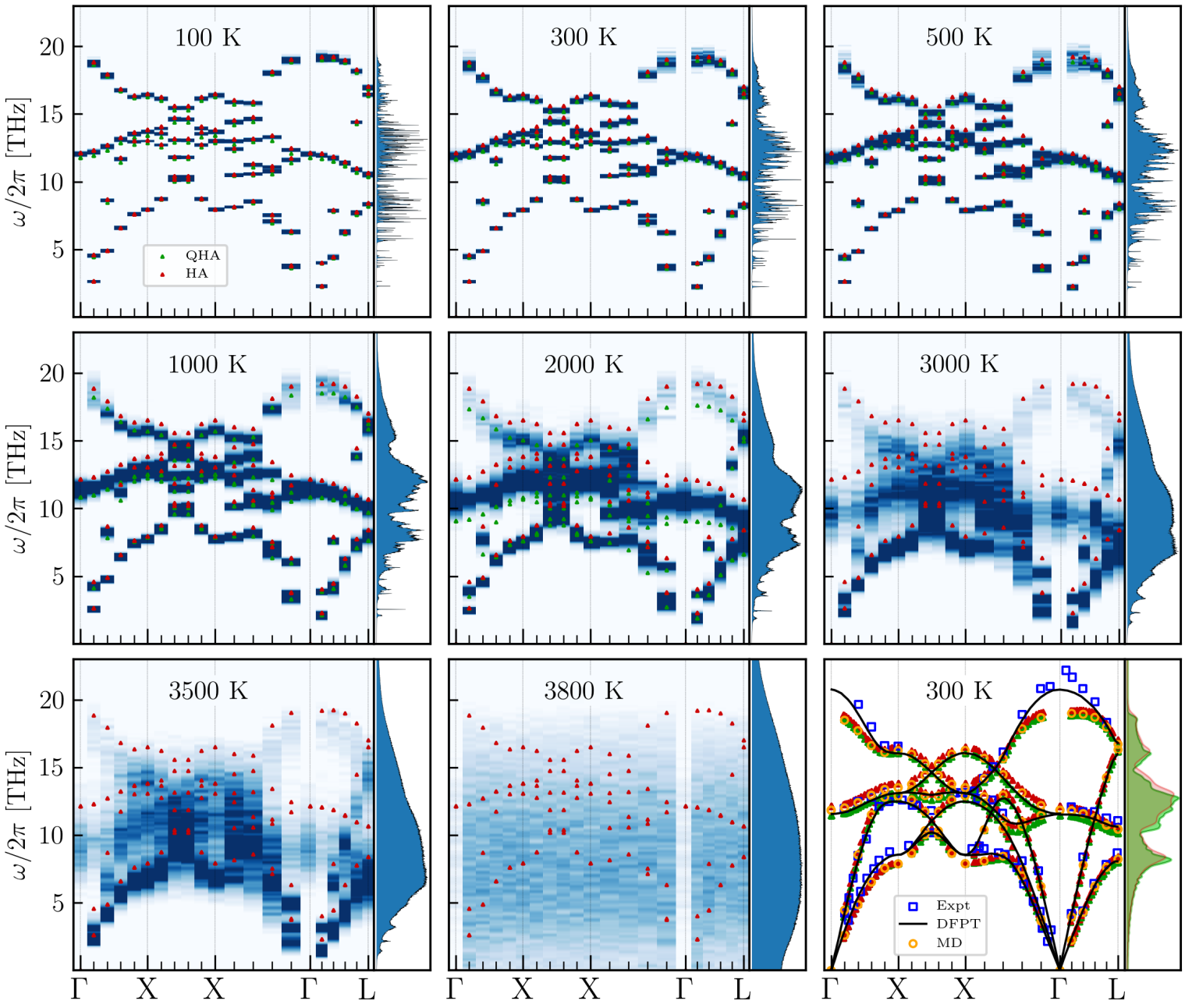



Figure 3.5: Distribution of vibrational energy in reciprocal spacetime, $\tilde{\mathcal{E}}(\omega, \boldsymbol{k})$, at a selection of temperatures ($T$) up to and above the melting temperature, $T_m$, computed for MgO after MD at constant pressure. The values of $T$ are approximate, precise values are provided in Sec. 3.2. The blue and white background image is data from the MD simulations using the *ab initio*-parameterized force field: at each $T$, $\tilde{\mathcal{E}}(\omega, \boldsymbol{k})$ was calculated and normalized to one so that the same map between colours and energy density values could be used at each $T$. The image is pixelated, with the width and height of each pixel equal to the resolutions imposed on our simulations by our finite simulation cell size and simulation times, respectively. We also project the full spectrum onto the normal mode eigenvectors calculated at zero temperature, and plot the locations of the quasiparticle peaks as orange symbols in the lower right panel. The red and green symbols on each plot are the phonon frequencies calculated with the force field at zero temperature and using the quasiharmonic approximation, respectively. The frequencies measured by Sangster *et al.* experimentally [106] are plotted with blue squares and the black lines have been calculated by density functional perturbation theory (DFPT) using the quasiharmonic approximation [52]. The side plots at each temperature are plots of $\tilde{\mathcal{E}}(\omega) = \sum_{\boldsymbol{k}} \tilde{\mathcal{E}}(\omega, \boldsymbol{k})$ versus $\omega$, with $\omega$ on the vertical axis.

each atom moves almost independently of all others, besides those in its close proximity.

We can note two gross features in the spectra and one striking specific feature which will be addressed in more details in the next sections.

**The softening of the phonon frequencies: MD vs QHA**

The first gross feature is that all phonons shift to lower frequencies as $T$ increases. This is a consequence of the weakening of the bonds caused by the crystal's thermal expansion. Consequently, one would expect that the QHA works well; on the contrary, we clearly observe that the QHA frequencies, which are plotted in green at each $T$ for which we found the crystal to be stable within the QHA, tend to be lower than many of the bands in the MD spectra, especially for the TO branch. Such discrepancy increases with increasing $T$ and results in an underestimation of the frequency of most of the modes. The QHA provides a reasonably accurate approximation to the phonon band structure up to at least 500 K, albeit one that is not noticeably closer to the MD band structure than the HA. However, its overestimation of the softening of TO frequencies is quite dramatic at $T = 1000$ K and $T = 2000$ K.

Apart from the classical approximation, which the use of Bose-Einstein occupation numbers in QHA calculations partly rectifies, all of the limitations of our MD calculations discussed in Sec. 3.3 also apply to our QHA calculations. Therefore, at least at high $T$, the full spectra, which do not rely on the additional simplistic assumption that phonons interact weakly enough for their spectrum to be a band structure, should be regarded as closer to reality. Referring to Table 3.1, we see that the QHA lattice parameter is larger than the MD lattice parameter at each $T$. Hence, when the $T$-dependent frequency of each mode is plotted as a function of $T$ through the $T$-dependent volumes, the QHA curves lie below the $V(T)$ MD curves, and the gap between them widens as $T$ increases. We shall return to this point in Sec. 3.4.2, where constant volume results are shown, and in Secs. 3.6-3.7.1, where we will quantitatively assess the phonon quasiparticle frequencies and assess the breakdown of the QHA.

**The degradation of higher-energy modes**

The second gross feature is that the higher-energy branches degrade more rapidly than the lower-energy ones as $T$ increases. In particular, the striking feature is that there is an anomalous broadening in $\omega$-space of the LO modes near the $\Gamma$ point in all directions of the BZ, even at low temperatures. While this is happening to LO bands at small wavevectors, the acoustic branches of the spectrum remain relatively robust. Hence, LO modes lose definition much more rapidly with increasing $T$ than acoustic bands. The anomalous broadening of the LO mode is investigated in detail in Sec. 3.5.

It is also interesting to notice that zone center modes lose definition much more rapidly than zone boundary modes: much of the intensity seen at high frequencies and small wavevectors at low $T$ gradually spreads out to lower frequencies and larger wavevectors as $T$ increases. This is easiest to see along the wavevector paths $\Gamma \to X$ and $\Gamma \to L$, which are straight line segments connecting the zone center to the high symmetry points $X$ and $L$ on the zone boundary. I will denote the wavevectors at $X$ and $L$ by $\boldsymbol{k}_X$ and $\boldsymbol{k}_L$, respectively. When analyzing spectra, I will ignore the point $\Gamma$ itself, which does not represent the limit $\boldsymbol{k} \to 0$, but the point $\boldsymbol{k} = 0$: the energy at $\boldsymbol{k} = \boldsymbol{k}_\Gamma$ is the energy of the rigid relative motion of the Mg and O sublattices in our simulations, which does not interest us. The redistribution, at high $T$, of most of the intensity away from optical frequencies at wavevectors of $\frac{1}{5}\boldsymbol{k}_X$, $\frac{2}{5}\boldsymbol{k}_X$, $\frac{1}{5}\boldsymbol{k}_L$, $\frac{2}{5}\boldsymbol{k}_L$, means that, at these $T$, the optical motion of the lattice cannot be described as *coherent* waves with wavelength greater than about five or ten lattice spacings. This is a manifestation of thermal disorder reducing the correlation times of collective motions along the cell eigenvectors of the affected modes, which I anticipated in Sec. 1.1 and which I will discuss in more detail in Sec. 3.5.

**The distribution of total kinetic energy $\tilde{\mathcal{E}}(\omega)$**

The broadening and progressive melting of optical modes is also reflected in the distribution of the total kinetic energy in $\omega$-space, $\tilde{\mathcal{E}}(\omega)$, plotted in the right hand side of each panel of Fig. 3.5. It is interesting to look at these plots, because most of the times that a band structure is

drawn, the lateral panels show the total phonon DOS, which is obtained by interpolating the phonon frequencies in the BZ after they have been calculated either within the HA or QHA [52]. These do not include the effect of the broadening of the phonon line shapes with $T$, because the phonon spectra are assumed to be $\delta$-functions in $\omega$-space. Within the FT-VVCF method, the line shape of each phonon broadens with increasing $T$, and $\tilde{\mathcal{E}}(\omega)$ is naturally affected by this. The global DOS can also be obtained from experimental measurements, but for MgO this was only done at 400 K [90] and 935 K [14].

Let us discuss the total $\tilde{\mathcal{E}}(\omega)$ from the simulations. At $T = 100$ K, it is composed of isolated narrow peaks corresponding to the frequencies at which lattice vibrations occur in the MD supercell. These peaks do not merge to form a smooth curve as a consequence of the finite size of the supercell. At $T = 300$ K, $\tilde{\mathcal{E}}(\omega)$ can be roughly subdivided into three regions, corresponding to the frequencies of the LO mode (at 15-20 THz), of the TO modes and of the bending of the LA branch (at 10-15 THz), and of the bending of the TA branch (at 5-10 THz). As $T$ increases, the peaks broaden and progressively shift towards lower frequencies. At $T = 3000$ K, the LO and TO+LA peaks in $\tilde{\mathcal{E}}(\omega)$ are barely recognizable, and at $T = 3500$ K $\tilde{\mathcal{E}}(\omega)$ consists of only one very broad peak, which corresponds to the bending of the TA mode. The TA mode, in fact, persists even at this $T$, while the optical modes have almost completely melted. Hence, at this $T$, the material is still in a crystalline structure, for the acoustic modes persist, but very little of the high-frequency part of its vibrational energy exists as *coherent* optical waves. Thermal disorder has almost completely disrupted the long-range order which phonons rely on for their existence. Crystal melting manifests itself in the spectra as the sudden total loss of definition and integrity of the acoustic bands. This occurs between $T = 3500$ K and $T = 3800$ K.

### 3.4.2 Phonon spectra at finite temperatures in the $V(0)$ simulations

The effect of thermal expansion can be disentangled from other mechanisms by which $T$ changes the spectra by fixing the simulated volume to its equilibrium value, $V(0)$. The resulting spectra are presented in Fig. 3.6.

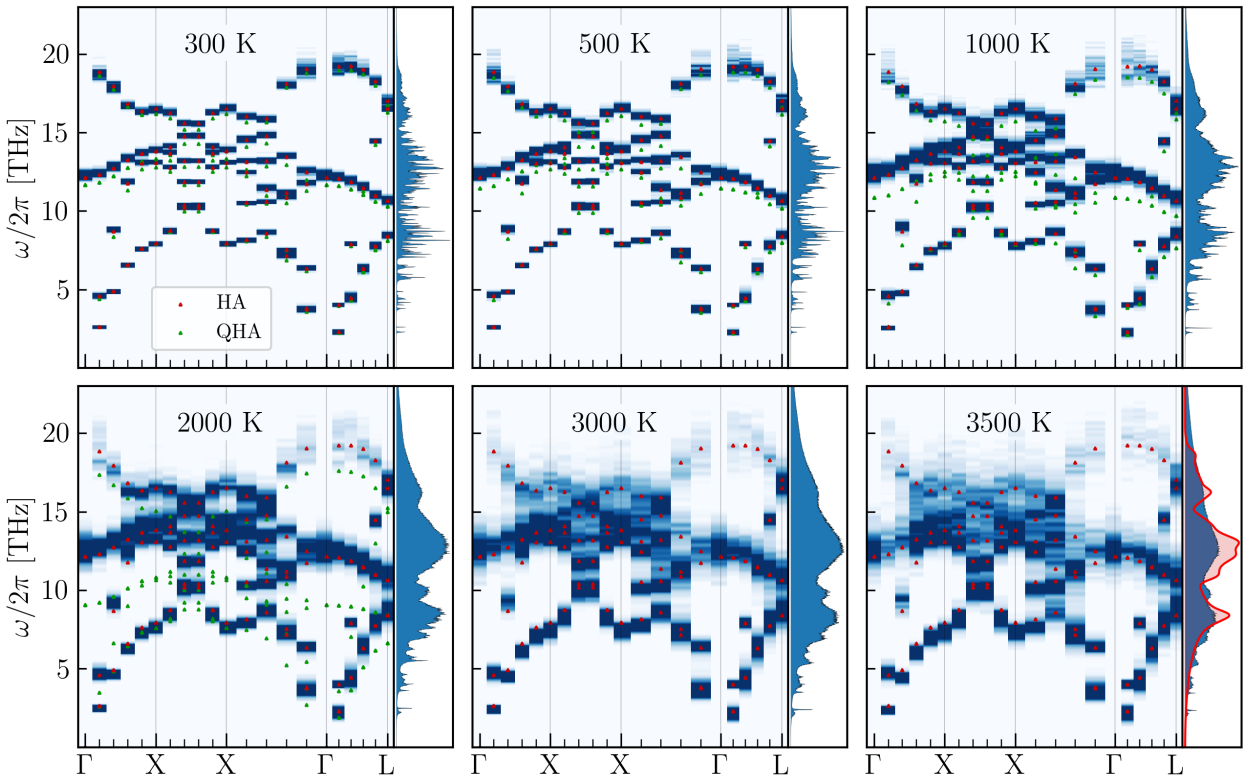



Figure 3.6: Distribution of vibrational energy in reciprocal spacetime, $\tilde{\mathcal{E}}(\omega, \boldsymbol{k})$, at a selection of temperatures ($T$) computed for MgO after MD at constant volume. The values of $T$ are approximate, precise values are provided in Sec. 3.2. For further details, see Fig. 3.5.

The direct comparison between the HA and QHA frequencies, or the comparison between Figs. 3.5 and 3.6, show that most of the negative phonon frequency shifts happen when the crystal is free to expand. This confirms the observation that thermal expansion is the most prominent anharmonic mechanism through which the phonons change their frequencies in simple crystals, and reinforces the reason for the success of the QHA at $T < 1000$ K. Bonds weaken when the crystal expands, hence the energy of the vibrations decreases.

Looking at the LO modes near Γ, it is interesting to notice that the anomalous broadening we discussed for the $V(T)$ simulations is present in the $V(0)$ case as well. Hence, we can rule out thermal expansion as its cause. However, it can be seen that the bands look much more like bands than they do in the $V(T)$ case.

## 3.5 The broadening of the LO mode near the Γ point

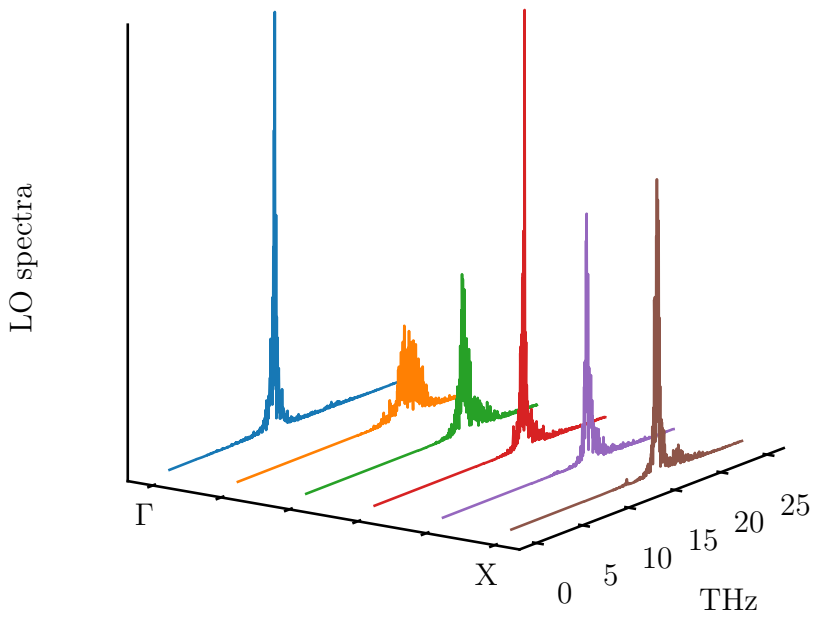



Figure 3.7: The LO spectra at $T = 1000$ K along the $\Gamma - X$ path, showing an anomalously large broadening at $\boldsymbol{k} = \frac{1}{5}\boldsymbol{k}_X$. The experimental spectra can be found in Fig. 2 of Ref. [52]. The LO frequency at Γ lacks the additional contribution of the long-range electric field, which is absent in the supercell calculation.

The specific striking feature of the spectra that I have chosen to discuss is that the loss of definition of the optical modes appears to begin with an anomalously-large broadening of the LO modes nearest to the $\Gamma$ point. The broadening of the mode is even visible in Fig. 3.5 at $T = 100$ K, which is the lowest $T$ at which I calculated the full spectrum, and it occurs for the LO phonons at all wavevectors $\boldsymbol{k}$ near $\Gamma$, regardless of their direction. To make apparent that the broadening of the LO is larger at smaller wavevectors, I plot the spectra of the LO mode at $T = 1000$ K along the path $\Gamma - X$ in Fig. 3.7, to show that the broadening is maximum at $\boldsymbol{k} = \frac{1}{5}\boldsymbol{k}_X$.

We are not the first to observe this: Giura *et al.* [52] reported the same result via inelastic X-ray scattering (Fig. 3.3) and via DFPT calculations (Fig. 3.4). Moreover, a similar broadening of the LO mode was found experimentally by Woods, Brockhouse, Cochran and Cowley [146, 145] for two alkali halides, namely NaI and KBr, and both experimentally and theoretically by Togo *et al.* [**?**] for NaCl and KCl, suggesting this is a characteristic feature common to many bi-atomic ionic compounds, or at least those crystallizing in the rock-salt structure.

The large broadening of the long wavelength LO mode (LWLO) has important physical consequences. One of them concerns the absorption of light when the radiation is in the energy range of the LWLO. The fact that decay channels open for the LWLO mode, in fact, means that similar decay channels open for the photon, since the conservation of energy and momentum is the same for photon-phonon and phonon-phonon collisions (cf. Sec. 3.1.2). Hence, a photon with frequency $E/\hbar \approx \omega_{\mathrm{LWLO}}$ can be absorbed with the creation of two or more phonons. Another consequence is a possible reduction of thermal conductivity. Thermal conductivity, in fact, depends on the phonon linewidths and on the phonon group velocity [34]. The larger the linewidth, the shorter is the phonon mean free path–which is the average spatial extent by which a phonon can travel through the crystal [38, 4]–and the lower the thermal conductivity. The larger the group velocity, the faster the lattice excitations can travel and hence transport heat [38, 4]. Acoustic modes contribute maximally to the thermal conductivity, whereas TO modes are usually poorly dispersive, hence contribute very little to it. LO modes, on the other hand, are dispersive as a result of the LO/TO splitting, which is large in strongly ionic crystals; hence, they can give a considerable contribution to the thermal conductivity. However, if the

LO modes are highly damped, their mean free path is shortened, and their contribution to the transport of heat is reduced. Hence, a large damping of the LO mode means that the thermal conductivity is reduced.

For these reasons, understanding the mechanism by which the LO dampens is important. I propose two explanations, or partial explanations, for why the melting of bands begins with the longest wavelength LO modes and why acoustic modes, and modes with shorter-wavelengths, are relatively stable. The first explanation is entirely based on the concept of conservation of energy and momentum for phonon-phonon scattering, while the second explanation can be framed within a completely classical picture of interactions between acoustic-optical phonons. These are discussed in Secs. 3.5.1 and 3.5.2.

### 3.5.1 The conservation of energy and momentum for the LO mode

The first explanation of the LO broadening stems from the concept of conservation of energy and momentum for the phonon-phonon collisions which are the physical interpretation of the mathematical form of the anharmonic potential. As we saw in Sec. 2.5.1, when discussing PT, Eq. 2.20 shows that, to second order in the perturbation, the phonon linewidth is essentially a weighted two-phonon density of states, where the weights are the Bose-Einstein prefactors and the phonon coupling constants. The TPDOS, defined in Eqs. 2.21-2.22 is an extension of the DOS that accounts for momentum and energy conservation in a three-phonon scattering process. There are two different scattering processes that can occur: the summation and the difference processes. A summation process is one in which the reference phonon $\lambda = (\boldsymbol{q}\nu)$ is annihilated (created) to create (annihilate) two phonons $\lambda_1 = (\boldsymbol{q}_1\nu_1)$ and $\lambda_2 = (\boldsymbol{q}_2\nu_2)$, and a difference process is one in which the reference phonon $\lambda = (\boldsymbol{q}\nu)$ is annihilated (created) together with a phonon $\lambda_1 = (\boldsymbol{q}_1\nu_1)$ to create (annihilate) a phonon $\lambda_2 = (\boldsymbol{q}_2\nu_2)$. In all cases the total momentum must be conserved up to a $\boldsymbol{G}$-vector, namely $\boldsymbol{q} + \boldsymbol{q}_1 + \boldsymbol{q}_2 = \boldsymbol{G}$, and energy must be conserved, namely $\omega - \omega_{\lambda_1} - \omega_{\lambda_2} = 0$ or $\omega + \omega_{\lambda_1} - \omega_{\lambda_2} = 0$. In order to understand the reason for the broadening of the LO, we first figure out whether it can participate to a greater extent in summation or difference processes. Being the highest frequency branch, it is obvious

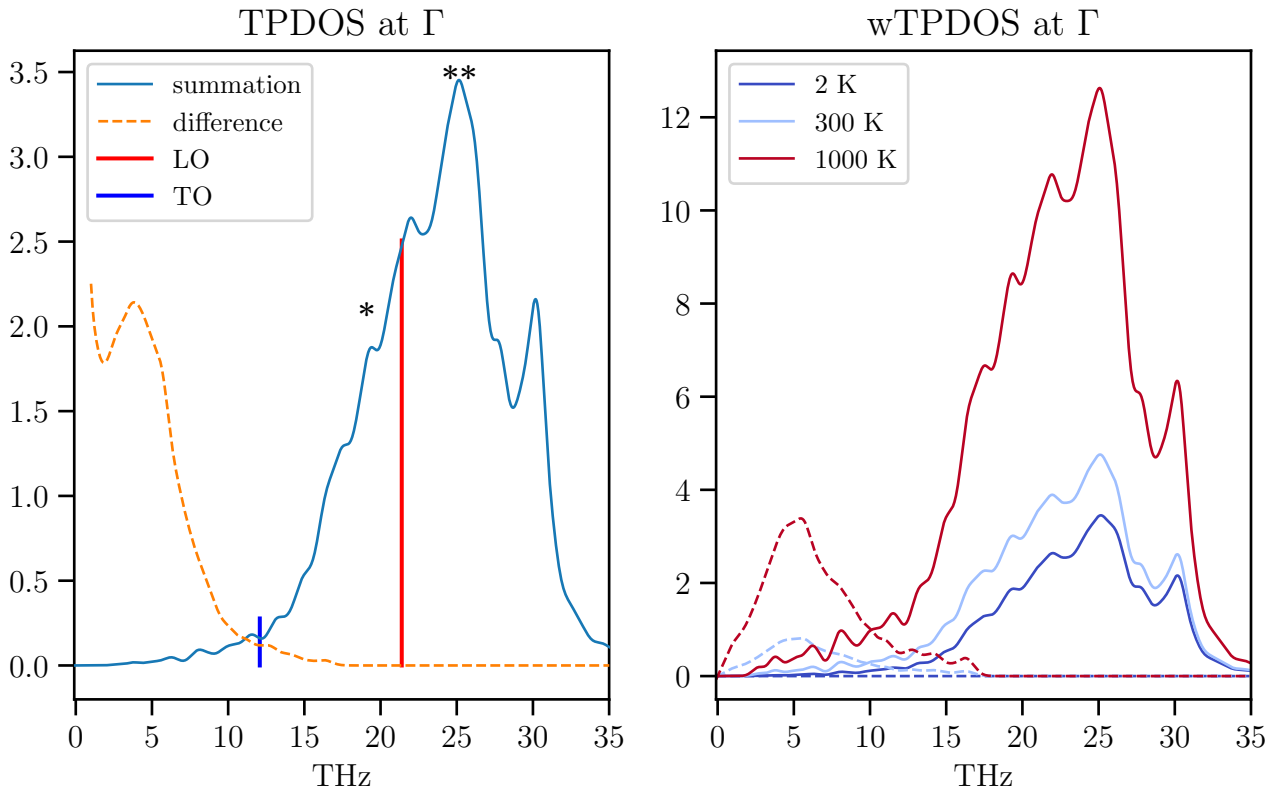



Figure 3.8: Two-phonon density of states (TPDOS, on the left) and weighted two-phonon density of states (wTPDOS, on the right) calculated for a reference Γ phonon. Solid lines and broken lines represent summation and difference processes, respectively. On the left, vertical lines are drawn in the correspondence of the TO and LO frequencies, the latter one of which has been augmented after applying the non analytical correction. The height of the vertical lines corresponds to the sum of the contributions of the summation and difference processes at the relevant frequency. The star "*" and double star "**" indicate peaks of the TPDOS where infra-red spectroscopy performed by Giura *et al.* and Calandrini *et al.* found excess of spectral weight [52, 16]. On the right, the evolution of the wTPDOS with increasing temperature is shown, highlighting that the Bose-Einstein prefactors open more and more decay channels as the crystal is heated, and that summation processes happen with greater probability than difference processes.

to expect that it can most likely participate in summation processes, i.e. it mostly decays into, rather than merges with, other phonons. This can be easily verified through the TPDOS and wTPDOS calculated for a reference phonon with vanishing wavevector, $\boldsymbol{q} = \mathbf{0}$, shown in Fig. 3.8. I chose to show $\boldsymbol{q} = \mathbf{0}$ for the time being, since it is the $\boldsymbol{k}$-point, commensurate with my supercell, which is closest to the $\boldsymbol{k}$-point that IR experiments probe, i.e. $\boldsymbol{q} \to \mathbf{0}$.

Looking at the left-hand side of Fig. 3.8, it is clear that summation processes dominate at high frequencies. This makes sense since they require $\omega = \omega_{\lambda_1} + \omega_{\lambda_2}$, while difference processes dominate at lower frequencies, since they require $\omega = \omega_{\lambda_1} - \omega_{\lambda_2}$. The LO mode frequency, which has been increased by applying the non-analytical correction effective at $\boldsymbol{k}$-points near the $\Gamma$ point, is indicated by a red vertical line and lies in a region of frequency of very high TPDOS. While the LO modes can only participate in summation processes (i.e., decay into two phonons), the TO modes can participate in both processes, but to a smaller extent. The heigths of the vertical lines drawn at the frequencies of the two modes indicate that the TPDOS is much higher for the LO than for the TO. This is because the TO mode falls in an energy window where the TPDOS for both summation and difference processes is low.

The right hand side of Fig. 3.8 shows the wTPDOS, i.e., the TPDOS weighted by the Bose-Einstein occupation numbers, at three temperatures. Differently than the graph of the left hand side of the same figure, temperature is now taken into account via the Bose-Einstein prefactors of Eq. 2.20. As $T$ is raised, we observe an increase of wTPDOS for the summation processes. This demonstrates that temperature all but enhances the ability of high-frequency modes to participate in summation processes. This is because the population of phonons increases with $T$, and there are far more decay channels for the LO at high $T$. Difference processes, on the other hand, cannot occur at $T = 0$, and their probability of happening also increases with $T$.

We can summarize the results of this subsection in two sentences: the broadening of the LO mode is high because the number of momentum- and energy-conserving phonons which it can couple to is high. Moreover, because the way it can couple with the other phonons is with a summation process, meaning that either it decays into two or two phonons decay into it, the probability of decaying is high and it increases steadily with $T$. Hence, the LO dampens a lot.

**How are the TPDOS and the experimental ESW related?**

I suggest in passing that the excess of spectral weight (ESW) measured in the optical conductivity of Giura *et al.* [52] and of Calandrini *et al.* [16], which we discussed in Sec. 3.1.2 and which they attributed to multiphonon processes, should correspond to the peaks in the TPDOS for the summation processes indicated by "*" and "**" in Fig. 3.8. The photon dispersion is much steeper than the phononic one, since light travels at a much faster speed than sound, therefore photons with energies similar to the phonon energies ($\sim$ meV) can be considered to have an almost vanishing wavevector, $\boldsymbol{k}_{\text{photon}} \to 0$. When light is absorbed (or scattered) by the crystal, it can excite one phonon or a number $n$ of phonons; the latter case is less and less probable as $n$ increases. In all cases, the momentum has to be conserved, which in the case $n = 2$ imposes that the two contributing phonons to have approximately equal and opposite wavevectors $\boldsymbol{q}_{\text{phonon1}} \approx -\boldsymbol{q}_{\text{phonon2}}$ [52] (cf. Sec. 3.1.2). The TPDOS shown in Fig. 3.8 imply the exact same conservation of momentum (cf. Eqs. 2.21-2.22). Hence, the TPDOS can be used once again to show the energy conservation for photon-phonon scattering, and features one shallower peak at $f \approx 19$ THz; this roughly corresponds to the frequencies at which Giura *et al.* and Calandrini *et al.* found ESWs, as can be seen in Figs. 3.1-3.2, which show their results. Moreover, the same authors reported additional weak but highly structured ESW at frequencies higher than the LO [16], and this should be attributed to the peak at $f \approx 25$ THz indicated by a "**".

We have used the TPDOS to understand the multiphonon contributions to the absorption of light by MgO. This is a higher-order contribution: in fact, the ESWs manifest as a weak signal in the IR spectra of Giura *et al.* and Calandrini *et al.*, but are not negligible even at room temperature [52, 16]. Hence, the present calculation shows that if one is confident that the theoretical model computes the phonon band structure and the phonon DOS correctly, then the (relatively simple) calculation of the TPDOS can be used to predict the opening of decay channels for the photons, even without any MD simulation. Conversely, if the IR absorption spectrum is measured, one can infer the most anharmonic phonons, at least the ones near the BZ center, by either directly checking on the spectral broadening of the resonant TO mode or

by looking at the additional peaks (ESWs) of the spectra: in fact, these represent frequencies where the conservation of energy is fulfilled, and this is a necessary condition for particle-phonon scattering events for any particle that the crystal can interact with, be it a photon, a neutron or another phonon.

### 3.5.2 Classical view of acoustic-LO coupling

In this section, I show the mechanism by which LO modes, which bear a long-range electric field that causes their frequency to be higher than the TOs, are disrupted by acoustic modes. This disruption can cause a modulation of the energy of the LO modes, which results in a higher broadening for these modes. I acknowledge that the concepts explained in this section mainly originate from the idea of my supervisor, Dr. Paul Tangney, and are discussed in Ref. [24].

The acoustic branches can be thought of as a skeleton on which the optical branches 'hang', because spatially-coherent countermotion of cations and anions about a reference structure would not happen unless the reference structure was itself spatially coherent. In other words, the displacements of primitive cells from their equilibrium structures are very unlikely to have order on length scale $\lambda$ if the crystal does not have order on length scale $\lambda$.

Crystalline order is gradually lost as $T$ increases, and this manifests as a gradual reduction of the correlation lengths and times of displacements along the modes' cell eigenvectors, and hence a gradual reduction of the modes' coherence lengths and times. The energy cost of acoustic distortions protects long range order in the time average of the crystal's structure. However, consider the example of an LO mode whose cell eigenvector is $\boldsymbol{e}(\boldsymbol{k},\ \mathrm{LO})$, where $|\boldsymbol{k}|$ is small. The crystal having long range order when averaged over several periods of a long-wavelength acoustic (LWA) mode is not sufficient to protect long range order in the set of primitive cell displacements along the LO mode's cell eigenvector. It is insufficient because the periods (frequencies) of zone center LO modes are much shorter (higher) than those of LWA modes. Therefore, long range order of cell displacements along an LO cell eigenvector relies, not on the degree to which the time average of LWA mode displacements preserve crystalline

order (i.e., vanish), but on the degree to which they preserve it in times much shorter than LWA mode periods. Long range order of the LO branch requires the *amplitudes* of LWA modes to be small, not their time-averaged displacements. The converse is not true and, in either the limit of large LO frequency, $\omega_{\boldsymbol{k}}^{\mathrm{LO}}$, or the limit of small LWA frequency, $\omega_{\boldsymbol{k}}^{\mathrm{LWA}}$, the coupling between LWA and LO modes is effectively unidirectional: LO vibrations are highly sensitive to acoustic mode displacements, whereas acoustic modes are much less sensitive to LO mode displacements.

The reason for the low sensitivity of LWA phonons to LO phonons is that an LO mode's period, $2\pi/\omega_{\boldsymbol{k}}^{\mathrm{LO}}$, is so short that LO displacements average to zero in much less than the period, $2\pi/\omega_{\boldsymbol{k}}^{\mathrm{LWA}}$, of an LWA phonon. Therefore the forces they exert on an LWA mode cancel one another before the LWA mode has had time to respond to them. This partial decoupling of a slow-moving degree of freedom from a much faster one is known as adiabatic decoupling. Adiabatic decoupling does not mean that the LWA modes do not exchange energy with the optical modes; it means that they exchange energy with them equitably, due to thermal equilibrium, and so rapidly that they do not notice.

Optical mode disorder changes so quickly that every complete LWA oscillation occurs in the presence of an equivalent background of optical displacements, whereas LWA disorder changes so slowly that every complete LO oscillation occurs in the presence of a unique and inequivalent background of LWA displacements. Therefore it is approximately true that LWA modes do not 'see', and are not influenced directly by, the highest-frequency LO modes, because they are adiabatically decoupled from them. Nevertheless, and at the same time, if there exists an effective LWA-LO coupling mechanism, the frequencies and coherence lengths and times of LO waves are strongly influenced by whatever LWA displacements exist during the LO waves' lifetimes. Of course, the adiabatic decoupling picture, in which optical modes see 'frozen' acoustic modes and acoustic modes do not see optical modes because the time averages of their displacements vanish, is very much an idealized limiting case. Adiabatic decoupling of acoustic modes from optical modes becomes a perfect decoupling in the $\boldsymbol{k} \to 0$ limit, but is likely to be far from perfect at the smallest finite wavevectors present in our simulations. Clearly this picture would not apply to the transverse acoustic (TA) and TO modes in the regions of

the BZ where they occupy the same small frequency window between about 10 THz and 15 THz. However, it does seem to help to explain why the lowest-frequency acoustic modes are broadened less than the highest-frequency optical modes.

As $T$ increases from the $T \to 0$ limit, it is the LWA modes that are the first to become active, because they are lowest in energy. Therefore, there may be a common explanation for why the LO branch of the band structure is the first to melt, or partially melt, for why zone center modes melt before zone boundary modes, and for why acoustic bands are degraded less at the highest $T$s than optical bands: acoustic modes are degraded less because of the partial immunity to optical disorder that adiabatic decoupling affords them. LO modes are not protected by adiabatic decoupling and, as we now explain, there is a very simple and effective mechanism by which they can be disrupted, and their frequencies changed, by acoustic disorder or even by a single quasistatic acoustic perturbation of the crystal.

**Acoustic warping of the LO electric field**

By modulating the relative displacements of cations and anions, an LO wave of wavevector $\boldsymbol{k}$ creates regions of excess charge at its nodes, from which emanates an electric field, $\boldsymbol{\mathcal{E}}_{\boldsymbol{k}}^{\mathrm{LO}}$, of the same wavelength, $\lambda_{\boldsymbol{k}}^{\mathrm{LO}} \equiv 2\pi/|\boldsymbol{k}|$. This field, which we referred to as the LO mode's intrinsic field above, exerts an additional force on the LO's motion, thereby increasing its frequency, $\omega_{\boldsymbol{k}}^{\mathrm{LO}}$. One way to understand the origin of $\boldsymbol{\mathcal{E}}_{\boldsymbol{k}}^{\mathrm{LO}}$ is to consider the case in which $\lambda_{\boldsymbol{k}}^{\mathrm{LO}}$ is orders of magnitude larger than a primitive lattice spacing; and to imagine partitioning the crystal into primitive unit cells of dipole moment $\boldsymbol{d}$, whose volume we will treat as infinitesimal. If the LO mode at wavevector $\boldsymbol{k}$ becomes active, it modulates $\boldsymbol{d}$ along an axis parallel to $\hat{\boldsymbol{k}} = \boldsymbol{k}/|\boldsymbol{k}|$ by modulating the displacements of Mg cations from the O anions with which they share a primitive cell. On length scale $\lambda_{\boldsymbol{k}}^{\mathrm{LO}} \gg |\boldsymbol{a}_1|, |\boldsymbol{a}_2|, |\boldsymbol{a}_3|$, we can define a local spatial average of the cell dipole moment per unit volume, $\boldsymbol{P} \equiv \langle \boldsymbol{d} \rangle / |\boldsymbol{a}_1 \cdot (\boldsymbol{a}_2 \times \boldsymbol{a}_3)|$, and treat it as a continuous function of position. The dependence of $\boldsymbol{d}$ on the choice of primitive cell makes $\boldsymbol{P}$ ill-defined; however its derivatives with respect to space and time are the same for every choice. Therefore the density $\rho_b \equiv -\nabla \cdot \boldsymbol{P}$ of excess charge or bound ('$b$') charge is independent of the choice of

primitive cell and is a well-defined physical quantity. If only the LO mode at $\boldsymbol{k}$ is active, $\rho_b$ varies in direction $\hat{\boldsymbol{k}}$ with wavelength $\lambda_{\boldsymbol{k}}^{LO}$. Its magnitude is largest at the wave's nodes, which is where the Mg-O displacement varies most from cell to adjacent cell along $\hat{\boldsymbol{k}}$. When multiple LO modes are active, $\rho_b$ has a contribution from each one and we will denote the contribution from the one with wavevector $\boldsymbol{k}$ by $\rho_{b,\boldsymbol{k}}^{\mathrm{LO}}$.

$\boldsymbol{\mathcal{E}}_{\boldsymbol{k}}^{\mathrm{LO}}$ is the field emanating from $\rho_{b,\boldsymbol{k}}^{\mathrm{LO}}$. If it was absent or negligible ($\boldsymbol{\mathcal{E}}_{\boldsymbol{k}}^{\mathrm{LO}} \approx 0$) the LO and TO modes would have the same frequency in the long wavelength limit by symmetry. Therefore near $\Gamma$, $\boldsymbol{\mathcal{E}}_{\boldsymbol{k}}^{\mathrm{LO}}$ increases the value of $\omega_{\boldsymbol{k}}^{\mathrm{LO}}/2\pi$ by almost 10 THz. It follows that any weakening or strengthening of $\boldsymbol{\mathcal{E}}_{\boldsymbol{k}}^{LO}$ could change $\omega_{\boldsymbol{k}}^{\mathrm{LO}}$ quite dramatically A quasistatic acoustic perturbation of the crystal changes $\omega_{\boldsymbol{k}}^{LO}$ by weakening or strengthening $\boldsymbol{\mathcal{E}}_{\boldsymbol{k}}^{LO}$, and different quasistatic acoustic perturbations would result in different frequencies. Therefore the distribution of the LO mode's energy among frequencies, which is localized at a single frequency in the $T \to 0$ limit, should broaden significantly as $T$ activates the acoustic modes.

There are some obvious mechanisms by which TA and longitudinal acoustic (LA) distortions would change $\boldsymbol{\mathcal{E}}_{\boldsymbol{k}}^{LO}$. The first is simply disorder: acoustic perturbations whose wavelengths differed from $\lambda_{\boldsymbol{k}}^{\mathrm{LO}}$ would break the periodicity of $\boldsymbol{\mathcal{E}}_{\boldsymbol{k}}^{LO}$ by breaking the periodicity of $\rho_{b,\boldsymbol{k}}^{\mathrm{LO}}$. This would reduce the LO wave's coherence and, in many or most cases, reduce $\omega_{\boldsymbol{k}}^{LO}$ by weakening $\boldsymbol{\mathcal{E}}_{\boldsymbol{k}}^{LO}$.

A second mechanism is that a TA or LA perturbation with wavevector $\boldsymbol{k}$ (or $m\boldsymbol{k}$, where $m \in \mathcal{Z}$), would change $\boldsymbol{\mathcal{E}}_{\boldsymbol{k}}^{LO}$ by perturbing the charge reservoirs at the antinodes of $\rho_{b,\boldsymbol{k}}^{\mathrm{LO}}$. A TA perturbation would displace the positive and negative reservoirs relative to one another along an axis perpendicular to $\hat{\boldsymbol{k}}$, whereas an LA perturbation would expand or compress them. Hence, a TA would reduce the magnitude of its component along $\hat{\boldsymbol{k}}$, thereby reducing $\omega_{\boldsymbol{k}}^{\mathrm{LO}}$. An LA perturbation, on the other hand, would modulate the magnitude of $\boldsymbol{\mathcal{E}}_{\boldsymbol{k}}^{LO}$ along $\hat{\boldsymbol{k}}$. If, at a given moment, the positive antinodes of $\rho_{b,\boldsymbol{k}}^{\mathrm{LO}}$ were compressed (expanded) by an LA wave of wavevector $\boldsymbol{k}$, its negative antinodes would be expanded (compressed) at that moment. However the phase velocities of LO and acoustic waves are different, in general, which means that the antinodes of an acoustic wave would be moving relative to those of $\rho_{b,\boldsymbol{k}}^{\mathrm{LO}}$, making it a

time-dependent perturbation of the LO wave.

A third mechanism is that a quasistatic acoustic perturbation of the crystal would create regions in which the crystal is compressed and regions in which it is expanded. Compressing an ionic crystal increases its Madelung energy and the magnitudes of local electric fields. Therefore, an acoustic wave with a wavelength much larger than $\lambda_{\boldsymbol{k}}^{\mathrm{LO}}$ might increase $\omega_{\boldsymbol{k}}^{\mathrm{LO}}$ in compressed regions of the crystal and reduce it in expanded regions.

The acoustic-LO coupling mechanisms discussed above suggest that, as soon as acoustic modes become active, we should see a range of LO frequencies corresponding to LO vibrations occurring in the presence of different backgrounds of acoustic deformations of the crystal. Let us now examine the spectra presented in Fig. 3.5 for consistency with this prediction. We will focus on the lowest-$T$ spectra and on what happens near $\Gamma$, which is the region of the BZ occupied by the first modes to become thermally-active as the crystal is heated from the $T \to 0$ limit. To see clearly how the degradation of the LO band depends on wavevector magnitude, let us focus again on the paths $\Gamma - X$ and $\Gamma - L$ at the left hand side and at the right hand side, respectively, of each spectrum in Fig. 3.5.

As $T$ increases, the earliest deviations from a perfect band structure occur close to $\Gamma$ along both paths (and also along other paths, which we do not discuss). For example, at 300 K and 500 K the LO modes at $\frac{1}{5}\boldsymbol{k}_X$ and $\frac{1}{5}\boldsymbol{k}_L$ have broadened noticeably in frequency. Along $\Gamma - X$ the LO broadening is accompanied by a noticeable broadening of the LA modes, whereas along $\Gamma - L$ it is accompanied by a noticeable broadening of the TA modes. In the latter case the broadening of the TA mode is smaller at $\boldsymbol{k} = \frac{1}{5}\boldsymbol{k}_L$ than it is further away from $\Gamma$, despite the largest broadening of the LO mode being at $\boldsymbol{k} = \frac{1}{5}\boldsymbol{k}_L$. However, $\frac{1}{5}\boldsymbol{k}_L$ is the wavevector at which the difference between LO and TA frequencies is greatest, which means that it is the wavevector at which the adiabatic decoupling of acoustic modes from optical modes discussed here would be most effective. Therefore, the low-$T$ broadening of the LO modes near $\Gamma$, its progression to larger wavevectors as $T$ increases, and the broadening of acoustic modes that accompanies it, all appear to be consistent with acoustic modes changing $\omega_{\boldsymbol{k}}^{\mathrm{LO}}$ and making LO waves less coherent by disrupting $\boldsymbol{\mathcal{E}}_{\boldsymbol{k}}^{\mathrm{LO}}$ . The main point of this section is that there exists a

mechanism for strong coupling between the acoustic and LO modes of an ionic crystal, which would degrade its LO bands but degrade its acoustic bands to a much lesser degree. We have provided simple physical reasons why we should see anomalous broadening of the LO mode in our spectra, and as we analyze the spectra of individual modes in more detail in Sec. 3.6 we will provide further indirect evidence that the mechanism we proposed is responsible for the observed broadening. However, a much more detailed analysis would be required to prove it conclusively.

Let us end this section by summarizing our physical reasoning. It is well known that the frequency of a long wavelength LO phonon is increased by its intrinsic electric field, $\boldsymbol{\mathcal{E}}_{\boldsymbol{k}}^{LO}$. It is also known that, as $T$ increases from the $T \to 0$ limit, the earliest contributions to thermal disorder come from the lowest energy modes, which are LWA modes. It is obvious that, by breaking the long range order of primitive cell displacements along LO cell eigenvectors, acoustic perturbations of the crystal would alter $\boldsymbol{\mathcal{E}}_{\boldsymbol{k}}^{LO}$. It follows that acoustic phonons would change the frequencies of LO waves and, by disordering the lattice, make them less coherent. As $T$ increases, the first manifestation of this effect in the spectra would be the LO band near the BZ center beginning to broaden and dissolve. As $T$ continues to increase, causing significant activity among higher-energy and larger-wavevector acoustic modes, we should expect to see the degradation of the LO band spread from BZ's center towards its boundary. All of this is consistent with what is observed in Fig. 3.5.

## 3.6 The quasiparticle approximation (QPA)

To quantitatively assess frequency shifts and linewidths of the phonons, in this section I show at the quasiparticle information. This means having fitted the phonon spectra to Lorentzians and plotting the finite-$T$ phonon frequencies, $\tilde{\omega}_{\boldsymbol{q}\nu}$, and linewidths $\Gamma_{\boldsymbol{q}\nu}$. The former quantity is defined as the peak of the Lorentzian distribution, the latter quantity is its full width at half maximum. It is important to note that this is an approximation, because it assumes that the phonon line shapes are well-fitted by Lorentzians, which is not the general case [75]. We shall

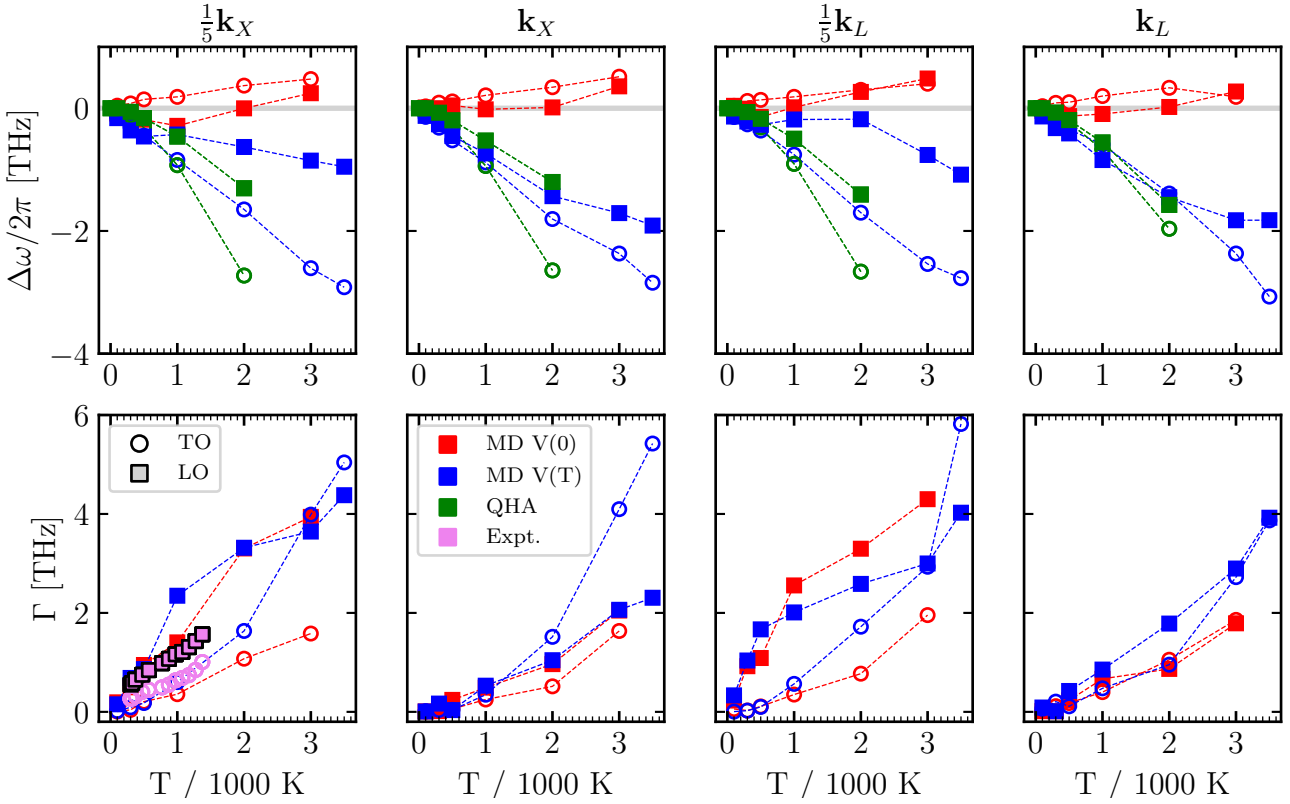



Figure 3.9: Results of fitting Lorentzian functions to optical mode spectra at, from left to right, the wavevectors $\frac{1}{5}\boldsymbol{k}_X$, $\boldsymbol{k}_X$, $\frac{1}{5}\boldsymbol{k}_L$ and $\boldsymbol{k}_L$. The upper panels show the phonon frequency shifts versus $T$, obtained through the difference between the fitted Lorentzian's peak frequency and the $T \to 0$ phonon frequency. The lower panels plot the fitted Lorentzians' full widths at half maximum versus $T$ and the left-most plot includes a comparison to the values measured by Calandrini *et al.* at a much smaller wavevector [16]. The insets specify the meanings of the symbols and their colors in all eight plots.

call this the quasiparticle approximation, QPA.

### 3.6.1 The phonon quasiparticles as a function of temperature

Let us now focus on some specific phonons, i.e. the optical modes, and let us assess their quasiparticle frequencies and linewidths as a function of temperature. Fig. 3.9 shows the phonon frequency shifts and linewidths of the Lorentzian fits to the phonon spectra for some of the most anharmonic modes, the TO and LO modes at $\frac{1}{5}\boldsymbol{k}_X$, $\boldsymbol{k}_X$, $\frac{1}{5}\boldsymbol{k}_L$ and $\boldsymbol{k}_L$ as a function of $T$. The shifts are compared between the QHA, drawn with green lines, and the two sets of simulations, $V(0)$ and $V(T)$, drawn with red and blue lines, respectively. I show the phonon frequency shifts with respect to their values at $T \to 0$, i.e. $\Delta\omega_{\boldsymbol{q}\nu}(T) = \tilde{\omega}_{\boldsymbol{q}\nu}(T) - \omega_{\boldsymbol{q}\nu}(0)$. In the

MD simulations, $\omega_{\boldsymbol{q}\nu}(0)$ is the frequency of the normal mode $(\boldsymbol{q}\nu)$ at the $V$ that minimizes the potential energy, whereas in the QHA case it is its frequency at the $V$ that minimizes the sum of the potential energy and the zero-point energy of the phonon modes.

**The phonon frequency shifts**

Let us comment on this plot by first looking at the frequency shifts (upper panels of Fig. 3.9). The upper panels demonstrate all phonon frequencies decrease as the temperature is raised in the $V(T)$ simulations, as we anticipated in Secs. 3.4.1-3.4.2. This is to be physically interpreted as the result of thermal expansion: when the crystal is allowed to expand, the interatomic force constants lower–and so do the phonon frequencies–due to the increased distance between atoms. On the other hand, when the volume is kept fixed, const-$V$ phonon-phonon interactions make the phonon frequencies increase and decrease, depending on the mode, as the red lines show.

Moreover, it is important to note that the phonon frequency shifts in the $V(T)$ condition are higher than in the $V(0)$ one: for example, the TO modes at $\frac{1}{5}\boldsymbol{k}_X$ show an almost linear negative trend of decrease, of about -1 ThZ/1000 K when thermal expansion is included, and a much smaller, positive trend when the volume is kept fixed.

With respect to QHA vs MD (green vs blue lines), we saw in Fig. 3.5 that the absolute values of the phonon frequencies are underestimated by the QHA with respect to the MD for some of the phonons, especially the TO branches, and I hinted that the MD spectra would be more reliable since they have been obtained in a fully non-perturbative way. Referring to the frequency *shifts* now, defined as $\Delta\omega_{\boldsymbol{q}\nu}(T) = \tilde{\omega}_{\boldsymbol{q}\nu}(T) - \omega_{\boldsymbol{q}\nu}(0)$ and plotted in Fig. 3.9, the QHA usually underestimates them at low $T$, and highly overestimates them at high $T$. The QHA lines are almost all concave down, signalling a departure from a linear $T$-dependence of the shifts. The difference between the QHA and the $V(T)$ values starts diverging at $T > 1000$ K.

These results suggest that, in the case of MgO, the thermal expansion makes the biggest part of the phonon frequency shifts when the pressure is low. It is therefore to be expected that the QHA method works relatively well at relatively low $T$. At the same time, it is not

surprising that the QHA is found to break down at $T > 1000$ K, since this result is in agreement with the independent calculations of Karki et al. [71] and E. Calandrini et al. [16]. The maximum temperature of validity of the QHA, $T = 1000$ K, is also roughly the $T$ at which we observe a divergence between the QHA and MD. Such breakdown forbids the calculation of thermodynamic properties at high $T$, since these depend on the phonon frequencies. In Sec. 3.7.1, I show how to overcome this issue.

In some references in the literature, a linear trend of the phonon frequency shifts versus $T$ is assumed [31]. I remark that some of the phonon frequencies show approximately linear trends with the temperature, at least at $T < 2000$ K, while some others do not (although in the latter case the phonons usually have very small shifts up to 2000 K). Fig. 3.9 makes it clear that there is a deviation from the linear trend vs $T$ for all the LOs; for example, the linearity of the LO shift vs $T$ at $\frac{1}{5}\boldsymbol{k}_X$ and at $\frac{1}{5}\boldsymbol{k}_L$ is broken at $T = 1000$ K.

**The phonon linewidths**

Of course, the QHA is a band calculation, and therefore does not include any phonon linewidth. To asses the phonon linewidths, therefore, we need to look at the MD results, shown in the lower panels of Fig. 3.9. Let us first focus on the case of $\boldsymbol{k} = \frac{1}{5}\boldsymbol{k}_X$: this is the commensurate $\boldsymbol{k}$-point nearest to $\Gamma$ in the $\{100\}$ direction of the BZ, and therefore corresponds to the longest wave length accessible in this direction to the supercell considered. Let us call the LO mode with such long wavelength LWLO. The linewidth of the LWLO, $\Gamma_{\mathrm{LWLO}}(T)$, shows a curve that is concave down, resulting in a remarkably high value even at low $T$. In fact, the LO linewidth is one order of magnitude higher than the TO one at room $T$ and it increases with $T$ faster than any other mode, reaching the value of $\Gamma_{\mathrm{LWLO}}(T) \gtrsim 3$ THz at $T = 2000$ K. A similar trend is found for the LO linewidth at $\boldsymbol{k} = \frac{1}{5}\boldsymbol{k}_L$, confirming the observation that that the anomalous broadening is common to all zone center LO modes.

The violet symbols in Fig. 3.9 show the experimental values for the LO and TO linewidths from Calandrini *et al.* obtained from IR reflectivity [16]. I have drawn them at $\boldsymbol{k} = \frac{1}{5}\boldsymbol{k}_X$ rather than $\boldsymbol{k} \to \boldsymbol{k}_\Gamma$, which is the point sampled by IR reflectivity, since the supercell calculation does

not allow to distinguish the TO and LO at $\boldsymbol{k} = \boldsymbol{k}_\Gamma$. The experimental and calculated values compare qualitatively well until at $T < 500$ K for the TO mode, but a bigger inaccuracy is found for the LO mode. However, the discrepancy between experimental and simulated linewidths might be due to the fact that I am comparing two different wavevectors, $\boldsymbol{k} \to 0$ (experiments) and $\boldsymbol{k} = \frac{1}{5}\boldsymbol{k}_X$ (simulations). The simulated linewidths might be larger than the experimental ones because the LO *near* $\Gamma$, and not *at* $\Gamma$, is the most anharmonic [52].

Some references, like Ref. [33], often assume a linear trend of the phonon linewidths vs $T$. The reason for this should be that $\Gamma_{\boldsymbol{q}\nu} \sim T$ is expected to be the leading-order contribution to the linewidths, within PT. In this respect, it is interesting to evaluate the broadening of the phonons from MD, which is non-perturbative. Interestingly, we observe a significant departure from a linear trend of the phonon broadenings vs $T$ for many phonons. The most striking non-linear trend is that of the LO mode near $\Gamma$, which we have discussed, and that of the TO mode at all $\boldsymbol{k}$-points.

At $T \approx 3000$ K, the TO and LO linewidths at $\boldsymbol{k} = \frac{1}{5}\boldsymbol{k}_X$ and $\boldsymbol{k} = \frac{1}{5}\boldsymbol{k}_L$ converge to the same value. This is in contrast with the PT calculation of Giura *et al.*, for which the ratio between the linewidths of the LO and of the TO modes increases steadily with $T$ [52]. This suggests that the mechanism of three-phonon scattering for the LO decay described in Sec. 3.5.1 is valid only until a temperature for which four-phonon scatterings are relevant. It also suggests that the PT calculations, unless higher-than-third-order terms are considered, are inadequate at elevated $T$s. This nothing but reinforces the power of the MD technique, which is fully non-perturbative.

At larger wavevectors, the LO and TO modes have a comparable broadening, at least at $T < 2000$ K, and one which is smaller than the broadening of BZ center modes. At $T > 2000$ K and for $\boldsymbol{k} = \boldsymbol{k}_X$ the TO linewidth diverges from the LO one, while the LO saturates at $\approx 2$ THz.

**Summary of the QPA**

One of the scopes of this section was to show the softening of the phonon frequencies when the crystal is allowed to expand. Another one was to show that the QHA overestimates the frequency shifts at high $T$. Another one was to show that the phonon linewidths are strongly dependent not only on temperature, but also on pressure. While temperature activates phonon-phonon scattering, a higher pressure is, most of the times, a suppressor of anharmonicity. Decreasing the volume confining the atoms results in a less anharmonic crystal, at equal $T$. This can be understood if we consider that a lower pressure allows the atoms to explore a greater portion of the energy landscape, i.e., to be more affected by non-quadratic terms in the potential expansion. Fig. 3.9 allows to see this because it shows that the magnitude of the phonon linewidths in the $V(T)$ simulations are usually higher than the ones in the $V(T)$ simulations, besides for the zone center LO modes, which are peculiar in this respect.

One of the physical consequences we can think of in this regard is how the thermal conductivity is impacted by this. Thermal conductivity is smaller if the phonon linewidths are larger. One can therefore trap the heat by stretching the crystal.

## 3.7 Quasiparticle thermodynamics

The theoretical basis of this section was explained in Sec. 2.7. In an ionic crystal, the thermodynamic state functions can be calculated from statistical mechanical formulae, and depend entirely on the phonon frequencies [38, 17]. Once the fully anharmonic phonon spectra are obtained at different temperatures, and as long as the phonons remain well defined quasiparticles (QP), one can use the quasiparticle frequencies to perform calculation of the basic thermodynamic quantities. In Sec. 2.7, I derived an equation which allows to calculate the heat capacity by using the phonon quasiparticle frequencies; this is of course an approximation, which we called quasiparticle approximation (QPA). The approach of calculating thermodynamic quantities in this way is called quasiparticle thermodynamics [31, 2].

The approach of using the finite-$T$ phonon frequencies in the calculation of thermodynamic state functions is not dissimilar to the usual way in which the heat capacity is calculated within the QHA [71, 41], which I discussed in Sec. 2.7. However, the QHA neglects phonon-phonon interactions and hence should be regarded as a poorer approximation than the QPA. The QPA, on the other hand, includes anharmonicity directly, and within the FT-VVCF method it includes anharmonicity virtually to all terms in the potential expansion. I am not the first to propose that the QP frequencies can be used into thermodynamic state functions. In fact, the quasiparticle thermodynamic calculation was performed by some authors specifically after the use of the velocity-velocity correlation function, in Ref. [128] (model system), Ref. [129] ($CaSiO_3$), Ref. [151] ($MgSiO_3$). However, the latter two studies were performed with a $2 \times 2 \times 2$ MD supercell and did not show any comparison to experimental results.

In this section, I focus on the *isobaric* heat capacity. I compare a hierarchy of methods, which, in increasing order of complexity, are: the HA, in its classical and quantum mechanical versions, the QHA, and the QPA. The HA and QPA calculations come from this work, the QHA from Karki *et al.* [71] and I also provide the experimental results from Ref. [67]. I chose the isobaric heat capacity for two reasons: firstly, being a constant pressure quantity, we can use the $V(T)$ set of simulations, for which some spectra and some frequency shifts are given in Fig. 3.5 and Fig. 3.9 (blue lines), respectively. Secondly, I chose the isobaric heat capacity because Karki *et al.* showed that the heat capacity in the QHA calculation does not compare well with experiments at $T > 1000$ K, and we are obviously keen on seeing if the fully-anharmonic calculation can overcome this problem.

One of the main outcomes of this section is that when one calculates the isobaric heat capacity with the fully anharmonic quasiparticle phonon frequencies, good agreement with experiment is obtained. The other outcomes will be discussed at the end of next section, after the results are shown.

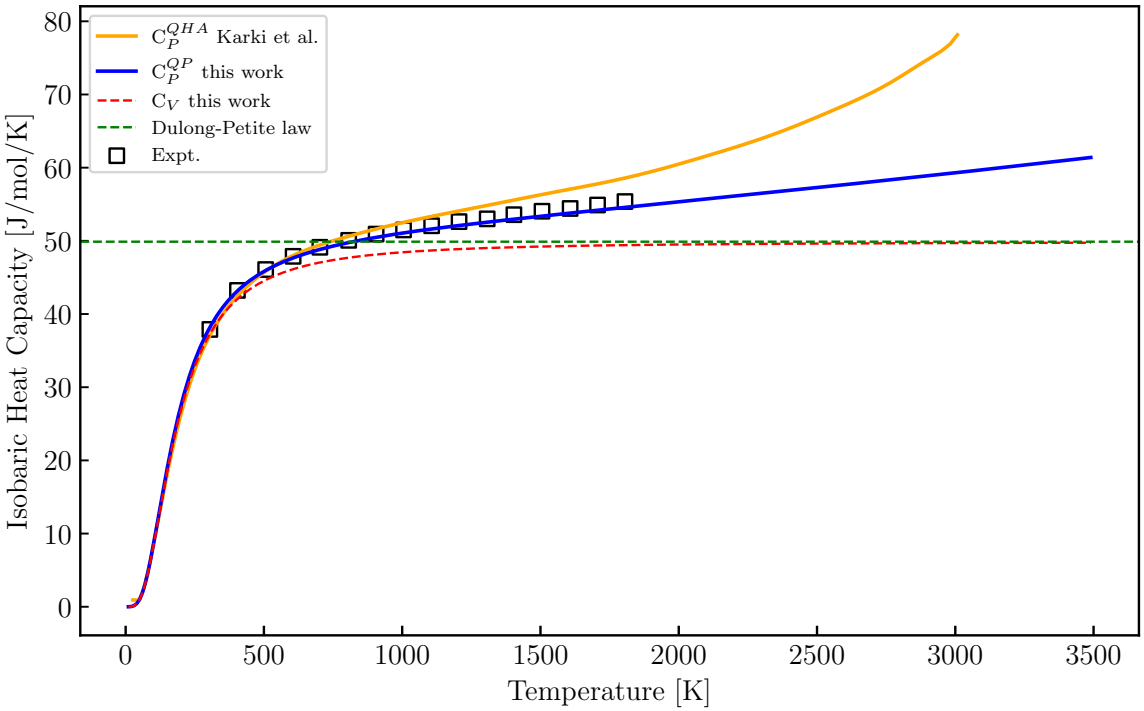



Figure 3.10: Hierarchy of methods for calculating the isobaric heat capacity. Symbols denote experimental values of Ref. [67], the yellow line denotes QHA calculation from Karki *et al.* [71] and the blue line corresponds to the quasiparticle calculation of $C_P^{\mathrm{QP}}$ from Eqs. 2.44-2.43. The broken lines denote $C_V$ computed from the HA through the quantum mechanical formula (in red) and the classical Dulong-Petite law (in green).

### 3.7.1 Isobaric heat capacity from quasiparticle thermodynamics

The formulae with which the isobaric heat capacity, $C_P(T)$, can be calculated from the phonon frequencies are reported in Eqs. 2.44-2.43. Within the QPA, the QP frequencies are defined as the peak positions of the Lorentzian fits to the phonon spectra at the different temperatures for which I run MD simulations. I then used the QP frequency *shifts* from their harmonic values in the BZ summation required by Eqs. 2.44-2.43.

The comparison between the heat capacity calculated with the classical Dulong-Petite law, the HA, QHA and QPA is presented in Fig. 3.10. The quasiparticle heat capacity, $C_P^{\rm QP}(T) = C_V(T) + C_{PA}(T)$, is drawn with a blue line, the QHA calculation from Karki *et al.* [71] with a yellow line and experimental values from Ref. [67] are denoted by symbols; the classical harmonic calculation, which corresponds to the Dulong-Petite law [4], is drawn with a green broken line, and the quantum mechanical HA calculation is drawn with a red broken line.

Fig. 3.10 can be used as a systematic assessment of the validity of the HA, in both its classical and quantum mechanical forms, the QHA and the QP thermodynamics. We shall comment on this hierarchy of methods from bottom to top, starting from the HA.

The HA obviously fails since it does not include any anharmonic effect, be it thermal expansion or phonon-phonon interactions. The classical version of it, the Dulong-Petite law, is very inaccurate at low $T$, as is well known [4]; on the other hand, the quantum mechanical HA is able to correctly reproduce the notorious S-shape of the heat capacity at low $T$, namely the $T^3$-law [4]. However, the HA is inaccurate at high $T$, since it does not include anharmonicity. In fact, the two flavours of the HA converge to the same value of $3n_a k_B$ (expressed in $\mathrm{JK^{-1}mol^{-1}}$ in Fig. 3.10) at high $T$, where $n_a$ is the number of atoms per unit cell, while the measured values of $C_P(T)$ increases almost linearly at high $T$. Note also that the discrepancy between classical and quantum mechanics reduces with increasing $T$.

The QHA is the second-best approximation in the hierarchy I am presenting: it works well at low $T$, it correctly reproduces the departure from the HA curve due to thermal expansion effects, but breaks down at $T > 1000$ K, giving values for the heat capacity that progressively

diverge from the experimental ones. The reason for the accuracy of the QHA at low $T$ lies on the fact that it mimics the crystal's thermal expansion by calculating the phonon frequencies with artificially expanded volumes. The reason for its inaccuracy at high $T$ is that the QHA does not account for the true anharmonicity of the crystal, and assumes that phonons do not interact.

The QPA, on the other hand, gives the correct quasi-linear trend at high $T$, and re-establishes agreement with the experiments. I cannot be confident enough that this agreement will be good also at $T > 1800$ K, because there is no available experimental data to compare with, but the $C_P^{\mathrm{QP}}(T)$ curve seems satisfactory. I have then shown that the fully-anharmonic phonon quasiparticles can be used to calculate anharmonic thermodynamic state functions. This suggests that the failure of the QHA is not caused by the approximation of treating the phonons as quasiparticles, but by incorrectly accounting for their self energies. Unfortunately, the lack of experimental data at very high $T$ makes it difficult to establish precisely at what temperature the quasiparticle picture of the phonons breaks down in MgO. However, Fig. 3.5 manifests that this surely happens close to the melting point $T_m$, where bands have disappeared completely.

### A high-$T$ approximation

Let us take Eq. 2.44 again, which this section is based on, and let us consider the high temperature limit $k_BT \gg \hbar\omega$. In this limit, the Bose-Einstein distribution becomes $\bar{n}_{\mathbf{k}\nu} \sim k_BT/\hbar\omega_{\mathbf{k}\nu}$, and assuming to first-order that $\Delta_{\mathbf{k}\nu} \approx a_{\boldsymbol{k}\nu}T$ [31], where $a_{\boldsymbol{k}\nu}$ is constant expressing the rate at which the phonon frequencies shift with $T$, then the second term in the square brackets of Eq. 2.44 vanishes, and the anharmonic part of the heat capacity is proportional to

$$C_{(V,P)A}^{\text{high } T} \sim -\sum_{\boldsymbol{k}\nu} k_B T \frac{\partial(\Delta_{\mathbf{k}\nu}/\omega_{\mathbf{k}\nu})}{\partial T} = -\sum_{\boldsymbol{k}\nu} \frac{a_{\boldsymbol{k}\nu}}{\omega_{\boldsymbol{k}\nu}} k_B T. \tag{3.1}$$

So, $C_{(V,P)A}^{\text{high } T} \sim T$, in agreement with thermodynamic perturbation theory [31, 77, 91, **?**]. Hence, thermodynamic perturbation theory, which is based on the truncation of the expansion for the partition function to first order [31], seems to corresponds to the QP thermodynamics when

the phonon frequency shifts are linear with $T$.

In other words, by assuming that phonons shifted linearly with temperature, $\Delta_{\mathbf{k}\nu} = a_{\boldsymbol{k}\nu}T$, we could have obtained a curve for the heat capacity valid at high $T$ so that $C_{(V,P)A}^{\text{high } T} \sim T$ by fitting the phonon frequency shifts to lines and obtaining the rates of the shifts, $a_{\boldsymbol{k}\nu}$'s. However, as we saw in Fig. 3.9 where I showed the frequency shifts of the phonon quasiparticles, the $\Delta_{\mathbf{k}\nu} = a_{\mathbf{k}\nu}T$ rule is not always respected, at least not for all phonons. In fact, many of the optical phonons frequencies shifts are very non-linear against $T$. Hence, first-order thermodynamic perturbation theory might fail at high $T$, and the correct values of the phonon self energies have to be computed instead.

It is also interesting to notice from Eq. 3.1 that the high-$T$ heat capacity increases if the phonon frequencies decrease, and viceversa. Moreover, we expect $C_P$ to increase with $T$ at a much greater pace than $C_V$, for two reasons: firstly, the magnitude of the phonon frequency shifts in the constant pressure simulations is much bigger than in the constant volume ones, and secondly, in the latter case the frequencies increase and decrease depending on the phonon involved, and so their opposite sign contributions in Eq. 2.44 may compensate.

Finally, bearing in mind again the high-$T$ limit of $C_P$, Eq. 3.1, the formula contains a sum over all phonon frequencies, as the heat capacity is an extensive properties. However, the heat capacity per atom (or per cell, or per mole) is an intensive property, and if the harmonic band structure is known, one can get an estimate of the term present in the formula for the heat capacity, $\frac{1}{N}\sum_{\boldsymbol{k}\nu}\frac{1}{\omega_{\boldsymbol{k}\nu}}$ (a sort of "inverse Einstein phonon"). Then, if the curve $C_P$ vs $T$ is known, one can get a (very rough) estimate of the phonon frequency shift rates $\hbar a_{\boldsymbol{k}\nu}$. That is, from very simple calorimetric measurements one can get a rough estimate of the true phonon frequency shifts at any temperature.

## 3.8 Conclusions

In this chapter, we have analyzed accurate vibrational spectra of crystalline MgO in a wide temperature range; I have presented what I believe to be the first detailed images of a real three-

dimensional crystal's spectrum as it transitions from a band structure, at low $T$, to having little observable structure upon melting. As far as I am aware, this work is the first investigation of strongly-interacting phonons in a real material that has produced vibrational spectra with enough detail to observe individual bands dissolve as $T$ increases up to the melting point.

The method I have used is generally-applicable: it does not require the material to be crystalline or to be at thermal equilibrium. For example it could be used, with equal validity, to calculate the vibrational spectrum of water, or a ferroelectric material, during resonant excitation of one of its IR-active modes. Therefore this method is a very powerful tool, which will have increasing importance as it becomes possible to calculate forces accurately and efficiently for more materials. It complements, and is complemented by, perturbation theories; but it is the only method that we are aware of that is as applicable to an amorphous material in a far-from-equilibrium stationary state as it is to a perfect crystal at equilibrium under ambient conditions.

I have identified, and discussed in some detail, two physical considerations about the spectra, which are likely to have important observable consequences for a wide range of crystals. The first is that phonons are likely to have a negative frequency shift when thermal expansion is allowed. The second is that zone center LO phonons are heavily damped at all $T$. I have provided two explanations for this, one which makes use of the concept of the two-phonon density of states, and one which highlights the classical picture of the phonons: waves which interact with each other. The first explanation treats the phonons as weakly interacting *quasi*particles, which can scatter from each other only if the momentum and energy are conserved. The second explanation supports the idea that the LO mode is highly sensitive to the amplitudes of acoustic phonons, because a large fraction of $\omega_{\boldsymbol{k}}^{\mathrm{LO}}$ is contributed by the LO mode's intrinsic field, which acoustic phonons warp and weaken. Despite this strong acoustic-LO coupling, long wavelength acoustic phonons are adiabatically decoupled from LO modes: they strongly modulate the energies and the frequencies of LO modes, while maintaining approximately-constant energies and frequencies themselves.

By calculating spectra at both constant volume and constant pressure, we have been able to

identify some features of the spectrum's $T$ dependence as consequences of thermal expansion, and to show that others, such as the rapid degradation of the LO band, are not.

I have also shed substantial light on the limitations of the quasiharmonic approximation and have shown that some of these are rectified by the quasiparticle approximation. By fitting the phonons to Lorentzian functions, I evaluated their frequency shifts and linewidths. We saw that many of the optical modes' frequencies and linewidths do not show linear trend with $T$.

I calculated the isobaric heat capacity within quasiparticle approximation. Taking the heat capacity as reference, we commented on a hierarchy of methods, which includes the classical HA, the quantum mechanical HA, the QHA and the QPA. The QPA has proven to be the most accurate: the calculation shows that agreement with experiment is recovered if the fully-anharmonic phonon quasiparticles are used to calculate thermodynamic state functions. Of course, this is valid only inasmuch as the phonon quasiparticles are well defined, namely, until temperatures close to the melting point. Finally, the high-$T$ limit of the equation for the heat capacity allowed me to suggest a link between calorimetric measurements and phonon frequency shifts.

# Chapter 4

# Interlude

So far we have discussed anharmonicity in MgO. The melting of the phonon bands which we referred to in the introduction of this thesis (Sec. 1.1) was apparent in Sec. 3.4.1. From what we saw in Fig. 3.5, the bands degrade *progressively* when the temperature is raised and phonons start to interact, and this process occurs to the optical modes first. The acoustic modes retain a good degree of integrity up to the melting point $T_m$. By calculating the isobaric heat capacity we saw that, until temperatures not too close to $T_m$, the phonons can still be considered quasi-excitations with a well-defined frequency and a linewidth: the quasiparticle picture holds. However, when $T \approx T_m$, bonds start to break and there is little to no structure in the distribution of kinetic energy in reciprocal space: $\tilde{\mathcal{E}}(\omega, \boldsymbol{k})$ is spread out and the delocalization of the energy signals a localization of the atomic motion; all the phonons have melted. This means that atoms do not participate in collective vibrations anymore, having lost correlation in length-scales of $\approx 1$ or 2 lattice constants, as expected in a liquid.

In the next chapters, I will present a material in which band melting occurs *suddenly* and for two bands only: this is the case of $BaTiO_3$. Just as in MgO the phonon bands' melting is a consequence of the complete loss of correlation in real spacetime of the atomic motions, so is for $BaTiO_3$. However, while for MgO the melting of optical and acoustic modes in MgO signals a phase transition solid-liquid, for $BaTiO_3$ the melting of the Slater modes (Sec. 7.7) determines a structural phase transition, ferroelectric solid - paraelectric solid.

The repercussions of band melting on the dynamics of $BaTiO_3$ are dramatic: across the phase transition, and well into the paraelectric phase, a new mode arises, whose character is rather different with respect to a vibrational mode in which the potential energy surface is quadratic. This mode is responsible for the peculiar ferroelectric and ferroelastic behaviour of this interesting perovskite, and for the formation of polar ferroelectric regions in the paraelectric phase.

# Chapter 5

# Introduction to $BaTiO_3$

## 5.1 Ferroelectricity and ferroelasticity of $BaTiO_3$

$BaTiO_3$ is a common perovskite. The term "perovskite" is the term used for the mineral $CaTiO_3$, which has given its name to the set of compounds isomorphous with it. Perovskites are minerals of the $ABX_3$ type with strong ionic bonds between atoms, and where A and B are cations, and the X atoms are the anions. Their primitive unit cell is illustrated schematically in Fig. 5.1.

Among the perovskites, $BaTiO_3$ is a particularly interesting one, because it is both ferroelectric and ferroelastic. Being ferroelectric it is also pyroelectric and piezoelectric.

Ferroelectricity is the most striking characteristic of $BaTiO_3$. A material is simply a polar dielectric when it exhibits a spontaneous electric polarization even without any applied electric field. The key aspect of ferroelectricity is the property of the electric polarization to be switched between symmetry-equivalent states by the application of an electric field of significant magnitude, where those states are related through a symmetry-breaking phase transition. Similarly, the spontaneous strain in ferroelastics can be switched between symmetry-related states by the application of a stress. Ferroelasticity is hence the "elastic version" of ferroelectricity. Piezoelectricity is the capability of a material to polarize, and hence produce an excess

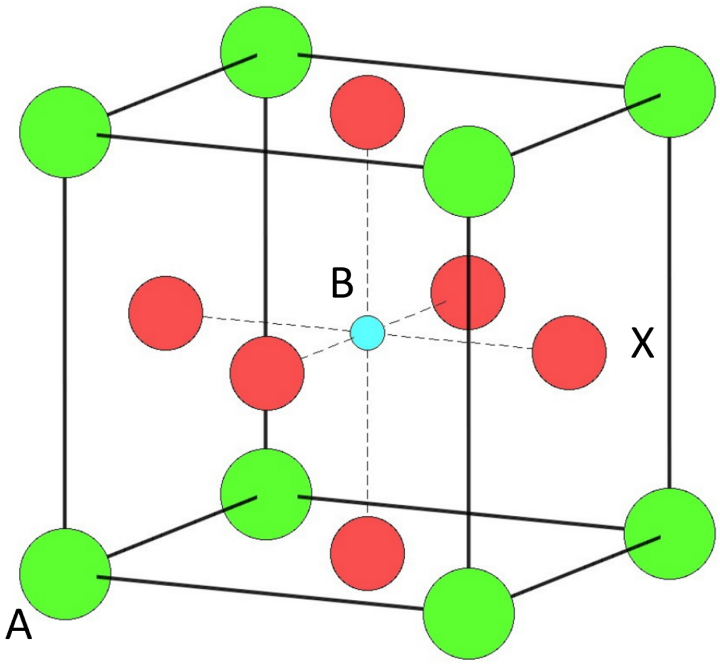



Figure 5.1: Schematic structure of perovskites, featuring the A and B cations and the X anions.

charge, during the application of a stress or strain. Pyroelectricity is a change in spontaneous polarization due to a change in temperature–it occurs in all polar dielectrics.

These properties are of course not entirely independent from one another. For example, a ferroelectric is obviously pyroelectric, and a pyroelectric is also piezoelectric [111]. However, ferroelectricity and ferroelasticity do not always come together: for example, triglycine sulphate is ferroelectric but not ferroelastic, since it does not change its crystal system [141]. Other materials, like $BiVO_4$, are ferroelastic but not ferroelectric [141]. Quartz manifests elastic anomalies across its phase transition, but it is not ferroelectric [38, 105, 141].

In $BaTiO_3$, ferroelectricity and ferroelasticity are inextricably linked. When the spontaneous polarization appears at $T_C$, the appearance of the spontaneous strain is an inevitable consequence of this–it is bound to happen through the so-called electrostrictive effect. Because in $BaTiO_3$ these interesting properties appear all together, this material has been studied extensively, and is suitable for many technological applications, some of which will be discussed in Sec. 5.5.

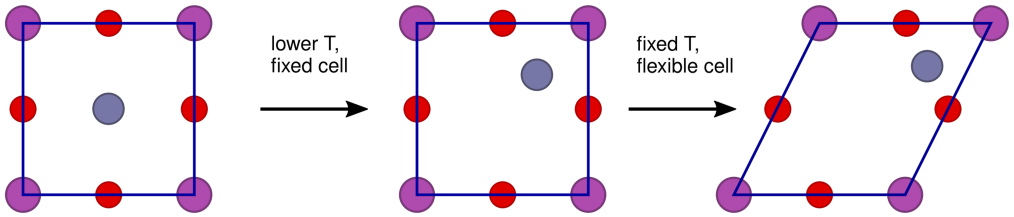



Figure 5.2: 2D model ferroelectric-ferroelastic lattice, readapted from Gigli *et al.* [50]. Different atoms are shown with different colors. The left plot shows the cubic cell, which is stable at high $T$, and since it has a center of inversion symmetry, gives a paraelectric phase. The middle plot shows the behaviour of a ferroelectric material as $T$ is lowered: the central atom displaces along the square diagonal, the inversion symmetry is broken and a spontaneous polarization appears. If the material is also ferroelastic, the cubic cell is unstable: as the right plot shows, if we allow to cell change its shape freely (no stress applied), it distorts along the direction of the Ti displacement.

## 5.2 The phases of $BaTiO_3$

At high $T$, the stable structure of $BaTiO_3$ has a cubic unit cell. Because the cubic structure possesses a center of inversion symmetry, it cannot have any spontaneous polarization [43]. Hence, the cubic phase of $BaTiO_3$ is paraelectric (PE). The PE phase is stable up to the melting point[1]. The ferroelectric-ferroelastic coupling of $BaTiO_3$ is responsible for it undergoing the following sequence of phase transitions as $T$ is decreased, starting from its paraelectric phase: cubic $Pm\bar{3}m$ (C) $\xrightarrow{\approx 400\text{ K}}$ tetragonal $P4mm$ (T) $\xrightarrow{\approx 278\text{ K}}$ orthorhombic $Amm2$ (O) $\xrightarrow{\approx 183\text{ K}}$ rhombohedral $R3m$ (R). This amounts to four stable phases, of which all but the C one are ferroelectric (FE).

When $T \to 0$, atoms oscillate about the crystal's minimum energy positions, $\{\mathbf{R}_i\}$. When $T > 0$, these positions can change gradually with $T$ as a result of thermal expansion. At $T = T_C$, namely at the transition temperature or Curie temperature, the material passes from one solid phase to another, and the average positions about which the atoms vibrate change abruptly. In the case of ferroelectric materials like $BaTiO_3$, the phase transition can occur between FE-FE phases or between FE-PE phases. Alongside the shift in the atomic average positions, often the unit cell's shape changes as a consequence of the reduced/enhanced symmetry and the altered balance between the atomic interactions.

[1] although another phase with hexagonal symmetry was found at $T > 1733$, but this phase seems to be unstable [43]

One of the ways atoms arrange and the cell distorts as a ferroelectric-ferroelastic material is cooled down through a PE-FE phase transition can be understood by looking at the schematic of Fig. 5.2, which is readapted from Gigli *et al.* [50]. This shows a dummy 2D ferroelectric-ferroelastic lattice; ideally, one could think of this lattice as a slice of a real $BaTiO_3$ crystal which contains Ba atoms (drawn in purple), O atoms (drawn in red) and the Ti atom (drawn in grey). However, it needs to be remembered that this is a schematic representation of $BaTiO_3$, and does not necessarily represents its real R-O-T-C transitions. We will use it merely to understand how a material can be both ferroelectric and ferroelastic. When $T$ is decreased, the Ti occupies a lower-symmetry position, and a new phase is established. Such phase is ferroelectric, because of the spatial unbalance between charges creates a non vanishing dipole moment in the unit cell. However, if the material is also ferroelastic this phase is unstable: if the cell's shape is allowed to change, it distorts in the direction of the Ti displacement, becoming rhomboidal. This creates a strain field within the crystal, which in the schematic case of Fig. 5.2 is a perfect shear. This is, qualitatively speaking, what gives $BaTiO_3$ its ferroelectric-ferroelastic behaviour, namely a coupling between elastic strains and ferroelectricity.

## 5.3 Theories for phase transitions

The reason for the rich phase diagram of $BaTiO_3$ has been debated for more than 50 years [25, 94], and a consensus has not been reached yet [125, 62, 94]. The debate revolves around the mechanism underpinning the phase transitions, which is commonly understood in terms of two competing theories: displacive vs order-disorder. It is quite surprising that, after so many years, there hasn't yet been a satisfactory agreement on which mechanism better describes the phase transitions.

I will now discuss the substantial differences between these two theories in detail, before looking at the experimental literature in Ch. 6.

### 5.3.1 Displacive theory

I now introduce the displacive theory. One way to understand why a phase transition occurs is to understand why a distorted cell is energetically favourable. A phase transition occurs when a change in $T$, $P$, applied stress or electric field, causes the Gibbs free energy ($G = U - TS + PV$) of another phase to be lower than the current one. $G$ can be lowered by increasing $S$, decreasing $V$, or if $U$ is lowered by distortions/displacements of the primitive cells. The free energy is a macroscopic property of the crystal, whereas $U$ contains local interactions between atoms (but may also have a contribution from long range interactions). Within the displacive theory, it is implied (but often overlooked) that we need to consider the free energy, i.e., a macroscopic thermodynamic state function, rather than the internal energy $U$.

Similarly to the way we expanded the potential energy in powers of the atomic displacements in Eq. 2.3, we could expand the free energy in powers of a macroscopic order parameter (about a reference state), and find out the values of the order parameter for which the free energy is at a minimum. This Taylor expansion is called "Landau free energy", and the resulting theory is the displacive theory. A beautiful and more comprehensive review of the displacive theory and phase transitions in crystals was given by Dove in Refs. [38, 39].

It is in general not easy to find a suitable macroscopic order parameter, and it is not my scope to do it here, but if a phonon mode exists whose eigenvector imposes a displacement pattern compatible with the phase transformation (e.g., referring to Fig. 5.2, the Ti must displace along a square diagonal), then *that* eigenvector can be taken as an order parameter. This means that the displacement pattern it imposes, or the polarization resulting from it, are suitable order parameters. Note that, because $BaTiO_3$ is also ferroelastic, the macroscopic strain associated to the change in the unit cell's shape should be considered as well. The reader interested in an accurate group-theoretical analysis of the search for an order parameter for $BaTiO_3$ is referred to Ref. [112]. I hereby limit myself to pointing out that the eigenvector of the mode generally considered responsible for the phase transition involves the displacement of the Ti against the O octahedron, as I will show in Chs. 6-7. This mode, in the spectroscopic community, is often called "Slater" mode [63].

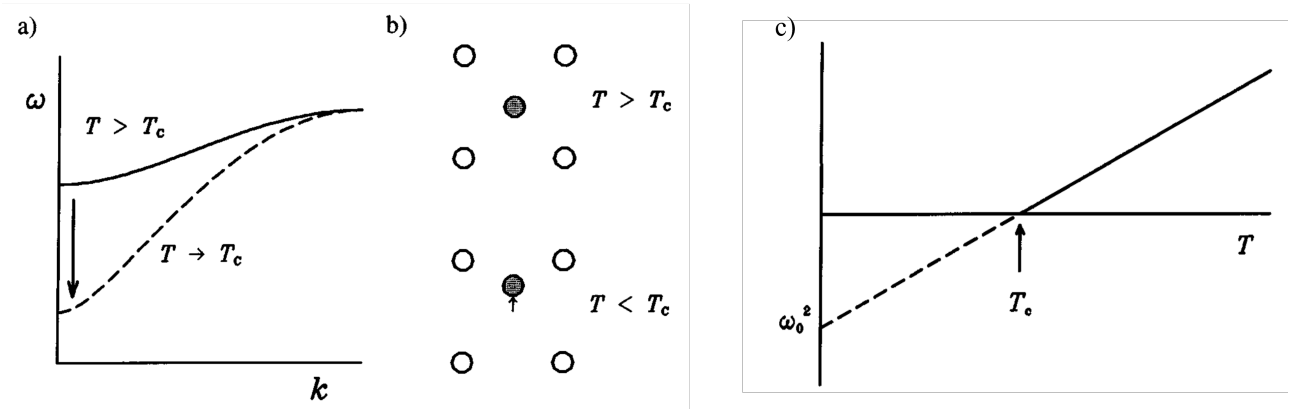



Figure 5.3: Schematic of a displacive phase transition, copied from Dove [38], where the soft mode is a BZ center one. Panel a) is a plot of the soft mode frequency as a function of the wavevector, showing the branch softening. Panel b) is the real-space picture showing that the atom in grey is displaced from the centrosymmetrical position when $T < T_C$. Panel c) shows the evolution of the soft mode at the BZ center vs temperature, according to Cochran's law.

Just as in Eq. 2.19 the quadratic terms in the Taylor expansion of the potential written as a function of the mode amplitudes are proportional to the square of the zero-$T$ harmonic phonon frequency $\omega^2_{\boldsymbol{q}\nu}$, the second derivative of the Landau free energy is proportional to the finite-$T$ square phonon frequency $\tilde{\omega}^2$, if a mode amplitude is taken as the order parameter. The displacive picture is a macroscopic picture, which is entirely based on the Landau expansion of the free energy and on the fact that $\tilde{\omega}^2$ is assumed to vary as $\tilde{\omega}^2 \sim (T - T_C)$ [38], where $T_C$ is the transition (or Curie) temperature. The $\tilde{\omega}^2 \sim (T - T_C)$ law was proposed for the first time by Cochran in 1960 [22], and for this reason it goes by the name of Cochran's law. I should highlight that this law is phenomenological.

Cochran's law implies that the phonon frequency softens perfectly as $T$ approaches $T_C$. This is schematically depicted in Fig. 5.3c, copied from Dove [38], which shows the $T$-dependence of an ideal BZ center soft mode. When $T < T_C$, the squared phonon frequency is negative and hence produces an imaginary phonon frequency, which of course is impossible. This means that the crystal is unstable with respect to displacements along the mode's eigenvector, i.e., the crystal's energy is lowered by distortions along the mode's eigenvector. This is why the phonon band structures calculated at $T = 0$ in the HA *for a high-symmetry phase* (e.g., the C phase of $BaTiO_3$) are often used to see if there are imaginary frequencies for the phonons [49]; if imaginary frequencies are found for some branches in some portions of the BZ, then the

high-symmetry phase is deemed unstable in the limit of $T \to 0$, where the HA holds. Or, as is often said, the equilibrium stable structure at low $T$ is equivalent to the higher-symmetry structure but with a phonon mode "frozen in". Let us continue our discussion on the displacive theory by looking at what happens when $T$ increases and the $\tilde{\omega}^2 \sim (T - T_C)$ law is assumed. At higher temperature, the phonon frequency increases so that it becomes real and positive at $T > T_C$, and the high-symmetry phase becomes stable. Fig. 5.3a shows the ideal soft mode's dispersion when $T > T_C$ and when $T \to T_C$, indicating that the branch softens with decreasing $|T - T_C|$, particularly near the BZ center.

A schematic depicting the real space picture of a displacive transition is presented in Fig. 5.3b, where a 2D view of a unit cell is shown, and the displacing atom is the dark one. At $T > T_C$, the atoms vibrate about highly-symmetrical positions, and the dark atom is at the center of the cell. When $T \to T_C$, the energy required to excite the soft mode is low, and when $T = T_C$ it vanishes; the crystal is unstable against a distortion along the eigenvector of the soft mode. Hence, the atoms displace along the eigenvector of the zero-energy mode, until a new, stable, lower-symmetry phase is established as in the lower plot of Fig. 5.3b. Of course, the soft modes need not be BZ center modes, like in the example above. When the soft mode is a BZ boundary mode, the real space picture is different, in that the atomic displacement have alternating phase factors in going from one unit cell to a subsequent one. For example, the zone boundary soft modes of $SrTiO_3$ [113] give rise to antiparallel rotations of the oxygen octahedra, resulting in an *anti*ferrodistortive behaviour [38]. In other words, the crystal displaces along an eigenvector of a mode with wavelength $2a$, where $a$ is the lattice parameter, which makes each cell and its neighbour inequivalent. This doubles the size of the primitive unit cell [113].

We can therefore summarize the displacive theory in the following way: *the displacive theory is the theory of a phase transition according to which a phonon mode softens completely in approaching the Curie temperature* $T_C$. Its theoretical foundations were laid by Cochran in 1960 in the historical review of Ref. [22]. The great success that the theory immediately earned is owed to its ability to describe some of the features and quantities that accompany the phase transitions, and that are of interest to the scientific community studying ferroelectric materials. One of these features is the increase in the static dielectric constant according to the Curie-

Weiss law. In fact, the Lyddane-Sachs-Teller relation states that the static dielectric constant $\varepsilon_s$ is proportional to the ratio between the longitudinal and transverse optical frequencies of the phonon modes in the $\boldsymbol{k} \to 0$ limit [4]. I will formally state this law in Sec. 8.1, where I will discuss the ferroelectricity of $BaTiO_3$ in some detail; for the moment, we shall continue with a qualitative discussion. If a transverse optical mode is soft, then $\varepsilon_s$ increases. The increase of $\varepsilon_s$ is typical of ferroelectrics, and it is of interest not only for the scientific community, but also for any technological application where a good capacitor is needed. Ferroelectricity is the subject of Sec. 8.1.

### 5.3.2 Order-disorder theory

The order-disorder theory was originally proposed for $BaTiO_3$ in 1966 by Bersuker [12], but received more widespread attention in 1968 when it was revived by Comes, Lambert and Guinier [25][2]. Let us denote the nominal structure as the spatially averaged structure as measured, for example, by X-ray diffraction. The authors envisaged, through their famous eight-site model, that at any $T$ each titanium would not be located at the very site of the nominal perovskite structure, i.e., in accordance with the space group of the crystal at that $T$. On the contrary, the Ti would be in all phases located at one of the eight equivalent off-centered positions, which are displaced from the center of the cell in the directions of the eight nearest Ba atoms.

Fig. 5.4, taken from the Comes, Lambert and Guinier paper [25], which dealt with the O phase, explains this pictorially: in each unit cell, the Ti is not located *at* the center of the unit cell, but is displaced in a $\langle 111 \rangle$ direction. Such displacement persists in all phases of $BaTiO_3$, even in the paraelectric one, where the position of the Ti in the nominal structure is the body center. In other words, the unit cell has a rhombohedral distortion at any given time and at any temperature, but its average over many cells at any given time gives the nominal structure.

It is important to notice that, in the eight-site model depicted in Fig. 5.4, the Ti displacement differ from one cell to another *only in their [010] component*, whereas their [100] and [001]

[2]most of the times, Bersuker is not even mentioned as the first author to promote the order-disorder theory. We should give credits to him, but in the following I will mostly refer to Comes, Lambert and Guinier.

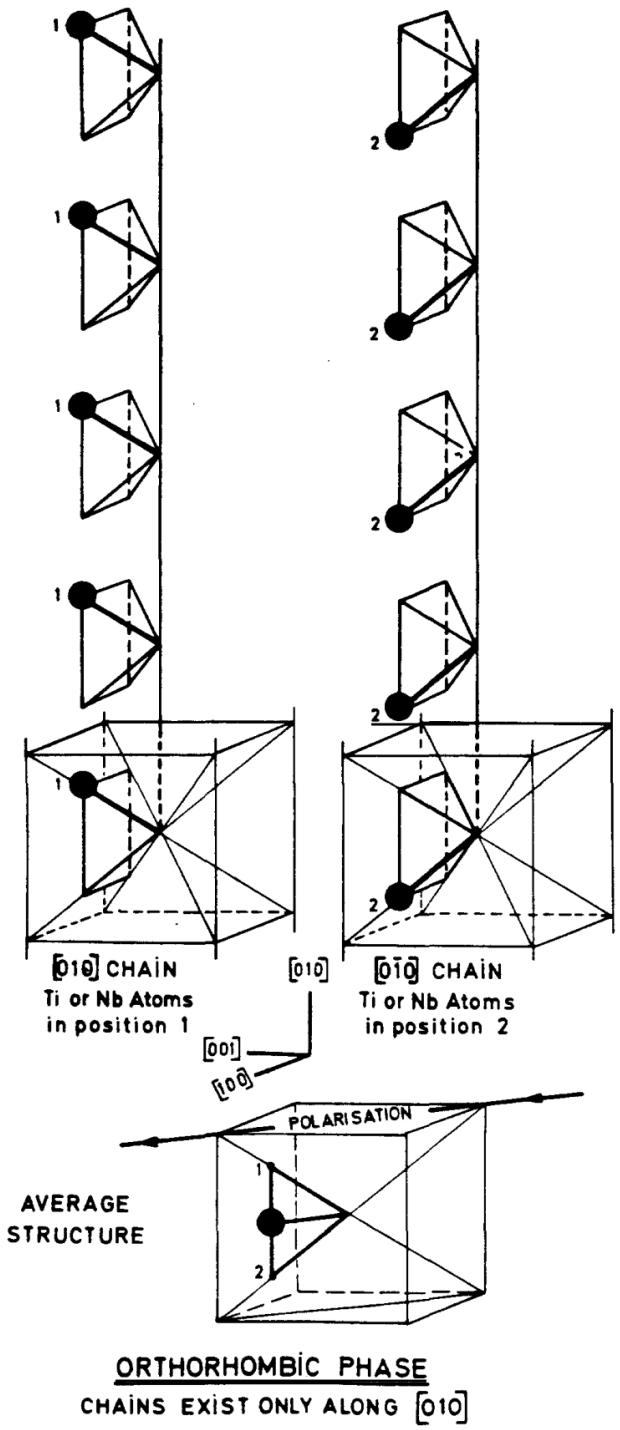



Figure 5.4: The eight-site model of Comes, Lambert and Guinier, taken from Ref. [25]. The upper panel shows the spatial arrangement of the titaniums: the atoms are displaced in one of the eight equivalent positions along the cube's body diagonal, and they align their displacements on a [010] direction forming chains. The chains are differently polarized: chain 1 is polarized up and chain 2 is polarized down. The middle panel shows an enlarged version of the eight possible orientations of the Ti displacement, and their orientations in the two chains. The lower panel shows the total net polarization of the crystal: this is along [101], because [010] chains and [0$\bar{1}$0] chains compensate: they average out in space to a net zero polarization along [010].

components are the same in all cells. For this reason, the total crystal's polarization is oriented along a [101] direction, while the polarization along [010] averages out to zero. Hence, the phase illustrated in Fi. 5.4 is orthorhombic. Another peculiarity of the eight-site model is that, along the [010] direction, the Ti displacements align, and atoms form linear chains. We can define a linear chain as a line of primitive face-sharing cells whose Ti displacements and strains are all along the same direction, the chain's axis. An example of two chains, denoted 1 and 2, is illustrated in Fig. 5.4.

The disorder in the O phase (and, by extension, in subsequent higher-symmetry phases) is caused by the loss of correlation between chains in the direction perpendicular to them. They alternate their polarization: if chain 1 is polarized up, chain 2 is polarized down, as we move perpendicularly to the chains' axes. Hence, the high-symmetry phase is disordered: the polarization of a plane of atoms containing the [010] axis, like the plane of Fig. 5.4, is zero, but only on a spatial average: locally, the polarization is finite and rhombohedral. The R phase, not displayed here, is generated by re-ordering the polarization along [010]; this is attained when all the Ti align their displacements in this direction. In other words, the R phase is realized when all the titaniums are equally displaced along one of the equivalent $\langle 111 \rangle$ directions.

We can therefore summarize the order-disorder theory in the following way: *the order-disorder theory is the theory of a phase transition according to which a phase is locally disordered, and it averages out in space (and/or time) to the high-symmetry phase.* Of course, the model of chain-like correlation of the Ti atoms and its consequent disorder, which was proposed by Comes, Lambert and Guinier, should not be regarded as the most general mechanism by which disorder can establish in a material. However, it is apt to understand how order-disorder transitions occur in $BaTiO_3$ [25, 126].

In the following of this thesis, I will present evidence consistent with the order-disorder picture, but the precise mechanism with which this happens is the subject of Ch. 7.

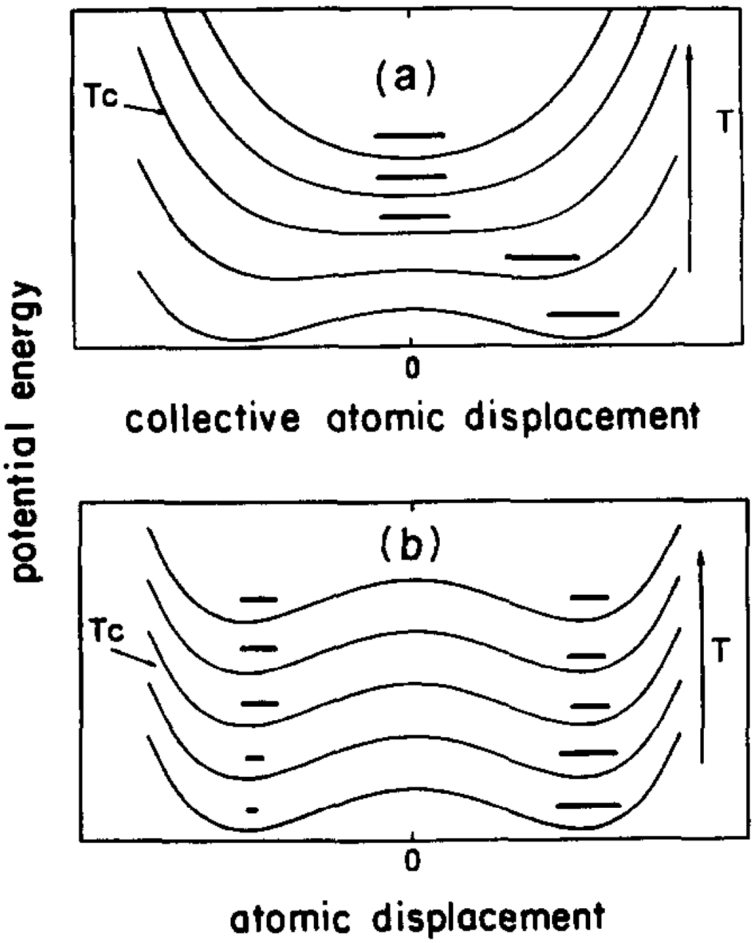



Figure 5.5: Potential energy as a function of the collective displacement imposed by a macroscopic parameter, in panel (a), and as a function of the displacement of a single atom in panel (b). Panel (a) represents the case of a displacive transition, whereby the potential energy is in the form of a double well at $T < T_C$ and becomes a quadratic potential at $T > T_C$, hence it changes with $T$. The collective motion of the atoms is about a well of the potential energy, hence the atoms displace altogether at $T \to T_C$. Panel (b) is the case of an order-disorder transition. The potential energy surface does not change with $T$, hence in the $T > T_C$ phase the atom hops from one minimum to another. The phase has higher symmetry, on spatial and time average. The figure is taken from Stern and Yacoby [126].

### 5.3.3 Displacive vs order-disorder

To better understand the difference between the displacive and order-disorder mechanisms, let us have a look at Fig. 5.5: this is copied from Stern and Yacoby [126], and depicts the potential energy function in a displacive phase transition in the top panel, and in an order-disorder phase transition in the bottom panel. It is important to note that the potential energy function is plotted against two different quantities in the two panels. In the top panel, potential energy is plotted against the *collective atomic displacements*, namely, a macroscopic order parameter. In the bottom panel, the potential energy is plotted against the *displacement of a single atom*. In Fig. 5.5, the length of the horizontal segments drawn on top of the potential wells indicate the fraction of cells/time that the quantity in the $x$ axis is found at that potential well.

#### Displacive transition

Let us begin with the displacive picture. In the top plot, the potential energy is shown as a function of the collective atomic displacements (the macroscopic order parameter) at different $T$s. The order parameter can be taken as the eigenvector of a soft mode. At low $T$, the energy surface of the order parameter is a double-well potential, and the average order parameter has a positive value. The phase is ferroelectric, since there is a spontaneous polarization, signalled by the fact that atoms are displaced to the right of the potential barrier. If we look back at Fig. 5.3b, we can think of this situation as the lower plot of that schematic. As $T$ is raised, *the energy landscape for the collective excitation rearranges so as to become quadratic*. When it does so, atoms vibrate about the center of the cell (indicated by $x = 0$ in Fig. 5.5), and this leads to a higher-symmetry phase. In going from a double-well to a single-well potential, there is a temperature, indicated by $T_C$ in the figure, at which the curvature of the potential is zero. Because the curvature is zero at the transition temperature, the squared phonon frequency is zero at this temperature. Hence, $\tilde{\omega}^2(T > T_C) > 0$, $\tilde{\omega}^2(T = T_C) = 0$ and $\tilde{\omega}^2(T < T_C) < 0$ because, at the center of the cell, which is the origin of the order parameter, the curvature is negative. Only locally, that is, at one of the two potential minima, is $\tilde{\omega}^2$ positive at $T < T_C$.

There are reasons why the potential energy surface against a collective vibration or order parameter can change its shape from a double well to a single well at different $T$s. The energy landscape of the atomic vibration in one particular unit cell at $\mathbf{R}_0$, in fact, depends on the interaction between the atoms inside the unit cell, and also on the interaction between them and the atoms in the surrounding unit cells. These interactions tail off as slow as $1/r$ or faster, but if we consider the first shell of neighbours, or if for some reason long range order is energetically favourable, the interactions with neighbouring cells can influence substantially the unit cell at $\mathbf{R}_0$. Fallon explained this very well in his thesis, Ref. [43], which also focused on $BaTiO_3$. When one unit cell is taken as reference, and the neighbouring cells are not polarized, meaning that the atoms are arranged according to the nominal C perovskite structure, the potential energy function calculated for a Ti displacement in the $\mathbf{R}_0$ cell is quadratic, with the minimum of the potential at the center of the cell. Hence, the structure at the minimum of the local potential energy surface of each cell is also the structure at the minimum of the potential energy surface of the macroscopic crystal, and is the nominal cubic structure. When, on the other hand, all neighbouring cells are equally polarized along a [111] direction, the potential function is also quadratic, but its minimum is shifted towards the same [111] polarization direction. Hence, the energetically favourable structure for the reference cell is also with the Ti displaced in the same direction. For a more quantitative description of this, see Fallon's thesis in Ref. [43], Sec. 7.4. Here, suffices it to say that the potential energy as a function of an order parameter *can* change shape because of the interactions within clusters of equally polarized unit cells. Such clusters can form as the result of more than one unit cell being polarized in the same direction, and this can be obtained when the temperature, and thermal disorder with it, is reduced and a greater degree of long-range order is established. Of course, the cluster needs to have a certain "critical" size, in a real macroscopic material, in order for it to be stable and to grow as the material is quenched. Fallon has shown that a minimum of a $5 \times 5 \times 5$ cells cluster is needed for the rhombohedral distortion of the reference cell to be energetically favourable in an MD simulation. This number is consistent with the other independent calculation of Ghosez, Gonze and Michenaud [48], but the critical cluster's size for a real macroscopic material is likely to be bigger.

**Order-disorder transition**

An order-disorder transition can be understood by looking at the bottom plot of Fig. 5.5. Here, the potential energy function is plotted against the displacement *of just one atom*; this can be the titanium, for us. The energy function *always stays in the form of a double-well potential, at any* $T$. At mechanical equilibrium ($T \to 0$), the atom occupies one of the minima. At low $T$, the energy barrier is so high that the atom stays at this minimum with high probability. When $T$ is raised, the probability that the atom hops to the other potential minimum increases. At $T \geq T_C$, the probability that the atom occupies either one of the two minima is the same: the thermal energy causes fluctuations that are big enough for atoms to easily overcome the barrier. In this case, a higher-symmetry phase is established which is doubly disordered. It is disordered in time, because at any given time $t$ the atom will be found in either one of the two minima, but at $t + \Delta t$ it can be found in the other minimum. It is disordered in space, because if in one unit cell the atom is displaced to the right, in a subsequent unit cell it can be displaced to the right or to the left, with equal probability. This is because we have plotted the energy surface for the motion of just one atom, and in doing so we have assumed no spatial correlation with neighbouring atoms, in sharp contrast with the displacive theory, whereby a collective motion is considered. As will be further explained later, the local disorder can occur when the strength of the inter-atomic interactions between neighbouring cells is smaller than the energy barrier [39], making the cells quasi-independent of one another. That is, no long-range correlations are established by means of an order parameter, like in the displacive picture.

Note that, in the model proposed by Comes, Lambert and Guinier, the atomic displacements really are correlated, but only along the chains' axes. In the eight-site model, correlation is only lost *perpendicularly to the chains*. In fact, the neighbouring chains denoted 1 and 2 in Fig. 5.4 are oppositely polarized, and hence uncorrelated in the direction orthogonal to the chains' axes, [010].

**The origin of the difference between displacive and order-disorder**

Let me emphasize once again the differences between the two pictures we have discussed. The displacive picture is essentially a macroscopic picture, while the order-disorder is a microscopic one. When I say that the displacive picture is macroscopic, it is because it involves the presence of an order parameter, which is a macroscopic quantity that changes as the phase changes. In the example of the top plot of Fig. 5.5, it is positive at $T < T_C$ and zero at $T \geq T_C$. When I say that the order-disorder picture is microscopic, it is because it implies the loss of correlation between unit cells, hence loss of long-range order.

At thermodynamic equilibrium, the free energy is the quantity that interests us. If we refer to the case of the isobaric-isothermal ensemble, the Gibbs free energy is $G = U - TS + PV$. Establishing whether a transition is displacive or order-disorder means establishing whether $G$ is minimized by an ordered phase or a disordered one. A disordered phase has a higher entropy, and hence the term $-TS$ favours a lowering of $G$. A displacive material, on the other hand, has soft modes which may lower the total energy $U$, but may have a lower entropy. This trade off between energy and entropy determines which phase is more stable.

Let us now focus on the internal energy $U$, and discuss a physical reasoning by which a transition can be displace or order-disorder. This reasoning was outlined by Dove [39], and resides on the ratio between the height of the potential energy barrier that atoms experience during a collective motion $Q_{\boldsymbol{q}\nu}$, $\Delta U(Q_{\boldsymbol{q}\nu})$, and the strength of the interactions between neighbouring atoms, $W$. $\Delta U(Q_{\boldsymbol{q}\nu})$ quantifies the energy penalty imposed by the collective motion to switch from a well to another. $W$ quantifies the strength with which neighbouring atoms are held together. If the height of the barrier is small with respect to the force constants between neighbouring cells, $\Delta U(Q_{\boldsymbol{q}\nu})/W \ll 1$, then the long-range order established by the collective motion is favoured, because $W$ is high. Hence, the motion is ordered. If, on the other hand, the height of the barrier is large with respect to the strength of the interactions between neighbouring cells, $\Delta U(Q_{\boldsymbol{q}\nu})/W \gg 1$, then the motion of the atoms is more influenced by the local potential than it is by the forces resulting by the interactions with atoms in other cells, and therefore it is quasi-independent of other atoms. Hence, the motion becomes disordered. A more detailed

analysis between these two limiting conditions is provided by Dove in Ref. [39].

### 5.3.4 Spectroscopic evidence of displacive *and/or* order-disorder transition

The spectroscopic community was initially guided by Cochran's theory of a soft mode, which dates back to 1960 [22], and at that time was the best model of the phase transitions available. For this reason, and because of the success of the displacive theory for other ferroelectrics or incipient ferroelectrics like $SrTiO_3$ and $KMnF_3$ [113], most of the early experimental efforts went in the direction of searching for a soft mode in $BaTiO_3$, and, as they found it, supported the displacive picture [82, 36, 56, 119, 94]. In general, in the spectroscopic community this rule of thumb is accepted [62]: *when the low-frequency spectrum of a material shows an optical mode with a well-defined underdamped line shape whose frequency softens to almost zero when $T \to T_C$, then the crystal is a* bona fide *displacive material.*

As it frequently occurs, however, this picture is complicated either by the abnormal dampening of the optical excitation, which manifests as a broad peak rather than a narrow peak with a well-defined frequency, or by the presence of an additional excitation which shows up as a peak around zero frequency: the central peak, or central mode.

When a central peak occurs, it can appear either very broad or very narrow. In order to understand what this means, we need to consider Fig. 5.6, copied from Ref. [148]. It plots the expected line shape of a damped phonon, namely, a Lorentzian with frequency $\omega_{\mathrm{TO}}$ and half width at half maximum $\Gamma$, in units of $\omega_{\mathrm{TO}}$ and for four values of $\Gamma$. Because the fitting of phonon spectra to Lorentzians is ubiquitous in the experimental literature, the concept I am discussing here is rather general and is valid irrespective of the type of experiment, and hence is valid whether the spectrum is an absorption or Raman or neutron scattering spectrum, and so on. In fact, the Lorentzian function is the response function of a damped harmonic oscillator whose phenomenological equation is $m\ddot{x} + \Gamma\dot{x} + \omega_{\mathrm{TO}}^2 x = 0$. What is important to notice is that, at fixed $\omega_{\mathrm{TO}}$, varying the value of the damping parameter $\Gamma$ results in a completely different

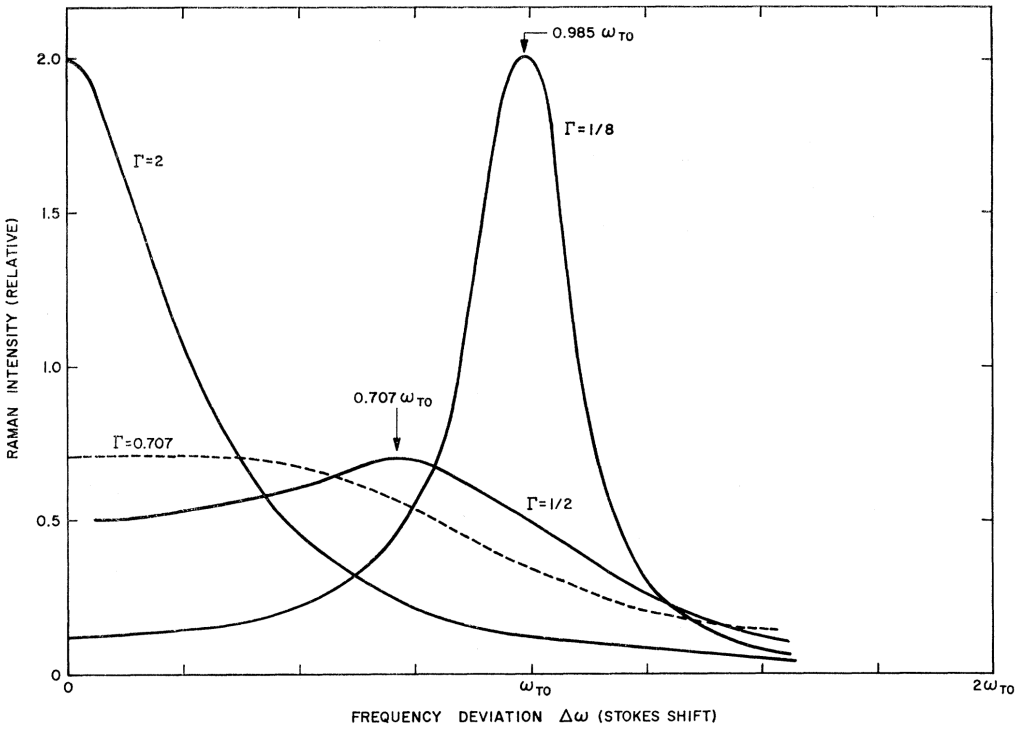



Figure 5.6: Lorentz-like spectrum of a phonon mode with frequency $\omega_{\rm TO}$ for four values of the damping factor $\Gamma$, taken from Ref. [148].

line shape. In Fig. 5.6, the peak positions are indicated with arrows. At small $\Gamma$, the mode is underdamped, and its peak position is very close to $\omega_{\rm TO}$. With increasing $\Gamma$, the peak position drifts to the left and the spectrum broadens, until a critical value $\Gamma = 2\omega_{\rm TO}$ after which the mode is deemed overdamped. In the case of an overdamped excitation, its line shape narrows down again, and its peak shifts to zero frequency; this is the so-called *critical slowing down* behaviour [62]. In all cases, the undamped excitation frequency is $\omega_{\rm TO}$, hence if this was deemed a soft mode, a potential phonon branch would be drawn at this frequency, not at the frequency of the spectral peak position. This is, in my opinion, a cause for a lot of headaches in the phonon dispersions proposed by the authors, because the phonon spectra are inevitably polluted by statistical and background noise which can make it hard to distinguish whether a mode is underdamped or overdamped. Moreover, the accuracy in the determination of the undamped phonon frequency $\omega_{\rm TO}$, depends on how well its spectrum can be approximated by a Lorentzian, or by how well the model of coupled modes proposed by the authors can fit the experimental spectra. We shall get back to this issue specifically when we will discuss the neutron scattering experiments in Sec. 6.3.

The purpose of this digression is to say that the spectrum of a soft excitation, be it a soft mode or a central mode, appears differently whether it is underdamped or heavily damped or overdamped. This depends on the ratio between its linewdith $\Gamma$ and its characteristic frequency, $\Gamma/\omega_{\mathrm{TO}}$. The precise estimation/calculation of this ratio is important in order to establish whether the mode is damped ($\Gamma/\omega_{\mathrm{TO}} < 2$) or overdamped ($\Gamma/\omega_{\mathrm{TO}} \geq 2$). If the soft excitation is overdamped, it is likely a central mode, and when a central mode is present, it is a signal of an order-disorder transition.

Let us see why. Let us assume, for simplicity, that the strength with which the atom is bound to the surrounding atoms is zero, $W = 0$ ($W$ was defined in the previous section). In other words, let as assume that the atom is isolated. The bottom plot of Fig. 5.5 shows that, in an order-disorder transition, the energy barrier $\Delta U$ between minima of the potential needs to be overcome. This, in classical mechanics, can only happen if the thermal energy per atom, $\approx k_B T$, is higher than $\Delta U$. Statistically, on the other hand, the probability that the atom overcomes the barrier is $\sim \exp[-\Delta U/(k_B T)]$, hence if $k_B T \gg \Delta U$, the probability of hopping is very high, and an atomic hop will happen frequently. If $k_B T > \Delta U$, but not much greater, the atom rattles from one minimum to another, but as it encounters the potential barrier it slows down conspicuously. With some probability, it will even bounce back. Hence, the motion looks on a time average a vibration about the center of the cell, but the rattling motion is hindered by the presence of $\Delta U$. This causes the phonon to dampen. In other words, the atom moves more slowly, when crossing the barrier, than when it is oscillating at the bottom of one of the potential wells. Therefore, despite the fact that it is rattling or hopping between minima, the fraction of time that it spends between minima may not be lower than the fraction spent in each potential well.

Hence, if a hopping mode exists, it will by all means be heavily damped or overdamped. An overdamped, low-frequency excitation is said to be of a *relaxational* type, and in the spectroscopic community it is often called a "Debye" mode[3]. The presence of a Debye mode is a clear

[3]The reason for the name relaxational comes from a statistical mechanical consideration. Suppose the equilibrium of a system is perturbed by a perturbation $f$, which couples to the dynamical variable $A$ (for example, $f$ can be an oscillating electric field and $A$ the system's dipole moment). $A$ will change from its equilibrium value $\bar{A}$; we denote this change $\delta A(t) = A(t) - \bar{A}$. From the fluctuation-dissipation theorem, the response function $\chi(t)$ is equal to $\chi(t) = 1/(k_B T)\frac{d}{dt}\langle \delta A(0)\delta A(t)\rangle$ [17]. The average $\langle\cdot\rangle$ is a thermal *equilibrium*

hint of an order-disorder transition. Let us state another rule of thumb: *when the low-frequency spectrum of a material shows an overdamped excitation, and hence an excitation which can be interpreted as a Debye mode, than the crystal likely undergoes an order-disorder transition.* In the last sentence, I wrote *likely*, because as I said it is often difficult to assess whether a mode is damped or overdamped, as this depends on the undamped frequency $\omega_{\mathrm{TO}}$, whose precise determination is often difficult.

In the spectroscopic community, it is accepted that if both an undamped soft mode **and** a Debye mode are found, then the displacive and order-disorder components coexist [62]. The displacive component would be caused by the softening (partial or total) of the phonon mode, and the order-disorder component would be caused by some sort of atomic hopping [62].

### 5.3.5 Other experimental evidence of displacive *and/or* order-disorder transition

Looking at phonon spectra is not the only way to understand whether a phase transition is displacive or order-disorder.

In fact, the very first authors to suggest, in 1968, that the higher-symmetry phases of $BaTiO_3$ could be disordered, namely Comes, Lambert and Guinier [25], based their argument on the interpretation of the anomalous X-ray diffuse scattering patterns of $KNbO_3$, a perovskite with a sequence of phase transitions identical to $BaTiO_3$. We shall see this in much more details in Sec. 6.2, but here I provide a brief outline. The main feature of an idealized X-ray diffraction experiment is the presence of sharp Bragg peaks. As long as the crystal remains ordered, the dynamical motion of the atoms makes the Bragg peaks broaden and elongate along very specific directions of reciprocal space. If the crystal becomes disordered, however, a new kind

average, and the quantity $\langle \delta A(0)\delta A(t)\rangle$ is the correlation function for the dynamical variable considered. Now, assume $\langle \delta A(0)\delta A(t)\rangle \sim \mathrm{Re}[\exp(i\omega_1 t - \Gamma t)]$; then, the response function is oscillatory with an exponential decay. The permittivity $\tilde{\chi}(\omega)$ is the Fourier Transform of $\chi(t)$, and it will be a Lorentzian with frequency $\omega_1$ and half with at half maximum $\Gamma$. If $\Gamma \gg \omega_{\mathrm{TO}}$, however, the oscillatory behaviour is screened by the exponential, and we can effectively write $\langle \delta A(0)\delta A(t)\rangle \sim \exp(-\Gamma t)$. Hence, when the time-scale $1/\Gamma$ of the exponential decay is much smaller than the period of the oscillations $1/\omega_{\mathrm{TO}}$, the response is purely relaxational. Debye was the first author to propose such a model of relaxational dielectric behaviour [89]

of diffuse patterns emerge, and it is these patterns that prompted Comes, Lambert and Guinier to identify $BaTiO_3$ as a disordered perovskite.

Another way to understand whether a phase is disordered or not is by means of X-ray absorption fine structure (XAFS) or nuclear magnetic resonance (NMR). These types of experiments are highly sensitive to the local environments of each atom. Both techniques allow to detect whether or not the Ti atom is placed **at** the center of the cell, on an average over the time scale of the experimental technique. If, on a time average, the titanium is found off the center of the cell, this is a clear indication that the phase is disordered, and this would suggest that the eight-site model is a good model. We will deal with local probes in Secs. 6.4-6.5.

Because a more specific discussion of each type of experiment seems at this point necessary, in the next chapter we will become acquainted with the experimental literature.

## 5.4 Taxonomy of phonon modes: group theoretical and spectroscopic notation

Before delving into the experimental literature, however, I need to introduce the notation and nomenclature used to label the phonon modes.

One way to do this is to name them with integer numbers by increasing order of frequency. This is surely the easiest thing to do, and it is sometimes necessary when the type or symmetry of the modes are not known. This often happens when one computes Brillouin sums over a grid in $\boldsymbol{k}$-space without calculating the eigenvectors of each mode, which results in the impossibility of distinguishing between, say, acoustic and optical modes.

This notation is quite poor as it does not say anything about the phonons other than how their frequencies are ordered. Group theory, on the other hand, tells us what kind of symmetry operations can be done to the eigenvector of a certain mode without changing it. In other words, it defines how the symmetry of the static lattice is lowered by the excitation of a specific phonon mode. The set of all symmetry operations which can be applied to the eigenvector of a

mode without changing it defines its irreducible representation (IRREP). Labelling a phonon mode by its IRREP is very convenient, because it gives information about its eigenvector.

**The group theoretical notation**

The unit cell of $BaTiO_3$ contains 5 atoms; hence there are 15 phonon branches: 3 acoustic and 12 optical. We will use the so-called "chemical notation" (as opposed to the physical one, an example of which is in Ref. [29]). Let us begin with the phases' symmetries, ordering them from highest to lowest. A group theoretical analysis shows that, in the $Pm\overline{3}m$ (cubic) phase, the point group is the highly-symmetrical $O_h$, and the optical modes' IRREPS at the BZ center, $\Gamma$, are:

$$\Gamma_{opt} = 3F_{1u} + 1F_{2u} \tag{5.1}$$

In the $P4mm$ (tetragonal) phase, the point group is $C_{4v}$, and the modes' IRREPS at $\Gamma$ are:

$$\Gamma_{opt} = 3(A_1 + E) + B_1 + E \tag{5.2}$$

In the $Amm2$ (orthorhombic) phase, the point group is $C_{2v}$, and the modes' IRREPS at $\Gamma$ are:

$$\Gamma_{opt} = 4(A_1 + B_1 + B_2) \tag{5.3}$$

In the $R3m$ (rhombohedral) phase, the point group is $C_{3v}$, and the optical modes' IRREPS at $\Gamma$ are:

$$\Gamma_{opt} = 3(A_1 + E) + A_2 + E. \tag{5.4}$$

In the C phase, the $F_{1u}$ and $F_{2u}$ modes are triply degenerate. In the lower symmetry phases, the $E$ modes are doubly degenerate, and the $A$ and $B$ modes are non degenerate. In all cases, the optical modes sum up to 12.

The T phase originates from the highly-symmetrical C phase through a distortion in the $\langle 100 \rangle$

direction. For this reason, the symmetry operations of $P4mm$ are a subset of the ones of $Pm\bar{3}m$. This means that, in cooling, a triply degenerate mode in the C phase splits into two modes of the T phase $F_{1u} \rightarrow A_1 + E$ and $F_{2u} \rightarrow B_1 + E$.

It is important to note that, since an $A_1$ mode and a $E$ mode belong to different IRREPS, their eigenvectors differ. However, as they all come from the same $F_{1u}$ mode, which is triply degenerate, the main difference is in the direction of the modes' eigenvectors. The $\langle 100 \rangle$ distortion, in fact, imposes a difference in modes polarized parallel to this direction, the $A_1$ and $B_1$ modes, and modes polarized perpendicularly to it, the $E$ modes. These modes experience different chemical environments, because the cell is elongated along the tetragonal axis, and their frequency is slightly different, hence the splitting. This is not true for the C phase, for which any Cartesian direction should be regarded as equivalent, and hence all the modes in the cubic phase are triply degenerate. This observation is important because, as we will see soon, according to standard spectroscopy (IR and neutron scattering), the alleged soft mode is an $E$ mode [62, 36, 56], i.e., a mode for which the eigenvectors belong to the plane perpendicular to the unit cell's polarization. $A_1$ modes with eigenvectors along the polarization axis are never soft.

Just as in the C-T transition, splitting of phonon modes can happen in the T-O transitions and O-R transitions. A schematic of the splittings/mergings in the R-O-T-C phases for the $F_{1u}$ mode is illustrated in Fig. 5.7, taken from Luspin *et al.* [82].

Of course, an additional splitting at the BZ zone center comes from the long-range electric field which longitudinal optical phonons produce in the limit of $\boldsymbol{k} \rightarrow \Gamma$.

### The spectroscopic notation

Despite its effectiveness in the characterization of the phonon modes, in the body of this thesis I decided to not use the group theoretical notation, or, better, to use it only when it is necessary to be able to relate to experimental papers.

Most of the times, I will use the "spectroscopic" notation [63] instead. In the C phase, out

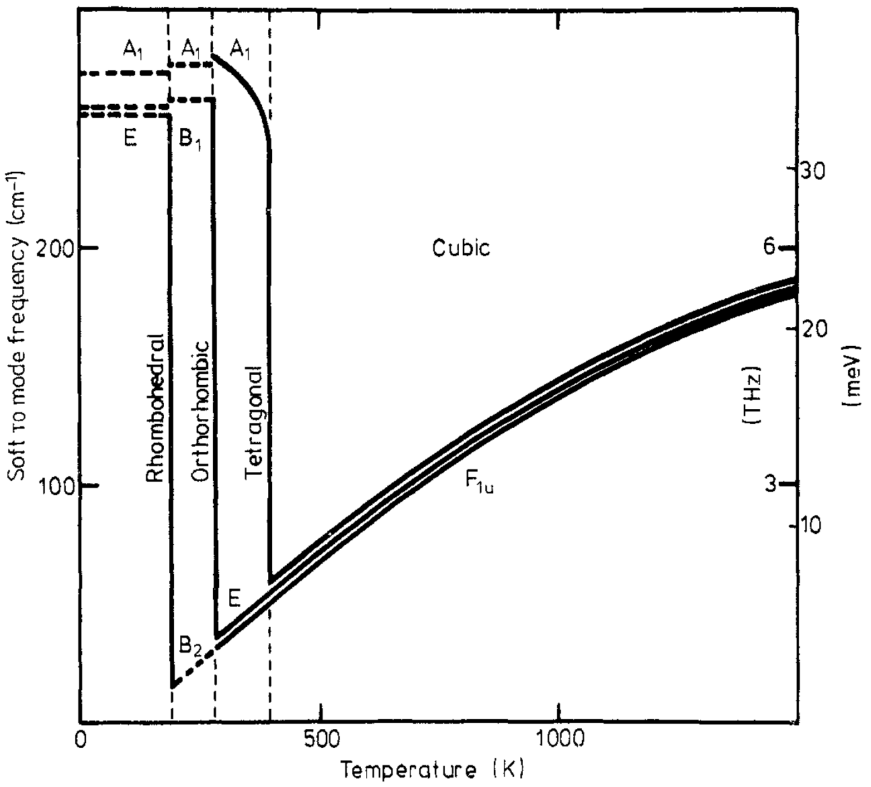



Figure 5.7: Schematic plot of the temperature dependence of the $F_{1u}$ mode, taken from Luspin *et al.* [82]. The figure shows the splitting of this mode with decreasing the temperature from the C phase. The $F_{1u}$ is triply degenerate in the C phase. In the T phase, characterized by a polarization along an axis [001], the $F_{1u}$ splits into a mode $A_1$ polarized along [001] and two degenerate modes $E$ polarized along [100]-[010]. In the O phase, characterized by a polarization along [011], the $A_1$ mode rotates and is polarized along [011], the $E$ mode further splits into a $B_1$ mode polarized along $[0\bar{1}1]$ and a $B_2$ mode polarized along [100]. In the R phase with polarization along [111], the $A_1$ mode is polarized along [111], and the doubly degenerate $E$ mode are polarized perpendicular to it. The solid lines represent a fit to reflectivity measurements from Luspin *et al.*, but the broken lines were drawn by adjusting data from other perovskites, so the temperature dependence of the frequencies is mainly qualitative. The plot does not account for the LO/TO splitting.

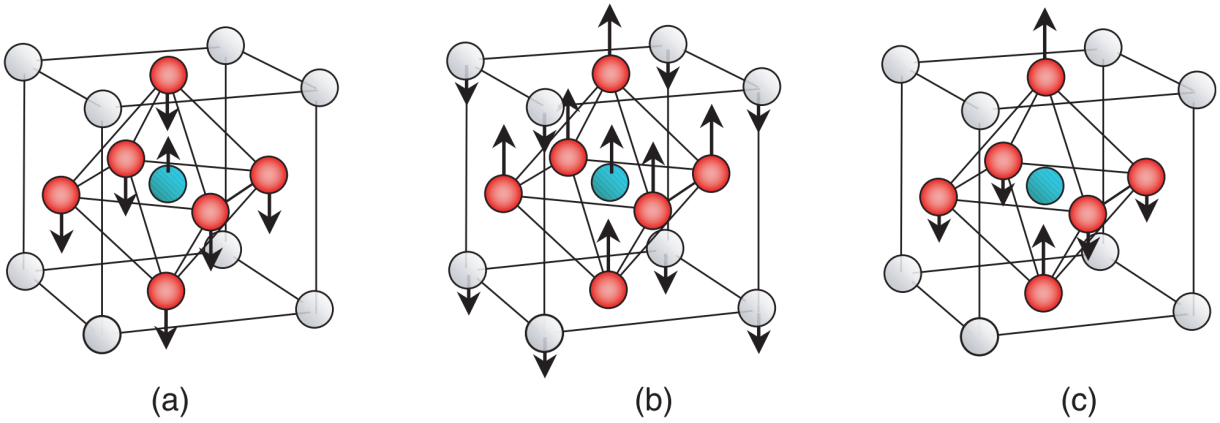



Figure 5.8: The eigenvectors of the $F_{1u}$ modes, from Hlinka *et al.* [63]. Panel (a) shows the Slater mode, panel (b) shows the Last mode and panel (c) shows the Axe mode.

of the four optic phonons, three are infra-red (IR) active, and these are the ones which were named, by increasing order of frequency (when the modes are hard): Last, Slater and Axe modes. Unfortunately, there is no widely-adopted name for the IR-inactive $F_{2u}$ mode–which however is not of great interest to us–so this mode will be called by its group theoretical name. The reader interested in a nice review about the taxonomy of phonon modes in $BaTiO_3$ will find Ref. [63] helpful (especially Table 1 of Ref. [63]).

**Modes' eigenvectors**

What do the modes' eigenvectors look like? I show some of the calculated eigenvectors in App. E, but because the determination of the eigenvectors is, in principle, a group-theoretical exercise, we shall also see the modes' eigenvectors here. We shall only see eigenvectors of $F_{1u}$ in the C phase, and remember that in the lower-symmetry phases there is a splitting of these modes depending on whether or not their eigenvector is along the ferroelectric axis.

Fig. 5.8, taken from Hlinka *et al.*'s review [63], draws the eigenvectors of the three IR-active modes, whose symmetry is $F_{1u}$. Barium atoms are drawn in grey, O atoms in red and the Ti atom in green. The O atoms are at the vertices of an imaginary octahedron around the Ti atom, and the Ba atoms form a sort of imaginary cubic cage around the other atoms. Plot (b) shows the Last mode, which entails the displacement of the Ti and of the O against the Ba. Plot (c) shows the Axe mode, which entails the displacement of just O atoms, against

each other. Plot (a) shows the Slater mode: this is the most important one, because it is most involved in the phase transitions, as we shall see. It is the displacement of the Ti against the O octahedron, with the Ba atoms standing still. The Slater mode is the subject of Ch. 6, where I review the experimental literature on $BaTiO_3$, and Ch. 7, where I show my results.

## 5.5 Applications of $BaTiO_3$

Ferroelectrics are materials which exhibit a spontaneous polarization. As a result, their static dielectric constant is high. Hence, $BaTiO_3$ is suitable for all applications in which a good capacitor is needed. Indeed, billions of $BaTiO_3$ condensers are made every year [111].

There is another property which ferroelectrics have and other simple dielectrics do not. For the sake of the argument, consider tetragonal $BaTiO_3$ having polarization $\boldsymbol{P} \parallel [001]$. Such polarization can be switched with the application of an electric field, which is called coercive electric field, $\boldsymbol{E}_c$. If an electric field is applied which is larger than the coercive field, the polarization becomes $\boldsymbol{P} \parallel [00\bar{1}]$. This switchability of stable polarization states makes ferroelectric materials very interesting to the semiconductors industry. The typical magnitude of the coercive field is $E_c \sim 50$ kV/cm [111, 70]. Hence, for a 1 mm bulk crystal, the voltage needed to switch the polarization would be $V_C \sim 5$ kV, which is unsuitable for most of the common applications. However, the miniaturization of modern devices has allowed to fabricate ferroelectric films as thin as 2 nm [139], with the result of a switching field as low as few V [32], which is the voltage at which computer devices work. From this, it has become possible to integrate ferroelectrics into electronic devices, with great avdantages with respect to non-ferroelectric components.

One of the applications of the switchability of polarization states is the production of ferroelectric random access memories (Fe-RAMs). In fact, two different polarization states can be considered as 0-1 states, and digital information can be stored through them. The advantage of Fe-RAMs with respect to ordinary RAMs is that ordinary RAMs are volatile, while Fe-RAMs are not. If ferroelectric capacitors are integrated into the field-effect transistors which compose the RAM, their polarization states are permanent, and hence the Fe-RAMs are non volatile,

lower power, and much less subject to fatigue [32]. Commercially available Fe-RAMs use lead zirconate titanate [32]; however, they are not widespread.

Other applications exploit the fact that polycrystalline samples of $BaTiO_3$ made up of domains with different polarizations exhibit domain walls. The domain walls possess a bound charge, which is the sum of the bound charges provided by the macroscopic polarizations of two adjacent domains. The bound charges can be screened with free charges, like electrons (or holes or mobile ions). In this case, the domain walls are strongly charged, and result in a quasi-2D electron gas within the insulating material [8]. Such electron gas has a conductivity similar to that of a metal, and around $10^9$ times the conductivity of a single crystal $BaTiO_3$ [123]. Moreover, the domain walls are mobile, because an electric field can easily change the domains' polarizations. In $BaTiO_3$, additional stability to the domain walls is given by ferroelasticity [8]. The fact that the domain walls are very responsive to external stimuli looks promising for future applications. One of these is domain wall memory: researchers have designed solid state devices which realize '0' and '1' states in $BiFeO_3$ through the absence and presence of walls, respectively [127]. Another application is domain logic: junctionless ferroelectric field-effect transistors have been designed which exploit the riconfigurability of the charged domain walls to realize logic gates, like AND, OR, etc. [127].

$BaTiO_3$ can be combined with other ferroelectrics or ferromagnetics. For example, ultrathin films of $BaTiO_3$ sandwiched between Fe and $La_{2/3}Sr_{1/3}MnO_3$ proved to have both a spontaneous magnetization and polarization [139]. This engineered and tunable multiferroicity is promising for spintronics. Another example is the possibility of controlling the in-plane polarization with an anisotropic strain at the interface $BaTiO_3$/PrScO [79].

Another applications stems from piezoelectricity. Piezoelectrics are materials which exhibit an electric field under a strain, and hence have numerous applications in the field of medical ultrasonic imaging, sensors, and actuators in general [69]. In an ordinary piezoelectric, the frequency of the electro-acoustic wave propagating in a direction is determined by the speed of sound divided by the length of the crystal in that direction. In a ferroelectric, this length must be replaced with the length of the ferroelectric domains, which can be much smaller than the

sample size, and hence produce higher frequency waves, or waves which are programmable [69].

These are only a few applications, and potential applications, of $BaTiO_3$.

# Chapter 6

# Experimental literature review for $BaTiO_3$

$BaTiO_3$ has been studied for over 60 years, and the experimental and theoretical literature is therefore extensive. In this chapter, I focus on those works that will aid in the understanding of the next chapter, Ch. 7, where I will discuss the results of my work.

**Two ways of reading the chapter**

I offer two possible ways of reading the thesis from now on. One is to follow the pages in the order they are written: in this case, the reader will be acquainted with the experimental literature first, and the results of my work later in Ch. 7. Another way is to jump across chapters. Many of the experiments I discuss in this chapter, in fact, are simulated in the next chapter. For example, the infra-red spectra I discuss in Sec. 6.1 are simulated in Sec. 7.5. The diffuse scattering patterns I discuss in Sec. 6.2 are simulated in Sec. 7.6. I discuss the neutron scattering spectra in Sec. 6.3, and simulate a quantity similar to the neutron cross-section in Sec. 7.7. I present the real spacetime picture of the atomic vibrations here when discussing the local probes, in Secs. 6.4-6.5, and I provide the results of the simulations in Sec. 7.8. In many of the sections of the next chapter, whenever I can I present my results alongside with the experimental spectra, to aid the comparison.

**Overview of the chapter**

This section is organized as follows. We will first see one of the experimental techniques that probe phonon modes near the BZ center, namely, infra-red/THz spectroscopy, in Sec. 6.1. We will then investigate the other parts of the BZ away from the $\Gamma$ point by looking at diffuse X-ray scattering in Sec. 6.2 and inelastic neutron scattering in Sec. 6.3. The real space picture of the atomic motions will be the focus of Secs. 6.4-6.5, which deal with X-ray absorption fine structure and nuclear magnetic resonance, respectively, and of Sec. 6.6, which is dedicated to electron microscopy. Finally, I will summarize this chapter in Sec. 6.7.

## 6.1 Infra-red and THz spectroscopy

In this section, we will see that the T-C phase transition of $BaTiO_3$ is characterized by the partial softening of one of its TO modes, whose widely used name in the spectroscopic community is Slater mode [63], and the additional emergence of a central peak, called "Debye" mode. I showed the eigenvectors of the optical modes, including the Slater mode, in Sec. 5.4, and I discussed the central mode, or Debye mode, in Sec. 5.3.4.

I will comment on the behaviours of these two modes and on the interpretation of the latter one.

One way that information about optical phonon spectra can be obtained is via infra-red (IR) spectroscopy. This is undoubtedly the easiest and cheapest method with which phonon frequencies and linewidths can be probed. It involves shining light on the crystal in the IR spectrum, the energy range of the atomic vibrations, so that phonons can be resonantly excited. The part of the electromagnetic spectrum relevant for lattice vibrations in crystals like $BaTiO_3$ is the far-IR, with wavelengths 25-100 $\mu$m (400-10 cm$^{-1}$). The region of the spectrum at the border of the microwave region, 0.77-5 mm (2-130 cm$^{-1}$), is commonly referred to as *THz region*, and it has now become customary to call experiments which makes use of such radiation "THz spectroscopy", but the principle behind it is the same as IR spectroscopy.

Because the photon dispersion is much steeper than the phononic one, photons in the IR range can be considered as having a vanishing wavevector with respect to the typical dimension of the BZ, which is $\sim \frac{2\pi}{a}$, where $a$ is the lattice constant, and so is of the order of $\sim 1$ A$^{-1}$. IR radiation has wavevectors in the order of $10^{-4} - 10^{-7}$ Å$^{-1}$, hence only optical phonon modes with wavevectors near the BZ center can be detected.

One of the issues that hindered IR studies for many years is the so-called "teraherz gap" [**?**], which is the region of the electromagnetic spectrum between about 100 GHz and $\approx$ 10 THz where detectors, and intense continuous wave or pulsed sources are either unavailable or not widely available. This is a cause for concern, if we consider that the region of the spectrum that interests us most is the low frequency region, where a central peak might be present. Luckily, the gap is closing [100, 62], and accurate low-frequency spectra can be obtained by means of THz spectrometers, like the one used by Hlinka *et al.* [62].

Typical IR/THz studies measure the reflectance of a bulk material [83, 99, 63]. From the reflectance, the real and imaginary parts of the dielectric function $\varepsilon(\omega) = \varepsilon'(\omega) + i\varepsilon''(\omega)$ are then obtained. The real part $\varepsilon'(\omega)$ can be used to evaluate the static dielectric constant $\varepsilon_s = \varepsilon'(\omega \to 0)$, while $\varepsilon''(\omega)$, being proportional to the absorption spectrum, shows peaks at the frequencies of the transverse optical (TO) polar phonon modes near $\Gamma$. The two functions are calculated either by means of the Kramer-König relations or by fitting $\varepsilon(\omega)$ to a set of harmonic oscillators [63]. The former method was used, among the others, by Luspin *et al.* [82]. The latter method is often the preferred one in recent experiments; it has the advantage of producing smoother spectra, but the disadvantage of having assumed a form for the dielectric function and decided on the number of harmonic oscillators to fit the spectra *ex ante*. Often, the assumption that the IR response is the sum of a set of independent harmonic oscillators breaks down as a result of strong coupling between polar phonon modes; in this case, expedients must be put in place by the spectroscopist, such as a thorough modelling of the coupling between the modes. This was done, for instance, by Hlinka *et al.* [62], and by Chaves, Katyiar and Porto, who showed that the absorption line shape changes a lot when the coupling is considered [19].

### The THz-IR spectrum of $BaTiO_3$

Let us analyze two important spectroscopic measurements, reproduced in Fig. 6.1; the figure shows the imaginary part of the dielectric function, $\varepsilon''(\omega)$, obtained from a collection of IR spectra in both the T (bottom plot) and the C (upper plot) phases, from Hlinka *et al.* [62] and from Luspin *et al.* [82], respectively. Hlinka *et al.*'s sample was found to have $T_C = 403.5$ K, and they used a light beam polarized along the tetragonal $c$ axis. Luspin *et al.* found $T_C = 395.15$ K, and polarized the light along a crystallographic $\langle 100 \rangle$ axis. The range of temperatures of these two works conveniently covers the T-C transition, and a joint look at these spectra should therefore be of help to understand what happens during a structural phase transition of $BaTiO_3$. Each peak in the spectra corresponds to one of the three IR-active TO phonon modes near the BZ center. The peaks are named according to the spectroscopic notation (see Sec. 5.4): D=Debye, L=Last, S=Slater and A=Axe [63].

In the T phase, the four polar modes show very different behaviours: the Axe and Last modes are almost temperature-independent, whereas the Debye and Slater modes depend strongly on $T$ and change drastically at the phase transition, suggesting that they are involved in it. The Slater peak softens–but not perfectly–upon heating, and a new central mode, the broad low frequency peak marked with a "D", emerges progressively: this is the Debye mode, and is highlighted in Fig. 6.1 by the shaded areas. The emergence of a low frequency central mode near the zero of frequency as $T \to T_C$ is concomitant with the shrinking of the Slater mode. At the onset of the C phase, the Slater peak seems to have disappeared.

In the C phase, the D peak dominates the spectrum in the 0-200 $cm^{-1}$ (0-5 THz) range until a temperature of 1000 K. Note the change in the scale of the $y$ axis between the lower and upper panels: the Debye mode grows abnormally at the onset of the C phase and overwhelms the Last mode. Upon heating, the Debye peak broadens, until its high-frequency tail overlaps with the Last mode. If we now follow the evolution of the Debye mode's undamped frequencies in the C phases, which are represented in Fig. 6.1 by the vertical arrows drawn beneath each D peak as reported by Luspin *et al.*[1], we clearly see that the Debye mode's frequency hardens

[1]Luspin *et al.* fitted the spectrum to a damped harmonic oscillator, while Hlinka *et al.* to a proper

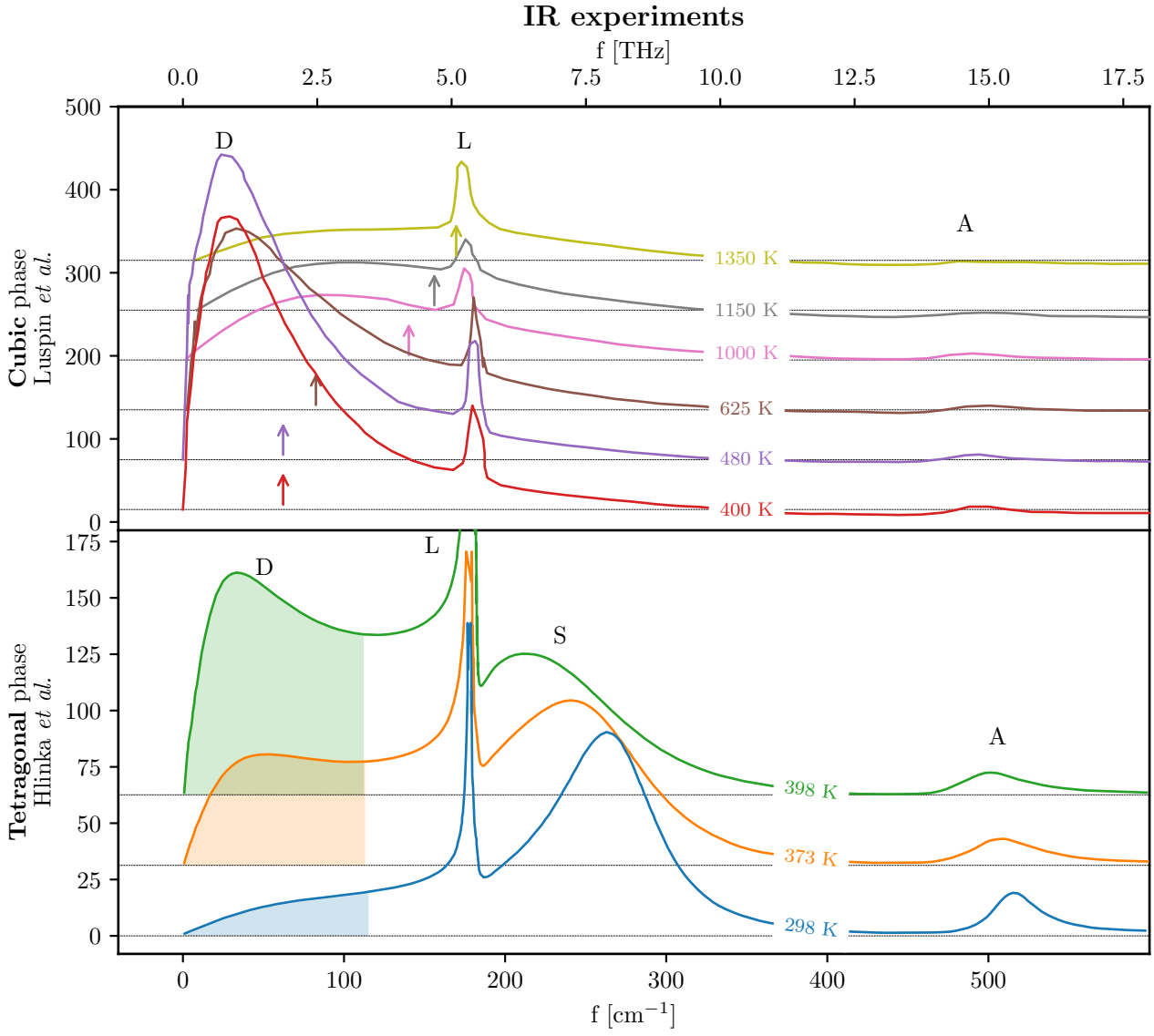



Figure 6.1: Imaginary part of the dielectric function $\varepsilon''(\omega)$ from two IR experiments from Hlinka *et al.* [62] and Luspin *et al.* [82]. The TO modes are labelled according to their spectroscopic names: D=Debye, L=Last, S=Slater and A=Axe. The shaded areas indicate the emergence of the Debye mode. Note the different scales for axes of the two plots: the Debye peak dominates the absorption spectrum at lower temperatures in the C phase. The vertical arrows indicate the undamped Debye frequencies as provided by Luspin *et al*, manifesting the hardening of the mode in the C phase.

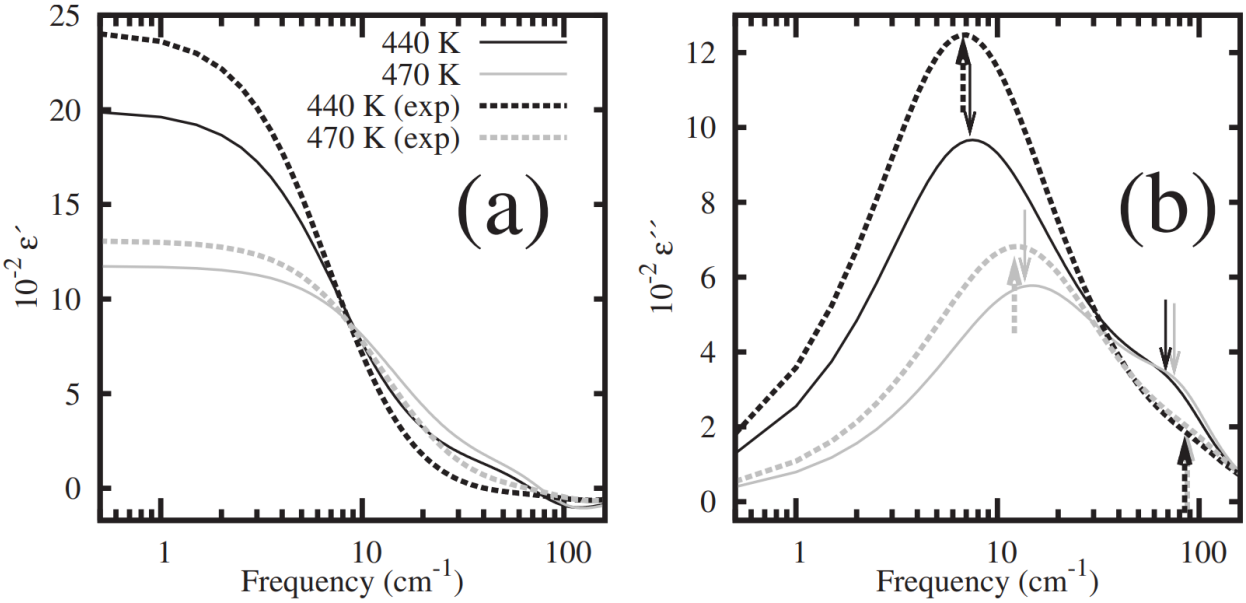



Figure 6.2: Real and imaginary parts of the low-frequency dielectric function of $BaTiO_3$ in the C phase, taken from Ponomareva *et al.* [100]. The solid and broken lines denote the calculated and experimental spectra, respectively. In the imaginary spectrum, the first peak is the Debye mode, and the authors have claimed that the second small bump at $\approx 90$ cm$^{-1}$ is the Slater mode.

with increasing $T - T_C$, until at 1350 K almost reaches the Last mode's frequency.

The absence of a Slater mode peak in the C phase prompted some authors to search for it in the low frequency range of the C phase's spectrum. For example, Ponomareva *et al.* claimed that the low frequency spectrum should be fitted not to one, but to two damped harmonic oscillator, D and S, the frequency of the latter being essentially temperature independent [100]. In other words, Ponomareva *et al.* claimed that there is indeed a Slater peak within the overdamped Debye signal, but that this S peak deviates from Cochran's law $\omega^2 \sim (T - T_C)$ and stays $T$-independent instead [100]. Fig. 6.2 shows Ponomareva *et al.*'s main result; in the right hand side of the figure, which shows $\varepsilon''(\omega)$ in the THz region, it is possible to identify the main central peak, which hardens with $T$ from 440 K to 470 K and therefore closely reflects the Debye mode seen in Fig. 6.1, and an additional small, almost imperceptible bump at $f \approx 90$ cm$^{-1}$, which the authors claim it corresponds to the Slater mode after it has crossed the Last mode during its softening.

relaxational-like Debye mode, and fitted the spectra to a model which considers coupling between all modes [62].

**Interpretation of IR/THz spectroscopy**

The striking feature revealed by these and all the other IR measurements of $BaTiO_3$ [92, 99, **?**, **?**] is the indubitable presence of a central peak, which we called a Debye mode for consistency with the nomenclature given to it by Hlinka *et al.* in 2008 when their study was performed. It certainly cannot be a proper soft mode in the sense described in Sec. 5.3.1, namely, a mode whose frequency softens to zero as $T \to T_C$. In fact, the authors found that in the T phase, namely at $T \leq T_C$, they could fit their spectra with *two modes*, a Debye *and* a Slater mode. So, the central peak *emerges progressively* with increasing $T - T_C$ when approaching the transition from below, at the same time that the Slater mode softens *partially*. The frequency of the Slater mode decreases little with $T - T_C$, while the frequency of the Debye mode was found to decrease more with $T - T_C$ [62].

The now widely accepted interpretation of the Debye mode relies on the concept of the eight-site model of Comes, Lambert and Guinier [25]: each time, the Ti atom is displaced from the center of each unit cell, and as the time evolves the thermal fluctuations make it jump from one basin to another in the same cell. This explains the equal occupancy, in time and space, of the potential minima which we saw in the lower plot of Fig. 5.5. Hence, the presence of the Debye mode is explained as inter-well hopping between minima of the local potential energy surface at each cell [62], and imposes a degree of order-disorder character in the phase transition. Such inter-well hopping motion does not only involve the Ti atom: it is a motion of each primitive cell along the cell eigenvector of the Slater mode. The motion occurs in one, two or three $\langle 100 \rangle$ directions of the pseudocubic perovskite cell, depending on whether the phase is orthorombic, tetragonal, or cubic, respectively. When this motion is small-amplitude vibrations about a local potential energy minimum, it is the S mode (T phase, $T - T_C < 0$). When $T$ is large (C phase, $T - T_C \approx 0$), it becomes a motion across the energy barrier and it is the Debye mode.

The interpretation of the Debye mode of Hlinka *et al.* is consistent with an order-disorder mechanism. On the other hand, the same authors suggested that the presence of a partially softening Slater mode in the T-C transition, and the alleged persistence of the Slater mode in the C phase, which Ponomareva *et al.* maintained, would give a degree of displaciveness.

Hence, both a soft mode and a Debye mode would coexist in the T-C transition, and therefore both characters, displacive *and* order-disorder, coexist in $BaTiO_3$ [62]. I personally do not fully understand this interpretation. My personal opinion is that the IR spectra are consistent with a pure order-disorder transition; I will substantiate this in the following of the chapter.

I have only selected a few works, but the presence of a central peak was confirmed by all IR spectroscopic studies. Besides the aforementioned works of Hlinka *et al.* [62], Luspin *et al.* [82] and Ponomareva *et al.* [100], other important studies are the one of Ostapchuck *et al.* [92], Petzelt *et al.* ([99] Fig. 3), Spitzer *et al.* ([**?**] Fig. 7), Barker [**?**], and Sanjurjo, Katiyar and Porto [107].

## 6.2 X-ray diffuse scattering

X-ray diffuse scattering is a powerful technique to probe atomic motions averaged over space. It is essentially the extension of standard X-ray diffraction. X-ray diffraction measures the constructive or destructive interference of light scattered from an incident beam by planes of atoms. Constructive interference produces sharp Bragg peaks at the reciprocal lattice $\boldsymbol{G}$-points, according to Laue's condition [4].

When the hypothesis that the atoms are fixed at their equilibrium positions is relaxed, the Bragg peaks inflate and elongate along specific directions, and produce patterns from which some features of the dynamics of the atoms can be inferred. These patterns are the *diffuse* scattering patterns. X-ray diffuse scattering extends standard diffraction by including processes in which a photon is scattered by the crystal with the creation or annihilation of one (or more) phonon(s). Such processes must conserve energy and momentum. If we denote the energy of the incident and scattered photon as $E_i$ and $E_f$, respectively, then the energy conservation for a one-phonon scattering is $E_f = E_i \pm \hbar\omega_{\boldsymbol{q}\nu}$, where $\hbar\omega_{\boldsymbol{q}\nu}$ is the energy of the excited phonon, and the plus (minus) stands for a scattering event whereby the photon gains (loses) energy by annihilating (creating) a phonon. The conservation of momentum has to be fulfilled within a $\boldsymbol{G}$-vector.In fact, because the energy of X-rays is in the scale of keV, the momentum $\hbar\mathbf{k}_i$ of

the incident radiation is much greater than the typical size of the BZ. For example, the beam line used in a 2018 X-ray scattering experiment on $BaTiO_3$ by Pasciak *et al.* had a wavelength of 0.2127 Å [94], which corresponds to a wavevector almost 20 times greater than the linear dimension of a BZ (the lattice constant is $\approx 4$ Å). Hence, the wavevectors of the incident and scattered radiation are much longer than the size of one BZ, and the conservation of momentum for X-rays is $\mathbf{k}_f = \mathbf{k}_i + \boldsymbol{q} + \boldsymbol{G}$, where $\boldsymbol{q}$ is a phonon wavevector in the first BZ.

Since the ratio of the change in the incident energy, $\hbar\omega$, to the incident energy is $\hbar\omega/E_i \sim$ meV/keV $\sim 10^{-6}$, spectrometers need to have a high resolution in frequency to be able to measure spectra $S(\boldsymbol{Q}, \omega)$ as a function of the scattered wavevector $\boldsymbol{Q} = \mathbf{k}_f - \mathbf{k}_i$ and energy shift $\hbar\omega = E_f - E_i$. Before the common use of synchrotrons, which started around the 1970s, obtaining detailed spectra as a function of the energy shift $\hbar\omega$ was impossible [4, 38, 118], and the experimentalist willing to use X-rays to probe phonon modes had to settle for the *total scattering cross section* $S(\boldsymbol{Q}) = \int d\omega S(\boldsymbol{Q}, \omega)$. In other words, in a diffuse scattering experiment we do not find the energy dependence of the spectra, but only its integrated value. Simply put, we shine X-rays of momentum $\hbar\mathbf{k}_i$ on $BaTiO_3$ single crystal, we position the detector to detect wavevector $\mathbf{k}_f$, and, as we switch the detector on, we count the number of photons *of any energy* arriving at the detector with wavevector difference $\boldsymbol{Q} = \mathbf{k}_f - \mathbf{k}_i + \boldsymbol{G}$, irrespective of whether they were elastically or inelastically scattered.

I formally defined the total scattering cross section, which is the quantity probed in neutron/X-ray diffuse scattering, in Sec. 2.8 (Eq. 2.45). In brief, it is the Fourier transform of the pair correlation function (PCF), $G(\boldsymbol{R})$, evaluated for any direction of space. Because the PCF measures the average distance between atoms in space, X-ray diffuse scattering gives information about the spatial correlations of the dynamical positions of the atoms, computed for all directions of space. For this reason, it is a very useful technique for the investigation of disorder in materials. A nice short review on the diffuse scattering technique for disordered materials is Ref. [**?**].

X-ray diffuse scattering experiments of $BaTiO_3$ are very important, and talked-about. In 1968, in studying the electron and X-ray diffuse scattering patterns of $BaTiO_3$ and $KNbO_3$, Comes,

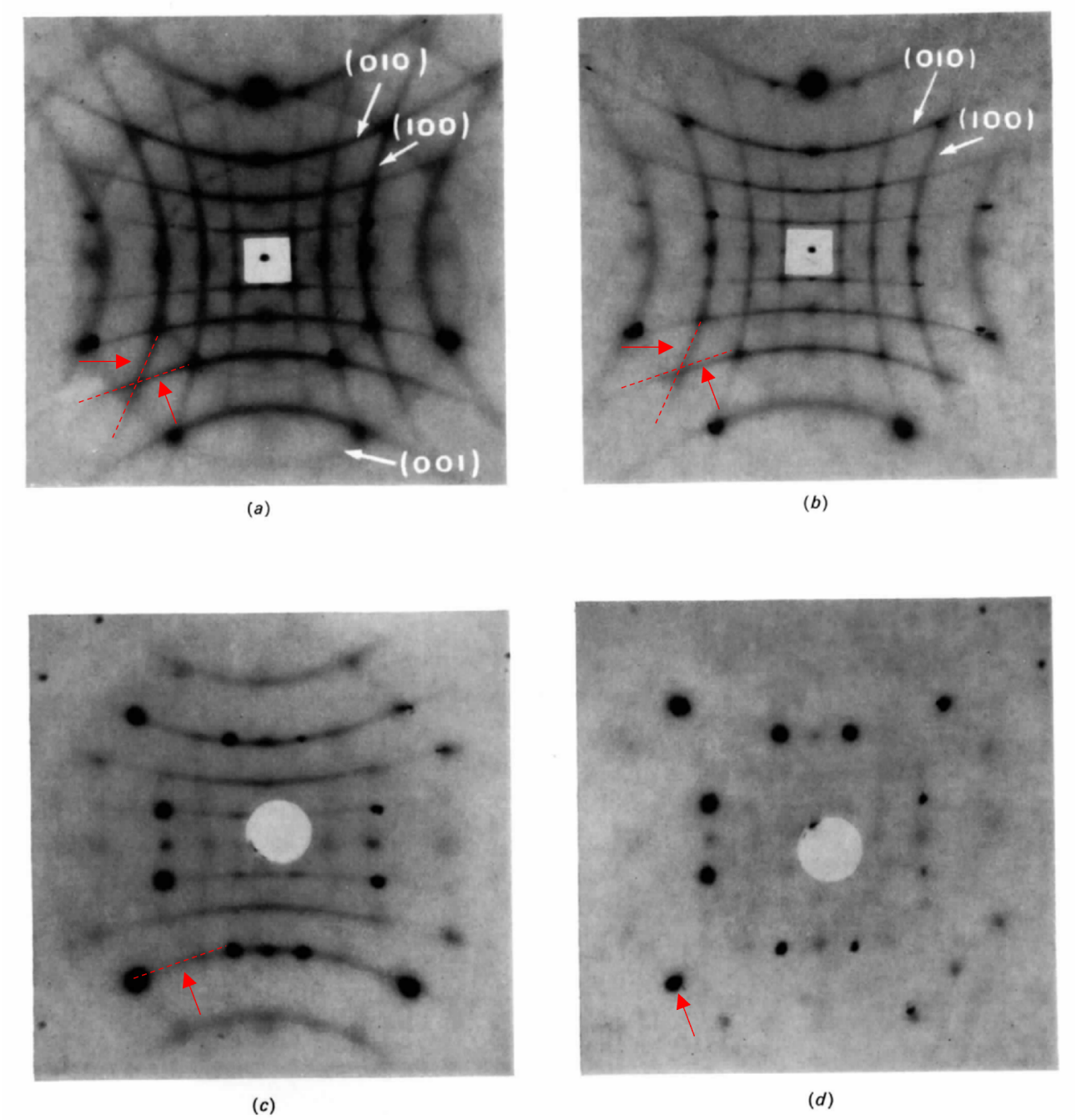



Figure 6.3: The X-ray diffuse patterns of $KNbO_3$, from Comes, Lambert and Guinier [26]. The panels (d)-(c)-(b)-(a) show the R-O-T-C phases of $KNbO_3$, which is isomorphous with $BaTiO_3$, respectively. I have added red arrows to point at the most striking features of the patterns. In the R phase, mainly the $\boldsymbol{G}$-points are visible. In the O phase, a set of horizontal $S_O$ appears. In the T phase, two sets of orthogonal $S_O$ appear. In the C phase, the two sets of tetragonal $S_O$ remain, but the background is darker, suggesting there is an additional diffuse *plane* parallel to the plane of the figure.

Lambert and Guinier [25] noticed some uncommon "diffuse streaks". The diffuse patterns are reproduced in Fig. 6.3. I shall mention that this picture has several issues: first, it is the result of an experiment on $KNbO_3$ (which however has an identical series of phase transitions and experimental behaviour as $BaTiO_3$); second, the original paper it is taken from is in French, Ref. [26][2]; third, the diffuse streaks appear bent, rather than orthogonal. This is caused by the experimental setting, which involved the use of a monochromatic X-ray and the collection of the diffracted rays on a planar photographic film placed at a certain distance from the sample. The result is the projection of all points which intersect the Ewald sphere, namely all points in reciprocal space satisfiying the condition for diffraction with the excitation of a phonon, onto a plane. This deforms the shape of the reciprocal space and the lines appear bent. A more detailed explanation of the experimental setting can be found in Ref. [27]. Nevertheless, I have decided to display it here because this figure is of historical importance, in the sense that it was a breakthrough in the understanding of $BaTiO_3$ and other perovskites as order-disorder materials. In spite of all of the problems I mentioned, the most striking features I want to discuss are still observable, and the fact that the diffuse patterns belong to all of the R-O-T-C phases allows us to see trends.

Let us begin discussing the R phase, reproduced in Fig. 6.3d. The only evident points are the $\boldsymbol{G}$ points, i.e. the Bragg peaks. Unfortunately, either the low temperature or the high noise or both things together completely masked the streaks caused by TA modes, which we call $S_A$ and which will be apparent in Fig. 6.4. The $S_A$ should be present at any finite $T$, because the X-ray cross section is inversely proportional to the frequency of the phonon involved in the scattering (see Sec. 2.8), and at any finite $T$ phonons, and especially the low frequency modes, are activated and should produce diffuse streaks. It is interesting to follow the evolution of the diffuse patterns: it is clear that the difference between one phase and a higher temperature one is the additional presence, in the latter phase, of horizontal and vertical *diffuse streaks*; we shall call these $S_O$. I have highlighted the $S_O$'s with red arrows, and with broken red lines, which are a guide for the eye for such patterns. For example, in going from the R to the O phase, horizontal $S_O$ appear. In going from the O to the T phase, vertical $S_O$ appear. In going

[2]the plots were later reproduced by Holma, Takesue and Chen [64] and commented in English.

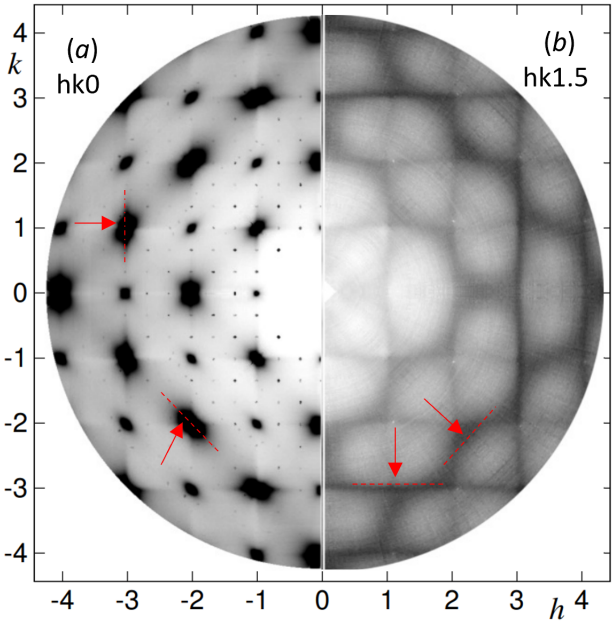



Figure 6.4: The X-ray diffuse scattering of $BaTiO_3$ obtained experimentally at 500 K, readapted from Pasciak *et al.* [94]. Panel (a) shows the reciprocal plane $[hk0]$, and panel (b) shows the reciprocal plane $[hk1.5]$. The latter plane does not show the Bragg peaks because it passes through the $X$ point, and hence allows to see the patterns more clearly. The red arrows point at the $S_A$ and $S_O$. Notice that diffuse streaks are present in both planes, suggesting they are diffuse sheets.

from the T to the C phase, the tetragonal patterns remain, but the background is darker. This suggests that the streaks are in fact diffuse *planes*. In the T-C transition, the additional diffuse plane is parallel to the plane of the sheet, and produces a grey background. Notice also that the increased temperature of the O-T-C phases produces a new set of streaks, which appear as concentric circles in Fig. 6.3; these are the $S_A$ streaks. The precise reason for the denomination $S_A$ and $S_O$ will be clearer soon.

The early experimental evidence provided by Comes, Lambert and Guinier for the presence of $S_O$ streaks was confirmed experimentally by others soon after [58, 57, 64], and in more modern measurements [94, 103]. We shall not discuss all of them, as the early measurements of Harada and Honjo [57] and Harada *et al.* [58] are hardly legible, and the figures provided by Ravy *et al.* [103], although interesting, do not add to what I have already shown. There is, however, an important recent (2018) X-ray study which is worth investigating: the one of Pasciak *et al.*. Fig. 6.4 shows the diffuse scattering patterns of $BaTiO_3$ in its PE phase measured by Pasciak *et al.* at 500 K. Note that Hlinka, whom we already encountered in the IR section, was one of

the corresponding authors of this work.

Fig. 6.4 shows two {100} planes in reciprocal space. In Cartesian coordinates, these are $[hkl]$ planes in the BZ where $l = 0$ in the left hand side and $l = 1.5$ in the right hand side. Hence, one plane contains the $\Gamma$ point, on the left of the figure, and one plane contains the $X$ point, on the right of the figure. Let us focus on the left hand side of Fig. 6.4. The first thing to note is the elongation, along 45°, of the Bragg peaks, which is due to TA modes and which produces the $S_A$ streaks; this will be shown in more detail in Sec. 7.6. Secondly, note the additional presence of $S_O$, which manifest as vertical and horizontal long streaks extending all the way from one $\boldsymbol{G}$-point to another, especially if one considers points away from [000]. The right hand plot is particularly interesting: in fact, it shows that the presence of the diffuse streaks $S_O$ is not limited to the $l = 0$ plane, but is observed in the $l = 1.5$ plane as well. This confirms that such diffuse streaks are not as much streaks, as they are planes, or *sheets*.

**Disappearance of the diffuse sheets at high pressure**

So far we talked about the $T$-dependence of the diffuse sheets. There was a brilliant study from Ravy *et al.* [103] which focused on the pressure ($P$) dependence of the streaks. At room $T$, $BaTiO_3$ undergoes a T-C phase transition at or above $P = 2$ GPa [103]. Interestingly, the authors found that the intensity of the streaks in $BaTiO_3$ vanishes at $P > 11$ GPa [103]. In other words, when the pressure is very high, the $S_O$'s disappear. The reason for this will be clearer in the next chapter, but I can anticipate that a high pressure decreases the volume of each unit cell, restricting the amount of anharmonic potential energy surface which the atoms can exprience, thereby reducing the degree of anharmonicity of the material. At some positive value of the pressure, the potential energy surface stops being a multiple-well potential, and becomes almost quadratic, causing the re-centering of the titaniums and the energetic preference of the nominal cubic structure. When this happens, anharmonicity, which causes the Ti-hopping motion between potential energy wells, is suppressed, and the material becomes much more harmonic [103].

### Summary of IXS

To summarize, the X-ray scattering patterns of $BaTiO_3$ are characterized by acoustic streaks $S_A$, which are expected for any material in the solid state, and some anomalous diffuse sheets $S_O$ orthogonal to the crystallographic $\langle 100 \rangle$ axes, of which the $h = \pm 3$ and $k = \pm 3$ sheets are the most pronounced in the C phase for the range of BZ vectors covered by the study of Pasciak *et al.* [94]. The diffuse sheets disappear at high pressure. These anomalous results, since the 1968 when they were discovered, became so pivotal that most of the papers on $BaTiO_3$ either cite the Comes, Lambert and Guinier paper [25] or try to give an explanation for the diffuse sheets. In the next section, I discuss how these diffuse sheets have been interpreted.

### Interpretation of the $S_O$ streaks

Comes, Lambert and Guinier assumed a simplistic model which considers only the Ti displacement, rather than the Ti-O combined displacements. According to this model, each Ti atom is not placed at the center of the unit cell, like in the nominal perovskite structure, but that it is at any time displaced towards the eight equivalent corners of the cube ($\langle 111 \rangle$ directions). I have already presented their eight-site model in Sec. 5.3.2; it is important to remember that, in the eight-site model of Comes, Lambert and Guinier, the displacements of the titaniums align along one or more of the crystallographic directions [100], [010] and [001], resulting in chains of equally polarized unit cells. The polarization of the chains differs from one chain to another, as depicted in Fig. 6.3, thereby creating *disorder* in space. The result is a "linearly-correlated" disorder, in the sense that atoms are correlated in chains, but the chains are *uncorrelated with each other*.

How is the eight-site disordered model related to the diffuse streaks? In a diffraction experiment the fundamental quantity measured is the scattering cross section. When atoms are assumed to be static, this is proportional to the static structure factor, which varies from crystal to crystal but is similar for materials with similar crystal structures. After calculating the static structure factor of their model of orthorhombic $BaTiO_3$, with Ti displaced by a quantity $+dy$

| $S(\boldsymbol{Q})$ - **Reciprocal space** | $G(\boldsymbol{R})$ - **Real space** |
|---|---|
| Sharp Bragg peaks | 3D periodic structure<br>$\rightarrow$ crystal with no defects |
| Diffuse streaks | 2D periodic structure<br>$\rightarrow$ perpendicular to the streaks<br>$\rightarrow$ disorder in streaks' direction |
| Diffuse planes | 1D periodic structure<br>$\rightarrow$ perpendicular to the planes<br>$\rightarrow$ disorder on planes |
| Diffuse clouds | no structure<br>$\rightarrow$ perfectly disordered or liquid |

Table 6.1: Features of $S(\boldsymbol{Q})$ and what they imply in the real space distribution of atoms. This table is entirely taken from [76].

or $-dy$ depending on the chain (cf. Fig. 6.3, Comes, Lambert and Guinier showed that such a disordered structure was able to qualitatively reproduce the orthogonal streaks they observed in the diffuse scattering experiments. In other words, a disordered, chain-like static structure would produce the $S_O$'s [25].

This interpretation of the diffuse streaks, namely that they are the result of linearly-correlated disorder, should not sound too audacious: it is well known from other studies, like the ones in Refs. [**?**, 148], that linearly-correlated disorder gives rise to diffuse streaks, as a result of a sharp decrease of transversal correlation in the atomic positions. Let us understand what this means. In Sec. 2.8 I showed that the scattering cross section $S(\boldsymbol{Q})$ is the Fourier transform of the pair correlation function (PCF) weighted by the atomic scattering lengths $b_i$, $G(\boldsymbol{R}) = \sum_{ij} b_i b_j \langle \delta(\boldsymbol{R} - \mathbf{R}_i + \mathbf{R}_j) \rangle$. Hence, if $S(\boldsymbol{Q})$ is spread out in $\boldsymbol{Q}$-space, then atoms lose spatial correlation in real $\boldsymbol{R}$-space. If $S(\boldsymbol{Q})$ shows up as sharp Bragg peaks, so that it has 0D structure, then the real-space arrangement of the atoms $G(\boldsymbol{R})$ is periodic in 3D space, hence it forms a perfect crystal. If $S(\boldsymbol{Q})$ produces diffuse lines, so that it has 1D structure, then the real-space arrangement $G(\boldsymbol{R})$ has 2D structure, hence the crystal is ordered on planes in real space, but there is disorder along lines in real-space perpendicular to 2D planes. In other words, it is made of a stack of ordered planes whose polarization changes from one plane to another. If $S(\boldsymbol{Q})$ shows diffuse planes, so that it has 2D structure, then the real-space arrangement $G(\boldsymbol{R})$ has 1D structure, namely it is made of linear chains of atoms whose polarization, defined as the combined displacements of the atoms of the chains, changes from one chain to another; hence

the presence of *uncorrelated linear chains*. If $S(\boldsymbol{Q})$ manifests as a uniform 3D background, then the material has 0D structure, so it is completely disordered or it is in a liquid or gaseous phase. This concept is summarized in Tab. 6.1. In $BaTiO_3$, because the diffuse planes are vertical and horizontal planes in reciprocal space, such as the $k = 3$ one visible in Fig. 6.4, the real-space correlations of atomic motions must be linear, namely, atoms must form linear chains, as in the eight-site model of Comes, Lambert and Guinier illustrated in Fig. 5.4. I can anticipate that this model is consistent with the model of this thesis, which I discuss in Sec. 7.8.

This said, there were some authors who rejected the interpretation of Comes, Lambert and Guinier of the presence of uncorrelated linear chains. In particular, these authors suggested that the streaks are due to the Slater TO being a soft mode. For example, Hüller, one year after the work of Comes, Lambert and Guinier, interpreted the diffuse sheets of $BaTiO_3$ as being a result of the anisotropy of the lowest TO branch (the Slater TO mode). He suggested that a simple dynamical model of a soft mode could explain such an anomaly [66]. Let us see briefly what his argument is. The diffuse sheets appear as streaks in one reciprocal plane. The streaks are caused by the lowering of symmetry when temperature activates phonon modes. We will see in Sec. 7.6 that the $S_A$ streaks are caused by acoustic modes. The $S_A$ streaks are more pronounced because the TA modes are the first to be activated at finite $T$. If a soft mode whose frequency is low exists, it will be have a large amplitude, and it will produce diffuse streaks. Now, if the phonon branch is soft along the whole $\Gamma - X$ path in the BZ, but it hardens quickly with an angle $\alpha$ between the [100] and [110] directions, the diffuse streaks it produces are elongated along the same [100] direction, that is, the $\Gamma - X$ path. In other words, the diffuse streaks appear as lines drawn in the BZs which are directions of reciprocal space along which the mode is soft. Hence, a very anisotropic mode, that is a mode whose dispersion changes a lot with $\alpha$, for example being soft along $\Gamma - X$ but hard along $\Gamma - M$, would produce the $S_O$ streaks of Fig. 6.3. It is for this reason that the subscripts $O$ for the horizontal/vertical streaks was used by Harada and Honjo [57] in 1966, and by Pasciak *et al.* in 2018 [94], to mean "optical", as the streaks were deemed to be caused by the lowest Slater TO branch, which was thought to be a soft phonon.

Hüller, as I said, was the author who first proposed, in 1969, that a displacive model could

explain the diffuse streaks and firmly advocated the soft mode picture, which was admittedly in contrast with the 1968's eight-site model of Comes, Lambert and Guinier [66]. After these years, authors supporting the one or the other interpretation alternated, and this ignited an intense debate on the origin of the phase transitions of $BaTiO_3$. Papers from the years 1968-1969 are in fact the most cited papers on $BaTiO_3$, because the questions posed during those years, namely whether the phase transition is displacive or order-disorder, remains unsettled. Is it displacive, as Hüller proposed, or is it order-disorder, as Comes, Lambert and Guinier thought?

## 6.3 Neutron scattering

Although IR spectroscopy is a valuable tool for obtaining optical spectra as a function of frequency, it only provides information about the phonon modes near Γ. To discuss phonon spectra in other parts of the BZ, we need to turn our attention to inelastic neutron scattering (INS). The rationale behind neutron scattering is the same as X-ray and Raman scattering: the crystal is irradiated with a beam of particles, and these particles are then collected at a detector with a change of energy $\Delta E = E_f - E_i$ and a change of momentum $\boldsymbol{Q} = \mathbf{k}_f - \mathbf{k}_i + \boldsymbol{G}$ after they have been scattered by the crystal.

Until it became common to use synchrotrons for producing highly brilliant and very monochromatic X-ray beams with the capability of detecting the scattered beam with less-than-meV resolution, neutrons were considered the only way to obtain phonon spectra over the whole BZ [38, 118]. In fact, neutrons possess qualities, with respect to photons, which make them excellent probes for studying lattice vibrations. Just to mention some: they do not have electrostatic charge, hence they do not interact with electrons like X-rays do; they have a mass in the same order of magnitude of, but smaller than, the nuclei, with which they interact; as a consequence of this, cold and thermal neutrons have energies up to $\sim$ 100 meV, which is the range of the phonon energies, as opposed to X-rays which have energies on the scale of $\sim$ keV. Among the drawbacks, neutrons have a magnetic moment through which they interact with

the nuclei; this produces the so-called *incoherent* scattering, which is very useful if one aims at getting insights into the magnetic properties of the sample, but is not useful if one only wants information about the phonons. Of course, neutrons need reactors or spallation sources to be produced and accelerated.

The rising interest in ferroelectric perovskites in the late 1960s and the desire for experimental verification of the soft mode model of the phase transitions, prompted many scientists to use neutrons to produce phonon spectra. Among these was a group working at the Brookhaven National Laboratory in New York, which included Axe, Shirane, Yamada, Harada, Linz and co-workers. We will primarily focus on the works of these authors, because they are the only INS experiments that I have found reported in the literature.

These authors decided to opt for neutron scattering to study a wide variety of perovskites in order to be able to work out the conundrums that light spectroscopy left unsolved. For example, the unstable modes of $SrTiO_3$ involve the tilting, around a $\langle 100 \rangle$ axis, of the oxygens' octahedra by angles that alternate going from one unit cell to another [39]; hence, among the unstable modes are modes at the $M$ and $R$ points, in the BZ boundary [29, 113]. Such points are not accessible to IR or Raman spectroscopy, and so the phase transition of $SrTiO_3$ simply could not be completely understood before the neutron scattering experiments were performed [113].

Here, we are mostly interested in the range of small frequencies, where the soft TO excitation and the acoustic branches lie. In this region of frequency, and in particular near a neutron energy shift of $\Delta E = \hbar\omega \to 0$ shift, INS spectra are polluted by two types of scattering which are not of interest to us. The first type, at $\boldsymbol{Q} = \mathbf{G}$, is the *elastic* scattering, i.e. one after which the neutron does not alter its energy, and which produces sharp Bragg peaks–the same we would encounter in a standard X-ray diffraction experiment. The second type, which can happen at any $\boldsymbol{Q}$, is the *incoherent* magnetic scattering. Both of these contributions need to be subtracted if only phononic excitations are to be extracted. There is a third spurious scattering, namely *isotope* scattering, which is caused by the fact that different isotopes have different masses and hence scatter neutrons in a different way. This latter type of scattering depends on the percentage of isotopes of the different elements present in the crystal, but we

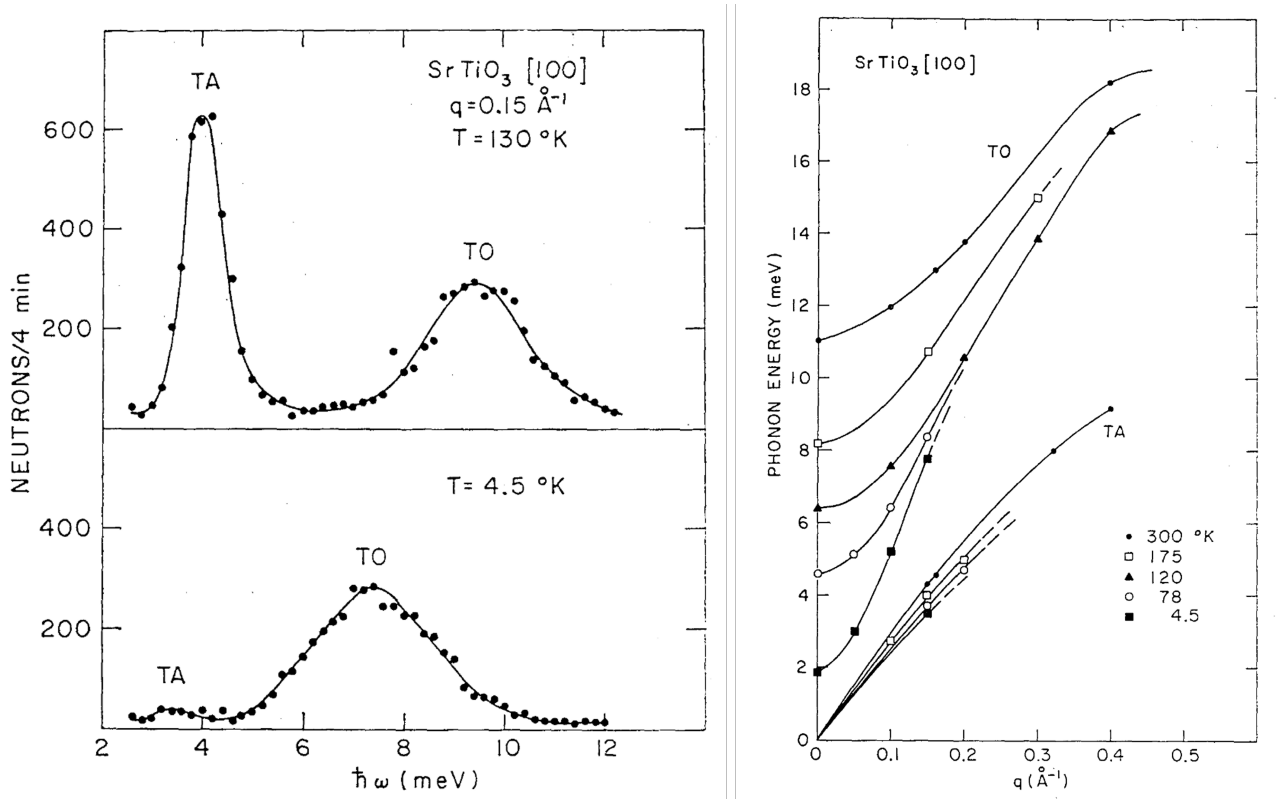



Figure 6.5: Neutron scattering spectra (left plot) and dispersion (right plot) of $SrTiO_3$ for the two lowest phonons, taken from Yamada and Shirane [147].

shall neglect it.

If a peak near the energy shift $\Delta E = \hbar\omega \to 0$ is found, which is due to inelastic scattering and not to the other types of scatterings mentioned above, in the experimental language it is often called *quasi-elastic* scattering, or, sometimes, *critical* scattering [148], as it is associated to a phase transition. It is this type of scattering we wish to examine.

### 6.3.1 $SrTiO_3$ and other perovskites

I start by very briefly summarizing the results found for other perovskites, as this will be useful for comparison with $BaTiO_3$. The behaviour of the soft mode of $SrTiO_3$ is evident in Fig. 6.5, taken from Yamada and Shirane [147], which shows, on the left hand side, a neutron scattering spectrum of the TA and of the lowest TO, at $q = 0.15$ A$^{-1}$ in the $\boldsymbol{q} \sim [100]$ direction of the BZ, measured for two temperatures, $T = 130$ K and $T = 4.5$ K. The plot clearly shows that the TO softens with decreasing $T$. On the right hand side is the phonon dispersion of

the lowest branches along a $\Gamma - X$ path, measured at different temperatures. It is clear that there are some striking features worth noticing: one is the progressive broadening of both the TO **and** TA modes as their line shapes overlap during the softening of the TO. Another one is the decrease of the sound velocity, which is observable in the softer dispersion of the TA mode with decreasing $T$. This should be caused by the repulsion between the TA and TO modes, which increases with decreasing $T$ as the latter branch softens and hence dangerously gets closer to the TA; however, the crossing is forbidden as the two modes belong to the same IRREP. Unfortunately, this is not the place to focus on this interesting incipient ferroelectric. However, what we need to note is that the spectrum of the soft TO branch of $SrTiO_3$, in the $\langle 100 \rangle$ direction of reciprocal space (and also in the $\langle 110 \rangle$ and $\langle 111 \rangle$ directions, see Ref. [120], Figs. 2 and 3) is underdamped (in the sense described in Sec. 5.3.4) at any $T$ and always stands at frequencies higher than the TA. As a result, the TO branch is very dispersive, because the TA mode is dispersive, being an acoustic mode.

On the other other hand, the behaviour of the Slater mode in $BaTiO_3$, which is the mode deemed soft by spectroscopists [119, 148, 56, 62], is rather different.

### 6.3.2 The early INS dispersion of the Slater mode in $BaTiO_3$

In this section, we will see the INS spectra of the low frequency excitations of $BaTiO_3$. I will show that the TO spectrum is (i) at lower frequencies than the TA and (ii) very non dispersive in $\boldsymbol{k}$-space.

The presence of a central peak in cubic $BaTiO_3$ was first observed by Shirane *et al.* in 1967 [119]. Their INS experiment showed that the peak of the Slater mode's spectrum lies below the TA peak, i.e., $\omega_{\mathrm{TO}}^{\mathrm{Slater}} < \omega_{\mathrm{TA}}$. Importantly, this happens throughout the whole $\Gamma - X$ path, and even at $T = T_C + 200$ K. The dispersion of the peak positions of the low-frequency spectra, published by Shirane *et al.* [119] and by Yamada and Shirane [148], is presented in Fig. 6.6. This is a first evidence that the Slater TO mode in $BaTiO_3$ behaves differently than the soft mode in $SrTiO_3$, because the dispersion of the Slater TO mode is very poorly dispersive across the BZ in the $\Gamma - X$ path. This is apparent if we compare Fig. 6.5 with Fig. 6.6.

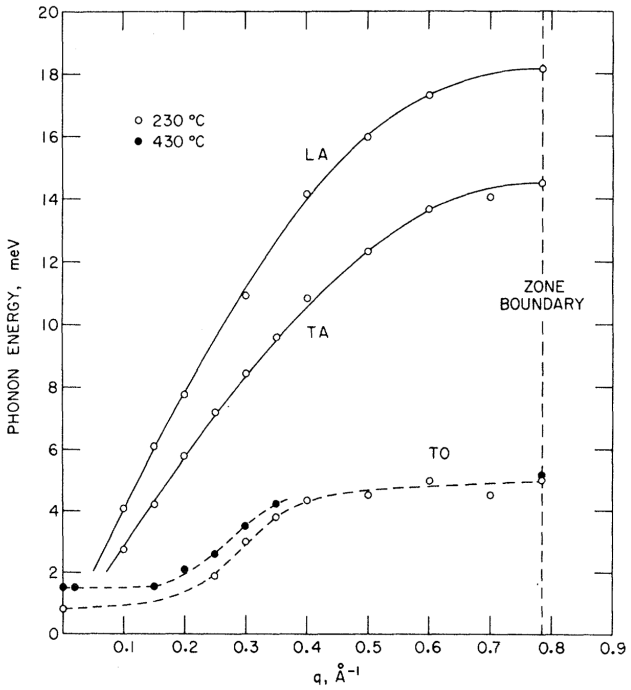



Figure 6.6: Neutron scattering dispersion of $BaTiO_3$ in the $\Gamma - X$ path featuring a soft TO excitation, from Shirane *et al.* [119]. These results were retracted by the same authors four years later in Ref. [56].

What Shirane *et al.* were the first to notice is that the "intensity of the [Slater] TO modes [near zero frequency] are unusually weak" [119]. This, as signalled two years later by Yamada and Shirane [148], is particularly difficult to understand if the optical peak at $\omega_{\mathrm{TO}}^{\mathrm{Slater}} < \omega_{\mathrm{TA}}$ was a proper vibrational mode. In fact, if we consider that the dynamical structure factor of a phonon mode is inversely proportional to its frequency (see Eq. 2.56), in a neutron experiment we would expect a high intensity for the signal of the soft TO compared to the signal of the TA, which lies at higher frequencies. Yamada and Shirane were expecting a ratio of the intensity of the two peaks, $I_{\mathrm{TO}}^{\mathrm{Slater}}/I_{\mathrm{TA}}$ as high as 60 times bigger than what they observed [148]. This is a hint that the optical low-frequency excitation found in neutron scattering and in the other experiments is not properly a soft vibrational mode, but something else: as we said in assessing the IR spectra, this should be a Debye mode, i.e. the hopping of Ti atoms among minima of the energy landscape. The precise reason for why the intensity of the Debye mode may not be high should be clearer later in this section.

Unfortunately, the same authors of the dispersion of Fig. 6.6 retracted these results four years later, in Harada, Axe and Shirane [56], motivating their retraction on the grounds that the

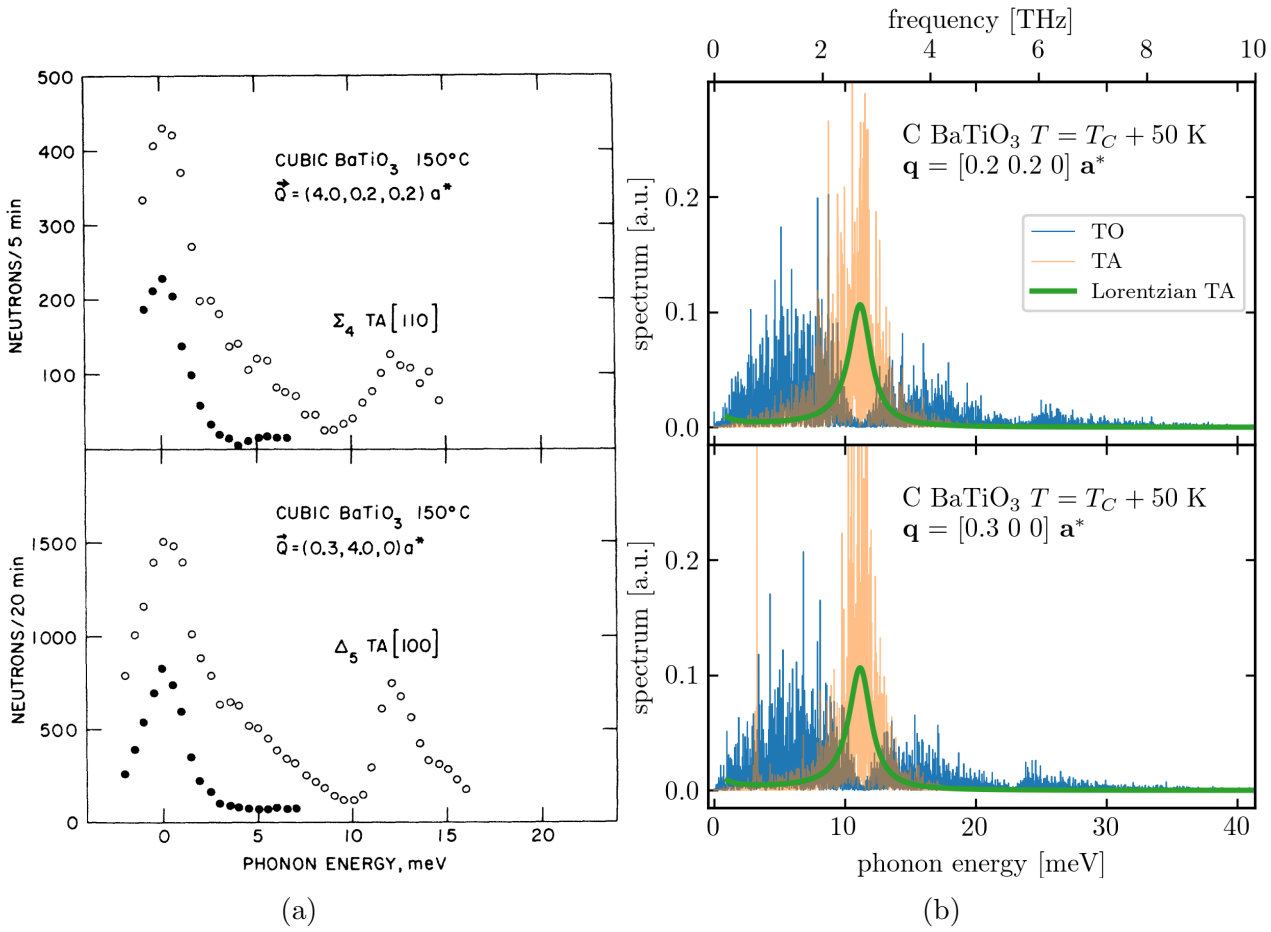



Figure 6.7: The low-frequency spectrum of the Slater TO and of the TA in cubic $BaTiO_3$. (a) the neutron scattering spectra, taken from Harada, Axe and Shirane [56], featuring a TO excitation softer than the TA (the black dots represent incoherent scattering and must be subtracted). (b) the spectra from the calculation of this work, obtained after MD, showing that the Slater TO melts and is spread out in $\omega$-space

.

signal-to-noise ratio they had in 1967 when they published these results was too low to be unreliable. I decided to report these results anyway, since they are the only ones that show the peak positions, rather than the calculated undamped phonon frequencies.

### 6.3.3 The spectra of the low-frequency excitations away from Γ

A typical spectrum at $\boldsymbol{q} = [0, 0.2, 0.2]\boldsymbol{a}^*$ and $\boldsymbol{q} = [0.3, 0, 0]\boldsymbol{a}^*$ in the C phase, measured by Harada, Axe and Shirane is displayed in Fig. 6.7a. The black dots denote the incoherent scattering, which must be subtracted from the white dots representing the experimental data. If we imagine doing so, we are left with a well defined excitation with a peak at an energy $\hbar\omega$

half way between 0 and 5 meV, and whose tail encounters the TA mode at $\hbar\omega \approx 10$ meV. Note that we are now away from $\Gamma$, so the low-frequency excitation cannot be a Bragg peak; in other words, it cannot be the result of elastic scattering. Hence, it is caused by inelastic scattering, that is, by a vibrational mode–exactly the Slater TO mode we were looking for. This confirms the presence of a central mode not only at the BZ center, as we learned from IR spectroscopy, but also in other portions of the BZ.

**The asymmetry of the TA spectrum**

It is worth lingering on these spectra a little. One thing to notice is the apparent broadening and asymmetry of the TA line shape. Both features are surprising, if we consider that the TA, being an acoustic mode, is usually underdamped, and its expected line shape is approximately Lorentzian[3] (as we saw for MgO in Fig. 3.5, for instance).

As for the broadening of the TA's line shape, this is a clear sign of TO-TA interaction [56], which in turn gives rise to the ferroelastic behaviour. We will return to this in the next chapter, especially in Sec. 7.7, and in Sec. 8.2. As for the asymmetry of the TA line shape, it is useful to compare the experimental phonon spectra with the simulated spectra from my MD simulations.

Let us look at Fig. 6.7b, which shows the TA and Slater TO raw spectra calculated after MD from Eq. 2.37 and convolved with the Bose-Einstein distribution in order to be comparable to INS. The TA mode is plotted with a transparent orange line, and I used a green line to plot the Lorentzian fit to the TA, in order to be able to assess its quality as a fit to the same mode. One of the few advantages that simulations have, with respect to experiments, is that we can single out the TA and the Slater TO contributions to the low-energy spectrum *individually*, while experiments of course cannot.

The simulated spectra show a very anomalous spread in $\hbar\omega$-space of the Slater TO mode. The broadening in $\hbar\omega$-space is apparent in Fig. 6.7b as we follow the mode's signal (blue line) in

[3]We have seen a similar anomalous broadening of the TA in $SrTiO_3$, in Fig. 6.5, but only at very low $T$, when the TO has almost totally softened, and moreover the signal's intensity was just too low to detect any asymmetry of the TA as $T \to 0$. A better-resolved INS spectrum of a TA mode is the one for $KTaO_3$ by Axe, Harada and Shirane, in Ref. [5]: at $T \gg T_C$, the TA is an underdamped, relatively narrow peak, and as $T$ is lowered towards $T_C$, its line shape broadens and shifts considerably (see Fig. 1 in Ref. [5]).

the whole range 0-40 meV, starting from low energies. The line shape of this mode produces a well defined peak at $\approx$ 5 meV, it then abruptly decreases to zero at $\approx$ 10-12 meV, in the correspondence of the TA peak position, it raises again to produce a second peak in the energy range $\approx$ 12-22 meV, and finally it even produces a shallow third peak at $\approx$ 25 meV.

The comparison INS vs MD spectra in Fig. 6.7 shows that the first simulated peak produced in Fig. 6.7b by the Slater mode at energies lower than the peak position of the TA, $\hbar\omega < \hbar\omega_{\mathrm{TA}}$, corresponds to the quasi-elastic scattering due to the soft TO mode observed in the INS spectra of Fig. 6.7a. Sadly, however, the frequency range $\hbar\omega > 16$ meV is not covered by the INS experiments, nor there is more data available in the literature, to my knowledge. For this reason, it is impossible to infer, from the available experimental data, whether the Slater TO mode produces other satellite peaks at higher frequencies, like my simulations suggest. I can only point out that a shoulder is clearly visible in the bottom plot of Fig. 6.7a, flanking the TA peak at its right. This shoulder resembles the second peak that the simulated Slater mode produces, at $\hbar\omega \approx$ 10-12 meV, visible in Fig. 6.7b. Hence, the simulated results shown in Fig. 6.7b suggest that the sharp asymmetry of the spectra to the right of the TA line shape is due to a satellite TO signal, rather than a feature of the TA of its own, and this would be a signature of an anomalously broadened Debye mode. This possibility–that the Slater mode would melt and therefore produce satellite peaks in a vast portion of $\omega$-space–was never considered in the literature, as the authors at that time, and still now [94], were in search of a single peak for the Slater mode, or, at worst, the soft excitation combined with a central peak, as for $SrTiO_3$ [113].

Once again, there is no experimental evidence to verify the spread in $\omega$-space, since the INS spectra terminate at 16 meV, and for this reason we need to find other experimental data.

**Constant energy scans**

Since const-$\boldsymbol{Q}$ scans are not of help, we can use also const-$E$ scans, and cross check between the two. In Fig. 6.8 I display all the spectra of Harada, Axe and Shirane 1969's work [56], which investigated the C phase. The central plot of Fig. 6.8 reports the dispersion proposed

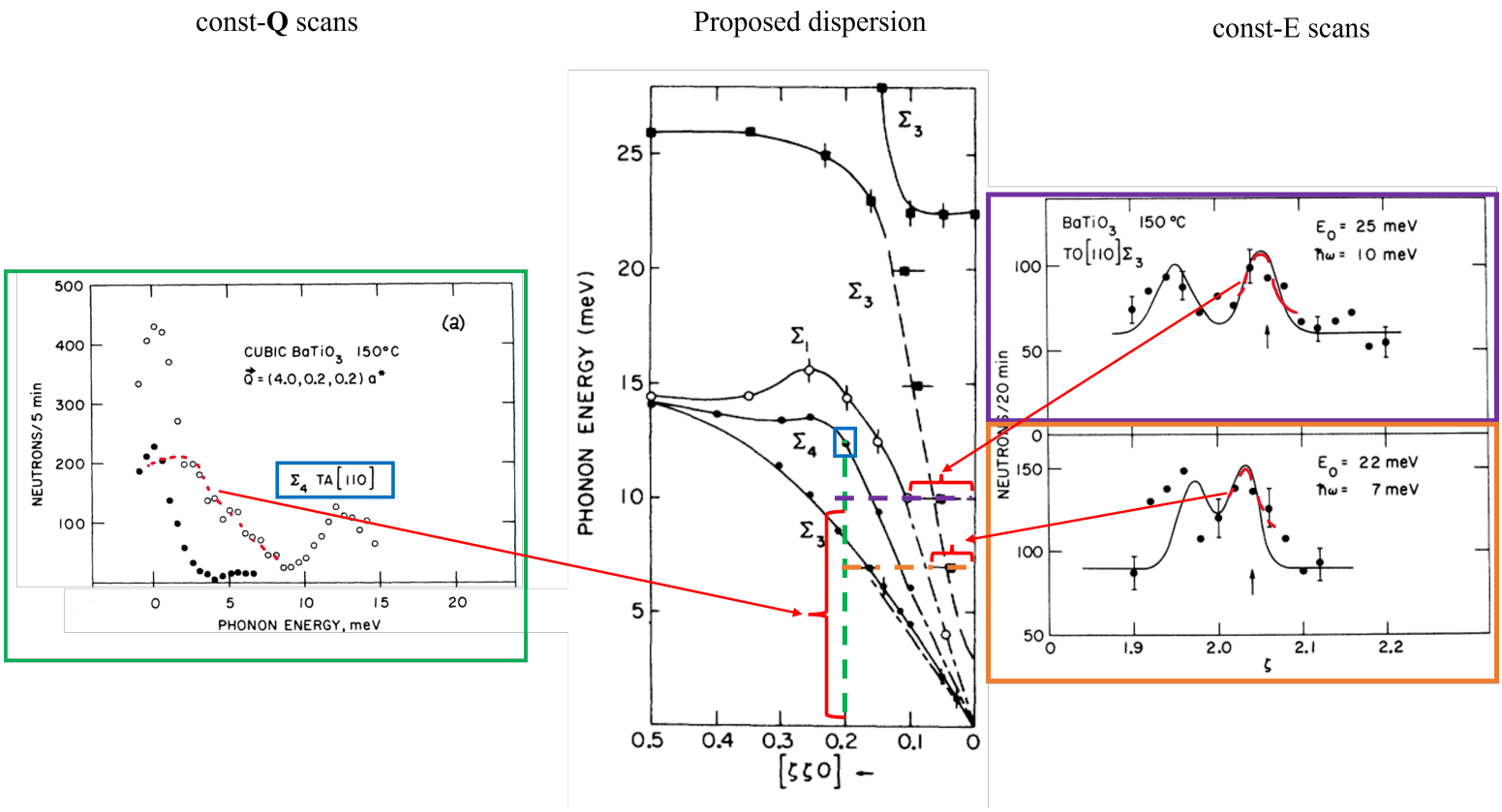



Figure 6.8: Neutron scattering results for C-$BaTiO_3$, taken from Harada, Axe and Shirane [56] in the $\boldsymbol{q} \sim \langle 110 \rangle$ path in reciprocal space. The left plot shows a const-$\boldsymbol{Q}$ scan, the right plot shows two const-$E$ scans and the central plot shows the proposed dispersion. Note that the authors suggest that the Slater branch (indicated by the physical group theoretical notation $\Sigma_3$) stands at frequencies higher than the acoustic modes. The red lines denote the Slater activity, the blue line indicates the TA mode and the broken lines denote the portions of the dispersion to which the scans correspond.

by the authors along a $\langle 110 \rangle$ direction of the BZ, after they fitted the spectra to a model that considered TA-TO interaction (See Ref. [56] for more details). Differently from Fig. 6.6, which dates back to 1967, the TO branch, denoted $\Sigma_3$ and drawn with a broken line, is very dispersive and always stands at higher frequencies than the TAs and LA branches; the authors seem to have had in mind, when drawing the $BaTiO_3$'s band structure, the band structure of other displacive perovskites, like $SrTiO_3$. The coloured thick lines that I added in the dispersion plot represent the only three scans for which the spectra are given. The red lines indicate the Slater mode's activity.

There are some things which do not seem clear or that are worth noticing from Fig. 6.8. First of all, the const-$\boldsymbol{Q}$ scan on the left is supposed to show only $\Sigma_4$ modes[4], i.e. modes polarized along the $\langle 100 \rangle$ direction [56]; among these modes is the TA. I framed the TA mode with light blue rectangles, one around its label in the spectrum and one around the corresponding point in the dispersion. The soft TO, on the other hand, which is also a $\Sigma_4$ mode, traced with a dotted red curve in the spectrum, does not find any correspondence in the dispersion. Where is it? Is it possible that its undamped energy is higher than 25 mev? This seems unreasonable.

Secondly, let us have a look at the const-$E$ scans: they manifest TO peaks near $\Gamma$, approximately at $\boldsymbol{q} = [0.05, 0.05, 0]\boldsymbol{a}^*$. As indicated inside these plots, they are $\Sigma_3$ modes, i.e. modes polarized along $\langle 110 \rangle$. Now, if we consider the intersection between the green and the orange broken lines in the dispersion, we have two Slater modes, of type $\Sigma_3$ and $\Sigma_4$, whose activity, following the orange broken line across the $\Gamma - M$ path, is present before (const-$E$ scans) and after (const-$\boldsymbol{Q}$ scan) the acoustic modes. This situation is similar to Fig. 6.7b, where we saw that the TO peaks appear at frequencies lower and higher than the TA peak position. This gives credibility to the early INS dispersion of Fig. 6.6, which shows that the intensity of the Slater TO mode is very spread out in $\boldsymbol{k}$-space, and to the next chapter, where this spread will become apparent, especially in Fig. 7.6.

[4] this is the physical notation which I mentioned in Sec. 5.4.

**Interpretation of neutron scattering**

We now have several reasons to suspect that the "soft" TO mode is not in fact a soft phonon mode. Firstly, because its cross-section is much lower than we would have expected, as Shirane, Yamada, Litz *et al.* [119, 148] warned. Secondly, because the signal of the Slater TO mode seems anomalously spread out in $\omega$-space, as I observe in my simulations. Thirdly, because if we cross-check between const-$\boldsymbol{Q}$ and const-$E$ scans, the signal of the Slater TO mode seems spread out also in $\boldsymbol{k}$-space, at least in the $\Gamma - M$ path where spectra were made available by Harada, Axe and Shirane [56]. This is in contrast, for example, with the behaviour of the soft TO branches in $KTaO_3$ and $SrTiO_3$, which are very dispersive, as pointed out by Yamada and Shirane [147] and reproduced in Fig. 6.5.

The neutron spectroscopists who poured a lot of effort into the study of ferroelectric perovskites in the late 1960s and early 1970s, when analyzing $BaTiO_3$ hinted that it might have been partially an order-disorder material. The first INS paper to talk about the possibility of a disordered paraelectric phase is the one of Yamada, Shirane and Lintz [148]: they suggested that the presence of an overdamped central peak, i.e. the quasi-elastic "critical" scattering, resembles the magnetic disordering which is established in magnetic substances beyond the transition point (see Sec. III of Ref. [148]). However, the neutron spectroscopists at that time appear to have been influenced by Cochran's concept of the soft mode, developed in 1960 in Ref. [22], which at that time was the prominent model of materials' structural phase transition. In fact, it was only two years after the 1969 publication of Ref. [148] (and of Hüller's paper [66] on the soft mode interpretation of the X-ray diffuse scattering), that authors of the same group changed their minds, advocating that a well-defined, but highly-anisotropic soft mode could explain the INS spectra and of course the X-ray diffraction patterns, which are the major evidence of a disordered phase. Moreover, it is interesting to notice that in their analysis after the 1969 the undamped TO branch was always drawn at a frequency higher than the TA branch, although the peak positions of the spectra lie well below it, as we saw in the figures of this section. As a result, $BaTiO_3$'s dispersion resembles the dispersion of $SrTiO_3$–a soft mode material.

Let us conclude this section with a final remark. It is clear, in my opinion, that the potential of INS experiments has not been sufficiently exploited. The first reason for asserting this is that the energy range allowed by INS spectrometers in the past was not sufficient, if we look at Fig. 6.7a, to cover the whole spectrum of the Slater excitation of $BaTiO_3$. A second reason is related to the choice of $\boldsymbol{G}$-vectors in all of the INS studies. The use of *even* $\boldsymbol{G}$-points, like [200], [400], [220] guarantees a higher signal-to-noise ratio, as the structure factor of the perovskite crystals is high at this points (as can be seen in Fig. 6.4). On the other hand, if one considers the *dynamical* structure factor (Eq. 2.57), which depends on the modes' eigenvectors, such choice favors the TA acoustic modes, which therefore always stand in the way of the Slater TO spectrum. This results in the TA being over-represented in the spectra, and creates overlap between the two modes which is very hard to disentangle. In other words, the spectra that the authors measured enhances the TA mode, rather than the TO. Though it is not possible to remove the acoustic peaks completely, it should be possible to enhance the TO signal with respect to the TA signal, for example by choosing *odd* $\boldsymbol{G}$-vectors, like [100], [300] or [110]. In this way, it would be possible, not to exactly distinguish between the TA and TO mode separately, as we did in Fig. 6.7b, but at least to have a purer, and more complete optical spectrum. More on this, and the precise way I would plan a neutron scattering experiment, is presented in Appendix D.

## 6.4 Local probes: X-ray absorption fine structure (XAFS)

The very reason why $BaTiO_3$, and most similar perovskites, were originally deemed displacive by spectroscopists is that a soft mode was found in all of them, in agreement with Cochran's theory [22]. On the other hand, we highlighted in the previous sections quite a few hints that the PE-FE transition of $BaTiO_3$ might be of the order-disorder type: the fact that IR measurements found a Debye mode which emerges and is very coupled to the shrinking of the Slater mode, the presence of diffuse sheets found in X-ray diffuse scattering experiments, which suggest linear disorder, and the fact that the the Slater mode is very spread out in $\omega$-space and very flat in $\boldsymbol{k}$-space, as it appears with neutron scattering. After the 1968 eight-site model

of Comes, Lambert and Guinier was rejected by Hüller in 1969 and by the same Comes few years later [28], the order-disorder picture of the phase transitions of $BaTiO_3$ and other similar perovskites gained new popularity with XAFS measurements.

The "fine structure" is the small oscillations of the X-ray absorption of an atom at energies near its absorption edges. When the energy of the X-ray is sufficiently high so as to dislodge core-level electrons, the absorbing atom is promoted to an excited state with a core hole plus a photoelectron. This electron is scattered back by the surrounding atoms, and interference occurs between the ejected and backscattered photoelectron's wavefunctions. This interference produces an oscillatory modulation of the absorption coefficient, with maxima or minima when constructive or destructive interference occur: the fine structure of the X-ray absorption.

The X-ray absorption is plotted either vs the energy of the incident X-ray or vs its wavevector; in the latter case, it is usually denoted $\chi(k)$. The XAFS depends on the number, type and position of the atoms surrounding the excited one. For example, the frequency of the oscillations are directly proportional to the distance between the excited and the backscattering atom: the lower the frequency, the closer the atom. It also depends on the temperature, because the greater the atomic fluctuations the greater will be the extent of the influence of the surrounding atoms on the scattered photoelectron. XAFS is a local probe, namely it gives information about the local structure around an atom. Analysis of the XAFS gives information about the lattice constant $a$, the local relative positions of the atoms $\mathbf{R}_{ij}$, the displacement of an atom with respect to the center of the cell $\delta_{\text{atom}}$ and its orientation $\alpha_{\text{atom}}$ with respect to an axis, the mean square deviation of a bond distance $\sigma_{ij}^2$ and so on. Since the energy of the X-ray can be tuned so as to match the absorption edges of the different species present in the crystal, the XAFS technique is very element-selective: in perovskites of the type $ABO_3$, the probe atoms are usually chosen to be the the A and B cations. In the case of $PbTiO_3$ and $BaTiO_3$, for instance, the excitation of the Pb $L_{III}$ edge at 13035 eV, of the Ba $L_{III}$ edge at 5247 eV and of the Ti $K$ edge at 4966 eV [122, 102] gives information on the local environments around these atoms.

The local structure within the bulk of a crystal can be inferred from the pair correlation function (PCF), which I have defined in Eq. 2.48. I restate the equation for the PCF, neglecting the

scattering lengths or atomic form factors: $G(\boldsymbol{R}) = \sum_{ij}\langle\delta(\boldsymbol{R} - \mathbf{R}_i + \mathbf{R}_j)\rangle$. The PCF is the probability of finding an atom $i$ at a distance $\mathbf{R}_{ij} = \boldsymbol{R}_j - \boldsymbol{R}_i$ from an atom $j$, weighted by the atomic scattering lengths in the case of neutron experiments or atomic form factors in the case of X-ray experiments. It is the inverse Fourier transform of the scattering cross section measured by X-ray diffraction (see Eq. 2.47). However, there is an important difference between X-ray diffraction and XAFS: while X-ray diffraction measures the *average* crystallographic structure, XAFS enables to determine the PCF of a single *probe atom* with respect to its neighbours. That is, XAFS allows to measure $g(\boldsymbol{R}) = \sum_j \delta(\boldsymbol{R} - \mathbf{R}_0 + \mathbf{R}_j)$ or a quantity proportional to it [126]. This is just the nuclear density around the probe atom. The maximum value of $j$ is defined by the spatial extent of the experiment; depending on the experimental setup, this comprises the first, second, third and in some cases fourth shell of neighbouring atoms [126].

The PCF obtained from XAFS gives information about the local interaction energy $U(\boldsymbol{R}; T)$ of the atoms at different $T$s [126]. Let us take the cubic phase as an example. If this phase remains ordered, then its potential energy surface becomes quadratic at $T > T_C$, in accordance with the displacive theory (cf. Fig. 5.5), with a minimum at the center of symmetry of the cell. Hence, the PCF of the relative position between two atoms, say the Ti and an O atom, would reveal a presumably Gaussian shape with its maximum exactly half way between the two atoms. If the C phase is disordered, on the other hand, $U(\boldsymbol{R}; T > T_C)$ remains in the form of a multiple-well potential, and the low-$T$ and high-$T$ phases differ by the occupancy of the wells: this will be high for the one well and low for the other at $T < T_C$, and will be approximately equal for opposite wells at $T > T_C$. Hence, if a phase is disordered and we imagine to freeze the atoms at time $t$, we would find that the probe atom is not *at* the center of the cell, with high probability, and the PCF should reflect this by having its peak position off-centered. XAFS allows to calculate the PCF and therefore to investigate whether a phase is locally ordered or not.

It is important to note that the structural information about local environments is obtained by fitting $\chi(k)$ to some theoretical model. This model includes parameters which depend on the absorbing atoms and which are calculated *ab initio* [102], and other parameters which are called the "condensed matter contribution" [102], like the unit cell's shape, local positions

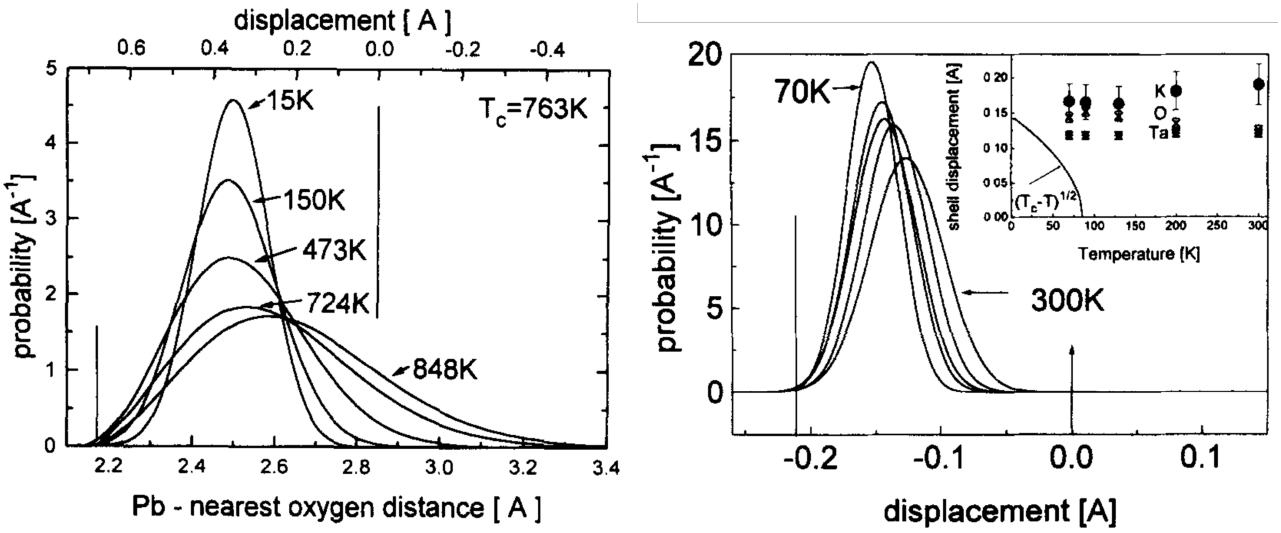



Figure 6.9: The pair correlation function obtained from XAFS for the Pb-O distance in $PbTiO_3$ [126, 122] (left plot) and for the Nb-O distance in $KTaO_3$:9%Nb [126] (right plot).

of the atoms and their mean square displacements. The latter parameters, the ones which mainly interest us, are obtained through a fit of the theoretical model to $\chi(k)$. Within the XAFS technique, there can be distinguished the Extended XAFS (EXAFS), that is, the region stretching to much more than 20 eV above the absorption edge, and the X-ray Absorption Near Edge Structure (XANES), which is the region of the X-ray absorption near the edge.

**Results for other perovskites**

Let us briefly mention the results for some perovskites: $PbTiO_3$ and Nb-doped $KTaO_3$. The calculated PCFs, taken from Ref. [126], are presented in Fig. 6.9. On the left hand side is the Pb-to-nearest-O pair correlation function for $PbTiO_3$; the origin of the top $x$-axis indicates the half distance between two adjacent O atoms located along a face diagonal. The study indicates that at any $T$, even in the C phase ($T > T_C$), the peak of the PCF of the Pb-O distance is not at zero, indicating that the Ti atom is displaced away from the center of the unit cell's face, and specifically along the tetragonal axis [126]. The calculated PCF for $KTaO_3$:9%Nb of the Ti-O distance, shown on the right plot of Fig. 6.9, also shows that the Nb is not half way between the O atoms, at all temperatures. This suggests that the average positions of the atoms do not correspond to the ones predicted by the nominal perovskite structures as found by X-ray diffraction, and that there is a local distortion in each unit cell in these two materials.

### 6.4.1 The XAFS of $BaTiO_3$

I now discuss the main results for $BaTiO_3$, and show that the work of Ravel *et al.* [102] gives a clear indication that all of the phases have a rhombohedral distortion at any given time. The authors performed EXAFS measurements on the Ba $K$ edge, and XANES on the Ti $K$ edge.

#### EXAFS

Let us first analyze the EXAFS results from Ravel *et al.* [102]. These were obtained at nine temperatures in all phases of $BaTiO_3$. The authors used five structural parameters to fit $\chi(k)$, whose variation allowed for the possibility of a rhombohedral or a cubic structure: the rhombohedral angle, $\alpha$, the rhombohedral displacement of the Ti, $\delta_{Ti}$, the displacement of the O atom in the $z$ direction, $\delta_{O_z}$, the lattice parameter, $a$ and the displacement of the O atom in the $x$ and $y$, $\delta_{O_{xy}}$. By analyzing the best fit parameters, they came to the conclusion that a good fit *in all phases* was found with the rhombohedral structure. This is the first hint that the phases of $BaTiO_3$ would be characterized by a rhombohedral distortion.

If this is an indication that a rhombohedral distortion of the unit cell is present in all phases of $BaTiO_3$, it is certainly not a proof of it. In fact, the authors repeated the same analysis considering other sets of structural parameters which were fixed so as to represent the R-O-T-C nominal phases. After fitting $\chi(k)$ to these sets of parameters, they found that the statistical significance of the nominal phases was not worse than the statistical significance of the data interpreted with a rhombohedral distortion.

Because the statistical analysis was insufficient to settle the question, they proceeded by analyzing another variable that they obtained in their fit of $\chi(k)$, which is the mean square of the Ba-Ti distance, which they called $\sigma^2$ [102]. They compared $\sigma^2$ obtained from the rhombohedral fit and from the fit to the nominal R-O-T-C structures, and they found that the optimal $\sigma^2$ obtained with the nominal structures was much larger than the $\sigma^2$ obtained with the rhombohedral distortion. Because $\sigma^2$ is the mean square variation of a bond length, it is inversely proportional to the bond stiffness. Hence, a greater $\sigma^2$ could be explained by the softening of a

spring constant, which would prove the presence of a soft mode and hence that the material is displacive, in principle. However, the small variations of the bond length $\delta_{\text{Ba-Ti}}$ and of the other bond lengths from phase to phase are not consistent with such big values of $\sigma^2$. In fact, the authors found that the bond lengths change by only $\approx 3$ % in passing from a phase to another [102]. If the springs were softening, then at $T \approx T_C$ the atoms would displace noticeably, and the bond lengths would likely have a big percentage difference. Then, the larger values of $\sigma^2$ when the nominal structures are chosen should be due to the fact that the nominal structures have to compensate for the Ti off-centering, that is for static disorder. On the other hand, the presence of a rhombohedral local symmetry is perfectly compatible with all the measurements.

**XANES**

The XANES measurements were performed at the Ti $K$ edge. XANES spectra include the fluctuations of $\chi(E)$ within $\approx 60$ eV of the absorption edge. Because this range of energy is just too small to obtain information on the structural parameters like in an EXAFS spectrum, the XANES spectrum is used in a slightly different way. For example, it is used to infer the oxidation states of certain atoms. The absorption edges of certain transition metals, in fact, are strongly affected by the oxidation (loss of electrons) of the metal atom when it binds with other atoms.

There is another important way in which a XANES spectrum can be used, which is relevant for $BaTiO_3$ in particular. Because the dominant effect of the interaction of radiation with an atom is caused by electric dipole transitions, the selection rule for a photoelectron being initially in state $1s$ with angular momentum $l = 0$ is that $l$ must increase by one. Hence, transitions to $p$ states should be dominant. The signature of an $s$-to-$p$ transition is the presence of a peak *before* the absorption edge. The O atom has valence $p$ states, but the Ti atom has unoccupied states of the $d$ type, instead. Hence, if an $s$-to-$p$ peak is found by XANES, then the only possible explanation is that a displacement of the Ti towards the O octahedron has occured, and that this displacement has caused a mixing between the Ti $d$ states and the O $p$ states. So, *the presence of a peak before the absorption edge is a strong indication that the Ti has displaced*

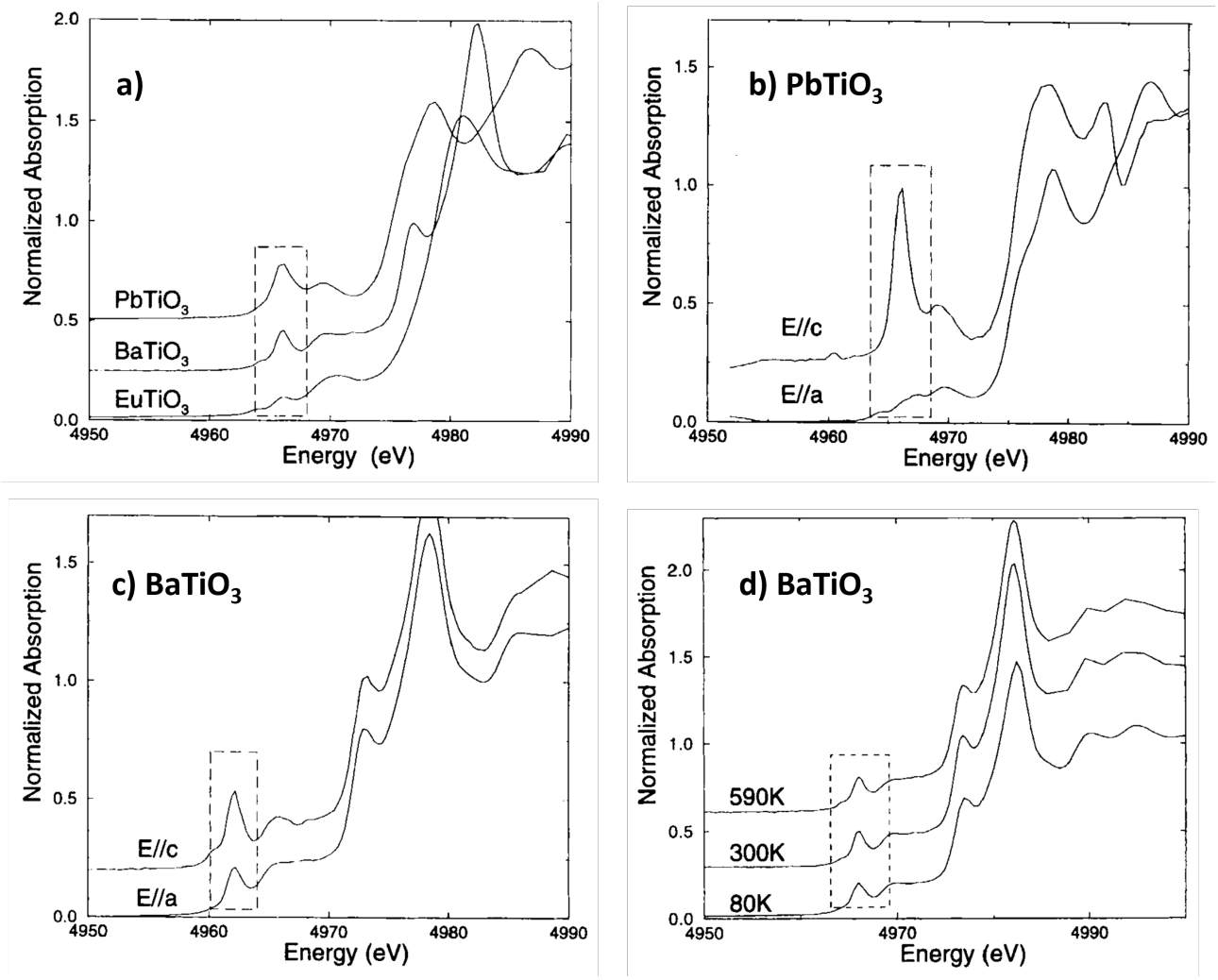



Figure 6.10: XANES spectra of perovskites, taken from Ravel *et al.* [102]. (a) comparison between T-$PbTiO_3$, T-$BaTiO_3$ and C-$EuTiO_3$ at 300 K showing that the pre-edge peak almost disappears in a cubic perovskite. (b) pre-edge peak in T-$PbTiO_3$ for the electric field polarized parallel and perpendicular to the tetragonal axis $c$, showing that the peak disappears in the latter case. (c) pre-edge peak in T-$BaTiO_3$ for the electric field parallel and perpendicular to the tetragonal axis $c$, showing that the peak almost does not change with the orientation of the electric field. This is the best XAFS indication that the T phase (and, by extension, the other phases) is characterized by a local rhombohedral distortion, hence is disordered. (d) temperature evolution of the pre-edge peak of $BaTiO_3$, showing that the distortion is present in all phases.

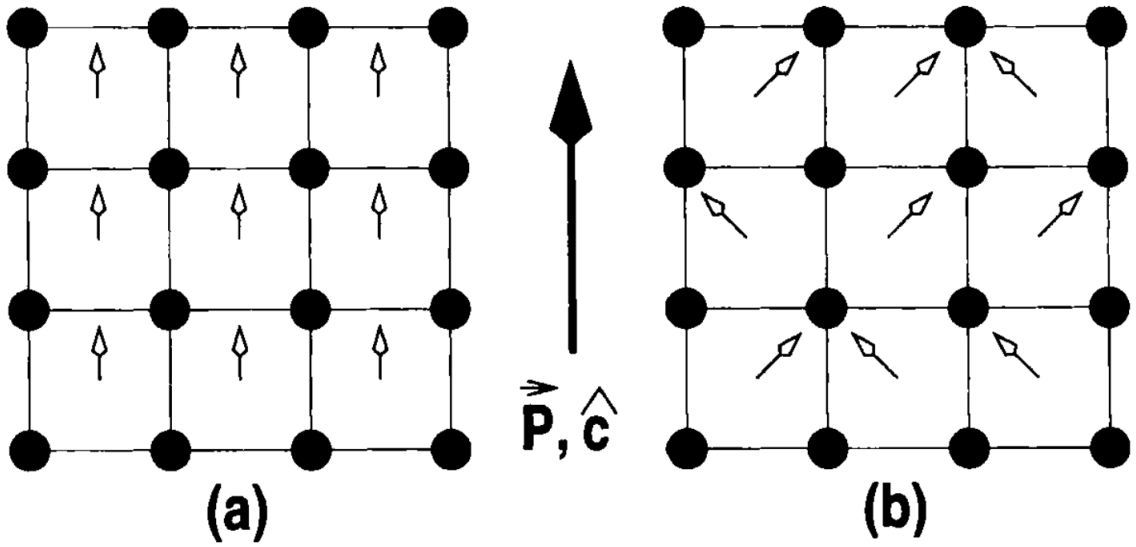



Figure 6.11: Model of T phases of $PbTiO_3$ (a) and of $BaTiO_3$ (b), according to XAFS authors Ravel *et al.* [102]. The T phase of $PbTiO_3$ is ordered, while the T phase of $BaTiO_3$ is disordered.

*from the centrosymmetrical position of the unit cell* [102].

Fig. 6.10a shows the XANES spectra of three polycrystalline samples of $BaTiO_3$, $PbTiO_3$ and $EuTiO_3$, at 300 K. $BaTiO_3$ and $PbTiO_3$ are tetragonal at this $T$ (and $PbTiO_3$ remains tetragonal at $T < 763$ K), while $EuTiO_3$ is cubic at all $T$s. Clearly the pre-edge peak is present for the first two perovskites, and almost disappears for the third. Fig. 6.10b shows data obtained for a $PbTiO_3$ single crystal, with the polarization of the electric field from the light beam $\boldsymbol{E}$ parallel to the crystal's polarization axis $\boldsymbol{E}||c$ and orthogonal it, $\boldsymbol{E}||a$. The two spectra reveal a qualitative different behaviour before the edge: the peak is present in the $\boldsymbol{E}||c$ case and absent in the $\boldsymbol{E}||a$ one. This suggests an asymmetric distortion of the cell or off-center displacement of the titanium in $PbTiO_3$ along the $c$ axis; in other words, the local structure of this perovskite would be tetragonal at all $T$s. On the other hand, the XANES spectra for $BaTiO_3$ , reproduced in Fig. 6.10c, do not change significantly with the orientation of the electric field. In fact, the pre-edge peak is present regardless of the orientation of $\boldsymbol{E}$, albeit being slightly shallower when $\boldsymbol{E}||a$. Moreover, the XANES spectra of $BaTiO_3$ do not change significantly with $T$, as Fig. 6.10d shows. This is the best XAFS indication that the local structure of $BaTiO_3$ is rhombohedral at all temperatures, hence it is disordered.

The model of Ti displacements in the two perovskites is qualitatively explained by the schematic

of Fig. 6.11, also taken from Ref. [102]. On the left hand side is $PbTiO_3$ in its T phase. This phase appears perfectly ordered because all the Ti atoms are displaced coherently towards the $c$ axis. The model that Ravel *et al.* advocate for $BaTiO_3$ in the T phase is disordered, and is shown in the right hand side of Fig. 6.11. Because the Ti would have a $\langle 111 \rangle$ distortion $\boldsymbol{\delta}_{\mathrm{Ti}}$, the angle between $\boldsymbol{\delta}_{\mathrm{Ti}}$ and the polarization of an electric field along the $c$ and the $a$ axis would be 45° in both cases, hence the $\boldsymbol{E}||a$ and $\boldsymbol{E}||c$ XANES spectra would not differ substantially, as Fig. 6.10c indicates.

In reality, as the authors note, the $\boldsymbol{E}||a$ and $\boldsymbol{E}||c$ XANES spectra of $BaTiO_3$ do differ somewhat. Firstly, the area of the pre-edge peak changes, although little, with $T$. By computing the ratio between the areas of the peaks taking the 35 K area as reference, Ravel *et al.* found that the Ti distortion decreases by only 13% from its value at 35 K as obtained from the EXAFS. Secondly, the areas change, again little, with the orientation of the electric field (see Fig. 6.10c). By calculating the two areas, Ravel *et al.* estimated that the Ti displacement $\boldsymbol{\delta}_{\mathrm{Ti}}$ would make a $\approx 12°$ angle from the $\langle 111 \rangle$ direction towards the $c$ axis. This latter feature is called "re-orientation of the minima" [43]. The possible responsible for it is the strain, along the $c$ axis, caused by the macroscopic polarization being in the $c$ direction when the phase is tetragonal [102][5].

Finally, note that, in the model of Fig. 6.11b, the authors seem to not have appreciated the results from X-ray diffuse scattering, which suggest that the Ti distortions are linearly correlated along non-ferroelectric directions. The way they are drawn in Fig. 6.11b, in fact, suggests that the distortions along an $a$ axis are not correlated for more than two unit cells. This is in contrast with the eight-site model of Comes, Lambert and Guinier discussed in Sec. 5.3.2. One of the possible explanations of this is that XAFS is a local probe: the spatial extent of the experiment may be just too limited to appreciate atomic correlations within a relevant portion of material.

[5]It should be noted, however, that in the single crystal measurements of Ravel *et al.*, an electric field of 600 V/cm was applied in the tetragonal direction. This was done so that the measurements would not be polluted by the possibility that the surfaces of the crystal were differently oriented with respect to the bulk. This procedure is sometimes called poling. Although the x-rays are highly penetrating, in fact, the authors preferred to avoid any surface effects by applying an electric field so that surfaces and bulk would be equally polarized.

**Summary of XAFS**

EXAFS experiments performed by Ravel *et al.* [102] on $BaTiO_3$ revealed that the local structure of the material can be approximated well with a rhombohedral distortion in all phases, and even at temperatures well into the C phase. A rhombohedral distortion is a displacement of the Ti atom along a $\langle 111 \rangle$ direction, with respect to their neighbouring atoms. XANES spectra confirmed this observation in the T and C phases, and revealed that the local distortions deviate from the $\langle 111 \rangle$ directions by 12° towards the $c$ axis [125]. This in an interesting result: the unit cells are locally *quasi-rhombohedrally* distorted, because such distortion does not exactly happen towards the cubic body diagonals, according to XAFS measurements.

Hence, we can summarize the XAFS results by Ravel *et al.* [102] and the later analysis of Stern [125] as follows: all the phases of $BaTiO_3$ are characterized by an off-centering of the Ti approximately along the body diagonal; hence, all but the R phase are disordered in space (and time). For example, the disorder of the T phase along an $a$ axis averages out the Ti distortions to zero. At any given time, and at any $T$, the Ti distortion changes not as much in its magnitude as it does in its *orientation* with respect to the ferroelectric axis. It is this slight orientational misalignment with respect to the $\langle 111 \rangle$ direction, according to Stern, that makes a displacive component in $BaTiO_3$ [125]. As a result of this small displacive component, the Ti in the T phase would be slightly displaced towards the $c$ ferroelectric axis.

A beautiful discussion on the possibility that the PE phase of $BaTiO_3$ is disordered is in the paper by Stern and Jacoby[6], in Ref. [126].

## 6.5 Local probes: nuclear magnetic resonance (NMR)

When a magnetic field is applied to an ensemble of particles, any elementary particle which possesses a spin, characterized by a quantum number $m$, will tend to align it to the direction

[6]E. Stern is known for his great contribution on the development of the XAFS techninque, and Jacoby was one of the authors of the theoretical development of a spin-phonon Hamiltonian for order-disorder perovskites, Ref. [51].

of the field. Nuclei having an even number of protons and neutrons have nuclear spin quantum number $I = 0$, hence they have a vanishing magnetic moment and do not interact with the magnetic field. The proton $^1$H and atomic isotopes with $I = \frac{1}{2}, 1, \frac{3}{2}, \ldots$, on the other hand, interact with it.

When a magnetic field $\mathbf{B}$ is applied to a $I = \frac{1}{2}$ spin nucleus, the Zeeman effect [40] occurs. The Zeeman effect produces a splitting of the nuclear energy levels into two non-degenerate levels, $m = -\frac{1}{2}$ and $m = \frac{1}{2}$. Such levels correspond to a state with the spin aligned with the magnetic field (lower energy $E_-$) and to a state with the spin directed opposite to it (higher energy $E_+$). The splitting is proportional to the strength of the magnetic field, $\Delta E_L = E_+ - E_- = \hbar\gamma B$ [40], where $\gamma$ is the gyromagnetic ratio of the isotope, dependent on the nucleus type. The frequency $\nu_L = \Delta E_L/\hbar$ is called Larmor frequency. It is the frequency at which spins precess around $\mathbf{B}$.

As long as $\mathbf{B}$ is applied and we wait for long enough, the system goes from random orientations of the nuclear spins to all spins oriented along $\mathbf{B}$, though with different phase factors. If now a radio frequency (RF) electromagnetic pulse is applied in a direction perpendicular to the spins, it will perturb them perpendicularly to $\mathbf{B}$, and this perturbation allows transition from states $-\frac{1}{2} \leftrightarrow \frac{1}{2}$ to be observed if the frequency $\nu$ of the oscillating pulse matches the Larmor frequency $\nu_L$, creating resonance with the nuclear transition. Such transition is called central transition, and is dependent on (i) the type of isotope, through the factor $\gamma$ and (ii) its chemical environment, namely, the effect of the screening on the magnetic field caused by the electrons around the probe nucleus. The higher the screening effect, the lower the Larmor frequency of the nuclear transition.

When the RF pulse is turned off, the spins undergo relaxation to their equilibrium state, which is with the spins oriented towards the $\mathbf{B}$ field. There are two types or relaxation: spin-lattice relaxation and spin-spin relaxation. The latter mechanism is the time needed for the spins to create decoherence between the spins' phases so that the equilibrium condition with the presence of $\mathbf{B}$ is recreated. The time needed for this type of relaxation to occur is usually called $T_2$.

**Nuclear quadrupole transitions**

Any atomic nucleus having more than one unpaired nucleon, that is having $I \geq 1$, in addition to its magnetic moment has an electric *quadrupole* moment. The electric quadrupole moment is the result of a non-spherical charge distribution within the nucleus, and it can couple with the electric field provided by the electrons. If such field has a non-symmetrical spatial distribution, it exerts a force on the nuclear quadrupole. Hence, the quadrupole can couple to an electric field which changes from a point in space to another in the proximity of the nucleus. Such field change is called electric field gradient (EFG). Being the gradient of a vector, mathematically it is a $3 \times 3$ tensor.

In the absence of an applied magnetic field, and taking $I = \frac{3}{2}$ as an example, the nuclear energy levels corresponding to states $m = \pm\frac{1}{2}$ are degenerate, as are states $m = \pm\frac{3}{2}$, and the two couples of levels are separated by an energy difference corresponding to the quadrupole energy $\Delta E_Q = E_{m=3/2} - E_{m=1/2} = e^2Qq/2$, where $e$ is the elementary electric charge, $Q$ is the quadrupole moment of the nucleus (its values are tabulated for many isotopes [40]) and $q$ is an isotropic EFG applied to the nucleus. Hence, nuclear quadrupolar transitions can be observed at frequencies $\Delta E_Q/\hbar$, which are proportional to the EFG that valence electrons provide to the nucleus.

As in the case $I = \frac{1}{2}$, also for nuclei with $I \geq 1$ the application of an external magnetic moment produces an energy shift of the quadrupole nuclear levels and a splitting of their degeneracies. For example, in $^{47}$Ti ($I = \frac{5}{2}$), there are six nuclear states $m = \frac{5}{2}, \frac{3}{2}, \frac{1}{2}, -\frac{1}{2}, -\frac{3}{2}, -\frac{5}{2}$. The presence of a magnetic field makes them all non-degenerate. In the hypothesis of only $\Delta m = \pm 1$ allowed transitions, there can happen the following transitions: $\frac{5}{2} \leftrightarrow \frac{3}{2}$, $\frac{3}{2} \leftrightarrow \frac{1}{2}$, $\frac{1}{2} \leftrightarrow -\frac{1}{2}$, $-\frac{1}{2} \leftrightarrow -\frac{3}{2}$, $-\frac{3}{2} \leftrightarrow -\frac{5}{2}$. The transition $\frac{1}{2} \leftrightarrow -\frac{1}{2}$ is the central transition, and the others are called satellite transitions.

It is important to note that, while the central transition is possible even for nuclei with no quadrupoles, *the satellite transitions are only possible if there is quadrupole-EFG coupling.* Such coupling, in turn, is made effective by the presence of an EFG $q$, which is produced by

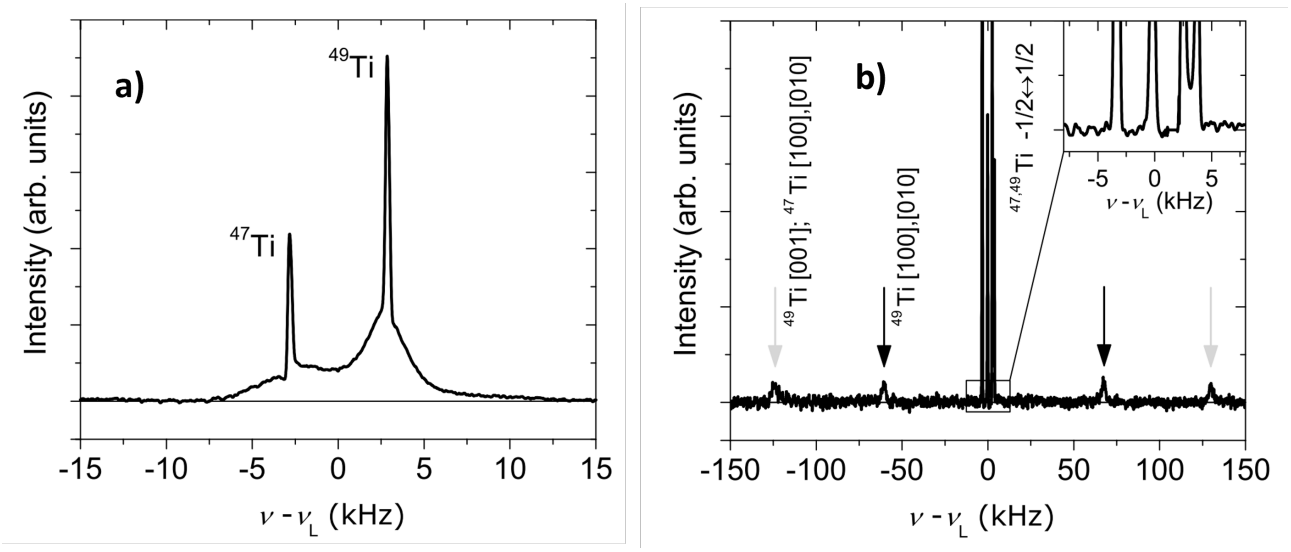



Figure 6.12: NMR spectra of $BaTiO_3$ from Zalar, Laguta and Blinc [150], with $\mathbf{B}||[001]$. a) C phase, with the central transitions of $^{47}$Ti and $^{49}$Ti sitting on a broad background. b) T phase, with well-resolved satellite peaks. The black arrows indicate $^{49}$Ti transitions in [100] or [010] domains, while the grey arrows indicate $^{47}$Ti transitions in [100] or [010] domains or $^{49}$Ti transitions in [001] ferroelectric domains [150]. The presence of a broad background in plot (a) indicates that the Ti atom is locally off-centered.

the electrons only if the nucleus sits in a position of non-cubic symmetry. If the nucleus sits on a site of symmetry $O_h$, then an EFG is impossible, by symmetry, and nuclear quadrupolar transitions are not expected. Hence, the presence of satellite peaks in the NMR spectra of the Ti atoms can reveal whether or not the Ti sits on the body center of the nominal perovskite structure.

Let us look at Fig. 6.12. It shows the NMR spectrum of the $^{47}$Ti ($I = \frac{5}{2}$) and $^{49}$Ti ($I = \frac{7}{2}$) in a $BaTiO_3$ single crystal, taken from the work of Zalar, Laguta and Blinc [150], at $T > T_C$ (C phase, left plot, a) and $T < T_C$ (T phase, right plot, b). These two isotopes are not abundant in nature (7.3% abundance the first and 5.5 % the latter), but when many NMR scans are collected, the signal is clearly visible. The intensity of the signal is plotted against the frequency shift from the Larmor frequency, $\nu - \nu_L$. In the presence of a 9.2 T magnetic field, the theoretical Larmor frequency of the two isotopes is nearly identical, and equal to 21.42 MHz [150], but the little difference in the gyromagnetic ratios of the two isotopes make their magnetic moments slightly different, and the $m = \pm\frac{1}{2}$ nuclear levels of $^{47}$Ti and $^{49}$Ti shift downwards and upwards in frequency, respectively. So, the $^{47}$Ti central transition is at $\approx -2.6$

kHz, and the $^{49}$Ti central transition is at $\approx 3.1$ kHz with respect to $\nu_L$; their difference is 5.7 kHz [150]. This difference is appreciable both in the C-phase spectrum of Fig. 6.12a and in the inset of the T-phase spectrum in Fig. 6.12b. The presence of four peaks in the inset of spectrum b) and of the other peaks is caused by ferroelectric domains oriented differently from the ferroelectric axis [001], denoted [100]-[010] in the figure [150].

It is important to recognize the difference between Figs. 6.12a and b. In the T phase (Fig. 6.12b), the spectrum is composed of sharp lines corresponding to different central and satellite transitions. In Fig. 6.12a, on the other hand, the two central lines sit on a broad background. This broad background has been interpreted by Zalar, Laguta and Blinc as the result of nuclear quadropolar transitions $\Delta m = \pm 1$. In other words, the sharp satellite peaks of the T phase "condense" in the C phase in the broad background visible in Fig. 6.12a. Now, satellite peaks *are not expected* in the nominal C perovskite structure, as the Ti sits on a highly symmetrical position, and no EFG is expected. The only reason for the presence of satellite quadrupolar peaks, then, the authors have claimed, is that the C phase of $BaTiO_3$ is disordered, in the sense that the Ti is not placed at the center of the cell.

And where is the Ti placed then? The authors proceeded with obtaining the angular dependence of the satellite peaks (this calculation was previously done in Ref. [**?**]): the C crystal was rotated so that one of its crystallographic axis $a$ would make an angle $\theta$ with the magnetic field. By changing the angle between the field and the crystal's axis, information was extracted on the symmetry of the EFG tensor. In fact, tetragonal symmetry would result in a diagonal EFG tensor, orthorhombic symmetry would make two off-diagonal components non-zero, and rhombohedral symmetry would make all off-diagonal components of the EFG tensor non-zero. As a result of this, the principal axis of the EFG, namely the direction of the maximum eigenvalue of the EFG tensor, in the T symmetry would be parallel to a cube edge along one of the C crystal's axis $\langle 100 \rangle$. In the R symmetry, the principal axis would be parallel to the body diagonal along a $\langle 111 \rangle$ direction. In order to infer the type of symmetry of the EFG, Zalar, Laguta and Blinc fitted the observed angular dependence of the NMR spectra to a theoretical model, and found the best agreement with a *tetragonal distortion* (cf. Fig. 3 of Ref. [150]).

Hence, NMR would indicate that the Ti atoms are off-centered and tetragonally displaced. This is in disagreement with XAFS and the eight-site model, which predict a displacement of the Ti along the body diagonal. The authors of the NMR study proposed that the presence of a tetragonal distortion is to be attributed to a displacive component of the phase transition: the fact that Ti are off-centered is an indication of an order-disorder transition, but the fact that they have four preferential sites among the eight available is an indication of a rigid displacement of the Ti atom, hence of a displacive transition. So, both character coexist above $T_C$, Zalar, Laguta and Blinc have claimed [150]. Below $T_C$, the T distortion becomes static, and the EFG increases by a factor of 100 [150].

### 6.5.1 Summary of experimental results for local probes: NMR vs XAFS

It seems necessary to compare XAFS and NMR results. Let us first recall that both methods probed the local environments around the Ti, and that both found that the Ti does not sit at the body center of the nominal cubic cell in the T and C phases. This agreement among local probes strongly suggests that the phases of $BaTiO_3$ are indeed disordered.

At the same time, we cannot neglect that there is a disagreement between XAFS and NMR. In the paraelectric phase, according to the XAFS experiments, in fact, the Ti distortions are *quasi-rhombohedral* (cf. Sec. 6.4), while according to NMR the local distortions are *tetragonal* (cf. Sec. 6.5). If we consider the additional complication that diffraction experiments observe a cubic phase [125], it seems that all the experiments disagree with each other.

This issue prompted Stern, one of the main authors of the XAFS measurements, to write a comment on these two experimental techniques and on the origin of their disagreement, in Ref. [125]. He warned that it is important to bear in mind, when assessing different experimental techniques, the typical time-scales of the experiments.

NMR's spin-spin relaxational time $T_2$, which is the time needed by the nuclear spins to relax to their equilibrium distribution after the radio-frequency pulse is turned off [40], was measured to

200 $\mu$s for $BaTiO_3$ by Zalar, Laguta and Blinc [150]. This means that the nuclear quadrupolar transitions revealed by NMR happen on a time scale of $T_2$, corresponding to a frequency of $\nu_{\mathrm{NMR}} = 1/T_2 \sim 10^8$ Hz. Hence, NMR produces results which are averaged over a time scale of $10^{-8}$ s = 10 ns.

The typical time scale of X-rays, on the other hand, is much smaller. XAFS, in fact, occurs at time scales typical of a photoelectron which is dislodged from core levels. The fluctuations of the absorption coefficient it creates happen at energies of the order of keV, and hence has the characteristic time in the order of $\sim$ fs [125]. Atoms are almost immobile in a fs, unless $T$ is insanely high (but in this case the crystal would probably have melted). X-ray diffraction in principle is fast, but it only probes average crystalline structures, and hence does not provide information on the local structures.

The importance of the experimental time scales is evident: if any dynamical or structural change is happening in the crystal, the time scale of the measurement must be smaller than the time scale in which the change happens. Almost no spectroscopic technique is as fast as XAFS, and so it seems natural to give credibility to it, and be in favor of the interpretation that the local distortions in $BaTiO_3$ are rhombohedral. A question remains: why does NMR find a tetragonal distortion? One possible explanation is this. If we suppose average the atomic vibrations on a small time scale, we may find, with high probability, the Ti atom away from the center of the cell. In the T phase with tetragonal axis $c$ || [001], the Ti can hop to any of the four minima which are placed at the positive values of $z$. Hence, the hopping motion happens on the $aa$ crystallographic plane, which is the $xy$ plane. When $T$ is higher but not too far from $T_C$, the time scale of the atomic hopping in the previously ferroelectric $c$ direction might be longer than the time scale of the hopping in the $a$ direction. In other words, the frequency at which hops along $z$ happen might be $\nu_{\mathrm{hop}||c} < \nu_{\mathrm{NMR}}$, and the frequency of atomic hopping in the $xy$ plane might be $\nu_{\mathrm{hop}||a} \gg \nu_{\mathrm{NMR}}$. If this is the case, then the EFG experienced by the Ti isotopes, which is time averaged over the time scale of the experiment, would have tetragonal symmetry. For this reason, NMR would find tetragonal distortion [125].

One of the possible reasons for this asymmetry of the hopping time scales stems from the

property of ferroelasticity and from an understanding of what happens to a macroscopic crystal as it is heated up. When the crystal is passing from a T to a C phase, tetragonally polarized clusters of atoms persist in the C phase within a temperature range after $T_C$ [74]. Such clusters remain stable until thermal disorder is high enough to make them shrink completely. This is one of the consequences of ferroelaticity: among the factors that stabilize these clusters is that the tetragonal strain field persist when $T$ is higher but not much higher than $T_C$. Such strain field makes it harder for the Ti atom to hop along the $z$ direction, because an additional amount of elastic energy is needed to reverse the strain. This may favor the presence of tetragonally polarized clusters within the C phase, when the material is heated up. This may explain why NMR, which is relatively slow with respect to atomic fluctuations and which was performed at $T = T_C + 35$ K by Zalar, Laguta and Blinc [150], found tetragonal distortions. This explanation, or rather this suspicion, is strengthened by the observation that *all NMR spectra were obtained upon heating* [150]. It would be very instructive, and relatively easy, to repeat the experiment, but this time *on cooling* and with the crystal heated up to much more than $T_C \approx 450$ K. Note that, even on cooling, at some point of the hysteresis loop, the crystal has to choose a T distortion (along [001] or along $[00\bar{1}]$), and that might reveal a tetragonal distortion again, but there should be a certain $T$ which is far away enough from $T_C$ so that the R distortion can be seen, and not too high so as to avoid high thermal fluctuations which may mask the Ti hopping motion.

The above explanation is even more credible if we consider the also XAFS found that, in the C phase, the Ti distortions are not exactly in a $\langle 111 \rangle$ direction, but are skewed towards one of the cubic $\langle 100 \rangle$ axis by $\approx 12°$. This is the reason why I called them *quasi*-rhombohedral distortions. The fact that the Ti displacement is slightly directed to one $\langle 100 \rangle$ direction as revealed by XAFS is another argument in favour of a slight tetragonal distortion which should be caused by the tetragonal strain field which the C phase inherits from the T phase. This issue of the Ti being slightly misoriented with respect to the cube diagonals was addressed in better details by, among the others, Fallon, and, as I said, goes by the name of re-orientation of the minima [43].

In summary, both NMR and XAFS confirmed that the Ti atoms are off-centered, with the

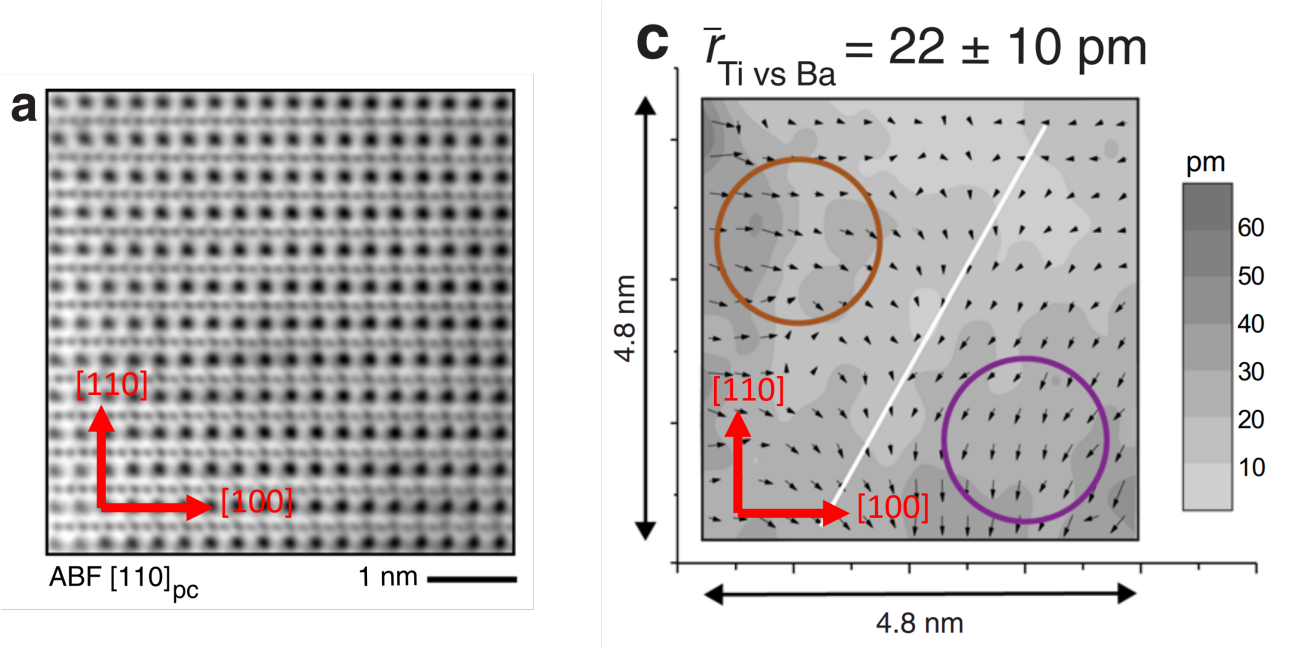



Figure 6.13: Scanning transmission electron microscopy (STEM) of a single-crystal domain within a polycrystalline sample of $BaTiO_3$ from Bencan *et al.* [9]. The left hand side shows the STEM image, and the right hand side shows the Ti vs Ba displacements according to the analysis of the authors.

difference that NMR found tetragonal distortions while XAFS found quasi-rhombohedral distortions, and the discrepancy between the two might be caused by the longer time scale of NMR.

## 6.6 Electron microscopy

Microscopy is probably the most immediate experiment one can think of when the structure at the nanoscale is unknown. In 2021, Bencan *et al.* [9] performed scanning transmission electron microscopy (STEM) to obtain images of $BaTiO_3$ in its C phase. The advances in this type of technique allow to have a resolution in space so high as to be able to see the single atoms. If the space resolution has had a great deal of improvements, the time resolution has not, unfortunately. The supplemental information of Ref. [9], in fact, shows that, at best, the shutter speed for the image acquisition was 1.6 $\mu$s. This is at least six order of magnitudes greater than the time scale of the atomic motion. Hence, the images that the authors provided are not an instantaneous picture of the atoms in $BaTiO_3$, but a time-averaged one. For this

reason, one can probably have little confidence that these pictures can reveal whether or not the C phase of $BaTiO_3$ is disordered. Nonetheless, we shall briefly discuss the STEM results, as they reveal an interesting feature.

The STEM pictures of C $BaTiO_3$ are displayed in Fig. 6.13. The left hand side shows the image of a (110) plane in the cubic phase of $BaTiO_3$ at 473 K (this sample had $T_C = 403$ K), with the Ba atoms appearing as the darkests and largests spots, the O atoms right above them and the Ti atoms in between oxygens. The right hand side shows the analysis of Ti vs Ba displacements calculated by Bencan *et al.* The authors suggested that the areas indicated by brown and purple circles are a clear signature of the presence of polar nanoclusters in the PE phase. Unfortunately, the plane chosen by the authors is a (110) plane, and makes it harder to infer information about polarizations on the {100} planes, which are the planes on which the linear chains predicted by Comes, Lambert and Guinier lie. The fact that Ti vs Ba displacements align in *regions* of a handful of unit cells suggests that mechanisms by which polar nanoclusters can form exist.

The authors suggested that one of the possible mechanisms is the presence of defects, which create differently oriented strain fields. This spatially-varying strain field can polarize portions of the material, which is ferroelastic, thereby creating polar ferroelectric nanoclusters whose polarization can be permanent, or having a lifetime greater than $\sim \mu$s.

## 6.7 Summary of experimental literature

Let us briefly summarize, in bullet points, the experimental literature we have seen in this chapter.

IR and THz spectroscopy revealed:

- the presence of a central peak, whose interpretation is that of a Debye mode [62, 82];
- this peak *emerges* progressively as the Slater mode softens *partially*, in doing so overlaps with the Last mode, shrinks and then slowly drowns in the T-C transition [62];

- some authors have claimed that the Slater mode shows up as a small bump somewhere in the low-frequency region [100];
- the Debye mode is ascribed to the inter-well hopping motion of the Ti atom against the O cage [62].

X-ray diffuse scattering revealed that:

- the higher-symmetry O-T-C phases are characterized by anomalous diffuse sheets [25, 26, 64, 57, 66, 94];
- these diffuse sheets are either caused by disorder on crystallographic planes (Comes, Lambert and Guinier's interpretation with the eight-site model [25]) or by a soft mode (Hüller's interpretation [66, 94]);
- the intensity of the diffuse streaks decreases progressively until zero when pressure is increased [103].

Neutron scattering revealed that:

- the line shape of the soft TO mode at $\Gamma$ in $SrTiO_3$ is underdamped at $T \gg T_C$, it softens according to Cochran's law as $T \to T_C$, and dampens during the softening, but it never becomes overdamped [147, 120];
- the line shape of the Slater TO mode in $BaTiO_3$ behaves much differently: it stands at lower frequencies with respect to the TA [119], and it is widespread and non dispersive along $\Gamma - X$ [148, 118, 56];
- the integrated intensity of the TO, or critical scattering, is not higher than the integrated intensity of the TA, as we would expect if the TO was a perfect phonon mode [119, 148];

NMR and XAFS revealed that:

- in the paraelectric phase the Ti atom is locally displaced from the body center of the cell, suggesting this phase is disordered [150, 102, 126, 125];

- the Ti distortion is quasi-rhombohedral according to XAFS [102], and tetragonal according to NMR [150], but the disagreement should be caused by NMR's typical time scale being longer than the hopping frequency of the atoms in non-ferroelectric directions [125].

Electron microscopy revealed that:

- polar nanoregions can form permanently as a result of the presence of defects, which create a strain field which varies from point to point in space [9].

In the next table, I summarize these results, and indicate whether they are a sign of displacive or order-disorder phase transitions. The black crosses 'X' indicate the interpretation of the authors, and the red crosses 'X' indicate my personal interpretation of the experimental results. Although I have not discussed Raman spectroscopy in this chapter, I have included the highlights from some important Raman papers, in case the reader were interested in them.

| | paper | year | highlights | disp. | o-d |
|---|---|---|---|---|---|
| IR | Luspin *et al.* [82] | 1980 | hardening of Debye mode in the C phase | X | X |
| | Hlinka *et al.* [62] | 2008 | partial softening and shrinking of the Slater mode in the T phase, and consequent emergence of Debye mode | X | X X |
| | Ponomareva *et al.* [100] | 2008 | alleged presence of a shallow Slater peak within the Debye mode | X | X X |
| | Sanjuro, Katiyar and Porto [107] | 1980 | model of coupled polar phonons | | |
| Raman | Di Domenico *et al.* [36] | 1968 | presence of a central peak in the T phase<br>presence of broad bands at $\approx$ 250 cm$^{-1}$ and 520 cm$^{-1}$<br>failure of the Lyddane-Sachs-Teller relation (see Sec. 8.1) | X | X |
| | Scalabrin *et al.* [110] | 1977 | presence of a central peak in the T phase<br>disappearance of the 250 cm$^{-1}$ and 520 cm$^{-1}$ bands upon perfect alignment of the laser to the crystal's crystallographic axis<br>failure of the Lyddane-Sachs-Teller relation indicates disorder (see Sec. 8.1) | X | X X |
| | Fontana and Lambert [45] | 1972 | presence of 250 cm$^{-1}$ and 520 cm$^{-1}$ bands even in the Raman-inactive C phase | | X X |
| | Quittet and Lambert [101] | 1973 | ” | | X X |
| | Bencan *et al.* [9] | 2021 | $T$-evolution of the FE peaks in the R-T-C phases | | X X |
| | Vogt, Sanjuro and Rossbroich [140] | 1982 | hyper-Raman, highly resolved spectrum of the central peak | X | |
| | Perry and Hall [98] | 1965 | early $T$-dependence of Raman spectrum | | |

| | paper | year | highlights | disp. | o-d |
|---|---|---|---|---|---|
| IXS | Comes, Lambert and Guinier [25] | 1968 | X-ray evidence of diffuse streaks<br>first proposal of eight-site model and of uncorrelated linear chains | | X X |
| | Hüller [66] | 1969 | rejection of eight-site model and explanation of the diffuse streaks with a highly anisotropic soft mode | X | |
| | Pasciak *et al.* [94] | 2018 | recent X-ray diffuse scattering experiment of the group of Hlinka<br>interpretation of the diffuse streaks as a soft mode | X | X |
| | Harada and Honjo [57] | 1966 | early X-ray diffuse scattering experiment<br>streaks interpreted as result of a soft mode | X | X |
| | Ravy *et al.* [103] | 2007 | pressure dependence of the X-ray diffuse streaks<br>disappearance of the diffuse streaks at high pressure (C phase) | | X X |

| | paper | year | highlights | disp. | o-d |
|---|---|---|---|---|---|
| INS | Shirane *et al.* [119] | 1967 | the Slater TO mode in the C phase lies below the TA | | X X |
| | Yamada, Shirane and Litz [148] | 1969 | the Slater TO mode in the C phase has a very weak intensity<br>the Slater TO intensity grows as $T \to T_C$<br>the integrated cross-section creates the diffuse streaks as in X-ray scattering | X | X X |
| | Shirane *et al.* [118] | 1970 | the undamped Slater TO frequencies are very anisotropic<br>Slater TO dispersion drawn below the TA branch along $\Gamma - X$ and above it along $\Gamma - M$<br>X-ray diffuse streaks are caused by the anisotropy of the Slater TO mode | X | |
| | Harada, Axe and Shirane [56] | 1971 | the Slater TO peak in the C phase is overdamped<br>a TO central peak is found in the [100] and [110] directions of the BZ<br>asymmetry of the TA | X | X X |
| | Herlihy *et al.* [59] | 2022 | $P$-dependence of the PCF from INS<br>rhombohedral symmetry at all $T$s<br>recovery of harmonic behaviour at high pressure | | X X |
| | Senn *et al.* [112] | 2016 | $T$-dependence of the PCF from INS<br>presence of local rhombohedral Slater-like distortion at all $T$s<br>such distortions correlate *linearly* in real space to produce the X-ray diffuse streaks<br>a spin-Hamiltonian with spin correlations can describe the X-ray diffuse streaks | | X X |

| | paper | year | highlights | disp. | o-d |
|---|---|---|---|---|---|
| NMR | Zalar, Laguta and Blinc [150] | 2003 | Ti has tetragonal distortion in the C phase | | X X |
| XAFS | Stern and Yacoby [126] | 1996 | $PbTiO_3$ and $KTaO_3$:9%Nb are disordered | | X X |
| | Ravel *et al.* [102] | 1998 | Ti has quasi-rhombohedral distortion in the T phase<br>re-orientation of the minima: Ti is displaced 12° closer to the *c* axis | X X | X X |
| | Stern [125] | 2004 | comments on NMR vs XAFS<br>the time scale of NMR is larger than the time scale of XAFS<br>hence NMR averages *aa* plane Ti fluctuations and gives a T distortion<br>XAFS gives the correct instantaneous and local distortion<br>displacive component coming from the 12° re-orientation of Ti distortion | X X | X X |

**Open questions**

The experimental interpretations of the dynamics of $BaTiO_3$ were not free from afterthoughts and retractions. For example, the work of Hlinka *et al.* [62], which combined THz and IR spectroscopy, appeared to have solved the dispute in 2008: the Debye peak arises when approaching the phase transition from below and it is not a softening mode. The peculiar behaviour of the Slater mode and the presence of a Debye mode was claimed to be a clear signature of both a displacive *and* order-disorder phase transition [62]. The order-disorder component was ascribed to the atomic inter-well hopping of Ti between minima of the energy landscape–the Debye mode–[62], but it is not clear what the displacive component should be attributed to, since there are no traces of proper soft modes.

Moreover, the group of Hlinka has recently proposed, in the 2018 work of Pasciak *et al.* which focused on X-ray diffuse scattering, that a (very anharmonic) soft mode would describe the presence of diffuse sheets [94]. So, some of the authors who accepted disorder after IR spectroscopy changed their minds and later leaned towards a totally displacive character of the transition.

Even Comes, the very author who first proposed the eight-site model and the Ti-hopping mechanism forming uncorrelated linear chains, changed his mind in later works, especially after performing neutron scattering [28, 125]. The main reason for this is in the apparent inability of the disordered model to explain the enormous increase of the static dielectric constant during the FE-FE and FE-PE transitions, which follows a Curie-Weiss law. The dislacive model, on the other hand, is able to explain such increase by means of the Lyddane-Sachs-Teller relation because, when one mode's frequency softens completely, the static dielectric constant diverges. We will see in Sec. 8.1 that the eight-site model and the presence of uncorrelated linear chains is perfectly compatible with a high value of the static dielectric constant.

It is surprising that still to this day there is a lack of agreement on whether or not the central peak of $BaTiO_3$ is a Debye mode or a soft mode, and that a definitive theoretical understanding of it is still missing. Hence, an accurate and definitive microscopic understanding of the phase transitions at the atomic level is still of great scientific value for $BaTiO_3$, and could naturally be extended to other perovskites, such as $PbTiO_3$ and $KNbO_3$, which show similar experimental behaviours [64].

Is the central mode a soft phonon or a proper Debye mode? Are the diffuse sheets an indication of disorder or of a soft and highly anisotropic mode? Does the Slater mode melt in $(\omega,\boldsymbol{k})$-space, or it is dispersive across high-symmetry paths in the BZ? Can a computational model tell us if the Ti are off-centered or not, on a small time scale? Can MD confirm/rule out the possibility of uncorrelated linear chains? It is these questions that we will address in the next chapter.

# Chapter 7

# Sudden melting of the transverse optical Slater phonon in $BaTiO_3$

## 7.1 Scope of the chapter

We left the last chapter with some open questions, which the experimental literature left unanswered.

One of the sources of confusion about the lattice dynamics of $BaTiO_3$ arises from intrinsic differences in what different experimental techniques measure. Experiments like XAFS, NMR and electron microscopy probe aspects of the local structure, such as the off-center displacements of Ti atoms and their chemical environments. Probes of local structure agree that the titanium is found with high probability off the body center of the nominal perovskite structure in all phases [150, 102, 126, 125], giving credibility to the eight-site model of Comes, Lambert and Guinier and suggesting an order-disorder transition. Spectroscopy, on the other hand, be it IR, Raman, Brillouin [74, 44], or neutron/X-ray scattering, is only able to probe collective excitations (phonons) and structures averaged over time and space; hence it provides the macroscopic picture, but not the local one. For this reason, and because of the success of Cochran's theory of the soft mode for other ferroelectrics like $SrTiO_3$ [**?**], all or most of the early [82, 36, 56, 119] and recent [94] spectroscopic efforts on $BaTiO_3$ supported the displacive picture, or at best a

combination of both components [62].

However, the two theories with which phase transitions are understood, namely the displacive and the order-disorder theories, might not be distinguishable in a macroscopic sense. As we have seen in Sec. 5.3.3, in fact, the displacive picture is a thermodynamic perspective, whereby the mechanism that drives the phase transition is understood in terms of the free energy surface (FES). The order-disorder picture, on the other hand, describes local dynamics and energetics, and the mechanism that drives the phase transition is understood in terms of the potential energy surface (PES) of each atom, dipole moment, or primitive unit cell. In an order-disorder phase transition, the unit cells are *locally* distorted, but the *spatial average* can be of a high symmetry phase. Hence, on a spatial average, the displacive and order-disorder mechanisms may be confused. It is hard to understand the microscopic picture if only the macroscopic one is known. At the same time, it is difficult to infer the macroscopic structure of the phase if only the microscopic one is known.

Classical MD simulations are not limited by these constraints, other than the small time- and length- scales that can be simulated. They are limited to providing relatively-local information, because the computational cost of MD restricts the size of the supercell which can be simulated. However, ergodicity allows to use time averages to infer thermodynamical and macrostructural information. Therefore, they are an invaluable tool for understanding both local structure and dynamics *and* macroscopic structure and thermodynamics. The local (and/or instantaneous) dynamics can be easily investigated once atomic trajectories are computed with MD, while the vibrational spectrum, which characterizes the collective dynamics (phonons), can be calculated by Fourier transforming the velocity-velocity correlation function (FT-VVCF). I showed in Chapter 3 that accurate polarizable-ion force fields, together with the calculation of the FT-VVCF, are capable of describing the thermal broadening and frequency shift of the phonon dispersion in MgO. I did so through the calculation of the ($\omega$,$\boldsymbol{k}$)-resolved distribution of the vibrational energy, $\tilde{\mathcal{E}}(\omega, \mathbf{k})$, whose formal definition is in Sec. 2.6. In this chapter, we will see a similar calculation for $BaTiO_3$.

It is clear from the previous chapter that $BaTiO_3$ is a very anharmonic material. Since velocities

are calculated with MD, the FT-VVCF approach is non-perturbative, and therefore not limited in applicability to low $T$ or small amplitudes of vibrations. It contains all anharmonic terms, unlike perturbation theory. Moreover, MD is by no means limited by the degree to which a material is ordered or disordered. Hence, the FT-VVCF can be used even for disordered phases, like the PE phase of $BaTiO_3$ is deemed to be. We shall see in the course of this chapter that the PE phase of $BaTiO_3$ is characterized by an anomalous phonon power spectrum, which is perfectly compatible with the presence of disordered uncorrelated linear chains.

### 7.1.1 Overview of this chapter

This chapter is organized as follows.

Simulation details are presented in Sec. 7.2, and the phases which I can simulate and the sources of inaccuracy of the force field are discussed in Sec. 7.3.

An overview of the results sections is outlined in Sec. 7.4. In brief, I present the simulated IR spectra in Sec. 7.5, the simulated X-ray diffuse scattering in Sec. 7.6, and I show how the distribution of vibrational energy manifests the melting of the Slater TO mode, which may be my most important result, in Sec. 7.7. The real spacetime picture of the dynamics, that completes the understanding, is then presented in Sec. 7.8.

I use Sec. 7.9 to discuss what I mean by phonon melting, and Sec. 7.10 to discuss the mechanism of the phase transitions which stems from the model. I conclude with final remarks in Sec. 7.11.

## 7.2 Simulation details

### 7.2.1 Force field

The atomistic force field used in this work has the same mathematical form as the one I used for MgO: it is a classical polarizable-ion potential of the form quoted in Sec. 2.11. Its parameters

were fitted to DFT data collected for all phases of $BaTiO_3$, as described in Ref. [43], where the reader can find a useful discussion on the fitting technique. The force field parameters are quoted in appendix B. The accuracy of the force field is discussed in the Sec. 7.3.

### 7.2.2 Molecular Dynamics

My supercell was a 10×10×10 repetition of the 5-atom primitive unit cell of $BaTiO_3$, and simulations were performed under periodic boundary conditions.

The structure from which I began was the structure at mechanical equilibrium ($T \to 0, P \to 0$). It was obtained by relaxing the atomic positions and the supercell's vectors. The relaxed structure is rhombohedral ($R3m$). The length of the primitive lattice vectors is $a \approx 4.004$ Å, and the angles between them are $\alpha = 89.69°$. They compare well with experiment ($a = 4.001$ Å, $\alpha = 89.87°$ [43, 60]), and with DFT calculations ($a = 3.921$ Å, $\alpha = 89.99°$ [43]).

I performed one 10 ps MD simulation in the NVT ensemble, to equilibrate the temperature. The production runs can be subdivided into two sets of simulations, one in the NPT and one in the NVT ensemble. The NPT simulations were the primary source of my analysis, but I decided to complement them with constant-$V$ simulations in order to exclude the possibility that my physical results were spurious artifacts of the barostat.

In all simulations, the temperature was kept constant by means of a Nosé-Hoover thermostat (described in Sec. 2.10.1) whose frequency was set to 10 THz, which is roughly half of the highest phonon frequency. The pressure was kept constant by means of a Parrinello-Rahman barostat (described in Sec. 2.10.2), whose mass has been set to 100 times the mass of one unit cell. Such a big value of the barostat's mass guaranteed that the maximum frequency of the cell fluctuations is 0.5 THz smaller than the lowest LA phonon frequency. I will discuss the problem of tuning of the barostat's mass and its effect on the MD trajectories in Sec. 7.5.

In all runs, I used a timestep of $\approx 0.7257$ fs and simulated for $\approx 500$ ps. Out of the 500 ps, I excluded the first $\approx 100$ ps in the NPT simulations to guarantee equilibration of the volume, and used the remaining 400 ps for the analysis. The atomic positions were saved for analysis

every 20 time steps, and the velocities were approximated from the finite differences of the positions of two successive snapshots.

The first set of simulations, in the NPT ensemble, allowed the energy $E(t)$ and the volume $V(t)$ to fluctuate in time so as to simulate a coupling with a bath at fixed temperature $T$ and pressure $P$. I simulated at $T = 50, 100, 125, 150, 200, 250, 300$ K, and the pressure was set to zero in all runs ($P = 0$). The second set of simulations, in the NVT ensemble, were run at the same temperatures as the NPT ones, and at the average volumes $V = \langle V(t) \rangle_t$ of the NPT simulations. This was done so as to have constant volume simulations at the volumes predicted by the force field, and to disentangle and evaluate the effect of the barostat on the MD trajectories.

### 7.2.3 Calculation details

#### IR spectra

The simulated IR spectra were calculated from Eq. 2.61. To compute the supercell's total dipole moment, I first computed the dipole moments in each unit cell as $\boldsymbol{p}_l(t) = \sum_{i=1}^{n_a} q_i \boldsymbol{r}_i(t) + \boldsymbol{d}_i(t)$, where $n_a$ is the number of atoms in each cell, the first term denotes the rigid-ion contribution, and the second term the electronic contribution, which the force field calculates as described in Sec. 2.11. Then, I summed the dipole moments of all unit cells to obtain $\boldsymbol{M}(t) = \sum_{l=1}^{N_c} \boldsymbol{p}_l(t)$. The values of $V$ and $T$ in Eq. 2.61 are the average volumes and temperatures of the simulations, $V = \langle V_{\mathrm{NPT}}(t) \rangle_t$ and $T = \langle \mathcal{T}(t) \rangle_t$. The Fourier transform of the dipole moments' correlation function appearing in the equation was computed using the convolution theorem [1]. The spectra were convolved with Gaussians of standard deviation $\sigma = 0.1$ THz to reduce the inevitable MD noise.

### Diffuse scattering

For the simulated diffuse scattering, I performed two calculations: one in the harmonic approximation (HA), and one from MD.

For the harmonic calculation, I used Eqs. 2.58-2.57. The calculation was performed on a regular grid of commensurate points. Commensurate points means that, because the supercell is a $10 \times 10 \times 10$ repetition of one unit cell, the $\boldsymbol{k}$-points are defined by the regular grid $\boldsymbol{k} = h\boldsymbol{b_1} + k\boldsymbol{b_2} + l\boldsymbol{b_3}$, where $h$, $k$ and $l$ are integer multiples of $\frac{1}{10}$, and the $\boldsymbol{b}_i$'s are the reciprocal lattice vectors, obtained for the system at mechanical equilibrium ($T \to 0, P \to 0$). The phonon frequencies and eigenvectors were computed from this equilibrium structure, which was obtained after relaxation and is rhombohedral. I used values of the atomic scattering lengths equal to 5.07 fm, 3.438 fm and 5.8 fm for the Ba, Ti, and O atoms, respectively. I did not use atomic form factors, which are relevant if X-ray scattering is to be simulated, hence the present calculation simulates a neutron diffuse scattering experiment.

For the MD calculation, I chose again $\boldsymbol{k}$-points commensurate with the MD $10\times10\times10$ supercell, as in the case of the HA calculation. Because the supercell's shape changes with $T$, however, the reciprocal lattice vectors $\boldsymbol{b}_1$, $\boldsymbol{b}_2$ and $\boldsymbol{b}_3$ are calculated from the average unit cell vectors of the NPT simulation. In other words, the MD unit cell vectors $\mathbf{a}_i(t)$ fluctuate at each run, and they vary from simulation to simulation because the supercell shape changes with $T$. Hence, also the reciprocal space vectors change. I decided to use the average cell vectors $\langle \mathbf{a}_i \rangle$ to get the $\boldsymbol{b}_i$'s. This means that $\boldsymbol{b}_1$ was calculated through the formula $\boldsymbol{b}_1 = 2\pi \langle \mathbf{a}_2 \rangle \times \langle \mathbf{a}_3 \rangle / (\langle \mathbf{a}_1 \rangle \cdot \langle \mathbf{a}_2 \rangle \times \langle \mathbf{a}_3 \rangle)$, and $\boldsymbol{b}_2$ and $\boldsymbol{b}_3$ were calculated similarly. To give an example, $\boldsymbol{b}_1 \approx [1.569, -0.004, -0.004]$ $[2\pi/\text{Å}]$ at 50 K (R phase), and $\boldsymbol{b_1} \approx [1.567, 0, 0]$ $[2\pi/\text{Å}]$ at 300 K (C phase).

### Velocity-velocity correlation function

The VVCF was calculated in the exact same way as was done for MgO. The Fourier transform was computed exploiting convolution theorem, as explained in Ref. [1].

The atomic trajectories were projected onto the phonon eigenvectors, as explained in Sec. 2.6.

In particular, the results which I show in Sec. 7.7 are obtained with a projection onto one of the two transverse Slater branches. The eigenvectors were obtained numerically through two sets of harmonic calculations: one at mechanical equilibrium after relaxation ($T \to 0, P \to 0$, R phase), and one with an artificial cubic structure with lattice constant $a = 4$ Å. The choice of the rhombohedral and cubic eigenvectors is consistent with the phases obtained with the NPT simulations: I used the rhombohedral eigenvectors for temperatures 50 K to 125 K, and the cubic eigenvectors for the other temperatures, because such were the phases that the variable cell MD predicted. The choice of two different sets of eigenvectors allowed better visualization of the phonon bands, because, when the phase is cubic, the rhombohedral eigenvectors are not normal modes, and vice versa.

The vibrational energy distribution of the Slater mode in ($\omega$,$\boldsymbol{k}$) space, $\tilde{\mathcal{E}}_{\text{Slater TO}}(\omega,\boldsymbol{k})$, was obtained through Eq. 2.37 and divided by $k_B T$. The $\boldsymbol{k}$-points chosen are commensurate with the MD supercell and belong to the high-symmetry path $\Gamma - X - M - \Gamma - R$. The spectra were convolved with Gaussians with a standard deviation of $\sigma = 0.05$ THz, for visualization purposes.

## 7.3 Simulated phases and accuracy of the force field

Before discussing the main results, we shall embark in a brief assessment of the force field, and briefly discuss some of the issues of simulating classically a material like $BaTiO_3$. I will focus in particular on the issue of the inevitable finite size effects which make classical MD inaccurate when the size of the MD supercell is small, the lack of quantum mechanical effects, and the difficulty of parametrizing a force field accurately for all the phases.

The accuracy with which we simulate the different phases of $BaTiO_3$ is apparent in Fig. 7.1, which shows the supercell vectors and angles averaged over the NPT simulations. The error bars denote the standard deviations of the same quantities. We observe a phase transition at $T_C \approx 150$ K. Before discussing the phases we are able to compute, however, there are a few details to notice. First, the fluctuations of the lengths of cell vectors increase as the phase

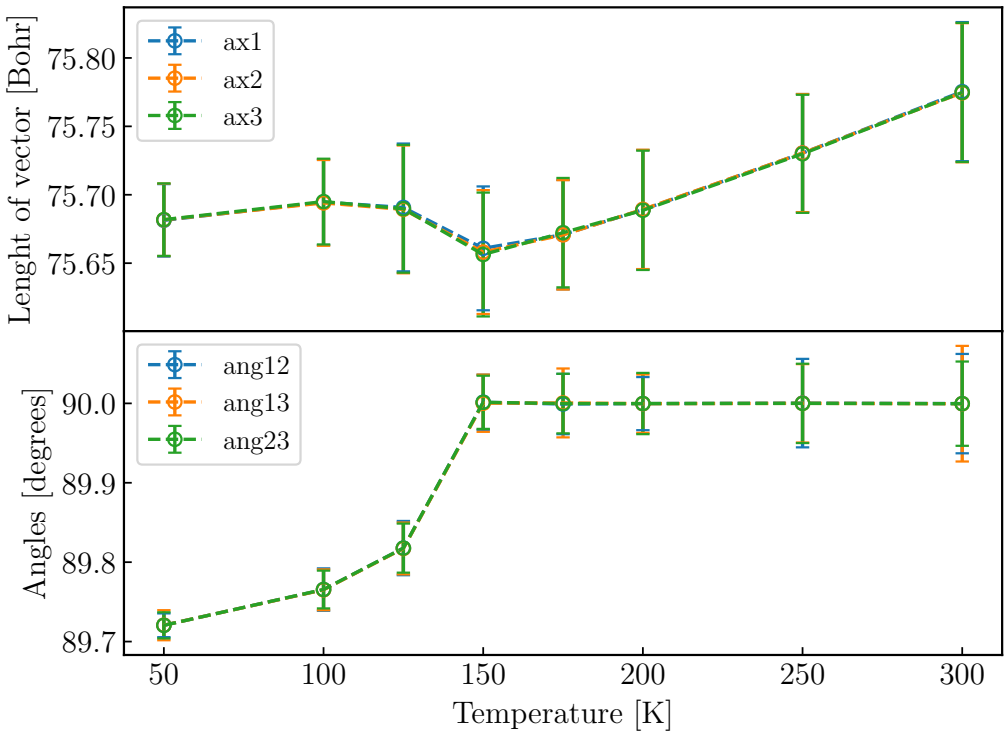



Figure 7.1: The average MD 10×10×10 supercell vectors' lengths and angles. Error bars denote the standard deviations of the same quantities.

transition is approached. This is because, due to finite size effects, the phase transition happens gradually over a finite range of temperatures where higher fluctuations are to be expected, the "critical region" [148, 114, 121]. At higher $T$, fluctuations increase as a consequence of thermal disorder. Second, there is a volume decrease at the phase transition, signalled by the decrease of the cell vectors' lengths. This feature has been confirmed experimentally [114, 121, 102] and theoretically [136].

Let us now discuss the phases that the force field predicts. We only observe two phases of $BaTiO_3$: the rhombohedral (R), at $50 \leq T < 150$ K, and the cubic (C), at $T \geq T_C = 150$ K. This can be inferred from the values of the supercell vectors' angles at $T < T_C$, which are all less than 90°, and lengths, which are equal at each $T$. The values of the angles at 50 K are in good agreement with the machine-learned potential recently developed by Gigli *et al.* [50]. Two are evidently the issues of the simulations. First, the R-C phase transition we can simulate does not represent the true R-O-T-C transitions of $BaTiO_3$, and not even a subset of that. Second, the transition temperature $T_C$ is not the correct one. As for the inability to

describe the real R-O-T-C transitions, which appears to be the most serious issue, Fallon has shown [43] that there are strong finite size effects which compress the $T$ range of stability of the O and T phases, so that these phases become lost in the fluctuations evident in Fig. 7.1.

In general, both issues are caused by finite size effects and by the inevitable inaccuracy of the simulations. Many are the sources of inaccuracy; I shall try to disclose the most striking ones.

**The trade off between including quantum mechanical effects and reaching larger length scales**

Firstly, one problem is the use of classical simulations, rather than quantum mechanical. This means that forces are calculated classically at each MD step, that nuclei are treated as classical particles, and that phonons are treated as classical oscillators.

We discussed in Sec. 1.2 the concepts of *accuracy* and *resolution*. Although quantum mechanical methods like *ab initio* MD can guarantee a much better accuracy, their high computational cost imposes limitations on the length and time scales affordable with such methods, so that their resolution is poor. The use of a relatively big supercell is vital for our purposes: Fallon has shown that MD simulations at the same temperature performed using MD supercells of different sizes result in different phases, with the bigger supercells being the more accurate [43]. This can be understood in terms of the energy fluctuations. From statistical mechanics, the magnitude of the fluctuations in the potential energy per atom scales as $1/\sqrt{N}$, where $N$ is the number of atoms, meaning that the energy fluctuates more in relation to its average value when the supercell is small. When the size of the MD supercell is too small, Fallon has shown that the total polarization of the supercell precesses, and averages in time to zero. The result is that the phase appears cubic [43]. The same simulations performed with bigger MD supercells, on the other hand, produced correctly a rhombohedral phase [43]. This is because the polarization domains are nucleated: if the supercell is too small, the sizes of polarized clusters that can form are small, and they are unstable: they precess their polarization and it is easier for them to shrink, thereby favouring the higher-symmetry cubic phase, on a time average. Other theoretical calculations have led to similar conclusions: for example, Ghosez, Gonze and

Michenaud found that the C phase is unstable at mechanical equilibrium only with a minimum of 5 distinct unit cells [48], hence with at least at $10 \times 10 \times 10$ supercell.

The convenience of classical simulations can also be understood if we consider that at least one of the phase transitions of $BaTiO_3$, the T-C one ($T_C \approx 400$ K), happens at a temperature for which quantum mechanical effects should be not too large, since the Debye temperature is $\approx$ 500 K [108]. Hence, treating the nuclei as classical particles is unlikely to change the picture qualitatively.

For these reasons, I believe that classical MD simulations, with parameters fitted to DFT data, are an excellent compromise between accuracy and the necessity of reaching bigger length and time scales.

**The issue of simulating the correct transition temperature**

Concerning the issue of predicting too small a $T_C$, I am not the first to report the problem: it was shown by Fallon [43], by Gigli *et al.* [50], and by Zhong, Vanderbilt and Rabe [152], that this is in part a consequence of the inaccuracy of the exchange-correlation functionals, which were used to fit the parameters of the present model within density functional theory. These functionals, especially within the local density approximation, tend to underestimate the equilibrium volume, and because the phase transition is very sensitive to the pressure, the value of $T_C$ can disagree with experiments [43, 50, 152]. The same authors showed that $T_C$ can be easily tuned by artificially increasing the MD volume, for example by applying a negative pressure. This strategy was adopted in Refs. [152] (pressure applied $P = -4.8$ GPa) and [50] (pressure applied $P = -2$ GPa) to arbitrarily increase $T_C$ so that it more closely matched the experimental value. Nonetheless, I have decided not to do this. My justification of this choice is that working at a smaller $T$s means protecting ourselves from the effect of too high a thermal disorder, which could have obscured the important features I want to show.

**The issue of modelling the atomic interactions as perfect ionic interactions**

Another source of inaccuracy is the use of a relatively simple ionic model (described in Sec. 2.11) to describe atomic interactions. Studies have found that there is a certain degree of covalency in the Ti-O bond (Ref. [54] and Refs. therein). For this reason, there are examples in the literature of potentials developed for other similar perovskites which modelled covalency explicitly [117]. However, Ref. [54] showed that when only a small portion of the valence electron density $n$ is "shared" between two atoms, so that the overlap between the atomic electron clouds is small, then the energy differences and interatomic forces can be accurately described with an ionic potential. The effect of the hybridization between atomic orbitals can be modelled for example by reducing/increasing the amount of ionic charge sitting at each ion. For a more thorough discussion on the terms "covalent" and "ionic", the reader is referred to Ref. [54].

Furthermore, polarizable potentials of the same form of the one used here were successfully employed for other oxides: not only MgO, which we discussed in Ch. 3, but also silica [130], alumina [55] and $TiO_2$ [109]. Furthermore, relatively simple shell models were able to accurately describe the phonon band structure of $BaTiO_3$ [72] and its dynamics and thermodynamics [135]. A force field almost identical to the one I used in this work was parametrized and tested by Fallon and proved itself capable of describing many features of $BaTiO_3$'s lattice dynamics [43], and a photo-excited version of it was successfully employed by Gu [53].

Hence, although there certainly is a degree of covalency in $BaTiO_3$, in light of the discussion provided in Ref. [54] and of the tests performed by Fallon [43] and by other independent force fields [94], I have found that an ionic model is accurate enough to understand the phase transitions in $BaTiO_3$.

**The issue of "transferability"**

One of the problems of force fields of this kind is the difficulty to make them transferable: after the fitting procedure to obtain its parameters, the force field might behave well for one

phase and less well for another. Although the configurations used to fit the present force field were taken to be representative of all the phases of $BaTiO_3$, as is described by Fallon [43], it is in general quite hard to find a parameter set that is adequate for all phases. I have not parametrized the force field myself, and the reader interested in a thorough discussion on this is referred to Sec. 4.3 of Ref. [43].

This drawback could in principle be overcome with the use of effective Hamiltonians, whereby one or more order parameters (local soft modes, acoustic modes, strains) are considered in the model and determine a lowering/increase of the symmetry of the unit cell in the various phases. Effective Hamiltonians have been utilized by many authors and were capable of describing the R-O-T-C transitions of $BaTiO_3$ [142, 152]. They are often constructed as a combination of the energetics of physical ionic interactions and of one or more order parameters [152], and hence really are expressions for the free energy surface. These methods are based on assumptions over which phonon modes are responsible for the phase transitions, and often only BZ center soft phonons were considered [152]. As a result of this, they are inevitably biased by the choice of the order parameter, and often lead to a transition which has some character of a displacive transition [152].

Effective Hamiltonians inevitably reduce the degrees of freedom of the dynamics. An MD simulation with a force field based only on the energetics of some agreeable physical interactions (Coulomb, short-range, etc.), on the other hand, does not limit the atomic degrees of freedom taken into consideration, other than the ones that the computational cost allows. It is very important to have a fully atomistic simulation, so that we do not bias towards a particular mechanism.

All this said, I believe that, if not representative of the true $BaTiO_3$, the force field I used can be a qualitative description of a $BaTiO_3$-like material, or at least give a wealth of information about what happens, in the atomic scale, when a perovskite like $BaTiO_3$ undergoes a phase transition. This will hopefully become apparent in the following part of this chapter.

## 7.4 Results: an overview of the sections

In the next sections, I discuss the main results of this thesis for $BaTiO_3$.

**Short overview**

In brief, I show the simulated IR spectra in Sec. 7.5, the simulated diffuse scattering in Sec. 7.6, the distribution of vibrational energy in Sec. 7.7, and the real spacetime picture of atomic vibrations in Sec. 7.8. The results Secs. 7.5-7.8 can be read in parallel with Secs. 6.1-6.5, where I discussed the same experimental techniques whose observables I simulate here, or similar quantities. To ease the comparison, whenever I can I show the simulated and the experimental results in the same plot.

**Extended overview**

The results sections are presented in order of the amount of information that each result gives.

The IR spectra, which I present in Sec. 7.5, give limited information, because they only show optical modes at the BZ center, $\boldsymbol{k} \to \boldsymbol{k}_\Gamma$. I will show that the phase transition is characterized by a partial softening of the Slater TO mode and the emergence of a central peak, which I interpret as a Debye mode, i.e., a mode which represents inter-well hopping of Ti-O atoms. A Debye mode is an indication that the local PES retains the aspect of a multiple-well surface, whereby atoms hop among minima as a result of thermal fluctuations. Hence, the Debye mode differs from a soft mode, which relies on the fact that the PES remains quadratic at $T \geq T_C$ (cf. Sec. 5.3.3). This interpretation goes in favor of an order-disorder transition, and echoes the interpretation given in one of the most prominent spectroscopic papers by Hlinka *et al.* [62]. However, the IR evidence alone is not enough to understand the phase transitions in $BaTiO_3$.

To substantiate the possibility of uncorrelated Ti-O hops between minima of the PES, which generate spatial disorder (cf. Sec. 5.3.2), the simulated neutron diffuse scattering patterns are of help. I show them in Sec. 7.6. The patterns provide information about a much wider

portion of reciprocal space, and can be used to assess the presence of spatial disorder, with the aid of table 6.1. Looking at the scattering patterns will help us to (i) suggest the possible presence of linearly-correlated disorder, namely, the presence of uncorrelated linear chains of atoms, which are consistent with the eight-site model of Comes, Lambert and Guinier [25], and (ii) connect with the large amount of literature available for this experimental technique (cf. Sec. 6.2). However, the scattering cross section $S(\boldsymbol{Q})$ is integrated over the frequency space, hence it should be regarded as a probe of the structure averaged over time. It is not possible to obtain the spectra of the single phonon modes with this technique.

The distribution of kinetic energy in reciprocal spacetime projected onto the Slater TO eigenvectors, $\tilde{\mathcal{E}}_{\text{Slater TO}}(\omega, \boldsymbol{k}; T)$, which I show in Sec. 7.7, will allow us to have the spectra of the mode responsible for the phase transitions over different wavevectors and as a function of frequency and for different temperatures. I will show that the Slater TO mode melts, meaning that it is abnormally spread out in $\omega$-space and in $\boldsymbol{k}$-space. The broadening in $\omega$-space is consistent with an inter-well hopping motion, because of the slowing down effect of the energy barrier at the center of the cell which occurs if the PES retains the aspect of a multiple-well potential. The spread out in $\boldsymbol{k}$-space happens over a whole $\{100\}$ plane in reciprocal space, and confirms the presence of diffuse sheets in the simulated neutron diffuse scattering. In fact, the areal spread of the Slater mode suggests the presence of 1D order in the atomic motions, and so the presence of uncorrelated linear chains. Computing $\tilde{\mathcal{E}}_{\text{Slater TO}}(\omega, \boldsymbol{k}; T)$ is the most complete and informative way in which spectra can be obtained. However, the link between reciprocal spacetime and real spacetime will be still missing at this point in the chapter.

To complete the understanding, I show the real spacetime picture of the vibrations in Sec. 7.8. The hopping of Ti-O atoms, we will see, are linearly correlated at $T > T_C$. Hence, the onset of a phase transition is characterized by the preference of atoms to form linear chains directed along the crystallographic $\langle 100 \rangle$ axes. The polarizations of the chains are uncorrelated with one another, creating disorder on planes containing the chains. The disorder is dynamical, not static, in the sense that the chains flip their polarization every so often, as a result of inter-well hops. This study confirms almost entirely the intuition of Comes, Lambert and Guinier, but extends it in a dynamical way.

## 7.5 IR spectra

I presented the experimental IR results in the last chapter, in Sec. 6.1. Here, I re-propose the experimental spectra, but this time alongside the spectra simulated in this work, in order to compare experiment and simulation. I show the results of the NPT simulations; this will allow us to briefly discuss the effect of the barostat during MD. By reproducing the main features of experimental spectra with our simulations, I show that they can be explained by an incomplete softening of the Slater TO mode, and the emergence of a Debye mode as $T$ increases towards $T_C$.

On the left hand side of Fig. 7.2 I replot the measured IR spectra in the T phase from Hlinka *et al.* [62] (bottom plot) and in the C phase from Luspin *et al.* [82] (top plot). On the right hand side, I show the calculation of the imaginary part of the permittivity function, $\chi''_{xx}(\omega)$, from the dipole-dipole correlation function (Eq. 2.61) obtained from MD simulations in the NPT ensemble. One reason for discussing the calculated spectra is that they can be regarded as a first sanity check of our model of $BaTiO_3$, which will be further tested in the subsequent sections. Before discussing the comparison between experimental and simulated spectra, it is important to check that the results are not artifacts of the barostat.

#### The effect of the barostat

The way $P$ is kept constant during the MD trajectory is through a barostat. We have discussed the Parrinello-Rahman barostat in Sec. 2.10.2, and its equations of motion are quoted in Eq. 2.75. The barostat imparts additional forces on the atoms and, inevitably, has an impact on the cells' dipole moments $\boldsymbol{p}_l = \sum_{i=1}^{n_a} q_i \boldsymbol{r}_i + \boldsymbol{d}_i$, which determine the dipolar response $\boldsymbol{\chi}''(\omega)$. This is evident in the presence of three additional peaks at low frequencies, labeled 'MD' in Fig. 7.2, where we would not expect any optical phonon mode. These peaks correspond to the frequencies of the volume fluctuations, hence they are caused by the barostat. We shall neglect such peaks: these are an artifact of the simulations and of the finite size of the MD supercell. The volume's fluctuations, in fact, exactly like the energy fluctuations, are a statistical mechanical effect, and

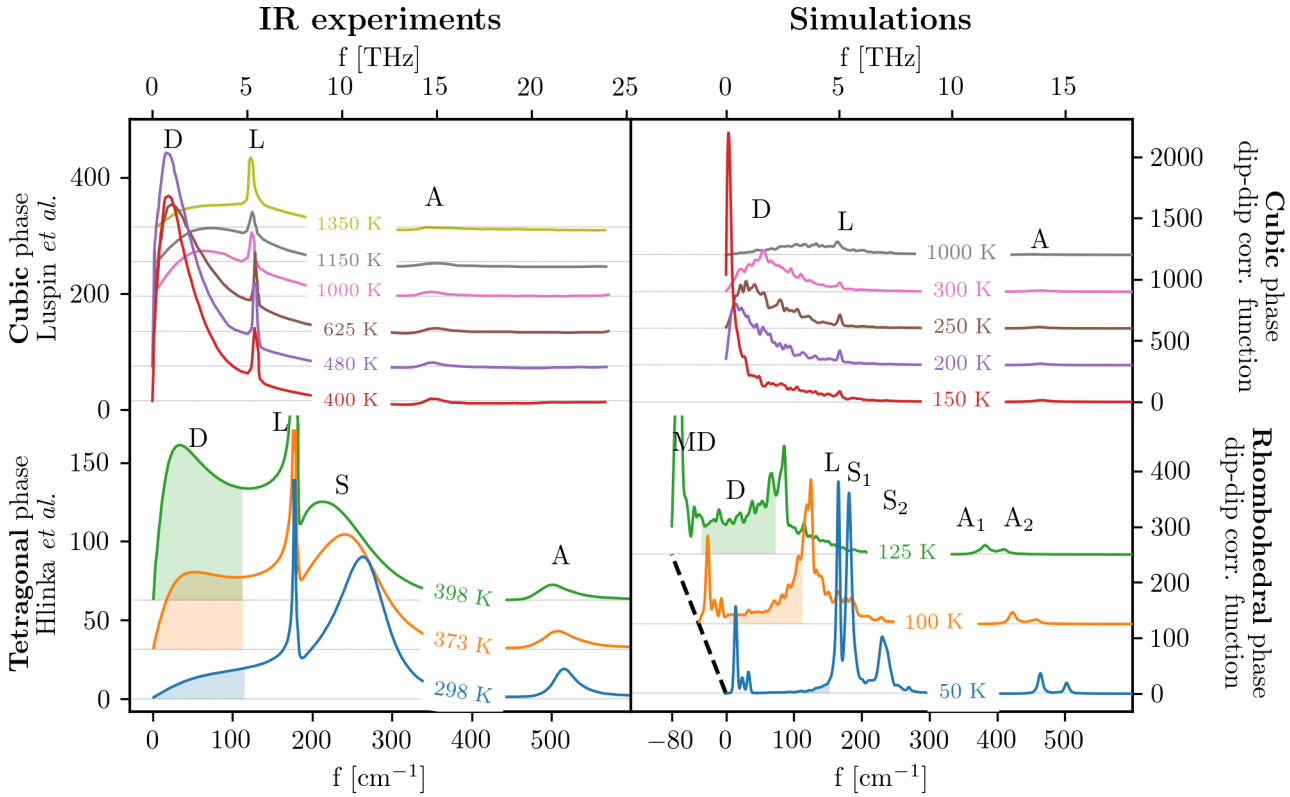



Figure 7.2: Experimental and simulated dielectric spectra of $BaTiO_3$. On the left is the imaginary part of the dielectric function $\varepsilon''_{zz}(\omega)$, and on the right is the permittivity $\chi''_{xx}(\omega)$ from NPT simulations. Both sides contain dielectric spectra of TO modes near Γ. The left hand plots are, in the bottom, experimental spectra of $A_1$ modes in the T phase from Hlinka *et al.* [62], and in the top, experimental spectra of $F_{1u}$ modes in the C phase from Luspin *et al.* [82]. In right hand plots are the simulated IR spectra, calculated from Eq. 2.61, in the R phase (bottom plot) and C phase (top plot). In the bottom right plot, I shifted the 100 K and 125 K spectra by 40 $cm^{-1}$ and 80 $cm^{-1}$ for visualization purposes. The naming of the modes follows the spectroscopic notations described in Sec. 5.4: D=Debye, L=Last, $S_1$ and $S_2$ are the two non degenerate Slater modes, and $A_1$ and $A_2$ are the two non degenerate Axe modes. The MD peaks are caused by the barostat, and are discussed in the body of the text. The Debye mode is highlighted by shaded areas in the bottom plots. In the simulated R-C transition, the two Slater modes shrink, and a Debye mode emerges. The Debye mode initially manifests as a noisy signal in between the MD and the Last peaks. Then, at $T \gtrsim T_C$ in the C phase, it dominates the spectrum and appears as a narrow peak (critical slowing down). The Debye peak then broadens and hardens, until it overlaps with the Last modes.

vanish in the thermodynamic limit, i.e., they are negligible in a macroscopic sample.

The frequencies of the volume and cell angles fluctuations can be tuned by tuning the mass of the Parrinello-Rahman barostat. A smaller mass means a higher frequency. This can in principle allow a faster equilibration of the volume, since in relatively little simulation time the volume has gone through many oscillations, and hence a shorter time is needed to complete the simulation. However, a very small mass can mean that the frequency of the volume fluctuations might become too high, and this is unphysical. Andersen, one of the first authors to propose the barostat device for MD simulations [3], suggested that for a liquid the time scale of the fluctuations $\tau_B$ (the inverse of the barostat's frequency $f_B$) should be set to a value approximately equal to the length of the sample $L$ divided by the velocity of sound of the liquid $v_s$ [3], hence $\tau_B = L/v_s$. This should correspond to the time scale at which pressure waves propagate through the liquid. In a solid, this corresponds to choosing a barostat frequency $f_B$ equal to the frequency of the longest wavelength acoustic phonon (LWA), $\omega_{\mathrm{LWA}}/(2\pi)$, accessible with the MD supercell chosen.

One way to prevent the barostat from negatively interfering with the atoms' dynamics is to choose a bigger barostat's mass. This allows to have slower fluctuations of the volume, and stay protected against too large spurious additional external forces exerted on the atoms. In my production MD runs, I set the barostat's mass to 100 times the mass of a unit cell. This value of the mass allowed the highest frequency of the volume fluctuations, which is $\approx 1$ THz, to be smaller than the frequency of the lowest LA mode, which is $\approx 1.52$ THz. The frequencies of the volume fluctuations are then far from being resonant to the hard optical phonon modes, as can be seen from the R phase spectra of Fig. 7.2. I can safely say that the barostat did not undesirably interact with the relevant polar modes which are the objects of this investigation and correctly mimics the quasi-elastic fluctuations of a chunk of bulk material interacting with the surroundings.

It goes without saying that NVE or NVT simulations do not require one to accurately tune the barostat. An obvious alternative to NPT simulations is to fix the supercell's shape to one of the nominal phases of $BaTiO_3$ and opt for constant volume simulations. However, one should be

very cautious when doing so, because $BaTiO_3$ is ferroelastic, and the coupling between optical modes and elastic strains is at the heart of ferroelasticity. Elastic strains can of course occur even in an NVT simulation, but these might be underestimated, because the supercell's volume and shape are fixed. For this reason, I used the NPT simulations as the reference simulations for my analysis.

To make sure that the barostat has not polluted my spectra, however, I have run NVT simulations with supercells averaged from the NPT simulations. As explained in Sec. 7.2.3, I run NVT simulations with $V = \langle V_{\mathrm{NPT}}(t)\rangle_t$, where $V_{\mathrm{NPT}}(t)$ is the fluctuating volume of the NPT runs. The NVT simulations allowed me to stay protected against artifical strains imposed on the system. In this section, I am showing the results of the NPT simulations, but I have redone the calculation of the imaginary permittivity $\chi''_{xx}(\omega)$ from the NVT runs. The results are shown in appendix F, and Fig. F.1, combined with Fig. 7.2, is a useful comparison between NVT and NPT simulations and between NVT simulations and experiments.

**The simulated IR spectra from NPT simulations**

Let us look at the right hand side of Fig. 7.2, which shows the simulated IR spectra of the TO modes of $BaTiO_3$. As we saw in Sec. 7.3, we simulate a different temperature range and observe a different phase transition (R-C) than experiments; this apparently gross inadequacy of our force field was discussed there. A look at the R phase shows that the degeneracies of the T phase are broken in the R phase, as expected. In fact, we observe two Slater peaks and two Axe peaks. The two Last peaks are very close in frequency because they are almost degenerate.

The R-C phase transition from our simulations is a bit more complicated than the real T-C one, because in the T-C transition, at $T < T_C$, it is one Slater mode that softens partially and loses intensity, while in our simulations we have two Slater modes that do so. This is inevitable: the T-C transition happens when the tetragonal axis [001] distorts so as to become equivalent to the [100] and [010] axes. Hence, in the T-C transition, the transverse Slater mode along the T axis, which is an $A_1$ mode, softens and shrinks. In a R-C transition, it is the [111] axis that distorts in the same direction. Hence, in the R-C transition, two transverse

non degenerate Slater modes soften partially and lose intensity. These modes are transverse because the imaginary part of the permittivity plotted in Fig. 7.2 only contains TO modes, and they are Slater modes because their peaks correspond to the Slater modes' frequencies.

What is important to note is that, with respect to experiments, we witness a very similar trend for the relevant polar phonon modes: while the two Slater TO modes soften partially and shrink, the Debye mode, highlighted by the shaded areas in between the MD and the Last peaks, grows with increasing $T - T_C$. In transitioning from the R to the C phase, the simulated Debye mode signal is almost constant from the MD peaks to the Last peak. At the onset of the C phase, at $T = 150$ K, the Debye mode dominates the low frequency part of the spectrum and appears as a very narrow peak at almost zero frequency. This is the "critical slowing down" behaviour of the central peak [62], which we discussed in Sec. 5.3.4. Such central peak then broadens and hardens as $T$ is raised, until at $T = 1000$ K it almost reaches the peak position of the Last mode.

The interpretation of the Debye mode as a hopping mode was discussed in Sec. 6.1, and throughout much of the last chapter, and we shall not discuss it any further. The purpose of this section was to show that (i) the barostat did not undesirably interact with the polar modes we are interested in, (ii) the simulations give a qualitatively correct picture of the underlying physics and (iii) the R-C transition, although not one which the real $BaTiO_3$ undergoes, can still be used as a basis for understanding what happens when $BaTiO_3$ changes phase.

A last thing to notice is the shape of the Debye mode. The experimental spectra, in fact, show a very clear peak for this mode. However, we must remember that the experimental lines from Hlinka *et al.* are obtained through a fit of the experimental data to the the sum of three damped oscillators, L, S and A, and one Debye-like relaxational mode [62]. A damped harmonic oscillator (DHO) has spectrum as in Eq. 2.63, and a relaxational mode is just a DHO whose exponential decay is faster than the frequency of the oscillation. Hence, with respect to the simulated spectra, the experimental spectra look much smoother curves. However, notice that the D mode overlaps quite substantially with the L mode. If we look at the $T = 373$ K experimental spectra of Fig. 7.2, the D peak is not very pronounced: it is almost constant in the

range $50 \lesssim f \lesssim 180$ cm$^{-1}$. If we consider this, and the fact that the THz-range experimental data were in the frequency window $0 \ll f \ll 50$ cm$^{-1}$ [62], there are reasons to believe that the experimental line shape is not too different than the line shape of the simulated Debye mode at, for example, $T = 125$ K. Of course, we here have to make an effort to neglect the MD peaks. The reader interested in how the MD peaks disappear in an NVT simulation, and in how the Debye mode grows from $f = 0$ will find the constant volume spectra in appendix F.

## 7.6 Diffuse scattering

We saw, in Sec. 6.2, that X-ray diffuse scattering experiments on $BaTiO_3$ showed some anomalous diffuse sheets, which Comes, Lambert and Guinier were the first to interpret as a result of spatial disorder [25], in 1968. We also saw that Hüller, and other authors after him, rejected this interpretation and proposed that a soft mode could produce the diffuse sheets [66]. This controversy sparked a long-lasting debate, with authors either supporting the order-disorder [25, 112] or the displacive picture [66, 94, 57].

In this section, I compare the simulated and experimental diffuse scattering patterns. The simulations can be subdivided into two sets of results: one comes from a calculation in the HA and the other comes from the NVT simulations. The HA results will be useful to illustrate the patterns which arise in the scattering cross section when the phonons are activated by temperature, and to understand how to interpret an image of diffuse scattering. I then show that our MD model of $BaTiO_3$ is able to reproduce the diffuse patterns observed in the X-ray diffuse scattering experiments. We will see that the PE phase of $BaTiO_3$ is characterized by the presence of diffuse *sheets*. The diffuse sheets are interpreted in the same way as we discussed in Sec. 6.2, and summarized in table 6.1. The interpretation is that the diffuse sheets appear on $\{100\}$ planes in reciprocal space and are caused by 1D-correlated disorder in real space. 1D-correlated disorder means that atoms align their displacements forming chains along $\langle 100 \rangle$ directions, with each parallel chain uncorrelated with another.

The harmonic and MD calculations of the scattering cross section are performed according to Eqs. 2.58 and 2.45, respectively. In comparing the two calculations, we will be able to assess the difference between the idealized phononic lattice dynamics (in the R equilibrium phase) and the MD dynamics in all phases. The concept is similar to the one I have used for MgO in Fig. 3.5, where I compared the harmonic phonon frequencies with the MD spectra; however, while there we looked at how the *energy* is distributed in $(\omega,\boldsymbol{k})$-space, here we look at how the relative *positions* of the atoms are distributed in $\boldsymbol{k}$-space, i.e. how accurately they can be described in terms of plane waves of different $\boldsymbol{k}$-vectors.

As we saw in Sec. 2.8, in fact, the scattering cross section $S(\boldsymbol{Q})$ is the Fourier transform of the pair correlation function (PCF) $G(\boldsymbol{R}) = \sum_{ij} b_i b_j \langle \delta(\boldsymbol{R} - \mathbf{R}_i + \mathbf{R}_j) \rangle$ (Eq. 2.47). The PCF is the average probability of finding an atom $i$ at a distance $\mathbf{R}_{ij} = \mathbf{R}_i - \mathbf{R}_j$ from atom $j$, weighted by the atomic scattering lengths $b_i$ and $b_j$. Hence, it quantifies the correlation in space of the relative atomic positions.

In a static periodic lattice, atoms are placed at the sites $\{\boldsymbol{R}_i\}$, the atomic spatial correlation is constant and the scattering cross section produces the sharp Bragg peaks at the $\boldsymbol{G}$-points which are found in a standard diffraction experiment, in accordance with the Laue condition $\boldsymbol{Q} = \boldsymbol{G}$ [4]. When the motion of the atoms is considered, the symmetry of the periodic lattice is lowered by the atomic vibrations. In the limit of $T \to 0$, where the HA holds, these vibrations can be described by perfect plane waves. A plane wave of atoms with wavevector $\boldsymbol{q}$ has periodicity $l_{\boldsymbol{q}} = 2\pi/|\boldsymbol{q}|$ and correlation length $\lambda_{\boldsymbol{q}} \to \infty$. Such wave imposes a constraint on the dynamical positions of the atoms $\{\boldsymbol{r}_i\} = \{\mathbf{R}_i + \boldsymbol{u}_i\}$. This constraint is that the relationship between the displacements of atoms $i$ and $j$ which are placed $\mathbf{R}_{ij}$ apart from each other in the direction of $\boldsymbol{q}$ is $\boldsymbol{u}_i = \boldsymbol{u}_j \exp(i\boldsymbol{q} \cdot \mathbf{R}_{ij})$. So, atoms are perfectly correlated in the sense that they participate in the motion of an infinitely long wave. When $T$ is raised so that phonons are activated, the assumption of the lattice being characterized by static atoms breaks down, and the sharp Bragg peaks which characterize the regular lattice broaden. This broadening can be imaged when the crystal is radiated with external particles, be them neutrons or photons or electrons, and it creates patterns in $\boldsymbol{Q}$-space: the diffuse scattering patterns.

The Bragg peaks broaden because the values of $\boldsymbol{Q}$ at which there is correlation in real space are not limited by the Laue condition $\boldsymbol{Q} = \boldsymbol{G}$ anymore. They are not limited because spatial correlation is now found *at any* $\boldsymbol{Q} = \boldsymbol{G} + \boldsymbol{q}$ *point where a phonon mode exists.* Hence, in the whole reciprocal space. Furthermore, if a particular mode $(\boldsymbol{q}\nu)$ exists that is highly populated, a good amount of the crystal dynamics is described by the eigenmotion of such mode; hence, this mode will contribute a lot to the diffuse scattering. Transverse acoustic modes at small $\boldsymbol{q}$'s are the lowest-frequency phonon modes, hence it is obvious to expect that they contribute maximally to the scattering. So, the $\boldsymbol{q}$-points near the $\boldsymbol{G}$-points are the ones with highest signal: the Bragg peaks inflate because of TA modes.

Let us now be more specific. In a neutron/X-ray experiment, we would use an incident (i) beam directed along $\hat{\mathbf{k}}_i$, we would place ourselves with the detector at the direction $\hat{\mathbf{k}}_f$, and count the number of neutrons/photons arriving at the detector after being scattered by any collective lattice vibration. I restate the equation for the scattering cross section in the hypothesis that the beam excites only one phonon, Eq. 2.58:

$$S_1^{\mathrm{ph}}(\boldsymbol{Q}) = \sum_{\nu} \frac{\hbar}{2\omega_{\boldsymbol{q}\nu}} |F_\nu(\boldsymbol{Q})|^2 (1 + 2n_{\boldsymbol{q}\nu}).$$

Here, $\boldsymbol{Q} = \mathbf{k}_f - \mathbf{k}_i = \boldsymbol{q} + \boldsymbol{G}$, where $\boldsymbol{q}$ is the phonon wavevector, $\omega_{\boldsymbol{q}\nu}$ is the frequency of the phonon, $F_\nu(\boldsymbol{Q})$ is defined in Eq. 2.57 and $n_{\boldsymbol{q}\nu} = n_{\boldsymbol{q}\nu}(\omega, T)$ is the Bose-Einstein occupation number. Hence, to a first approximation, $S(\boldsymbol{Q}) \sim S_1^{\mathrm{ph}}(\boldsymbol{Q})$ depends on three factors. First, it depends on the frequency of the phonons which propagate at that $\boldsymbol{Q}$, through the factor $1/\omega_{\boldsymbol{q}\nu}$ (the lower the energy, the easier it is for the beam to excite that phonon). Second, it depends on the frequency of the phonon and temperature through the factor $(1 + 2n_{\boldsymbol{q}\nu})$ (the higher the temperature, the higher the population of phonons that can contribute to the scattering). Third, it depends on the term $F_\nu(\boldsymbol{Q})$; this term contains the static structure factors $\exp(i\boldsymbol{Q}\cdot\boldsymbol{R}_j)$, the Debye-Waller factors $\exp(-W_j)$, and the "selection rule" $\boldsymbol{Q}\cdot\mathbf{e}(\mathbf{q}\nu, j)$. All of these terms are defined in Sec. 2.8. Of course, it also depends on the atomic scattering lengths $b_j$, in the case a beam of neutrons is used (different atoms, and even different isotopes, scatter neutrons in a different way). In the case of X-ray scattering, the scattering lengths should be replaced with the atomic form factors [4, 73]. In this work, I decided to use the scattering lengths, and to simulate a neutron scattering experiment; the scattering lengths I used, together with further details of the calculation, can be found in Sec. 7.2.3.

### 7.6.1 Harmonic diffuse scattering

Fig. 7.3 shows the harmonic calculation. Details of the calculation were provided in Sec. 7.2.3. The patterns are shown as a pixelated contrast and contour plots. A high value of $S(\boldsymbol{Q})$ is indicated by a dark pixel in the left hand plot, and a yellow line in the contour plot. The other lines and symbols will be explained below. We shall use the harmonic calculation as a key to

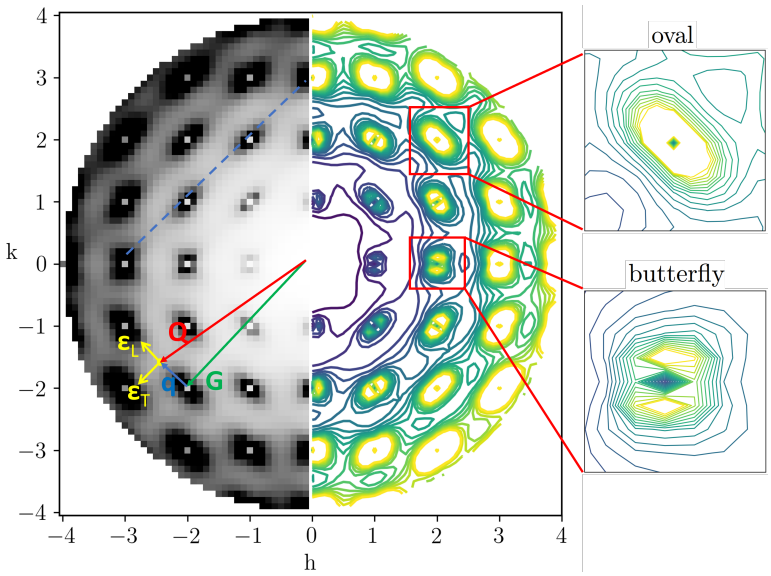



Figure 7.3: Harmonic calculation of diffuse scattering. Left: pixelated contrast plot. The $\boldsymbol{G}$-points are colored in white, because Bragg scattering has been subtracted. The broken blue line is a guide for the eye to identify the diffuse streaks, which are elongation of the Bragg peaks from the $\boldsymbol{G}$-points along a direction at 45° from the Cartesian axes. The coloured arrows in the bottom show an example of the scattering cross section around $\boldsymbol{G}$ = [-2 -2 0], showing that, for phonons propagating in the direction $\boldsymbol{q}$, the transverse modes having eigenvector $\boldsymbol{\varepsilon}_T$ have a maximum value of the selection rule $\boldsymbol{Q} \cdot \boldsymbol{\varepsilon}$, and hence form the 45° streaks. Right: a contour plot showing the typical butterfly and oval shapes around the $\boldsymbol{G}$ vectors. Mode decomposition of the scattering cross section is available in appendix G.

interpret the MD results, which are more important.

The white spots at the $\boldsymbol{G}$ vectors are the Bragg peaks, and appear white because I subtracted Bragg scattering from the total scattering, so that only diffuse scattering could be seen unambiguously (cf. Sec. 2.8). The phonon calculation makes all Bragg peaks elongate in a 45° direction. The broken blue line is a guide for the eye to visualize such elongation. This oblique deformation of the Bragg peaks can extend far away from the $\boldsymbol{G}$ vectors, resulting in oblique streaks. The 45° pattern is typical of TA modes, for two reasons. First, the TA modes are the lowest-energy ones, and make the terms $\frac{1}{\omega_{\boldsymbol{q}\nu}}$ and $n_{\boldsymbol{q}\nu}$ in $S_1^{\mathrm{ph}}(\boldsymbol{Q})$ very large for such modes. Secondly, at many $\boldsymbol{G}$-points the selection rule for inelastic scattering, $\boldsymbol{Q}\cdot\boldsymbol{e}(\boldsymbol{q}\nu,j)$ (Eq. 2.57), favors the TA modes along lines at 45° from a $\langle 100\rangle$ direction, since the eigenvectors of such modes are roughly along the same direction of $\boldsymbol{Q}$. In Fig. 7.3, this is schematically illustrated with a green, blue and red arrow as an example of a $\boldsymbol{G}$, $\boldsymbol{q}$ and $\boldsymbol{Q}$ vector, respectively, and with yellow arrows as schematic vectors representing the polarization of transverse (T) and longitudinal (L) modes. For the particular $\boldsymbol{G}$-point considered in Fig. 7.3, L modes have an eigenvector almost perpendicular to the scattering wavevector $\boldsymbol{Q}$, and hence do not contribute much to the cross section at that $\boldsymbol{Q}$. T modes, and especially TA modes, on the other hand, contribute maximally.

For this reason, I follow the notation of Harada and Honjo [57] and call these streaks $S_A$. Of course, the patterns depend on the position in reciprocal space: the $\boldsymbol{Q}$ vector drawn in red in Fig. 7.3 is just an example. The insets of Fig. 7.3 show the typical butterfly-like shape at $\boldsymbol{G} = [200]$ and the oval shape at $\boldsymbol{G} = [220]$. Such shapes, which are caused by the TA modes, are in fact prototypical: other interesting sources where the butterfly and oval diffuse patterns from solids were imaged are Ref. [94] (Fig. 1 or supplemental material), Ref. [61] (Fig. 3) or Ref. [47] (Fig. 1).

The scattering cross section displayed in Fig. 7.3 was calculated by summation of all the fifteen phonon modes. The reader interested in the breaking down of $S(\boldsymbol{Q})$ into each mode, which can be calculated by virtue of Eq. 2.58, is referred to appendix G, where I show that the contribution of the high energy modes to $S(\boldsymbol{Q})$ is essentially negligible, because $\omega_{\boldsymbol{q}\nu}$ is large for

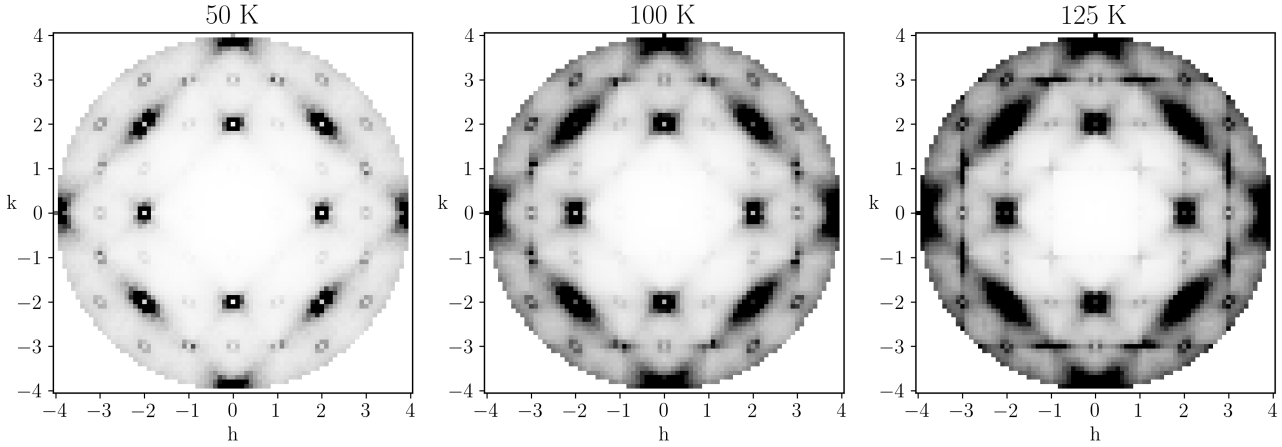
such modes. The harmonic calculation I have just shown can be of help to foresee where to expect a greater scattering cross section. This, for example, can guide the experimentalist in the selection of $\boldsymbol{G}$-vectors in a scattering experiment [29]: in fact, the const-$\boldsymbol{Q}$ scans obtained at different $\boldsymbol{Q}$s can differ even if the phonons involved ($\boldsymbol{q}\nu$) in the scattering are the same [56]. This is because, in a one-phonon process, $\boldsymbol{Q} = \boldsymbol{q} + \boldsymbol{G}$, and the integrated scattering cross section varies from $\boldsymbol{G}$ to $\boldsymbol{G}$, as Fig. 7.3 shows.

The HA is an approximation which is valid in the limit $T \to 0$, as we have learned in this thesis. Things can fundamentally change when the MD dynamics is considered.

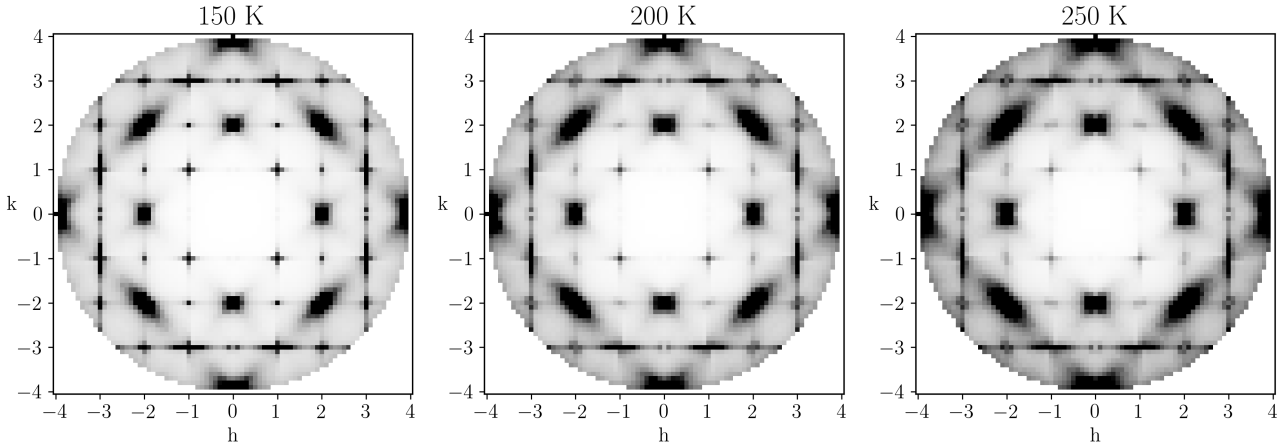
### 7.6.2 MD diffuse scattering

I calculated the scattering cross section, $S(\boldsymbol{Q})$, for the temperatures simulated via MD. Details of the calculation can be found in Sec. 7.2.3. The results are displayed in Fig. 7.4. The images of diffuse scattering are displayed as pixelated plots, since the values of $S(\boldsymbol{Q})$ were obtained only at commensurate points in reciprocal space. Because $S(\boldsymbol{Q})$ increases with $T$, in Fig. 7.4 for visualization purposes the color scheme is the same for three plots belonging to the same row, but different between one row and another. This allowed to reduce the contrast at the higher temperatures.

There is another decision which I made, which can sound contradictory to what I said in Sec. 7.5: here, I am showing the NVT results. The reason for this is simple: the barostat induces volume fluctuations which have low frequencies (see the IR spectra of Fig. 7.2). Such additional spurious fluctuations inevitably appear in the diffuse scattering, and can (and in fact they do) overshadow the features I want to show. In fact, the volume fluctuations produce streaks which are very similar to the $S_O$ which we mentioned in Sec. 6.2. The problem is that, when the barostat is applied, the $S_O$ streaks are present also in the R phase, and do not allow to see differences between the R and C phases. The barostat streaks are artificial; in a real material these would be absent, or different, since a real material is macroscopic. To be able to compare our results with experiments, I decided to avoid a useless complication and look at the NVT results. The reader interested in the NPT diffuse streaks can find them in appendix H.




(a) Evolution of the total scattering cross section for BZ [$hk0$] planes in the rhombohedral (R) phase. The max value has been set to 0.4 $10^{-5}$ [bohr$^2$].




(b) Evolution of the total scattering cross section for BZ [$hk0$] planes in the cubic (C) phase. The max value has been set to 1 $10^{-5}$ [bohr$^2$].

Figure 7.4: The neutron diffuse scattering in the R and C phase simulated from MD in the NVT ensemble. The phase transition is signalled by the additional presence of horizontal and vertical streaks $S_O$, of which [±3k0] and [h±30] are the most pronounced.

Let us analyze the $T = 50$ K simulation shown in Fig. 7.4a: we observe the same oblique streaks as in Fig. 7.3 at the even $\boldsymbol{G}$-points (like [200], [400], [220]). Note the presence of butterfly and oval spots at $\boldsymbol{G}$=[200] and $\boldsymbol{G}$=[220]. These are the same patterns which we saw in the harmonic calculation reported in Fig. 7.3. It is to be expected that harmonic patterns are seen from MD at 50 K: at low temperature, and with a stable R phase, the harmonic lattice dynamics should be adequate to approximate the MD dynamics. There is, however, one striking difference between the HA and MD at $T = 50$ K: the absence of streaks at odd $\boldsymbol{G}$-points. I define odd $\boldsymbol{G}$-points as points characterized by at least one odd number, like [100], [110], [210] and so on. The absence of signal at the odd $\boldsymbol{G}$-points is due to the much lower value of the static structure factors $\exp(i\boldsymbol{Q} \cdot \boldsymbol{R}_j)$ appearing in Eq. 2.46 at these points. Dove calls this the "systematic absences of crystallography" [38]. Such absences are, probably, obscured in the harmonic calculation, because in Eq. 2.58 the term $\boldsymbol{Q} \cdot \boldsymbol{e}$ favors $\boldsymbol{G}$ vectors away from [000].

Let us now turn our attention to what happens when the temperature is raised: Fig. 7.4a shows that as $T$ increases the patterns become darker, because the total cross section increases in magnitude. This is because the population of phonons is higher at higher $T$. Hence, there is higher contrast for the diffuse patterns. The most important trend which can be understood from the plots as $T - T_C$ increases is the gradual emergence of vertical and horizontal diffuse streaks $S_O$, which cross both even and odd $\boldsymbol{G}$ vectors. The most evident ones are the streaks $h, k = 3$. This result looks familiar: it is what Comes, Lambert and Guinier found experimentally in 1968 [25, 26, 64], and that was confirmed by the recent experiment of Pasciak *et al.* [94] and other investigations [58, 57, 64, 103], and which we discussed in Sec. 6.2.

A comparison between the experimental result of Pasciak *et al.* [94] and the simulated results in the PE phase is plotted in Fig. 7.5 at different values of $l$: $l = 0$ and $l = 1.5$. As we noted in Sec. 6.2, the use of $l = 1.5$ plane passing through the $X$ point is a clever expedient which Pasciak *et al.* used. In fact, it allows to observe the presence of $S_O$ streaks in both planes in reciprocal space, and to state that the diffuse streaks are actually planes, or *sheets*. The sheets I am referring to are planes perpendicular to the plane of Fig. 7.5, and whose normal are along the [100] and [010] directions, namely, the $h$ and $k$ axes.

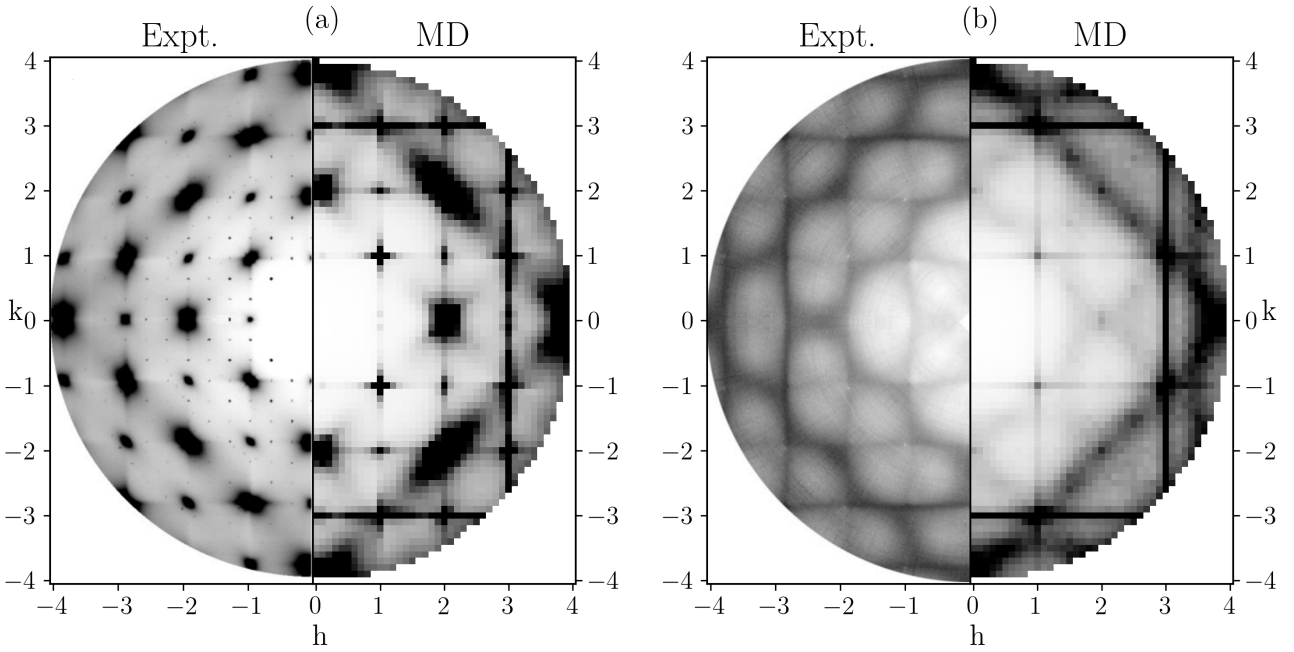



Figure 7.5: Comparison between the diffuse scattering obtained experimentally at 500 K [94] (left) and from MD at 150 K (right) for the planes (a) $[hk0]$ and (b) $[hk1.5]$. Notice that diffuse streaks are present in both planes, suggesting they are diffuse sheets orthogonal to the plane of the figure.

My interpretation of the diffuse sheets is the same as the one discussed in Sec. 6.2. The sheets which appear as {100} planes in reciprocal space (2D structure) appear to be caused by the presence of linear correlation (1D structure) in real space of atomic motions. Such linear correlation creates *uncorrelated linear chains* of atoms, predicted by the early theoretical model of Comes, Lambert and Guinier [25] which we discussed in Sec. 5.3.2. The polarizations of the chains belonging to one {100} plane are disordered, in the sense that they are differently oriented so that they average out to zero. Hence, when the spatial average of the chains polarization is zero, the phase is cubic.

This interpretation can sound quite premature at this point, because we only looked at the reciprocal space picture, not at the real space one. In order to demonstrate the presence of such linearly-correlated disorder, I show the real space picture of the dynamical displacements of $BaTiO_3$ in Sec. 7.8. The reader can either accept my interpretation for the time being and follow the flow of the chapter (which leads to the next section where I show the melting of the Slater TO mode) or skip the next section and jump directly to Sec. 7.8.

**Comments on the simulated diffuse scattering**

Besides the interpretation of the diffuse sheets, the other message of this section is this: it appears that the similarity between the experimental and simulated scattering cross sections that we saw in the figures is satisfactory. We were able to reproduce the diffuse $S_A$ and $S_O$ streaks qualitatively well. The fact that we can relate to experiments, at least qualitatively, is vital to us, because it gives credibility to our theoretical model of $BaTiO_3$. This does not mean, of course, that simulations are superior to experiments: experiments are "true" (although they insist on particular observables), and simulations are often so complicated to set up that one is forced to settle for a qualitative comparison. However, simulations do have an advantage with respect to experiments: they allow us to break up a quantity into its several components, whereas experiments most often are not able to disentangle each component. This will be clear in the next section, where I will show the dispersion of the Slater TO mode, and only of *that* mode, and we will be able to assess what it does during a phase transition in a material like $BaTiO_3$.

## 7.7 The melting of the Slater TO

In this section, I present what may be the most important result of this thesis. I use the NPT simulations to calculate the vibrational energy distribution of the Slater TO mode in $(\omega, \boldsymbol{k})$-space, $\tilde{\mathcal{E}}_{\text{Slater TO}}(\omega, \boldsymbol{k}; T)$. This quantity is defined in Eq. 2.37. I show that in approaching the R-C transition from below, at $T \lesssim T_C$ the Slater TO modes soften and in the process encounter the Last modes, which are very close in frequency. Then, the Slater modes burrow through the Last modes and lose much of their intensity to the 0-5 THz range, as they turn into an incipient Debye mode. At $T \geq T_C$, $\tilde{\mathcal{E}}_{\text{Slater TO}}(\omega, \boldsymbol{k}; T)$ is spread out dramatically from the regions of reciprocal spacetime where it was localized at $T < T_C$. It becomes very delocalized over a whole $\{100\}$ plane in $(\omega, \boldsymbol{k})$-space, appearing as a blotch. I do not interpret this as a phonon mode, and explain why. On the contrary, I interpret the delocalization of vibrational energy in $\boldsymbol{k}$-space as a result of loss of correlation in the atomic motions in real space, and the delocalization in $\omega$-space as a result of a large anharmonicity caused by the multiple-well potential energy surface. I will suggest that the fact that the PES retains the aspect of a multiple-well potential causes an inter-well hopping motion of Ti-O atoms, and provide a simplistic model for the understanding of this peculiar motion, before discussing it in more details in Sec. 7.8.

For what we have seen so far, it would be obviously interesting to look at the energy distribution in reciprocal spacetime of the Slater TO, $\tilde{\mathcal{E}}_{\text{Slater TO}}(\omega, \boldsymbol{k}; T)$. The details of the calculations can be found in Sec. 7.2.3. In brief, I project the atomic velocities onto the eigenvectors of the Slater branches. These branches are highlighted in red and blue in the lower right panel of Fig. 7.6, which shows the R and C phonon band structures with solid and broken lines, respectively, with imaginary frequencies shown as negative numbers. In red is one of the transverse Slater modes in the R phase, and in blue one of the transverse Slater modes in the C phase. To visualize the eigenvectors of one of the $\boldsymbol{k}$-points of the branches I chose for projecting the MD trajectories, the reader is referred to appendix E.

I chosen to show the spectra of these branches because they include one of the two transverse Slater eigenvectors, although we must keep in mind that there is a high degree of mode mixing

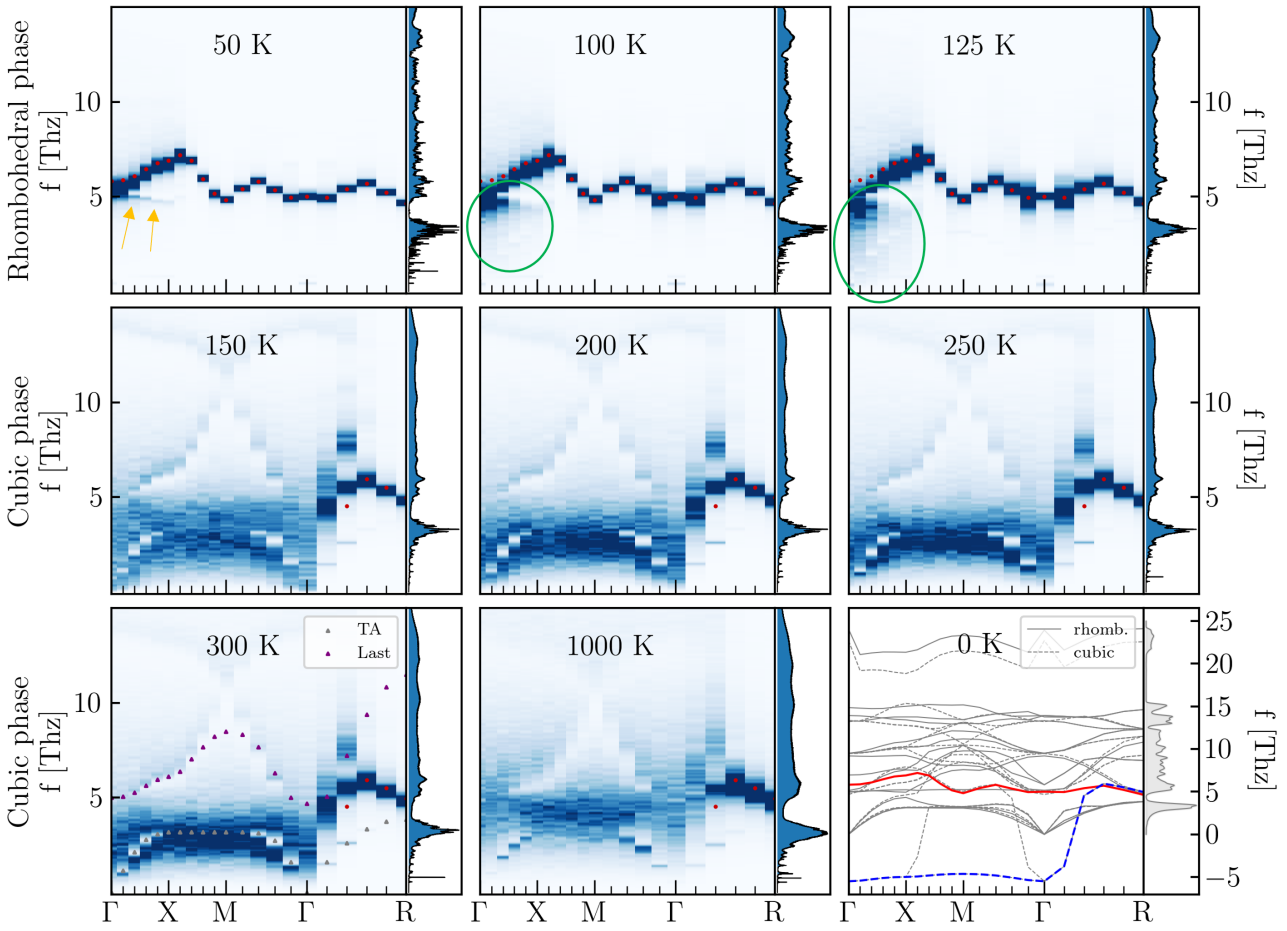



Figure 7.6: The distribution of vibrational energy, $\tilde{\mathcal{E}}(\omega, \boldsymbol{k})$ of $BaTiO_3$ along $\Gamma - X - M - \Gamma - R$ at several temperatures calculated after NPT simulations of a $10 \times 10 \times 10$ cell. In each panel, the right hand side plot is the plot of $\tilde{\mathcal{E}}(\omega) = \sum_{\boldsymbol{k}} \tilde{\mathcal{E}}(\omega, \boldsymbol{k})$. The Slater TO branches chosen in the rhombohedral (R) phase and cubic (C) phase are highlighted in the lower-right panel, which shows the harmonic band structures computed for the R and C unit cell. The red dots denote the harmonic phonon frequencies of the selected Slater branches for comparison with the limit of zero temperature. The upper panels show that in the R phase the Slater mode partially softens, burrows through the Last mode (orange arrow at 50 K), as explained in the text, and cedes its energy to the 0-5 THz range to create a Debye mode (green circles). The middle and lower panels show that the Slater mode forms an anomalous blotch in the C phase, which extends to the whole {100} plane in the Brillouin zone. The purple and grey triangles in the $T = 300$ K panel show the HA frequencies of the Last and TA modes, respectively. The presence of white spots whose frequencies coincide with the TA and Last modes suggests mixing with these modes, which is at the heart of the ferroelectric-ferroelastic coupling.

away from the BZ center, and therefore the eigenvectors at, say, $X$, might differ quite a lot from the eigenvectors at $\Gamma$. The reader interested in the whole dispersion, with the contribution of all the modes, or in the distribution of vibrational energy of the other modes (Last, Slater LO, etc.) will find other projections in appendix I.

In each panel of Fig. 7.6, a darker blue stands for a higher value of the $\tilde{\mathcal{E}}_{\text{Slater TO}}(\omega, \boldsymbol{k})$. The plots appear pixelated. The resolution in $\omega$-space and $\boldsymbol{k}$-space is defined by the duration of the simulation and the size of the MD supercell; these are $\approx 0.00255$ THz and $\frac{1}{10}$ of a reciprocal lattice vector ($= 0.0830$ bohr$^{-1}$), respectively. The red dots denote the harmonic phonon frequencies for comparison with the low temperature limit. The grey and purple triangles in the $T = 300$ K panel denote the frequencies of one TA branch and one Last TO branch.

### 7.7.1 The Slater TO at $T < T_C$

I now discuss the spectra presented in Fig. 7.6. The upper panels show the phonons in the R phase: at $T = 50$ K, the MD peaks are narrow and almost perfectly coincide with the red harmonic dots, signalling a low degree of anharmonicity; this should be expected because of the relatively low $T$. Nonetheless, I highlight with orange arrows in Fig. 7.6 an interesting feature: the Slater TO phonon in the $\Gamma - X$ path shows double peaks. This seems odd, at first, since the R harmonic eigenvectors should be a good, if not almost perfect, basis set for the displacement decomposition at low $T$, and therefore we would have expected each phonon spectrum to show a single peak. Within the approximation of perturbation theory, we also know that we would expect the phonon line shape to be a Lorentzian [15]. Of course, the eigenvectors at any $\boldsymbol{k}$-point form a complete set, and *any* choice of a complete and orthonormal set of eigenvectors would reproduce the full dispersion (I plot the full dispersion in Fig. I.1). However, since at 50 K the phase is rhombohedral, it is particularly interesting to see what happens to the *pure rhombohedral* Slater TO mode, i.e., whether the atomic dynamics can be effectively described by such eigenmotion. The presence of double peaks makes it easy to deduce that the harmonic Slater TO obtained with a rhombohedral supercell is not a perfect eigenmode of the atomic motions, even at 50 K when the phase is rhombohedral. What is happening to the Slater TO

mode?

**Mixing between modes: burrowing of the Slater mode through the Last mode**

Let us try to understand the reason for the double peaks. During its softening, which is barely starting to occur at 50 K but it happens more and more as $T$ is raised, the Slater mode encounters the Last mode. When a mode softens so that its peak position gets closer to another mode, their spectra overlap. However, if two modes have the same symmetry, namely, if they belong to the same IRREP (cf. Sec. 5.4), such overlap is strongly hindered.

This concept is the concept of band crossing and anti-crossing: two bands of different symmetries can cross harmlessly, but two modes of the same symmetry can mix, and their bands do not cross [38]; the bands appear to repel one another, and there is an anti crossing. This occurs because of interactions between motions along the eigenvectors of the two bands, which cause their eigenvectors to mix. When I say that two modes' eigenvectors mix, I always refer to their eigenvectors at $\Gamma$. So, if at $\boldsymbol{k} = \boldsymbol{q}$ there is mixing between mode 1 and mode 2, I mean that the eigenvectors of mode 1 and mode 2 at $\boldsymbol{q}$ are an admixture of the eigenvectors of mode 1 and mode 2 at $\boldsymbol{k} = \boldsymbol{0}$. The mixing of the bands' characters changes the modes' frequencies: it increases the frequency of one and lowers the frequency of the other, such that the dispersion of the bands change and they avoid crossing one another.

The inset of Fig. 7.7 shows the acoustic, Last, and Slater phonon bands obtained at the relaxed configuration of the atoms (R phase). In the band structure, I have put labels to indicate the IRREP of each mode. At $\Gamma$, the triplets of Lasts and Slaters are of the type $E + A_1$, where $E$ is doubly degenerate (cf. Sec. 5.4). The $\Gamma$ point represents the highest point group, that is, the $\boldsymbol{k}$-point which has the highest symmetry, because it is the limit $\boldsymbol{k} = \boldsymbol{0}$, and the translational symmetry is $Q(\boldsymbol{R}) = Q(\boldsymbol{R} + \boldsymbol{a})$, where $Q$ is any quantity and $\boldsymbol{a}$ is a lattice constant. Any finite $\boldsymbol{k}$ reduces the symmetry of the crystal when a phonon with such wavevector is activated. Hence, in order to classify the phonon modes away from $\Gamma$, one should consider the little group of each $\boldsymbol{k}$-point. A group theoretical analysis[1] shows that, in the R phase (space group $R3m$),

[1] consider the correlation table between the $C_{3v}$ and the $C_s$ point groups.

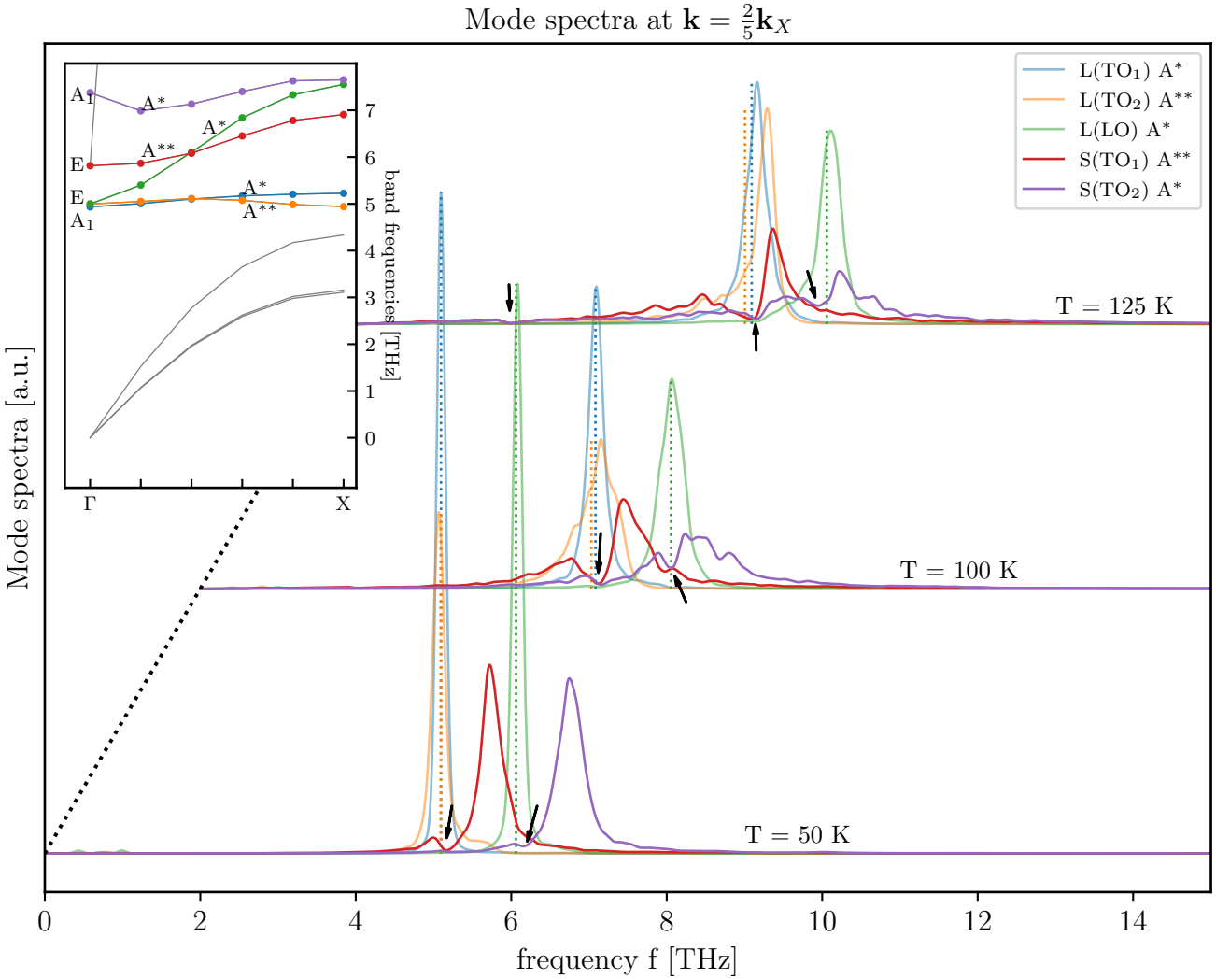



Figure 7.7: Phonon spectra at $\boldsymbol{k} = \frac{2}{5}\boldsymbol{q}_X$ in the R-C transition of the model of $BaTiO_3$ obtained from NPT simulations. Each mode is drawn with a different color, as is described in the legend. In the legend, S stands for Slater, L stands for Last, TO and LO stand for transverse optical and longitudinal optical, respectively, and $A^*$ and $A^{**}$ denote the group theoretcial IRREPs of the modes. In the inset is shown the band structure in the harmonic approximation, at the relaxed configuration of the atoms (R phase). The coloring scheme is consistent with the spectra. The vertical dotted lines denote the average positions of the spectra, as explained in the text. Each Slater mode burrows through the Last mode with which it shares the same IRREP. This causes the presence of dips, highlighted by black arrows, in the Slater spectra at frequencies corresponding to the average positions of the Last modes. The more the Slater modes burrow through the Last modes, the more their spectra are sucked up in the 0-5 THz range, and they broaden heavily in this range. At the same time, the Last modes broaden noticeably the more the burrowing occurs, and its average frequency downshifts.

the little group of a point $\boldsymbol{k}$ in the $\Gamma - X$ path reduces to $C_s$, and the modes' symmetries in this path change according to the little group. In particular, the phonons transform, from their IRREP at $\Gamma$, as $A_1 \to A^*$ and $E \to A^* + A^{**}$. Hence, the $A_1$ mode simply changes its character, and the $E$ modes split into two non degenerate modes. I have indicated the modes' IRREPs in the inset of Fig. 7.7 near each band. Note that one of the $E$ modes becomes a longitudinal mode ($A^*$) and that the Slater LO is at a much higher frequency because of the huge LO/TO splitting, and it does not interest us.

What is important to realize is that pairs of modes $A^*$-$A^{**}$ can cross, and in fact they do. At $\boldsymbol{k} = \frac{2}{5}\boldsymbol{k}_X$, the Last LO crosses the Slater $\mathrm{TO}_1$. At $\boldsymbol{k} = \frac{3}{5}\boldsymbol{k}_X$, the Last $\mathrm{TO}_1$ crosses the Last $\mathrm{TO}_2$. On the other hand, modes of the same symmetry, $A^*$-$A^*$ and $A^{**}$-$A^{**}$, repel each other, and cannot cross. Moreover, when they get closer to each other, like the Last LO and Slater $\mathrm{TO}_2$ at $\boldsymbol{k} = \boldsymbol{k}_X$, there is where interaction is maximum and their eigenvectors mix the most.

Let us now look Fig. 7.7. It shows the spectra of the Last and Slater modes at $\boldsymbol{k} = \frac{2}{5}\boldsymbol{k}_X$ in the R-C transition. I chose this point because $\tilde{\mathcal{E}}_{\text{Slater TO}}(\omega, \boldsymbol{k}; T = 50\text{ K})$ shows double peaks for the Slater spectrum, as we learned from Fig. 7.6. The vertical dotted lines are important: they denote the average frequency of the Last modes when such modes' spectra are considered as probability distributions. In other words, I took each spectrum $\tilde{\mathcal{E}}_\nu(\omega, \boldsymbol{k} = \frac{2}{5}\boldsymbol{k}_X)$, I normalized it to 1 obtaining $p_\nu(\omega)$, and I have calculated the value $\bar{\omega}_\nu = \int d\omega p_\nu(\omega)\omega$. These average frequencies would correspond to the peak positions of the spectra if these were $\delta$-functions or Lorentzians or Gaussians. However, because the Last modes' spectra clearly do not resemble these functions, I preferred calculating the average frequencies, rather than fitting the spectra to Lorentzians and plotting their peak positions. In the following, I will refer to them as average frequencies.

Let us start off with the spectrum at $T = 50$ K. I will use Slater $\mathrm{TO}_1$ and Slater $\mathrm{TO}_2$ to denote the two transverse Slater modes; these are indicated with a red and purple line in Fig. 7.7. The Slater $\mathrm{TO}_1$ is an $A^{**}$ mode and can mix with another $A^{**}$ mode, like the Last $\mathrm{TO}_2$. As a result of this mixing, the Slater $\mathrm{TO}_1$ clearly mainfests a secondary peak, at around 5 THz, namely at frequencies very near and lower than the dip indicated in Fig. 7.7 by a black arrow.

The frequency of this dip coincides with the average frequency of the Last $TO_2$ mode (and of the Last $TO_1$, since they happen to be nearly degenerate). The spectral dip happens because the Slater $TO_1$ and Last $TO_2$ belong to the same IRREP. Hence, the Slater $TO_1$ softens, but during its softening it encounters the Last $TO_2$, with which it is impeded to overlap, because they have the same symmetry. Then, the only chance for the Slater mode to continue its softening is that it burrows through the Last mode. There is no other way, because the Slater $TO_1$ mode cannot pass unharmed through the Last $TO_2$ mode. Let us focus on the Slater $TO_2$ now: this is an $A^*$ mode, and can mix with the other $A^*$ modes, namely, the Last LO and the Last $TO_1$. At $T = 50$ K, the Last $TO_1$ is too far away from it in frequency for the overlap to occur. However, the Last LO is not too far away. Hence, there is a incipient burrowing of the Slater $TO_2$ through the Last LO. This is indicated in Fig. 7.7 by the black arrow at $\approx 6$ THz. These two secondary peaks which form for the two Slater TO modes are peaks highlighted by orange arrows in Fig. 7.6.

The burrowing results in the presence of a dip in the spectrum of the Slater mode in the correspondence of the average frequency of the Last mode with which it mixes, with the consequential presence of two peaks for the Slater mode. The burrowing, in fact, splits the modes' spectra into two parts, one corresponding to the original spectrum of the excitation, and one corresponding to the burrowed spectrum. This happens because the original (pure) Slater mode, when it overlaps with the Last modes and mixes with them, changes its eigenvector becoming an admixture of the two. As a consequence of this, there is no distinct peak for the pure Slater mode anymore.

If we now raise the temperature, we can observe what kind of dramatic effects the burrowing has with respect to the phonon modes. At $T = 100$ K, the portion of the Slater $TO_1$ spectrum which has burrowed through the Last $TO_2$ has increased. At the same time, the burrowed portion of the Slater $TO_2$ mode has increased. Note that the lower-frequency burrowed portion of the Slater $TO_2$ mode (purple line) lies at frequencies close to the peak position of the Last $TO_1$, hence a second burrowing occurs. This is indicated by the first black arrow on the left in the $T = 100$ K spectrum in Fig. 7.7.

Importantly, the burrowing does not come without consequences for the Last modes as well. In fact, their line shapes broaden considerably after the burrowing. At $T = 100$ K, the Last $TO_2$ seems to be the one which has been impacted the most, as it appears very dampened. This is because the amount of burrowing which has occurred through it is large at this $T$. A similar broadening is observed for the Last $TO_1$. Moreover, note that the average frequency of the Last $TO_2$ (orange dotted line) downshifts noticeably, and it downshifts more than the Last $TO_1$ (dotted blue line). The reason for plotting the average frequencies, rather than the peak positions, should be clear now. A non negligible portion of the spectrum of the Last mode, in fact, is in a way drawn to lower frequencies by the burrowing of the Slater mode, and the presence of this portion of the spectrum moves its mean position to lower frequencies as well. The broadening and shifting of the Last modes when the burrowing occurs should be caused by the mixing of these modes with the Slater modes. This means that, at $T = 125$ K, the excitations which happen at $\boldsymbol{k} = \frac{2}{5}\boldsymbol{k}_X$ (and in all $\boldsymbol{k}$-points along $\Gamma - X$) are a mixture of *pure* Slaters and *pure* Lasts. Hence, the *pure* Last mode gets some degree of character of the Slater mode, and its spectrum broadens.

Interestingly, at $T = 125$ K the burrowed portion of the Slater modes spreads out in frequency so much that it is difficult to assign a single peak to it. It is difficult because the burrowed spectrum is very spread out in $\omega$-space, meaning that the linewidth is huge and quasiparticle theory breaks down; furthermore, it is difficult because there are small remnants of the original Slater peaks at higher frequencies. Note also that at this $T$ another interference effect is starting to form, this time with a TA mode. This is indicated in Fig. 7.7 with the first black arrow on the left hand side in the $T = 125$ K spectrum.

Inelastic neutron scattering experiments found a similar interference effect between the soft mode and the TA [56] (see Fig. 6.7). We shall talk about the interference TA-Slater in the next section. However, the circumstance that there is mixing between the Last and Slater modes is often not taken into account by some IR spectroscopists, who tend to consider the TO soft mode as "isolated" [99]. Other IR spectroscopists calculated that the interaction is largest with the Axe modes [62, 110, 19, 107].

Even at the very beginning of its softening, the Slater modes overlap with the Last modes. When two excitations overlap, mixing occurs between them. This means that neither one of the two modes are pure Slater or pure Last modes anymore, but they are of mixed character. I used the example of two bands repelling each other because it is the same logic. In the case of $BaTiO_3$, the two bands *are forced* to cross, because one of them is softening, hence their eigenvectors mix. It is important to realize that the requirement for the mixing of two excitations is not only that they share the same symmetry: in addition to this, their spectra also need to overlap. This means that they also need to share *the same time scale*. Two excitations which can couple but which have very different time scales do not mix noticeably. The concept of, for example, the Born-Oppenheimer approximation, which allows to decouple the electronic and nuclear degrees of freedom of the atomistic wavefunction, can be applied to our case as well. Hence, two modes of very different frequencies can be thought of being adiabatically decoupled, as we saw in Sec. 3.5.2. N.B.: this does not mean that two excitations of different frequencies cannot interact. Interaction and mixing are two different concepts, which should not be confused. Electrons can interact with phonons and phonons can interact *adiabatically* with other phonons even if they have very different frequencies (like the acoustic-LO interaction described in Sec. 3.5.2), but they cannot mix, to a first approximation.

I also highlight that this interpretation–that when one mode overlaps with another it mixes strongly with it–could be extended to other soft-mode materials, but only inasmuch as the soft mode encounters, during its softening or partial softening, another lower-energy mode. In the case of perovskites $ABO_3$, depending on the bond strengths and the masses of the A cation, the Last mode can be at a higher or lower frequencies than the Slater mode. For example, when the A cation has a relatively big mass, then the Last modes frequencies can be lower than the Slater modes ones. This is because the Last mode involves the displacement of the A cations against the $BO_3$ octahedra, and when an atom with a big mass is involved, the phonon frequency is lower. In $BaTiO_3$, a material whose phase transitions have order-disorder character, as we have learned in Ch. 6, the Last mode is at a lower frequency, but this is not the case for other perovskites. For example, in $SrTiO_3$, which is a material thought to be displacive [147], there are no optical modes at $\Gamma$ whose frequencies are softer than its soft mode (see e.g. the INS

spectra of Fig. 6.5).

**Summary of the behaviour of the Slater mode in the R-C transition**

Let us now summarize what the Slater mode is going through.

The Slater mode is softening, as thermal disorder reduces the depths of the off-center wells in each primitive unit cell's local PES; this occurs because disorder among primitive cells' dipole moments flattens each cell's PES [43]. Moreover, thermal fluctuations increase, so that the probability that the atoms overcome the energy barrier of the local PES increase. The first feature softens the Slater spectrum, the second feature broadens it.

During this process, the Slater mode encounters the Last mode, burrows through it, increases the Last mode's broadening because it mixes with it, and then its burrowed part is sucked up in the 0-5 THz window of the spectrum. With respect to the emergence of a Debye mode, we can now draw a reasonable picture for what is happening. The Slater mode "cedes" part of its spectrum to the 0-5 THz range, *thereby creating a Debye mode*. Then, we expect the Debye mode to share with the Slater mode the same eigenvector.

In a way, we forecast this behaviour from the IR spectra of Fig. 7.2, where we saw that the more the Debye peak arises, the more the Slater mode loses intensity. There, the progressive emergence of a Debye mode seemed *consequent* to the shrinking of the Slater mode. Here, we can make this statement with more confidence, since we have the full energy distribution of the Slater TO mode in reciprocal spacetime: the Slater mode's energy is "taken away" from the regions of ($\omega$,$\boldsymbol{k}$)-space where it was localized in the R phase, and flows into other regions of frequency, the 0-5 THz range, to form a Debye mode.

This behaviour is clearly not the behaviour of an ideal soft mode, which we discussed in Sec. 5.3.1. In fact: (i) the softening is not complete, since there is no clearly identifiable phonon peak whose frequency approaches zero, and (ii) the vibrational energy distribution at $T = 100$ K and $T = 125$ K also shows a non-negligible activity in the frequency range 0-5 THz, highlighted with green circles in Fig. 7.6.

### 7.7.2 The Slater TO at $T \geq T_C$

Let us look at Fig. 7.6 again and discuss the phonon spectra in the cubic phase. What we witness in the C phase is something dramatic: we observe a "blotch" in the calculated energy distribution $\tilde{\mathcal{E}}_{\text{Slater TO}}(\omega, \boldsymbol{k}; T)$. The blotch is energy that is strongly smeared out both in $\omega$-space and in $\boldsymbol{k}$-space. The abnormal broadening along the frequency axis suggests that the PES remains a multiple-well potential, which dampens the atomic motions and hence broadens the spectral lines in $\omega$-space. The abnormal broadening in $\boldsymbol{k}$-space is remarkable: it extends all the way to the $X$ and $M$ points. The consequence is the presence of a *diffuse* energy density in the whole BZ $[hk0]$ plane. The presence of vibrational energy at low frequencies away from $\Gamma$ was confirmed by all the inelastic neutron scattering experiments [56, 119, 118, 148], which I discussed in Sec. 6.3. Moreover, the fact that energy is spread out over $\{100\}$ planes in reciprocal space agrees with the results of X-ray diffuse scattering experiments [25, 64, 103, 94], which we saw in Sec. 6.2

#### The mixing of the Slater TO mode with TA modes

Before trying to interpret the blotch, it is interesting to notice the presence of white spots in $\tilde{\mathcal{E}}_{\text{Slater TO}}(\omega, \boldsymbol{k})$ in the C phase. The white spots stand exactly at the frequencies of the peak positions of the transverse acoustic (TA) spectra. This can be understood by looking at the TA modes' frequencies calculated in the HA drawn with grey symbols in the $T = 300$ K panel of Fig. 7.6.

The lack of intensity of the Slater TO spectra at these spots means that there is no overlap, or limited overlap, between the spectra of the Slater modes and the spectra of the TA modes. Let us then try to understand what the white spots mean.

Recall what we have said about the Slater and Last modes mixing: two modes belonging to the same IRREP can mix, or "interact". When the C phase is realized, the space group changes, and the symmetries of the normal modes of vibrations change. In the cubic phase (space group $Pm\bar{3}m$), the point group at the $\Gamma$ point is $O_h$, and the $F_{1u}$ and $F_{2u}$ modes are all triply

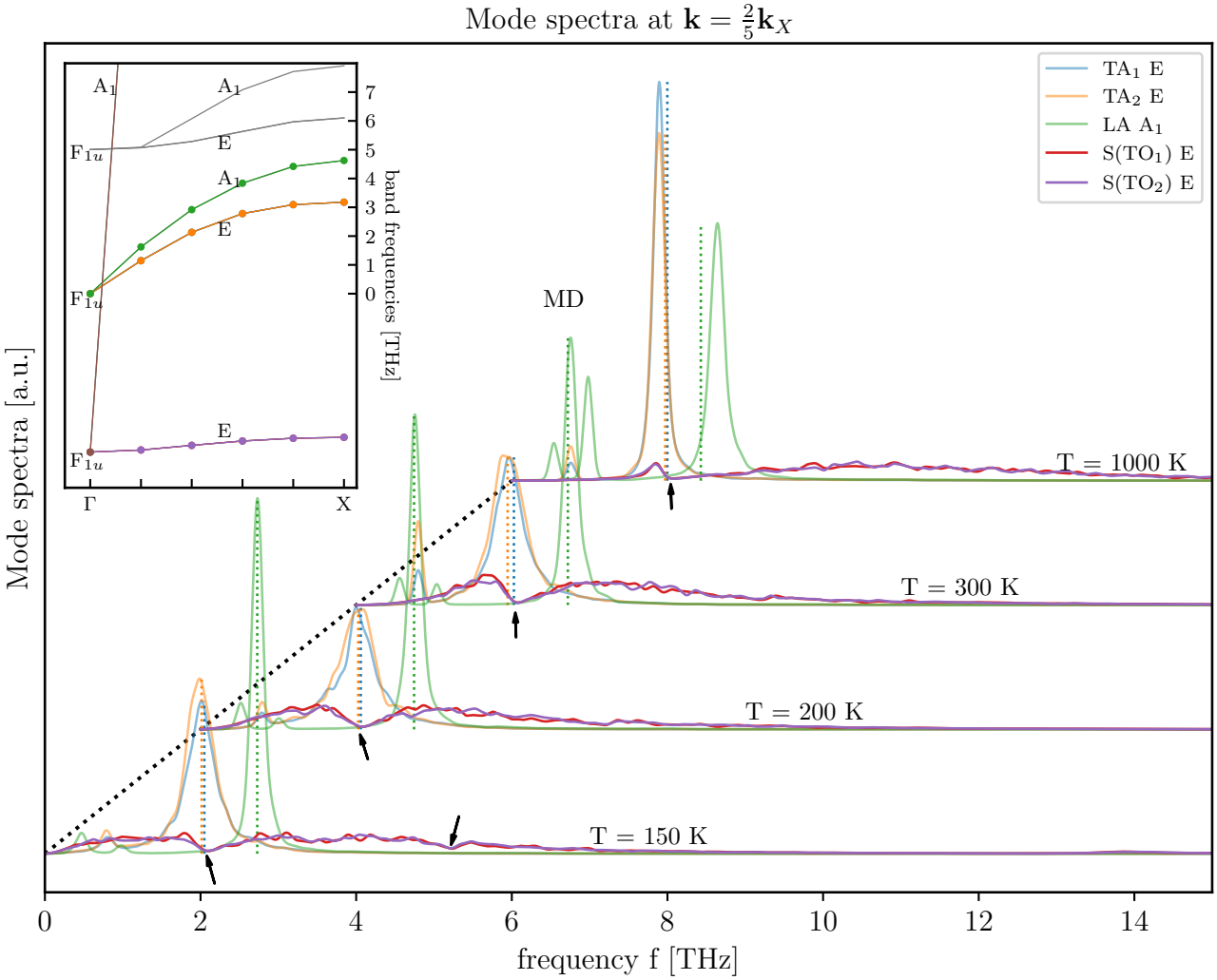



Figure 7.8: Phonon spectra at $\boldsymbol{k} = \frac{2}{5}\boldsymbol{q}_X$ in the C phase of the model of $BaTiO_3$ obtained from NPT simulations. Each mode is drawn with a different color, as is described in the legend. In the legend, S stands for Slater, and TA and LA stand for transverse acoustic and longitudinal acoustic, respectively, and $A_1$ and $E$ denote the group theoretcial IRREPs of the modes. The peaks denoted 'MD' are due to the fluctuations of the volume caused by the barostat, as explained in Sec. 7.5. In the inset is shown the band structure in the harmonic approximation, with the structure taken as the C phase. The coloring scheme is consistent with the spectra. The vertical dotted lines denote the average positions of the spectra, as explained in the text. The Slater mode is dramatically spread out in frequency, and the mixing with the TAs causes the interference dips indicated by the black arrows. The burrowing of the blotch through the TAs causes a large broadening of the latter modes. Such broadening is very non monotonic: it is large at $T \gtrsim 150$ K and small at $T = 1000$ K. the broadening of the LA mode is small throughout all temperatures.

degenerate. Now consider the $\Gamma - X$ path in reciprocal space: the little group of a point $\boldsymbol{q}$ in this path reduces to $C_{4v}$, and the modes split so that $F_{1u} \to A_1 + E$. Hence, along the $\Gamma - X$ path, for each triplet of phonons there are two degenerate modes, which are polarized orthogonally to $\boldsymbol{q}$ and hence correspond to the TAs or TOs, and one mode polarized along $\boldsymbol{q}$, which correspond to LAs or LOs. The band structure in the inset of Fig. 7.8 was computed with a C structure with lattice constant $a = 4$ Å, and the modes' IRREPs are written near each band. The Slater modes have imaginary frequencies, which are plotted as negative numbers. Modes with the same symmetry, like $E$-$E$ or $A_1$-$A_1$, can mix, and modes with different symmetries, $E$-$A_1$ cannot. Hence, the Slater modes can mix with the TA modes, because they belong to the same IRREP.

In the dramatic case where the spectrum of the blotch occurs *at the same frequencies of the TA*, the overlap between spectra is inevitable, but is forbidden by symmetry. Hence the presence of the white spots in the blotch. Fig. 7.8 shows the spectra of the TAs, LA and of the two Slater modes, S($TO_1$) and S($TO_2$) at $\boldsymbol{k} = \frac{2}{5}\boldsymbol{k}_X$. The interference dips (indicated in Fig. 7.8 by black arrows) which we observed in the previous section are present in the C phase in the correspondence of the TA average frequencies, and in the correspondence of the Last frequencies. These are very similar to the dips which were found at 10 mev between the soft peak and the TA peak in neutron scattering experiments by Harada *et al.* [56], which I reported in Fig. 6.7a, and which the authors called "interference effect" [56]. It might be now useful, in order to compare experiments and simulations, to look back at Fig. 6.7, but in doing so the reader should be aware that the spectra provided in Fig. 6.7b are convolved to the Bose-Einstein distribution, in order to be compared with neutron scattering spectra.

Note that, in Fig. 7.8, additional acoustic peaks are present in the frequency range 0-2 THz. These are caused by the barostat, and are denoted 'MD' in the figure. Note also that we have said in the last section that the burrowing of the Slater mode through the Last mode makes the latter one broaden in frequency space. For the same reason, the burrowing of the blotch through the TAs makes the line shape of the TAs broaden. The linewidth of the TAs is very non monotonic with $T$: it is high at $T \gtrsim T_C$ but much lower at $T \gg T_C$. This anomalous behaviour will be further investigated in Fig. 8.3.

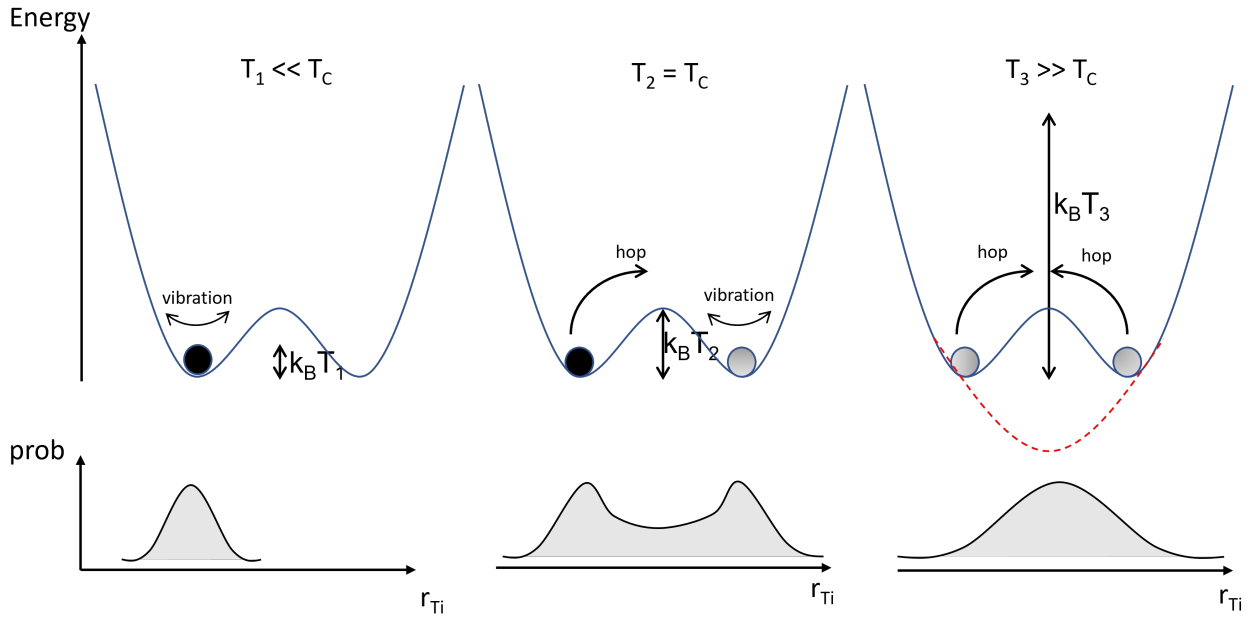



Figure 7.9: Schematic of the different dynamical regimes that occur to a disordered model of $BaTiO_3$ as $T$ is varied. The motion of only *one titanium* (the black bead) in only *one unit cell* is considered. The $x$ axis corresponds to one direction of space. In the top panels the energy surface is plotted against the Ti displacement, and is assumed to have the form of a double well. In the bottom panels, I plot the expected probability distribution of the Ti position. The double arrows $\leftrightarrow$ indicate the scale of the thermal energy, $k_BT$,at each temperature. The figure shows the three different dynamical *regimes* that can happen. At $T_1 \ll T_C$, the motion is purely vibrational about one minimum of the potential. At $T = T_C$, the atom can overcome the barrier by hopping to the other minimum, and the vibrational and hopping motion coexist. At $T \gg T_C$, the motion is effectively a vibration about the center of the cell. The frequency of such vibration is proportional to the curvature of the broken red line.

Just as two modes of the same IRREP can interact because their eigenvectors can mix, so can the blotch and the TA. What does it mean that the blotch and the TA mix? It means that the dynamical motions they represent is affected by one another. At finite $T$, one cannot excite a TA mode without producing an effect on the optical vibration represented by the blotch, and vice versa. In other words, the presence of white spots suggests coupling between the motion represented by the blotch and transverse acoustic waves travelling through the crystal. In the long wavelength limit, acoustic modes represent elastic waves. So, the blotch-TA coupling mechanism is consistent with the ferroelectric-ferroelastic coupling of $BaTiO_3$. I will dedicate a section to ferroelasticity in the next chapter, in Sec. 8.2.

**My interpretation of the blotch: the model I propose**

We have discussed the white spots present in the blotch, and their possible meaning. Let us now try to interpret what kind of motion the blotch represents. Note that the results I show in Fig. 7.6 are somewhat similar to the calculation of Pasciak *et al.* [94]; however, my interpretation differs quite a lot from theirs. I don't consider the anomalous energy density $\tilde{\mathcal{E}}_{\text{Slater TO}}(\omega, \boldsymbol{k})$ a soft phonon, but a proper Debye mode. To be more specific, I interpet it as a result of the combination of hopping motion and vibrational motion of Ti-O atoms which happens in an uncorrelated way from one linear chain to another. This particular atomic motion produces disorder, i.e. a loss of correlation in real space for the atomic displacements, and makes the Slater TO branch melt. This interpretation will be explained in this and the next sections.

Before justifying why I do not consider it a soft phonon, I now discuss what kind of dynamical model I propose to explain the anomalous power spectrum which we saw in Fig. 7.6. Let us consider the drawings in Fig. 7.9: these offer a simplistic and schematic view of the dynamics of a Ti atom within one unit cell. In the top part of the figure, I plot the double well potential energy surface (PES) against the displacement of the Ti atom with a blue line, under the simplistic assumption that the PES does not change with $T$, and that the height of the energy barrier $\Delta U$ is large compared to the strength of the interactions between the atom and its neighbours. These two assumptions are simplistic, because Fallon [43] has shown that the energy barrier is not so high when the PES is plotted against the displacement of only the Ti atom, and that the PES does change as a result of the surrounding unit cells being polarized. In fact, Fallon has shown that the potential energy barrier flattens even further at $T > T_C$ because the disorder among the neighbouring cells' dipoles causes the magnitude of the negative curvature which forms the double well PES to reduce [43]. The other, very simplistic assumption is that the atom is isolated, in the sense that interactions with its neighbours are not large; we shall relax this approximation later in this chapter. In the bottom part of the figure, I plot the schematic distribution of Ti positions which I expect from an MD run in each case. The double arrows $\leftrightarrow$ indicate the scale of the thermal energy in the three different situations.

In the model I am proposing, I focus on only the Ti atom, for simplicity, and neglect the O

and Ba atoms. This is surely inaccurate. In fact, the Slater mode, which is the mode whose spectrum is plotted in Fig. 7.6, involves the displacement of Ti *against* the O octahedron. Hence, the whole dynamics involves not only the Ti atom, as I am going to describe, but involves a motion along the Slater eigenvector. Hence, whenever I say that the Ti vibrates, I mean that Ti-O vibrate against each other. And whenever I say that the Ti hops, I mean that the Ti displaces and at the same time the O cage displaces in the opposite direction. Hence, not only there is a displacement of Ti atom, $\delta_{\text{Ti}}$, but a displacement of the Ti *against* the O atom, $\delta_{\text{Ti-O}}$. Another way to see this is to consider that the cell displacements along optical eigenvectors can be thought of the modulation of the cells' dipoles. It is such dipoles which I refer to, even though I am only considering the Ti atom.

At $T = T_1 \ll T_C$, the magnitude of the thermal energy per degree of freedom is $\langle E_i \rangle \approx k_B T \ll \Delta U$, and there is a limited chance $\sim \exp(-\Delta U / k_B T)$ that the atom will overcome the potential barrier. Hence, the probability that the atoms escapes from the well in which it sits at mechanical equilibrium is just too little, and the titanium will be practically "stuck" in a well. The dynamics is purely vibrational: the Ti atom vibrates about this well. The probability of finding it in this well is very high, and the probability of finding it in the other well is almost zero.

At $T = T_2 = T_C$, the titanium hops to the other well, because $k_B T \sim \Delta U$. However, the event of hopping happens only with a certain probability, hence with a certain frequency. During the time between an hopping event and a subsequent one, the atom sits on either well with high probability, and its motion is vibrational about that well. Hence, the vibrational and hopping motions coexist. The motion is dampened because every time the atom encounters the barrier, it is forced to slow down. The positional distribution of the Ti atom will feature two peaks, one at the one well and one at the other well. Note, however, that the distribution is not zero at the midpoint. In fact, the slowing-down effect of the energy barrier lowers the velocity of the atom at this point, and is proportional to the height of the barrier. Hence, we expect a non zero probability distribution at the center of the cell, or even a peak, depending on the height of the barrier.

At $T = T_3 \gg T_C$, the scale of the thermal energy per atom is $k_B T \gg \Delta U$, and atoms do not "experience" an energy barrier anymore. In this case, the energy surface has *effectively* become quadratic. It is not quadratic, because there remains an energy barrier, but this barrier is just too small, with respect to $k_B T$, for the atom to notice it. The Ti atom, in this case, effectively (approximately) vibrates according to the overall curvature drawn with a broken red line in Fig. 7.9. The positional distribution broadens up significantly, because the amplitude of the vibration includes a larger amount of space, with respect to the case $T = T_1 \ll T_C$.

Let us now check this model for consistency with the spectra of Fig. 7.6. At $T \ll T_C$, we expect only a vibration. Hence, we expect the vibrational energy distribution $\tilde{\mathcal{E}}(\omega, \boldsymbol{k}; T \ll T_C)$ to be very localized around the points $(\omega_{\boldsymbol{q}\nu}, \boldsymbol{q})$ which represent lattice vibrations commensurate with the MD supercell. This is consistent with the $T = 50$ K plot of Fig. 7.6. The presence of double peaks for the Slater mode, which happen when it burrows through the Last mode, suggests that the Slater mode is softening as a result of the flattening of the energy barrier, which decreases the curvature of the potential's single wells. This also demonstrates that the model I propose in Fig. 7.9 is simplistic, because the PES does not change with $T$ in that model. At $T \leq T_C$ or at $T \approx T_C$, we expect both vibrational *and* hopping motion to coexist. This is consistent with the $T = 125$ K plot of Fig. 7.7, where the Slater excitation is composed of the original peak and the burrowed spectrum. The original peak at higher frequencies should be the feature of the intra-well vibration, and the highly damped burrowed spectrum should be the feature of the inter-well hopping motion. Such inter-well motion should be highly dampened because of the large slowing down effect caused by the energy barrier. For this reason, the $\tilde{\mathcal{E}}(\omega, \boldsymbol{k}; T \approx T_C)$ must be very delocalized in $\omega$-space. Moreover, because the hoppings of Ti atoms are very uncorrelated from one unit cell to another in our simplistic model, there is a delocalization of the energy in $\boldsymbol{k}$-space. Atoms fail to move altogether in form of plane waves, and $\tilde{\mathcal{E}}(\omega, \boldsymbol{k})$ spreads out in reciprocal space. At $T \gg T_C$, the hopping motion *effectively* mimics a vibration about the center of the unit cell. This *effective* vibration follows the overall curvature denoted with a broken red line in Fig. 7.9. Hence, the phononic behaviour is recovered: at high $T$, the Ti effectively vibrates about the center of the cell. The Slater branch will have a relatively large broadening, because it is still a damped mode, but a broadening which is smaller than

the case $T \approx T_C$.

This counter-intuitive behaviour–that a phonon mode becomes less broadened at increasing $T$–is caused by the *different dynamical regimes* which occur at different $T$s. Note also that the overall curvature at $T \gg T_C$ is smaller than the curvature at the bottom of each of the two basins of the wells, hence the phonon spectrum $\tilde{\mathcal{E}}(\omega, \boldsymbol{k}; T \gg T_C)$ will have peaks at lower frequencies with respect to the case $T \ll T_C$. In other words, the Slater TO at high $T$s cannot be harder than the Slater TO at $T \ll T_C$.

The Slater TO at high $T$s may produce a smaller standard deviation of the Ti distribution than the case $T = T_C$. To see this, compare the distributions at $T = T_C$ and $T \gg T_C$ in Fig. 7.9. If this is the case, then we expect the Slater TO to harden with increasing $T - T_C$. In fact, the variance of the atomic displacement distribution is the sum of the squared amplitudes of the phonon modes. These are inversely proportional to the frequency of the oscillations [129]; if the amplitude is smaller, it means that a phonon is hardening. Hence, we expect the spectrum of $\tilde{\mathcal{E}}_{\text{Slater TO}}(\omega, \boldsymbol{k})$ to harden with increasing $T - T_C$. In other words, the atoms get a smaller and smaller slowing down from the energy barrier as $T$ increases, and the time between two consecutive hoppings diminishes. Then, the time needed to complete a hopping cycle decreases with $T$, hence the hopping motion becomes a vibrational motion with an increasing frequency. This is consistent with the hardening of the blotch which we observe in Fig. 7.6 at increasing $T - T_C$ in the C phase.

The model I just discussed, as I stated in the beginning of this section, is simplistic. Once again, it is simplistic because it assumes that the PES does not change with $T$, and because it assumes that $\Delta U$ is large, and because the displacement of the Ti atom within each unit cell is uncorrelated with its neighbours. The model is admittedly similar to the model of order-disorder of Stern [126], which is illustrated in Fig. 5.5. The "true" dynamics of the atoms in $BaTiO_3$ is surely not that simple. For example, we discussed, in Ch. 6 and in Sec. 7.6 (and we shall further discuss this in Sec. 7.8), the tendency of Ti displacements to align along $\langle 100 \rangle$ axes to form chains. In the model I presented, each atom is independent of each other and there is no chain-like correlation between them. All this said, this model serves as a reference

model for the understanding of what follows.

**Reasons to believe that the blotch is not a phonon**

I now justify why I think that the blotch in $\tilde{\mathcal{E}}_{\text{Slater TO}}(\omega, \boldsymbol{k})$ in the PE phase is not a phonon, in the sense that it is not a soft mode with a precise frequency $\omega_{\boldsymbol{q}\nu}$ and wavevector $\boldsymbol{q}$.

First of all, the blotch appears very broad in $\omega$-space; if we were looking at a phonon branch, we would be witnessing an almost flat phonon dispersion of a frequency $\tilde{f} \approx 2.5$ THz and a linewidth $\tilde{\Gamma}$ comparable to that value. The magnitude of this linewidth would contradict the concept of phonon quasiparticles, for which $\tilde{\Gamma}$ should be much smaller than $\tilde{f}$ [88]. The fact that the Slater branch is largely spread out in frequency space is a strong indication that the PES retains the aspect of a multiple-well potential. In fact, if the PES has multiple wells, the energy barrier placed at the center of the cell induces a relatively large slowing down to the motion of Ti-O atoms, thereby damping the motion along a Slater eigenvector. In one direction, a double-well potential can be written as $V(x) = ax^2 + bx^4$, where $a$ is negative and therefore the frequency of the motion along a Slater eigenvector is imaginary. Perturbation theory *fails in this case*, because there is no bound state for the vibration of the atoms, and this forbids the calculation of the phonon self energy [42]. Hence, the large broadening of the Slater branch is more likely an effect of the multiple-well character of the PES rather then an effect of small anharmonicity coming from cubic or quartic terms in the potential expansion.

Secondly, a look at $\tilde{\mathcal{E}}_{\text{Slater TO}}(\omega, \boldsymbol{k})$ shows that the blotch appears clearly to emerge at $100 \leq T \leq 125$ K in the frequency range 0-5 THz and to harden at $T \geq 150$ K, and this behaviour closely reflects the trend observed for the Debye peak in the IR spectra of Fig. 7.2. We discussed the meaning of Debye mode in Sec. 5.3.4: the Debye mode is widely interpreted as the dynamical result of the inter-well hopping of Ti atoms [62], so it seems natural to interpret the blotch as a proper Debye mode.

Thirdly, such energy density appears very much smeared out in $\boldsymbol{k}$-space. Of course, a phonon branch can in principle be flat or almost flat: this would represent a set of standing waves of a

certain frequency and different wavelenghts, and can in principle be the case of optical phonon bands. Just as an electronic flat band is known to give rise to localized electronic states, a phonon flat band means localized vibrations, i.e. atomic vibrations that are not correlated in space. However, the energy distribution we observe is spread out *over a whole* $\{100\}$ *plane in the BZ*, and not over a line in reciprocal space, like a flat band. Recall that $\tilde{\mathcal{E}}(\omega, \boldsymbol{k})$ is related to the VVCF by a Fourier transform. Hence, anything localized in $\boldsymbol{k}$-space is delocalized in real space (through the plane wave $\exp(i\boldsymbol{k}\cdot\boldsymbol{r})$), and vice versa, if anything is delocalized in $\boldsymbol{k}$-space then it is localized in real space, with the consequence of a loss of long-range order in real space. A loss of long-range order means that the optical atomic motions which happen in the 0-5 THz range are poorly described by wave-like collective motion of planes of atoms. There seems to happen an almost complete decoherence of the Slater TO lattice waves travelling through the crystal.

We can say that the whole Slater TO phonon branch, which is dispersive in the $T \to 0$ limit, has "melted" at $T \approx T_C$. The use of such language is figurative but effective. In fact, the loss of correlation in real space contradicts *in toto* the concept of phonons: plane waves with an infinite correlation time and length. It also contradicts the concept of phonon *quasi*particles: plane waves with a finite correlation time and infinite correlation length. We can say that phonon theory breaks down for the Slater mode at $T \gtrsim T_C$. The breakdown of phonon theory shouldn't be too surprising in the case we are discussing: the presence of imaginary frequencies for the phonon bands when the harmonic calculation is performed in the C phase (see bottom right plot of Fig. 7.6 or Fig. E.3 for an enlarged version) means that the curvature of the potential energy surface at the center of each cell is negative. Now, the Taylor expansion about the equilibrium positions, upon which the HA is based, is useless if atoms do not perform small-amplitude oscillations or if they are moving over energy barriers and between minima. This does not necessarily means that *all* materials which have imaginary bands manifest phonon melting at $T \sim T_C$. In an ideal displacive material, the free energy surface rearranges dynamically so that long-range order is established even at finite $T$. As we saw in in Sec. 5.3.3, and in particular in Fig. 5.5, the collective motion in a displacive material is characterized by a double-well potential in the FE phase and a single-well potential in the PE phase. On the other hand, this

is not the case of order-disorder materials, for which the long-range order is destroyed in the high $T$ phase. But how can this happen?

I showed in the chapter dedicated to MgO, Sec. 3.4.1, that when a material melts the phonon dispersion loses structure completely, resulting in a continuous "sea", and no bands at all can be identified. I here would like to establish an analogy between what we saw for MgO in Fig. 3.5 at temperatures close to its melting point, $T \sim T_m$, and the blotch we observe at $T \gtrsim T_C$ for $BaTiO_3$ in Fig. 7.6. That is, the melting of phonon bands. Only, for MgO the melting happens to all branches at $T \sim T_m$, and produces the liquid phase, here the melting concerns just the Slater modes, and produces a disordered PE phase. My interpretation of the blotch is similar to the interpretation of the vibrational spectrum in liquid MgO: the energy gets dispersed in ($\omega$,$\boldsymbol{k}$)-space because the atomic motions become more localized in time and space.

There is one last thing to notice. In $\boldsymbol{k}$-space, the blotch is spread out on a $\Gamma - X$ path *and* on a $\Gamma - M$ path, hence it is spread out over a $\{100\}$ plane in reciprocal space. Recall that the total scattering cross section is the integral over the phonon frequencies of a const-$\boldsymbol{Q}$ scan, $S(\boldsymbol{Q}) = \int d\omega S(\boldsymbol{Q}, \omega)$ (see Sec. 6.2). Although $\tilde{\mathcal{E}}(\omega, \boldsymbol{k}) \neq S(\boldsymbol{k}, \omega)$, it is obvious that the integral of $\tilde{\mathcal{E}}(\omega, \boldsymbol{k})$ would produce the same diffuse sheets which I have shown in Fig. 7.5. Fig. 7.6 can then be regarded as a "variable-$\omega$ view" of the diffuse sheets of Fig. 7.5. Such diffuse sheets suggested the presence of uncorrelated linear *chains*. In other words, the fact that the blotch is spread out over a $\{100\}$ plane in reciprocal space suggests **linear** disorder in real space, in the sense described in table 6.1.

It is obvious that we need to better understand what it means that a phonon melts. I will discuss this in Sec. 7.9. Before doing that, however, it is instructive to look at the real spacetime picture of the atomic vibrations. This is presented in the next section.

**Summary of the results**

In summary, I have shown what happens to the Slater TO mode during a phase transition. We saw that, during its softening in the R-C transition, it overlaps with the Last mode and

burrows through it. Thereafter, the burrowed portion of its spectrum becomes the Debye mode in the 0-5 THz range. When the Slater mode cedes its energy to the Debye mode, its intensity starts to become spread out in $\boldsymbol{k}$-space and in $\omega$-space. In $\boldsymbol{k}$-space, the incipient delocalization happens over a $\Gamma - X$ path in the BZ. In $\omega$-space, the delocalization is mainly in the 0-5 THz range, but is forbidden at the frequency ranges of the TA peaks.

When the C phase is perfectly realized, namely when the supercell's lattice vectors form 90° angles with each other on average, the Slater mode melts completely, resulting in a blotch. Such a blotch is soft and spread out in $\omega$-space, and very spread out in $\boldsymbol{k}$-space. In $\omega$-space, the blotch extends in the 0-5 THz range, but there are satellite peaks present also at even higher frequencies. In $\boldsymbol{k}$-space, it extends to a whole $\{100\}$ plane of the BZ.

I interpreted the Debye mode similarly to the way some spectroscopic papers did [62]: that the Debye mode should be the hopping of atoms between energy wells placed away from the center of the cubic cell. I have offered a simplistic view of the dynamical regime that can describe the anomalous diffuse vibrational energy. The hopping of Ti cation attracts the neighbouring O anion, and the motion is effectively along a Slater eigenvector. When $T \ll T_C$, the Slater motion is purely vibrational. When $T \lesssim T_C$ or $T \gtrsim T_C$, the inter-well hopping motion and the intra-well vibrational motion of Ti-O atoms coexist, and share the same Slater eigenvector. When $T \gg T_C$, the motion becomes effectively a highly damped oscillation about the center of the cell. This explained the anomalous trend of the blotch vs $T$: the blotch becomes less broad in $\omega$-space and hardens with increasing $T$, because the dynamical regime switches from a hopping+vibrational motion to a pure, although damped, vibration, as the multiple-well potential gradually and effectively becomes quadratic as $T$ increases further.

The sharp delocalization of the blotch in reciprocal space was interpreted as a result of disorder: the delocalization of energy in $(\omega,\boldsymbol{k})$-space suggests a localization in $(t,\boldsymbol{r})$-space, where spatial localization means that the atomic hopping motion is *uncorrelated* from one cell to another in real space. The fact that the blotch is smeared out over a whole $\{100\}$ sheet in reciprocal space suggested that the disorder is linear, in the sense that *uncorrelated linear chains* form at $T \sim T_C$. This will be shown in more details in Secs. 7.8-7.9.

The information I show in Fig. 7.6 is about how the energy is distributed in reciprocal space. The picture is not complete until we look at the positions of the atoms in real space. This is what we are going to see next.

## 7.8 Displacements in real spacetime

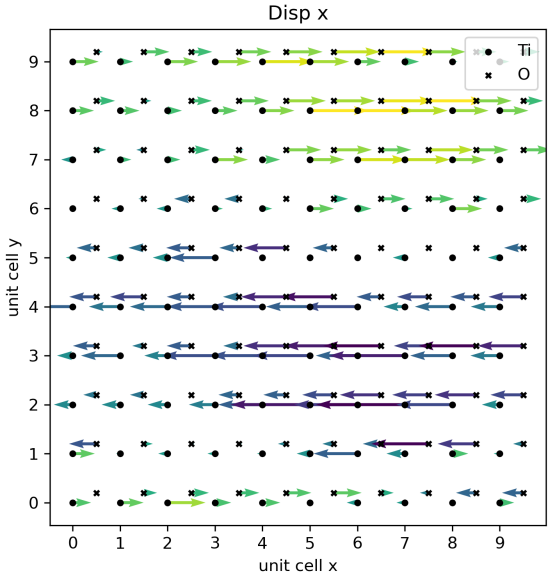
In Secs. 7.6 and 7.7 we saw that, in the C phase, both the scattering cross section and the distribution of kinetic energy are diffuse on sheets corresponding to {100} planes in reciprocal space. We interpreted the two results as the presence of linearly-correlated motions Ti and O atoms along a Slater eigenvector.

In this section, I show the real spacetime picture of the vibrations. It is an important section, because it completes the understanding, and validates the interpretation of the spectra given in the last two sections. We shall see that the PE phase of $BaTiO_3$ is characterized by the presence of linear chains of Ti-O atoms. The chains form because Ti atoms displace coherently along lines in the $\langle 100 \rangle$ directions, and the O atoms displace towards them. The distribution of the displacement of the chains is sharply double peaked, meaning that chains of atoms spend more time displaced coherently in a $\langle 100 \rangle$ direction, and that the chains can flip their polarization every so often. The visualization in real spacetime of such chains should shine some light on the anomalous X-ray diffuse sheets and on the anomalous melting of the Slater TO mode in $BaTiO_3$'s PE phase.

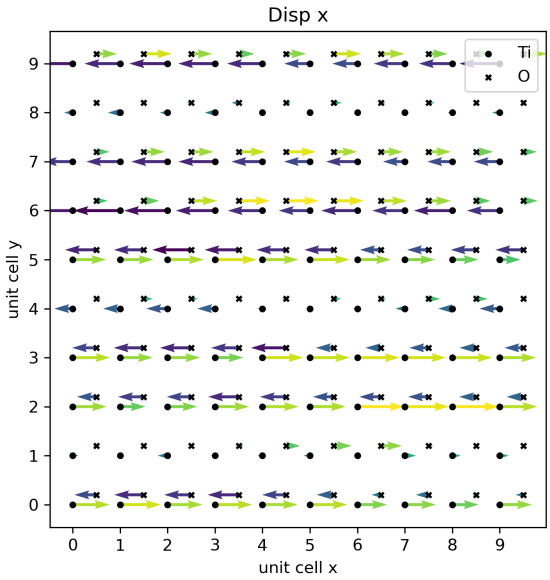
### 7.8.1 The displacements of Ti and O atoms

In the last section we saw that the main region of frequency where the blotch appears in the distribution of vibrational energy is the region 0-5 THz. The midpoint is $\tilde{f} \approx 2.5$ THz. Hence, the motion which corresponds to the blotch should roughly have a time scale $\tilde{\tau} = 1/\tilde{f}$.

The arrows in Fig. 7.10 show the $x$ components of the displacements of the Ti and O atoms during an NVT simulation averaged over a time period of $\Delta t = 0.5$ ps. The displacement of




(a)




(b)

Figure 7.10: $x$ components of the displacements of Ti and O atoms on the plane [$x$ $y$ 0.05] (scaled coordinates) averaged over a 0.5 ps time window, at 50 K in the R ferroelectric phase (a), and at 150 K in the C paraelectric phase (b). The Ti atoms positions averaged over time are denoted with a black dot, and the O atoms positions with a cross. These have been offset for visualization purposes. In the R phase, Ti-O couples are in phase, and the motion is characterized roughly by half of the plane being polarized to the right and half of it to the left, hence it indicates that we are probing a TA mode propagating in the $y$ direction of space. In the C phase, Ti-O are in anti phase: this suggests that the motion is characterized by a Slater eigenvector. The displacements of Ti vs O align to form chains in real space. The polarizations of the chains are uncorrelated with each other. If one chain is positively polarized, the chain above or below it can be polarized either positively or negatively, indifferently.

each atom $j$ is defined with respect to the average position, $u_x^j(t) = r_x^j(t) - \langle r_x^j \rangle_t$, and it is averaged over $\Delta t$. I show one specific time window, $(t_0, t_0 + \Delta t)$, of the simulation, but the general features I am presenting in Fig. 7.10 are common to all time windows I investigated. The atoms considered lie on only one of the equivalent $\{100\}$ planes, specifically a (001) plane, namely, an $xy$ plane. The black dots and crosses denote the positions of Ti and O, $\langle r^{\mathrm{Ti}_j} \rangle_t$ and $\langle r^{\mathrm{O}_j} \rangle_t$, respectively, averaged over the whole 400 ps production run. I have vertically offset the O positions for visualization purposes.

**Displacements averaged over 0.5 ps at 50 K**

Let us start with Fig. 7.10a, obtained for the simulation at $T = 50$ K. We note two features: (i) for most of the 100 Ti-O pairs belonging to a same unit cell in the plane, Ti and O are displaced in phase with one another and (ii) there is a clear polarization of the upper half plane to the right, and of the lower half plane to the left. Here, polarization means combined displacement. Both are clear features of a TA mode: the longest wavelength TA mode (LWTA) propagating in the $y$ direction, with wavevector $\boldsymbol{q} = 0\boldsymbol{b}_1 + \frac{1}{10}\boldsymbol{b}_2 + 0\boldsymbol{b}_3$, has a frequency $\omega_{\mathrm{LWTA}} \approx 1$ THz. So, the time window considered for the averaging corresponds to half a TA cycle, hence we are probing this mode. Of course, many spurious artifacts complicate a clear depiction of such a lattice wave: anharmonicity, the unphysical fluctuations caused by the Nosé-Hoover thermostat, and the presence of other phonons, such as an LA travelling on the same plane or a TA of the same frequency travelling in the $z$ direction and for which the polarization is along the $xy$ plane. However, it is quite clear, from the way the plane is polarized, that we are looking at the TA mode. It cannot be anything else, since there are no lower-frequency modes in the R phase, and higher-frequency modes average out in less or much less than the time scale we are considering.

**Displacements averaged over 0.5 ps at 150 K**

If we now look at Fig. 7.10b, obtained for the simulation at $T = 150$ K, the first temperature for which I compute a C phase, the picture is completely different. Firstly, note that most of the titaniums and oxygens are now in anti phase. This shows that, at this $T$, the dynamics of

low frequency is dominated by an optical eigenvector, and it is obvious to think of the Slater mode, for which Ti and O atoms displace against each other. Barium atoms, being heavy, do not move much in this time scale, and if they do, they mainly participate in an acoustic mode whose period is $\Delta t = 0.5$ ps time[2]. Most importantly, note that there is an alignment of Ti and O displacements in rows along the $x$ axis: couples of Ti-O form linear chains. The linear chains are made of Ti atoms which, *when averaged over a time window* $\Delta t = 0.5$ *ps*, are all displaced to the right, or to the left, of the time averaged position of the Ti atom, which corresponds to the body center of the unit cell. At the same time, the chains are made of O atoms which displace *towards* the Ti atoms, and align similarly. The chains are not correlated in the $y$ direction, in the sense that if a chain is pointing to, say, the right, the chain next up might be pointing right or left, or might have spent equal times being polarized to the right and to the left, like the chains in rows #1, #4 and #8. For this reason, we shall call them *uncorrelated linear chains*.

These results agree very well with the eight-site model of Comes, Lambert and Guinier [25] which we discussed in Sec. 5.3.2. Importantly, they were confirmed by other theoretical MD models, like the one of Pasciak *et al.* [94] and Gigli *et al.* [50]. Particularly interesting to notice is the striking similarity with the chain correlations in Pasciak *et al.*'s work, which can be seen by comparing Fig. 7.10b with Fig. 2 of Ref. [94]. A qualitatively identical result was found by Gigli *et al.* [50] (Fig. 2 of Ref. [50]). Note that, from the work of Pasciak *et al.*, the linear chains are approximately 10-20 unit cells long, which is greater than the size of our MD supercell. The chain-like correlations were observed also by other theoretical works, like the one of Senn *et al.* [112], who used a simple spin Hamiltonian to describe the alignment of the Ti displacements along chains. Moreover, these results agree well with the results of Fallon [43], who investigated the spatial correlations of the polarizations of the unit cells of $BaTiO_3$ in all of its phases. He found that, in the C phase, the $x$ components of the polarizations of the cells along an $x$ axis remain very well correlated, while the $y$ components of the polarizations of the cells along an $x$ axis are very poorly correlated (see Figs. 8.8-8.11 of Ref. [43]).

[2]this can be inferred from the density of states projected onto the atomic species, see e.g. Ref. [49].

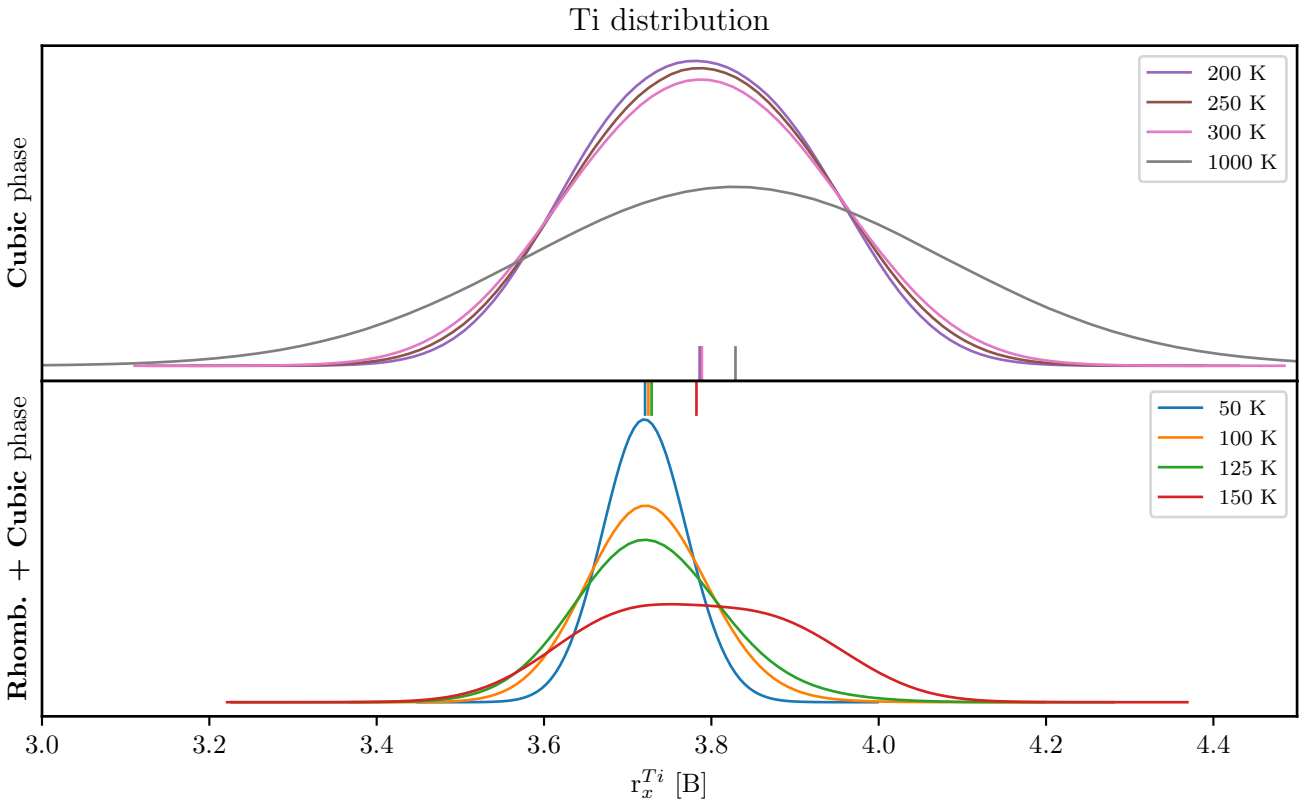



Figure 7.11: Displacement distribution function (DDF) of the Ti atom from MD simulations. The vertical segments denote the averages of the distributions. The DDF broadens progressively with $T$ at $50 < T < 125$ K, but there is a sharp broadening at $T = 150$ K $\approx T_C$. The DDF becomes very flat and asymmetrical at this temperature, and its average shifts a lot. In the top plot, the DDF is less flat. The view in the top plot is enlarged, so that the two plots share the $x$ axis but not the $y$ axis.

### 7.8.2 The displacement distribution function of the titaniums

In order to have a clearer understanding of the dynamics in the C phase, we need to collect statistics of the *local* atomic positions of the Ti atoms. To do this, we can simply look at the displacement distribution function (DDF). This is defined as the frequency (amount of times / unit of time) with which an atom is at $\boldsymbol{r}$ during the MD simulation. Being a probability density function, the DDF integrates to 1.

Note that, in the case of just one harmonic oscillator, which is quite pathological in this respect, the DDF is not exactly the probability that an atom is found at $\boldsymbol{r}$. In fact, this is defined at thermal equilibrium as $\rho(r,p) = \frac{1}{Z}\exp[-\beta H(r,p)] = \frac{1}{Z}\exp[-\beta(k\frac{r^2}{2} + \frac{p^2}{2m})]$, where $H(r,p)$ is the Hamiltonian of the oscillator, $p$ is the momentum, $\beta = 1/(k_B T)$, $k$ is the spring constant and $m$ is the mass. Hence $\rho(r,p)$ is Gaussian in $r$ [85] when $p$ is integrated out. However,

when the DDF is calculated from the trajectory of the oscillator, the distribution is very non Gaussian. It is shallow at $r = 0$ and has a maximum at $r = A$, where $A$ is the amplitude of the oscillation. This is because the mid position, $r = 0$, is where the oscillator has the highest velocity, whereas the point $r = A$ is the one with the slowest velocity. Hence, the time spent by the mass near $r = A$ is larger than near $r = 0$. All this said, many, but not all, of the DDFs I am going to show are bell-shaped, as can be found in other examples in the literature [129]. This is because the oscillation of an atom is composed of the *sum* of phonons with different frequencies. If one considers a trajectory defined by the sum of cosines of random frequencies, $x(t) = \cos(\omega_1 t) + \cos(\omega_2 t) + \ldots \cos(\omega_n t)$, a bell-shaped DDF is obtained when $n$ is large. There are $3N$ modes of vibration, with $N = 5000$ for the supercell which I consider, so we expect the DDFs to be bell-shaped, in most cases. The only reason why a DDF would not be bell-shaped is either if all the normal modes are very correlated, in which case the central limit theorem would not apply, or if there is one or more modes which have a very high amplitude and a very low frequency with respect to the others. In fact, the trajectory of an atom can be written as $x(t) = A_1 \cos(\omega_1 t) + A_2 \cos(\omega_2 t) + \ldots A_n \cos(\omega_n t)$, where each harmonic term is a normal mode of vibration. If one of the harmonics, say the $i$th, has a very low frequency, and hence large amplitude, with respect to the others, it can make the DDF increase at $r = A_i$, and decrease at $r = 0$, hence we expect a non bell-shaped DDF.

I consider NPT simulations and I only plot the displacements in the $x$ direction, neglecting the $y$ and $z$ components (which are equivalent by symmetry in the C phase). The way I calculate the DDF is simply by considering the displacement of each Ti atom in each unit cell during the MD run. The $x$ Cartesian component of the displacement of Ti atom $j$ at time $t$ is defined as $u_x^{\mathrm{Ti}_j}(t) = r_x^{\mathrm{Ti}_j}(t) - \langle r_x^{\mathrm{Ti}} \rangle_t$, where $\langle r_x^{\mathrm{Ti}_j} \rangle_t$ is the time average, over the 400 ps production run, of the position of the same atom. After I compute the distribution of a $u_x^{\mathrm{Ti}_j}(t)$, I offset the distribution by $\langle r_x^{\mathrm{Ti}_0} \rangle_t$, which is the time average over the whole production run of the position of the titanium in a reference unit cell whose lattice point is $\mathbf{R}_0 = 0$. I do this because, for the way it is defined, the DDF is a distribution with zero mean, i.e. $\langle u \rangle = \int \mathrm{DDF}(u) u du = 0$, but I want to show the Ti position, rather than its displacement. Ergodicity allows us to be confident that the time average of one Ti trajectory, $\langle r_x^{\mathrm{Ti}_0} \rangle_t$, should correspond to the ensemble

average, because all titaniums are equivalent.

The DDF of the Ti position is reproduced in Fig. 7.11, where I also indicate the average Ti positions as vertical line segments, which are coloured based on the temperature of the simulation. Let us comment on the R phase, in the bottom panel of Fig. 7.11. The distribution at $T = 50$, 100, 125 K is bell-shaped: the titanium spends most of its time around the minimum of the potential energy surface (PES) where it sits at mechanical equilibrium. Note, from the vertical segments, that the position about which the titanium vibrates does not shift considerably with $T$ in the R phase, suggesting that volume expansion, is small.

Increasing $T$ in the R phase produces curves which are more and more shallow: this is because the area under each curve is constant and equals 1, but the spatial extent, or amplitude, of the atomic vibration is larger at higher $T$. This can be understood by considering that, assuming for simplicity an Hamiltonian composed of only one harmonic oscillator with frequency $\omega_{\boldsymbol{q}\nu}$, the mean square displacement is [38] $\langle u_j^2 \rangle = \int \mathrm{DDF}(u_j) u_j^2 du_j \overset{CL}{=} 3k_B T/(m_j \omega_{\boldsymbol{q}\nu}^2)$, where $m_j$ is the mass and $CL$ means classical limit. Hence, the second moment of the DDF is the mean square displacement of an atom, and it increases with $T$.

Let us now comment on the DDF at $T = 150$ K. The standard deviation of the DDF increases sharply between $T = 125$ K and $T = 150$ K. The average position of the Ti shifts considerably, and at this $T$ corresponds to the center of the C cell. A close look at the DDF at $T = 150$ K shows that it is not Gaussian, because it features a bump to the left of the average position, at or close to the position of the PES minimum in the R phase. Importantly, the distribution is *very flat* at the average position. This suggests that the local potential energy surfaces on which the titaniums move are also flat, and this observation is consistent with Fallon's thesis [43].

Let us now focus on the upper plot of Fig. 7.11. At $T = 200, 250, 300$ K, the standard deviation of the DDF does not increase much. This suggests that the amplitude of the Ti motion is not increasing. We shall return to this point in the next section. At higher $T$ in the C phase, at 1000 K, the DDF is more spread.

From Fig. 7.11, it is hard to tell whether the real spacetime dynamics corresponds to a displacive or order-disorder picture. The DDFs for the single titanium, in fact, can be interpreted with either one of the two theories. The fact that the Ti DDF approximately does not change its shape from $T \leq T_C$ to $T \geq T_C$ could lead to the interpretation that the FES rearranges in the C phase to become quadratic, with its minimum at the center of the cell. This would happen if and only if all the local PES on which titaniums move become quadratic at $T \geq T_C$. This interpretation would support the displacive theory. On the other hand, the combination of the fact that the DDF's shape is very non Gaussian at $T = 150$ K, the fact that it is very flat at the center of the cell, and the fact the that standard deviation of the DDF does not increase at $T = 200, 250, 300$ K, could lead us to the interpretation that the PES retains a double well, though with a small energy barrier, and that when the Ti hops from a minimum to another of the PES, it is slowed down by the energy barrier, resulting in a flatter DDF at the center of the cell. This would support the order-disorder theory.

### 7.8.3 The displacement distribution function of chains and planes of titaniums

Because looking at the individual Ti atom provides limited information, we need to proceed differently. I define two different quantities: the chain and the plane displacement distribution functions. Let us consider the $x$ components of the displacements of Ti atoms ordering them in rows along $x$, and let us arrange them in an array $\mathbf{u}$ so that $\mathbf{u} = [u^{\mathrm{Ti}_1}_{\mathrm{chain1}}, u^{\mathrm{Ti}_2}_{\mathrm{chain1}}, \dots, u^{\mathrm{Ti}_{11}}_{\mathrm{chain2}}, \dots]$. The chain and plane DDFs are the frequency distribution of the following quantities:

$$u_x^{\mathrm{chain}}(t) = \frac{1}{10} \sum_{j=i\cdot 10}^{(i+1)\cdot 10} u_x^{\mathrm{Ti}_j}(t) \tag{7.1}$$

and

$$u_x^{\mathrm{plane}}(t) = \frac{1}{100} \sum_{j=i\cdot 100}^{(i+1)\cdot 100} u_x^{\mathrm{Ti}_j}(t). \tag{7.2}$$

Here, the dynamical quantities and averages are the same as I defined in the previous section.

In the chain DDF, $i$ runs from 0 to 99, so that the DDF considers atoms belonging to the 100 chains parallel to the $x$ axis in the MD supercell. In the plane DDF, $i$ runs from 0 to 9, so that the DDF considers atoms belonging to the 10 (001) planes of the MD supercell. After I compute these two variables from MD, I plot their histogram and I offset the distribution by $\langle r_x^{\mathrm{Ti}_0} \rangle_t$.

Let us see the reason for doing this calculation: the DDF of the single $u_x^{\mathrm{Ti}_j}(t)$ allows to evaluate the displacement distribution over the MD run for a single Ti atom $j$. Instead, summing the $u_x^{\mathrm{Ti}_j}(t)$ over atoms aligned in a [100] direction gives us information about the dynamics of a whole 1D *chain*, rather than that of a single atom. Recall that the displacements of atoms in a chain are summed up in Eq. 7.1. Hence, the chain DDF can be considered as the distribution of the "centroid" of the Ti displacements along chains. If titaniums belonging to a chain are completely independent from each other, then their motion would be disordered along a chain, and we should expect a very narrow (possibly bell-shaped) chain DDF, because positive and negative contributions would compensate in Eq. 7.1: the chain's centroid would not move much. If, on the other hand, there exists a mode whose excitation creates linear correlation of the atoms, then the motion of Ti atoms belonging to a chain is ordered, because Ti belonging to a chain move in unison. i Inspection of the chain DDF will allow us to understand what kind of correlation there is. A similar reasoning can be applied to the plane DDF: summing over a plane gives information about a 2D plane of atoms. Offsetting by $\langle r_x^{\mathrm{Ti}_0} \rangle_t$ allows to figure out whether or not the DDF of the chains' and planes' centroids are centered about the average Ti position, hence to see if there is a local instantaneous distortion. I did not normalize the chain and plane DDFs, so they do not integrate to 1, for visualization purposes. Hence, strictly speaking, they are not proper density distribution functions.

**The chain DDF**

The DDFs for all the simulated temperatures are depicted in Fig. 7.12. Let us start commenting on the chain DDF in the R phase. At $T = 50$ K, the chain distribution is bell-shaped: the Ti atoms along the chains spend most of their times around their average positions, which at

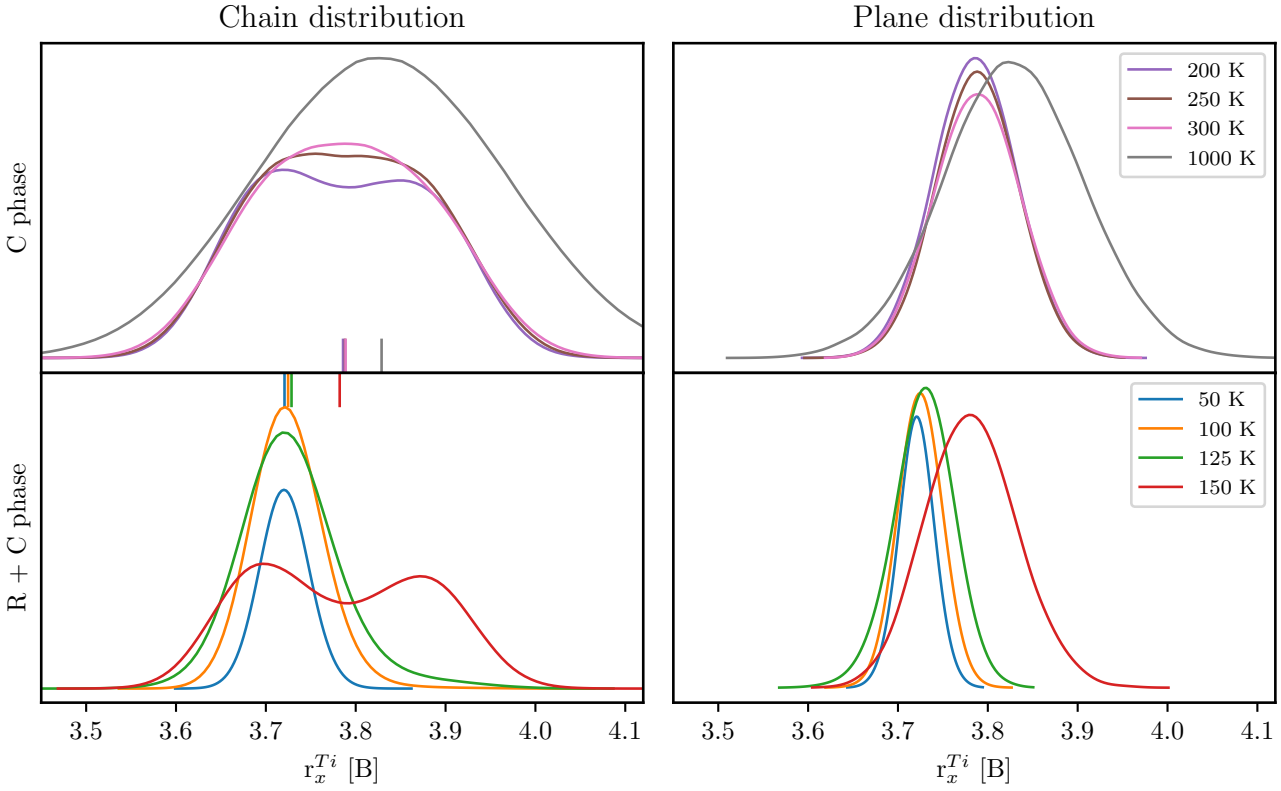



Figure 7.12: Displacement distribution function (DDF) of one chain (left) and of the whole plane (right) of atoms from MD. The distributions are not normalized. The chain DDF is narrow at $T = 50$ K, and it spreads at $T = 100$ K and $T = 125$ K. At $T = 150$ K, the DDF is sharply double peaked: this suggests that the motion of the centroid of the chains is not a pure oscillation. Increasing $T$, the chain DDF flattens out in the midpoint, signalling that the atomic hopping is increasing. The plane DDF remains roughly Gaussian at all temperatures, meaning that the different polarizations of the chains compensate, and the polarization of a plane is zero at any given time.

this $T$ almost corresponds to their position at mechanical equilibrium, i.e. the ones for which the potential energy is at a minimum (at $P \to 0$). At $T = 100$ K, the distribution is taller and wider; this is an obvious consequence of increasing the temperature and of not dividing the curves by their integrals. Now, if the PES were harmonic, we would expect a monotonic increase of the height of the distribution as we increase $T$. Instead, the monotonicity is broken at $T = 125$ K. At this temperature, the distribution is shallower and non-symmetrical, being slightly skewed towards positive values of $r_x^{\mathrm{Ti}} - \langle r_x^{\mathrm{Ti}} \rangle$. This suggests that we are at the onset of the formation of a Debye mode, when there is an increased probability of Ti hopping.

Remarkably, at $T = 150$ K the chain distribution is sharply double-peaked: it is apparent that the centroid of the chain is more frequently to the right or to the left of the Ti average position, which at these temperatures corresponds to the center of the C cell. The fact that the DDF is double-peaked, whereas the DDF of the single titanium is not, suggests that the motion of Ti atoms *along a chain* is very correlated. The amplitude of the chains' motion is $A_{\mathrm{chain}} \approx 0.1$ bohr. Increasing $T$, at $T = 200$ K the highest value of the chain DDF is still placed at $\Delta r \approx 0.1$ bohr away from the center of the cell. This suggests two important things, which I discuss next.

**The combination of vibrational and hopping motions**

The histograms of Fig. 7.12 suggest that the motion of Ti is a combination of vibration *and* hopping motion. The amplitude of the motion of the chain's centroid, in fact, *does not change* from the value $A_{\mathrm{chain}} \approx 0.1$ B at $T = 150, 200, 250, 300$ K, as can be seen observing the standard deviations of the chain DDFs. This suggests that the dynamical regime at these temperatures is the one I schematically illustrated in Fig. 7.9, and corresponds to the case $T \approx T_C$. At $T \approx T_C$, the probability of Ti *hopping* is high, and the time that the titaniums spend *in between* one minimum and another (inter-well hopping) increases with respect to the time that they spend vibrating about one minimum (intra-well vibration). Hence, when the flipping frequency of the chains increases, it tends to level off the middle part of the distribution, because Ti atoms spend more time *at* the center of the cell, as they are hopping among wells more often. In fact, what really appears to change from the DDF at $T = 150$ K to the DDF at $T = 200$ K is that the

dip in the middle of the chain DDF remains at $T = 200$ K, but it gets filled up more and more as the $T$ is raised. At $T = 300$ K, the fraction of time for which a chain is off-centered almost equals the fraction of time spent flipping, hence the distribution is almost bell-shaped. We can consider this $T$ to be close to the temperature at which $BaTiO_3$ completes its transition from a dynamical regime characterized by hopping+vibrational motion to a regime of pure vibrational motion *about the center of the cell*. In saying so, we must remember that the PES is probably quite flat, as we have noticed from the previous section in Fig. 7.11, and hence the concept of atomic hopping is schematic and simplistic.

At $T = 1000$ K, thermal fluctuations have won against the proclivity of titaniums to form chains, and the DDF is effectively Gaussian, as expected. At such high temperature, there is no special hopping motion of Ti atoms anymore, or, better, the hopping motion cannot be distinguished from a vibrational motion. This is consistent with the recovery of the Slater phonon at $T = 1000$ K that we mentioned in Sec. 7.7 when talking about the hardening of the blotch. If we look back at Fig. 7.6, we immediately see that at $T = 1000$ K the spectrum of the Slater mode resembles a band with a small broadening. In other words, the Slater mode looks a damped optical phonon branch. These results are also consistent with the different dynamical regimes I have discussed in Sec. 7.7 and illustrated in Fig. 7.9. There, I hinted that the recovery of a phononic behaviour might have been caused by the thermal energy being so high as to overshadow the presence of an energy barrier. When this happens, the Ti atoms do not experience an energy barrier anymore, and the local potential energy surface becomes effectively quadratic, or almost so.

**The possibility of controlling the hopping motions by varying the pressure**

There is a second interesting thing to notice. We have seen that the off-center positions in which the titaniums hop, which should correspond to the minima of the PES, do not change much with the temperature, and are placed $\Delta r \approx 0.1$ bohr away from the body center of the cell, in the Cartesian directions. This suggests that the distance between minima of the PES only depends on temperature through the volume expansion $V(T)$. This would mean that the

aligned hopping motion of chains of titaniums can be controlled by increasing/decreasing the pressure $P$. Pressure, in fact, is a thermodynamic variable which affects the volume directly.

We are in a position to guess what can happen when $P$ is increased: by reducing the unit cell's volume, pressure can reduce the distance between the off-center positions about which the chains' centroids spend most of their times, until a point where the two peaks of the distribution merge to become a single peak distribution. The observation that the chain mechanism can be controlled by tuning the pressure is consistent with the X-ray and neutron diffuse scattering experiments which were conducted at finite pressure, and which we discussed in Sec. 6.2. In brief, they highlighted that the diffuse sheets of $BaTiO_3$ disappear when the pressure is raised [103, 59]. The diffuse sheets, we said, are caused by disorder, which in turn is caused by the formation of uncorrelated chains. In this light, we can understand that the recovery of a "more harmonic behaviour" at high pressure pointed out by Ref. [103] is caused by the decreased amount of space available for the rattling of the Ti within a cell when $P$ is high. In this case, the short range repulsion between ions increases and wins against the Coulombic interaction between Ti-O atoms which favors off-center displacements, thereby killing the energy barrier. Atoms experience a quadratic PES when the Slater mode is excited at high $P$, and the hopping motion becomes a vibration about the center of the cell.

I did not focus on the pressure dependence of the phonon spectra of $BaTiO_3$, but I did perform a trial MD run at high $P$. In the conclusions of this thesis, in Sec. 9.2, I show how $\tilde{\mathcal{E}}_{\text{Slater TO}}(\omega, \boldsymbol{k}; P)$ changes dramatically when an MD simulation is performed at high pressure, and resembles a dispersive and narrow phonon branch–so, no blotch, and no hopping motion.

**The plane DDF**

The right hand side of Fig. 7.12 is also interesting. It shows the distribution of the plane average of the Ti displacement. This can be regarded almost as the distribution of an ensemble average, only the ensemble is a $xy$ plane of the MD supercell. Interestingly, all the curves show one peak. This is the result of the loss of correlation in real space of the chains: there is an equal amount of chains pointing to the right and to the left in Fig. 7.10b, and these opposite

contributions compensate in Eq. 7.2.

Importantly, at $T = 150$ K, at the onset of the formation of the chains, there is a sharp increase in the standard deviation of the plane distribution. This is caused by the "unblocking" of the hopping motion, that is, the aligned off-centering of Ti, which naturally causes the Ti to explore greater portions of the unit cell. At $200 \leq T \leq 300$ K in the C phase, the standard deviation of the plane average does not increase much, even though the temperature is increasing. This is the same odd behaviour which we observed for the chain DDF at the same temperatures. It can be explained by realizing that the thermal energy, at these temperatures, is being "used" to increase the hopping frequency of titaniums (i.e., to "fill up" the middle part of the chains' DDF). Hence, the amplitudes of the atomic motions do not increase much as long as the chains are present, meaning that the Ti atoms hop between minima which are placed at the same positions in the unit cell. At $T = 1000$ K, the distribution broadens up again, because the greater thermal fluctuations make the motion become a damped vibration, and the amplitude of this vibration will increase with $T$ again.

### 7.8.4 The local structure of $BaTiO_3$ and the chain dynamics

The results of this section lead to the conclusion that the local structure of our model of $BaTiO_3$ possesses an *approximately rhombohedral distortion* at any given time. It is rhombohedral by symmetry, because we only considered an $x$ direction, but this is equivalent to a $y$ or $z$ directions, in the C phase, hence we expect the same distributions along $y$ and $z$. It is approximately rhombohedral because the PES appears to be quite flat for the displacement of a single Ti atom, on average, and so the atom slows down at the center of the cell during its hopping motion, and the fraction of time at which it is found *at* the center is large. These observations are consistent with XAFS measurements by Ravel *et al.* [102], which we discussed in Sec. 6.4.

The collective motions of chains of atoms seems far from being perfectly vibrational, i.e., an oscillation of planes of atoms. A swinging motion, corresponding to the correlated oscillation of dipoles in a wave with wavevector $\boldsymbol{q}$, is not the flipping motion of chains. The two motions can be confused, but they are rather different, because the potential energy surfaces which produce

them are different. A phonon implies that the PES is quadratic at any given temperature, or that the amplitude of the vibrations are always small, so that the Taylor expansion of the potential energy can harmlessly be truncated at the quadratic terms. A Debye mode implies that the PES stays in the form of a multiple-well potential, and that when $T$ increases the amplitude of the atomic motions is large enough to allow atoms to explore the available space in the unit cell by hopping to the other minima. The relation between the chains' dynamics and the phases of $BaTiO_3$ is discussed in Sec. 7.10.

## 7.9 The melting of the Slater TO mode and the loss of correlation

In Sec. 7.7 we have seen that the energy distribution of the motion along the Slater TO mode's eigenvector, $\tilde{\mathcal{E}}_{\text{Slater TO}}(\omega, \boldsymbol{k})$, is very diffuse in $(\omega, \boldsymbol{k})$-space: we have called the appearance of this broad flat band the melting of the Slater mode. We hinted that the delocalization of $\tilde{\mathcal{E}}(\omega, \boldsymbol{k})$ is a signature of a localization in space and time of the atomic vibrations, i.e., a loss of spatial and temporal correlations of the cell dipoles. In Sec. 7.8 we have seen the real spacetime picture of the dynamics, which is characterized by the tendency of Ti-O atoms to align in chains. In this section, we shall see that the relationship between the two pictures, the reciprocal spacetime one and the real spacetime one. We will see that the melting of the Slater mode determines, or is determined by, a loss of correlation in real spacetime of the atomic motion, which produces the chain dynamics of Ti-O atoms.

In Sec. 7.7, I have stated that the Slater TO melts. But what does it mean that a phonon melts, exactly? In light of what we have discussed, we need to better understand this.

### 7.9.1 Cases where the energy is perfectly localized

Suppose that the distribution of vibrational energy, $\tilde{\mathcal{E}}(\omega, \boldsymbol{k})$, is perfectly localized at a point $(\omega, \boldsymbol{k}) = (\omega_{\boldsymbol{q}\nu}, \boldsymbol{q})$ in reciprocal spacetime. Then, we can identify the wavevector of a phonon with a point $\boldsymbol{q}$ in reciprocal space (the point has 0D structure). The distance and the direction of this point from the $\Gamma$ point defines the three components of the wavevector $\boldsymbol{q} = [q_x, q_y, q_z]$. A phonon with such wavevector corresponds to a wave propagating in the direction $\hat{\boldsymbol{q}}$ and with a certain eigenvector $\boldsymbol{e}(\boldsymbol{q}\nu)$. Assume that the phonon is a transverse optical (TO) phonon. Then, the displacement pattern that this mode imposes on the crystal is the one illustrated in Fig. 7.13. In this figure, I draw the wavevector with a blue arrow, the direction of the eigenvector with a green arrow, and the direction of the atomic displacements along rows in the $x$ direction with black arrows. Parallel planes of atoms perpendicular to $\boldsymbol{q}$ are represented in grey. The phonon displaces the atoms *coherently along planes perpendicular to* $\boldsymbol{q}$. This is because the

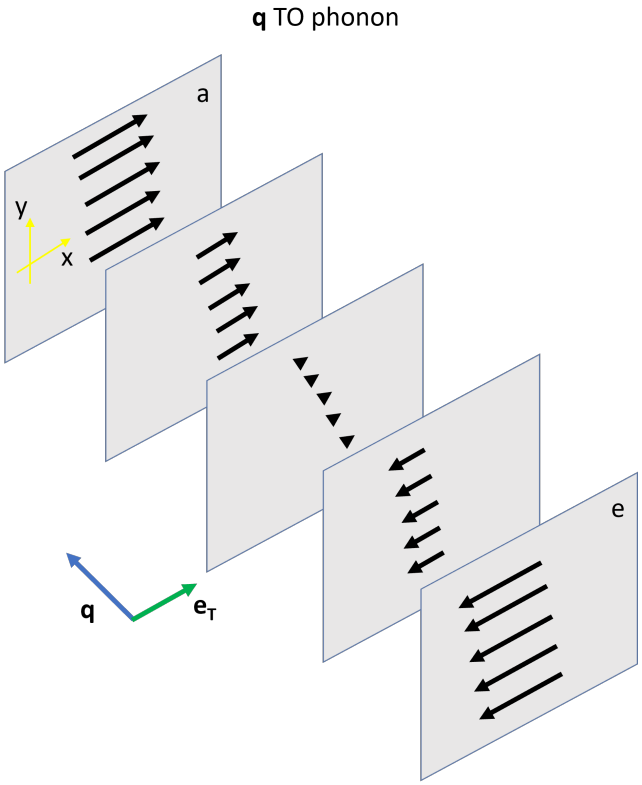



Figure 7.13: Schematic of the displacement pattern imposed by a mode of wavevector $\boldsymbol{q}$. The wavevector is drawn with a blue arrow, and the black arrows are schematic vectors indicating the direction of the eigenvector $\boldsymbol{e}(\boldsymbol{q})$ of the phonon involved. A TO phonon produces the coherent displacements of atoms belonging to a plane perpendicular to $\boldsymbol{q}$; the correlation in the displacements in parallel planes is modulated by the phase factor $\exp(i\boldsymbol{q}\cdot\boldsymbol{R})$. The transversal correlation of the atomic displacements is infinite: the planes are ordered.

phase factors of the displacements are $\exp(i\boldsymbol{q}\cdot\boldsymbol{R})$, hence planes orthogonal to $\boldsymbol{q}$ have the same phase factors.

In order to better visualize this, I draw Cartesian axes in yellow on one of these planes. It is clear that the correlation of the atomic displacements within the same plane is perfect in both the $x$ and the $y$ directions, because rows of atoms along $x$ all displace by the same amount, and different rows placed at different $y$ positions displace also by the same amount. Then, the whole atomic plane displaces coherently. Moreover, there is a perfect correlation of atomic displacements along the $z$ axis, because the wave $\exp(i\boldsymbol{q}\cdot\boldsymbol{R})$ imposes a perfect oscillatory modulation of the displacements. Hence, atoms belonging to planes even very far away from each other, like the planes (a) and (e) in Fig. 7.13, are perfectly correlated, despite being far. They do not displace of the same amount or direction, but they are correlated through an infinite plane wave in space.

In summary, the correlation in the atomic motion for a phonon which can be represented as a point (0D structure) in $\boldsymbol{k}$-space is perfect over the crystal's volume (3D structure).

### 7.9.2 Cases where the energy is delocalized

Let us now discuss the cases where $\tilde{\mathcal{E}}(\omega,\boldsymbol{k})$ is delocalized.

#### Flat bands

The simplest case is that of a flat band. This can be the case of optical bands, which can be non-dispersive or poorly-dispersive. A flat band is a band of constant frequency $\omega_\nu(\boldsymbol{k})=\tilde{\omega}\quad\forall\boldsymbol{k}\parallel\hat{\boldsymbol{q}}$. Here, $\forall\boldsymbol{k}$ means all the commensurate $\boldsymbol{k}$-points, and $\hat{\boldsymbol{q}}$ is the direction, in reciprocal space, along which the band is flat. For example, $\hat{\boldsymbol{q}}$ could be the $\Gamma-X$ direction and $\boldsymbol{k}=\frac{1}{5}\boldsymbol{k}_X,\frac{2}{5}\boldsymbol{k}_X,\ldots$. We can think of a flat band at $\tilde{\omega}$ as an excitation whose energy is $\tilde{\mathcal{E}}(\boldsymbol{k})\delta(\omega-\tilde{\omega})$, and is dispersed along a line in $\boldsymbol{k}$-space (1D structure). In other words, the energy which, in the last section, was localized on one single point in reciprocal spacetime, $(\omega,\boldsymbol{k})=(\omega_{\boldsymbol{q}\nu},\boldsymbol{q})$, is now delocalized along the line $(\omega,\boldsymbol{k})=(\tilde{\omega},\boldsymbol{k}\parallel\hat{\boldsymbol{q}})$.

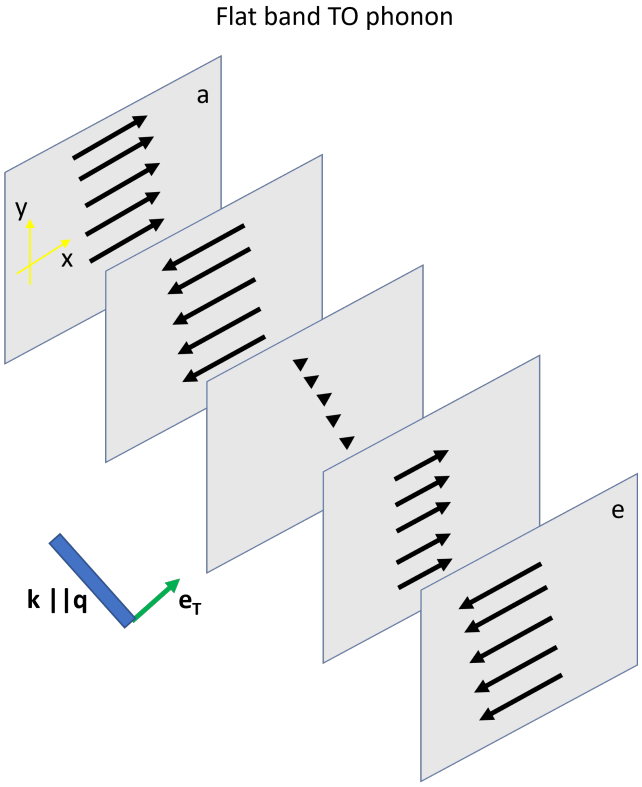



Figure 7.14: Schematic of the displacement pattern imposed by a flat band. The narrow rectangle in blue shows the direction $\hat{\boldsymbol{q}}$ (1D structure) of the spread of the energy in reciprocal space. The black arrows are schematic vectors indicating the direction of the eigenvector $\boldsymbol{e}(\boldsymbol{k})$ of the flat band. A flat band induces displacements which are perfectly correlated on *planes* (2D structure) perpendicular to $\hat{\boldsymbol{q}}$. The correlation along $z$ between parallel planes is lost: each plane displaces independently from another.

A delocalization in reciprocal space means a localization in real space. In particular, a delocalization in reciprocal space along a line $\boldsymbol{k} \parallel \hat{\boldsymbol{q}}$ means a loss of correlation of atomic vibrations happening over real planes perpendicular to $\hat{\boldsymbol{q}}$. The displacement pattern of a flat band is illustrated in Fig. 7.14. In this figure, the blue needle-like rectangle indicates the direction of the spread of $\tilde{\mathcal{E}}(\omega, \boldsymbol{k})$ in reciprocal space, i.e., the direction $\hat{\boldsymbol{q}}$. Let us comment on the displacement pattern imposed by a flat band. The planes are ordered, in the sense that atoms displace *coherently* on planes perpendicular to $\hat{\boldsymbol{q}}$. However, the planes are perfectly uncorrelated with each other. This means that their displacements are completely independent from each other: if one plane displaces positively, the subsequent parallel plane can displace either positively or negatively, indifferently. The correlation along $\hat{\boldsymbol{q}}$ is destroyed, because the energy is dispersed along $\hat{\boldsymbol{q}}$. Hence, if the energy is delocalized along a line in reciprocal space (1D structure), the correlations in real space are planar (2D structure).

A flat band means that correlation is preserved along planes in real space, but this is not the general feature of melted phonons. The displacement pattern which we observed for $BaTiO_3$ at $T \sim T_C$ and which we discussed in Sec. 7.8, in fact, is not quite that of a flat band. We observed a chain-like correlation, not a planar correlation.

**A 2D melted phonon**

Let us now extend the reasoning to the case in which the energy is delocalized over an *area* in reciprocal space. Suppose for simplicity that the energy is localized in $\omega$-space, so that $\tilde{\mathcal{E}}(\omega, \boldsymbol{k}) = \delta(\omega - \tilde{\omega})\tilde{\mathcal{E}}(\boldsymbol{k})$, and we do not have to carry the complication of the spread in frequency space as well. If the energy is delocalized over an area in reciprocal space, then the frequency of our excitation is $\omega_\nu(\boldsymbol{k}) = \tilde{\omega} \quad \forall \boldsymbol{k} \in A(\boldsymbol{q})$. Here, $\forall \boldsymbol{k}$ means all the commensurate $\boldsymbol{k}$-points, and $A(\boldsymbol{q})$ is the area in reciprocal space where the energy is delocalized. The plane which this area belongs to could be identified with its normal, which we can call $\boldsymbol{n}$. For example, $\boldsymbol{n}$ could be the [001] direction, and $\{\boldsymbol{k}\}$ would be the set of points belonging to a (001) plane in reciprocal space and which lie within $A(\boldsymbol{q})$. If $A(\boldsymbol{q})$ spans all of the (001) plane, then the energy is perfectly delocalized over the whole plane.

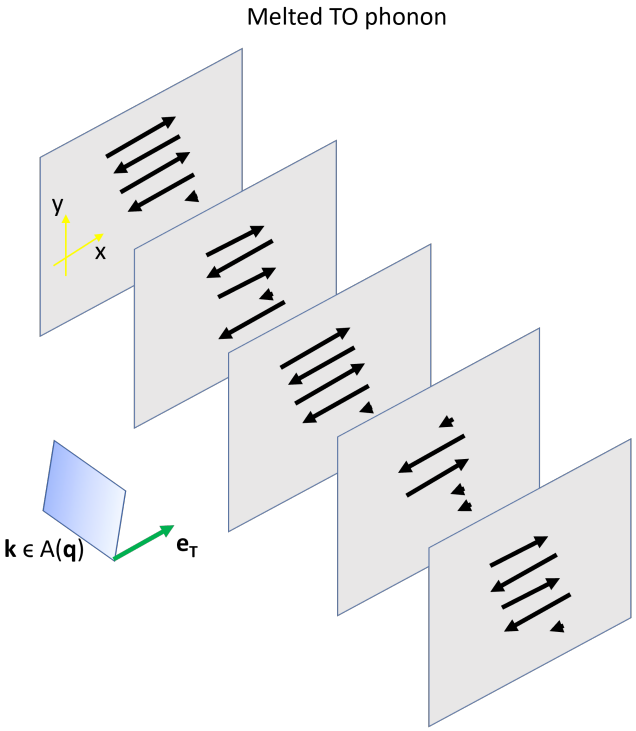



Figure 7.15: Schematic of the displacement pattern imposed by a melted phonon. The rectangle in blue shows the area $A(\boldsymbol{q})$ (2D structure) of the spread of the energy in reciprocal space. The black arrows are schematic vectors indicating the direction of the eigenvector $\boldsymbol{e}(\boldsymbol{k})$ of the melted phonon. A melted phonon induces displacements which are perfectly correlated on *lines* (1D structure) perpendicular to $A(\boldsymbol{q})$. The correlation along $z$ between parallel planes is lost, and the correlation along $y$ between rows of atoms is also lost: each row of atoms along $x$ moves independently from another.

Now, it is harder to visualize the displacement pattern of an excitation of this kind, because we are not used to it. However, we could think of it by extension to the case of the flat band. In that case, the atoms displace coherently on planes perpendicular to $\hat{\boldsymbol{q}}$. In this case, atoms displace coherently along lines perpendicular to the area $A(\boldsymbol{q})$. This is illustrated in Fig. 7.15. The area drawn in shaded blue represents the set $\{\boldsymbol{k}\}$ of $\boldsymbol{k}$-points which share the same energy, namely, the area in reciprocal space over which the energy is dispersed. The green arrow represents the eigenvector of the collection of such set of $\boldsymbol{k}$-points. Note that the melted branches share the same eigenvector in this simplistic picture. The displacement pattern imposed by the melted phonon is such that the there is a perfect correlation of atomic displacements along *lines* in the $x$ direction, which is the direction perpendicular to the area $A(\boldsymbol{q})$. However, the correlation along $z$ and $y$ is destroyed. Along $z$, it is destroyed because the parallel planes in Fig. 7.15 are uncorrelated with each other, like in the previous case of a flat band. Along $y$, it is destroyed because the energy is diffuse along the $\boldsymbol{k}_y$ direction in reciprocal space.

In other words, any delocalization of the energy $\tilde{\mathcal{E}}(\omega, \boldsymbol{k})$ along any direction $\hat{\boldsymbol{q}}$ imposes a localization along the direction $\hat{\boldsymbol{r}} = \boldsymbol{J}\hat{\boldsymbol{q}}$ in real space. Here, $\boldsymbol{J}$ is the Jacobian between real and reciprocal space. In a cubic crystal, this is just the identity matrix, hence a delocalization along an $x$ Cartesian direction in reciprocal space means a localization in an $x$ Cartesian direction in real space.

In $BaTiO_3$, the formation of chains at $T \gtrsim T_C$ is consistent with the melting of the Slater phonon. Compare Fig. 7.15 with Fig. 7.10b: Ti-O displace along the Slater TO eigenvector in chains, and each chain is independent from another. Note that a flat band cannot explain the displacement pattern of Fig. 7.10b, because that would impose a planar correlation, which is not what we observe.

This is what I mean when I say that the Slater TO mode has melted: that the displacement pattern it produces can be identified neither as a proper wave propagating along $\boldsymbol{q}$ as in Fig. 7.13, nor as a soft flat band as in Fig. 7.14. The phonon has melted because we can think of its wavevector as an *area* in reciprocal space (2D structure). We can do so because the excitation is actually composed of a collection of phonons which share the same energy and

the same eigenvector, and whose wavevectors are all different *but all lie on the same plane*. Such area *is* the area which I compute in the diffuse scattering patterns of Fig. 7.5, and it is the area over which the Slater TO mode manifests as a blotch in Fig. 7.6. The blotch in $\tilde{\mathcal{E}}(\omega, \boldsymbol{k})$ then determines 1D structure in the atomic correlations; hence, *uncorrelated linear chains*. Because the areal wavevector of the melted phonon belongs to a {100} plane in the BZ, then the chains are perpendicular to a {100} plane in real space, which means they belong to another {100} plane in real space, since by symmetry orthogonal planes are equivalent in the C phase. Moreover, because the areal wavevector spans *the whole* {100} plane, the chains are perfectly uncorrelated, in our model, in the sense that the chains' transversal correlation along $y$ in Fig. 7.15 is one unit cell long.

Of course, this does not necessarily have to be the case. The transversal correlation of the chains can be, or probably is, greater than one unit cell in the real material. From the work of Pasciak *et al.* [94], in fact, the transversal correlation seems to be $\approx$ of 3-4 unit cells, and the correlation length in the direction of the chains is roughly 10-20 unit cells (see Fig. 2 of Ref. [94]).

**A 3D melted phonon**

Of course, this reasoning can be extended to the case in which $\tilde{\mathcal{E}}(\omega, \boldsymbol{k})$ is spread over a volume (3D structure). In this case, the excitation is composed of a sum of wavevectors in a volume in reciprocal space, and we can think of it as a phonon whose wavevector is a volume in $\boldsymbol{k}$-space. Then, the atomic correlations in real space would have 0D structure, hence the crystal would be perfectly disordered. This means that each atom in each unit cell would rattle independently from each other. There would not be any correlation in the atomic displacements, neither volumetric, nor planar, nor linear. We expect the diffuse scattering to manifest as diffuse clouds in this case (see Tab. 6.1). This is what we would expect, for example, in a liquid or gas.

Note that disorder from a "3D melted phonon" is not exactly equivalent to thermal disorder. Thermal disorder is generated by the activation of the $3N$ normal modes of the crystal, each

with a different energy so that they are all differently populated, and each with a different eigenvector so that the displacement patterns imposed by each mode is different, in general. Hence, thermal disorder occurs even without any phonon having melted. A 3D melted phonon would impose disorder just by itself, without requiring other modes to be activated.

## 7.10 Discussion

We saw in Sec. 7.5 and 7.7 that the phase transition in $BaTiO_3$ is accompanied by a partial softening of the Slater TO mode, and the transfer of a part of its energy to the Debye mode. In Sec. 7.6 I showed that the difference in the scattering cross section between phases is in the presence of diffuse sheets orthogonal to the cubic axes, and interpreted this as a consequence of disorder. Such disorder was depicted in Sec. 7.8 and is caused by the presence of uncorrelated linear chains of Ti-O.

In this section, I will try to give an explanation for why the linear chains are formed, pointing out the possible mechanism that drives the phase transitions of all phases of $BaTiO_3$. Although our simulations are only able to describe a R-C transition, it is natural, if not obvious, to generalize the reasoning to the other phases as well.

### 7.10.1 The phase transitions from the point of view of a single unit cell

Let us consider the case $T \to 0$: the free energy surface (FES) coincides with the potential energy surface (PES) in this limit, and features eight minima positioned along the eight equivalent $\langle 111 \rangle$ directions [43]. At mechanical equilibrium, the Coulomb attraction between cation and anion makes it favorable for the Ti to displace against the O cage along a Slater eigenvector. This means that the energy is lowered if the Ti and O sublattices displace against each other in one of the $\langle 111 \rangle$ directions, until the short range repulsion raises the energy again. When these two competing fractions of the energy balance, the PES is at a minimum. When the Ti and O sublattices displace against each other, the cells distort, and become rhombohedral. This happens because such elastic distortion lowers the energy even more. As a result of the Ti-O displacements and of the elastic distortion, the unit cell is polarized in a $\langle 111 \rangle$ direction: the phase is ferroelectric, because there is a spontaneous polarization along this direction.

Let us now raise $T$. The FES does not coincide with the PES anymore, but the results of this

chapter strongly suggest that the FES does not change its shape, retaining the aspect of an eight-well potential. Moreover, because of the large loss of correlation in real space of atomic motions, and because the FES is a thermodynamic quantity and hence involves macroscopic order parameters and time averaged quantities, we shall more properly focus on the local PES and on the local degrees of freedom.

During the dynamics, at low $T$, the atoms are "stuck" in the minima of the PES where they were at equilibrium, vibrate about them, and $BaTiO_3$ is still in its R phase. The motion is entirely vibrational. As $T$ is increased, however, the energy of the thermal fluctuations increases proportionally, and the probability that a Ti atom hops to another well of the potential increases. At the same time, the PES flattens out as a result of the interactions with the neighbouring cells. When the range of temperatures of the "critical fluctuations" is reached (for us, $100 \leq T \leq 150$ K, but this temperature range is likely overestimated by finite size effects), the probability for the hopping of a Ti atom is high. When the Ti atom hops to another minimum in, say, the $x$ direction, it attracts the opposite O atom via an electrostatic interaction cation-anion, so that the oxygen moves towards it, like in Fig. 7.10b. During the hopping, the polarization of the cell changes sign, in the $x$ direction. If the amount of time spent by the titanium in one minimum is roughly the same as the amount of time spent in the other minimum, the $x$ component of the polarization averaged over the whole simulation is zero, hence we say that $BaTiO_3$ is in its orthorhombic phase, with a net polarization in the [011] direction. If the $x$ and $y$ components of the polarization averaged over the whole simulation are zero, then we say that $BaTiO_3$ is in its tetragonal phase, with a net polarization in the [001] direction. When all components of the polarization averaged over the whole simulation are zero, then we say that $BaTiO_3$ is in its C phase. The cubic phase is locally and instantaneously rhombohedral, but its polarization averages out in time to zero. Of course, it takes some energy for this hopping to occur, in a similar way as it takes energy for an atom to vibrate about an equilibrium position. Such hopping energy must be "taken away" from a phonon mode: the Slater mode.

It is important to state once again that, although the PES retains the aspect of a multiple-well surface, the energy barrier flattens considerably at finite $T$. This can happen as a result of

disorder among neighbouring cells, which, as Fallon has shown, favors the C phase, locally. If all the neighbouring cells are polarized, so that there is a macroscopic polarization $\boldsymbol{P}$, it is favorable for the reference cell to polarize at any time $t$ in the same direction. However, when the polarizations of the neighbouring cells average to zero, so that $\boldsymbol{P} = \boldsymbol{0}$, it is favorable for the reference cell to have a net zero polarization at any time $t$. Hence, for $T$s not too far from $T_C$, the energy barrier reduces from the value it has at $T \to 0$, and the displacement distribution function is almost flat at the center of the cell.

### 7.10.2 The phase transitions from the point of view of many unit cells

Let us now see what happens when the presence of other unit cells is considered.

The results of this chapter have elucidated that Ti-O atoms align to form uncorrelated linear chains. Fig. 7.16, taken from Senn *et al.* [112], describes the chain formation very well. The upper row is a schematic view of a supercell in the bulk of the crystal: the arrows inside the cubic supercell denote the polarizations of the cells, and the black and white arrows outside the supercell define the sum of the polarizations of each row of face-sharing cells, that is, the polarization of each chain. The sum of the black and white arrows defines the total polarization $\boldsymbol{P}$. The lower row shows the calculated diffuse scattering obtained from each static configuration of atoms.

Let us consider the R phase, Fig. 7.16(b). It is made of a collection of cells all polarized in the same [111] direction of space, and hence is ferroelectric. The three sets of chains, which are perpendicular to each one of the three {100} planes, are all equally polarized. We can think of them as being "frozen". The atoms vibrate about one of the eight equivalent minima of each local PES. In the O phase, the hopping of Ti-O unfreezes in one direction. In Fig. 7.16(c), this is indicated by the presence of an equal number of black and white arrows on the supercell face which has [010] as normal. The chains can flip in the [010] direction, and hence the spatial average polarization along [010] is zero at any given time. The phase is still

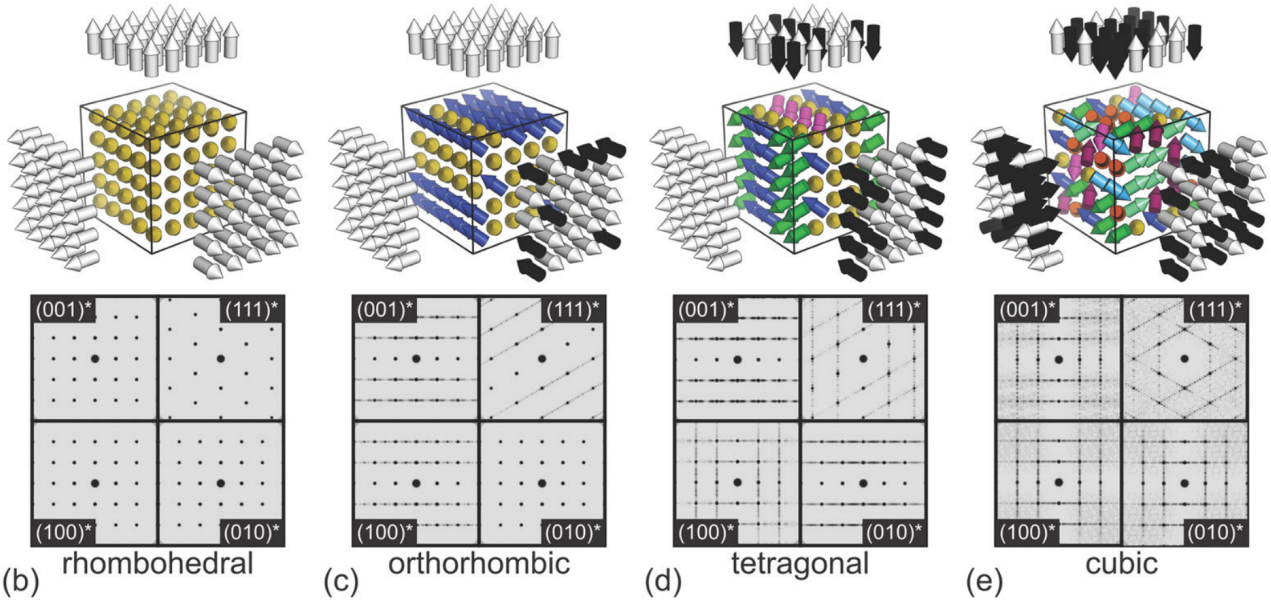



Figure 7.16: Schematic of the chain formation in $BaTiO_3$, taken from Senn *et al.* [112]. The upper row shows a view of a supercell, with the arrows representing the polarization of each cell in the bulk of the material. The black and white arrows represent the sum of the polarizations of face-sharing cells, along the Cartesian directions [100], [010] and [001]. There are three sets of chains, each pointing at a different Cartesian direction. In the R phase, each set is made of chains which are polarized all in the same direction, and the phase is ordered. In the O phase, the chains belonging to two sets are equally polarized, and the ones belonging to one set are disordered, meaning that they alternate their polarizations so that their spatial average is zero along one direction. In the T phase, one set is polarized and two sets are disordered, meaning that their averaged polarization is zero. In the C phase, all the three sets are disordered. The lower row shows the calculated diffuse scattering from the static structures indicated by the upper rows.

ferroelectric because the polarization along the [101] direction is non-zero. In the T phase, two sets of chains in two crystallographic directions are allowed to flip, and only one set remains frozen. In Fig. 7.16(c), this is indicated by the presence of an equal number of black and white arrows on two supercell faces. The total polarization is finite, but only along one axis, and the phase is again ferroelectric. In the C phase, all sets of chains are allowed to flip, and the phase is paraelectric.

All phases are locally and instantaneously rhombohedral, because at any given time one chain is polarized along a $\langle 111 \rangle$ direction. The different phases are realized because of the freezing/unfreezing of one or more orthogonal sets of chains. It is important to note that the chains are not only disordered in space, but also flip their polarization every $\Delta t = 0.5$ ps, in our model. This means that, in the non-ferroelectric directions, the polarization of a plane of atoms is zero *both on a time average and on a spatial average*.

I have not investigated the precise reason for the proclivity of atoms to align in chains. The theoretical work of Ghosez, Gonze and Michenaud [48] showed that, with at least five distinct unit cells (i.e., a $10 \times 10 \times 10$ supercell minimum), DFT energy calculations show a negative eigenvalue for the force constant matrix when a Ti vs O motion in a chain is excited. A negative eigenvalue of the force constant matrix means that the total energy of the crystal is lowered by the Ti-O motion along the Slater eigenvector. Hence, it is likely that it is energetically favourable for the atoms to align in chains. Once again, note also that from other theoretical studies the longitudinal correlation length of the chains is 10-20 unit cells [94], but it is likely to be bigger in a macroscopic material with defects [9].

## 7.11 Conclusions

**Summary of the results of this chapter**

We discussed the dynamics of $BaTiO_3$ across its phase transitions by means of classical MD. I have shown the simulated IR spectra, the diffuse scattering patterns, the distribution of vibrational energy of the Slater TO modes and the real spacetime picture of the atomic vibrations.

The IR spectra confirmed the experimental evidence of a central peak [62, 100, 82], which arises progressively as the transition temperature is approached from below. The central peak was interpreted as a proper Debye mode, namely, the hopping of Ti-O atoms among minima of the potential energy surface.

The diffuse scattering patterns from MD featured diffuse sheets on {100} planes in reciprocal space, and were in qualitatively good agreement with X-ray/electron diffuse scattering experiments [25, 64, 94]. I interpreted the diffuse sheets as the result of linear correlations of atomic motions: atoms lose correlation in two directions of space, while they retain an almost perfect correlation along the third direction: Ti-O form uncorrelated linear chains.

I have then shown the spectra of the Slater TO modes during a R-C transition. During their softening at $T \lesssim T_C$, the Slater modes encounter the Last modes, and burrow through them. The burrowed portions of the Slater modes constitutes the spectrum of the Debye mode. At $T \geq T_C$, the Slater modes melt, in the sense described in Sec. 7.9, and their kinetic energy distribution is dramatically spread out in reciprocal spacetime, resulting in a blotch. The blotch extends in $\boldsymbol{k}$-space over a whole {100} plane, and in $\omega$-space mainly in the 0-5 THz range (but it produces higher frequency satellite peaks as well). The only forbidden regions of frequency are the ones corresponding to the TA and Last TO modes, because they belong to the same IRREP of the Slater modes. This suggested that there is high mixing between the blotch and the TA modes, and some mixing between the blotch and Last modes. I hinted that the mixing of the blotch with the TA modes is linked to ferroelasticity.

The chains dynamics is characterized by the vibration of the chains' centroids about off-centered

positions at $\Delta r \approx 0.1$ bohr from the center of the cells and by their flips which happens in a time scale approximately equal to $\Delta t = 0.5$ ps. Hopping and vibrational motions of linearly-correlated atoms coexist in $BaTiO_3$ at at $T \gtrsim T_C$. This combination makes the displacement distribution function of a whole chain sharply double-peaked. In my simulations, the combination of hopping+vibrational motion persists until $T \approx 300$ K $\approx T_C + 150$ K, temperature after which the chain displacement distribution function becomes bell-shaped. Thermal fluctuations are able to flip the chains' polarization in time, winning against the energy gain which exists for the chains' formation. Hence, the higher-symmetry FE and PE phases of $BaTiO_3$ are characterized by a polarization which is zero both on ensemble average, because of disorder, and on a time average, because of the flips.

**The novelty of my work**

As the reader must have noticed by now, many of the results which I have shown in this chapter were already present in the literature, in some form.

If Sec. 7.5 on IR spectra and Sec. 7.6 on the diffuse scattering do not include any new finding, I believe that Sec. 7.7, where I show the distribution of vibrational energy, $\tilde{\mathcal{E}}_{\text{Slater TO}}(\omega, \boldsymbol{k})$, provides the first clear image of the spectra of the alleged soft branch of $BaTiO_3$ in frequency and reciprocal space. The frequency resolution was good enough to appreciate the large broadening of this branch in $\omega$-space, and the size of the MD supercell allowed to sample a good amount of points in reciprocal space so as to appreciate the spread of the energy in $\boldsymbol{k}$-space. These two spreads constitute the main point of this chapter, which is the melting of the Slater TO mode. The spread over a whole $\{100\}$ plane in $\boldsymbol{k}$-space is the signature of linear correlation of atomic motions, namely, of the formation of uncorrelated linear chains. The spread in $\omega$-space strongly suggests that the local PES over which atoms move along a Slater eigenvector remains a multiple-well surface, with the energy barrier slowing down the atoms at the center of the cell and hence dampening the mode.

I have highlighted in the last chapter and at beginning of this chapter that there is still disagreement in the literature around the mechanism that drives the phase transitions of $BaTiO_3$,

which have been historically thought to be of a displacive type [58, 66, 94]. Overall, the results of this chapter strongly suggest that $BaTiO_3$ is an order-disorder material.

What in the early IR spectroscopies was believed to be a soft mode [82, 107, 36, 110, 140], in fact, we learned is more properly a central peak which can be interpreted as a Debye mode, namely, an inter-well hopping motion. One of the reasons for the early interpretation of this central peak as a soft mode is that the *dielectric function* at low frequencies, which contains the intensity of the Debye mode, is narrow at $T \sim T_C$ (Fig. 7.2), and therefore the Debye mode can be confused with an underdamped soft mode. Nonetheless, we saw from the plots of $\tilde{\mathcal{E}}_{\text{Slater TO}}(\omega, \boldsymbol{k})$ that, at $T \approx T_C$, the *spectrum* of the Slater mode is very smeared out in $\omega$-space (central plots in Fig. 7.6). Such a large spread is, once again, very probably caused by the presence of an energy barrier in the local PES over which atoms move.

The fact that the anomalous diffuse scattering patterns which I simulated are in qualitative agreement with X-ray experiments suggests that they are effectively caused by linear correlations of the atoms, which I demonstrate by showing the real spacetime picture of atomic vibrations averaged over 0.5 ps in Fig. 7.10. The linear correlations of the atomic motions along the Slater eigenvector creates disorder across {100} planes, because the chains are not correlated with one another. This is in sharp contrast with the interpretation, pioneered by Hüller [66] in 1969, and revived in 2018 by Pasciak *et al.* [94], that a very soft and anisotropic mode would cause the diffuse sheets. In fact, I show that the Slater branch is very *diffuse* over a whole {100} plane in the BZ, and hence *is not anisotropic* on this plane. It is the opposite of an anisotropic mode: it is a phonon band which remains flat over a whole area, hence it has melted.

The possibility that the soft mode would be anisotropic was in part confirmed by some of the inelastic neutron scattering (INS) experiments [119, 148, 118, 56], which we discussed in Sec. 6.3. These studies, however, disagree on the dispersion of the soft TO mode: those performed before the 1969 found the band relatively flat in the $\Gamma - X$ path [119, 148], those performed after the 1969 found this mode very dispersive [118, 56], and with a dispersion that changes a lot depending on the direction of propagation of the mode. To see this, compare Fig. 6.6,

which shows the spectral peaks from Shirane *et al.* [119] (1967) with Fig. 6.8, which shows the undamped phonon frequencies across the $\Gamma - M$ path according to the fit of phonon spectra of Harada *et al.* [56] (1971; for the $\Gamma - X$ path, the reader can look at Fig. 5 of Ref. [56]). According to the present theoretical work, the distribution of vibrational energy $\tilde{\mathcal{E}}_{\text{Slater TO}}(\omega, \boldsymbol{k})$, which I plot in Fig. 7.6, shows that the Slater mode is very flat in $\boldsymbol{k}$-space. Another problem of the INS experiments is that they produced spectra which did not exceed the frequency of 3.6 THz (cf. Sec. 6.3), which is not enough to appreciate the broadening of the Slater TO mode in $\omega$-space, and its burrowing through the TA modes. It is difficult to comment on the INS spectra any further, because the number of $\boldsymbol{k}$-points for which data is available is quite limited.

Finally, XAFS/NMR experiments are useful to probe the local structure, and they agree with the results of this chapter that there is a higher probability for the off-centering of the Ti at any given time. However, we have learned that such off-centering is apparent only when *chains* of Ti-O are considered, because only then is the displacement distribution sharply double-peaked. It is unclear how local probes like XAFS or NMR could capture such linear correlations, since by definition they happen on a certain length scale. Electron microscopy is also not of help, because it averages the atomic images over a time scale which is just too large when compared to the time scale of the atomic motions or of the chains' flips. In this regard, MD simulations gave us a big advantage over these types of experimental techniques, because they allowed us to probe both the local motion of the atoms *and* the collective Slater motion.

One of the possible reasons for the disagreement among experimental results (cf. Sec. 6.7) and between experimental analysis and my analysis is that the hopping motion due to a Debye mode and the swinging motion due to a soft phonon are very similar, and can be confused. The word "hop", in fact, is symbolic, and in reality the Ti-O atoms rattle within a cell, with the energy barrier slowing down the motion when the atoms traverse it.

This also suggests that the difference between an order-disorder and a displacive material is subtle, and can be understood as the difference between a macroscopic picture whereby the free energy surface is quadratic at $T \geq T_C$, and a microscopic picture whereby the potential energy surface features multiple wells. However, in the latter case, if the height of the energy barrier

is low, as it appears to happen in $BaTiO_3$, the PES is *almost quadratic*, and the difference between the displacive and order-disorder limits almost vanishes. It is important to note that this difference can be appreciated mostly by the very large spread of the Slater mode throughout frequency space, which is the best sign that the PES features multiple wells even at finite $T$. The spread in $\boldsymbol{k}$-space only means that there are linear correlations of atomic motions, but it might not be incompatible with the concept of a soft mode, per se.

The fact that Ti-O atoms align in chains confirms the old intuition of Comes, Lambert and Guinier of the eight-site model [25], and by many other authors after them [112]. Only, they considered disorder in a static way, whereas here we extended the same logic in a dynamical way, as we analyzed the motion of the atoms in space and time. A real-world material is macroscopic, and therefore the real behaviour of $BaTiO_3$ is surely not exactly identical to what we have discussed. It is possible that in a macroscopic sample the transversal correlation of the chians does not drop to zero, but remains finite. This would mean that the atomic chains might not be exactly *linear* chains, but elongated polar *nanoregions* [74, 9]. The dynamics of the polar nanoregions interacts (or mixes, in the sense described in Sec. 7.7) with the macroscopic density fluctuations caused by long-range acoustic modes, giving the ferroelectric-ferroelastic coupling, and with the inevitable presence of defects and impurities, which creates a strain field that can cause the polar nanoregions to permanently polarize in the direction of the strain [9].

Finally, I do not think that this is the last words on $BaTiO_3$: many things are still to be understood. I will point some of them out in Sec. 9.2.

# Chapter 8

# The physical consequences of the melting of the Slater TO phonon

In the last chapter, I have discussed the dynamics of $BaTiO_3$ during a phase transition, and I have shown that the Slater TO mode melts. In this chapter, I attempt to link the microscopic understanding developed in the last chapter to some of the macroscopic properties of $BaTiO_3$. The most obvious ones are ferroelectricity and ferroelasticity. Ferroelectricity is the subject of Sec. 8.1, and ferroelasticity is the subject of Sec. 8.2.

## 8.1 Ferroelectricity

In this section, we shall see how the dynamics of the uncorrelated chains of $BaTiO_3$ can determine ferroelectricity.

A ferroelectric material is a material which exhibits a macroscopic polarization $\boldsymbol{P}$ even with no applied electric field $\boldsymbol{E}$, and whose polarization is switchable between states that are symmetrically equivalent. Because the macroscopic polarization and the electric field are related to the susceptibility via $\boldsymbol{P} = \boldsymbol{\chi E}$, the phase transitions are accompanied by a sharp increase of the susceptibility $\chi(T)$, or equivalently of the static dielectric constant $\varepsilon_s(T)$ (see Sec. 2.9). The

diagonal part of the susceptibility tensor, $\chi_{\alpha\alpha}$, measures how easy it is to create a macroscopic polarization density $\boldsymbol{P}$ along a certain axis $\alpha$ when an electric field $\boldsymbol{E}$ is applied to the same axis.

The early understanding of ferroelectricity was guided by Cochran's concept of a soft mode [22]: a phonon mode softens when reducing $T - T_C$. Near the phase transition, at $T \to T_C$, atoms are easily displaced along the eigenvector of the soft mode, and hence can react much more easily to an external electric field. When the frequency of the soft mode reaches zero, the energy required to activate such motion vanishes, and the atoms begin oscillating about new equilibrium positions in a structure which has a spontaneous polarization, i.e. a polarization without any applied field. When this happens, the static dielectric constant must be infinite, in principle, very high in practice.

### The Curie-Weiss law

It is common in the literature to fit the $T$-dependence of the static dielectric constant $\varepsilon_s$ to the Curie-Weiss law [50, 36, 82]

$$\varepsilon_s = \varepsilon_{T\to\infty} + \frac{C}{T - T_C}, \tag{8.1}$$

where $\varepsilon_{T\to\infty}$ is the value at which $\varepsilon_s$ saturates at high temperatures, and $C$ and $T_C$ are the Curie constant and temperature. The Curie constant is usually of the order of $10^5$ K [50], while $\varepsilon_{T\to\infty}$ is of the order of 10 [50], therefore, for temperatures not too far from $T_C$, $\varepsilon_{T\to\infty}$ can be neglected.

### The Lyddane-Sachs-Teller relation

The static dielectric constant is often mentioned in conjunction with the Lyddane-Sachs-Teller (LST) relation, which contains the ratios between polar phonon modes. In the cubic phase, the LST is [36, 110],

$$\frac{\varepsilon_s}{\varepsilon_\infty} = \prod_j \left(\frac{\omega_j^{LO}}{\omega_j^{TO}}\right)^2 = \left(\frac{\omega_{\text{Last}}^{LO}}{\omega_{\text{Last}}^{TO}}\right)^2 \left(\frac{\omega_{\text{Axe}}^{LO}}{\omega_{\text{Axe}}^{TO}}\right)^2 \left(\frac{\omega_{\text{Slater}}^{LO}}{\omega_{\text{Slater}}^{TO}}\right)^2, \tag{8.2}$$

where $\varepsilon_\infty$ is the electronic dielectric constant. It is important to remember that the LST relation, as it is written in Eq. 8.2, can only be applied to cubic crystals, where $\varepsilon_s^{xx} = \varepsilon_s^{yy} = \varepsilon_s^{zz} = \varepsilon_s$. In crystals with different space groups the equation should be modified to include the directions of the phonons' eigenvectors [23] [1]. The LST therefore links the ratio $\varepsilon_s/\varepsilon_\infty$ to the ratios of the frequencies of LO and TO modes.

The ratio between the LO and TO of the Last and Axe modes is very weakly temperature-dependent, and can practically be considered constant. The strongest dependence on temperature in the right hand side of Eq. 8.2 is of course due to $\omega^{TO}_{\text{Slater}}(T)$, which is the subject of our investigation.

**Combining the Curie-Weiss law with the LST relation**

Combining Eq. 8.2 and Eq. 8.1, in the hypothesis that $\varepsilon_{T\to\infty}$ can be neglected, we have the following Cochran's law for the Slater TO mode [**?**]

$$(\omega^{TO}_{\text{Slater}})^2 = \frac{\varepsilon_\infty r(T)}{C}(T - T_C) \approx A(T - T_C), \tag{8.3}$$

where $r(T) = (\omega^{LO}_{\text{Slater}})^2(\omega^{LO}_{\text{Last}}/\omega^{TO}_{\text{Last}})^2(\omega^{LO}_{\text{Axe}}/\omega^{TO}_{\text{Axe}})^2$, and the second equality is approximate because $r(T) \approx$ const. This equation is present in Cochran's historical paper, Ref. [22], only in a different form. All the quantities in Eq. 8.3 can be easily evaluated from the simulations. In fact, the equation contains the LO and TO phonon frequencies, which can be obtained from the peak positions of their spectra $\tilde{\mathcal{E}}_\nu(\omega, \boldsymbol{q})$, the electronic dielectric constant which can be computed from the force field's description of ionic polarization in response to an applied $\boldsymbol{E}$ field, and the Curie constant and temperature, which can be obtained from a fit to the observed static dielectric constant. Hence, Eq. 8.3 can be used to assess the consistency of our model with Cochran's law.

The rationale for what I propose to do here is simple: if we believe that the polarization response is entirely caused by the excitation of a soft phonon (and, but to a lesser extent, by the other

[1] or, more generally, to replace $\varepsilon_s$ with the determinant of the dielectric tensor [**?**].

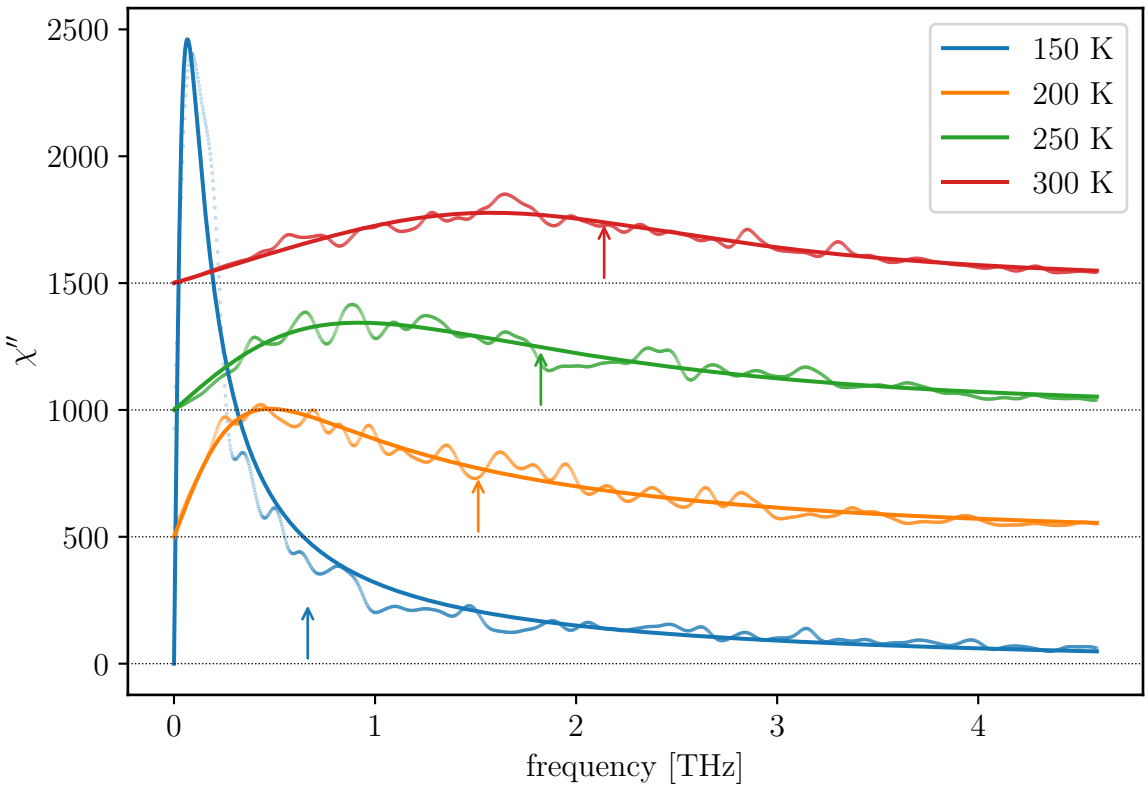



Figure 8.1: The low-frequency part of the susceptibility $\chi''(\omega)$ computed from MD (wiggly dotted lines) and from a fit to damped harmonic oscillators, Eq. 2.63 (solid lines). The vertical arrows indicate the undamped oscillators' frequencies.

harder optical phonons), then we must accept the LST relation. Now, for ferroelectrics the Curie-Weiss law usually holds, and even if it didn't, $\varepsilon_s$ increases a lot as $T \to T_C$. Hence, from the LST, $\omega^{TO}_{\text{Slater}}$ has to decrease a lot. Is such decrease consistent with the simulated IR spectra? If so, Cochran's law is correct and the Slater mode softens according to Eq. 8.3. If not, we have to rule out the possibility of a soft mode.

### 8.1.1 The fit of the Debye mode to a damped harmonic oscillator

Let us first look at the IR spectra. They were already presented in Sec. 7.5. Here, I show only the low-frequency dielectric spectrum, where the central peak is present, and its fit to a damped harmonic oscillator (DHO). I have convolved the raw spectra, obtained from MD via Eq. 2.61, to Gaussians with standard deviation $\sigma = 0.04$ THz, and then I have fitted each spectrum to a DHO, whose equation can be found in Eq. 2.63.

Note that I have not considered any coupling between the modes, which can in principle change the line shapes of the spectra [6]. However, this is the same approach used by Hlinka *et al.* [62], who fitted the low-frequency part of the spectrum to a Debye mode (Fig. 1 of Ref. [62]), without considering any coupling. This is also the same approach that was used by Gigli *et al.* in fitting this part of the optical spectrum (Figs. 8 and 10 of Ref. [50]).

The dielectric spectra in the range $0 \leq f \lesssim 5$ THz and their fits are plotted in Fig. 8.1. The quality of the fits looks good. I have noticed that the fits are sensible to the amount of frequency range considered for the fit. For example, when the frequency range is $0 \leq f \lesssim 6$ THz, the DHO fits change, as it should be. However, the undamped oscillators' frequencies do not change of a considerable amount. I found that all the oscillators are overdamped, namely, that $\Gamma > 2\omega_0$ (see Sec. 5.3.4). This is already an indication that this excitation is a proper Debye mode, as we have learned in Ch. 7, but here we shall pretend we do are unsure about it and give the soft mode a last chance. The vertical lines represent the undamped frequencies of the oscillators. Note that when the oscillators are heavily damped, the undamped oscillator frequency can be quite different than the peak position.

### 8.1.2 The simulated static dielectric constant

Let us now check the static dielectric constant, which has been calculated after MD from the dipole moments' fluctuations (Eq. 2.60). This is plotted in Fig. 8.2 with blue dots. Error bars are calculated by means of the standard formulae for the (time) variance of the fluctuations, in which the total number of timesteps has been adjusted to account for the correlation time of the dipole moments' autocorrelation function, as in Ref. [50]. We should regard these as the "true" values of $\varepsilon_s$ (within the limitations of the force field), since they have been calculated from an Einstein relation (Eq. 2.60) which does not make any assumption other than the one of linear response theory.

We observe a sharp increase in $\varepsilon_s$ at the phase transition, as expected, since the material is ferroelectric. The trend is qualitatively consistent with the experimental dielectric measurements in the T-C tranisiton of, for example, Li *et al.* (cf. Fig. 2 of Ref. [80]). I find that the

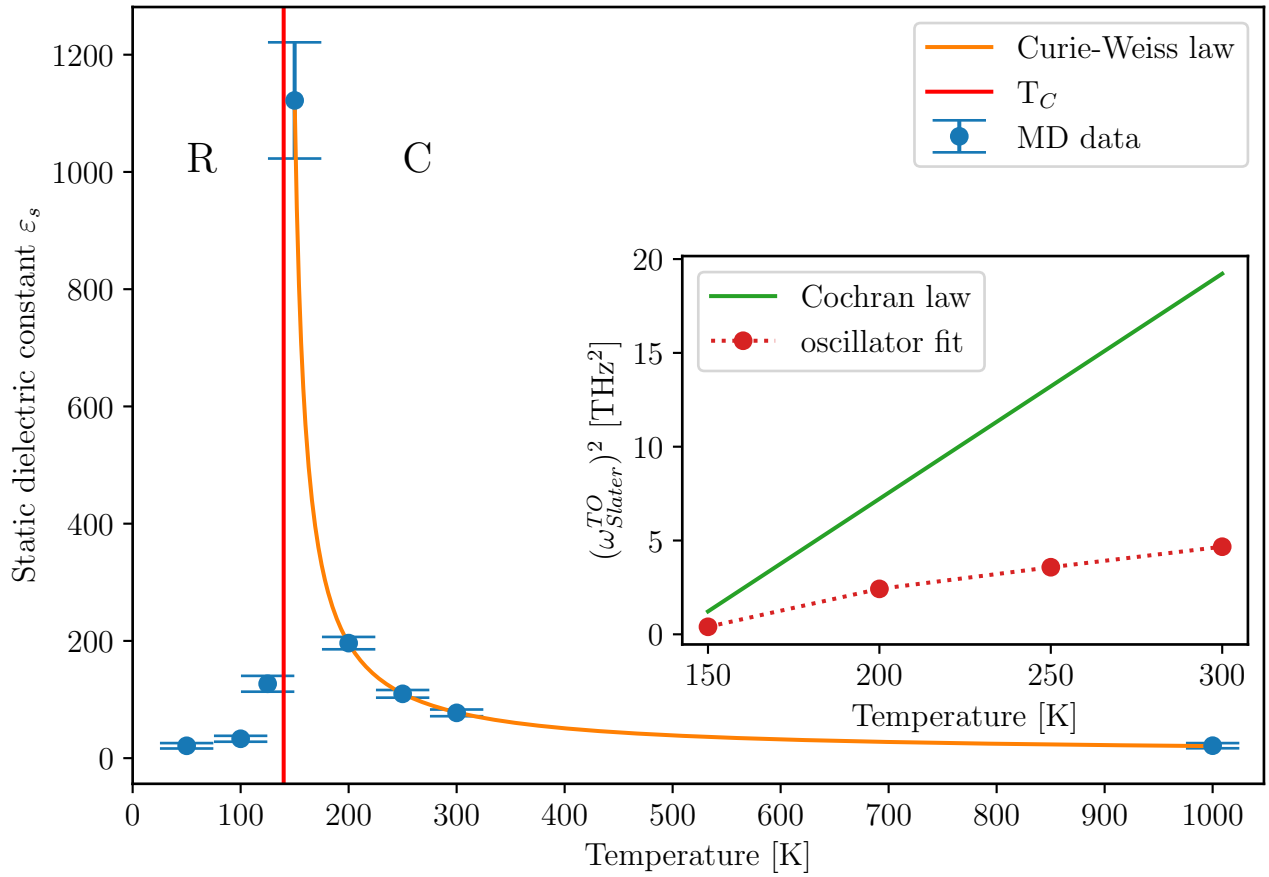



Figure 8.2: Static dielectric constant as a function of temperature. The orange line is the Curie-Weiss fit. The red vertical line denotes the transition (Curie) temperature $T_C$. The errorbars are computed by means of the standard statistical formulae for the variance of the variance, as in Ref. [50]. Inset: Cochran's law and oscillator fit of the low-frequency spectrum, showing that the evolution of the Debye mode vs $T$ is not consistent with Cochran's law.

Curie-Weiss law 8.1 is an excellent fit to the calculated values of $\varepsilon_s$, and the best fit parameters are $C = 11328.8$ K, $T_C = 140$ K and $\varepsilon_{T\to\infty} = 7.36$. The maximum value of $\varepsilon_s$ is realized at $T_C$, and is $\varepsilon_s(T_C) \approx 1120$; this is smaller than, but in the same order of magnitude of, the experimental value found in the T-C transition by Luspin *et al.* (Fig. 10 of Ref. [82]) and by the theoretical calculation of Gigli *et al.* (Fig. 7 of Ref. [50]).

**Checking on Cochran's law**

I have computed the phonon frequencies appearing in Eq. 8.2 from the peaks of the Lorentizan fits to the phonon spectra, $\tilde{\mathcal{E}}_\nu(\omega, \boldsymbol{q})$, of the Axe TO and LO, Last TO and LO and Slater LO modes. I have done this to test the hypothesis of the phonons being quasiparticles. If they are, then PT predicts that the phonon spectra are Lorentzians [15]. I considered the spectra of the TO/LO phonons at the smallest commensurate $\boldsymbol{k}$-point, $\boldsymbol{q} = \frac{1}{5}\boldsymbol{k}_X$, since the distinction between TO and LO modes vanishes at the $\Gamma$ point. I calculated a practically temperature-independent value of the electronic dielectric constant, $\varepsilon_\infty = 3.24$, which is somewhat smaller than the experimental value of $\varepsilon_\infty \approx 5$ [36]. Then, I plugged the values of $r(T)$, $\varepsilon_\infty$ and $C$ into Eq. 8.3 and obtained a practically temperature-independent value of $A \approx 0.12$ [THz$^2$/K].

The resulting Cochran's law, Eq. 8.3, is plotted in the inset of Fig. 8.2, and is compared with the DHO frequencies which I plotted as vertical arrows in Fig. 8.1. We observe a significant departure of the DHOs' frequencies from Cochran's law. This is surely not a proof of the failure of Cochran's law. However, it suggests that a dynamical model whereby all phonons are quasiparticles and whereby one of the TO modes softens perfectly with $T - T_C$ is incompatible with our MD model. This indication was largely substantiated in the last chapter. It is not surprising that we observe a divergence of the DHOs frequencies to Cochran's law; this law, in fact, lies at the heart of the soft mode (displacive) theory, but in the last chapter I have provided evidence that this is not the mechanism for the phase transitions of $BaTiO_3$.

**Experimental evidence of the possibility of the failure of the LST relation**

A similar issue with the LST relation was found by Di Domenico *et al.* [36], who used the LST to predict the value of $\omega^{TO}_{\text{Slater}}$ at 430°C and compared it to the fit of inelastic neutron scattering spectra from Ref. [119]. They highlighted that there is striking disagreement between the LST and inelastic neutron scattering: the LST would predict, at 430°C, $\omega^{TO}_{\text{Slater}} = 70$ cm$^{-1}$, while the neutron scattering spectra found $\omega^{TO}_{\text{Slater}} = 11$ cm$^{-1}$, a much lower value [36]. This disagreement is similar to the disagreement between the DHO frequencies and Cochran's law in the inset of Fig. 8.2: the DHO fit to the low-frequency spectrum is incompatible with the LST relation. Di Domenico *et al.* could find no cause for this apparent discordance.

Other authors, like Scalabrin *et al.*, pointed out that the disagreement between the *measured* static dielectric constant and the static dielectric constant *calculated* according to the LST relation should be caused by the contribution of "statistical disorder" caused by some non-vibrational mode (Sec. 3 of Ref. [110]).

Finally, I need to mention, as we saw in Sec. 6.1, that Ponomareva *et al.* [100] fitted the low-frequency spectrum with *two* DHOs, rather than only one. Of these two, one would correspond to the Slater TO mode, and one to the Debye hopping mode. However, just as in other theoretical calculations, like the one of Gigli *et al.* (Figs. 8 and 10 of Ref. [50]), I did not attempt to find the Slater TO peak in the low-frequency part of the spectrum, since the MD noise and the overwhelming Debye mode make it impossible to distinguish it.

### 8.1.3 Ferroelectricity and the chains dynamics

But if ferroelectricity is not caused by a soft mode, what is it caused by? Qualitatively speaking, we can be convinced that this has to do with the chains dynamics. We saw that, in the C phase, the chains flip, as a result of thermal fluctuations, every $\approx 0.5$ ps, in our simulations.

It is obvious to acknowledge that the presence of an electric field $\boldsymbol{E}$ applied to the crystal will cause the chains to align to its direction, resulting in a net macroscopic polarization $\boldsymbol{P}$. Let us

consider the C phase at $T \gg T_C$, which is a paraelectric, hence $\boldsymbol{P} = 0$. The chains which, at the time of application of the electric field, were already pointing in the direction of the field will persist. The chains which were pointing at the opposite direction of the field, on the other hand, will flip, with the result of a large increase in $\boldsymbol{P}$, from zero to a positive value. This means that the value of $\varepsilon_s$ must be relatively large, and $BaTiO_3$ is a good dielectric.

$BaTiO_3$ becomes ferroelectric in the T,O and R phases. Let us consider the C-R transition that we observe from the simulations. During this transition, the chains stop being disordered in space and orient themselves altogether in a $\langle 111 \rangle$ direction, causing the material to be polarized even in the absence of an electric field. Because this happens *spontaneously*, i.e., without any applied $\boldsymbol{E}$, $\varepsilon_s$ is very large at $T \sim T_C$.

**The difference between a soft mode and a melted mode**

If a dielectric material has a soft optical mode with wavevector $\boldsymbol{q} \to 0$, when the soft mode is activated *all atoms* in the crystal displace coherently along its eigenvector. If the mode is soft but its frequency is not zero, when an electric field $\boldsymbol{E}$ is applied, all the atoms in the crystal displace about their average positions along the eigenvector of the soft mode (and of the other optical modes), of an amplitude which depends on the frequency of the soft mode (and of the other optical modes). The result is a macroscopic polarization $\boldsymbol{P}$. The softer the optical phonon mode, the larger $\boldsymbol{P}$, at fixed $\boldsymbol{E}$.

If, however, the soft phonon has melted, the spatial disorder that it creates imposes a different physical mechanism by which a polarization can occur. In fact, it is not anymore the case that all atoms displace coherently. Depending on whether the phonon is a flat band or it has melted over an area in $\boldsymbol{k}$-space, the spatial correlations in the atomic motions have shortened in the way described in Sec. 7.9. In the case of $BaTiO_3$, the melted Slater mode generates uncorrelated linear chains in real space. When an electric field is applied in the C phase, there is an inevitable difference between chains of atoms that are polarized parallel to the direction of the electric field and chains which are polarized oppositely to it. There is an equal amount of chains belonging to either one of the two sets, because the spatial average of the chains'

polarization is zero, in non-ferroelectric directions. Then, half of the chains will polarize even further, and only half of them have to reverse their polarization. This can mean that the crystal is easier to polarize, with respect to a crystal with a soft mode. In terms of atomic motion, half of total number of Ti-O atoms will polarize even more when $\boldsymbol{E}$ is applied, and half of them will be forced to "hop" to the opposite well where they were, inducing a macroscopic polarization $\boldsymbol{P}$.

## 8.2 Ferroelasticity

Ferroelasticity is caused by the coupling between optical modes and elastic strains. Unfortunately, the ferroelastic behaviour in $BaTiO_3$ has not gathered the same attention that ferroelectricity has. One way to experimentally investigate the interaction between strains and optical modes is via Brillouin spectroscopy, which allows to detect long wavelength acoustic (LWA) modes. Acoustic modes with very long wavelength, in fact, represent elastic strains. Despite the potential of Brillouin spectroscopy, however, there is a limited amount of Brillouin studies [74, 68, 44], and even those studies do not seem definitive.

Ferroelasticity is responsible for a lot of very interesting phenomena which occur at the phase transitions. These phenomena are mostly elastic anomalies. For example, in the T-C transition, the anomalies are, chiefly, a softening and broadening of a long wavelength LA mode (LWLA) [74], and in the O-T transition a softening and broadening of a long wavelength TA mode (LWTA) [44]. All anomalies are more pronounced when $T \sim T_C$.

In this section, I do not attempt to include a thorough and quantitative study of ferroelasticity, but limit to point out some of the consequences of acoustic anomalies and the mechanism which can cause the dampening of the acoustic modes.

**The macroscopic consequences of the *softening* of acoustic modes**

The softening of LWA modes implies a softening of the elastic constants. In the T-C transition, it was found experimentally that the LWLA softens, but the LWTA mode's frequency does not shift considerably [74]. In the O-T transition, the TA softens [44]. The result of the softening of a LWLA is a softening of the $C_{11}$ elastic constant (which is proportional to $\omega^2_{\mathrm{LWLA}}$ [38]), and the result of a softening of a LWTA is a softening of the shear modulus $C_{44}$ (which is proportional to $\omega^2_{\mathrm{LWTA}}$ [38]). Here $C_{11}$ and $C_{44}$ are the elastic constants representing the stress $\sigma_{xx}$ when a unitary strain $\epsilon_{xx}$ is applied and the shear stress $\sigma_{xy}$ when a unitary shear strain $\epsilon_{xy}$ is applied, respectively.

The reason for the softening of $\omega^2_{\mathrm{LWLA}}$, and hence of $C_{11}$, during a T-C phase transition is that the unit cell changes its shape, from tetragonal to cubic. The decrease of volume found experimentally [114, 121, 102] indicates that the $c$ tetragonal axis shrinks. Hence, the crystal is softer against a strain along $c$. The reason for the softening of $\omega^2_{\mathrm{LWTA}}$, and hence of $C_{44}$, during a O-T transition is that this transition produces a change in the unit cell's shape compatible with an in-plane strain $\epsilon_{xy}$. Hence, the crystal is softer against a shear deformation.

One possible consequence of the softening of $C_{11}$ in the T-C transition is a change of the material Poisson's ratio, $\nu$. Because the Poisson's ratio is, in the hypothesis of an isotropic medium, $\nu = \frac{1}{2}(C_{11} - 2C_{44})/(C_{11} - C_{44})$, the softening of $C_{11}$ and the $T$-independence of $C_{44}$ may result in a negative value of $\nu$ for a certain range of temperatures [37], making $BaTiO_3$ auxetic in this range. The possibility of an auxetic bulk material is very rare, or even totally new, in the literature. For this reason, I dedicate Sec. 9.2.3 to suggest possible future work on this subject.

**The coupling between Slater modes and acoustic modes**

Let us consider, for the sake of the argument, the C phase, and let us imagine applying a strain along the $x$ axis, $\epsilon_{xx}$. This strain causes atoms to displace along $x$ of an amount which is proportional to $x$, $u_x = \epsilon_{xx}x$. This can cause, within a cell, an imbalance of the dipole moments, and this imbalance inevitably creates a dipole moment, which can be described as

the excitation of a Slater mode. The vice versa is also true. It is not possible to decouple the optical Slater mode and the elastic strain field it creates along the direction of its eigenvectors.

Let us now check this simplistic reasoning for consistency with the results of this thesis. Recall that we observed white spots in the kinetic energy distribution of the Slater mode, in Fig. 7.6. This suggested mixing between the Slater mode and the TA mode. This mixing, we said in Sec. 7.7, means that the excitation of a Slater mode would partially activate a TA mode, and vice versa. In other words, it is not possible to entirely disentangle the Slater mode and the TA mode. This gives the ferroelastic-ferroelectric coupling. One way to understand this is to acknowledge that a long wavelength TA mode travelling along a [100] direction imposes a shear distortion of the cells [38]. A shear distortion of all unit cells (together with a volume reduction [114]) is what happens to our model of $BaTiO_3$ during the transition R-C. Hence, if one shear-strains the C phase, where the Slater mode is soft, they can obtain the R phase, where the Slater modes are hard. In this light, we can understand why there is coupling between elastic strains and the ferroelectric modes: the Slater mode is very sensitive to a shear strain, or to a LWTA mode in our small supercell.

The different strains which can bring from a crystal class to another during the R-O-T-C phase transitions of $BaTiO_3$ define which LWA modes are more dampened during a Brillouin scattering experiment. In a O-T transition, an in-plane shear strain $\epsilon_{xy}$ can be taken as a macroscopic order parameter that defines the difference between the two phases, and the *TA mode was found to be heavily damped* by Brillouin spectroscopy [44]. In a T-C phase transition, the cell distorts along the tetragonal $c$ axis, hence it is a strain $\epsilon_{zz}$ which takes from one phase to another, and an *LA mode was found to be heavily damped* by Brillouin spectroscopy [74].

**Ferroelasticity and the *broadening* of acoustic modes**

These observations prompted me to have a closer look at the LWA modes. I obtained the frequency shifts and broadenings of the LWTA and LWLA modes at $\boldsymbol{q} = \frac{1}{5}\boldsymbol{k}_X$, which is the longest wavelength accessible to the supercell, through fitting the phonon spectra $\tilde{\mathcal{E}}_\nu(\omega, \boldsymbol{q} = \frac{1}{5}\boldsymbol{k}_X)$ to Lorentzians. In Fig. 8.3, I plot the frequency shifts of the LWA modes with respect to

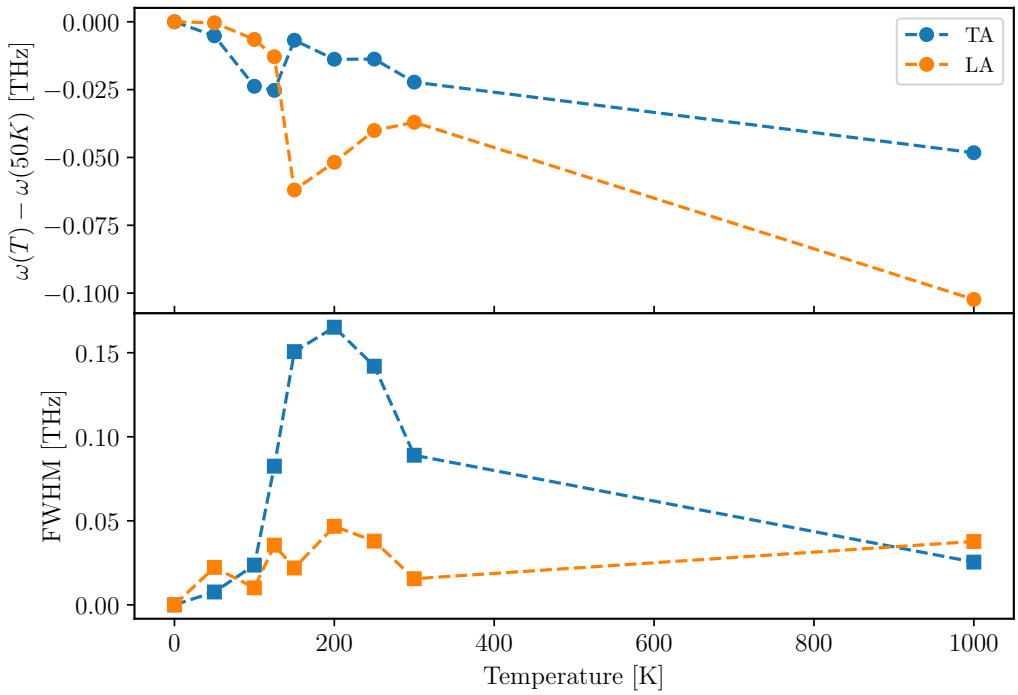



Figure 8.3: Temperature dependence of the LA and TA frequency shift (upper part) and broadening (lower part), obtained by fitting the phonon spectra to Lorentzian, and computing their peak positions and full width at half maximum at the simulated temperatures. Note the dip in the LA frequency, signalling a softening of the bulk modulus due to the unit cell's change of shape and the very non-monotonic behaviour of the TA broadening.

their frequencies at $T = 50$ K, and the full width at half maximum (FWHM) of the Lorentzian fits.

Although the R-C transition is not real, there are some features which are consistent with experiments. For example, the upper panel of Fig. 8.3 shows that the LWLA frequency dips across the phase transition, while the LWTA stays almost constant, in agreement with the experimental results [74]. The softening of the LWLA and the consequent softening of $C_{11}$ and of the bulk modulus $K$ is to be attributed to the ongoing change of the unit cell's shape, from R to C.

Interestingly, the broadening of the LWTA and LWLA is very non-monotonic, having a maximum at $T = 200$ K, and tailing off after this temperature. The broadening of the LWTA at $T = 1000$ K is one order of magnitude smaller than the one at $T = 200$ K; this is a clear indication that the mechanism for the acoustic broadening does not have anything to do with anharmonicity in the usual sense, according to which the broadening of a mode increases with

$T$ because phonon-phonon interactions increase with $T$.

A simple mechanism to understand why the LWTA mode has a large linewidth is to understand how it *interferes* with the Slater mode. If we look back at Fig. 7.10b, where I showed the real spacetime picture of the atomic vibrations, we can immediately see that a LWTA, which moves the center of mass of half plane to the right, and half of it to the left, exactly like in Fig. 7.10a, is incompatible with the Slater mode, which tends to align the atoms in linear chains. Hence, the the activation of a LWTA can disrupt the Slater mode, because it tends to recreate the transversal correlation among chains, and vice versa, the motion caused by the Slater mode can disrupt the propagation of a TA mode. This can happen because the two modes have the same time scale: the frequency of the LWTA is $\omega_{\mathrm{LWTA}} \approx 1$ THz, and the thermal flipping of the chains happens every $\Delta t \approx 0.5$ ps, hence they need 1 ps to complete a cycle. In the R phase (where the Slater mode is hard), and at $T = 1000$ K (where the Slater mode recovers a phononic behaviour and is hard), the TA can propagate with no obstacles other than the usual thermal phonon-phonon scattering. Because of this entanglment between atomic motions, the TA is very dampened, hence it has a large broadening.

**How come the thermal conductivity does not decrease at $T \approx T_C$?**

I finally want to remark that an increased broadening of acoustic modes should, in principle, lower the thermal conductivity, according to the common understanding of phonon-phonon scattering [38, 33]. Although the broadening of the LA, which is on the order of GHz [74], is surely not large enough to call $BaTiO_3$ a thermoelectric, it is tempting to draw a parallel between $BaTiO_3$ and other materials which feature "rattler modes", like $Ba_8Ga_16Ge_3$ [21]. Rattler modes are uncorrelated and local oscillations of one atom within some atomic cage which can enormously suppress the thermal conductivity [21].

On the contrary, the thermal conductivity of $BaTiO_3$ is not found to decrease at the onset of the phase transitions, but to increase instead [84]. I suggest that this has to do with the capability of the chains to transport heat, somehow. However, I did not investigate this to any extent; in Sec. 9.2, I point out that this could be the subject of some future work and I provide

a possible way in which thermal conductivity can be calculated from MD.

# Chapter 9

# Conclusion

## 9.1 Summary of thesis achievements

In this thesis, we have explored the breakdown of phonon theory in MgO at extreme conditions of temperature, and in $BaTiO_3$ near its phase transition temperatures.

We first saw what I mean by breakdown of phonon theory in Ch. 1: when temperature reduces the correlation lengths and times of lattice waves to less than their periods in space and time, they cease to be wave-like and become localized in spacetime. I called this event the "melting" of a phonon.

### Theoretical achievements

The most important result of this thesis is the calculation of the distribution of kinetic energy, $\tilde{\mathcal{E}}(\omega, \boldsymbol{k})$. I have defined this quantity in Sec. 2.6, and I have shown that it corresponds to the distribution of kinetic energy among frequencies and wavevectors in App. C. It is important to emphasize that the interpretation I have given of $\tilde{\mathcal{E}}(\omega, \boldsymbol{k})$ differs from the interpretation that others have given to it. In fact, this quantity has been commonly termed "vibrational density of states" (weighted by $k_B T$) [38, 129], but this is only valid at $T \to 0$ when anharmonicity

vanishes. At finite $T$, $\tilde{\mathcal{E}}(\omega, \boldsymbol{k})$ should be simply regarded as the distribution of kinetic energy. A more rigorous treatment is in Ref. [132].

**MgO**

MgO was the first material investigated. We saw that, in MgO, phonon melting happens progressively with temperature (Sec. 3.4.1), and it occurs most rapidly to the LO mode, then occurs to the other optical modes and finally to the acoustic modes: when acoustic modes melt, the crystal melts.

I proposed two possible explanations for why the LO is the most anharmonic phonon in MgO (Sec. 3.5). One is based on the conservation of energy and momentum for phonon-phonon collisions when such collisions involve three phonons. This explanation, which makes use of the two-phonon density of states, is a general feature of anharmonicity and can surely be extended to all materials, as long as $T$ is not too high and perturbation theory applies. I have shown that the calculation of the two-phonon density of states, which is relatively inexpensive, allows to interpret the multiphonon absorption of light by a crystal, namely, processes in which a photon is absorbed with the creation of two phonons. These processes manifest in IR spectra as additional peaks [52, 16]. The second explanation for the degradation of the LO band near the BZ center is based on a mechanism by which an acoustic mode can warp the LO mode's intrinsic field, and can also be extended to other binary ionic materials, especially if the long-range electric field born by the LO mode is large and therefore the LO/TO splitting is large.

I then assessed the accuracy with which the phonons can be regarded as quasiparticles in MgO. There is a wide range of temperatures for which the quasiparticle picture of the phonons holds, and the fit of the phonon spectra to Lorentzians is justified. This suggests that the material is poorly anharmonic.

I have derived an equation (Eq. 2.44) that allows to compute the isobaric or isochoric heat capacity from the phonon quasiparticle frequencies. I have shown that thermodynamic properties

calculated in this way give excellent agreement with experiments, overcoming the inadequacy of the quasi-harmonic approximation. The calculation of the isobaric heat capacity, and its comparison with experiment, has allowed us to quantitatively assess a hierarchy of methods. In order of increasing accuracy: the harmonic approximation (in its classical and quantum mechanical forms), the quasi-harmonic approximation, and the quasiparticle approximation.

**$BaTiO_3$**

I then investigated what happens to a model of $BaTiO_3$, which is likely to share many features with other order-disorder multiferroic perovskites, when it undergoes a phase transition.

I have shone some light on the debate about whether the $T$-induced phase transitions in $BaTiO_3$ are displacive or order-disorder transitions. We saw that the softening of the Slater modes is impeded by the presence other optical modes of the same symmetry: the Last modes. Hence, the Slater mode burrows through the Last modes, with dramatic consequences thereafter. Right after the phase transition temperature is reached, in fact, the Slater TO mode melts completely, and its molten state is known as the central mode or Debye mode (Sec. 7.7).

I have provided a simplistic model for interpreting the melting of the Slater mode: the potential energy surface retains the aspect of a multiple-well function, with a certain energy barrier $\Delta U$. In this energy landscape, the atoms hop, along the Slater eigenvector, from one minimum to another, and do not vibrate about the center of the cell.

Hence minimization of the free energy is achieved, not by the Ti sublattice displacing such that each Ti is at the center of a primitive cell, on average, but when the Ti sublattice becomes a superposition of either two (orthorhombic), four (tetragonal) or eight (cubic) sublattices, each of which has 1/2, 3/4, or 7/8 of its Ti sites vacant. In each of the sublattices contributing to each superposition the lattice sites are located at a different one of the eight symmetry-equivalent potential energy minima of the Ti atom's local PES in the primitive unit cell. Of course, in this simplistic picture the off-center displacement of each Ti atom to one of the eight potential energy minima of a primitive cell, really represents a more complex distortion of the

ideal cubic perovskite primitive cell, which also involves motion of the centroid of the three O atoms towards the Ti atom, and a strain that deforms the cube with Ba atoms at each of its eight corners. This complex distortion is a superposition of a displacement along the eigenvectors of the Slater mode and the acoustic modes.

We saw that the melting of the Slater mode means that we cannot identify its wavevector with a point in reciprocal space, but with an area (Sec. 7.9). In real space, this is equivalent to the existence of correlations along one axis, and disorder in the plane perpendicular to this axis, i.e., there exist parallel chains of correlated primitive cells and these chains are not correlated with one another. I illustrated the linear disorder in real spacetime (Sec. 7.8), and shown that this is a key for interpreting the X-ray patterns of this material (Sec. 7.6).

The study of the reciprocal and real spacetime pictures allowed us to suggest a mechanism for the phase transitions of $BaTiO_3$: a higher-symmetry phase is generated by the flipping of the atomic chains in time and by their disorder on crystallographic planes in real space (Sec. 7.10). The amplitude of the motion of the chains does not change much with temperature, suggesting that the PES remains a multiple-well surface at $T > T_C$.

Finally, we explored some of the physical consequences of our microscopic understanding to some of the macroscopic properties of $BaTiO_3$, which makes it a multiferroic: ferroelectricity (Sec. 8.1) and ferroelasticity (Sec. 8.2). I have rejected the possibility that the transitions occur by a complete softening of a phonon mode, which causes relative sublattice displacements to a new crystal structure, i.e., simple displacive transitions, by observing the inconsistency of the Lyddane-Sachs-Teller relation with the DHO's fit of the IR spectra. I have discussed qualitatively, and in part quantitatively, the striking features of ferroelasticity: acoustic modes' softening and broadening.

## 9.2 Future work

I believe that my work can be substantially extended. I hereby highlight some roads for future work.

### 9.2.1 MgO: phonon sidebands

In Sec. 3.4, I noted that there would be some interesting feature in the rich phonon spectra of MgO which I would not touch upon. I show one of these here, and hint at some of the interesting recent theoretical advances in the understanding of it.

Recent highly-resolved inelastic neutron scattering measurements revealed the presence of sidebands, or "ghost" (G) bands, in NaBr [115]. These are low-intensity phonon bands in regions of reciprocal space where there is no harmonic dispersion. The G band is visible in Fig. 9.1a, which reports the neutron scattering results from Ref. [115]; the ghost band is indicated by a white G in the plot, and is clearly noticeable at room $T$.

Fig. 9.1b shows $\tilde{\mathcal{E}}(\omega, \mathbf{k})$ for MgO at 300 K, where I have chosen a different colour scheme and increased the contrast to guarantee a better visualization. The white arrows point at what seems to be a clear indication of a G band: there is some structured intensity outside the harmonic phonon bands. Fig. 9.1c-9.1d show the same spectra projected onto optical and acoustic modes, respectively, indicating that the sideband appears as a high-frequency tail of the optical modes, or at least modes of higher frequency; the acoustic modes do not contribute to the G band considerably. Finally, Fig. 9.1e shows the temperature evolution of the spectrum of the G band at the $X$ point: the sideband appears very shallow at low $T$, and it then softens and eventually overlaps with the LO spectrum.

The theoretical understanding proposed in Ref. [115] makes use of the quantum Langevin model [**?**], whereby the coupling between phonons is mediated by a thermal bath: when, say, a TO phonon interacts with, say, a TA phonon, this interaction occurs together with the coupling of both modes with a bath of other phonons. It can be shown that this can be described by quantum Langevin equations for the phonon operators, which can determine the presence of sidebands in the phonon spectra [115].

It might be worth exploring this further. The quantum Langevin model is one which can predict the presence of sidebands, as opposed to perturbation theory, for which the spectrum of a mode is always a Lorentzian. Some open questions then come to the mind: where does the G band

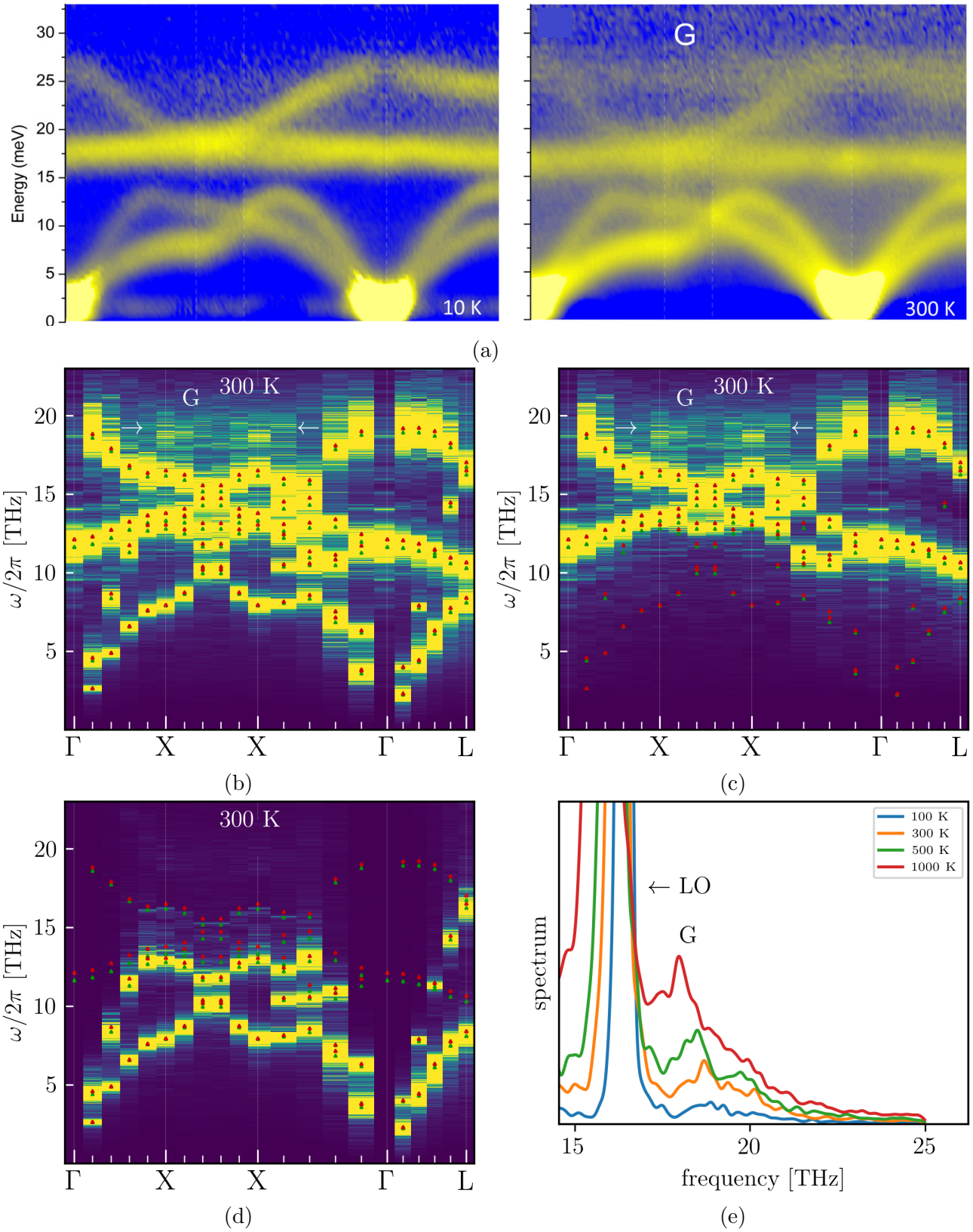



Figure 9.1: Emergence of a "ghost" (G) band in the phonon dispersion of NaBr and MgO. (a) inelastic neutron scattering results for NaBr, at 10 K and 300 K, taken from Ref. [115]; (b) the all-bands result of this work at 300 K for MgO; (c) the spectra projected onto the optical eigenvectors, with the G band being clearly visible; (d) the spectra projected onto the acoustic eigenvectors, with the G band basically disappeared; (e) the temperature evolution of the G band in the high-frequency spectrum of the phonons at the $X$ point, zoomed in so as to see the G band: the G band is very shallow at low temperatures, and its peak softens and gets more structured at higher temperatures.

come from? Maybe it comes from an interaction of the LO phonon with other phonons? Is the quantum Langevin model a more accurate description of phonon-phonon interactions than PT? Does the G band affect considerably the optical spectra in the IR range? Is it detectable by IR spectroscopy? Does it correspond to the excess of spectral weight in the IR spectra of Refs. [52, 16], or to the secondary peaks in the two-phonon density of states of Fig. 3.8? Is it exploitable technologically?

### 9.2.2 $BaTiO_3$: the effect of pressure

In Sec. 6.2 I briefly discussed the effect of pressure on the X-ray diffuse scattering of $BaTiO_3$. In Ch. 7 we investigated the effect of temperature on the dispersion of the Slater TO phonon. We noticed in Sec. 7.8 that the off-centered positions about which the Ti vibrate in the cubic phase remain 0.1 bohr far from the center of the cell, regardless of the value of $T$. I then pointed out that the minima of the free energy surface might depend on $T$ only through the volume expansion $V(T)$. Hence, the Ti hopping mechanism and the chain formation, I hinted, might be controlled by the pressure $P$. Pressure is a thermodynamic variable that can increase or decrease the degree of anharmonicity. However, it behaves very differently than temperature, because it directly controls the volume, and in turn the energy surface experienced by the atoms. It is therefore interesting to try to understand what happens to $BaTiO_3$ when the pressure, instead of the temperature, is varied.

Unfortunately, there are only a few studies of the effect of pressure on $BaTiO_3$. Among these, I highlight Ref. [103] and Ref. [59]. The experiment of Ref. [59] showed that, at 300 K (tetragonal phase when $P = 0$), there is a phase transition to a cubic phase at $P \approx 2.5$ GPa. Being a cubic phase, we would expect to see the usual diffuse sheets in a X-ray diffusion experiment. On the contrary, Ref. [103] showed that such diffuse sheets are absent when $P$ is high. Why is that? Ref. [103] provided a partial explanation for that, pointing out that an increase of pressure can cause the centering of the positions about which the Ti vibrate thereby making the material more harmonic.

I have run a trial simulation at $T = 50$ K at high pressure and I plot $\tilde{\mathcal{E}}_{\text{Slater TO}}(\omega, \mathbf{k})$ for the

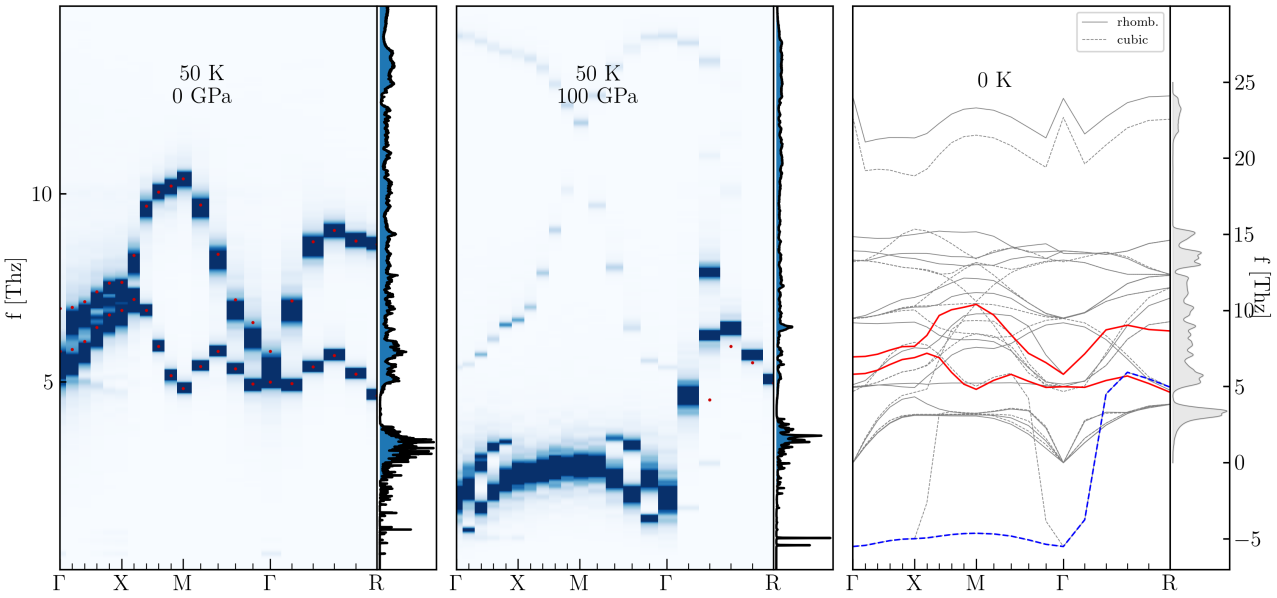



Figure 9.2: Vibrational energy distribution in reciprocal space of the Slater TO phonons of $BaTiO_3$ highlighted in the rightmost panel after NPT simulations at $(T, P)$ = (50 K, 0 GPa) and (50 K, 100 GPa). Pressure stabilizes the Slater Ti-O vibrations, making it resemble a phonon.

Slater TO phonon when $P = 0$ and when $P = 100$ GPa in Fig. 9.2. It seems clear that pressure stabilizes the Slater Ti-O vibrations, making it resemble a phonon band. Here the spectrum of the Slater TO mode is highly dispersive and does not resemble a blotch, in contrast with Fig. 7.6; hence, it is acceptable to argue that the Slater TO is a phonon, in this case. The reason should be that the volume reduction due to the increased pressure makes the double well potential become basically single-well and hence the hopping motion of Ti-O almost disappears. Note that the branch is split into two peaks, one above and the other below the TA white spots, suggesting that there is still mixing with the TA. Moreover, there are still satellite peaks at higher frequencies. It seems worth looking at this in more details.

### 9.2.3 $BaTiO_3$: ferroelasticity and other elastic anomalies. Is the material auxetic?

Ferroelasticity, in my opinion, has not gathered the same attention that ferroelectricity has.

One of the interesting phenomena that were pointed out by some studies [37] on the elastic properties of $BaTiO_3$ is auxeticity. Auxeticity means that the Poisson's ratio of the material

assumes negative values. The Poisson's ratio, in the hypothesis of an isotropic response, is $\nu = \frac{1}{2}(C_{11} - 2C_{44})/(C_{11} - C_{44})$, where $C_{11}$ and $C_{44}$ were defined in Sec. 8.2. Hence, a negative value of $\nu$ can occur as a result of the softening of the elastic constant $C_{11}$ with respect to $C_{44}$.

The possibility of a softening of $C_{11}$ is connected with the concept of ferroelastic phase transitions. Ferroelasticity is the presence of an elastic strain even when no external stress is applied [105]. The softening of $C_{11}$ was detected by the Brillouin study of Ref. [74]. This is caused by the change in the shape of the unit cell of $BaTiO_3$ during its phase transitions. A deformation of the cells in which the crystal can be partitioned, in fact, can be seen as the result of an external strain, and because in $BaTiO_3$ this happens naturally at $T_C$ with no stress applied, an elastic constant has to soften. Now, if $C_{11}$ softens more than $C_{44}$, $\nu$ can become negative: the material becomes auxetic. Hence, ferroelastic phase transitions and auxeticity seem to be strongly interconnected.

Auxeticity determines a very unusual and counter-intuitive elastic response: when the material is stretched in one direction, it expands, rather than contracts, transversely. Albeit being an interesting phenomenon, most of the times experimental studies did not even mention auxeticity. If we apply the isotropic formula $\nu = \frac{1}{2}(C_{11} - 2C_{44})/(C_{11} - C_{44})$ to get the Poisson's ratio $\nu$ to the data presented in Ref. [74] [1], we would find that $BaTiO_3$ is auxetic well into its PE phase, and for a wide range of temperatures–as much as 300 K after $T_C$. This seems very unlikely. This absurd result should be caused by the inadequacy of the isotropic formulae, rather than a real property of the material. Hence, there are reasons to believe that the elastic response of $BaTiO_3$ is very anisotropic, even in its cubic phase, at least close to $T_C$. In fact, it is known by other Brillouin [68] and neutron scattering [28] studies that the acoustic modes show a strongly anisotropic dispersion, meaning that the isotropic formulae would have to be ruled out, even in the C phase.

Ref. [37] was the only one, to my knowledge, to talk about auxeticity directly: it asserted that $BaTiO_3$ is auxetic, but only at $T \approx T_C$. The application of isotropic formulae, in this case, was justified by the use of a polycrystalline sample, where the orientation of the grains are

[1] Ref. [74] Fig. 4

random and hence we should expect an isotropic elastic response. Hence, we can confidently say that the Poisson's ratio of $BaTiO_3$ becomes negative for at least a range of temperatures near $T_C$. However, the precise mechanism for why this happens is neither understood, nor has been investigated in any detail.

Auxeticity is a very exotic phenomenon in the engineering community: it determines an increase in the shear modulus, a higher absorbance of impacts, fracture resistance and other interesting properties. However, the feeling is that it remained a "niche". One of the reasons is that, in the common understanding of it, the auxetic behaviour is given by rigid rotations of large portions of the material upon stretching/compression, and this can only happen if the material features holes, which can accommodate the rotation of the solid portions. A typical example of this is the honeycomb structures. As a result, the auxetics commonly proposed by engineers are hollowed, or in form of foams, and hence soft. There are very few or possibly no examples of *bulk* auxetic materials.

From a theoretical/computational point of view, finite element methods techniques are typically used by engineers; these have the capability of reaching much larger length scales, but pay the price of renouncing the whole physics of the atomic interactions at the nanoscale. Fully-atomistic MD can only simulate a handful of atoms, but this has proven enough to understand the mechanism underpinning the atomic dynamics of the phase transitions of $BaTiO_3$. Because auxeticity seems to happen only at $T \sim T_C$ [37], it is natural to blame the peculiar atomic dynamics of $BaTiO_3$ at the phase transitions for it. Hence, MD might work as a bridge between physics and engineering, and help us understand, study, and engineer bulk auxetic materials with tunable characteristics.

### 9.2.4 $BaTiO_3$: the thermal conductivity

When mentioning ferroelasticity and the dampening of acoustic modes in Sec. 8.2, I touched upon the thermal conductivity. The disruption of the acoustic modes due to the chains' flipping mechanism should decrease the thermal conductivity at the onset of phase transitions. This would be natural to believe, since acoustic modes acquire a relatively high linewidth in $\omega$-space,

and in the common understanding of thermal transport in crystals, the thermal conductivity is inversely proportional to the phonon linewidth [38, 4, 33].

On the contrary, experiments have shown that the thermal conductivity increases at the onset of the transitions [84]. I suspect that this apparently odd result has to do with the fact that the chains, which form at $T \sim T_C$, can more easily transport the thermal energy. However, I am far from satisfied with my understanding of this. It would be interesting to perform calculations of this (and maybe other?) transport property. This could be done, within linear response theory, by means of a Green-Kubo formula (or its equivalent Einstein relation version) which allows to calculate the thermal conductivity from MD simulations, as explained in standard textbooks of statistical mechanics [89, 1]. This calculation would not be dissimilar to the way I calculated the static dielectric constant in Sec. 8.1.

## 9.3 Other avenues of future work

The chief method I have used throughout this work, the FT-VVCF method, is not new, as I have mentioned. However, its full power has not been exploited sufficiently, in my opinion. For example, the method was used in Refs. [128, 151, 129], but the $2 \times 2 \times 2$ supercell used in these references only allowed to obtain spectra at the BZ center and boundaries, hence phonon band structures were not obtained. Another example is Ref. [133]: this is a 2006 study of carbon nanotubes which used a relatively fast and inaccurate force field. The wavevector resolution achieved at that time, and for that one dimensional material, was achieved in this thesis in approximately the same amount of computational time for three dimensional materials like MgO and $BaTiO_3$ and using much more sofisticated force fields. Hence, the FT-VVCF method appears to not have been extensively used in the literature, especially when compared to PT, despite it being fully non-perturbative.

Besides allowing to calculate phonon spectra non-perturbatively, this method is flexible with respect to how the atomic trajectories are computed. For example, it can be used when trajectories are calculated with *ab inito* MD, so that the electronic quantum mechanical effects can be

included (but only within the Born-Oppenheimer adiabatic approximation). The advances in computer hardware (like the integrated use of CPUs and GPUs and the improvements of RAM memories that allow to store big amounts of data) and software (for example in linear-scaling DFT codes), are making *ab initio* techniques more and more affordable. Hence, I foresee that the FT-VVCF, calculated after *ab initio* MD or other first principle methods, can have a big impact in the future of phononics.

# Appendix A

# The force field parameters for MgO

The parameters of the potential are summarized in table B.1.

| | Mg | O | Mg-Mg | Mg-O | O-O |
|---|---|---|---|---|---|
| charges | | | | | |
| q | 1.415382 | -1.415382 | | | |
| $D$ | | | 0 | $3.0945 \times 10^{-3}$ | $2.161\times 10^{-3}$ |
| $\gamma$ | | | 25.1073 | 10.1621 | 8.9925 |
| $r^0$ | | | 26.9788 | 4.9640 | 6.1491 |
| dipoles | | | | | |
| $\alpha$ | 0 | 9.6565 | | | |
| $b$ | | | 0 | 1.8713 | 0 |
| $c$ | | | 0 | -1.6809 | 0 |

Table A.1: The force field parameters for MgO in atomic units.

# Appendix B

# The force field parameters for $BaTiO_3$

The parameters of the potential are summarized in table B.1.

| | O | Ti | Ba | O-O | O-Ti | O-Ba | Ti-Ti | Ti-Ba | Ba-Ba |
|---|---|---|---|---|---|---|---|---|---|
| charges | | | | | | | | | |
| q | -1.338693 | 2.506673 | 1.509406 | | | | | | |
| $D$ | | | | 1.5048E-07 | 3.9134E-03 | 8.3600E-03 | 3.4815E-04 | 5.1423E-02 | 1.0142E-02 |
| $\gamma$ | | | | 1.8629E+01 | 1.0719E+01 | 9.4084E+00 | 7.3084E+01 | 9.2656E-01 | 6.5269E+00 |
| $r^0$ | | | | 1.4726E+01 | 4.8614E+00 | 5.6453E+00 | 7.1587E+00 | 2.1852E+01 | 7.1900E+00 |
| dipoles | | | | | | | | | |
| $\alpha$ | -1.13111552 | 1.42377371 | 0.57364597 | | | | | | |
| $b$ | | | | 1.3567E+00 | 3.6966E+00 | 1.6832E+04 | 1.6833E+04 | 1.4924E+00 | 9.7493E+03 |
| $c$ | | | | 1.5679E+00 | -9.2528E+00 | 0 | 0 | -2.0683E+00 | 0 |

Table B.1: The force field parameters for $BaTiO_3$ in atomic units.

# Appendix C

# The relationship between the distribution of kinetic energy and the velocity-velocity correlation function

Let us consider only one atom of mass $m$ and moving along one dimension with velocity $\dot{u}(t)$, and let us assume that its trajectory is only observed at $t \in (-\frac{\mathcal{T}}{2}, \frac{\mathcal{T}}{2})$. This will allow us to integrate over all real numbers rather than over a specific time interval, namely, to write $\int_{\mathbb{R}} dt \equiv \int dt$ instead of $\int_{-\mathcal{T}/2}^{\mathcal{T}/2} dt$. Let us define the $\frac{1}{\sqrt{2}}\sqrt{\text{mass}}$-weighted velocity $v(t) = \frac{1}{\sqrt{2}}\sqrt{m}\dot{u}(t)$. In the following, I will denote the Fourier transform (FT) of a quantity either by $\mathfrak{F}[\cdot]$) or by a tilde $\tilde{\cdot}$. For example, $\tilde{v}(\omega) = \mathfrak{F}[v(t)] = \int dt v(t) e^{-i\omega t}$.

The kinetic energy of the atom at time $t$ is

$$\mathcal{K}(t) = v^2(t). \tag{C.1}$$

The average kinetic energy is

$$K = \langle \mathcal{K}(t) \rangle_t = \frac{1}{\mathcal{T}} \int dt v^2(t) = \frac{1}{2\pi\mathcal{T}} \int d\omega \tilde{v}^2(\omega) = \tag{C.2}$$

$$\frac{1}{2\pi\mathcal{T}} \int d\omega \tilde{v}^*(\omega)\tilde{v}(\omega) = \frac{1}{2\pi\mathcal{T}} \int d\omega \tilde{v}(-\omega)\tilde{v}(\omega). \tag{C.3}$$

In the last equation of Eq. C.2, I have used *Parseval's theorem*, which states that the integral over *time* $t$ of the square of a quantity equals the integral over *frequencies* $f$ of the FT of the same quantity, and I divided by $2\pi$ because I considered the cyclic frequency $\omega$, rather than $f$. In Eq. C.3 I used the fact that the trajectory of the atom is a real function, hence $\tilde{v}(\omega)^* = \tilde{v}(-\omega)$. Clearly the quantity $\frac{1}{2\pi\mathcal{T}}\tilde{v}(-\omega)\tilde{v}(\omega)$ defines how the kinetic energy is distributed over frequencies.

Let us now write the velocity-velocity correlation function (VVCF),

$$C(t) = \langle v(t_0)v(t_0+t)\rangle_{t_0} = \frac{1}{\mathcal{T}}\int v(t_0)v(t_0+t)dt_0. \tag{C.4}$$

The FT of $C(t)$ is

$$\tilde{C}(\omega) \equiv \mathfrak{F}[C(t)] = \frac{1}{\mathcal{T}}\int dt \int dt_0 v(t_0)v(t_0+t)e^{-i\omega t} = \tag{C.5}$$

$$\frac{1}{\mathcal{T}}\int ds \int dt_0 v(t_0)v(s)e^{-i\omega(s-t_0)} = \frac{1}{\mathcal{T}}\int dt_0 v(t_0)e^{i\omega t_0}\int ds v(s)e^{-i\omega s} = \frac{1}{\mathcal{T}}\tilde{v}^*(\omega)\tilde{v}(\omega), \tag{C.6}$$

where to go from Eq. C.5 to C.6 I have changed the integration variable $t_0+t \to s$. Alternatively, one could have noticed that $C(t)$ is similar to the convolution between $v$ and itself, $v * v$, and used *convolution theorem* that states that the FT of the convolution between two functions is equal to the product of the FT of each function. Eq. C.6 demonstrates that the FT of the VVCF is $2\pi$ the quantity in the integral of Eq. C.3, hence it is the *distribution of kinetic energy in $\omega$-space of the trajectory of the single atom.*

**Extension to the case of a vibrating string**

The extension to the case where multiple atoms are present is straightforward. For simplicity, and without loss of generality, let us consider a vibrating string of length $L$, and whose uniform mass per unit length is $\rho$. The string can be considered a continuum along the $x$ axis, and its ends are fixed at $x = -\frac{L}{2}$ and $x = \frac{L}{2}$. The displacement of an infinitesimal portion of the string from equilibrium is $u(x,t)$, and let us define the $\frac{1}{\sqrt{2}}\sqrt{\text{mass}}$-weighted velocity $v(x,t) \equiv \frac{1}{\sqrt{2}}\sqrt{\rho dx}\dot{u}$.

The kinetic energy of an infinitesimal portion $dx$ of the string is

$$\mathcal{K}(x,t) = \frac{1}{2}\rho dx\dot{u}^2(x,t) = v^2(x,t). \tag{C.7}$$

The average kinetic energy of the string is obtained by averaging over time $t$ and space $x$,

$$K = \left\langle \langle \mathcal{K}(x,t)\rangle_x \right\rangle_t = \frac{1}{L\mathcal{T}}\int dx \int dt v^2(x,t) = \frac{1}{4\pi^2 L\mathcal{T}}\int dk \int d\omega \tilde{v}^2(k,\omega), \tag{C.8}$$

where I have used Parseval's theorem again in two dimensions.

The VVCF is

$$C(x,t) = \left\langle \langle v(x_0,t_0)v(x_0+x,t_0+t)\rangle_{x_0} \right\rangle_{t_0} = \frac{1}{L\mathcal{T}}\int dx_0 \int dt_0 v(x_0,t_0)v(x_0+x,t_0+t). \tag{C.9}$$

Because space and time are independent of one another, the FT in $x$ and $t$ of the VVCF can be performed separately in the same manner as in Eq. C.6, yielding

$$\tilde{C}(k,\omega) \equiv \mathfrak{F}_k\mathfrak{F}_\omega[C(x,t)] = \frac{1}{L\mathcal{T}}\int dx dt dx_0 dt_0 v(x_0,t_0)v(x_0+x,t_0+t)e^{-i(kx-\omega t)} = \tag{C.10}$$

$$\frac{1}{L\mathcal{T}}\tilde{v}^*(k,\omega)\tilde{v}(k,\omega). \tag{C.11}$$

Hence, the quantity in the integral of C.8 is $1/(2\pi)^2$ the FT of the VVCF in space and time. Hence, the FT-VVCF is the distribution of the kinetic energy in reciprocal spacetime, or ($\omega$,$\boldsymbol{k}$)-space.

# Appendix D

# Planning on a modern neutron scattering experiment

In Sec. 6.3, we pointed out some of the problems in the INS spectra produced for $BaTiO_3$. Among them is the maximum energy shift allowed by the spectrometer. This value determines the range of frequencies at which phonon spectra can be measured without the signal vanishing and being deteriorated by background noise. One of the factors it depends on is the quality of the neutrons utilized. Until the late '60es, mainly cold neutrons, that is neutrons of energy between 0 and 25 meV, were used. Consequently, the neutrons were so slow that often only phonon-annihilation processes could be detected with low noise [106]; furthermore, if we consider not-too-high a sample temperature, and bearing in mind the Bose-Einstein distribution, modes at frequencies $\omega > k_B T/\hbar$ are not highly populated, and some authors, like Sangaster, referred that only modes below 10 THz could be detected in some cases [106]. The situation changed when thermal neutrons, i.e. neutrons with energies of 25 meV and beyond, could be used after the installation, on many laboratories, of hot sources [106, 30]. These do not only guarantee higher-energy neutrons, but also higher intensity beams, that is beams with better signal-to-noise ratio. For example, the neutron beam used by Sangaster for computing the dispersion of MgO was thermalized by passing through a block of BeO kept at 1100 °C [106], while Currat *et al.*, around the same years, reported that the high-energy phonons of $KNbO_3$ could

be detected by using neutrons up to 80 meV [30]. Nowadays measurements allow the whole phonon dispersion to be probed with an accuracy so high that details of the phonon bands can be detected–see for instance the low-signal phonon sidebands clearly visible with the INS experiment performed by Shen *et al.* for NaBr in Ref. [115] (and whose data is reported in Fig. 9.1a). Of course, besides the neutrons' energies, other devices are important that determine the quality of the beams, like the use of monochromators. Another expedient is to subtract the instrument background from the spectra *ex post*, as Shen *et al.* did [115].

Although the studies performed for $BaTiO_3$ in the Brookhaven National Laboratory used thermal neutrons, they do not seem utterly satisfying, in that the maximum energy shift recorded was $< 20$ mev, corresponding to $\approx 5$ THz. One of the open questions I highlight in Sec. 6.3 is whether or not there is Slater TO activity at $\omega > \omega_{\rm TA}$. Experimental evidence of this would be of paramount importance: it would in fact confirm/reject the concept of the melting of the Slater mode–that is, its spread out in $(\omega,\boldsymbol{k})$-space.

The fact that higher-frequency portions of $\omega$-space are now available with the modern apparatuses could probably be enough to say whether or not the melting of the Slater mode happens; in fact, we have shown, in Fig. 6.7b or Fig. 7.6, that part of the Slater TO activity lies in between the TA and the Last mode, where there is no phonon dispersion. Hence, if activity is found between, say, 5 THz and 10 THz, then that would already be an answer.

However, something more elaborate can probably be done. One thing could be to choose odd $\boldsymbol{G}$-vectors to produce the phonon spectra. Assuming that the scattering happens with the excitation of only *one* phonon, the scattering cross section is proportional to [38, 147, 29]:

$$S_1(\boldsymbol{Q},\omega) = \sum_\nu \left\{ \frac{\hbar}{2\omega_{\boldsymbol{q}\nu}} |F_\nu(\boldsymbol{Q})|^2 \big[ [1+n(\omega)]\delta(\omega+\omega_{\boldsymbol{q}\nu}) + n(\omega)\delta(\omega-\omega_{\boldsymbol{q}\nu}) \big] \right\}, \tag{D.1}$$

where the sum runs over the number of modes, $\omega_{\boldsymbol{q}\nu}$ is the frequency of the phonon involved, $n(\omega)$ is the Bose-Einstein population and in the big parenthesis are the two processes which can happen: the neutron loses energy to the crystal and excites one phonon ($n+1$ term), or the neutron gains energy from the crystal by absorbing one phonon ($n$ term); the $\delta$-functions

assure energy conservation for the two processes, and $|F_\nu(\boldsymbol{Q})|$ is the *dynamical structure factor*. The dynamical structure factor, as we saw in Sec. 2.8, is an extension of the static structure factor used in standard diffraction crystallography, and is defined as [38, 147, 29]

$$F_\nu(\boldsymbol{Q}) = \sum_j \frac{b_j}{\sqrt{m_j}} e^{-W_j} e^{i\boldsymbol{Q}\cdot\boldsymbol{R}_j} \boldsymbol{Q}\cdot\boldsymbol{e}(\boldsymbol{Q}\nu, j),$$

where the sum runs over the atoms in the unit cell, $b_j$ is the atomic scattering length (substitute with the atomic form factor if X-rays are used), $m_j$ is the atomic mass, $W_j$ is the Debye-Waller factor [38] and $\boldsymbol{e}(\boldsymbol{Q}\nu, j)$ is the eigenvector of the mode.

Now, let us focus on the C phase, and assume some simple TA and Slater TO eigenvectors for simplicity. Let us take $\boldsymbol{e}(\boldsymbol{G}+\delta\boldsymbol{q}, \text{TA}) = [[1,1,0],[1,1,0],[1,1,0],[1,1,0],[1,1,0]]$ and $\boldsymbol{e}(\boldsymbol{G}+\delta\boldsymbol{q}, \text{Slater TO}) = [[0,0,0],[1,1,0],[-1,-1,0],[-1,-1,0],[-1,-1,0]]$. Here, $\delta\boldsymbol{q}$ is a small phonon wavevector along the $[\bar{1}10]$ direction of the BZ, and the arrays define the displacements of Ba, Ti, and the three O atoms. Note that in the actual Slater mode the ratio between the O atoms' displacements is not exactly one, but we want to keep this a paper-and-pen calculation.

If we choose an even $\boldsymbol{G}$-vector, like $\boldsymbol{G} = [220]$, and we define a reduced dynamical structure factor as below, for the TA mode we have:

$$\begin{aligned}\sum_j e^{i(\boldsymbol{G}+\boldsymbol{\delta q})\cdot\boldsymbol{R}_j} \boldsymbol{Q}\cdot\boldsymbol{e}(\boldsymbol{G}+\delta\boldsymbol{q}, \text{TA}) \approx \exp(i2\pi[2,2,0]\cdot[0,0,0]) \times [2,2,0]\cdot[1,1,0] + \\ \exp(i2\pi[2,2,0]\cdot[\tfrac{1}{2},\tfrac{1}{2},\tfrac{1}{2}]) \times [2,2,0]\cdot[1,1,0] + \\ \exp(i2\pi[2,2,0]\cdot[\tfrac{1}{2},\tfrac{1}{2},0]) \times [2,2,0]\cdot[1,1,0] + \\ \exp(i2\pi[2,2,0]\cdot[\tfrac{1}{2},0,\tfrac{1}{2}]) \times [2,2,0]\cdot[1,1,0] + \\ \exp(i2\pi[2,2,0]\cdot[0,\tfrac{1}{2},\tfrac{1}{2}]) \times [2,2,0]\cdot[1,1,0] = \\ 4+4+4+4+4 = 20, \qquad \text{(D.2)}\end{aligned}$$

where we have used only scaled coordinates. Let us calculate the dynamical structure factor

for the Slater TO mode:

$$\sum_j e^{i(\boldsymbol{G}+\boldsymbol{\delta q})\cdot\boldsymbol{R}_j}\boldsymbol{Q}\cdot\boldsymbol{e}(\boldsymbol{G}+\delta\boldsymbol{q},\text{Slater TO}) \approx \exp(i2\pi[2,2,0]\cdot[0,0,0])\times[2,2,0]\cdot[0,0,0]+$$
$$\exp(i2\pi[2,2,0]\cdot[\frac{1}{2},\frac{1}{2},\frac{1}{2}])\times[2,2,0]\cdot[1,1,0]+$$
$$\exp(i2\pi[2,2,0]\cdot[\frac{1}{2},\frac{1}{2},0])\times[2,2,0]\cdot[-1,-1,0]+$$
$$\exp(i2\pi[2,2,0]\cdot[\frac{1}{2},0,\frac{1}{2}])\times[2,2,0]\cdot[-1,-1,0]+$$
$$\exp(i2\pi[2,2,0]\cdot[0,\frac{1}{2},\frac{1}{2}])\times[2,2,0]\cdot[-1,-1,0]=$$
$$0+4-4-4-4=-8, \quad \text{(D.3)}$$

Hence, we expect a lower signal for the Slater TO.

Let us now choose an *odd* $\boldsymbol{G}$-vector, like [110]:

$$\sum_j e^{i(\boldsymbol{G}+\boldsymbol{\delta q})\cdot\boldsymbol{R}_j}\boldsymbol{Q}\cdot\boldsymbol{e}(\boldsymbol{G}+\delta\boldsymbol{q},\text{TA}) \approx \exp(i2\pi[1,1,0]\cdot[0,0,0])\times[1,1,0]\cdot[1,1,0]+$$
$$\exp(i2\pi[1,1,0]\cdot[\frac{1}{2},\frac{1}{2},\frac{1}{2}])\times[1,1,0]\cdot[1,1,0]+$$
$$\exp(i2\pi[1,1,0]\cdot[\frac{1}{2},\frac{1}{2},0])\times[1,1,0]\cdot[1,1,0]+$$
$$\exp(i2\pi[1,1,0]\cdot[\frac{1}{2},0,\frac{1}{2}])\times[1,1,0]\cdot[1,1,0]+$$
$$\exp(i2\pi[1,1,0]\cdot[0,\frac{1}{2},\frac{1}{2}])\times[1,1,0]\cdot[1,1,0]=$$
$$2+2+2-2-2=2, \quad \text{(D.4)}$$

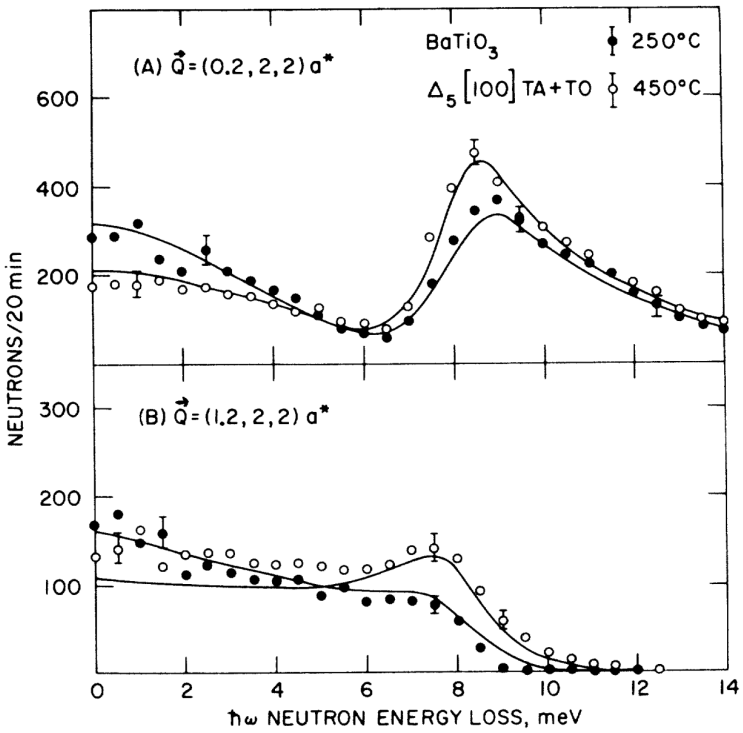



Figure D.1: The variation of the neutron spectra obtained for a same $\boldsymbol{q}$ point, $\boldsymbol{q} = [0.2, 0, 0]\boldsymbol{a}^*$, around different $\boldsymbol{G}$-points, $\boldsymbol{G} = [0, 2, 2]\boldsymbol{a}^*$ (upper plot) and $\boldsymbol{G} = [1, 2, 2]\boldsymbol{a}^*$ (lower plot). The lines are fit to the experimental data, which is indicated by symbols. The spectra are obtained at two temperatures. Note that the acoustic peak is weaker at $\boldsymbol{Q} = [1.2, 2, 0]\boldsymbol{a}^*$.

and

$$\sum_j e^{i(\boldsymbol{G}+\delta\boldsymbol{q})\cdot\boldsymbol{R}_j}\boldsymbol{Q}\cdot\boldsymbol{e}(\boldsymbol{G}+\delta\boldsymbol{q}, \text{Slater TO}) \approx \exp(i2\pi[1,1,0]\cdot[0,0,0]) \times [1,1,0]\cdot[0,0,0] +$$
$$\exp(i2\pi[1,1,0]\cdot[\frac{1}{2},\frac{1}{2},\frac{1}{2}]) \times [1,1,0]\cdot[1,1,0] +$$
$$\exp(i2\pi[1,1,0]\cdot[\frac{1}{2},\frac{1}{2},0]) \times [1,1,0]\cdot[-1,-1,0] +$$
$$\exp(i2\pi[1,1,0]\cdot[\frac{1}{2},0,\frac{1}{2}]) \times [1,1,0]\cdot[-1,-1,0] +$$
$$\exp(i2\pi[1,1,0]\cdot[0,\frac{1}{2},\frac{1}{2}]) \times [1,1,0]\cdot[-1,-1,0] =$$
$$0+2-2+2+2=4, \quad \text{(D.5)}$$

Hence, the ratio between the Slater TO and TA reduced factors is 4/2, so we expect a greater signal for the TO. This would mean that a purer optical spectrum can be obtain if $\boldsymbol{G} = [110]$ is used, rather than $\boldsymbol{G}$=[220]. In literature, examples of exploiting the $\boldsymbol{Q}$-dependence of the dynamical form factor to tune the characters of the spectra are very rare. One of the few of

them is in Harada, Axe and Shirane [56]. Their spectra are presented in Fig. D.1, and shows the difference between neutron spectra obtained at the same $\boldsymbol{q}$-point around different $\boldsymbol{G}$-points, namely, $\boldsymbol{G}$=[022] and $\boldsymbol{G}$=[122]. The phonon wavevector $\boldsymbol{q}$ is the same in both spectra, and one would in principle expect an exact same line shape. On the contrary, they found that (i) the acoustic peak is shallower at $\boldsymbol{G}$=[122], and (ii) that the interference which causes a pronounced dip between the TO and the TA disappears at the same point. However, the authors did not use odd $\boldsymbol{G}$-vectors systematically.

Of course, one of the problems in using odd G-vectors is that the expected signal is lower. This is because the structure factors for $\boldsymbol{G}$=[110] are lower than the case $\boldsymbol{G}$=[220]. This problem can be partly corrected by going as far as possible from $\boldsymbol{G}$=[000], which can be attained if high-energy neutrons are used; a $\boldsymbol{G}$-vector like $\boldsymbol{G}$=[330] or $\boldsymbol{G}$=[320] might be enough. Moreover, there are now techniques to remove the inevitable background from the instrument (cf. Ref. [115], which focuses on a 2021 highly-resolved INS study on NaBr, and its supplemental material), so poor signal is nowadays probably no longer an issue.

The calculation we have done here of the "reduced structure factors" is of course at the level of the cartoon. This paper-and-pen calculation should be replaced with a proper calculation of the dynamical structure factors $S(\boldsymbol{Q})$ of the phonon modes in many different $\boldsymbol{Q}$-points of reciprocal space. This calculation needs a good model of the atomic interactions, since the eigenvectors, the Debye-Waller factors and the phonon frequencies must be known in the summation of Eq. D.1. I provide the HA and MD calculations of $S(\boldsymbol{Q})$ in Sec. 7.6.

Of course, neutron scattering is not an in-house-lab procedure, and is costly. Nonetheless, this qualitative discussion, and the brilliant ($\omega$,$\boldsymbol{k}$) resolution of nowadays spectrometers (see for example Fig. 9.1a, where I report the neutron spectra of Ref. [115]), should in my opinion justify a new INS investigation of $BaTiO_3$.

# Appendix E

# The phonon band structures of $BaTiO_3$

In this section, I show the phonon band structure of $BaTiO_3$ in the HA. Fig. E.1 shows the bands at mechanical equilibrium in the R phase. Fig. E.3 shows the bands when they are calculated with the cubic nominal structure with lattice constant $a = 4$ Å. Fig. E.2 shows the eigenvectors of the Slater modes in the R phase for wavevector $\boldsymbol{k} = \frac{1}{5}\boldsymbol{k}_X$. Figs. E.4 and E.5 show the eigenvectors of the imaginary Slater modes in the C phase for wavevectors $\boldsymbol{k} = \frac{1}{5}\boldsymbol{k}_X$ and $\boldsymbol{k} = \frac{1}{5}\boldsymbol{k}_M$, respectively.

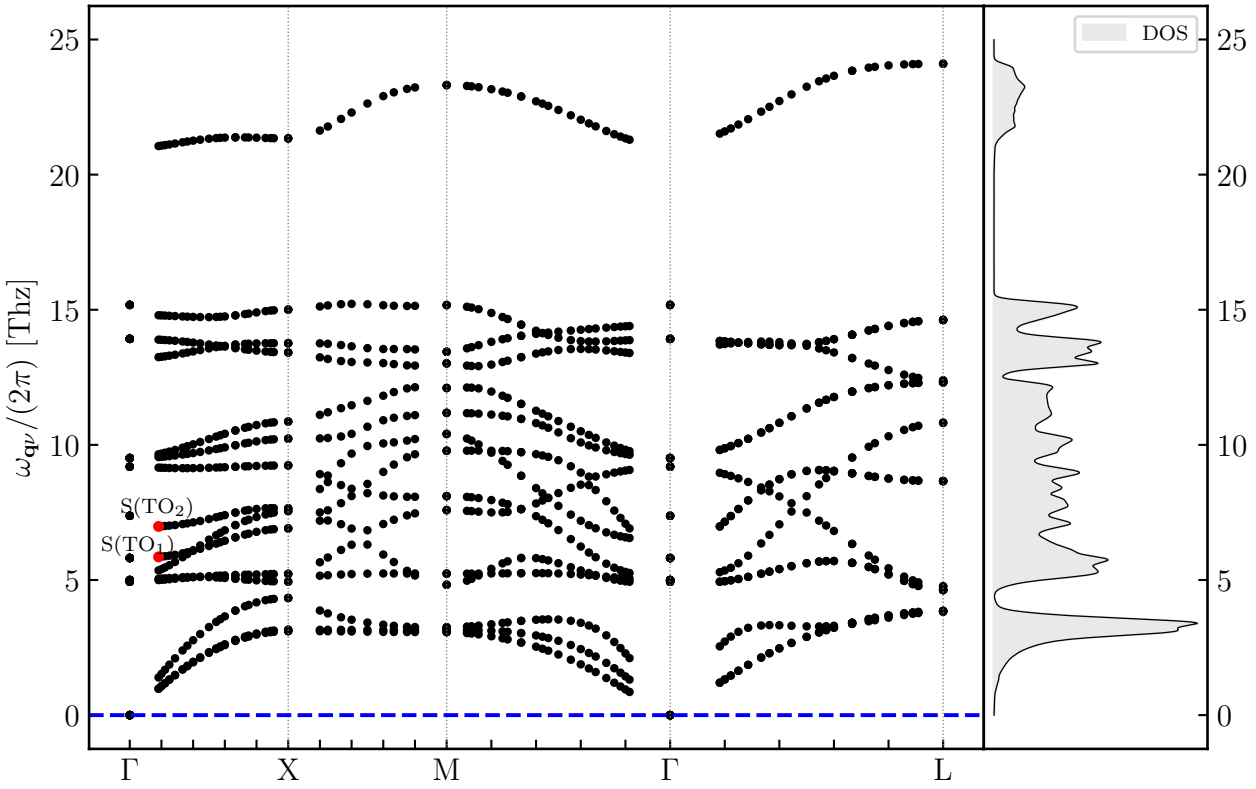



Figure E.1: The phonon band structure of $BaTiO_3$ in the HA at mechanical equilibrium. I have highlighted the Slater TO phonon modes near Γ.

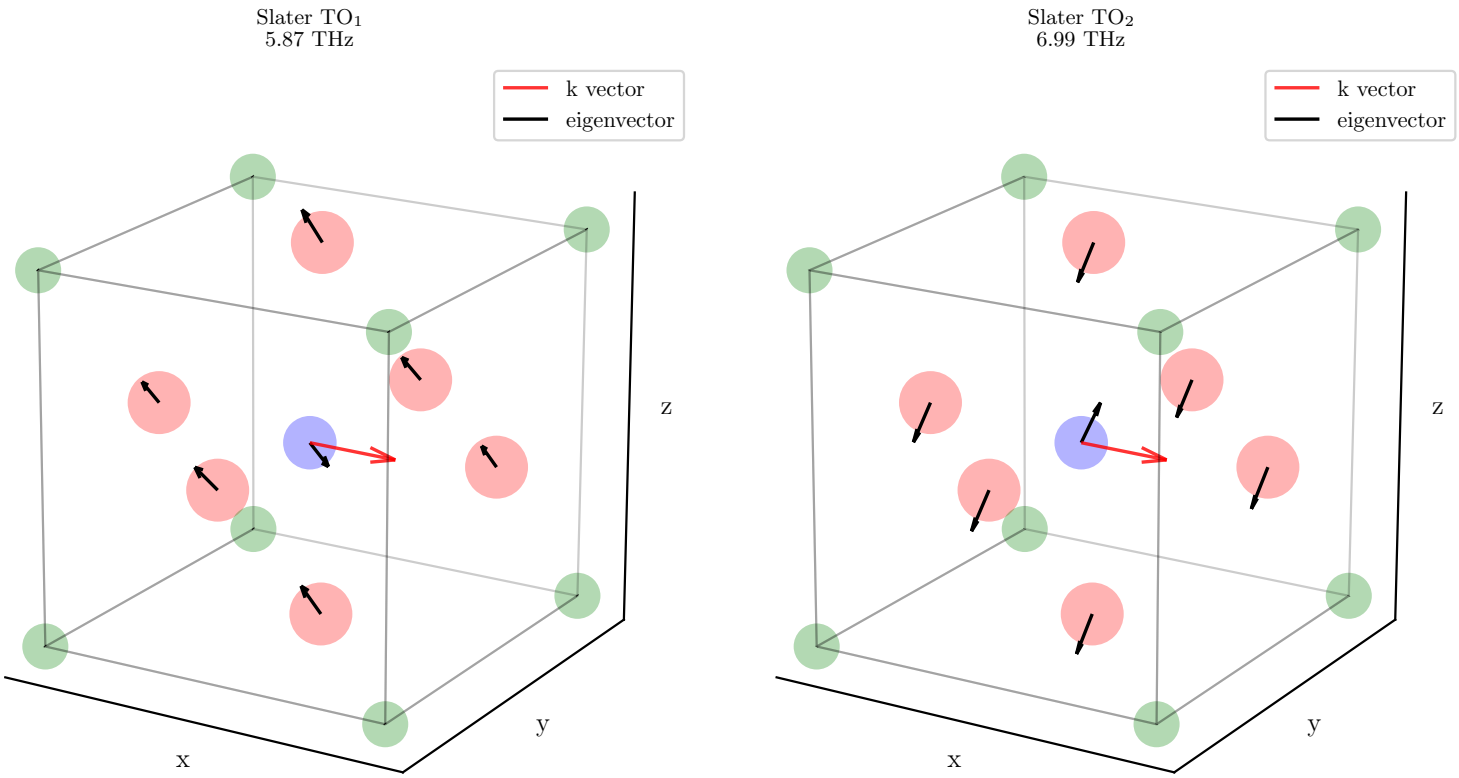



Figure E.2: The Slater TO modes at $\boldsymbol{k} = \frac{1}{5}\boldsymbol{k}_X$ for the R band structure at mechanical equilibrium. The red arrow is the wavevector, and the black arrows represent the eigenvector.

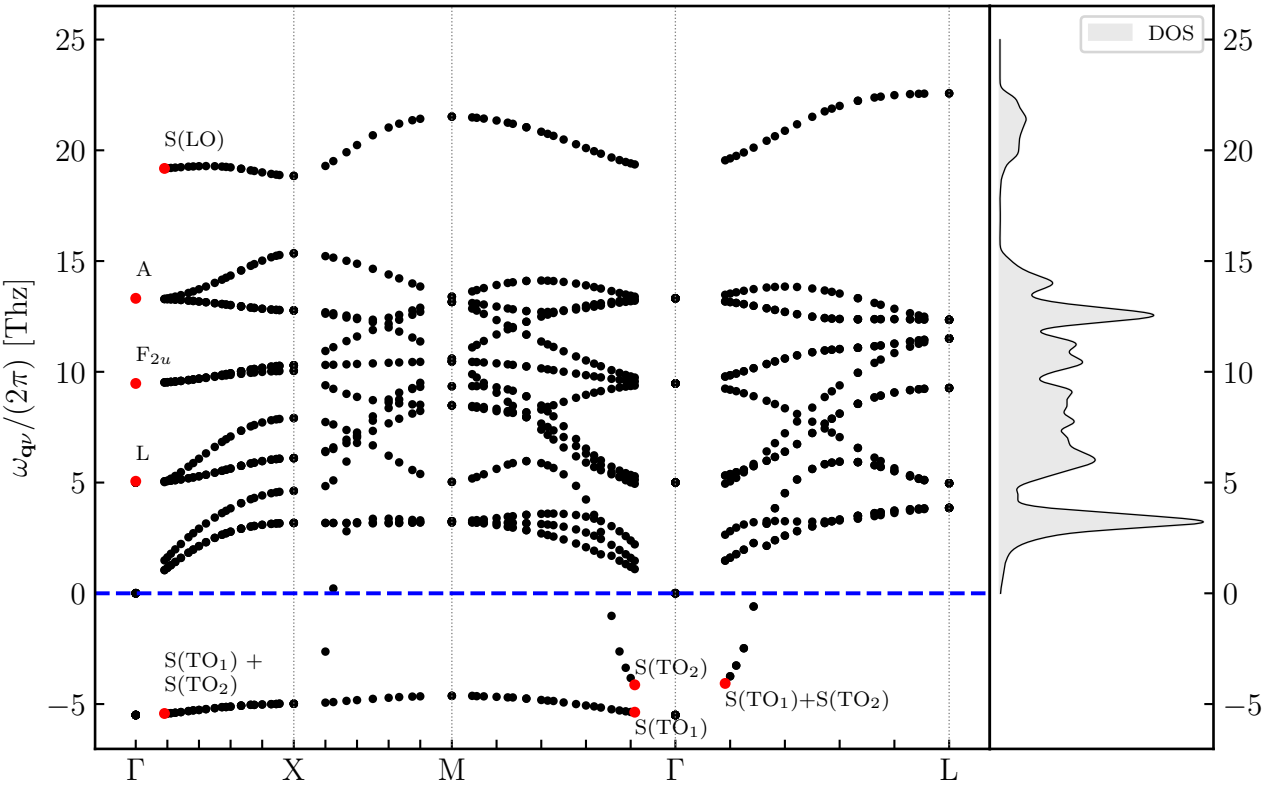



Figure E.3: The phonon band structure of $BaTiO_3$ in the HA for the nominal C band structure with lattice parameter $a = 4$ Å. I have highlighted the optical phonon modes near Γ and at Γ.

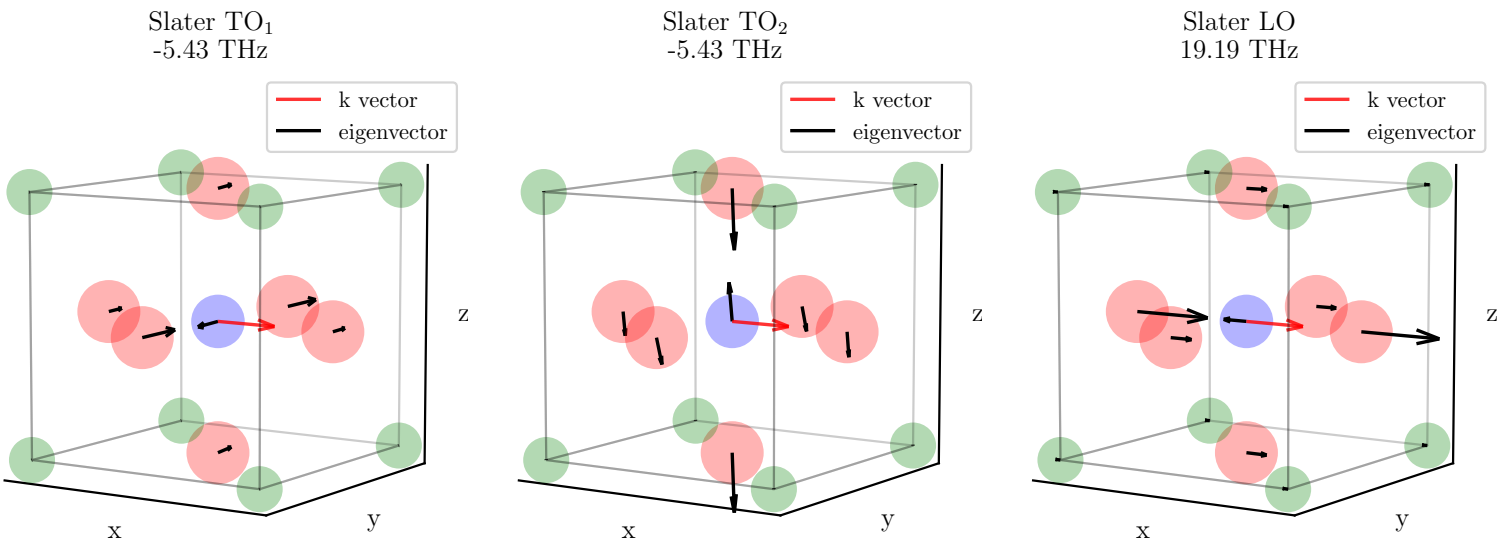



Figure E.4: The Slater TO modes at $\boldsymbol{k} = \frac{1}{5}\boldsymbol{k}_X$ for the C band structure. The red arrow is the wavevector, and the black arrows represent the eigenvector.

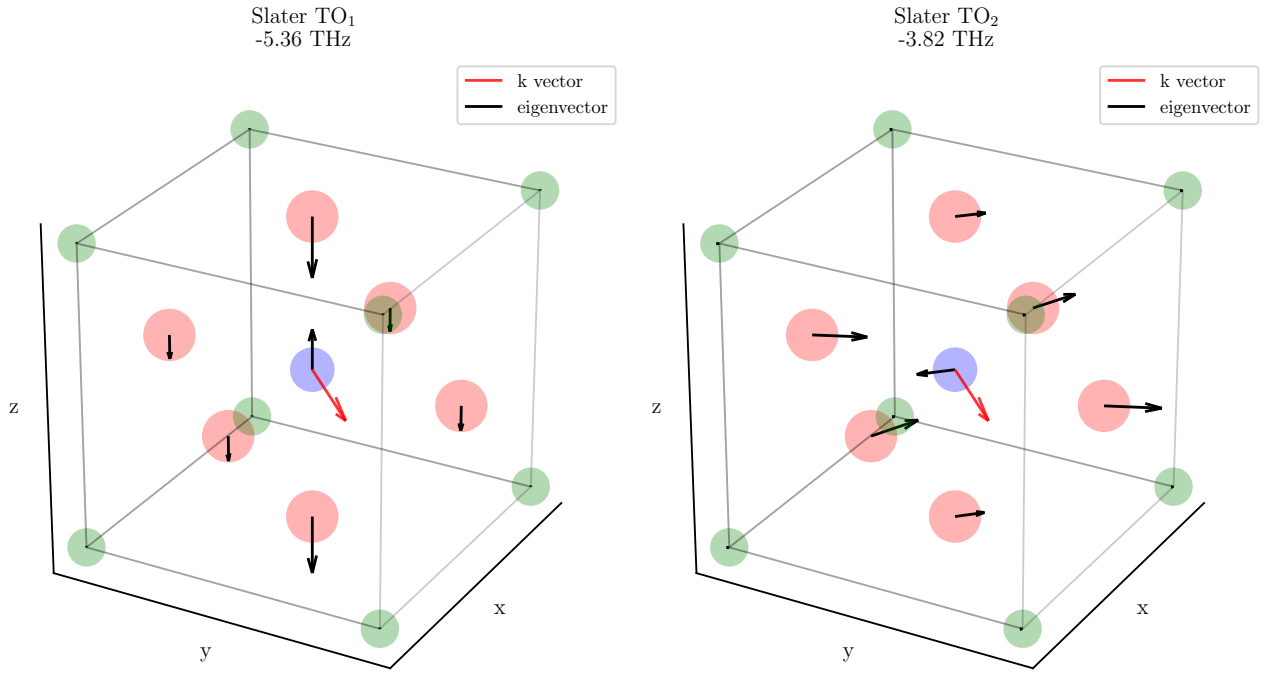



Figure E.5: The Slater TO modes at $\boldsymbol{k} = \boldsymbol{k}_M$ for the C band structure. The red arrow is the wavevector, and the black arrows represent the eigenvector.

# Appendix F

# The simulated IR spectra from NVT simulations

In this section, I show the imaginary part of the permittivity, $\chi''_{xx}(\omega)$, from NVT simulations. The results are in Fig. F.1. This plot, used alongside Fig. 7.2, allows to compare NPT and NVT simulations, and to compare both of them with experiments. Note that the MD peaks caused by the barostat disappear in an NVT simulation.

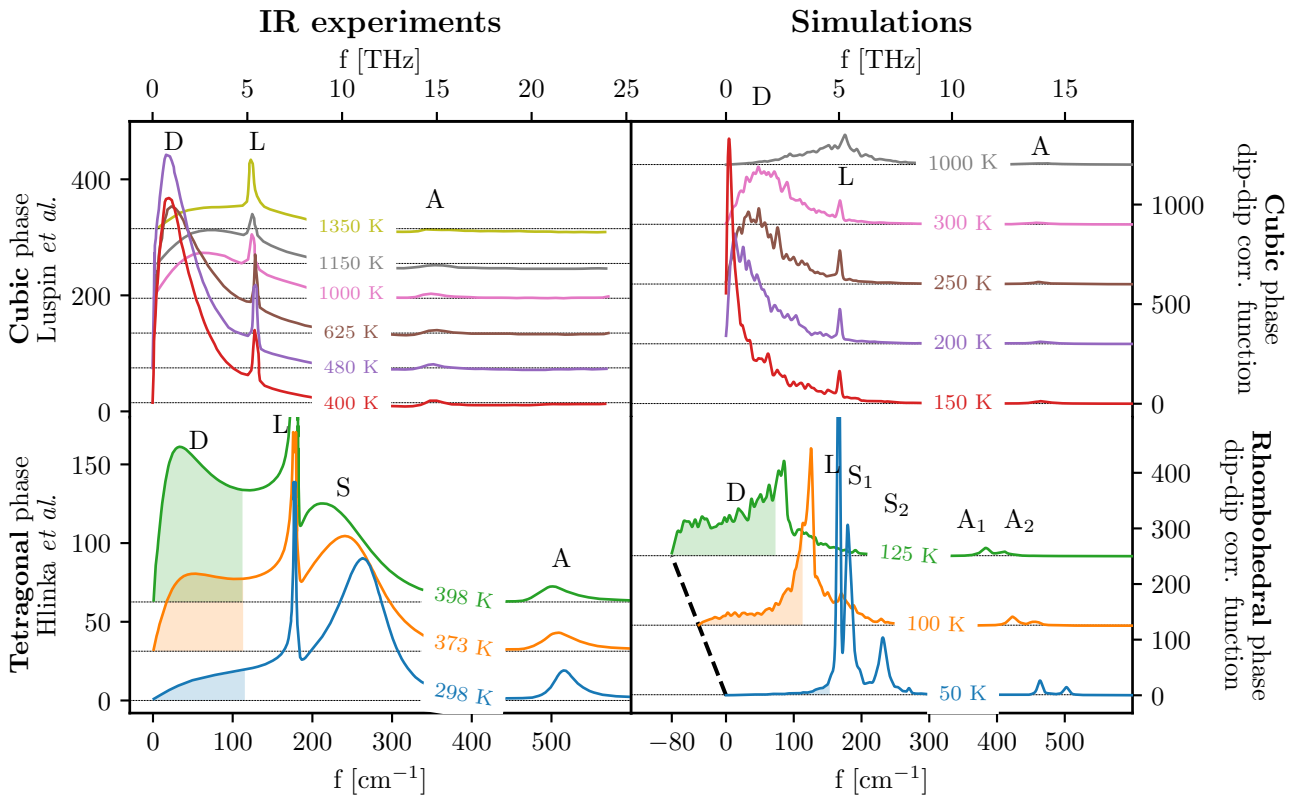



Figure F.1: Imaginary part of the dielectric function $\varepsilon''_{zz}(\omega)$ (left) and permittivity obtained from NVT simulations, $\chi''_{xx}(\omega)$ (right), containing the spectra of polar TO modes near Γ. The left hand side plots are, in the bottom, experimental spectra from Hlinka *et al.* [62] of $A_1$ modes in the T phase, and in the top, $F_{1u}$ modes in the C phase from Luspin *et al.* [82]. In the right hand side are the simulated IR spectra, calculated from Eq. 2.61, in the R phase (bottom plot) and C phase (top plot). In the bottom plot, I shifted the 100 K and 125 K spectra by 40 $\text{cm}^{-1}$ and 80 $\text{cm}^{-1}$ for visualization purposes. The naming of the modes follows the spectroscopic notations described in Sec. 5.4: D=Debye, L=Last, $S_1$ and $S_2$ are the two non degenerate Slater modes, and $A_1$ and $A_2$ are the two non degenerate Axe modes. This figure can be compared to Fig. 7.2, which shows the NPT results. Note the disappearance of the MD peaks in the NVT simulations. For the rest, the NPT and NVT spectra are similar. The Debye mode is highlighted by shadowed areas in the bottom plots. In the R-C transition, the two Slater modes shrink, and a Debye mode emerges. The Debye mode initially manifests as a noisy signal in the range $0 < f < 180$ $\text{cm}^{-1}$, which grows with approaching $T_C$ from below. Then, at $T \gtrsim T_C$ in the C phase, the Debye peak dominates the spectrum and appears as a narrow peak (critical slowing down). It then broadens and hardens, until it overlaps with the Last modes.

# Appendix G

# The diffuse scattering for $BaTiO_3$ in the HA broken down into modes

In Sec. 7.6, I showed the calculation of the diffuse patterns in the harmonic approximation. The patterns were obtained with the sum over the fifteen phonon modes (see Eq. 2.58). Here, I show the contribution of each mode to the diffuse scattering, in Fig. G.1. the color scheme is equal for all plots: yellow means higher values, blue means lower values. Note that optical modes contribute very little to the diffuse scattering, due to their higher frequency. Note that the denomination of the modes is only indicative, because there is high mixing of the Last and Slater modes away from $\boldsymbol{Q} = \boldsymbol{G}$.

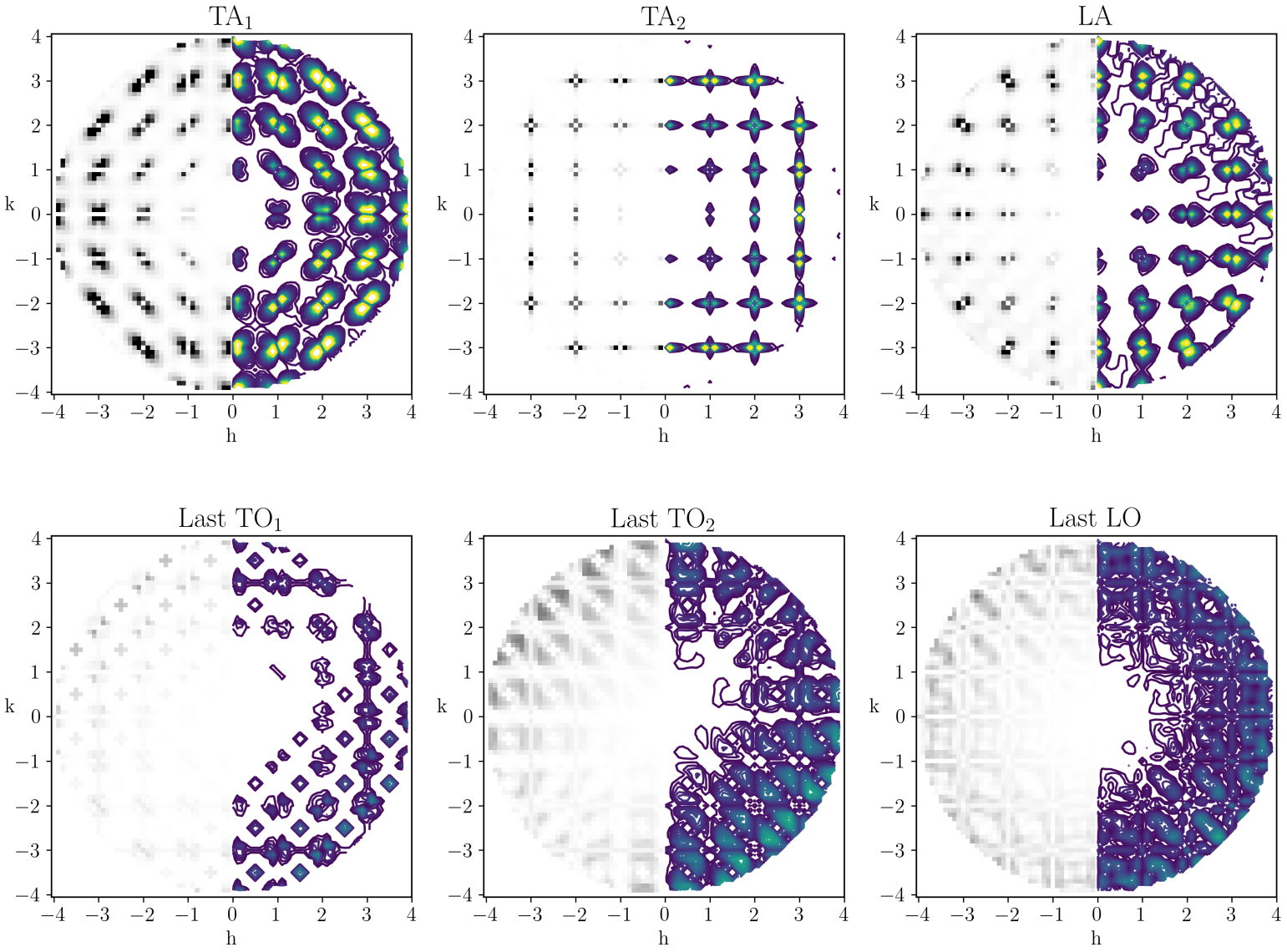
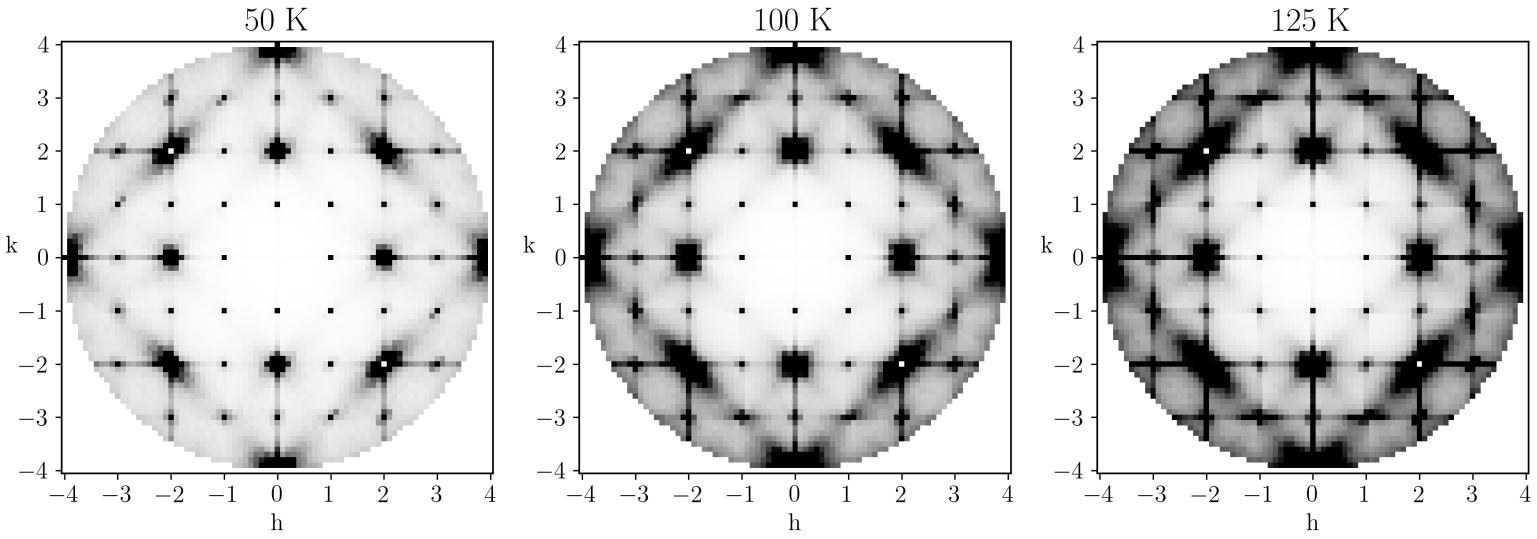



Figure G.1: Decomposition of harmonic diffuse scattering into phonon branches. First row: acoustic modes ($TA_1$ $TA_2$ LA). Note that characteristic butterfly and oval shapes caused by the $TA_1$ mode, and compare this with Fig. 7.3. The $TA_1$ contributes maximally to the scattering. Second row: Last modes. Note that higher energy modes contribute much less than acoustic modes. The color scheme is the same for all plots.

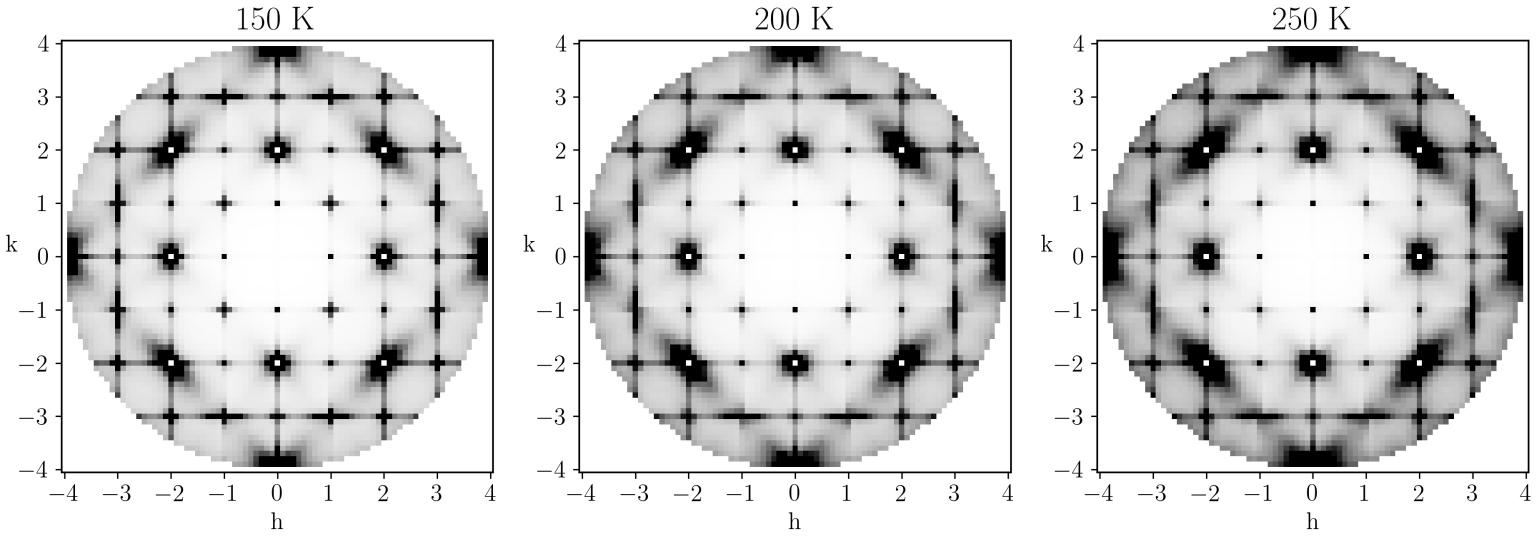
# Appendix H

# The diffuse scattering of $BaTiO_3$ from NPT simulations

In Sec. 7.6, I showed the diffuse scattering patterns from NVT simulations. I here provide the diffuse scattering from the NPT simulations. Note the additional presence of horizontal and vertical streaks in the R phase, which are due to the fluctuation of the MD volume caused by the barostat. I decided not to show the NPT results in the body of the thesis, because the barostat's streaks $S_B$ could be confused for $S_O$.




(a) NPT diffuse scattering at the rhombohedral phases. The horizontal and vertical streaks $S_B$ are caused by the barostat, which imposes MD supercell's fluctuations. In fact, they are absent in the NVT patterns of Fig. 7.4a. The max value for the color scheme has been set to 0.4 E-05 [$B^2$].




(b) NPT diffuse scattering at the cubic phases. The horizontal and vertical streaks are caused by the MD supercell's fluctuations $S_B$ *and* by the uncorrelated linear chains $S_O$. The max value for the color scheme has been set to 1 E-05 [$B^2$].

Figure H.1: The neutron diffuse scattering in the R and C phase simulated from MD in the NPT ensemble. Note that additional vertical and horizontal streaks appear in both phases, which are caused by the barostat.

# Appendix I

# The distribution of vibrational energy for $BaTiO_3$ projected onto different eigenvectors

In Sec. 7.7 I show the vibrational energy distribution, $\mathcal{E}(\omega, \boldsymbol{k})$, projected along the eigenvectors of one of the Slater modes. In this section, I show $\mathcal{E}(\omega, \boldsymbol{k})$ projected onto different sets of eigenvectors.

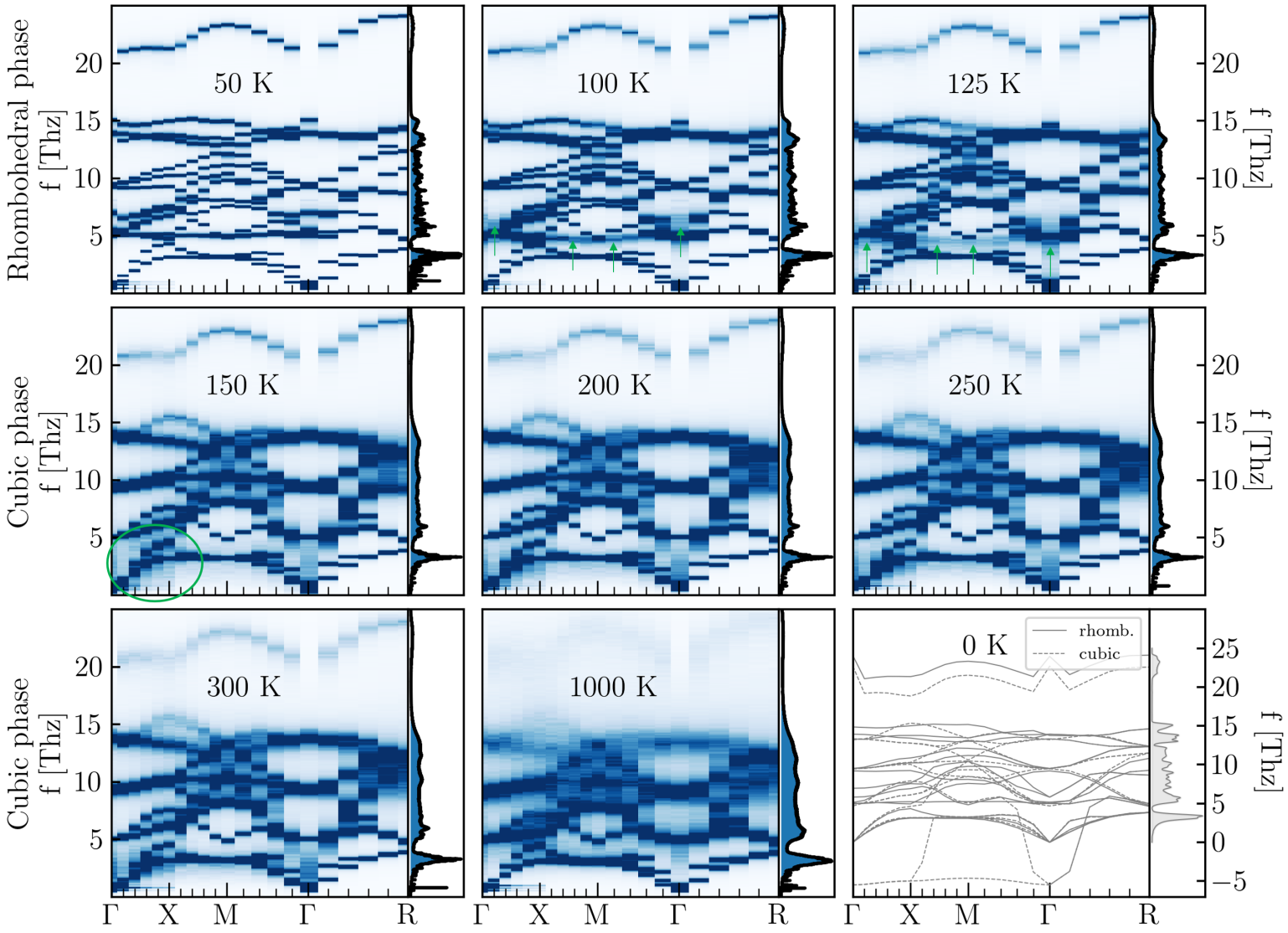



Figure I.1: The calculated vibrational energy $\mathcal{E}(\omega, \mathbf{q})$ of $BaTiO_3$ for all modes. The three peaks at low frequencies along $\Gamma - X$ visible at all $T$s are the MD peaks which I find in the IR spectrum of Fig. 7.2 as well, and result from the volume fluctuations caused by the barostat. I highlight with green arrows the partial softening and broadening of the Slater modes in the R-C transition, at 100 K and 125 K. At 150 K, I draw a green circle around $\Gamma - X$ where the melting of the mode is more apparent. Note that there is an evident splitting between $A_1$ or $B_1$ modes and $E$ modes at $\Gamma$ in the R phase, but in the C phase the phonon modes recover their degeneracies at $\Gamma$. Note also that the dispersion becomes broader at higher $T$; one striking feature is that the Slater LO mode, which is the highest frequency mode, becomes very broad at high $T$.

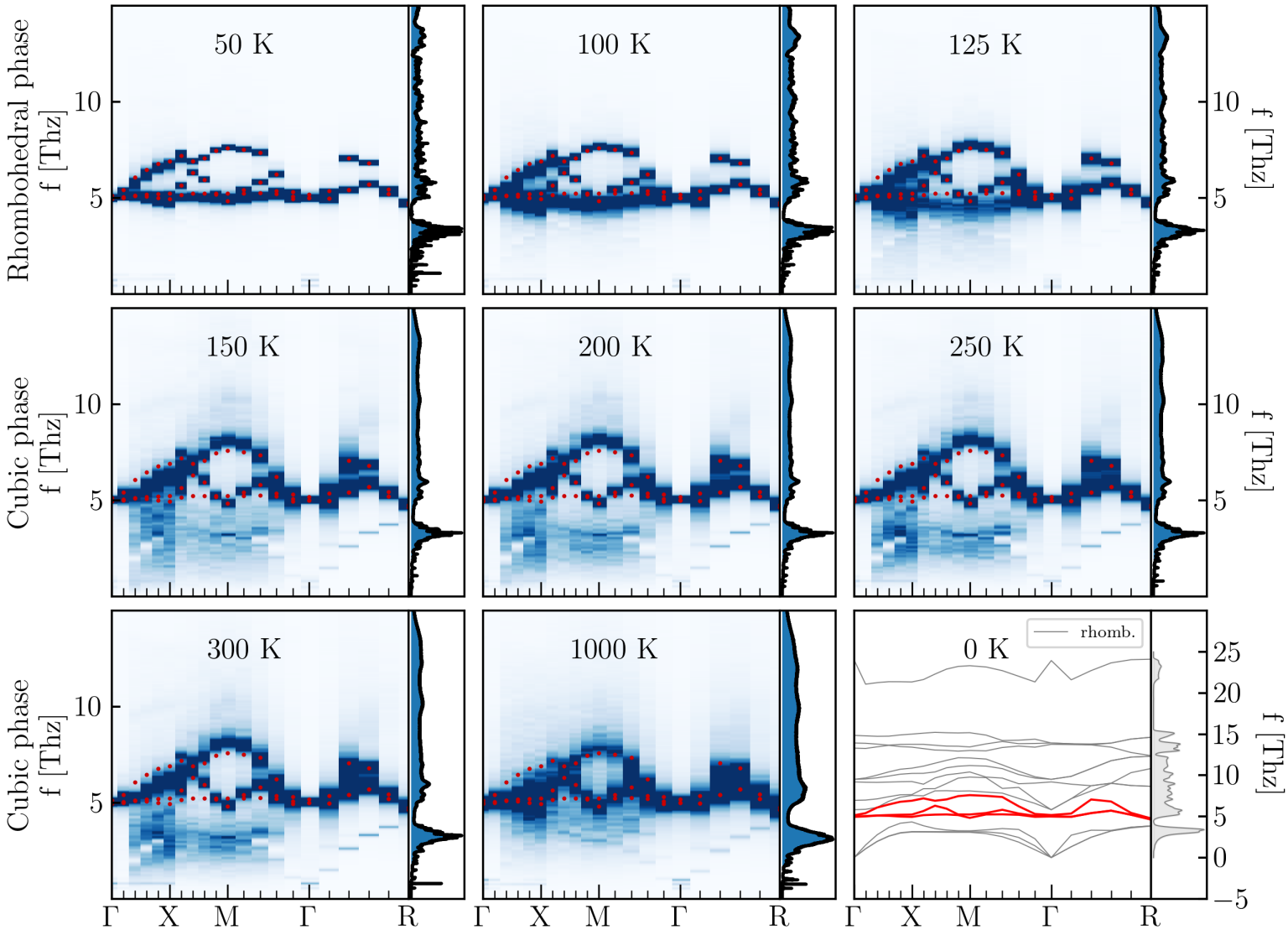



Figure I.2: The calculated vibrational energy $\mathcal{E}(\omega, \mathbf{q})$ of $BaTiO_3$ projected onto the eigenvectors of modes 4,5,6 of the rhombohedral phase, denoted in red in the lower right panel. This set of modes includes the Last modes at Γ. However, because of the high mixing of the modes away from the BZ center, the modes at $X$ can differ quite a lot from the pure Last modes at Γ. This is evident if we consider that these three branches contribute to the blotch, as it is apparent from 150 K to 1000 K. In the body of the thesis, in Fig. 7.6, the blotch is contributed maximally by the Slater branch obtained for the C phase. Hence, there is mixing, in the R phase, between Last modes and Slater modes.

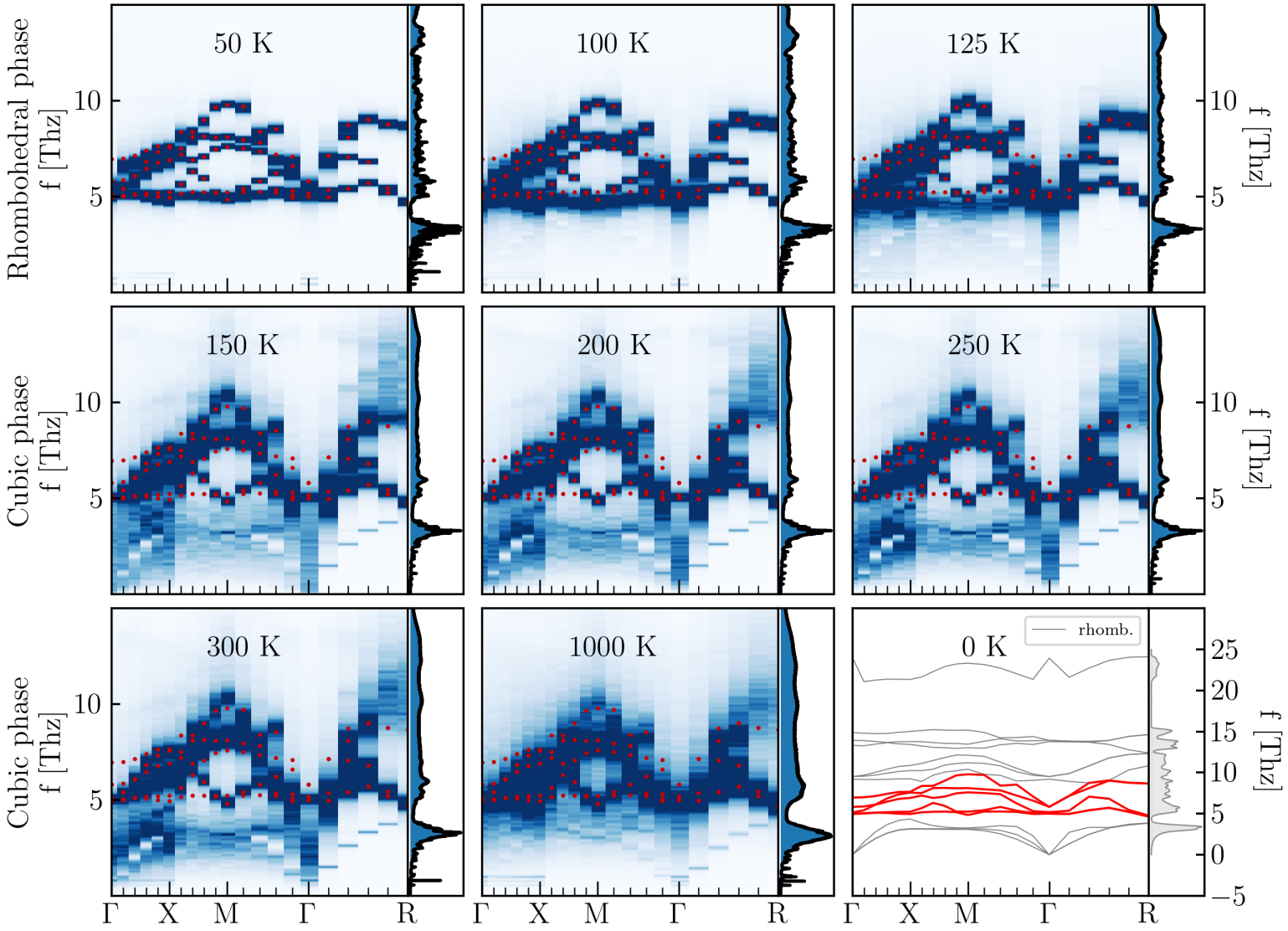



Figure I.3: The calculated vibrational energy $\mathcal{E}(\omega, \mathbf{q})$ of $BaTiO_3$ projected onto the eigenvectors of modes 4,5,6,7,8 of the rhombohedral phase, denoted in red in the lower right panel. These modes cover the frequency range 5-10 THz in the spectrum, where the Slater modes lie. The melting of the Slater modes is clearly visible.

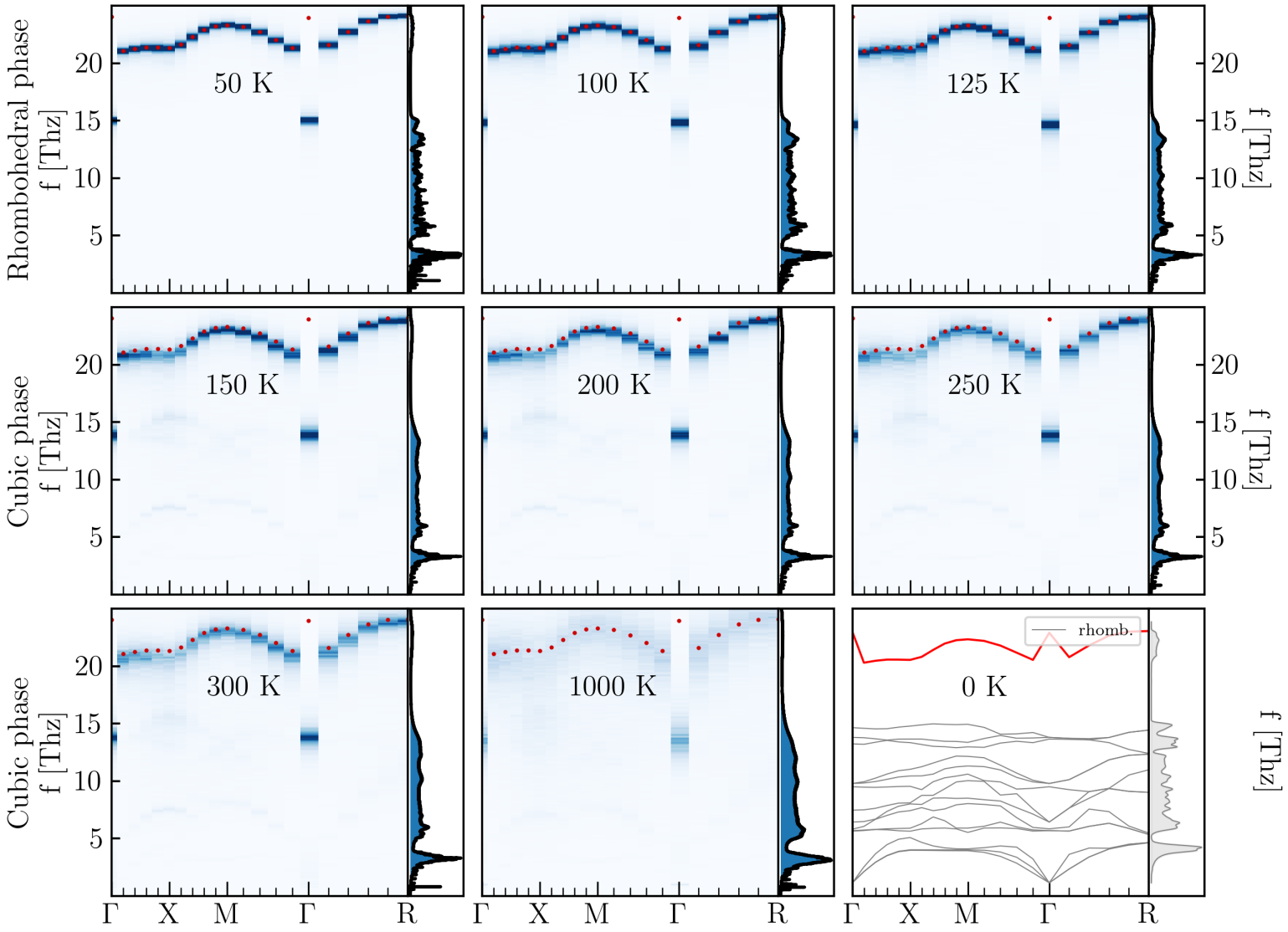



Figure I.4: The calculated vibrational energy $\mathcal{E}(\omega, \mathbf{q})$ of $BaTiO_3$ projected onto the eigenvectors of mode 15 (Slater LO) of the rhombohedral phase, denoted in red in the lower right panel. Note that it always stays hard, and broadens a lot with $T$.

# Bibliography


[1] Michael P. Allen and Dominic J. Tildesley. *Computer Simulation of Liquids*. Oxford University Press, second edition.

[2] Philip B. Allen. Anharmonic phonon quasiparticle theory of zero-point and thermal shifts in insulators: Heat capacity, bulk modulus, and thermal expansion. *Physical Review B - Condensed Matter and Materials Physics*, 92(6):1–10, 2015.

[3] Hans C. Andersen. Molecular dynamics simulations at constant pressure and/or temperature. *The Journal of Chemical Physics*, 72(4):2384–2393, 1980.

[4] Neil W Ashcroft and N David Mermin. *Solid State Physics*. Harcourt College Publishing, 1976.

[5] J. D. Axe, J. Harada, and G. Shirane. Anomalous acoustic dispersion in centrosymmetric crystals with soft optic phonons. *Physical Review B*, 1(3):1227–1234, 1970.

[6] A. S. Barker and J. J. Hopfield. Coupled-optical-phonon-mode theory of the infrared dispersion in BaTiO3, SrTiO3, and KTaO3. *Physical Review*, 135(6A):1732–1737, 1964.

[7] Stefano Baroni, Stefano De Gironcoli, Andrea Dal Corso, and Paolo Giannozzi. Phonons and related crystal properties from density-functional perturbation theory. *Reviews of Modern Physics*, 73(2):515–562, 2001.

[8] Petr S. Bednyakov, Boris I. Sturman, Tomas Sluka, Alexander K. Tagantsev, and Petr V. Yudin. Physics and applications of charged domain walls. *npj Computational Materials*, 4(65), 2018.

[9] Andreja Bencan, Emad Oveisi, Sina Hashemizadeh, Vignaswaran K. Veerapandiyan, Takuya Hoshina, Tadej Rojac, Marco Deluca, Goran Drazic, and Dragan Damjanovic. Atomic scale symmetry and polar nanoclusters in the paraelectric phase of ferroelectric materials. *Nature Communications*, 12(3509):1–9, 2021.

[10] H. J.C. Berendsen, J. P.M. Postma, W. F. Van Gunsteren, A. Dinola, and J. R. Haak. Molecular dynamics with coupling to an external bath. *The Journal of Chemical Physics*, 81(8):3684–3690, 1984.

[11] Herman J C Berendsen. Computer Simulation in Materials Science. *Computer Simulation in Materials Science*, (February), 1991.

[12] I. B. Bersuker. On the origin of ferroelectricity in perovskite-type crystals. *Physics Letters*, 20(6):589–590, 1966.

[13] Nicola Bonini, Michele Lazzeri, Nicola Marzari, and Francesco Mauri. Phonon anharmonicities in graphite and graphene. *Physical Review Letters*, 99(17):1–4, 2007.

[14] Alexey Bosak and Michael Krisch. Phonon density of states probed by inelastic x-ray scattering. *Physical Review B - Condensed Matter and Materials Physics*, 72(22):1–9, 2005.

[15] Jonathan Breeze. *Temperature and Frequency Dependence of Complex Permittivity in Metal Oxide Dielectrics: Theory, Modelling and Measurement*. Springer Cham, 2016.

[16] Eugenio Calandrini, Lorenzo Paulatto, Daniele Antonangeli, Fei He, Ricardo P.S.M. Lobo, Francesco Capitani, Jean Blaise Brubach, Pascale Roy, Laetitia Vincent, and Paola Giura. Limits of the quasiharmonic approximation in MgO: Volume dependence of optical modes investigated by infrared reflectivity and ab initio calculations. *Physical Review B*, 103(5):54302, 2021.

[17] David Chandler. *Introduction to Modern Statistical Mechanics*. Oxford University Press.

[18] Laurent Chaput, Atsushi Togo, Isao Tanaka, and Gilles Hug. Phonon-phonon interactions in transition metals. *Physical Review B - Condensed Matter and Materials Physics*, 84(9):1–6, 2011.

[19] A. Chaves, R. S. Katiyar, and S. P.S. Porto. Coupled modes with A1 symmetry in tetragonal BaTiO3. *Physical Review B*, 10(8):3522–3533, 1974.

[20] A. Chopelas. Thermal expansion, heat capacity, and entropy of MgO at mantle pressures. *Physics and Chemistry of Minerals*, 17(2):142–148, 1990.

[21] Mogens Christensen, Asger B. Abrahamsen, Niels B. Christensen, Fanni Juranyi, Niels H. Andersen, Kim Lefmann, Jakob Andreasson, Christian R.H. Bahl, and Bo B. Iversen. Avoided crossing of rattler modes in thermoelectric materials. *Nature Materials*, 7:811–815, 2008.

[22] W. Cochran. Crystal stability and the theory of ferroelectricity. *Advances in Physics*, 9(36):387–423, 1960.

[23] W. Cochran and R. A. Cowley. Dielectric constants and lattice vibrations. *Journal of Physics and Chemistry of Solids*, 23(5):447–450, 1962.

[24] Gabriele Coiana, Johannes Lischner, and Paul Tangney. Breakdown of phonon band theory in MgO. *arXiv:2307.10944*, 2023.

[25] R. Comes, M. Lambert, and A. Guinier. The chain structure of BaTiO3 and KNbO3. *Solid State Communications*, 6(10):715–719, 1968.

[26] R. Comès, M. Lambert, and A. Guinier. Désordre linéaire dans les cristaux (cas du silicium, du quartz, et des pérovskites ferroélectriques). *Acta Crystallographica Section A*, 26(2):244–254, 1970.

[27] R. Comès, M. Lambert, H. Launois, and H. R. Zeller. Evidence for a Peierls Distortion or a Kohn Anomaly in One-Dimensional Conductors of the Type K2Pt(CN)4Br0.30.xH2O. *Physical Review B*, 8(2):571–575, 1973.

[28] R. Comès and G. Shirane. Neutron-scattering analysis of the linear-displacement correlations in KTaO3. *Physical Review B*, 5(5):1886–1891, 1972.

[29] R. A. Cowley. Lattice Dynamics and Phase Transitions of Strontium Titanate. *Physical Review*, 134(4):A981–A997, 1964.

[30] R. Currat, R. Comés, B. Dorneri, and E. Wiesendanger. Inelastic neutron scattering in orthorhombic KNbO3. *Ferroelectrics*, 8(1):581, 1973.

[31] D. C. Wallace. *Thermodynamics of Crystals*. Wiley, New York, 1972.

[32] M. Dawber, K. M. Rabe, and J. F. Scott. Physics of thin-film ferroelectric oxides. *Reviews of Modern Physics*, 77(4):1083–1130, 2005.

[33] Nico De Koker. Thermal Conductivity of MgO Periclase from Equilibrium First Principles Molecular Dynamics. *Physical Review Letters*, 103(12):1–4, 2009.

[34] Haruhiko Dekura, Taku Tsuchiya, and Jun Tsuchiya. Ab initio lattice thermal conductivity of MgSiO3 perovskite as found in earth's lower mantle. *Physical Review Letters*, 110(2):1–5, 2013.

[35] Raffaele Guido Della Valle and Piero Procacci. Equation of motion for the Greens function in anharmonic solids. *Physical Review B*, 46(10):6141–6149, 1992.

[36] M. Didomenico, S. H. Wemple, S. P.S. Porto, and R. P. Bauman. Raman spectrum of single-domain BaTiO3. *Physical Review*, 174(2):522–530, 1968.

[37] Liang Donga, Donald S. Stone, and Roderic S. Lakes. Softening of bulk modulus and negative Poisson ratio in barium titanate ceramic near the Curie point. *Philosophical Magazine Letters*, 90(1):23–33, 2010.

[38] Martin T. Dove. *Introduction to lattice Dynamics*. Cambridge University Press.

[39] Martin T. Dove. Theory of displacive phase transitions in minerals. *American Mineralogist*, 82(3-4):213–244, 1997.

[40] Russel Drago. *Physical Methods for Chemists*. 1992.

[41] A. Erba, M. Shahrokhi, R. Moradian, and R. Dovesi. On how differently the quasi-harmonic approximation works for two isostructural crystals: Thermal properties of periclase and lime. *Journal of Chemical Physics*, 142(4), 2015.

[42] Ion Errea. Approaching the strongly anharmonic limit with ab initio calculations of materials' vibrational properties – a colloquium*. *European Physical Journal B*, 89(11), 2016.

[43] Joseph John Fallon. *Multiscale theory and simulation of barium titanate*. PhD thesis, 2014.

[44] P. A. Fleury and P. D. Lazay. Acoustic-soft-optic mode interactions in ferroelectric BaTiO3. *Physical Review Letters*, 26(21):1331–1334, 1971.

[45] M. P. Fontana and M. Lambert. Linear disorder and temperature dependence of Raman scattering in BaTiO3. *Solid State Communications*, 10(1):1–4, 1972.

[46] Daan Frenkel and Berend Smit. *Understanding Molecular Simulations, from Algorithms to Applications*. Academic Press, second edition.

[47] P. Ganesh, E. Cockayne, M. Ahart, R. E. Cohen, B. Burton, Russell J. Hemley, Yang Ren, Wenge Yang, and Z. G. Ye. Origin of diffuse scattering in relaxor ferroelectrics. *Physical Review B - Condensed Matter and Materials Physics*, 81(14):1–7, 2010.

[48] Ph Ghosez, X. Gonze, and J. P. Michenaud. Ab initio phonon dispersion curves and interatomic force constants of barium titanate. *Ferroelectrics*, 206-207(1 -4; 1-2):205–217, 1998.

[49] Philippe Ghosez, E. Cockayne, U V Waghmare, and K. M. Rabe. Lattice dynamics of BaTiO3, PbTiO3, and PbZrO3: A comparative first-principles study. *Physical Review B*, 60(2):836–843, 1999.

[50] Lorenzo Gigli, Max Veit, Michele Kotiuga, Giovanni Pizzi, Nicola Marzari, and Michele Ceriotti. Thermodynamics and dielectric response of BaTiO3 by data-driven modeling. *npj Computational Materials*, 8(209), 2022.

[51] Yakov Girshberg and Yizhak Yacoby. Ferroelectric Phase Transition in Perovskites with Off-center Ion Displacements. *Solid State Communications*, 103(7):425–430, 1997.

[52] Paola Giura, Lorenzo Paulatto, Fei He, Ricardo P.S.M. Lobo, Alexei Bosak, Eugenio Calandrini, Luigi Paolasini, and Daniele Antonangeli. Multiphonon anharmonicity of MgO. *Physical Review B*, 99(22):220304, 2019.

[53] Fangyuan Gu. *Controlling structural change in BaTiO3 by ultrafast laser excitation*. PhD thesis, 2021.

[54] Fangyuan Gu, Eámonn Murray, and Paul Tangney. Carrier-mediated control over the soft mode and ferroelectricity in BaTiO3. *Physical Review Materials*, 5(3):1–17, 2021.

[55] X. J. Han, L. Bergqvist, P. H. Dederichs, H. Müller-Krumbhaar, J. K. Christie, S. Scandolo, and P. Tangney. Polarizable interatomic force field for TiO2 parametrized using density functional theory. *Physical Review B - Condensed Matter and Materials Physics*, 81(13):1–9, 2010.

[56] J. Harada, J. D. Axe, and G. Shirane. Neutron-scattering study of soft modes in cubic BaTiO3. *Physical Review B*, 4(1):155–162, 1971.

[57] Jimpei Harada and Goro Honjo. X-Ray Studies of the Lattice Vibration in Tetragonal Barium Titanate. *Journal of the Physical Society of Japan*, 22(1):45–57, 1966.

[58] Jimpei Harada, Masaharu Watanabe, Shiro Kodera, and Goro Honjo. Diffuse Streak Diffraction Pattern of Electron and X-Rays due to Low Frequency Optical Mode in tetragonal BaTiO$_3$. *Journal of the Physical Society of Japan*, 20:630–631, 1965.

[59] A. Herlihy, T. A. Bird, C. J. Ridley, C. L. Bull, N. P. Funnell, and M. S. Senn. Recovery of harmonic-like behavior of the polar mode in BaTiO3 at high pressures. *Physical Review B*, 105(9):1–7, 2022.

[60] A. W. Hewat. Structure of rhombohedral ferroelectric barium titanate. *Ferroelectrics*, 6(1):215–218, 1973.

[61] H. Hiraka, S. H. Lee, P. M. Gehring, Guangyong Xu, and G. Shirane. Cold neutron study on the diffuse scattering and phonon excitations in the relaxor Pb(Mg1/3Nb2/3)O3. *Physical Review B - Condensed Matter and Materials Physics*, 70(18):1–7, 2004.

[62] J Hlinka, T Ostapchuk, D Nuzhnyy, J Petzelt, P Kuzel, C Kadlec, P Vanek, I Ponomareva, and L Bellaiche. Coexistence of the Phonon and Relaxation Soft Modes in the Terahertz Dielectric Response of Tetragonal BaTiO3. *Phys. Rev. Lett.*, 101(16):167402, 2008.

[63] J. Hlinka, J. Petzelt, S. Kamba, D. Noujni, and T. Ostapchuk. Infrared dielectric response of relaxor ferroelectrics. *Phase Transitions*, 79(1-2):41–78, 2006.

[64] M. Holma, N. Takesue, and Haydn Chen. Linear chain structure in cubic knb03 and bati03. *Ferroelectrics*, 164(1):237–251, 1995.

[65] William G. Hoover. Canonical dynamics: Equilibrium phase-space distributions. *Physical Review A*, 31(3):1695–1697, 1985.

[66] Alfred Hüller. Displacement correlation and anomalous x-ray scattering in BaTiO3. *Solid State Communications*, 7(8):589–591, 1969.

[67] Donald G. Isaak, Orson L. Anderson, and Takayasu Goto. Measured elastic moduli of single-crystal MgO up to 1800 K. *Physics and Chemistry of Minerals*, 16(7):704–713, 1989.

[68] S. Ishidate, T.Sasaki. Elastic Anomaly and Phase Transition in BaTiO3. *Phys. Rev. Lett.*, 62(1), 1989.

[69] Yachin Ivry, Nan Wang, and Colm Durkan. High-frequency programmable acoustic wave device realized through ferroelectric domain engineering. *Applied Physics Letters*, 104(13), 2014.

[70] Y. Jiang, E. Parsonnet, A. Qualls, W. Zhao, S. Susarla, D. Pesquera, A. Dasgupta, M. Acharya, H. Zhang, T. Gosavi, C. C. Lin, D. E. Nikonov, H. Li, I. A. Young, R. Ramesh, and L. W. Martin. Enabling ultra-low-voltage switching in BaTiO3. *Nature Materials*, 21:779–785, 2022.

[71] B. Karki, R. Wentzcovitch, S. de Gironcoli, and S. Baroni. High-pressure lattice dynamics and thermoelasticity of MgO. *Physical Review B - Condensed Matter and Materials Physics*, 61(13):8793–8800, 2000.

[72] D. Khatib, R. Migoni, G. E. Kugel, and L. Godefroy. Lattice dynamics of BaTiO3 in the cubic phase. *Journal of Physics: Condensed Matter*, 1(49):9811–9822, 1989.

[73] Charles Kittel. *Introduction to solid state physics - 8th edition.* John Wiley & sons ltd., 2005.

[74] Jae Hyeon Ko, Tae Hyun Kim, K. Roleder, D. Rytz, and Seiji Kojima. Precursor dynamics in the ferroelectric phase transition of barium titanate single crystals studied by Brillouin light scattering. *Physical Review B - Condensed Matter and Materials Physics*, 84(9):1–9, 2011.

[75] Ryogo Kubo. A stochastic theory of line-shape and relaxation. In D. Ter Haar, editor, *Fluctuation, relaxation, and resonance in magnetic systems*, pages 23–68. Oliver and Boyd, Edinburgh, 1962.

[76] Neutron Sciences at Oak Ridge National Laboratory. Youtube video: Friday at ORNL - Ray Osborn Diffuse Scattering, min 24:34 https://www.youtube.com/watch?v=7gUqiJsbHtc, 2017.

[77] Daniel J. Lacks and Ramesh C. Shukla. Molecular dynamics and higher-order perturbation-theory results for the anharmonic free energy and equation of state of a Lennard-Jones solid. *Physical Review B - Condensed Matter and Materials Physics*, 54(5):3266–3272, 1996.

[78] Michele Lazzeri, Matteo Calandra, and Francesco Mauri. Anharmonic phonon frequency shift in MgB2. *Physical Review B - Condensed Matter and Materials Physics*, 68(22):2–5, 2003.

[79] J. W. Lee, K. Eom, T. R. Paudel, B. Wang, H. Lu, H. X. Huyan, S. Lindemann, S. Ryu, H. Lee, T. H. Kim, Y. Yuan, J. A. Zorn, S. Lei, W. P. Gao, T. Tybell, V. Gopalan,

X. Q. Pan, A. Gruverman, L. Q. Chen, E. Y. Tsymbal, and C. B. Eom. In-plane quasi-single-domain BaTiO3 via interfacial symmetry engineering. *Nature Communications*, 12(6784), 2021.

[80] Z. Li, M. Grimsditch, C. M. Foster, and S. K. Chan. Dielectric and elastic properties of ferroelectric materials at elevated temperature. *Journal of Physics and Chemistry of Solids*, 57(10):1433–1438, 1996.

[81] Gerald Löffler, Hellfried Schreiber, and Othmar Steinhauser. The frequency-dependent conductivity of a saturated solution of ZnBr2 in water: A molecular dynamics simulation. *Journal of Chemical Physics*, 107(8):3135–3143, 1997.

[82] Y. Luspin, J. L. Servoin, and F. Gervais. Soft mode spectroscopy in barium titanate. *Journal of Physics C: Solid State Physics*, 13(19):3761–3773, 1980.

[83] M. Born and K. Huang. *Dynamical Theory of Crystal Lattices*. Oxford University Press, 1954.

[84] A.J.H. Mante and J. Volger. The Thermal Conductivity of BaTiO3 in the Neighbourhood of its Ferroelectric Transition Temperatures. *Physics Letters*, 24(3):144–145, 1967.

[85] Glenn J. Martyna, Michael L. Klein, and Mark Tuckerman. Nosé-Hoover chains: The canonical ensemble via continuous dynamics. *The Journal of Chemical Physics*, 97(4):2635–2643, 1992.

[86] Glenn J. Martyna, Douglas J. Tobias, and Michael L. Klein. Constant pressure molecular dynamics algorithms. *The Journal of Chemical Physics*, 101(5):4177–4189, 1994.

[87] MASAYOSHI TONOUCHI. Cutting-edge terahertz technology. *Nature photonics*, 1:97–105, 2007.

[88] Richard D. Mattuck. *A Guide to Feynmann Diagrams in the Many-Body Problem*. Dover Publications, second edi edition, 1992.

[89] Donald A. McQuarrie. *Statistichal Mechanics*. Harper and Row, New York.

[90] A. B. Mei, O. Hellman, C. M. Schlepütz, A. Rockett, T. C. Chiang, L. Hultman, I. Petrov, and J. E. Greene. Reflection thermal diffuse x-ray scattering for quantitative determination of phonon dispersion relations. *Physical Review B - Condensed Matter and Materials Physics*, 92(17):1–7, 2015.

[91] Artem R Oganov and Peter I Dorogokupets. Intrinsic anharmonicity in equations of state and thermodynamics of solids. 2004.

[92] T. Ostapchuk, J. Petzelt, P. Kuzel, S. Veljko, A. Tkach, P. Vilarinho, I. Ponomareva, L. Bellaiche, E. Smirnova, V. Lemanov, A. Sotnikov, and M. Weihnacht. Infrared and THz soft-mode spectroscopy of (Ba,Sr)TiO3 ceramics. *Ferroelectrics*, 367(1 PART 1):139–148, 2008.

[93] M. Parrinello and A. Rahman. Polymorphic transitions in single crystals: A new molecular dynamics method. *Journal of Applied Physics*, 52(12):7182–7190, 1981.

[94] M. Paściak, T. R. Welberry, J. Kulda, S. Leoni, and J. Hlinka. Dynamic Displacement Disorder of Cubic BaTiO3. *Physical Review Letters*, 120(16):1–6, 2018.

[95] Lorenzo Paulatto, Francesco Mauri, and Michele Lazzeri. Anharmonic properties from a generalized third-order ab initio approach: Theory and applications to graphite and graphene. *Physical Review B - Condensed Matter and Materials Physics*, 87(21):1–18, 2013.

[96] Ashish Y. Pawar, Deepak D. Sonawane, Kiran B. Erande, and Deelip V. Derle. Terahertz technology and its applications. *Drug Invention Today*, 5(2):157–163, 2013.

[97] John P. Perdew, Adrienn Ruzsinszky, Gábor I. Csonka, Oleg A. Vydrov, Gustavo E. Scuseria, Lucian A. Constantin, Xiaolan Zhou, and Kieron Burke. Restoring the density-gradient expansion for exchange in solids and surfaces. *Physical Review Letters*, 100(13):1–4, 2008.

[98] C. H. Perry and D. B. Hall. Temperature dependence of the Raman spectrum of BaTiO3. *Physical Review Letters*, 15(17):700–702, 1965.

[99] J. Petzelt, G. V. Kozlov, and A. A. Volkov. Dielectric spectroscopy of paraelectric soft modes. *Ferroelectrics*, 73(1):101–123, 1987.

[100] I Ponomareva, L Bellaiche, T Ostapchuk, J Hlinka, and J Petzelt. Terahertz dielectric response of cubic BaTiO3. *Phys. Rev. B*, 77(1):12102, 2008.

[101] A. M. Quittet and M. Lambert. Temperature dependence of the Raman cross section and light absorption in cubic BaTiO3. *Solid State Communications*, 12(10):1053–1055, 1973.

[102] B. Ravel, E. A. Stern, R. I. Vedrinskii, and V. Kraizman. Local structure and the phase transitions of BaTiO3. *Ferroelectrics*, 206-207(1 -4; 1-2):407–430, 1998.

[103] Sylvain Ravy, Jean Paul Itia, Alain Polian, and Michael Hanfland. High-pressure study of X-ray diffuse scattering in ferroelectric perovskites. *Physical Review Letters*, 99(11):1–4, 2007.

[104] J. A. Reissland. *The Physics of Phonons*. John Wiley & sons ltd., 1973.

[105] Ekhard K.H. Salje. Ferroelastic materials. *Annual Review of Materials Research*, 42:265–283, 2012.

[106] M. J. L. Sangster, G. Peckham, and D. H. Saunderson. Lattice dynamics of magnesium oxide. *Journal of Physics C: Solid State Physics*, 3(1026), 1970.

[107] J. A. Sanjurjo, R. S. Katiyar, and S. P.S. Porto. Temperature dependence of dipolar modes in ferroelectric BaTiO3 by infrared studies. *Physical Review B*, 22(5):2396–2403, 1980.

[108] S. Sanna, C. Thierfelder, S. Wippermann, T. P. Sinha, and W. G. Schmidt. Barium titanate ground- and excited-state properties from first-principles calculations. *Physical Review B - Condensed Matter and Materials Physics*, 83(5):1–9, 2011.

[109] Joanne Sarsam, Michael W. Finnis, and Paul Tangney. Atomistic force field for alumina fit to density functional theory. *Journal of Chemical Physics*, 139(20), 2013.

[110] A. Scalabrin, A. S. Chaves, D. S. Shim, and S. P.S. Porto. Temperature dependence of the A1 and E optical phonons in BaTiO3. *Physica Status Solidi (B)*, 79(2):731–742, 1977.

[111] J. F. Scott. Applications of modern ferroelectrics. *Science*, 315(5814):954–959, 2007.

[112] M. S. Senn, D. A. Keen, T. C.A. Lucas, J. A. Hriljac, and A. L. Goodwin. Emergence of Long-Range Order in BaTiO3 from Local Symmetry-Breaking Distortions. *Physical Review Letters*, 116(20):1–5, 2016.

[113] S. M. Shapiro, J. D. Axe, G. Shirane, and T. Riste. Critical neutron scattering in SrTiO3 and KMnF3. *Physical Review B*, 6(11):4332–4341, 1972.

[114] L. A. Shebanov. X-ray temperature study of crystallographic characteristics of Barium Titanate. *Physica Status Solidi (a)*, 65(1):321–325, 1981.

[115] Y. Shen, C. N. Saunders, C. M. Bernal, D. L. Abernathy, T. J. Williams, M. E. Manley, and B. Fultz. Prediction and observation of intermodulation sidebands from anharmonic phonons in NaBr. *Physical Review B*, 103(13):1–7, 2021.

[116] Hyung Joon Shin, Jaehoon Jung, Kenta Motobayashi, Susumu Yanagisawa, Yoshitada Morikawa, Yousoo Kim, and Maki Kawai. State-selective dissociation of a single water molecule on an ultrathin MgO film. *Nature Materials*, 9:442–447, 2010.

[117] Young Han Shin, Valentino R. Cooper, Ilya Grinberg, and Andrew M. Rappe. Development of a bond-valence molecular-dynamics model for complex oxides. *Physical Review B - Condensed Matter and Materials Physics*, 71(5):1–4, 2005.

[118] G. Shirane, J. D. Axe, J. Harada, and A. Linz. Inelastic neutron scattering from single-domain BaTiO3. *Physical Review B*, 2(9):3651–3657, 1970.

[119] G. Shirane, B. C. Frazer, V. J. Minkiewicz, J. A. Leake, and A. Linz. Soft optic modes in barium titanate. *Physical Review Letters*, 19(5):234–235, 1967.

[120] G. Shirane and Y. Yamada. Lattice-Dynamical Study of the 110 K Phase Transition in SrTiO3. *Physical Review*, 177(2):858–863, 1969.

[121] Gen Shirane and Akitsu Takeda. *Transition Energy and Volume Change at Three Transitions in Barium Titanate.*

[122] N. Sicron, B. Ravel, Y. Yacoby, E. A. Stern, F. Dogan, and J. J. Rehr. Nature of the ferroelectric phase transition in PbTiO3. *Physical Review B*, 50(18):13168–13180, 1994.

[123] Tomas Sluka, Alexander K. Tagantsev, Petr Bednyakov, and Nava Setter. Free-electron gas at charged domain walls in insulating BaTiO3. *Nature Communications*, 4(1808), 2013.

[124] G. L. Squires. *Introduction to the theory of thermal neutron scattering.* Dover Publications, 1996.

[125] Edward A. Stern. Character of order-disorder and displacive components in barium titanate. *Physical Review Letters*, 93(3):1–3, 2004.

[126] Edward A. Stern and Yizhak Yacoby. Structural disorder in perovskite ferroelectric crystals as revealed by XAFS. *Journal of Physics and Chemistry of Solids*, 57(10):1449–1455, 1996.

[127] Jie Sun, An Quan Jiang, and Pankaj Sharma. Ferroelectric Domain Wall Memory and Logic. *ACS Applied Electronic Materials*, 2023.

[128] Tao Sun, Xiao Shen, and Philip B. Allen. Phonon quasiparticles and anharmonic perturbation theory tested by molecular dynamics on a model system. *Physical Review B - Condensed Matter and Materials Physics*, 82(22):1–10, 2010.

[129] Tao Sun, Dong Bo Zhang, and Renata M. Wentzcovitch. Dynamic stabilization of cubic CaSi O3 perovskite at high temperatures and pressures from ab initio molecular dynamics. *Physical Review B - Condensed Matter and Materials Physics*, 89(9):1–9, 2014.

[130] P Tangney and S Scandolo. An ab initio parametrized interatomic force field for silica. *The Journal of Chemical Physics*, 117(19):8898–8904, 2002.

[131] P. Tangney and S. Scandolo. A many-body interatomic potential for ionic systems: Application to MgO. *Journal of Chemical Physics*, 119(18):9673–9685, 2003.

[132] Paul Tangney. *Theory of lattice dynamics. Manuscript in preparation.* 2022.

[133] Paul Tangney, Marvin L Cohen, and Steven G Louie. Giant wave-drag enhancement of friction in sliding carbon nanotubes. *Physical Review Letters*, 97(19):1–4, 2006.

[134] Paul Tangney and Sandro Scandolo. Melting slope of MgO from molecular dynamics and density functional theory. *Journal of Chemical Physics*, 131(12), 2009.

[135] S. Tinte, M. G. Stachiotti, S. R. Phillpot, M. Sepliarsky, D. Wolf, and R. L. Migoni. Ferroelectric properties of BaxSr1-xTiO3 solid solutions obtained by molecular dynamics simulation. *Journal of Physics Condensed Matter*, 16(20):3495–3506, 2004.

[136] Silvia Tinte, Jorge Íñiguez, Karin M. Rabe, and David Vanderbilt. Quantitative analysis of the first-principles effective Hamiltonian approach to ferroelectric perovskites. *Physical Review B - Condensed Matter and Materials Physics*, 67(6), 2003.

[137] Atsushi Togo, Laurent Chaput, and Isao Tanaka. Distributions of phonon lifetimes in Brillouin zones. *Physical Review B - Condensed Matter and Materials Physics*, 91(9), 2015.

[138] Mark E. Tuckerman. *Statistical Mehcanics: Theory and Molecular Simulation.* Oxford University Press, 2010.

[139] S. Valencia, A. Crassous, L. Bocher, V. Garcia, X. Moya, R. O. Cherifi, C. Deranlot, K. Bouzehouane, S. Fusil, A. Zobelli, A. Gloter, N. D. Mathur, A. Gaupp, R. Abrudan, F. Radu, A. Barthélémy, and M. Bibes. Interface-induced room-temperature multiferroicity in BaTiO3. *Nature Materials*, 10:753–758, 2011.

[140] H. Vogt, J. A. Sanjurjo, and G. Rossbroich. Soft-mode spectroscopy in cubic BaTiO3 by hyper-Raman scattering. *Phys. Rev. B*, 26(10):5904–5910, 1982.

[141] V. K. Wadhawan. Ferroelasticity. *Bulletin of Materials Science*, 6(4):733–753, 1984.

[142] Laura Walizer, Sergey Lisenkov, and L. Bellaiche. Finite-temperature properties of (Ba,Sr) Ti O3 systems from atomistic simulations. *Physical Review B - Condensed Matter and Materials Physics*, 73(14):1–6, 2006.

[143] Y. Wang, J. J. Wang, W. Y. Wang, Z. G. Mei, S. L. Shang, L. Q. Chen, and Z. K. Liu. A mixed-space approach to first-principles calculations of phonon frequencies for polar materials. *Journal of Physics Condensed Matter*, 22(20), 2010.

[144] M. Wilson and P. A. Madden. Polarization effects in ionic systems from first principles. *Journal of Physics: Condensed Matter*, 5(17):2687–2706, 1993.

[145] A. D.B. Woods, B. N. Brockhouse, R. A. Cowley, and W. Cochran. Lattice dynamics of alkali halide crystals. II. Experimental studies of KBr and NaI. *Physical Review*, 131(3):1025–1029, 1963.

[146] A. D.B. Woods, W. Cochran, and B. N. Brockhouse. Lattice dynamics of alkali halide crystals. *Physical Review*, 119(3):980–999, 1960.

[147] Y. Yamada and G. Shirane. Neutron Scattering and Nature of the Soft Optical Phonon in SrTiO3. *J. Phys. Soc. Jpn.*, 26(2):396–403, 1968.

[148] Y. Yamada, G. Shirane, and A. Linz. Study of Critical Fluctuations in BaTiO3 by Neutron Scattering. *Physical Reviews*, 177(2):848–857, 1969.

[149] Shinji Yuasa, Taro Nagahama, Akio Fukushima, Yoshishige Suzuki, and Koji Ando. Giant room-temperature magnetoresistance in single-crystal Fe/MgO/Fe magnetic tunnel junctions. *Nature Materials*, 3:868–871, 2004.

[150] Boštjan Zalar, Valentin V Laguta, and Robert Blinc. NMR Evidence for the Coexistence of Order-Disorder and Displacive Components in Barium Titanate. *Physical Review Letters*, 90(3):4, 2003.

[151] Dong Bo Zhang, Tao Sun, and Renata M Wentzcovitch. Phonon quasiparticles and anharmonic free energy in complex systems. *Physical Review Letters*, 112(5):1–5, 2014.

[152] W. Zhong, David Vanderbilt, and Karin M. Rabe. Phase Transitions in BaTi03 from First Principles. *Phys. Rev. Lett.*, 73(13), 1994.